CERN-PH-LPCC-2015-001
SLAC-PUB-16364
DESY 15-167

September 3 2015

arXiv:1611.05079v1 [hep-ph] 15 Nov 2016

LHC Forward Physics

Editors: N. Cartiglia, C. Royon
The LHC Forward Physics Working Group

K. Akiba[21], M. Akbiyik[1], M. Albrow[2], M. Arneodo[3,4], V. Avati[5,6], J. Baechler[6], O. Villalobos Baillie[87], P. Bartalini[7], J. Bartels[8], S. Baur[1], C. Baus[1], W. Beaumont[9], U. Behrens[10], D. Berge[11], M. Berretti[6,12], E. Bossini[12], R. Boussarie[13], S. Brodsky[14], M. Broz[15], M. Bruschi[16], P. Bussey[17], W. Byczynski[81], J. C. Cabanillas Noris[18], E. Calvo Villar[19], A. Campbell[10], F. Caporale[22], W. Carvalho[21], G. Chachamis[22], E. Chapon[23], C. Cheshkov[24], J. Chwastowski[25], R. Ciesielski[26], D. Chinellato[83], A. Cisek[25], V. Coco[6], P. Collins[6], J. G. Contreras[15], B. Cox[27], D. de Jesus Damiao[21], P. Davis[28], M. Deile[6], D. D'Enterria[6], D. Druzhkin[29,6], B. Ducloué[30,31], R. Dumps[6], R. Dzhelyadin[82] P. Dziurdzia[6], M. Eliachevitch[1], P. Fassnacht [6] F. Ferro[32], S. Fichet[33], D. Figueiredo[21], B. Field[34], D. Finogeev[35], R. Fiore[29,36], J. Forshaw[27], A. Gago Medina[19], M. Gallinaro[37], A. Granik[82], G. von Gersdorff[33], S. Giani[6], K. Golec-Biernat[25,38], V. P. Goncalves[39], P. Göttlicher[10], K. Goulianos[26], J.-Y. Grosslord[24], L. A. Harland-Lang[40], H. Van Haevermaet[9], M. Hentschinski[41], R. Engel [1], G. Herrera Corral[42], J. Hollar[37], L. Huertas[21], D. Johnson[6], I. Katkov[1], O. Kepka[43], M. Khakzad[44], L. Kheyn[45], V. Khachatryan[46], V. A. Khoze[47], S. Klein[48], M. van Klundert[9], F. Krauss[47], A. Kurepin[35], N. Kurepin[35], K. Kutak[49], E. Kuznetsova[1], G. Latino[12], P. Lebiedowicz[25], B. Lenzi[6], E. Lewandowska[25], S. Liu[28], A. Luszczak[25,38], M. Luszczak[25], J. D. Madrigal[50], M. Mangano[6], Z. Marcone[34], C. Marquet[51], A. D. Martin[47], T. Martin[52], M. I. Martinez Hernandez[53], C. Martins[21], C. Mayer[25], R. Mc Nulty[54], P. Van Mechelen[7], R. Macula[25], E. Melo da Costa[21], T. Mertzimekis[55], C. Mesropian[26], M. Mieskolainen[31], N. Minafra[6,56], I. L. Monzon[18], L. Mundim [21], B. Murdaca[20,36], M. Murray[57], H. Niewiadowski[58], J. Nystrand[59], E. G. de Oliveira[60], R. Orava[31], S. Ostapchenko[61], K. Osterberg[31], A. Panagiotou[55], A. Papa[20], R. Pasechnik[62], T. Peitzmann[63], L. A. Perez Moreno[53], T. Pierog[1], J. Pinfold[28], M. Poghosyan[64], M. E. Pol[65], W. Prado[21], V. Popov[66], M. Rangel[67], A. Reshetin[35], J.-P. Revol[68], M. Rijssenbeek[34], M. Rodriguez [5]3, B. Roland[10], C. Royon[25.43,57], M. Ruspa[3,4], M. Ryskin[47,69], A. Sabio Vera[22], G. Safronov[66], T. Sako[70], H. Schindler[6], D. Salek[11], K. Safarik [6], M. Saimpert[71], A. Santoro[21], R. Schicker[73], J. Seger[64], S. Sen[73], A. Shabanov[35], W. Schafer[25], G. Gil Da Silveira[39], P. Skands[74], R. Soluk[28], A. van Spilbeeck[9], R. Staszewski[25], S. Stevenson[75], W.J. Stirling[86], M. Strikman[76], A. Szczurek[25,38] L. Szymanowski[77], J.D. Tapia Takaki,[57] M. Tasevsky[43], K. Taesoo[78], C. Thomas[75], S. R. Torres[18], A. Tricomi[79], M. Trzebinski[25], D. Tsybychev[34], N. Turini[12], R. Ulrich[1], E. Usenko[35], J. Varela[37], M. Lo Vetere[80], A. Villatoro Tello[53], A. Vilela Pereira[21], D. Volyanskyy [84], S. Wallon[13,85], G. Wilkinson[75], H. Wöhrmann[1]. K. C. Zapp[6], Y. Zoccarato[24].

[1] *Karlsruhe Institute of Technology (KIT), Karlsruhe, Germany*
[2] *Fermilab, Batavia, USA*
[3] *INFN Torino, Italy*
[4] *Universitá del Piemonte Orientale, Novara, Italy*
[5] *AGH University of Science and Technology, Krakow, Poland*
[6] *CERN, Geneva, Switzerland*
[7] *Central China Normal University (CCNU), Wuhan, Hubei, China*
[8] *University of Hamburg, Germany*
[9] *University of Antwerpen, Belgium*
[10] *DESY, Hamburg, Germany*
[11] *NIKHEF and GRAPPA, Amsterdam, Netherlands*
[12] *INFN Pisa, Pisa, Italy and Universita degli Studi di Siena, Siena, Italy*
[13] *LPT, Université Paris-Sud, CNRS, 91405, Orsay, France*
[14] *SLAC National Accelerator Laboratory, Stanford University, Stanford, CA, USA*
[15] *Faculty of Nuclear Sciences and Physical Engineering, Czech Technical University in Prague, Prague, Czech Republic*

[16] *Universita and INFN, Bologna, Italy*
[17] *University of Glasgow, UK*
[18] *Universidad Autonoma de Sialoa, Culiacan, Mexico*
[19] *Pontifica Universidad Catolica del Peru (PUCP), Lima, Peru*
[20] *Universita della Calabria, Cosenza, Italy*
[21] *Universidade do Estado do Rio de Janeiro (UERJ), Rio de Janeiro, Brazil*
[22] *Instituto de Fisica Teorica UAM/CSIC and Universidad Autonoma de Madrid, Cantoblanco, Madrid, Spain*
[23] *LLR, Ecole Polytechnique, Paliseau, France*
[24] *IPN, Institut de Physique Nucléaire, Université Claude Bernard Lyon-I, CNRS/IN2P3, Lyon, France*
[25] *Institute of Nuclear Physics Polish Academy of Sciences, Krakow, Poland*
[26] *The Rockefeller University, New York, USA*
[27] *School of Physics and Astronomy, University of Manchester, UK*
[28] *University of Alberta, Canada*
[29] *Research and Development Institute of Power Engineering (NIKIET), Moscow, Russia*
[30] *Department of Physics, University of Jyvaskyla, Jyvaskyla, Finland*
[31] *Department of Physics, University of Helsinki, Helsinki, Finland*
[32] *INFN Genova, Italy*
[33] *ICTP South American Institute for Fundamental Research, Instituto de Fisica Teorica, Sao Paulo State University, Brazil*
[34] *Stony Brook University, Stony Brook, New York, USA*
[35] *Russian Academy of Sciences, Institute for Nuclear Research (INR), Moscow*
[36] *Gruppo Collegato INFN of Cosenza, Italy*
[37] *LIP, Lisbon, Portugal*
[38] *University of Rzeszow, Rzeszow, Poland*
[39] *High and Medium Energy Group, Instituto de Fisica e Matematica, Universidade Federal de Pelotas, Pelotas, Brazil*
[40] *Department of Physics and Astronomy, University College London, UK*
[41] *Instituto de Ciencias Nucleares, Universidad Nacional Autonoma de Mexico, Mexico*
[42] *Centro de Investigacion y de Estudios Avanzados del IPN CINVESTAV , Dep. de Fisica and Dep. de Fisica Applicada, Mexico*
[43] *Institute of Physics, Academy of Sciences, Prague, Czech Republic*
[44] *IPM, Institute for Research in Fundamental Sciences, Tehran, Iran*
[45] *Moscow State University, Moscow, Russia*
[46] *Alikhanyan National Scientific Laboratory (ANSL), Armenia*
[47] *Institute for Particle Physics Phenomenology, Physics Department, University of Durham, UK*
[48] *Lawrence Berkeley National Laboratory, Berkeley, California, U.S.A.*
[49] *Instytut Fizyki Jadrowej Polskiej Akademii, Krakow, Poland*
[50] *Institut de Physique Théorique, CEA Saclay, Gif-sur-Yvette, France*
[51] *Centre de Physique Théorique, Ecole Polytechnique, CNRS, Palaiseau, France*
[52] *University of Warwick, UK*
[53] *Benemerita Autonomous University of Puebla, Mexico*
[54] *University College Dublin, Dublin, Ireland*
[55] *University of Athens, Greece*
[56] *Dipartimento Inter-ateneo di Fisica di Bari, Italy; INFN Sezione di Bari, Bari, Italy*
[57] *University of Kansas, Lawrence, USA*
[58] *Case Western Reserve University, Department of Physics, Cleveland, USA*
[59] *Department of Physics and Technology, University of Bergen, Bergen, Norway*
[60] *Departamento de Fisica, Universidade Federal de Santa Catarina, Florianopolis, Brazil*
[61] *Frankfurt Institute for Advanced Studies, Frankfurt am Main, Germany*
[62] *Theoretical High Energy Physics, Department of Astronomy and Theoretical Physics, Lund University, Sweden*
[63] *Utrecht University and Nikhef, Utrecht, Netherlands*
[64] *Creighton University, Omaha, USA*
[65] *Centro Brasileiro de Pesquisas Fisicas (CBPF), Rio de Janeiro, Brazil*
[66] *ITEP, Moscow, Russia*
[67] *Universidade Federal do Rio de Janeiro (UFRJ), Rio de Janeiro, Brazil*
[68] *Centro Studi e Ricerche "Enrico Fermi", Roma, Italy*
[69] *Petersburg Nuclear Physics Institute, Gatchina, St. Petersburg, Russia*
[70] *STEL/KMI, Nagoya University, Nagoya, Japan*
[71] *IRFU-SPP, CEA Saclay, Gif-sur-Yvette, France*
[72] *Ruprecht-Karls-Universitaet Heidelberg, Germany*
[73] *Hacettepe University, Ankara, Turkey*
[74] *School of Physics and Astronomy, Monash University, Clayton, Australia*
[75] *Department of Physics, University of Oxford, Oxford, UK*
[76] *Penn State University, University Park, USA*

[77] *National Center for Nuclear Research, Warsaw, Poland*
[78] *Yonsei University, Seoul, Corea*
[79] *University of Catania and INFN Sezione di Catania, Italy*
[80] *Università degli Studi di Genova, Dipartimento di Fisica and INFN, Genova, Italy*
[81] *Cracow University of Technology, Poland*
[82] *B.P. Konstantinov Petersburg Nuclear Physics Institute PNPI, Russia*
[83] *Universidade Estadual de Campinas (UNICAMP), Campinas Brazil*
[84] *Heidelberg, Max Planck Inst., Heidelberg, Germany*
[85] *UPMC Univ. Paris 06, faculté de physique, 4 place Jussieu, 75252 Paris Cedex 05, France*
[86] *Imperial College, London UK*
[87] *University of Birmingham, Birmingham, UK*

Abstract

The goal of this report is to give a comprehensive overview of the rich field of forward physics, with a special attention to the topics that can be studied at the LHC. The report starts presenting a selection of the Monte Carlo simulation tools currently available, chapter 2, then enters the rich phenomenology of QCD at low, chapter 3, and high, chapter 4, momentum transfer, while the unique scattering conditions of central exclusive production are analyzed in chapter 5. The last two experimental topics, Cosmic Ray and Heavy Ion physics are presented in the chapter 6 and 7 respectively. Chapter 8 is dedicated to the BFKL dynamics, multiparton interactions, and saturation. The report ends with an overview of the forward detectors at LHC. Each chapter is correlated with a comprehensive bibliography, attempting to provide to the interested reader with a wide opportunity for further studies.

Contents

Introduction **2**

1 Running conditions and beam induced backgrounds **5**
1.1 Acceptance of Forward Detectors . . . 5
1.2 Background: pp induced background . . . 8
1.3 Different running conditions . . . 10

2 Monte Carlo **13**
2.1 Introduction . . . 13
2.2 EPOS LHC . . . 13
2.2.1 Diffractive contribution . . . 14
2.2.2 Inclusive Cross Sections . . . 15
2.2.3 Diffractive Cross Sections . . . 16
2.3 PHOJET . . . 17
2.3.1 Inclusive and total cross sections . . . 17
2.3.2 Modelling of inelastic final states . . . 18
2.3.3 Plans and future developments . . . 19
2.4 POMWIG . . . 19
2.5 PYTHIA 6 & 8 . . . 20
2.5.1 Inclusive Cross Sections . . . 20
2.5.2 Dynamical modelling . . . 21
2.6 QGSJET-II . . . 23
2.7 SHRiMPS . . . 26
2.7.1 Inclusive properties and the KMR model . . . 26
2.7.2 Exclusive properties . . . 27
2.7.3 The link to hadrons . . . 30
2.7.4 Selected predictions . . . 30
2.7.5 Summary and outlook . . . 31
2.8 `Dime` . . . 32
2.9 `ExHuME` . . . 33
2.10 FPMC . . . 34
2.10.1 Introduction . . . 34
2.10.2 Two–photon interactions . . . 34
2.10.3 Implementation of pomeron and reggeon exchanges in inclusive diffraction . . . 36
2.10.4 Implementation of exclusive production . . . 37
2.11 STARLIGHT . . . 37
2.12 `SuperChic` . . . 39
2.12.1 Version 1 . . . 39
2.12.2 Version 2 . . . 40
2.13 LHC forward measurements and MC tuning . . . 40

3 Soft Diffraction and Total Cross section **48**
3.1 Introduction . . . 48
3.2 Detecting soft diffraction with Forward Detectors . . . 48
3.2.1 Per Interaction Probability of Single and Double Tag . . . 49
3.2.2 Soft Vertex Reconstruction . . . 50
3.2.3 Proton and Vertex reconstruction Conclusion . . . 51
3.3 Physics sources and properties of forward protons from inelastic interactions . . . 52
3.3.1 MC versions and tagged proton selection for inelastic studies . . . 55
3.3.2 Kinematics of tagged proton samples . . . 56
3.4 Soft pseudorapidity gaps . . . 56
3.4.1 Previous measurements . . . 56
3.4.2 Future soft pseudorapidity gaps studies with a proton tag . . . 58
3.4.3 Soft pseudorapidity gap studies with CASTOR . . . 60
3.4.4 Extending pseudorapidity gaps with forward shower counters . . . 62
3.4.5 Soft rapidity gap conclusion . . . 62
3.5 Measurements of the Inelastic Cross-Section . . . 63
3.6 Measurements of the Total, Elastic and Inelastic Cross-Section with the TOTEM detectors . 63
3.6.1 Total cross-section . . . 64
3.6.2 Elastic scattering . . . 66
3.6.3 Inelastic scattering . . . 67
3.6.4 TOTEM Plans at $\sqrt{s} = 13\,\text{TeV}$ . . . 68
3.7 Measurement Total and Elastic cross-section with ALFA . . . 68
3.7.1 ALFA Plans at $\sqrt{s} = 13\,\text{TeV}$ . . . 68
3.8 Conclusions & Running Conditions . . . 69

4 Inclusive Hard Diffraction **72**
4.1 Introduction . . . 72
4.2 Backgrounds . . . 72
4.2.1 Proton Tag . . . 73
4.2.2 One Vertex Requirement . . . 73
4.2.3 Relative Energy Loss Difference . . . 74
4.2.4 Running Conditions . . . 74
4.3 Factorisation Tests . . . 75
4.3.1 Predictions . . . 76
4.4 Single Diffractive Jet Production . . . 78
4.4.1 ATLAS Feasibility Studies for $\sqrt{s} = 13$ TeV . . . 79
4.5 Single Diffractive Z, W and J/Ψ Production . . . 82
4.5.1 CMS-TOTEM Feasibility Studies for $\sqrt{s} = 13$ TeV . . . 83
4.5.2 ATLAS Feasibility Studies for $\sqrt{s} = 13$ TeV . . . 86
4.6 Double Pomeron Exchange Jet Production . . . 88
4.6.1 ATLAS Feasibility Studies for $\sqrt{s} = 13$ TeV . . . 89

4.7 Double Pomeron Exchange Photon+Jet Production . . . 91
4.7.1 ATLAS Feasibility Studies for $\sqrt{s} = 14$ TeV . . . 92
4.8 Double Pomeron Exchange Jet-Gap-Jet Production . . . 93
4.8.1 ATLAS Feasibility Studies for $\sqrt{s} = 14$ TeV . . . 94
4.9 Conclusions . . . 95

Appendices **97**
4.A Expected Statistics of Single Diffractive Jet Measurement . . . 97
4.B Expected Statistics of Double Pomeron Exchange Jet Measurement . . . 97

5 Central Exclusive Production **102**
5.1 Introduction . . . 102
5.2 Analysis techniques and detectors to study exclusive processes at the LHC . . . 104
5.2.1 Analysis techniques . . . 104
5.2.2 Central exclusive production at LHCb and ALICE . . . 104
5.2.3 Central exclusive production at CMS and ATLAS . . . 105
5.3 QCD processes . . . 106
5.3.1 Introduction . . . 106
5.3.2 Forward proton tagging: phenomenological insight and advantages . . . 108
5.3.3 Conventional quarkonium production . . . 110
5.3.4 'Exotic' quarkonium production . . . 113
5.3.5 Photon pair production . . . 114
5.3.6 Light meson pair production . . . 115
5.3.7 Production of low mass resonances and glueballs . . . 118
5.3.8 Quarkonium Pair Production . . . 122
5.3.9 Jet production . . . 125
5.3.10 Jet production: ATLAS feasibility study . . . 127
5.3.11 Jet production: CT–PPS feasibility study . . . 130
5.4 Photon–induced and photoproduction processes . . . 133
5.4.1 Introduction . . . 133
5.4.2 Forward proton tagging: phenomenological insight and advantages . . . 134
5.4.3 Two-photon collisions . . . 135
5.4.4 Diffractive photoproduction $\gamma p \to V p$ . . . 137
5.5 Exploratory physics . . . 147
5.5.1 Search for invisible objects via the missing mass and momentum methods . . . 147
5.5.2 Searching for magnetic monopoles with forward proton detectors . . . 149
5.5.3 Standard Model exclusive production of $\gamma\gamma$, WW and ZZ via photon induced processes . . . 152
5.5.4 Anomalous gauge couplings: $\gamma\gamma\gamma\gamma$ . . . 154
5.5.5 Anomalous gauge couplings: $\gamma\gamma WW$ and $\gamma\gamma ZZ$ . . . 157
5.5.6 Anomalous $\gamma\gamma WW$ couplings: detailed studies . . . 159
5.5.7 New strong dynamics in exclusive processes . . . 165
5.6 Conclusion . . . 167

6 Cosmic Ray Physics, Particle multiplicities, correlations and spectra **176**
6.1 Introduction . . . 176
6.2 LHC and air showers . . . 178
6.2.1 LHC data and hadronic interaction models . . . 179
6.2.2 Hadronic interaction models and air showers . . . 180
6.2.3 Need for measuring proton-oxygen interactions . . . 181
6.3 Energy Flow . . . 183
6.3.1 Past Measurements of Energy Flow . . . 183
6.3.2 Future Measurements of Energy Flow . . . 184
6.4 Particle multiplicities . . . 187
6.4.1 Past measurements of charged particle multiplicities . . . 188
6.4.2 Future measurements of charged particle multiplicities . . . 189
6.5 Spectra . . . 191
6.5.1 Measurement of identified charged particle spectra in pp and p-Pb collisions with ALICE 191
6.5.2 Neutral particle spectra . . . 197
6.5.3 Heavy flavor particle spectra . . . 200
6.6 Beam . . . 202
6.6.1 Proton-proton collisions . . . 202
6.6.2 Light ion collisions . . . 203

7 Heavy Ion Physics **209**
7.1 Introduction . . . 209
7.2 Exclusive photonuclear processes . . . 209
7.3 Models for photonuclear production . . . 212
7.3.1 Models based on the vector dominance model . . . 213
7.3.2 Models based on LO pQCD . . . 214
7.3.3 Models based on the colour dipole approach . . . 215
7.4 Experimental results on exclusive photonuclear processes . . . 216
7.4.1 Exclusive J/ψ photoproduction off protons in ultra-peripheral p–Pb collisions . . . 216
7.4.2 Coherent and incoherent J/ψ photoproduction from ultra-peripheral Pb–Pb collisions . . . 216
7.4.3 Coherent ψ(2S) photoproduction from ultra-peripheral Pb–Pb collisions . . . 218
7.4.4 Coherent ρ^0 photoproduction from ultra-peripheral Pb–Pb collisions . . . 218
7.4.5 Four-pion production in ultra-peripheral Pb–Pb collisions . . . 220
7.5 Two-photon physics . . . 220
7.6 UPC lessons from LHC Run 1 . . . 220
7.7 Experimental prospects . . . 222
7.8 Experimental Summary . . . 223
7.9 Theoretical proposals . . . 223
7.9.1 Tracking fast small color dipoles through strong gluon fields at the LHC . . . 223
7.9.2 Studies of the color fluctuation phenomena . . . 224
7.9.3 Multiparton interactions in the direct photon kinematics . . . 225

7.10 Propagation of partons through nucleons and nuclei at ultrahigh energies . . . 225
7.10.1 Introduction . . . 225

8 BFKL and saturation **232**
8.1 Introduction . . . 232
8.2 Forward backward jet production in $p\bar{p}$ and pp: the BFKL program . . . 234
8.2.1 Theoretical remarks . . . 234
8.2.2 Signals based upon inclusive all-order summation . . . 235
8.2.3 Multiple parton interactions (MPI) vs BFKL contribution . . . 239
8.2.4 Exclusive radiation patterns: towards a new class of BFKL observables . . . 242
8.2.5 Previous measurements and experimental aspects . . . 245
8.2.6 RunII expectations . . . 249
8.2.7 Summary . . . 249
8.3 Inclusive forward di-jet production in pp . . . 250
8.3.1 Dijet production at forward and very-forward rapidities . . . 251
8.3.2 Trijet production at forward-central and purely forward rapidities . . . 252
8.3.3 Forward jet production - measurements at very large rapidities . . . 253
8.4 Saturation physics in p+p and p+A collisions . . . 257
8.4.1 Introductory remarks . . . 257
8.4.2 Forward Drell-Yan production - collinear vs small-x approach . . . 257
8.4.3 Forward Drell-Yan production - Further prospects in the collinear approach . . . 260
8.4.4 Forward Drell-Yan production - Further prospects in the small-x approach . . . 263
8.4.5 Forward photon production and gluon saturation - theoretical overview and measurement proposal . . . 267
8.4.6 Summary . . . 272
8.5 Large-x physics in p+p and p+A collisions . . . 272

9 Detectors **281**
9.1 ATLAS-ALFA Experiment . . . 283
9.2 TOTEM Experiment . . . 286
9.2.1 Standard TOTEM Detectors Operated during Run-I at High β^* . . . 287
9.2.2 Detector Upgrade for Vertical Roman Pots . . . 289
9.3 Forward Shower Counters in CMS . . . 299
9.4 CMS-TOTEM Proton Spectrometer (CT-PPS) . . . 300
9.4.1 Development of Low-Impedance Roman Pots . . . 302
9.4.2 Requirements on the Timing Detectors and Strategy . . . 312
9.4.3 Pixel Tracking System . . . 321
9.5 The AFP Detector . . . 324
9.5.1 Beam Interface . . . 325
9.5.2 Silicon Tracker . . . 325
9.5.3 Time-of-Flight Detector . . . 327

9.5.4 Data Acquisition . . . 332
9.6 LHCb Experiment . . . 333
9.6.1 HERSCHEL configuration . . . 333
9.6.2 Detector Design and Installation . . . 335
9.6.3 Conclusions . . . 338
9.7 AD: The Alice Diffractive Detector . . . 338
9.7.1 Design of AD . . . 338
9.7.2 Commissioning of AD . . . 339
9.8 LHCf Detectors . . . 339

Foreword

In early 2013 the LHC Forward Physics and Diffraction Working Group was formed, as part of the activities of common interest to the LHC experiments organized by the LHC Physics Centre at CERN (LPCC, http://cern.ch/lpcc). The primary goal of the WG was to coordinate, across the experiments and with the theoretical community, the discussion of the physics opportunities, experimental challenges and accelerator requirements arising from the study of forward phenomena and diffraction at the LHC. The mandate of the group included the preparation of a Report, to outline a coherent picture of the forward physics programme at the LHC, taking into account the potential of the existing experiments – including possible detector upgrades –, the possible beam configurations and performance of the accelerator, and the optimization of the LHC availability for these measurements, in view of the priority need to maximize the LHC total integrated luminosity.

The WG was set up by the LPCC in coordination with the management of the ALICE, ATLAS, CMS, LHCb, LHCf and TOTEM experiments, which nominated their representatives in the WG steering group and the WG co-chairs. The steering group identified theory conveners, to oversee the relevant sections of the Report, and created three subgroups to focus the WG activity, reflecting the physics goals appropriate to different LHC running conditions:

- low pileup and luminosity (few 10 pb^{-1}),
- medium luminosity (few 100 pb^{-1}),
- high luminosity (100 fb^{-1}).

All interested physicists were then invited to attend the 16 WG meetings held so far, and to contribute to the writing of this Report, which hopefully represents the unanimous views of the broad forward-physics community. The detailed information about the WG, including the composition of the steering committee and of the subgroups' conveners, the list of meetings, the link to the WG material and to its mailing list subscription, can be found in the WG web page at

http://cern.ch/LPCC/index.php?page=fwd_wg

As requested by the LHC experiments committee (LHCC), and following the several presentations delivered to the committee in the course of the WG activity, this final Report will be submitted to the LHCC, and will form the basis for its internal discussions and recommendations on the requests by the experiments for beam time and detector upgrades, related to forward physics, during Run 2 of the LHC and beyond. More in general, we trust that this Report will promote the deeper understanding and appreciation of the value of this component of the LHC physics programme, and will encourage further progress and the development of new ideas, both on the theoretical and experimental fronts.

The chairs of the LHC Forward Physics WG

Introduction

Editors: J. Bartels, N. Cartiglia, C. Royon
Internal Reviewers: M. Arneodo, V. Khoze

For a successful run of the LHC it is essential to have a full understanding of the complete final states. This includes, besides the central region, also the kinematic region as close as possible to the forward direction. New physics is mainly searched for in the central region where factorization theorems for inclusive cross sections allow the use of parton densities and hard subprocesses whose cross sections can be calculated by using perturbative theory. However, there is a rich physics content outside this kinematic region, in particular close to the forward directions. Prominent examples include the final states with high forward multiplicities, as well as those with rapidity gaps, notably in elastic, diffractive, and central exclusive processes. Some of these configurations originate from purely nonperturbative reactions, while others can be explained in terms of multiparton chains or other extensions of the perturbative QCD parton picture. Future progress in this field requires the combination of thorough experimental measurements and extensive theoretical work.

Monte Carlo generators are indispensable for analyzing experimental data and comparing them with theoretical predictions. Their further development requires detailed studies of the forward region. The most successful and most frequently used Monte Carlo event generators (Madgraph, Pythia, Herwig) were initially written with focus on the central region, considered as the most promising for discovering new physics. Higher order QCD calculations have been implemented, and corrections due to multiparton interactions are now being included. Nevertheless, there remain important aspects that require further attention. Most importantly, when extending these event generators to the forward direction, it becomes necessary to include diffractive (elastic and inelastic) final states. The importance of this rapidity gap physics has been demonstrated, in particular, by the HERA data. At the LHC, final states with rapidity gaps are ascribed to rescattering effects (multiparton chains) that reduce the probability of finding kinematic regions devoid of jets or particles. This suppression (commonly referred to as 'suppression due to survival factors') has to be taken into account by the event generators, a task that still presents both conceptual and practical difficulties. On the other hand, there are event generators specifically developed for the forward direction (EPOS, PHOJET, QGSJET) that have proven to be particularly successful in predicting, for example, forward energy flow and multiplicities. A third class of specialised Monte Carlo generators has been developed: CASCADE and HEJ for small-x and BFKL physics, POMWIG, FPMC and SuperCHIC for central exclusive production. What is still missing are Monte Carlo generators that simulate final states dominated by saturated parton distributions. In summary, the most ambitious goal in the field of Monte Carlo simulation is the development of generators that include precision QCD calculations, and simulate multiparton interactions as well as final states with rapidity gaps. Clearly, the study of forward physics plays a central role in making progress along these lines.

The measurement of elastic pp scattering at the highest available energies is a 'must' at the LHC. This includes the measurement of σ_{tot}, $d\sigma_{el}/dt$ over the largest possible t region (specially at small t-values), and, more generally, the study of the composition of the total cross section in terms of elastic, diffractive and inelastic contributions. These measurements represent a textbook example of forward physics. The observed rise of the total cross section at the ISR, the Tevatron and at HERA and its compatibility with unitarity has always been a topic of central interest in particle physics. One of the goals is the connection of pp scattering at collider energies with cosmic ray physics: we are now in the novel situation in which the

LHC energies are within the cosmic ray energy domain and it is thus possible to connect these two branches of particle physics. The high energy run of LHC will allow to provide new data points in the cosmic ray spectrum. On the theoretical side the rise of the total cross section raises the question of unitarity, one of the basic principles of particle physics. How do σ_{tot} and σ_{el} reach their respective unitarity bounds? Is there an Odderon, as predicted by perturbative QCD? Theoretical answers cannot be obtained from perturbative calculations alone: there are important nonperturbative aspects in high energy forward scattering that reside in the region of large impact parameter. In contrast to the static potential of low energy QCD, in the high energy scattering of two hadrons both the profile function and the transverse energy composition are energy dependent, and their understanding within QCD therefore requires new tools. In this situation, experimental measurements are most important.

The appearance of rapidity gaps in pp scattering as well as the presence of intact protons in the final state that can be measured - in particular when accompanied by a hard scale (jets or heavy particles) - is part of the complicated structure of multiple interactions. In contrast to deep inelastic scattering where, for diffractive final states, multiple interactions are strongly suppressed, in pp scattering a rapidity gap in a single parton chain is likely to be filled by production from another chain. This leads to the suppression of rapidity gaps and the destruction of the scattered protons, leading to a suppression of the visible diffractive cross section encoded in the survival factor $S^2 < 1$. The thorough measurement of final states with rapidity gaps and intact protons therefore serves as a valuable tool for understanding the event structure in pp scattering. The most promiment examples include the single diffractive production of jets, Z and W bosons, as well as the central exclusive production reactions (double Pomeron exchange). These events allow to further constrain the Pomeron structure in terms of quarks and gluons, as initially investigated at HERA, in the completely new kinematical domain reached at the LHC. Diffractive final states originating from double Pomeron exchange attract attention also from another perspective. Double Pomeron exchange allows the formation of new states from pure gluons: the glueball states that have been under discussion for many years, heavy flavor states as well as beyond-standard-model objects. Tagging of the intact protons allows for a clean spin-parity analysis of the produced states. The presence of rapidity gaps between the protons and the centrally produced system along with that of intact protons can also be due to photon exchange, i.e. in such final states LHC serves as a $\gamma\gamma$-collider. This opens the door to the electroweak sector, e.g. to the search for anomalous couplings of vector bosons and photons.

Forward physics allows to address specific aspects of QCD dynamics that go beyond the collinear approximation, notably BFKL and small-x physics. The BFKL Pomeron has been derived for the high energy scattering of partons, but its theoretical interest has become much broader, and now includes aspects of integrability and the connection with gravity and string theory. Consequently there is a strong motivation to establish its existence in the real world of strong interactions. Already at HERA and at the Tevatron special final states were identified as providing potentially clear signals, most notably the Mueller-Navelet jets with a large rapidity separation between between two jets of comparable transverse momenta, and the so-called jet gap jet events, where two jets are separated by a gap devoid of particles. Such configurations have already been investigated in previous runs of the LHC (in particular, angular decorrelations), but it has become clear that further evidence has to be searched for. Both the increase in energy and the recent theoretical developments strongly motivate new efforts. For example, with the higher machine energy it will be possible to address, apart from the celebrated angular decorrelation between the jets, also the BFKL intercept: a comparison of Mueller-Navelet jets at different machine energies (7 TeV and 13 TeV) with fixed momentum fractions of the parton densities allows a direct measurement of the cross section as a function of the rapidity separa-

tion, i.e. the BFKL interecpt. Another BFKL related measurement that has not been carried out yet consists of varying the transverse momenta of the two Mueller-Navelet jets: when the momenta are of the same order, the BFKL Pomeron should dominate, whereas for very different transverse momenta the DGLAP description applies. BFKL dynamics can be tested also in another way. With modern calculational tools it has become possible to address multiparton final states within the collinear factorization. In the region of large rapidities, these subprocesses generate logarithms of energy and thus can directly be compared with LO or NLO BFKL. A new Monte Carlo (BFKLex) has been designed and developed specially for probing BFKL dynamics. Interest in small-x corrections to parton densities has been stimulated by deep inleastic ep scattering at HERA and by heavy ion collisison, studied both at RHIC and in the previous LHC run. One of the prominent ideas is the saturation of gluon densities at small x and low Q^2 that arises from multi-parton chains and their recombination. At the LHC one of the most promising places for searching signals for saturation is the kinematic region very close to the forward directions, in particular the Drell-Yan production of lepton pairs. Here LHC energies allow to access a much larger kinematic region than previous machines. More information on saturation is expected from the measurements of two-particle correlations: here it is mandatory to have rapidity intervals as large as possible.

Understanding the sources and the propagation of cosmic rays are central questions of astroparticle physics. While there is increasing evidence that supernova remnants accelerate cosmic rays up to energies of $\sim Z \times 10^{14}$ eV (with Z the charge of the cosmic ray nucleus), the sources of the particles of energies up to 10^{20} eV are not known. Cosmic ray physics needs a good understanding of p-air collisions in the forward directions. Indeed, air shower simulations represent a key ingedient needed to analyze cosmic ray data. Monte Carlo generators developed for cosmic ray physics (EPOS, PHOJET, QGSJET) are already quite successful in describing pp collisions in the forward direction and, for further improvements, it will be useful to study proton-oxygen collisions at the LHC. LHC energies have now reached regions that are close to cosmic ray physics and thus will allow to understand and to fine-tune hadronic models used for air shower simulation.

Finally, we describe the relevance of forward physics for heavy ion physics. Ultraperipheral collisions (UPC) of nuclei (protons and nuclei) at the LHC provide a tool complementary to pp, pA collisions for testing high energy QCD dynamics. For example, studies of UPC allow to measure nucleon and nucleus PDFs in a wide range of x down to $x \geq 10^{-5}$ for much smaller virtualities than in pp and pA collisions. Photon induced processes can also be probed in ion-ion and p-ion interactions given the fact that the intensity of the photon flux grows as the square of the charge of the accelerated particle, implying that heavy ions are a more efficient source of photons than protons.

We finish the document by describing the new detectors that are being or will be installed at the LHC by the ALICE, ATLAS, CMS, LHCb, LHCf and TOTEM collaborations. They will allow fulfilling the rich program of forward physics mentioned above and described in detail in the document.

Chapter 1

Running conditions and beam induced backgrounds

Editors: V. Avati, C. Royon

In this chapter, we describe briefly the acceptance of the forward detectors in the ATLAS and CMS/TOTEM experiments, as well as the induced backgrounds and the different running conditions at the LHC, that will be used in the next chapters of this document.

1.1 Acceptance of Forward Detectors

In this chapter, the proton impact position at forward detector locations for various optics settings and at an energy of $\sqrt{s} = 14$ TeV is discussed in vicinity of the ATLAS Interaction Point (IP1). The detailed studies of the proton behaviour for other energies can be found in [1]. Similar results are expected for the CMS-TOTEM Interaction Point.

The amount of data delivered by a collider is described by its instantaneous luminosity, which can be calculated as:

$$L = \frac{n \cdot N_1 \cdot N_2 \cdot f \cdot \gamma}{4 \cdot \pi \cdot \varepsilon \cdot \beta^*} F,$$

where N_1 and N_2 are the number of particles per bunch in beam 1 and 2, correspondingly, n is the number of colliding bunches (beam pairs), f is the beam revolution frequency, ε is its emittance, β^* is the betatron function at the Interaction Point (IP), γ is beam Lorentz factor, and F is the geometric luminosity reduction factor due to the crossing angle at the Interaction Point:

$$F = \left(1 + \left(\frac{\theta_c^* \sigma_z^*}{2\sigma^*}\right)^2\right)^{-1/2},$$

where θ_c^* is the crossing angle, σ_z^* – the bunch length, and σ^* – the transverse beam size[1]. The crossing angle is introduced in order to avoid unwanted parasitic interactions, *i.e.* when the bunches collide with each other away from the IP.

In terms of the accelerator optics, the value of the betatron function, β, at a point is the distance from this point to the next at which the beam is twice as wide. The lower the value of the betatron function at the IP (β^*), the smaller the beam size is ($\sigma \sim 1/\sqrt{\beta}$), and thus the larger the instantaneous luminosity is. During standard data taking at the LHC, one tries to decrease the value of β^* in order to maximise the delivered luminosity. These settings are commonly referred as the collision optics. Such an approach introduces large pile-up, which, as will be shown later in this report, makes diffractive measurements very difficult, if not impossible. Therefore one would like to have a few runs dedicated to the studies of diffraction. In such runs the magnets settings may be unchanged, but the proton population in bunches should be decreased, in order to keep the pile-up at reasonably low level.

Processes at very small $|t|$ such as elastic scattering require a dedicated machine configuration, known as *high-*β^* optics. The modifications include:

[1] In this section, asterisk denotes values at the Interaction Point.

– a high value of the betatron function, which implies a very low beam angular divergence (angular momentum spread) at the IP,
– low intensity bunches, needed to minimise the intra-beam scattering effects and to avoid an additional proton transverse momentum smearing,
– small number of bunches, to operate without a crossing angle,
– parallel-to-point focusing – a special feature obtained with a phase advance of $\psi = \pi/2$ to the forward detectors that causes the protons scattered at the same angle to be focused at the same point in the forward detector (in case of the discussed ALFA detectors such focusing occurs in the vertical, y, coordinate),

Another important parameter is the beam emittance, ε, which is a measure of the average spread in the position-momentum phase space. The LHC has been designed to obtain $\varepsilon = 3.75\,\mu$m·rad, but due to its outstanding performance this value was about 2 μm·rad the average during Run 1. In the following, the design value of the emittance is used in the calculations of the beam properties around the forward detectors, whereas the actual one is employed when the beam behaviour at the IP is computed. Such an approach is consistent with the one of the LHC machine group and the real experimental conditions.

The beam sizes and the beam divergence (momentum angular spread) at the ATLAS Interaction Point for various LHC optics are listed in Table 1.1. These results were obtained using the MAD-X program [2, 3], input with the relevant LHC optics files [4].

Table 1.1: LHC beam transverse size and beam divergence at the ATLAS IP for $\sqrt{s} = 14$ TeV, various β^* optics modes and emittance values.

β^* [m]	beam transverse size [mm]		beam divergence [MeV]	
	$\varepsilon = 2$ μm·rad	$\varepsilon = 3.75$ μm·rad	$\varepsilon = 2$ μm·rad	$\varepsilon = 3.75$ μm·rad
0.55	0.012	0.017	150	210
90	0.16	0.21	12	17
1000	0.52	0.71	3.6	5.0

The beam size at the forward detector's location determines the minimum distance from the beam to which the detectors can be safely inserted. Its knowledge is important for both the event simulations and data analysis, as it defines the kinematic regions that are accessible for a given optics settings. The results for the AFP and ALFA cases are listed in Table 1.2. It is worth recalling that although beam 1 and beam 2 are not identical, the differences in their transverse size at the location of forward detectors are negligible. For the ALFA(AFP) detectors only $y(x)$ width is meaningful since they approach the beam in the vertical(horizontal) plane.

For all the measurements that are possible with forward detectors, it is crucial to understand the connection between the scattered proton momentum and the position in the detector. This is usually expressed in terms of the geometric acceptance, which is defined as the ratio of the number of protons with a given relative energy loss (ξ) and transverse momentum (p_{T}) that reached the detector to the total number of the scattered protons. Obviously, not all scattered protons can be measured in forward detectors as they can be too close to the beam to be detected or can hit some LHC element (a collimator, the beam pipe, a magnet) upstream of the detector. In the calculations presented below, the following factors were taken into account:

– beam properties at the IP,

Table 1.2: LHC beam size in x at AFP and in y at ALFA stations for different β^* optics modes for nominal and low emittance. Calculations were done for $\sqrt{s} = 14$ TeV.

β^*	σ_x^{204} [mm]		σ_x^{212} [mm]		σ_y^{237} [mm]		σ_y^{245} [mm]	
[m]	$\varepsilon = 2$	$\varepsilon = 3.75$	$\varepsilon = 2$	$\varepsilon = 3.75$	$\varepsilon = 2$	$\varepsilon = 3.75$	$\varepsilon = 2$	$\varepsilon = 3.75$
0.55	0.14	0.19	0.10	0.14	0.21	0.28	0.17	0.23
90	0.43	0.59	0.36	0.49	0.48	0.66	0.44	0.60
1000	0.56	0.76	0.48	0.65	0.17	0.23	0.16	0.22

– beam pipe aperture,
– properties of the LHC magnetic lattice,
– detector geometry,
– distance between the beam centre and the active detector edge.

The geometric acceptance of the first AFP station (planned to be installed 204 m from the IP1) for $\sqrt{s} = 14$ TeV is shown in Fig. 1.1. The distance from the beam centre was set to 15 σ for the collision optics, to 10 σ for the *high-*β^* ones (*cf.* Table 1.2). In order to account for the dead material of the Roman Pot window a 0.3 mm distance was added in all cases.

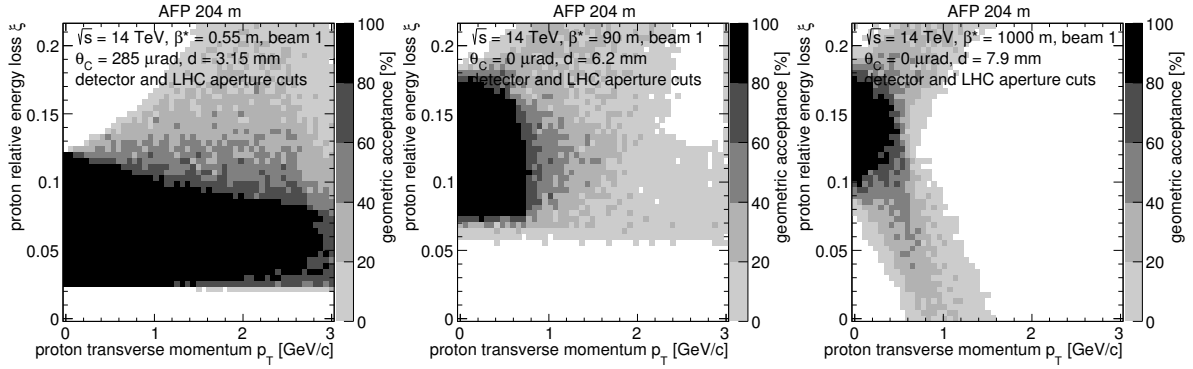
AFP 204 m
√s = 14 TeV, β* = 0.55 m, beam 1
θC = 285 µrad, d = 3.15 mm
detector and LHC aperture cuts
AFP 204 m
√s = 14 TeV, β* = 90 m, beam 1
θC = 0 µrad, d = 6.2 mm
detector and LHC aperture cuts
AFP 204 m
√s = 14 TeV, β* = 1000 m, beam 1
θC = 0 µrad, d = 7.9 mm
detector and LHC aperture cuts
proton relative energy loss ξ
proton transverse momentum pT [GeV/c]
geometric acceptance [%]

Fig. 1.1: Geometric acceptance of the AFP detector as a function of the proton relative energy loss (ξ) and its transverse momentum (p_{T}) for different LHC optics settings. The beam properties at the IP, the beam chamber and the detector geometries, the distance between the detector edge and the beam centre were taken into account. The beam energy was set to 7 TeV and the distance from the beam is calculated taking into account the nominal emittance value of 3.75 μm·rad and 0.3 mm of dead material.

For collision optics, the region of high acceptance is limited to $p_{\mathrm{T}} < 3$ GeV and $0.02 < \xi < 0.12$. These limits change to $p_{\mathrm{T}} < 1$ GeV and $0.07 < \xi < 0.17$ and $0.1 < \xi < 0.17$ for $\beta^* = 90$ and 1000 m optics, correspondingly.

The results for the first ALFA station (located 237 m from the IP1) are shown in Fig. 1.2. For this case the distance from the beam centre was set to 15 σ for collision optics and to 10 σ for the *high-*β^* ones and a 0.3 mm of dead material was added.

For collision optics the region of high acceptance ($> 80\%$) is limited by $p_{\mathrm{T}} < 0.5$ GeV and $0.06 < \xi < 0.12$, which is significantly smaller than in case of the AFP detectors. The picture changes drastically when *high-*β^* optics is considered, as these settings are optimised for the elastic scattering measurement in which access to low p_{T} values for $\xi = 0$ is crucial. One should also note that the limit on the minimum value of the proton p_{T} decreases with the

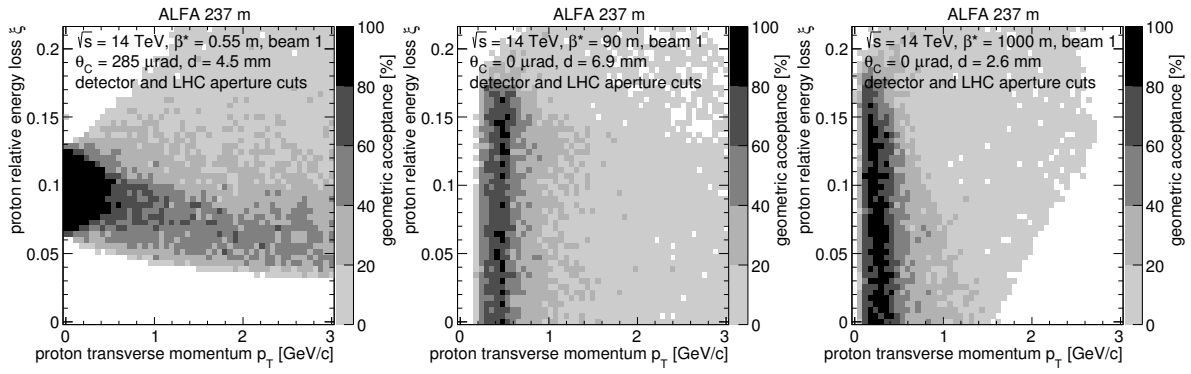
ALFA 237 m
√s = 14 TeV, β* = 0.55 m, beam 1
θC = 285 μrad, d = 4.5 mm
detector and LHC aperture cuts
ALFA 237 m
√s = 14 TeV, β* = 90 m, beam 1
θC = 0 μrad, d = 6.9 mm
detector and LHC aperture cuts
ALFA 237 m
√s = 14 TeV, β* = 1000 m, beam 1
θC = 0 μrad, d = 2.6 mm
detector and LHC aperture cuts
proton relative energy loss ξ
proton transverse momentum pT [GeV/c]
geometric acceptance [%]

Fig. 1.2: Geometric acceptance of the ALFA detector as a function of the proton relative energy loss (ξ) and its transverse momentum (p_{T}) for different LHC optics settings. The beam properties at the IP, the beam chamber and the detector geometries, the distance between the detector edge and the beam centre were taken into account. The beam energy was set to 7 TeV and the distance from the beam is calculated taking into account the nominal emittance value of 3.75 μm·rad and 0.3 mm of dead material.

increase of the β^* value. In other words, the higher the β^* is, the smaller t values are accessible. It is worth mentioning that the lower value of accessible p_{T} depends on the distance between the beam centre and the detector edge as was shown [5].

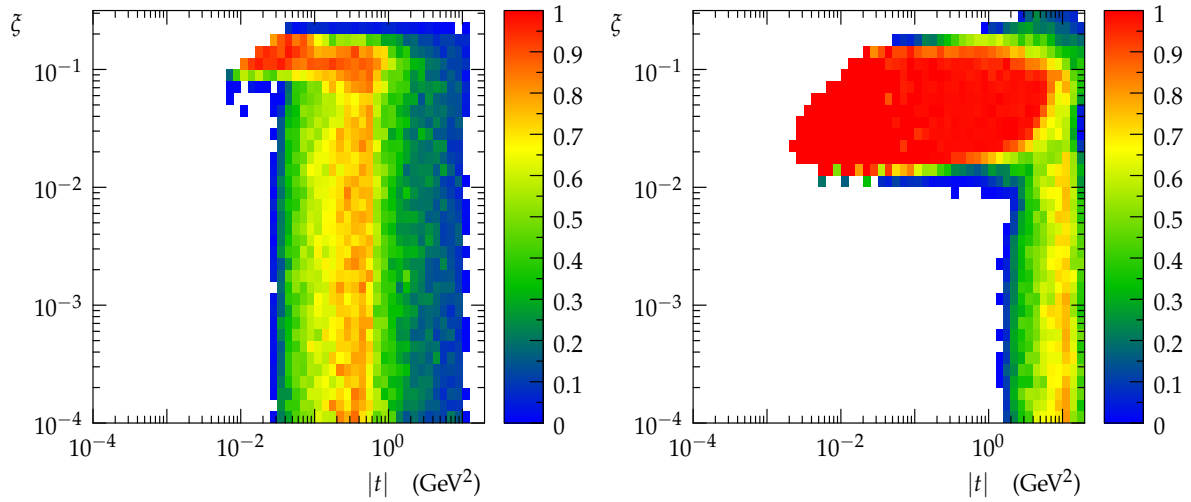

Fig. 1.3: Geometric acceptance of the TOTEM-RP detectors (vertical and horizontal) as a function of the proton relative energy loss (ξ) and its squared four-momentum transfer (t) for different LHC optics settings (left, β^*=90 m; right, low-β^*), at the beam energy of 7 TeV and at detector distance from the beam corresponding to 10σ+0.5 mm.

Similar considerations can be done for the acceptance in the leading proton detectors in IP5. The detailed acceptance studies of the TOTEM and CT-PPS detectors have been published already elesewhere ([7,8]). As example in Fig. 1.3 is shown the acceptance for high (90 m) and low beta optics, for both vertical and horizontal detectors.

1.2 Background: pp induced background

In addition to the genuine physics processes from the hard interaction or from pileup events, "machine-induced" backgrounds mainly due to beam halo or secondary particles must be taken

into account, as more than one track per bunch crossing can arrive to the RP. The electronics associated to the timing detector can measure without ambiguity only the traversing time of one particle per bunch crossing, hence the detector plane must be properly segmented as the deterioration of the timing detector resolution has a direct impact on the background suppression.

The contribution of the beam-related background has been added to the background from the physics interactions in many studies presented in this report.

The machine-induced background contribution at z=220 m is estimated by extrapolating the TOTEM measurements at $\sqrt{s} = 8$ TeV during Run-I to the Run-II data-taking conditions. The beam-related background has two components: the “collision debris" and the “beam halo" background. The “collision debris" contains particles from showers generated in the vacuum pipe aperture limitations that eventually produce a signal in the RPs. This fraction of the background scales with μ (defined as the mean number of inelastic interaction per bunch crossing) as the number of vertices (pile-up) generated in the bunch crossing. The “beam halo" contribution is due to beam protons travelling far from the central beam orbit and hitting the RPs; this contribution is expected to scale with the beam current ($\approx \sqrt{\mu}$). [2]. In this study the background is calculated per bunch crossing and the effective scaling is done based on the parameter μ.

Different approaches have been used to understand how to extract the background component from the data and how to extrapolate it to higher pile-up conditions. The detailed procedure is described in [6]. It can be summarized as in the following: the background probability per bunch-crossing is estimated from a zero-bias data sample (random trigger on bunch crossing). which includes all events, from both background and physics processes. In order to subtract the contribution from physics processes, the multiplicity of the leading protons reconstructed in the pots is estimated with a dedicated sample of simulated events (without pileup) for the very high pile-up case (low-β^*) or by using the information of the T2 telescope for moderate pile-up (high-β^*). By comparing the multiplicity of the primary tracks with the average cluster multiplicity per detector plane from the data (zero-bias data sample) it is then possible to subtract this contribution, and to extract the probability distribution of the background per bunch-crossing as well as its spacial distribution in the detector.

In the high-β^* scenario the beam-beam background has been estimated by selecting events with tracks in both arms of T2: in this sub-sample the probability to have at least a cluster in the RPs for events without elastic candidates was found to be 1.5%. In this estimate the contribution of the high-mass diffraction is already subtracted (about 0.5%). The beam halo contribution was calculated as the probability to have a proton track reconstructed in the vertical RPs when both T2 arms are empty and no elastic signature is present (i.e. no collinear protons on the other arm). The estimate is conservative and probably overestimates the beam-halo, as the selection includes contributions from low mass SD (no signal in T2 with possibly a single proton in the RPs acceptance) and a small fraction of elastic events with a proton on one arm escaping the detection (due to smearing and edge effects). This background, assumed to scale with $\sqrt{\mu}$, is $\approx 2-3\%$ for each vertical RP in condition with μ =0.5.

In conclusion, the beam-beam background probability estimated for a scenario with high-β^* and μ =0.5 is about 3% per BX.

In the low-β^* scenario, the probability per BX to have an additional track due to the beam-beam background has been found to be 80% at μ=50.

The extrapolated occupancies are shown in Figure 1.4 for $\mu = 50, 0.5$. The occupancy values reported in Figure 1.4 are not corrected by a factor 2-1.2 to account for the limited multi-

[2] In fact $I_{beam} \propto n_{bunch} N_{proton}$, where n_{bunch} is the number of bunches in the LHC ring and N_{proton} is the number of protons in a bunch, while the pile-up is proportional to N^2_{proton}.

track capability.

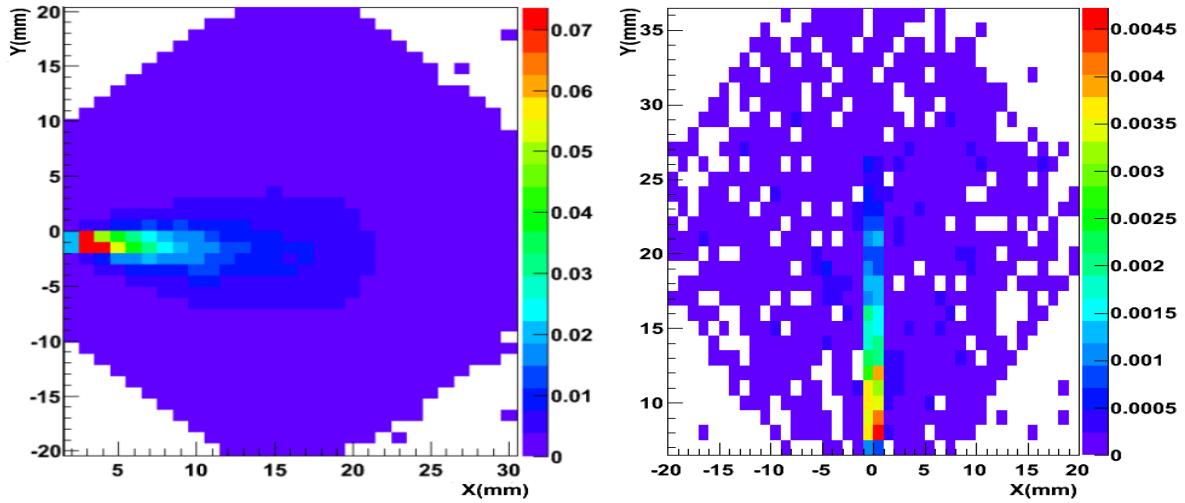

Fig. 1.4: Left: occupancy/BX*mm^2 in the horizontal RP (low-β^*, $\mu = 50$, 6σ approach). Right: occupancy/BX*mm^2 in the vertical RP (β^* =90m, $\mu = 0.5, 9.5\sigma$ approach). Not included in the plot the corrections factor 2 (1.2) which accounts for multiple tracks inefficiency (see text).

The beam background estimation is necessary for a proper optimization of the timing detector design: this extrapolation has been used for detectors development in the TOTEM Timing Upgrade TDR [7] and in the CT-PPS TDR [8]. Moreover several studies have been performed to understand the impact of such background on the physics process selection (see Chapter 5) and on the trigger optimization for high luminosity runs [6, 8].

1.3 Different running conditions

We briefly describe in this section the different running scenarii at the LHC, namely the low, medium and high luminosity runs (Table 1.3.

First we would like to stress that there is a complementarity between the low and high β^* measurements. At high β^* in the forward detector acceptance of ATLAS/ALFA and CMS-TOTEM it is possible to be sensitive to very low ξ values and thus to small diffractive masses, which corresponds to much higher cross section with respect to high diffractive masses. The small amount of luminosity available at high β^* will this be enough to fulfill the diffractive program at low masses.
On the contrary, at low β^*, the horizontal roman pots of ATLAS/AFP and CT-PPS will be needed and the acceptance is better at high ξ and thus high diffractive masses. The cross section for such processes is much smaller but high luminosity of the order of 100s of fb^{-1} will be available, allowing even searching for beyond standard model effects. In such high luminosity and high pile up conditions, the rapidity gap method to detect diffractive events in ATLAS/CMS is impossible.
An intermediary case is with LHCb that can acculumate a reasonable amount of luminosity (typically a few fb^{-1}) with little pile up and can use the rapidity gap method to measure diffraction since the beam are partially defocused close to LHCb. The Alice collaboration concentrates more on heavy ion and p-ion runs and will measure diffraction in those runs where pile up is negligible and the rapidity gap method can also be used.

The low luminosity runs (without pile up) allow performing multiplicity and energy flow

measurements useful to tune MC as well as to measure the total and soft diffractive cross sections in the ATLAS/ALFA and TOTEM experiments for a typical β^* up to 1000 m (see chapter 3). Additional measurements such as single diffraction, low mass resonances, glueballs, jet production in double Pomeron are possible at non-zero but little pile up, for β^* between 20 and 90 m. The default configuration studied in this document for these runs is at high $\beta^* \sim 90$m and the vertical forward detectors of ATLAS/ALFA and TOTEM can be used, together with the forward detectors such as T1/T2 from TOTEM. In a few days of data taking at a pile up of $\sim$0.1, typically 5 to 10 pb^{-1} can be acculmulated..

Medium luminosity runs are set-up specifically for the different LHC experiments. The CMS-TOTEM and ATLAS (ALFA and AFP) can accumulate low pile up data in low and high β^* special runs at low luminosity. It is then possible to accumulate 10 to 100 pb^{-1} at high β^* with a pile up $\mu \sim$1 with a couple of weeks of data taking and about the same amount of luminosity at low β^* with the same time scale at $\mu \sim$2 to 5. Let us mention again that both running conditions are usueful since they access different kinematical domains, namely small and large diffractive masses The LHCb experiment can accumulate a few fb^{-1} of data at small pile up..

High pile up data taking conditions means working at the same luminosity delivered to the experiments during standard data taking periods. The conditions in ATLAS and CMS are such to have a pile up μ between 20 and 100. It is also possible to collect data at a lower pile up $\mu \sim$25 by restricting data taking to end of store (we estimated that up to 40% of the total luminosity can be collected in this way) or to use events originating only from the tails of the vertex distribution, where the pile-up conditions are less severe. Typical luminosities will be 100s of fb^{-1} in such conditions.

Table 1.3: Summary of the machine parameters for the different running conditions.

Conditions	β^* [m]	N [10^{11} p]	N_b	μ (pileup)	L [cm^{-2}s^{-1}]	L_{int} [24h]	Physics
LOW	$\geq$ 1000	0.7	2	0.004	10^{27}	0.1/nb	σ_{tot}; Coulumb region
	19	0.1	40	0.01	$5{\cdot}10^{28}$	4.8/nb	Lhcf Run; Multiplicity; Energy flow; Inelastic cross section
MEDIUM	19	0.7	40	0.4	$2{\cdot}10^{30}$	0.17/pb	High cross section diffraction
	90	0.7	156–700	0.1	10^{30}–10^{31}	0.2–1/pb	σ_{tot}; low mass diffraction; Hard diffraction
	90	1.5	700	0.6	$5{\cdot}10^{31}$	4.4/pb	Glueball searches; CEP
HIGH	0.5	1.15	2800				LHCb programme
	0.5	1.15	2800	30	10^{34}	1/fb	Exclusive dijets, anomalous coupling

References

[1] M. Trzebiński, *Machine Optics Studies for the LHC Measurements*, in proceeding of Wilga 2014 Symposium, arXiv:1408.1836

[2] F. Schmidt, *Mad-X User's Guide*, CERN 2005, http://mad.web.cern.ch/mad

[3] E. Forest, F. Schmidt, E. McIntosh, CERN.SL.2002.044 (AP) KEK-Report 2002-3

[4] cern.ch/proj-lhc-optics-web/

[5] M. Trzebiński, R. Staszewski, J. Chwastowski, ISRN High Energy Physics, vol. 2012 (2012) 491460

[6] M. Berretti, “Performance studies of the Roman Pot timing detectors in the forward region of the IP5 at LHC", TOTEM-NOTE 2014-001

[7] TOTEM Collaboration, “Timing Measurements in the Vertical Roman Pots of the TOTEM Experiment, Technical Design Report”, CERN-LHCC-2014-020; addendum CERN-LHCC-2014-024.

[8] CMS and TOTEM Collaborations, ”Technical Design Report for CMS-TOTEM Precision Proton Spectrometer, CERN-LHCC-2014-021.

Chapter 2

Monte Carlo

Convener and Editor: L. Harland-Lang
Internal Reviewers: H. Jung, M. Ruspa

2.1 Introduction

Monte Carlo (MC) simulations of high energy physics are an essential part of the LHC forward physics programme. Such simulations are important as a means to compare the available models of diffractive physics with LHC measurements, as well as a tool to tune to hadronic data and hence provide a phenomenological description of soft QCD effects, an understanding of which is essential for a wide range of high energy physics analyses, including searches for BSM physics. In addition these are crucial in the modelling of cosmic ray physics, as described in Chapter 7. A large range of MC generators that deal with diffractive processes explicitly are available, many of which have been used in the experimental analyses described in this report, while conversely, these MC generators rely on future diffractive measurements at the LHC to constrain and improve the theoretical models contained within them. In Sections 2.2–2.7 some of the most widely used and up–to–date such MC generators for diffractive physics are described: the basics of the underlying theoretical models are summarised, and the outlook for the future is discussed, in particular in terms of the possibilities for and importance of future LHC measurements. Central exclusive production, discussed in Chapter 5, requires a different theoretical approach to standard inclusive processes and is not currently included in the available general purpose MC event generators. A selection of MC generators that deal dominantly with this exclusive process are on the other hand available, which are discussed in Sections 2.9–2.12. This (non–exhaustive) list of MC generators for diffraction and CEP is intended to serve as a reference point for some results in this report, where these MC generators are used. Finally, in Section 2.13 a selection of comparison plots between LHC Run I diffractive measurements and MC predictions are shown: this serves as an indication of the way in which, already, such measurements can be of great use for MC tuning, with future data increasingly allowing differentiation between the model inputs.

2.2 EPOS LHC

EPOS LHC [1] is a minimum bias MC hadronic generator used for both heavy ion interactions and cosmic ray air shower simulations. It is based on `EPOS` 1.99 [2, 3] retuned to reproduce LHC data on a higher precision level. `EPOS` is based on a hadronic model which provides a consistent treatment of the cross section calculation and particle production, taking into account energy conservation, in both cases according to parton-based Gribov-Regge theory [4]. In this approach, the basic ingredient is the purely imaginary amplitude of a single pomeron exchange, which is the sum of a (parameterized, Regge–like) soft contribution $G_0(\hat{s},b) = \alpha_0(b)\hat{s}^{\beta_0}$ and a semi-hard contribution based on the convolution of a soft pre-evolution (the part of the amplitude corresponding to a Regge–like soft evolution, from an arbitrary low virtuality Q^2 to the minimum hard scale Q_0^2 necessary to start the hard evolution), a DGLAP based hard evolution and a standard LO QCD $2\to2$ cross section. The latter needs complex calculations but can be

fitted to a simple Regge-like term: $G_1(\hat{s},b) = \alpha_1(b)\hat{s}^{\beta_1}$. $\hat{s} = sx^+x^-$ is the fraction of energy (mass) carried by the pomeron and b the impact parameter of the nucleon-nucleon collision. Further details can be found in [4].

Both cross sections and particle production are based on the total amplitude $G = \sum_i G_i$ via a complex Markov-Chain MC. The particle production process has two main components. Firstly, there are the strings composed from pomerons (2 strings per pomeron, with ISR and FSR and the soft contribution from the non-perturbative pre-evolution, below the fixed scale Q_0^2, included); at high energy many pomerons can be exchanged in parallel in each event (MPI), covering the mid-rapidity part. Secondly, there are the remnants, which carry the remaining energy and quarks and mostly cover the fragmentation region. A remnant can be as simple as a resonance or a string elongated along the beam axis if its mass is high enough and is treated the same way for both diffractive and non-diffractive events. Another particularity of EPOS is that on an event-by-event basis, if the particle density of the secondaries produced by the string fragmentation is too high (more than about 3 or 4 hadrons per fm^3), then string segments are merged to form clusters. Clusters are subsequently decayed following the microcanonical ensemble with additional flow to mimic the particle spectra obtained after hydrodynamical evolution and freezout hadronization (statistical collective hadronization).

2.2.1 Diffractive contribution

To generate inelastic events where new particles are produced, following standard AGK (Abramovski, Gribov, Kancheli [5]) cutting rules configurations of cut (inelastic) pomerons (with amplitude G) and uncut (elastic) pomerons (with amplitude -G) are generated. Configurations having the same number of cut pomerons, and any number of uncut ones, belong to the same class of inelastic events. As a consequence a class of inelastic event is defined by its number of cut pomerons and the sum of all possible elastic (uncut) pomeron exchanges.

A low mass diffractive event will be produced if only the remnants are excited and no inelastic (i.e. cut) pomeron is exchanged. To have such a contribution consistently produced by the MC, a third term G_2 is added to the total amplitude. Unlike the pomeron exchange discussed above, this diffractive exchange will not produce central strings (except in the case of central diffraction) but will allow the remnant to gain a heavier mass as some excited state. It can be defined as

$$G_2(x,s,b) = \alpha_2 x^{-\alpha_{diff}} \exp\left\{-\frac{b^2}{\delta_2(s)}\right\} \tag{2.1}$$

where α_2 is a free parameter depending on the remnant type. To use the same form as in the case of the soft pomeron, we have

$$\delta_2 = 4 \cdot 0.0389 \cdot \left(R_{diff}^{pro} + R_{diff}^{tar} + \alpha'_{diff} \ln s\right) \tag{2.2}$$

with 2 free parameters R_{diff}^{rem} and α'_{diff}. Since $\hat{s} = M^2$, α_{diff} is fixed at 1 to have a mass distribution following the usual $1/M^2 = \hat{s}^{-\alpha_{diff}}$. α_2, R_{diff}^{rem} and α'_{diff} can be fixed by fitting all cross sections (total, elastic, inelastic, single diffractive and elastic slope).

With G defined as

$$G(x^+,x^-,s,b) = \sum_{i=0}^{2} G_i(x^+,x^-,s,b) \tag{2.3}$$

it is possible to have a soft diffractive interaction if only G_2 is exchanged, while in the case of multiple interactions, G_2 can be produced together with G_0 and/or G_1. In future developments,

G_2 will be used to get the mass of the remnant in all cases (including non-diffractive events), while in EPOS LHC an independent $1/M^{2\alpha_{remn}}$ distribution is currently used to fix the mass of the excited remnants.

As a consequence, a high mass diffractive event will occur if a hard pomeron is exchanged without remnant excitation. A free parameter is introduced to fix this probability.

2.2.2 Inclusive Cross Sections

One fundamental quantity is the function Φ, due to the contribution of all elastic pomeron (virtual) exchanges, which can be written as :

$$\begin{aligned}\Phi\left(x^{\text{proj}},x^{\text{targ}},s,b\right) &= \sum_{l=0}^{\infty}\int\prod_{\lambda=1}^{l}dx_\lambda^+dx_\lambda^-\,\frac{1}{l!}\prod_{\lambda=1}^{l}-G(x_\lambda^+,x_\lambda^-,s,b) \\ &\times\; F_{\text{remn}}\left(x^{\text{proj}}-\sum_\lambda x_\lambda^+\right)F_{\text{remn}}\left(x^{\text{targ}}-\sum_\lambda x_\lambda^-\right).,\end{aligned} \tag{2.4}$$

where x^{proj} and x^{targ} are the momentum fractions not used in inelastic pomeron exchange and F_{remn} is a vertex function with the remnant to guarantee energy conservation ($\sum_{\text{ine}} x_{\text{ine}} + \sum_{\text{ela}} x_{\text{ela}} < 1$).

For x^{proj}=$x^{\text{targ}} = 1$, the Φ function can be seen as the probability to have only elastic pomeron exchange without any new particles produced, for a given impact parameter b. This then leads to the inelastic cross section definition

$$\sigma_{\text{ine}}(s) = \int d^2b\,(1-\Phi(1,1,s,b))\;. \tag{2.5}$$

An elastic scattering corresponds to the sum of elastic pomeron exchanges, with at least one exchange, which can be written as

$$\sigma_{\text{ela}}(s) = \int d^2b\left(1-\sqrt{\Phi(1,1,s,b)}\right)^2, \tag{2.6}$$

and then

$$\sigma_{\text{tot}}(s) = \sigma_{\text{ine}}(s)+\sigma_{\text{ela}}(s) = 2\int d^2b\left(1-\sqrt{\Phi(1,1,s,b)}\right)\;. \tag{2.7}$$

The elastic slope B ($d\sigma_{\text{ela}}/dt = A\exp(+Bt)$ for $t\to 0^-$) is then

$$B = \frac{1}{2}\frac{\int db^2b^2\left(1-\sqrt{\Phi(1,1,s,b)}\right)}{\int db^2\left(1-\sqrt{\Phi(1,1,s,b)}\right)}\;. \tag{2.8}$$

All free parameters entering in the definition of G and F_{remn} can be tuned by a combined fit of all hadronic cross sections (Fig. 2.1), particle multiplicity and the proton structure function F_2 (including the Q^2 independent correction at high energy/high mass needed to reduce the rise of the cross sections). For this reason minimum bias measurements are important for more exclusive channels, where special configurations of the amplitudes G_i are tested.

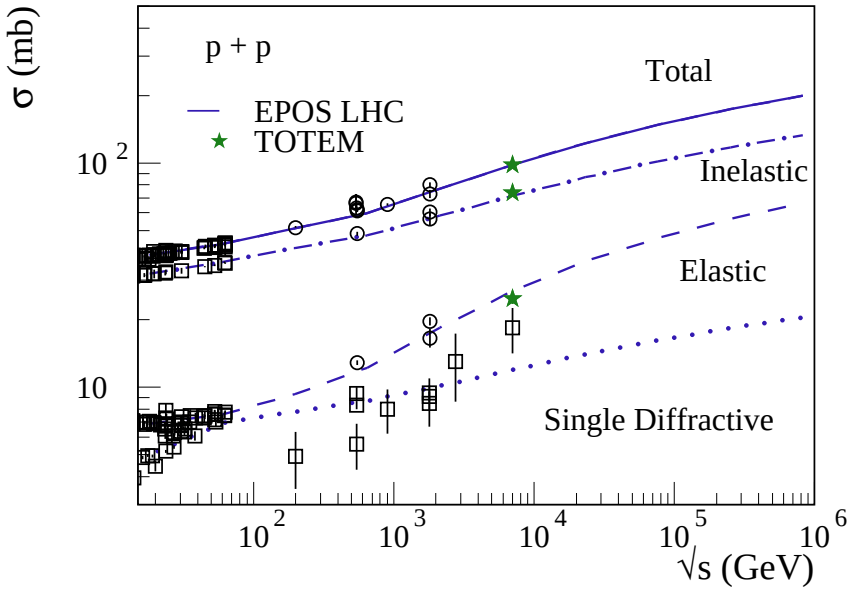

Fig. 2.1: Total, inelastic, elastic and single diffractive p-p cross section calculated with EPOS LHC. Points are data from [6] and the stars are the LHC measurements by the TOTEM experiment [7].

2.2.3 Diffractive Cross Sections

The diffractive cross section is now defined as that due to at least one inelastic exchange G_2, but with no other inelastic contribution; this can not be calculated analytically. Since G_2 is only dominant for $\sum x \ll 1$, we can write

$$\begin{aligned}\sigma_{\rm diff}(s,b) &\sim \Phi(1,1,s,b) \qquad (2.9)\\ &\times \left[\sum_{m=0}^{\infty}\frac{1}{m!}\prod_{\mu=1}^{m}\int dx_\mu^+ dx_\mu^- G_2(x_\mu^+,x_\mu^-,s,b)-1\right]\\ &\sim \Phi(1,1,s,b)\left[\exp\left\{\int dx^+dx^-G_2(x^+,x^-,s,b)\right\}-1\right]. \qquad (2.10)\end{aligned}$$

In practice, a parameter *MCorr* is introduced to evaluate the diffractive cross section without making such an approximation. The numerical value of *MCorr* can be fixed by a fit to the cross section obtained from exact MC simulations (equivalent to numerical integration) using

$$\sigma_{\rm diff}(s) = \int d^2b\left(\Phi(1,1,s,b)\left[\exp\left\{\frac{\chi}{MCorr}\right\}-1\right]\right), \qquad (2.11)$$

with $\chi = \int dx^+dx^-G_2(x^+,x^-,s,b) = \frac{\alpha_2}{(1-\alpha_{diff})^2}\exp\left\{-\frac{b^2}{\delta_2(s)}\right\}$.

Then defining the probability $R_{\rm pro}$ and $R_{\rm tar}$ to have projectile or target excitation respectively, the single diffractive cross section can be written as

$$\sigma_{\rm sd}(s) = R_{\rm pro}.(1-R_{\rm tar}).\sigma_{\rm diff}(s) + (1-R_{\rm pro}).R_{\rm tar}.\sigma_{\rm diff}(s), \qquad (2.12)$$

and as a consequence the double diffractive cross section is simply

$$\sigma_{\rm dd}(s) = R_{\rm pro}.R_{\rm tar}.\sigma_{\rm diff}(s), \qquad (2.13)$$

and the low mass (soft) central diffraction cross section is

$$\sigma_{\rm cd}(s) = (1-R_{\rm pro}).(1-R_{\rm tar}).\sigma_{\rm diff}(s). \qquad (2.14)$$

For central diffraction, since none of the remnants are excited, two strings without remnant connections are used to produce particles at mid rapidity (with two rapidity gaps). This is very similar to the method used to treat high mass diffraction but without any hard contribution (only soft strings). A better treatment of central diffraction with resonance production is under development.

Future LHC measurements of diffractive mass and rapidity gap distributions are extremely important to further constrain the parameters of the model for both low mass (soft) diffraction and high mass (hard) diffraction.

2.3 PHOJET

PHOJET is a MC event generator [8, 9] designed for simulating soft and semi–hard hadronic interactions, suited for describing accelerator events selected with minimum bias triggers. Special care is taken to have a self–consistent model for all partial cross sections, including the interplay of soft, hard, as well as diffractive and non–diffractive interactions [8]. Each inelastic interaction configuration is related through unitarity to a contribution to the elastic amplitude.

While PHOJET was originally developed for hadron–hadron, photon–hadron, and photon–photon interactions (hadron = p/π/K) [9], it has later been extended and included as a building block in the DPMJET III MC package [10] to also apply it to hadron–nucleus [11], nucleus–nucleus [12], and photon–nucleus interactions [13, 14]. The description of hadronic interactions of photons is limited to real and weakly–virtual photons, and no attempt is made to model deep–inelastic scattering.

The theoretical framework of the model is the Dual Parton Model [15] in which color flow topologies derived from the expansion of QCD for large numbers of color and flavour [16, 17] are unitarized in an eikonal–like model. The Dual Parton Model is closely related to the the Quark–Gluon–String Model [18], although there are differences in the practical implementations.

2.3.1 Inclusive and total cross sections

A detailed description of all partial cross sections can be found in [19]. In the following only a very brief summary is given.

Applying the optical theorem an elastic scattering amplitude is constructed from the sum of soft and hard interactions. All interactions leading to transverse momenta of partons smaller than $p_\perp^{\text{cutoff}}$ are attributed to soft interactions, for which the parton interpretation is only valid in analogy to the topological expansion of QCD. The Born cross section for soft interactions is parameterized by $\sigma_s = g^2 s_{\text{eff}}^{\Delta}$. Interactions with large momentum transfer, corresponding to partonic final states with $p_\perp > p_\perp^{\text{cutoff}}$, are called hard (or semi–hard) interactions and described by leading–order perturbative QCD

$$\frac{\mathrm{d}\sigma_{\text{hard}}}{\mathrm{d}^2 p_\perp} = \int \mathrm{d}x_1 \mathrm{d}x_2 \sum_{i,j,k,l} \frac{1}{1+\delta_{kl}} f_{i|A}(x_1,\mu^2) f_{j|B}(x_2,\mu^2) \frac{\mathrm{d}\hat{\sigma}_{i,j\to k,l}(\hat{s})}{\mathrm{d}^2 p_\perp}. \tag{2.15}$$

The transverse momentum cutoff is increased with the collision energy [20] to obtain a good description throughout the collider energy range [21]. Charm quarks are treated as massless and heavier quarks are not included in the calculation. The parameters of the amplitude for soft interactions are fitted to obtain a good description of the total, elastic, and diffractive cross sections and the forward slope of the differential elastic cross section at collider energies. Therefore, the soft parameters, and in particular Δ_{eff}, depend on the set of parton densities and the $p_\perp^{\text{cutoff}}$ used for the fit.

The sum of the amplitudes of soft and hard interactions form the pomeron amplitude, the basic building block of PHOJET. Pomeron–pomeron interactions are only explicitly included at lowest order for a number of graphs of interest (triple–pomeron for single diffractive dissociation, loop–pomeron for double–diffraction dissociation, and two combined triple–pomeron graphs, sometimes called double–pomeron scattering, for central diffraction [22]). All unitarity cuts of these graphs are accounted for following the AGK cutting rules [5].

The partial (soft, hard, triple–pomeron, loop–pomeron, double–pomeron) amplitudes are unitarized in a two–channel eikonal model [23]. The two channels are the ground states of the scattering particles and effective low–mass excitations of the ground states, that are used to describe low–mass diffraction dissociation, similar to the Good–Walker model [24]. Low–mass excitations are limited to $M_D^2 < 5\,\mathrm{GeV}^2$.

Photon interactions are described using the Vector Dominance Model (VDM) for soft (resolved) photon processes and QCD/QED matrix elements are used for hard processes and point–like photon interactions. VDM form factors are taken to extend the description from real photons to photons of virtuality up to $Q^2 \sim 1 - 2\,\mathrm{GeV}^2$.

2.3.2 Modelling of inelastic final states

As a first step the cross sections for different inelastic final states (diffractive and non–diffractive topologies) are calculated. Thanks to the two–channel unitarization of the amplitudes the sizes of the diffractive cross sections are directly linked to, for example, the multiplicity distribution in non–diffractive interactions, leading to strong model constraints. A high–energy event can be built up of a superposition of unitarity cuts of all the aforementioned amplitudes and exhibits, in general, a very complex topology. Hard interactions are sampled first without considering any phase space constraints. In the next step, working from the highest $p_\perp$ downward, the generated hard interactions are completed with angular ordered initial state radiation and, if needed, soft partons. The algorithm for generating initial state radiation is very similar to that described in [25]. Sometimes, depending on the number of interactions and available phase space, it may not be possible for all of the soft and hard interactions to be realized: in this case, priority is given to those with the highest $p_\perp$.

The partonic color flow of each event is sampled explicitly in the large N_c limit [16]. An option for soft color reconnection is implemented but currently not activated as it would not be compatible with the underlying ideas of the topological expansion of QCD. Partons are combined to color–neutral strings according to their color charges and PYTHIA 6 [26] is used to generate final state radiation for hard interactions. String fragmentation and hadronization is also done with PYTHIA 6 using an optimized set of fragmentation parameters.

One special feature of PHOJET is the generation of multiple soft and hard interactions in single and double diffractive dissociation, and in double pomeron scattering. A description of the single interaction scenario is given in [27] and the extension to multiple interactions is discussed in [28]. Inspired by the Ingelman–Schlein approach [29] the implementation of multiple interactions is analogous to that in non–diffractive interactions except that a virtual pomeron state is used to replace one or two of the scattering hadrons. Correspondingly, hard interactions are generated with parton densities for the pomeron (i.e. diffractive parton densities). The suppression of hard interactions with large rapidity gaps, due to the gap survival probability, is accounted for by generating multiple–interaction graphs. A prediction of this model is that the increase with the mass/energy of the pseudorapidity plateau of charged particles in diffractive interactions is similar to or faster than that observed for non–diffractive interactions [28].

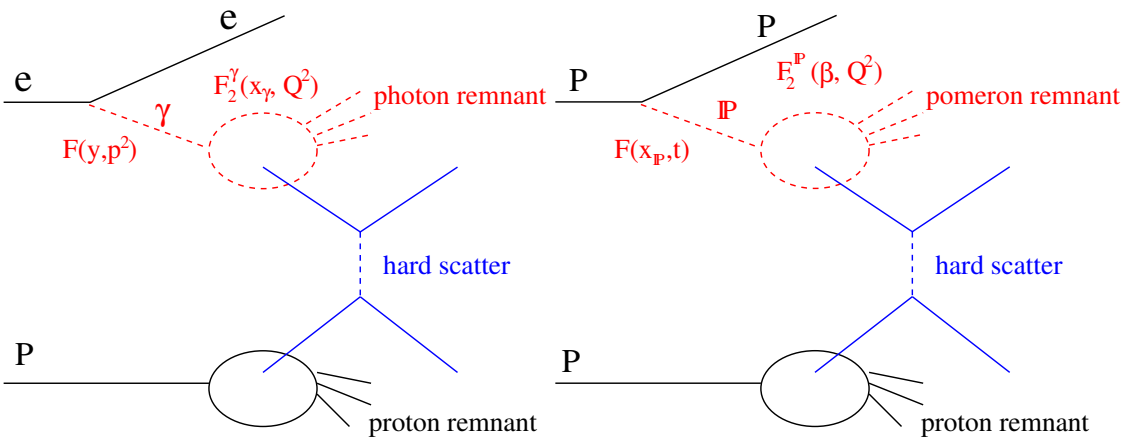

Fig. 2.2: The POMWIG model. Photoproduction in ep (or ee) collisions is replaced with pomeron or reggeon exchange in pp (or ep) collisions.

2.3.3 Plans and future developments

Work is ongoing to implement new parton densities in PHOJET and to carry out the corresponding cross section fits and fragmentation parameter optimization within a timescale of one year. On a somewhat longer time scale the implementation of a microscopic model of parton density saturation, which is currently accounted for only in a rather crude way and independent of the impact parameter of the collision, is foreseen.

2.4 POMWIG

POMWIG is a modification to the HERWIG event generator that allows for the simulation of diffractive interactions. The modifications are simple once it is noticed that pomeron exchange events in hadron–hadron collisions look very much like resolved photoproduction events in lepton–hadron collisions [30]. In resolved photoproduction in electron–proton collisions, for example, the process is modelled by the incoming electron radiating a quasi–real photon according to a flux formula. The photon is then treated as a hadronic object with a structure function, which undergoes a collision with the beam proton. Similarly, single diffractive interactions in proton–proton collisions may be modelled by assuming that one of the beam protons emits a pomeron, again according to some flux formula, which subsequently undergoes an interaction with the other beam proton (see Fig. 2.2). HERWIG will automatically choose to radiate a photon from a beam lepton if a hard subprocess is selected which requires a hadronic structure for the beam lepton. An example would be choosing HERWIG subprocess 1500 (QCD $2 \to 2$ scattering) in an electron–proton collision.

To simulate a single diffractive interaction in pp collisions, therefore, the photon flux should be replaced with a suitable pomeron flux factor, and the photon structure function with a pomeron structure function, and HERWIG should be run in ep mode rather than pp mode. The electron is identified with the proton which remains intact after the diffractive scattering, and POMWIG replaces the final–state electron by an intact, forward going proton in the event record. This process may be generalised to include sub-leading Regge exchanges, and to simulate double pomeron collisions.

The code can be obtained from [31]. The routines supplied function with all currently available Fortran versions of HERWIG from 5.9 onwards. Full installation details can be found at [31]. The example main program provided generates double pomeron $\to$ Higgs events at the

Quantity	Value
$\alpha_{I\!P}$	1.203
$\alpha_{I\!R}$	0.50
$\alpha'_{I\!P}$	0.26
$\alpha'_{I\!R}$	0.90
$B_{I\!P}$	4.6
$B_{I\!R}$	2.0
$C_{I\!R}$	16

Table 2.1: The default parameters in POMWIG

LHC, for a Higgs mass of 115 GeV, and using H1 2006 pomeron Fit A parton densities.

The default parameters for the pomeron and reggeon fluxes are those found by the H1 Collaboration in [32], for the case in which no interference is assumed between the pomeron and reggeon contributions to $F_2^{D(3)}$, as shown in Table 2.1. The reggeon contribution is not well constrained by the H1 data, but is only important at high $x_{I\!P}$ and low-β. In hadron–hadron collisions, the variable $x_{I\!P}$ is commonly referred to as ξ. The fluxes are parameterised as

$$f_{I\!P/p}(x_{I\!P}) = N \int_{t_{max}}^{t_{min}} \frac{e^{\beta_{I\!P}(t)}}{x_{I\!P}^{2\alpha_{I\!P}(t)-1}} dt \tag{2.16}$$

$$f_{I\!R/p}(x_{I\!P}) = C_{I\!R} \int_{t_{max}}^{t_{min}} \frac{e^{\beta_{I\!R}(t)}}{x_{I\!P}^{2\alpha_{I\!R}(t)-1}} dt \tag{2.17}$$

where $\alpha_{I\!P}(t) = \alpha_{I\!P}(0) + \alpha'_{I\!P} t$ and $\alpha_{I\!R}(t) = \alpha_{I\!R}(0) + \alpha'_{I\!R} t$. The normalisation of the flux is arbitrary in the case of the H1 pomeron structure function. The `H1QCD` routine is implemented such that the generated cross section will always match $F_2^{D(3)}$ as measured by H1 at $x_{I\!P} = 0.003$, irrespective of the parameters chosen for the flux. The normalisation of POMWIG diffractive cross sections is not expected to match LHC data. In particular, rapidity gap survival effects are not taken into account in POMWIG. The CMS Collaboration estimated a gap survival probability in single diffractive dijet production of approximately 0.1 in the range $0.0003 < x_{I\!P} < 0.002$ [33].

Finally, details of the `POMPYT` MC for diffractive interactions, based on a similar approach to that described above, can be found in [34].

2.5 PYTHIA 6 & 8

The starting point for the modelling of soft–inclusive QCD processes is common to both PYTHIA 6 [26] and PYTHIA 8 [35]. Both generators are therefore discussed together here, with the new features that are only available in PYTHIA 8 being pointed out where they occur. (Note that PYTHIA 6 has been in a legacy state since 2013, and is now no longer officially maintained.)

2.5.1 Inclusive Cross Sections

The default total, elastic, and inelastic cross sections are obtained from Regge fits. For pp, the 1992 Donnachie–Landshoff parametrization [36] is used, with one pomeron and one reggeon term,

$$\sigma_{\rm tot}^{pp}(s) \;=\; 21.70\, s^{0.0808} + 56.08\, s^{-0.4525} \text{ mb}, \tag{2.18}$$

with the pp CM energy squared, s, in units of $(\mathrm{GeV})^2$. For $p\bar{p}$ collisions, the reggeon coefficient changes to 98.39. (See [26, 36, 37] for other beam types.) The elastic cross section is approximated by a simple exponential falloff with momentum transfer, t (valid at small t), related to the total cross section via the optical theorem,

$$\frac{\mathrm{d}\sigma_{\mathrm{el}}^{pp}(s)}{\mathrm{d}t} = \frac{(\sigma_{\mathrm{tot}}^{pp})^2}{16\pi}\exp\left(B_{\mathrm{el}}^{pp}(s)\,t\right) \quad \rightarrow \quad \sigma_{\mathrm{el}}^{pp}(s) = \frac{(\sigma_{\mathrm{tot}}^{pp})^2}{16\pi B_{\mathrm{el}}^{pp}(s)}\,, \tag{2.19}$$

with $B_{\mathrm{el}}^{pp} = 5 + 4s^{0.0808}$ being the pp elastic slope (in GeV^{-2}), defined using the same power of s as the pomeron term in σ_{tot}, to maintain sensible asymptotics at high energies. The inelastic cross section is defined by

$$\sigma_{\mathrm{inel}}(s) = \sigma_{\mathrm{tot}}(s) - \sigma_{\mathrm{el}}(s)\,. \tag{2.20}$$

The relative breakdown of the inelastic cross section into single–diffractive (SD), double–diffractive (DD), and non–diffractive (ND) components is given by the following parametrizations [37, 38]:

$$\frac{\mathrm{d}\sigma_{\mathrm{SD}}^{pp\to Xp}(s)}{\mathrm{d}t\,\mathrm{d}M_X^2} = F_{\mathrm{SD}}\frac{g_{3\mathbb{P}}\beta_{p\mathbb{P}}^3}{16\pi M_X^2}\exp\left(B_{\mathrm{SD}}^{Xp}t\right) \tag{2.21}$$

$$\frac{\mathrm{d}\sigma_{\mathrm{DD}}^{pp}(s)}{\mathrm{d}t\,\mathrm{d}M_1^2\mathrm{d}M_2^2} = F_{\mathrm{DD}}\frac{g_{3\mathbb{P}}^2\beta_{p\mathbb{P}}^2}{16\pi M_1^2M_2^2}\exp\left(B_{\mathrm{DD}}\,t\right)\,, \tag{2.22}$$

$$\sigma_{\mathrm{ND}}^{pp}(s) = \sigma_{\mathrm{INEL}}^{pp}(s) - \int\left(\mathrm{d}\sigma_{\mathrm{SD}}^{pp\to Xp}(s) + \mathrm{d}\sigma_{\mathrm{SD}}^{pp\to pX}(s) + \mathrm{d}\sigma_{\mathrm{DD}}^{pp}(s)\right)\,, \tag{2.23}$$

with M_X, M_1, M_2 being the diffractive masses, and the pomeron couplings ($g_{3\mathbb{P}}$, $\beta_{p\mathbb{P}}$), diffractive slopes (B_{SD}, B_{DD}), and "Fudge Factors" (F_{FD}, F_{DD}) given in [26, 37–39]. Note in particular that the ND cross section is only defined implicitly, via eq.(2.23). Note also that, in PYTHIA 8, a central–diffractive (CD) component has recently been added as well, with a cross section $\sigma_{\mathrm{CD}} \sim 2\,\mathrm{mb}$.

Precision measurements at high energies, in particular by TOTEM [40, 41], have highlighted that $\sigma_{\mathrm{tot}}(s)$ actually grows a bit faster at large s, and more recent fits [42, 43] are consistent with using a power $s^{0.096}$ for the pomeron term. Updating the total cross section formulae in PYTHIA 8 is planned for a future revision. Alternatively, PYTHIA 8 optionally allows a Minimum Bias Rockefeller (MBR) model to be used, which comes with its own parametrizations of all pp and $p\bar{p}$ cross sections [44]. As a last resort, it is also possible to set your own user–defined cross sections (values only, not functional forms), see the HTML manual's section on "Total Cross Sections".

Cross sections for hard (parton–initiated) processes are obtained from perturbative $2 \to 1$ and $2 \to 2$ matrix elements folded with parton distribution functions (PDFs). There are also extensive (and automated) facilities to interface higher–order processes and/or matrix–element corrections from external matrix–element generators such as ALPGEN [45] or MADGRAPH [46]. For inclusive QCD samples, internal cross sections are defined in such a way that the high–$p_\perp$ tail of the inclusive QCD cross sections (above) is correctly normalized to the perturbative $2 \to 2$ result [47].

2.5.2 Dynamical modelling

In PYTHIA, the modelling of hard (parton–initiated) physics processes is based on a factorized picture of perturbative matrix elements, combined with the standard machinery of initial– and

final–state parton showers, interfaced with the Lund string hadronization model [48]. In the context of multi–parton–interaction (MPI) models, this picture can be extended to cover all $p_\perp$ scales (including soft ones) [47], via the introduction of an infrared regularization scale, $p_{\perp 0}$, which is a main tuning parameter of such models. Physically, $p_{\perp 0}$ expresses a colour screening / saturation scale, which is assumed to modify the naive LO QCD $2 \to 2$ cross sections in the following way,

$$\frac{\mathrm{d}\sigma_{2\to 2}}{\mathrm{d}p_\perp^2} \propto \frac{\alpha_s^2(p_\perp^2)}{p_\perp^4} \to \frac{\alpha_s^2(p_\perp^2 + p_{\perp 0}^2)}{(p_\perp^2 + p_{\perp 0}^2)^2} , \tag{2.24}$$

such that the divergence for $p_\perp \to 0$ is regulated. In practice, the optimal value for $p_{\perp 0}$ (and its scaling with the hadron–hadron CM energy) depends on several factors: the PDFs at low x [49, 50], the IR behaviour of α_s, the IR regularization of the parton showers, and the possible existence of other significant IR physics effects, such as colour (re)connections [47, 51–54]. There is also an implicit dependence on the assumed transverse mass–density of the proton [55]. Accepting the presence of these caveats and dependencies, MPI is the basic concept driving the modelling of all inelastic non–diffractive events in both PYTHIA 6 and 8, with the latter using a more recent formulation [56] with more advanced options. (The modelling of diffraction differs more significantly between the generators, and will be discussed below.)

In PYTHIA 6, two explicit MPI models are available, an "old" one based on virtuality–ordered showers [57–59] with no showers off the additional MPI interactions and a comparatively simple beam–remnant treatment [47], and a "new" one based on (interleaved) $p_\perp$–ordered showers [60], including MPI showers and a more advanced beam–remnant treatment [61]. In both cases, only partonic QCD $2 \to 2$ processes are included among the MPI (hence no multiple–J/ψ, multiple–Z, etc type MPI processes). Most LHC tunes (e.g., the "Perugia" ones [62]) use the "new" $p_\perp$–ordered framework. Diffractive events are treated as purely non–perturbative, with no partonic substructure: a diffractive mass, M, is selected according to the above formulae, and the final state produced by the diffractively excited system is modeled as a single hadronizing string with invariant mass M, stretched along the beam axis (with two strings in the case of double diffraction).

In PYTHIA 8, there is (so far) only one MPI model, extending and improving the $p_\perp$–ordered one from PYTHIA 6. The main differences are: full interleaving of final–state showers with ISR and MPI [56]; a richer mix of MPI processes, including electroweak processes and multiple–J/ψ and –Υ production (see the HTML manual under "Multiparton Interactions:processLevel"); an option to select the second MPI "by hand" (see the HTML manual under "A Second Hard Process"); an option for final–state parton–parton rescattering [63] (mimicking a mild collective–flow effect in the context of a dilute parton system, see the HTML manual under "Multiparton Interactions: Rescattering"); colour reconnections are handled somewhat differently (see the HTML manual and [51, 52]); and an option for an x–dependent transverse proton size [55]. Furthermore, future development of PYTHIA will only occur in the context of PYTHIA 8, so more advanced models are likely to only be available there, and not in PYTHIA 6. An example where the treatment in PYTHIA 8 already far surpasses the one in PYTHIA 6 is hard diffraction (for soft diffraction, the modelling is the same between 6 and 8, though the diffractive and string–fragmentation tuning parameters may of course differ). The default modelling of hard diffraction in PYTHIA 8 is described in [39] and follows an Ingelman–Schlein approach [29] to introduce partonic substructure in high–mass diffractive scattering. ("High–mass" is defined as corresponding to diffractive masses greater than about 10 GeV, though this can be modified by the user, see the HTML manual under "Diffraction".) This gives rise to harder $p_\perp$ spectra and diffractive jets. A novel feature of the PYTHIA 8 implementation is that hard diffractive interactions can include MPI (inside the pomeron–proton sys-

tem such that the rapidity gap is not destroyed), with a rate governed by the (user–specifiable) pomeron–proton total cross section, $\sigma_{p\mathbb{P}}$. This predicts that there should be an "underlying event" also in hard diffractive events, which could be searched for, say, in the region "transverse" to diffractive jets, and/or in association with diffractive Z production, which is currently being implemented in PYTHIA 8. Finally, as mentioned above, an alternative treatment relying on the min–bias Rockefeller (MBR) model is also available in PYTHIA 8 [44].

The most recent PYTHIA 8 tune is currently the Monash 2013 tune [49], which however did not explicitly attempt to retune the diffractive components. Important remaining open questions include dedicated tuning studies in the context of diffraction, for instance to constrain the total pomeron–proton cross section, $\sigma_{p\mathbb{P}}$, which controls the amount of MPI in hard diffractive processes, the sensitivity to the diffractive PDFs, and dedicated tests of string–fragmentation parameters in the specific context of diffractive final states, as compared with LEP–tuned parameters. The question of colour reconnections (CR) is likewise pressing [51–54], and disentangling its causes and effects is likely to be a crucial topic for soft–QCD studies to unravel during the coming years. This will require the definition and study of CR–sensitive observables and a detailed consideration of the interplay between PDFs, MPI, and diffractive physics, with MPI possibly contributing to destroying rapidity gaps in "originally" diffractive events, and CR possibly creating them in "originally" non–diffractive ones [54, 64].

2.6 QGSJET-II

The QGSJET-II model [65,66] has been developed within the Reggeon Field Theory (RFT) [67] framework. The underlying physics picture is one of multiple scattering processes: the interaction is mediated by multiple parton cascades which develop between the projectile and the target. Using the RFT language, those cascades are represented by exchanges of composite objects characterized by vacuum quantum numbers – pomerons. The properties of the underlying "elementary" parton cascades thus define the behavior of the pomeron amplitude. In order to match with perturbative QCD, one applies the "semihard pomeron" scheme: describing the parton evolution in the region of relatively high virtualities $|q^2| > Q_0^2$ using the DGLAP formalism and using a phenomenological soft pomeron amplitude for non–perturbative ($|q^2| < Q_0^2$) parton cascades [68, 69]. The respective RFT scheme is thus based on the amplitude of the "general pomeron" which is the sum of the soft and the semihard ones.[1] The Q_0^2 scale has no fundamental meaning here, being just a border between the two treatments applied to otherwise smooth parton dynamics.

The beauty of the RFT scheme is that it allows one to develop a coherent framework for calculating total and elastic cross sections for hadron–hadron (hadron–nucleus, nucleus–nucleus) scattering and for deriving partial cross sections for various configurations of inelastic final states, including diffractive ones [70]. This is based on the optical theorem and on the AGK cutting rules [5]. While the former states that the total cross section, being the sum of all the respective partial cross sections, including the elastic one, is equal to the s–channel discontinuity of the elastic scattering amplitude, the latter, expressed qualitatively, states that in the high energy limit there is no interference between final states of different topologies. This allows one to calculate partial cross sections *for all possible configurations of final states* by considering unitarity cuts of various elastic scattering diagrams and identifying the contributions of cuts of certain topologies with the desired cross sections.

A particular configuration for an inelastic collision thus contains a number of "elemen-

[1] It is worth stressing that the respective amplitude is no longer that of the pomeron pole, being characterized by more complicated s– and t–dependences [4].

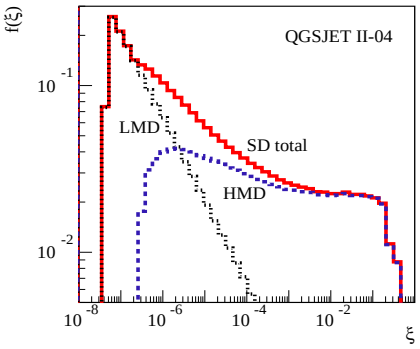

Fig. 2.3: $f_{\rm SD}(\xi) = \frac{\xi}{\sigma_{\rm SD}} \frac{d\sigma_{\rm SD}}{d\xi}$ for single diffractive pp collisions at $\sqrt{s} = 7$ TeV (solid); partial contributions of low (LMD) and high (HMD) mass diffraction are shown by dotted and dot–dashed lines respectively.

tary" production processes described by cut pomeron contributions and an arbitrary number of elastic (virtual) re–scattering processes described by uncut pomerons (see also the discussion in Section 2.2.1). To obtain the respective partial cross section, one has to sum over all the relevant contributions, i.e. ones which have the desirable cut pomeron topology and *any number of uncut pomerons*. This is rather easy to do within the eikonal framework: considering independent pomeron exchanges between the projectile and the target. In this way one arrives at the usual simple expressions for the inelastic cross section, and for relative probabilities of multiple inelastic interactions, which are employed in most MC generators. The scheme can be further generalized to include a treatment of *low mass diffraction* by applying the Good–Walker formalism [24]: considering the projectile and target hadron states to be superpositions of a number of elastic scattering eigenstates characterized by different vertices for their coupling to the pomeron [23]. However, to treat nonlinear processes, like the splitting/fusion of parton cascades *or high mass diffraction*, one has to consider so–called enhanced pomeron diagrams, which describe pomeron–pomeron interactions [71–73].[2]

An explicit treatment of nonlinear contributions to the interaction dynamics, based on an all–order re–summation of enhanced pomeron diagrams [74–76], is the distinctive feature of the QGSJET-II model. Various (generally complicated) final states, including diffractive ones, for inelastic collisions are generated by the MC procedure in an iterative fashion, based on the respective partial cross sections [66]. It is noteworthy that the positive–definiteness of the latter is a very nontrivial fact; it is only achieved after a full resummation of all the contributions for a particular final state of interest, i.e. summing over any number (and topology) of virtual rescatterings described by uncut pomerons [66, 76]. In the particular case of diffractive production, this generates important absorptive corrections (the rapidity gap 'survival factor' discussed throughout this report) which, on the one hand, assure s–channel unitarity of the scheme and on the other result in a nontrivial dependence of the respective cross sections on the masses M_X of the diffractive states produced [76, 77].

As an illustration, in Fig. 2.3 the calculated $\xi = M_X^2/s$ distribution for single diffraction is shown. Apart from the sharp peak at small M_X, which is due to the contribution from low mass diffraction, with decreasing M_X one observes a strong steepening of the M_X–dependence of high mass diffraction. This effect is produced by a strong impact parameter b dependence of the absorptive corrections discussed above: at small b, strong absorptive effects lead to an approximate $\propto dM_X^2/M_X^2$ shape of the mass spectrum, while in peripheral (large b) collisions,

[2] In principle, high mass diffraction may be treated within the Good–Walker framework. However, such a scheme would have a weak predictive power as one has to parameterize empirically the energy–dependence of Good–Walker eigenstates.

M_X range	< 3.4 GeV	$3.4 - 1100$ GeV	$3.4 - 7$ GeV	$7 - 350$ GeV	$350 - 1100$ GeV
TOTEM [79, 80]	2.62 ± 2.17	6.5 ± 1.3	$\simeq 1.8$	$\simeq 3.3$	$\simeq 1.4$
QGSJET-II-04	3.9	7.2	1.9	3.9	1.5

Table 2.2: $\sigma_{pp}^{\rm SD}$ (mb) at $\sqrt{s} = 7$ TeV for different ranges of mass M_X of diffractive states produced.

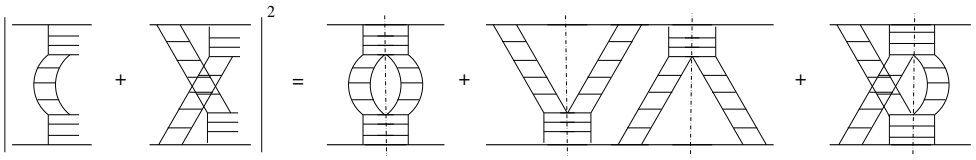

Fig. 2.4: Lowest order contributions to $\sigma_{\rm DD}$: squared sum of the respective amplitudes (lhs) and the corresponding cut diagrams (rhs); the cut plane is indicated by dot–dashed lines.

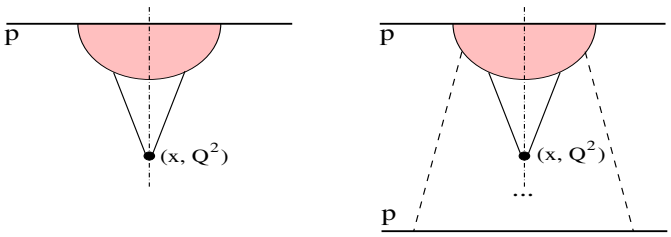

Fig. 2.5: Schematic view of parton distributions as "seen" in DIS (left) and in pp collisions (right). A low x parton (sea quark or gluon) originates from the initial state "blob" and interacts with a virtual "probe". The universal PDFs measured in DIS are affected by the rescattering of intermediate partons from the initial state cascade (hidden in the "blob") off the parent proton. In pp interactions the initial "blob" is affected itself by the collision process: due to the rescattering of intermediate partons off the partner (here, target) proton, as indicated by dashed lines.

the M_X–dependence approaches the triple–pomeron asymptotics [76, 77]. Such a behavior has indeed been observed by CMS and TOTEM, as discussed in [78] and illustrated in Table 2.2.

Another nontrivial predicted effect is the interference between different contributions to the double diffractive cross section $\sigma_{\rm DD}$ [76], which is illustrated for the lowest order (with respect to the triple–pomeron coupling) graphs in Fig. 2.4. Because of the finite pomeron slope, at large b the process is dominated by the usual "pomeron loop" contribution - 1st graph in the right–hand side (rhs) of the figure. On the other hand, moving to smaller b, one obtains a significant contribution from a superposition of two (projectile and target) single diffraction processes characterized by overlapping rapidity gaps - 2nd graph in the rhs. In addition, the interference between the two contributions produces a (negative) contribution corresponding to the 3rd graph in the rhs.

Finally, it is worth recalling the relationship between absorptive corrections due to enhanced pomeron graphs and the breakdown of collinear QCD factorization for quantities that are not fully inclusive, e.g. for jet production in specially triggered events or for diffractive dijet production. Unlike the universal parton distribution functions (PDFs) measured in deep inelastic scattering (DIS), cross sections for particular inelastic final states depend on non–universal PDFs which are influenced by absorptive corrections due to intermediate parton rescattering off the partner hadron and hence depend on the properties of the particular final state of interest [65], as depicted in Fig. 2.5.

2.7 SHRiMPS

2.7.1 Inclusive properties and the KMR model

The SHRiMPS MC generator aims at a complete description of Minimum Bias QCD events at hadron colliders and, most notably, at the LHC. It is based on the model by Khoze, Martin, and Ryskin (KMR) [81, 82]. The model rests on the description of the incident hadrons through the superposition of $N_{\rm GW}$ diffractive or Good–Walker states [24, 83], typical for models of soft interactions. Interactions between these states are described through single eikonal factors, related to the incident eigenstates, which emerge from effective parton densities, Ω_{ik}, associated with them:

$$\Omega_{ik}(Y,B_\perp) = \frac{1}{\beta_0^2}\int \mathrm{d}^2 b_\perp^{(1)} \mathrm{d}^2 b_\perp^{(2)} \delta^2\left(\vec{B}_\perp - \vec{b}_\perp^{(1)} + \vec{b}_\perp^{(2)}\right) \Omega_{i(k)}\left(y, b_\perp^{(1)}\right) \Omega_{(i)k}\left(y, b_\perp^{(2)}\right) . \quad (2.25)$$

Here $B_\perp$ is the impact parameter of the two hadrons, while the individual $\vec{b}_\perp^{(1,2)}$ label the partonic position with respect to the two incident hadrons in the transverse plane; β_0^2 is a normalisation factor with units of area (or cross section) and of the typical size of a hadronic total cross section and Y is the beam rapidity. With this form of the eikonal, the total, elastic and inelastic cross sections are for instance given by

$$\begin{aligned}
\sigma_{\rm tot}^{pp}(Y) &= 2\int \mathrm{d}^2 B_\perp \left\{ \sum_{i,k=1}^{N_{\rm GW}} |a_i|^2 |a_k|^2 \left\{ 1 - \exp\left[-\frac{\Omega_{ik}(Y,B_\perp)}{2} \right] \right\} \right\} \\
\sigma_{\rm el}^{pp}(Y) &= \int \mathrm{d}^2 B_\perp \left\{ \sum_{i,k=1}^{N_{\rm GW}} |a_i|^2 |a_k|^2 \left\{ 1 - \exp\left[-\frac{\Omega_{ik}(Y,B_\perp)}{2} \right] \right\} \right\}^2 \\
\sigma_{\rm inel}^{pp}(Y) &= \int \mathrm{d}^2 B_\perp \left\{ \sum_{i,k=1}^{N_{\rm GW}} |a_i|^2 |a_k|^2 \left\{ 1 - \exp\left[-\Omega_{ik}(Y,B_\perp) \right] \right\} \right\} \equiv \sum_{i,k=1}^{N_{\rm GW}} \sigma_{\rm inel}^{(ik)}(Y) .
\end{aligned} \quad (2.26)$$

Here, the a_i are the coefficients in the expansion of the proton wave function in terms of Good--Walker states. Low-mass diffractive dissociation can proceed in three ways, namely by the transition of either one of the two hadrons or of both of them into excited states. They can be labeled as single diffraction of hadron 1 or 2, $SD1$ and $SD2$, respectively, or by double diffraction, DD. For instance, the differential cross section with respect to the momentum transfer $t = -Q^2$ for the sum of elastic scattering and single diffraction of hadron 1 can be written as

$$\begin{aligned}
\frac{\mathrm{d}\sigma_{el+SD1}(Y)}{\mathrm{d}t} = \frac{1}{4\pi} \sum_{i,j,k=1}^{N_{\rm GW}} \Bigg\{ |a_i|^2 |a_k|^2 |a_j|^2 \int \mathrm{d}^2 B_\perp \exp\left[i\vec{Q}_\perp \cdot \vec{B}_\perp \right] \left\{ 1 - \exp\left[-\frac{\Omega_{ik}(Y,B_\perp)}{2} \right] \right\} \\
\times \int \mathrm{d}^2 B'_\perp \exp\left[i\vec{Q}_\perp \cdot \vec{B}'_\perp \right] \left\{ 1 - \exp\left[-\frac{\Omega_{ij}(Y,B'_\perp)}{2} \right] \right\} \Bigg\} .
\end{aligned} \quad (2.27)$$

The incident parton densities $\Omega_{i(k)}\left(y, b_\perp^{(1)}\right)$ and $\Omega_{(i)k}\left(y, b_\perp^{(2)}\right)$ of Good–Walker state i or k in the presence of k or i are the solutions of coupled differential equations, describing their evolution in rapidity. Their boundary values, the initial parton densities at the incident hadronic rapidities of

$$Y = \pm \log \frac{E_{\rm cm}}{m_{\rm had}} \quad (2.28)$$

with $E_{\rm cm}$ the centre-of-mass energy of the hadron collision and $m_{\rm had} = 1$ GeV a typical hadronic scale, are fixed through form factors. In the SHRiMPS implementation of the KMR model, $N_{\rm GW} = 2$ with initial parton densities given by dipole-like form factors modified with an exponential to guarantee numerical stability,

$$\mathscr{F}_{1,2}(q_\perp) \;=\; \beta_0^2\,(1\pm\kappa)\frac{\exp\left(-\dfrac{\xi(1\pm\kappa)q_\perp^2}{\Lambda^2}\right)}{\left(1+\dfrac{(1\pm\kappa)q_\perp^2}{\Lambda^2}\right)^2}\,, \tag{2.29}$$

and therefore

$$\begin{aligned}\Omega_{i(k)}(-Y/2, b_\perp^{(1)}) \;&= F_i(b_\perp^{(1)})\\ \Omega_{(i)k}(+Y/2, b_\perp^{(2)}) \;&= F_k(b_\perp^{(2)})\,,\end{aligned} \tag{2.30}$$

where $F_j(b_\perp)$ are the Fourier transforms of the form factors $\mathscr{F}_j(q_\perp)$. The parton densities increase with increasing rapidity distance from the hadron, driven by a parameter Δ, which could be identified as a reggeon, and in particular a pomeron intercept. This exponential "gain" term is counteracted by an absorptive correction, $\mathscr{W}_{\rm abs}$ which is interpreted as parton recombination. It is parametrised by a constant λ, which could consequently be identified as being connected to the triple-pomeron vertex, and reads

$$\mathscr{W}_{\rm abs}^{(ik)}(y, b_\perp^{(1)}, b_\perp^{(2)}) \;=\; \left\{\frac{1-\exp\left[-\frac{\lambda}{2}\Omega_{i(k)}(y, b_\perp^{(1)}, b_\perp^{(2)})\right]}{\frac{\lambda}{2}\Omega_{i(k)}(y, b_\perp^{(1)}, b_\perp^{(2)})}\right\}\left\{\frac{1-\exp\left[-\frac{\lambda}{2}\Omega_{(i)k}(y, b_\perp^{(1)}, b_\perp^{(2)})\right]}{\frac{\lambda}{2}\Omega_{(i)k}(y, b_\perp^{(1)}, b_\perp^{(2)})}\right\}. \tag{2.31}$$

Together, therefore

$$\begin{aligned}\frac{{\rm d}\Omega_{i(k)}(y, b_\perp^{(1)}, b_\perp^{(2)})}{{\rm d}y} \;&= +\mathscr{W}_{\rm abs}^{(ik)}(y, b_\perp^{(1)}, b_\perp^{(2)})\cdot\Delta\cdot\,\Omega_{i(k)}(y, b_\perp^{(1)}, b_\perp^{(2)})\\ \frac{{\rm d}\Omega_{(i)k}(y, b_\perp^{(1)}, b_\perp^{(2)})}{{\rm d}y} \;&= -\mathscr{W}_{\rm abs}^{(ik)}(y, b_\perp^{(1)}, b_\perp^{(2)})\cdot\Delta\cdot\,\Omega_{(i)k}(y, b_\perp^{(1)}, b_\perp^{(2)})\,,\end{aligned} \tag{2.32}$$

Taken together this yields a reasonably good description of total, elastic, inelastic and diffractive cross sections in pp and $p\bar{p}$ collisions at various centre–of–mass energies, see Fig. 2.8.

2.7.2 Exclusive properties

2.7.2.1 Parton–parton interactions

In order to link the KMR model with a truly exclusive partonic language, the SHRiMPS model assumes, in a first step, that while the proton is a superposition of Good–Walker eigenstates, the interaction projects onto one of these states. This happens for both colliding hadrons, and the corresponding contributions for each possible combination of Good–Walker states to the inelastic cross section can be read off from (2.26). After choosing the channel ik in which the interaction is taking place, the impact parameter distribution is given by ${\rm d}\sigma_{\rm inel}^{(ik)}(Y)/{\rm d}B_\perp$. The number of partonic interactions is given by a Poissonian in the eikonal $\Omega_{ik}(B_\perp)$ and the positions of the individual parton–parton scatters is determined probabilistically according to the parton densities $\Omega_{i(k)}(y, b_\perp^{(1)}, b_\perp^{(2)})$ and $\Omega_{(i)k}(y, b_\perp^{(1)}, b_\perp^{(2)})$.

The individual interactions between partons are interpreted as being given by cut pomerons, effectively multiple gluon emissions along a gluon-ladder ordered in rapidity. Since the KMR model has no notion of energies or light–cone momenta of the partons constituting the incident hadron states, suitable PDFs must be constructed, which are then convoluted with a total parton–parton cross section mediated through pomeron exchange, or a reggeised t–channel gluon, to yield the inelastic cross section,

$$\sigma_{\text{inel}}^{(ik)}(s_{\min}) = \frac{1}{2S}\sum_{\tilde{i},\tilde{k}}\int_{s_{\min}}^{s_{\max}} \mathrm{d}\hat{s}\int \mathrm{d}\hat{y}\left[f_{\tilde{i}/h_1}(x_1,\mu_F^2) f_{\tilde{k}/h_2}(x_2,\mu_F^2)\left(\frac{\hat{s}}{s_{\min}}\right)^{\eta_{ik}}\right]. \tag{2.33}$$

Here, the lower limit for the centre-of-mass energy squared of the partonic $2\to 2$ scattering, $s_{\min}$ is a parameter, and the corresponding upper limit can be conveniently set to the hadronic centre-of-mass energy squared, $s_{\max} = S = E_{\text{cm}}^2$. The parameter $s_{\min}$ is fixed by equating this cross section with the one obtained from the eikonal,

$$\sigma_{\text{inel}}^{(ik)}(Y) \;=\; \sigma_{\text{inel}}^{ik}(s_{\min})\,, \tag{2.34}$$

and therefore depends on the Good–Walker eigenstates. The exponent η_{ik} is given by the product of Δ and $\mathscr{W}_{\text{abs}}$ for the given combination of i and k. It is interesting to note that this typically reduces the bare pomeron intercept $\Delta \approx 0.3$ to $\eta \approx 0.1$, in remarking agreement with parametrisations of the pomeron, e.g. in [36].

2.7.2.2 Infrared–continued parton density functions and strong coupling

In order to also capture the dominant non–perturbative parts of the cross section, the PDFs in the SHRiMPS model are continued into the infrared region, allowing $\mu_F = 0$ to be set in the calculation of the cross section above. In the SHRiMPS model, the basic assumption is that at $\mu_F = 0$ only valence components of the proton exist, where the valence gluon distribution follows in shape the valence quarks. The transition between the perturbative regime and the non–perturbative extension is smooth: starting from an IR–cut parameter $Q_{\text{cut}} \approx 2\,\text{GeV}$, the sea components of the PDFs are phased out linearly with μ_F^2 such that

$$f_{\text{sea}/h_1}(x,\mu_F^2) = \begin{cases} f_{\text{sea}/h_1}(x,\mu_F^2) & \text{for} \quad \mu_F \geq Q_{\text{cut}} \\ \frac{\mu_F^2}{Q_{\text{cut}}^2}\, f_{\text{sea}/h_1}(x,Q_{\text{cut}}^2) & \text{for} \quad \mu_F < Q_{\text{cut}}\,, \end{cases} \tag{2.35}$$

while the quark valence distributions behave as

$$f_{q_{\text{val}}/h_1}(x,\mu_F^2) \;=\; f_{q_{\text{val}}/h_1}(x,\max\{\mu_F^2,Q_{\text{cut}}^2\})\,. \tag{2.36}$$

The valence gluon component is normalised such that the momentum sum rule is satisfied.

For each individual partonic $2\to 2$–scattering, a gluon t–channel exchange is assumed; incoming flavours and kinematics are selected according to (2.33), and the outgoing partons are supplemented with a transverse momentum according to the form factors of (2.29). These initial configurations serve as starting points for further gluon emissions off the t–channel gluon. The strong coupling which appears in the additional radiation off the t–channel gluon is infrared continued, as

$$\bar{\alpha}_S(\mu^2) \;=\; \alpha_S(\mu^2+q_0^2) \tag{2.37}$$

with q_0^2 being $\mathscr{O}\left(1\ \text{GeV}^2\right)$.

2.7.2.3 *Building gluon ladders*

The $2 \to 2$–scattering provides the starting point of further emissions and defines an active rapidity interval $[y_{i-1}, y_{i+1}]$ for them. However, at this point the model includes a diffractive component by allowing the t–channel gluon to either be in an octet state or to be re–interpreted as a colour singlet, a pomeron. Phrased differently, a decision is to be made as to whether the exchange corresponds to a cut pomeron or not, which is thereby related to the absorption part of the evolution equation. This choice is achieved probabilistically, based on the parton densities. The corresponding weights for singlet or octet exchange along the active interval is given by

$$\begin{aligned} \mathscr{W}_1 &= \left[1 - \exp\left(-\frac{1}{2}\lambda^2 \frac{\Omega_{i(k)}(y_{i+1}) - \Omega_{i(k)}(y_{i-1})}{\Omega_{i(k)}(y_{i-1})}\right)\right]^2 \\ \mathscr{W}_8 &= 1 - \exp\left(-\lambda^2 \frac{\Omega_{i(k)}(y_{i+1}) - \Omega_{i(k)}(y_{i-1})}{\Omega_{i(k)}(y_{i-1})}\right), \end{aligned} \tag{2.38}$$

following the logic already encoded in the expressions for the elastic and inelastic cross sections, c.f. (2.26). Of course, if the active rapidity interval is associated with a singlet exchange, no further emissions will happen off this part of the ladder.

The additional emission off the t–channel are driven by a Sudakov form factor–like structure, $\Delta(y_{i-1}, y_{i+1})$, which yields the probability for no emission in the active rapidity interval,

$$\Delta(y_{i-1}, y_{i+1}) = \exp\left\{-\int_{y_{i-1}}^{y_{i+1}} \mathrm{d}y_i \int \frac{\mathrm{d}k_{\perp,i}^2}{k_{\perp,i}^2 + Q_0^2(y_i)} \frac{C_A \bar{\alpha}_S(k_{\perp,i}^2)}{\pi} \mathscr{W}_{\mathrm{abs}}(y_i)\right\}. \tag{2.39}$$

The IR regulator Q_0^2 appearing in the equation above, guaranteeing the convergence of the integration over the transverse momentum of the emitted gluon, $k_{\perp,i}$ scales with the parton densities as

$$Q_0^2(y_i) = \frac{\lambda q_0^2}{\left(\frac{\Omega_{i(k)}(-Y, b_\perp^{(1)}, b_\perp^{(2)})}{\Omega_{i(k)}(y, b_\perp^{(1)}, b_\perp^{(2)})}\right)^2 + \left(\frac{\Omega_{(i)k}(Y, b_\perp^{(1)}, b_\perp^{(2)})}{\Omega_{(i)k}(y, b_\perp^{(1)}, b_\perp^{(2)})}\right)^2}, \tag{2.40}$$

where λ is introduced in (2.31). In other words, the denser the parton soup at the emission rapidity, the more transverse momentum the emitted gluon must have in order not to be absorbed. However, after each emission, the available rapidity interval shrinks, with y_i replacing y_{i-1}. Some example ladder types are exhibited in Figure 2.6. Each ladder is finally reweighted in such a way that its hardest interaction follows a rough estimate of perturbative QCD cross sections.

2.7.2.4 *Rescattering*

Another important aspect of the model is that it allows the rescattering of partons produced at the same position in impact parameter space, giving rise to a cascade of further ladders and potentially mixing the offsprings of different such ladders, as exemplified in Figure 2.7. In the SHRiMPS model, the rescattering appears probabilistically, with a rescattering probability between two partons i and j given by

$$\mathscr{P}_{\mathrm{resc}}(y_i, y_j) = \frac{1}{N_{\mathrm{resc}}!} \left(\frac{s_{ij}}{\max\{s_{ij}, s_{\min}\}}\right)^\eta \mathscr{W}_8, \tag{2.41}$$

where N_{resc} counts the number of rescatters that already happened before arriving at this pair of partons.

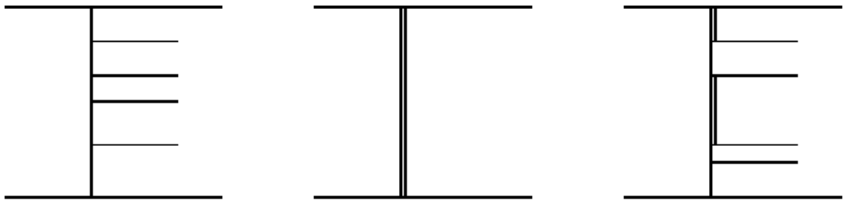

Fig. 2.6: Ladders with different colour topologies: one with only octet propagators (left), a pure singlet exchange (middle), and a ladder with both singlet and octet exchanges (right). Octet propagators are denoted by single, singlets by double lines.

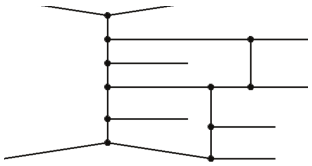

Fig. 2.7: Rescattering of partons off a primary ladder and the subsequent secondaries. In the SHRiMPS model they are all located at the same position in impact parameter space, and the rescatter probability is given by the parton densities.

2.7.3 The link to hadrons

The emerging parton ensemble undergoes further (collinear) parton showering; in the SHERPA event generator [84, 85] this is achieved through the native parton shower based on Catani–Seymour subtraction kernels [86, 87] with suitably defined starting conditions (avoiding double counting), typically given by the relative transverse momentum the partons have w.r.t. their colour partner. After the generation of all ladders and parton showering but before hadronization, colour is re–arranged through a colour reconnection model. The transition to hadrons is facilitated through SHERPA's cluster fragmentation model, in the spirit of [88], and supplemented with the intrinsic modelling of hadron decays, QED final state radiation etc.

2.7.4 Selected predictions

The parameters entering the eikonal (Eq. 2.30 and 2.32) are constrained by the total, inelastic and elastic as well as the differential elastic cross sections. The version of the KMR model forming the basis of the SHRiMPS model can be seen to yield a decent description of these quantities at various beam energies (Fig. 2.8).

The charged hadron transverse momentum distribution in minimum bias events (i.e. requiring at least two charged particles with $p_\perp > 100\,\text{MeV}$ within the detector acceptance) in SHRiMPS is compared to experimental data in the left panel of Fig. 2.9. In contrast to the very global observables of the minimum bias measurements, the underlying event observables study the correlation between soft and hard components of the event. An example can be seen in the right panel of Fig. 2.9, namely the charged particle density in the region transverse (in azimuthal angle, $60^\circ < |\Delta\phi| < 120^\circ$) to the hardest track in the event. This region is considered to be mainly populated by the interactions of partons not involved in the hard process.

Overall, SHRiMPS is in reasonable agreement with a variety of different measurements.

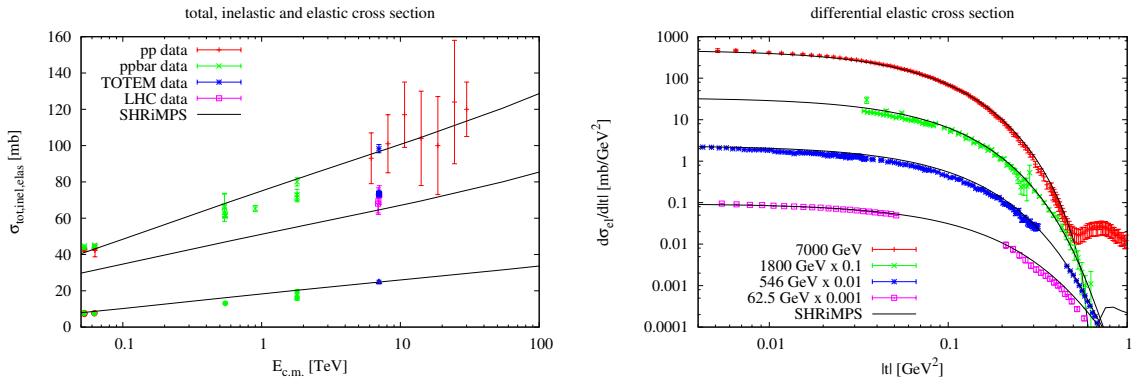

Fig. 2.8: **LHS:** Total, inelastic and elastic cross section compared data from $p+p$ and $p+\bar{p}$ collisions [89] and LHC data from TOTEM [90], ATLAS [91], CMS [92] and ALICE [93]. **RHS:** Differential elastic cross section compared to data from the LHC [94,95], the ISR [96,97], the SPS [98–100] and Tevatron [101,102].

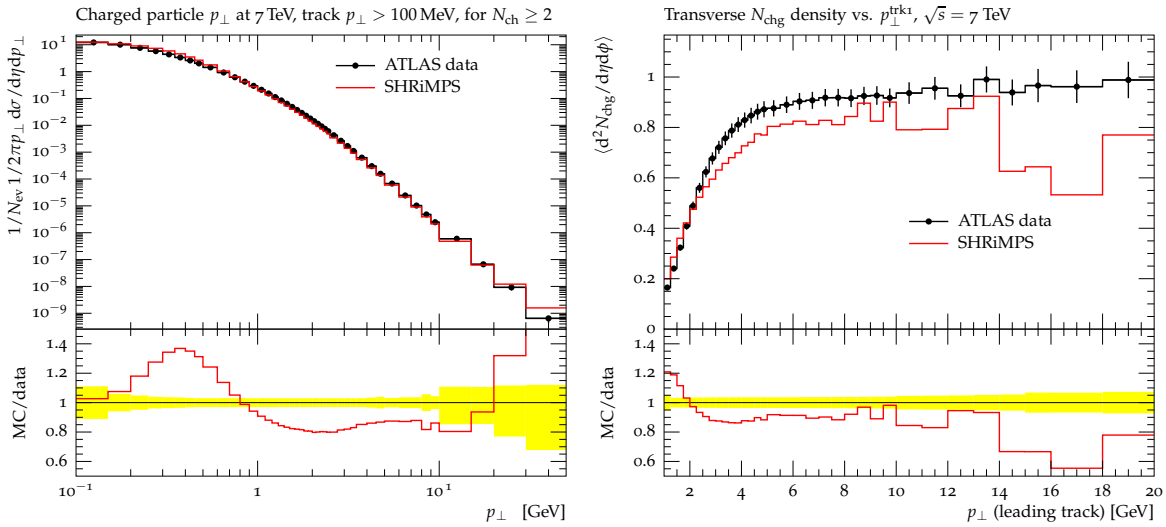
Charged particle p⊥ at 7 TeV, track p⊥ > 100 MeV, for N_ch ≥ 2
ATLAS data
SHRiMPS
1/N_ev 1/2πp⊥ dσ/dηdp⊥
MC/data
p⊥ [GeV]
Transverse N_chg density vs. p_⊥^trk1, √s = 7 TeV
⟨d²N_chg/dηdφ⟩
p⊥ (leading track) [GeV]

Fig. 2.9: **LHS:** Charged particle transverse momentum spectrum as an example for minimum bias observables measured by ATLAS [103] at $\sqrt{s} = 7\,\text{TeV}$ requiring at least two charged particles with $p_\perp > 100\,\text{MeV}$ within the acceptance; **RHS:** Charged particle density in the transverse region as example for underlying event observables measured by ATLAS [104] at $\sqrt{s} = 7\,\text{TeV}$ for $p_\perp > 500\,\text{MeV}$.

2.7.5 Summary and outlook

The SHRiMPS model aims at describing minimum bias QCD interactions in hadronic collisions, and in particular at the LHC. Starting from the inclusive model of Khoze, Martin, and Ryskin [81, 82], it adds an interpretation of this fairly inclusive interaction picture in terms of an exclusive partonic language, fit for implementation in a MC event generator, which in turn would take care of subsequent parton showering, i.e. a DGLAP evolution for the fragmentation of the hard partons, and the hadronization. This has been realised through an implementation as a new module, the SHRiMPS module, of the multi–purpose MC event generator SHERPA; somewhat in parallel the ideas of this implementation also form the base of the more theory–driven considerations of [105]

2.8 Dime

The Dime MC is an event generator [106] for meson pair CEP, proceeding via the double reggeon exchange mechanism of the type show in Fig. 5.7. In this 'one–meson exchange' model (see for instance [107–109]) the mesons are produced via pomeron–pomeron fusion, with an intermediate off–shell meson exchanged in the t–channel. The CEP cross section is given by

$$\sigma^{CEP} = \frac{1}{16\pi(16\pi^2)^2}\int dp_{1\perp}^2 dp_{2\perp}^2 dy_3 dy_4 dk_\perp^2 \frac{|\mathscr{M}|^2}{s^2}\,, \tag{2.42}$$

where $\sqrt{s}$ is the c.m.s. energy, $p_{1\perp}, p_{2\perp}$ are transverse momenta of the outgoing protons, $k_\perp$ is the meson transverse momentum and $y_{3,4}$ are the meson rapidities. Ignoring secondary reggeon contributions and soft survival effects for simplicity (these will be discussed below), the production amplitude, $\mathscr{M}$, is given by the sum $\mathscr{M} = \mathscr{M}_{\hat{t}} + \mathscr{M}_{\hat{u}}$ of the t and u–channel contributions, with $\hat{t} = (P_1 - k_3)^2$, $\hat{u} = (P_1 - k_4)^2$, where P_i is the momentum transfer through pomeron i, and $k_{3,4}$ are the meson momenta. We have

$$\mathscr{M}_{\hat{t}} = \frac{1}{M^2 - \hat{t}} F_p(p_{1\perp}^2) F_p(p_{2\perp}^2) F_M^2(\hat{t}) \sigma_0^2 \left(\frac{\hat{s}_{13}}{s_0}\right)^{\alpha_{I\!P}(p_{1\perp}^2)} \left(\frac{\hat{s}_{24}}{s_0}\right)^{\alpha_{I\!P}(p_{2\perp}^2)}\,, \tag{2.43}$$

where M is the meson mass, $s_0 = 1\,\text{GeV}^2$ and $\alpha_{I\!P}(p_{i\perp}^2) = 1.08 - 0.25\,p_{i\perp}^2$, for $p_{i\perp}^2$ measured in GeV^2 [36], and $s_{ij} = (p_i' + k_j)^2$ is the c.m.s. energy squared of the final–state proton–meson system (ij). The proton form factors are often taken for simplicity to have an exponential form, $F_p(t_i) = \exp(B_i t_i/2)$, although as in [110] a slightly different parameterization is taken here.

We can see from (2.43) that the cross section normalisation is set by the total meson–proton cross section $\sigma_{\text{tot}}(Mp) = \sigma_0 (s_{ij}/s_0)^{\alpha(0)-1}$ at the relevant sub–energy; the factor σ_0 can be extracted for example from the fits of [36]. While this is therefore well constrained for the cases of $\pi\pi$ and KK production, there remain other elements and possible additions to the model, which are in general less constrained by the available data. These are: the form factor $F_M(\hat{t})$ in (2.43) of the pomeron coupling to the off–shell meson, the possibility to produce additional particles in the pomeron fusion subprocess, and the effect of Reggeization of the meson exchange in the t–channel.

In Dime three different choices for the form factor $F_M(\hat{t})$ can be chosen, an exponential ($\sim \exp(b_{\text{exp}} t)$, an 'Orear–like' form ($\sim \exp(b_{\text{or}}\sqrt{-t})$) and a power–like form ($\sim 1/(1 - t/b_{\text{pow}})$), with the parameters fitted to ISR data on $\pi^+\pi^-$ CEP [111]. Any possible effect of meson Reggeization is currently omitted from the MC, as it is not clear that this effect will be important in the relevant kinematic regime, when the mesons are produced relatively centrally, without a large separation in rapidity between them. A simple phenomenological model is used for the possibility to produce additional particles in the pomeron fusion subprocess that would ruin the exclusivity of the event; this may be turned off or on in the MC. Finally soft survival effects are included using the approach of [110]; all four model implementations described there are included in the MC. It is important to emphasise that a full treatment of the survival factor is given in the MC: it is included at the amplitude level, accounting for the differential dependence of the survival factor on the particle kinematics, rather than simply applying an overall multiplicative factor. For further discussion of these issues and description of the MC, see [106].

Currently, the Dime MC implements $\pi^+\pi^-$, K^+K^-, $\pi^0\pi^0$, K^0K^0 and $\rho_0(770)\rho_0(770)$ production. In the $\rho_0\rho_0$ case the mesons are decayed via $\rho_0 \to \pi^+\pi^-$, including the finite ρ_0

width, according to phase space only[3], while the factor σ_0 in (2.43) is set by default to the reasonable estimate $\sigma_0^{I\!P} = 10\,\text{mb}$, i.e. of order the $\pi^+\pi^-$ cross section, but taking a lower value due the larger ρ_0 mass. This somewhat arbitrary input is necessary due to the lack of $\rho_0 p$ scattering data with which to set the normalization (another reasonable choice may be to take $\sigma_0^{I\!P}$ =13.63 mb as in $\pi^{\pm} p$ scattering [36]). For $\rho_0\rho_0$ production, secondary reggeons are not included and any spin effects are currently ignored in the production subprocess. Given the relative uncertainty in the $\rho_0\rho_0$ cross section normalisation, any effect from additional particle production is currently omitted, although this could in principle be included in the future.

2.9 ExHuME

The Exclusive Hadronic MC Event (ExHuME) generator [112] produces events for CEP processes. It is based on the 'Durham' model described in Section 5.3.1 but with some simplifying assumptions. The starting point is to write the CEP cross section for the production of system X of invariant mass M_X and rapidity y_X in the factorized form

$$\sigma = \mathscr{L}\left(M_X^2, y_X\right)\hat{\sigma}\left(M^2\right) \tag{2.44}$$

where $\hat{\sigma}$ is the subprocess cross section, which is written in terms of a colour averaged amplitude (5.2), see e.g. [5, 114] for more details. The factor $\mathscr{L}$ corresponds to the effective luminosity for producing the system X, and is written as (see also (5.1))

$$M_X^2\frac{\partial\mathscr{L}}{\partial y_X \partial M_X^2 \partial t_1 \partial t_2} = \left\langle S^2\right\rangle F_p(t_1)F_p(t_2)\left(\frac{\pi}{N_C^2-1}\int\frac{\mathrm{d}\mathbf{Q}_\perp^2}{\mathbf{Q}_\perp^4} f_g(x_1,x_1',Q_1^2,\mu^2) f_g(x_2,x_2',Q_2^2,\mu^2)\right)^2, \tag{2.45}$$

where the $F_p(t_i)$ are the elastic proton form factors, for momentum transfer $t_i \approx -\mathbf{p}_{i\perp}^2$, and are taken to have a simple exponential form. The f_g's in (5.1) are the skewed unintegrated gluon densities of the proton, described in Section 5.3.1. The factor $\left\langle S^2\right\rangle$ is the *average* survival factor, which is taken to have a constant value.

ExHuME generates events for the CEP of a Standard Model Higgs boson, via the $gg \to H$ subprocess, and dijet and diphoton production, via the $gg \to gg$, $gg \to q\bar{q}$ and $gg \to \gamma\gamma$ subprocesses, respectively. However, it should be noted that certain simplifying assumptions that have been made in this MC, and in the FPMC generator discussed in Section 2.10 which uses a similar framework, are not always reliable. In particular, as discussed in Section 5.3.2 the soft survival factor is not constant, but rather will depend on and effect the distribution in the proton transverse momenta $\mathbf{p}_\perp$. Moreover, the factorization of (2.44) only holds if the effect of any non–zero proton $\mathbf{p}_\perp$ inside the hard process matrix element is neglected. That is, it only includes a $J_z^P = 0^+$ component, with $q_{1_\perp} = q_{2_\perp} = -Q_\perp$ taken when calculating $\hat{\sigma}$. For some processes, such as $\chi_{c(1,2)}$ production [115] this can be a very bad approximation. Thus, in such situations as when the $J_z^P = 0^+$ component is not necessarily dominant and/or the protons are tagged, these approximations may be very bad indeed. Conversely, if the $J_z^P = 0^+$ component is indeed strongly dominant, and/or the proton transverse momenta are simply integrated over, these simplifications are more reliable.

[3] A more complete treatment should account for the different ρ polarization states, which may in general have distinct form factors $F_M(\hat{t})$, however given the lack of information about these such possible polarization effects are omitted in the current version of the MC.

NFLUX	Flux
9	QCD factorized model, Pomeron flux
10	QCD factorized model, Reggeon flux
12	QED flux from Cahn, Jackson; $R \sim 1.2A^{\frac{1}{3}}$
13	QED flux from Drees et al., valid for heavy ions only
14	QED flux in pp collisions, from Papageorgiou
15	QED flux in pp collisions, from Budnev et al.
16	QCD KMR flux
17	QCD factorized model, Pomeron–Reggon flux
19	QCD factorized model, Pomeron Reggeon fluxes
20	QED flux Budnev – QCD factorized model, Photon–Pomeron
21	QCD factorized model, Reggeon–Pomeron fluxes
22	QED flux Budnev – QCD factorized model, Pomeron–Photon

Table 2.3: Overview of available fluxes which are implemented in the FPMC generator. The QED flux corresponds to the photon exchange. The QCD flux corresponds to the pomeron/reggeon exchange, or to the gluon exchange in the case of the CEP predicted by the KMR calculation.

2.10 FPMC

2.10.1 Introduction

The idea of FPMC is to produce single diffraction, double pomeron exchange, exclusive diffraction and photon–induced processes within the same framework. The diffractive and exclusive processes are implemented by modifying the HERWIG routine for the $e^+e^- \to (\gamma\gamma) \to X$ process. In case of the two–photon pp events, the Weizsäcker–Williams (WWA) formula describing the photon emission off point–like electrons is substituted for the photon flux which properly describes the coupling of the photon to the proton, taking into account the proton electromagnetic structure. For central exclusive production, a look–up table of the effective gluon–gluon luminosity computed by `ExHuME` [112], see Section 2.9, is implemented. In case of pomeron/reggeon exchange, the WWA photon fluxes are replaced by the pomeron/reggeon fluxes multiplied by the diffractive parton density functions.

For processes in which the partonic structure of the pomeron is probed, the existing HERWIG matrix elements for non–diffractive production are used to calculate the production cross sections. The list of particles is corrected at the end of each event to change the type of particles from initial–state electrons to hadrons and from the exchanged photons to pomerons/reggeons, or gluons, depending on the process.

All these fluxes are implemented in the `FLUX` routine. The user selects the desired production mechanism by selecting the `NFLUX` parameter. Their overview is shown in Table 2.3. The energy which is carried by the exchanged object (photon/pomeron/reggeon/gluon) from the colliding particles is driven by the parameters `WWMIN` and `WWMAX`, representing the minimal and maximal momentum fraction loss ξ of the collided hadron.

2.10.2 Two–photon interactions

Two–photon production in pp collisions is described in the framework of the Equivalent Photon Approximation (EPA) [116]. The almost real photons (with low photon virtuality $Q^2 = -q^2$) are emitted by the incoming protons, producing an object X in the $pp \to pXp$ process, through two–photon exchange $\gamma\gamma \to X$. The precise form for the photon spectrum is given by (5.13). Integrating the product of the photon fluxes $f(E_{\gamma 1}) \cdot f(E_{\gamma 2}) \cdot \mathrm{d}E_{\gamma 1} \cdot \mathrm{d}E_{\gamma 2}$ from both protons over

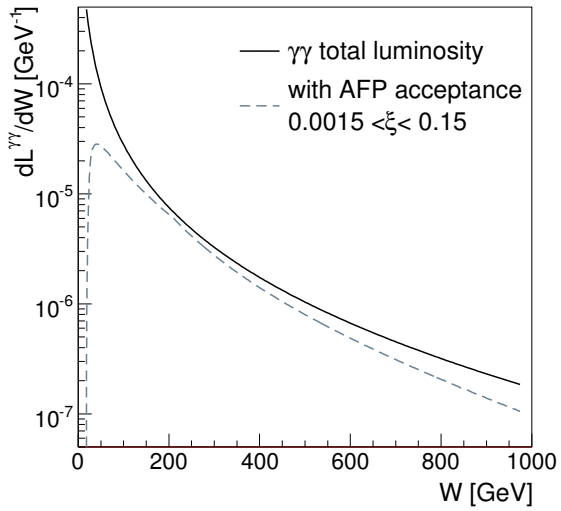

Fig. 2.10: Relative effective $\gamma\gamma$ luminosity in pp collisions at 14 TeV as a function of the two–photon invariant mass. The maximal virtualities of the emitted photons are set to $Q^2_{max} = 2$ GeV^2. The dashed curve shows the photon spectrum within the ATLAS or CMS forward detector acceptance.

the photon energies while keeping the two–photon invariant mass fixed to W, one obtains the two–photon effective luminosity spectrum $\mathrm{d}L^{\gamma\gamma}/\mathrm{d}W$.

The effective $\gamma\gamma$ luminosity is shown in Fig. 2.10 as a function of the mass W. The production of heavy objects is particularly interesting at the LHC, where new particles could be produced in a very clean environment. The production rate of massive objects is however limited by the photon luminosity at high invariant masses. The integrated two–photon luminosity above $W > W_0$ for $W_0 = 23$ GeV, $2 \times m_W \approx 160$ GeV, and 1 TeV is 1%, 0.15% and 0.007%, respectively, of the luminosity integrated over the whole mass spectrum. The luminosity spectrum for $0.0015 < \xi < 0.15$ is also shown in the figure (calculated in the limit of low Q^2, thus setting $E_\gamma = \xi E$).

Using the effective relative photon luminosity $\mathrm{d}L^{\gamma\gamma}/\mathrm{d}W$, the total cross section reads

$$\frac{\mathrm{d}\sigma}{\mathrm{d}\Omega} = \int \frac{\mathrm{d}\sigma_{\gamma\gamma\to X}(W)}{\mathrm{d}\Omega} \frac{\mathrm{d}L^{\gamma\gamma}}{\mathrm{d}W} \mathrm{d}W \tag{2.46}$$

where $\mathrm{d}\sigma_{\gamma\gamma\to X}/\mathrm{d}\Omega$ denotes the differential cross section of the sub–process $\gamma\gamma \to X$, dependent on the invariant mass of the two–photon system.

In FPMC, the formula (2.46) is implemented in the routine FLUX. It is normalized by the beam energy and is actually dimensionless, parameterized by the momentum fraction loss of the proton $\xi = E_\gamma/E$.

Many photon–induced processes have been implemented in FPMC, namely:

- dilepton production
- standard model $\gamma\gamma$ production including lepton, quark and W loops
- anomalous quartic coupling production of WW, ZZ and $\gamma\gamma$
- anomalous trilinear production of WW and ZZ
- SM Higgs boson production

Fit parameter	Fit A	Fit B
$\alpha_P(0)$	1.118 ± 0.008	1.111 ± 0.007
n_R	$(1.7 \pm 0.4) \times 10^{-3}$	$(1.4 \pm 0.4) \times 10^{-3}$
α'_P	$0.06^{+0.19}_{-0.06}$ GeV^{-2}	
B_P	$5.5^{-2.0}_{+0.7}$ GeV^{-2}	
$\alpha_R(0)$	0.5 ± 0.10	
α'_R	$0.3^{+0.6}_{-0.3}$ GeV^{-2}	
B_R	$1.6^{-1.6}_{+0.4}$ GeV^{-2}	

Table 2.4: Diffractive structure function parameters of QCD Fit A and Fit B fits [32]. These structure functions are used as defaults in FPMC.

IFIT	**PDF set**	Source
10	H1 (old)	[117]
20	Zeus (old)	[117]
30	combined H1 and Zeus (old)	[117]
100	H1 Fit B	[32]
101	H1 Fit A	[32]

Table 2.5: Implemented diffractive parton density functions in FPMC. The most recent are the H1 Fits A and Fit B IFIT=101, 100.

2.10.3 Implementation of pomeron and reggeon exchanges in inclusive diffraction

Diffractive parton density functions (DPDF) were measured at HERA. The outcome of the fits are the values of the pomeron and reggeon trajectories $\alpha_{I\!P}(t) = \alpha_{I\!P}(0) + \alpha'_{I\!P}$t, $\alpha_{I\!R}(t) = \alpha_{I\!R}(0) + \alpha'_{I\!R}$t governing the corresponding flux energy dependence, and the pomeron/reggeon parton distribution functions $f_{P/p}(\beta, Q^2)$, $f_{R/p}(\beta, Q^2)$. Only the normalization of the product of the diffractive structure function $f_i^D(x, Q^2, x_P, t)$ and of the pomeron/reggeon flux is fixed by the QCD fits. Therefore, the normalization of the fluxes is conventionally fixed at $x_P = x_R = 0.003$ such that

$$x_P \int_{t_{\rm cut}}^{t_{\rm min}} f_{P/p}\, {\rm d}t = 1 \tag{2.47}$$

where $|t_{\rm min}| \simeq m_p^2 x_P^2/(1-x_P)$ is the minimum kinematically accessible value of $|t|$, m_p is the proton mass and $|t_{\rm cut}| = 1.0$ GeV^2. The normalization of the reggeon flux is defined in the same way.

The pomeron and reggeon parameters obtained in the most recent H1 QCD fits are shown in Table 2.4. The implemented diffractive parton densities are summarized in Table 2.5 and can be selected with the IFIT parameter. The flux parameters are fixed in the routine HWMODINI where the initial parameters are set. The parton densities are used in the routine HWSFUN where the call to the H1 tables (the source code can be found at [32]) is made.

Predictions for the single diffractive and double pomeron exchange dijet cross sections for various jet p_T thresholds are summarized in Table 2.6. They are given assuming pomeron exchange only, since the contribution from sub–leading exchanges is found to be negligible at the LHC. Similarly, the single diffractive W and Z production cross sections are shown in Table 2.7. All numbers are calculated with the H1 Fit B parton density functions, with a cut on the maximum momentum fraction loss of the proton $\xi_{max} = 0.1$. The rates are not corrected for the survival probability which is expected to be 0.06 at the LHC [118].

$\sqrt{s} = 1.96$ TeV

PTMIN [GeV]	SD dijets [pb]	DPE dijets [pb]
10GeV	$180 \cdot 10^5$	$429 \cdot 10^3$
15GeV	$29 \cdot 10^5$	$42 \cdot 10^3$
25GeV	$23 \cdot 10^5$	$1.3 \cdot 10^3$

$\sqrt{s} = 14$ TeV

PTMIN [GeV]	SD dijets [pb]	DPE dijets [pb]
15GeV	$107 \cdot 10^6$	$5.2 \cdot 10^6$
25GeV	$14 \cdot 10^6$	$5.4 \cdot 10^5$
35GeV	$3.5 \cdot 10^6$	$1.1 \cdot 10^5$

Table 2.6: Single diffractive and double pomeron exchange dijet cross sections for various thresholds at the Tevatron and the LHC. No survival probability factor, which is expected to be approximately 0.06, is applied.

process	$\sqrt{s} = 1.96$ TeV	$\sqrt{s} = 14$ TeV	
$W \to$ anything+Gap	468 pb	9570 pb	IPROC=11499
$Z/\gamma \to$ anything+Gap	640 pb	6292 pb	IPROC=11399
Flags: TYPEPR='INC', TYPINT='QCD', PART1='P', PART2='E+', WWMAX=.1			

Table 2.7: Total single diffractive production cross section of W and Z/γ bosons at $\sqrt{s} = 14$ TeV. No survival probability factor, which is expected to be 0.06, was applied.

Recently, jet–gap–jet events were also implemented in DPE following the Mueller–Tang formalism [119].

2.10.4 Implementation of exclusive production

The implementation of central exclusive Higgs and dijet productions is not done in terms of a flux, as in the cases discussed above, but rather in terms of the effective gluon–gluon luminosity. The calculation of the effective gluon–gluon luminosity in exclusive events [5] is available in the ExHuME generator, see Section 2.9. It is convenient to study the forward processes in the same framework with the same hadronization model. We therefore adopted the ExHuME calculation of the gluon–gluon luminosity in FPMC.

CEP is implemented by means of look–up tables of the gluon–gluon luminosity calculated by ExHuME (Lumi()routine) as a function of the momentum fraction losses of the scattered protons ξ_1, ξ_2. It is evaluated and added to the event weight after generation of both of ξ_1, ξ_2. The rest of the event is then generated with the $gg \to q\bar{q}, gg, H$ matrix elements respecting the $J_z = 0$ selection rule. The effective gluon–gluon luminosity included in FPMC and the one calculated by ExHuME (v1.3.3) are in good agreement.

2.11 STARLIGHT

STARLIGHT is a MC event generator for electromagnetic interactions in nucleus-nucleus, proton-nucleus, and proton-proton collisions [120]. Simulations are performed for ultra-peripheral collisions, where the nuclei/protons are separated by impact parameters larger than the sum of their radii. In these collisions, purely hadronic interactions are strongly suppressed while the cross sections for electromagnetic interactions remain large [9, 122]. Two-photon and photonuclear/photon-proton interactions are included in the model. The main focus is on ex-

clusive particle production where the nuclei remain intact, $A+A \to A+A+X$, but general photonuclear interactions $\gamma+A \to X$ are included through an interface to the DPMJET MC. The model is primarily developed for interactions at high energy colliders such as RHIC, the Tevatron, and the LHC.

The electromagnetic field is treated as an equivalent flux of photons, and the photon spectrum is calculated in impact parameter space. Working in impact parameter space is preferable when dealing with hadronic beams, since it provides the clearest way to suppress interactions where the beams interact hadronically. In simple terms, this means that interactions with impact parameters $b < R_1 + R_2$ have to be excluded ($R_{1,2}$ are the nuclear radii). In STARLIGHT, the exclusion of hadronic interactions is done through a calculation of the hadronic interaction probability using the Glauber model.

The dominating exclusive particle production mechanism in high-energy nucleus-nucleus collisions is photonuclear vector meson production [14]. In these interactions, the photon fluctuates to a vector meson, which becomes real by scattering "elastically" off the target nucleus. For momentum transfers $|t| < (1/R)^2$, the vector meson couples coherently to all nucleons in the target and the cross section is enhanced. For larger momentum transfers, the vector meson may scatter quasi-elastically off a single nucleon. Coherent and incoherent photonuclear production of the ρ^0, ω, ϕ, J/ψ, $\psi(2S)$, and $\Upsilon(1S, 2S, 3S)$ vector mesons are included in STARLIGHT. In all cases, including asymmetric systems such as proton-nucleus collisions, either projectile can act as photon emitter or target.

The photonuclear vector meson production cross section is calculated from the corresponding $\gamma + p \to V + p$ cross section using the Glauber model. The photon-proton cross section is obtained from phenomenological fits to data, mostly from the electron-proton collider HERA. Interference between the two photon emitter and target configurations will modify the transverse momentum spectrum at low momenta [124]. This interference may be optionally included.

STARLIGHT also includes two-photon production of single pseudo-scalar and tensor mesons as well as dilepton pairs [125]. The total cross section is obtained by convoluting the photon spectra from the two beams with the two-photon cross section, $\sigma(\gamma\gamma \to X)$, under the requirement that there should be no accompanying hadronic interaction in the same event. For single meson production, $\sigma(\gamma\gamma \to M)$ is proportional to the two-photon decay width, $\Gamma_{\gamma\gamma}$, while for dilepton pair production the Breit–Wheeler cross section $\sigma(\gamma\gamma \to l^+l^-)$ is calculable from lowest order QED. Both for two-photon and photonuclear production of single mesons, the decay into two charged daughter particles is simulated taking into account the effects of polarization on the decay angle for mesons with $J > 0$.

In collisions of truly heavy ions (e.g. Au at RHIC or Pb at the LHC), the probabilities of exchanging multiple photons in a single event is high [15]. These additional photons typically have low energy but can lead to the breakup of one or both nuclei. Two-photon and photonuclear particle production can be simulated in STARLIGHT for various breakup scenarios of one or both beam nuclei.

General photonuclear interactions $\gamma+A \to X$ can be simulated with the DPMJET model [13]. STARLIGHT includes an interface to run DPMJET with photon spectra appropriate for heavy-ion beams. Emission of a photon from one or both nuclei in the same event can be simulated, with photon spectra calculated as described in [127].

STARLIGHT has been found to give a good description of two-photon production of dilepton pairs in heavy-ion collisions at RHIC [53, 128] and the LHC [69, 130]. Exclusive photonuclear production of ρ^0 mesons in heavy-ion collisions [63, 69, 133] and J/ψ mesons

in $pp/p\overline{p}$ collisions [134, 135] are also well reproduced. The cross section for photonuclear J/ψ production at the LHC is found to be overestimated, presumably because nuclear gluon shadowing is not included in the model [130].

2.12 SuperChic

2.12.1 Version 1

The original version of SuperChic was designed to generate events for the CEP of $\chi_{c,b}$ and $\eta_{c,b}$ quarkonia, as described in [114, 115]. Rather than integrating (5.1) directly, with the dependence on the outgoing proton $\mathbf{p}_\perp$ included inside the integral, an expansion was performed, so that for small proton $\mathbf{p}_\perp$, the χ_{c0} amplitude may for example be written as

$$\begin{aligned} T_0 &\propto \int \frac{\mathrm{d}^2 Q_\perp (\mathbf{q}_{1_\perp}\cdot\mathbf{q}_{2_\perp})}{Q_\perp^2 \mathbf{q}_1^2 \mathbf{q}_2^2} f_g(x_1,x_1',Q_1^2,\mu^2) f_g(x_2,x_2',Q_2^2,\mu^2) \\ &\approx C_0 + C_1(\mathbf{p}_{1_\perp}^2 + \mathbf{p}_{2_\perp}^2) + C_{12}(\mathbf{p}_{1_\perp}\cdot\mathbf{p}_{2_\perp}) + \cdots . \end{aligned} \tag{2.48}$$

Squaring (2.48) and keeping only the leading terms in $p_{i_\perp}^2$, we can see that this expansion is equivalent to making the replacement (at lowest order in $p_{i_\perp}^2$)

$$e^{-b\mathbf{p}_{i_\perp}^2} \to e^{-(b-2\frac{C_1}{C_0})\mathbf{p}_{i_\perp}^2} . \tag{2.49}$$

Thus to a first approximation we expect the inclusion of non–zero $p_\perp$ in the amplitude calculation to simply result in a change in the effective slope of the proton form factor. This approach may be readily extended to the higher spin $\chi_{1,2}$ and odd-parity η states, see [115]. This allows a more precise inclusion of non–zero proton $\mathbf{p}_\perp$ effects than is given by simply assuming the forward proton limit when calculating the subprocess matrix element (an assumption that would moreover give a vanishing cross section for the $\chi_{1,2}$ and η states). The decay $\chi_c \to J/\psi\gamma \to \mu^+\mu^-\gamma$ is also included in the MC, including full spin correlations, see [115]. This MC treatment was subsequently extended to include $\gamma\gamma$ [114] and meson pair ($\pi\pi$, KK, $\rho\rho$, $\eta(')\eta(')$) CEP within the approach of [136, 137].

In addition, SuperChic models the photoproduction process of C–odd vector mesons (J/ψ, $\Upsilon(1S)$, $\psi(2S)$). The cross sections are normalised using a fit to HERA data [43]

$$\frac{\mathrm{d}\sigma(\gamma^* p \to X + p)}{\mathrm{d}\mathbf{p}_{2\perp}^2} = \frac{N}{b}\left(\frac{W}{1\mathrm{GeV}}\right)^\delta e^{-b\mathbf{p}_{2\perp}^2} , \tag{2.50}$$

with $\delta = 0.72$, $N = 3$ nb in the case of J/ψ production, while for $\Upsilon(1S)$ production the fit of [139] is taken, which gives $\delta = 1.63$ and $N = 0.12$ pb. In the case of $\psi(2S)$, the same value of $\delta = 0.72$ as for the J/ψ is taken, with $N = 0.498$ nb: any difference in the energy scaling cannot be reliably determined from the limited statistics HERA data [140]. The photon flux is given as in [141], while a simplified form for the survival factor, as in [142], is used. A Regge scaling behaviour is taken for the slope b, with

$$b = b_0 + 4\alpha' \log\left(\frac{W}{W_0}\right) , \tag{2.51}$$

with $b_0 = 4.6\,\mathrm{GeV}^{-2}$, $W_0 = 90$ GeV, and $\alpha' = 0.16\,\mathrm{GeV}^{-2}$. For the J/ψ and $\Upsilon(1S)$ the decay to $\mu^+\mu^-$ is included, with full spin correlations, while the $\psi(2S) \to J\psi\pi^+\pi^- \to \mu^+\mu^-\pi^+\pi^-$ is also included, distributed according to phase space. In addition, in the case of J/ψ and Υ production, the simple leading order QCD cross section is also included, as in [23], with both MSTW08 [144] and CTEQ6 [145] PDFs.

2.12.2 Version 2

An update of `SuperChic` is currently close to release, which will address some of the limitations present in the previous version. In particular, the approximation (2.49) is no longer applied: instead, the exact $p_\perp$ dependence of the matrix element is used and, significantly, soft survival effects are included at the amplitude level, that is differentially and not as an overall constant factor. In this way the influence of the survival factor on the distribution of the outgoing protons, which as discussed in Section 5.3.2 can be quite significant, is included. In addition to this, the code has been re-written to allow all elements of the Durham model (PDF choice, skewness effects, model of soft survival) to be adjusted by the user in a relatively straightforward way. Finally, the range of processes generated is increased to include 2 and 3 (quark and gluon) jet, Higgs boson and double J/ψ production, in the first instance. This project is ongoing, and further developments are planned for the future.

2.13 LHC forward measurements and MC tuning

In this section a small selection of comparison plots between LHC diffractive measurements and MC predictions are shown, in all cases made using the MCPLOTS repository [146]. These are intended to serve as an indication of the way in which already such measurements can be of great use in tuning the available MCs, with further data to come increasingly allowing a differentiation between the model inputs.

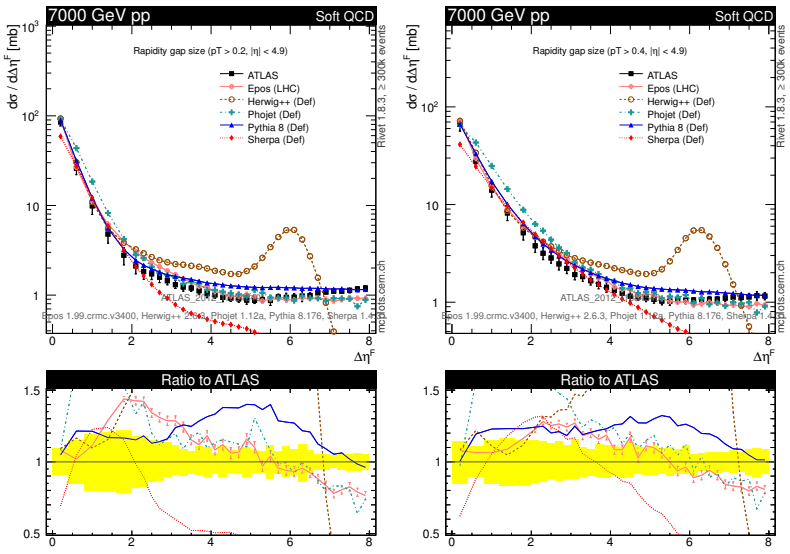

Fig. 2.11: Comparison of MC distributions with ATLAS forward rapidity gap cross section [147] at $\sqrt{s} = 7$ TeV, as a function of the gap size $\Delta\eta_F$ in which no final state particles are produced above some threshold $p_\perp^{\rm cut}$.

In Fig. 2.11 a comparison with the ATLAS forward rapidity gap cross section [147] at $\sqrt{s} = 7$ TeV, as a function of gap size, $\Delta\eta_F$, in which no final state particles are produced above a transverse momentum threshold $p_\perp^{\rm cut}$, is shown. Such data is invaluable for tuning the various input parameters of the MCs, such as the form of the pomeron flux. Overall it is clear that there is a large spread in MC predictions: Herwig++ has no explicit diffractive model, although it nevertheless generates quite large rapidity gap events, but clearly fails to describe the shape or magnitude of the data; PYTHIA tends to overestimate the data, a result which remains true for other available tunes; Sherpa clearly struggles to describe the shape and size of the data at higher η_F; EPOS (LHC re–tune) gives the best overall agreement.

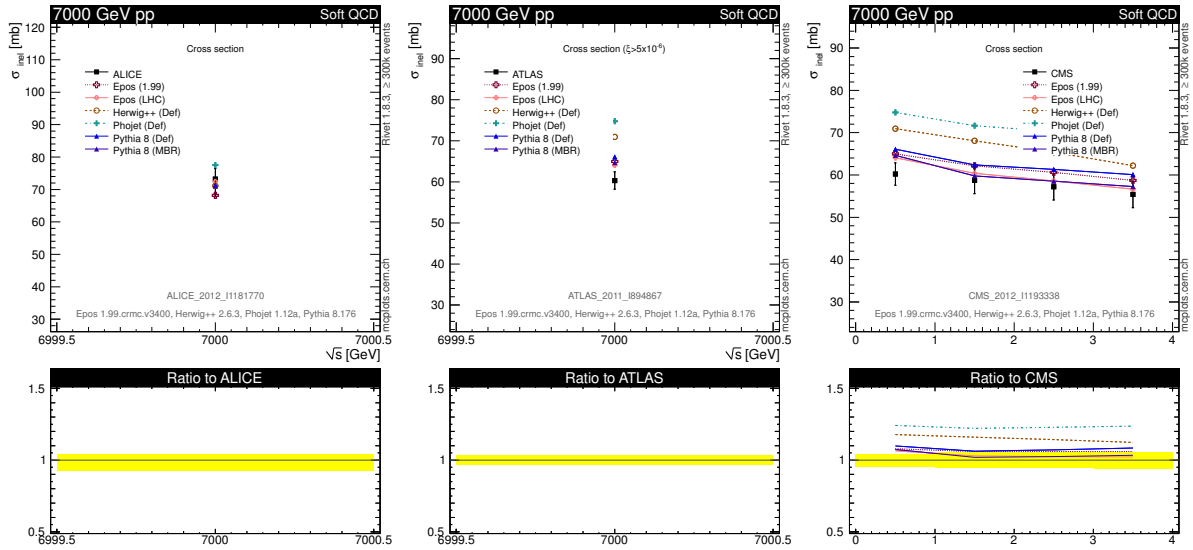

Fig. 2.12: Comparison of MC predictions with ALICE [148], ATLAS [91] and CMS [92] measurements of the inelastic cross section at $\sqrt{s} = 7$ TeV.

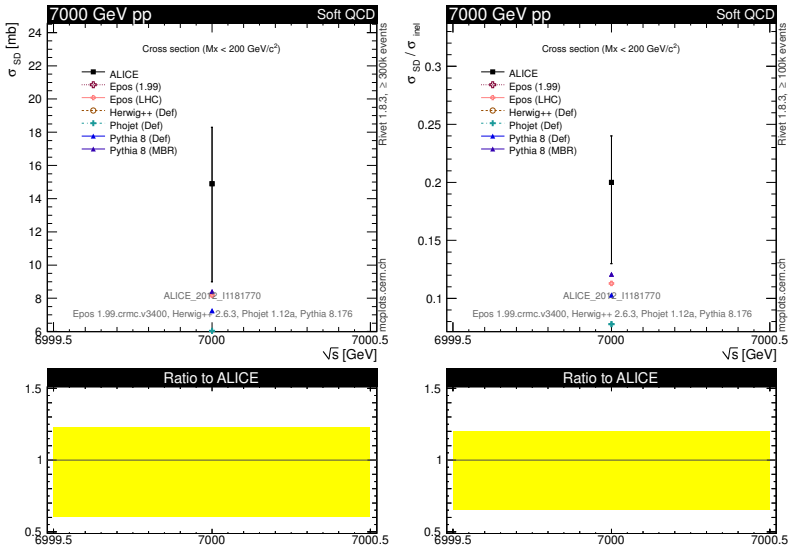

Fig. 2.13: Comparison of MC predictions to the ALICE [148] measurements of the ratios of the single–diffractive (for a diffractive mass $M_X < 200$ MeV) and double–diffractive cross sections (for a gap $\Delta\eta > 3$) to the inelastic cross section.

In Fig. 2.12 ALICE [148], ATLAS [91] and CMS [92] measurements of the inelastic cross section at $\sqrt{s} = 7$ TeV are shown. The CMS data correspond to two independent methods, one using the forward calorimeters (first bin in figure), and another using the central tracker, with requirements of there being more than one, two or three tracks with $p_\perp > 200$ MeV and $|\eta| < 2.4$; these measurements are therefore sensitive to different phase space regions. The ATLAS and CMS (calorimetry) measurements corresponds to the region $\xi = M_X^2/s > 5 \times 10^{-6}$, below which low mass diffraction is not seen within the detector acceptance, while the ALICE measurement corresponds to an extrapolation to this low M_X region. We can see that all MCs tend to overestimate the ATLAS and CMS ($\xi > 5 \times 10^{-6}$) measurements, but the agreement is better for the CMS central track–based measurement. Altogether there is broad agreement

between the MCs and data, but with higher precision measurements in the future, it will be possible to place more stringent constraints on these predictions.

Finally in Fig. 2.13 the ALICE [148] measurements of the ratios of the single–diffractive (for a diffractive mass $M_X < 200$ MeV) and double–diffractive cross sections (for a gap $\Delta\eta > 3$) to the inelastic cross section are shown. The MC predictions agree broadly within the quite large experimental uncertainties, but clearly the higher precision that will come from CMS, TOTEM and CMS+TOTEM measurements, combined with this data, will be of great use in tuning the MCs.

MC simulations are an essential part of the LHC forward physics programme, both as a means to compare the available models of diffractive physics with LHC measurements, as well as a tool to tune to hadronic data and hence provide a phenomenological description of soft QCD effects, an understanding of which is essential for wide range of high energy physics analyses, including searches for BSM physics. In addition such models are crucial in the modelling of cosmic ray physics. In this chapter a range of MC generators for diffractive and exclusive processes have been considered. A description of these MCs, which are widely used in the analyses presented in this report, as well as discussion of the possibilities for further constraints from future LHC data, have been presented.

References

[1] T. Pierog, I. .Karpenko, J. M. Katzy, E. Yatsenko and K. Werner, arXiv:1306.0121 [hep-ph].

[2] K. Werner, F. -M. Liu and T. Pierog, Phys. Rev. C **74** (2006) 044902 [hep-ph/0506232].

[3] T. Pierog and K. Werner, Nucl. Phys. Proc. Suppl. **196** (2009) 102 [arXiv:0905.1198 [hep-ph]].

[4] H. J. Drescher, M. Hladik, S. Ostapchenko, T. Pierog and K. Werner, Phys. Rept. **350** (2001) 93 [hep-ph/0007198].

[5] V. A. Abramovski, V. N. Gribov, and O. V. Kancheli, "Character of inclusive spectra and fluctuations produced in inelastic processes by multipomeron exchange," *Sov. J. Nucl. Phys.*, vol. 18, p. 308, 1974.

[6] C. Caso *et al.* [Particle Data Group Collaboration], Eur. Phys. J. C **3** (1998) 1.

[7] T. Csörgö *et al.* [TOTEM Collaboration], Prog. Theor. Phys. Suppl. **193** (2012) 180 [arXiv:1204.5689 [hep-ex]].

[8] R. Engel, "Photoproduction within the two component dual parton model: amplitudes and cross-sections," *Z. Phys.*, vol. C66, pp. 203–214, 1995.

[9] R. Engel and J. Ranft, "Hadronic photon-photon interactions at high energies," *Phys. Rev.*, vol. D54, pp. 4244–4262, 1996.

[10] S. Roesler, R. Engel, and J. Ranft, "The Monte Carlo event generator DPMJET-III." in Proc. of Int. Conf. on Advanced Monte Carlo for Radiation Physics, Particle Transport Simulation and Applications (MC 2000), Lisbon, Portugal, 23-26 Oct 2000, A. Kling, F. Barao, M. Nakagawa, L. Tavora, P. Vaz eds., Springer-Verlag Berlin, p. 1033-1038 (2001), 2000.

[11] F. W. Bopp, J. Ranft, R. Engel, and S. Roesler, "Antiparticle to Particle Production Ratios in Hadron-Hadron and d-Au Collisions in the DPMJET-III Monte Carlo," *Phys. Rev.*, vol. C77, p. 014904, 2008.

[12] F. W. Bopp, J. Ranft, R. Engel, and S. Roesler, "Learning from RHIC data with DPMJET-III," *Acta Phys. Polon.*, vol. B35, pp. 303–307, 2004.

[13] R. Engel, J. Ranft, and S. Roesler, "Photoproduction off nuclei and point-like photon interactions. I: Cross sections and nuclear shadowing," *Phys. Rev.*, vol. D55, pp. 6957–6967, 1997.

[14] S. Roesler, R. Engel, and J. Ranft, "Photoproduction off nuclei: Particle and jet production," *Phys. Rev.*, vol. D57, pp. 2889–2902, 1998.

[15] A. Capella, U. Sukhatme, C.-I. Tan, and J. Tran Thanh Van, "Dual parton model," *Phys. Rept.*, vol. 236, pp. 225–329, 1994.

[16] G. 't Hooft, "A planar diagram theory for strong interactions," *Nucl. Phys.*, vol. B72, p. 461, 1974.

[17] G. Veneziano, "Large N Expansion in Dual Models," *Phys. Lett.*, vol. B52, p. 220, 1974.

[18] A. B. Kaidalov, "Soft interactions of hadrons in QCD," *Surveys High Energ. Phys.*, vol. 13, pp. 265–330, 1999.

[19] R. Engel, "Hadronic interactions of photons at high energies," *PhD thesis, Universität Siegen (see https://web.ikp.kit.edu/engel/phojet.html)*, 1997.

[20] F. W. Bopp, D. Pertermann, R. Engel, and J. Ranft, "New parton structure functions and mini-jets in the two component dual parton model," *Phys. Rev.*, vol. D49, pp. 3236–3247, 1994.

[21] A. Moraes, C. Buttar, and I. Dawson, "Prediction for minimum bias and the underlying event at LHC energies," *Eur. Phys. J.*, vol. C50, pp. 435–466, 2007.

[22] R. Engel, M. A. Braun, C. Pajares, and J. Ranft, "Central diffraction, an important background to photon-photon collisions via heavy ion beams at LHC," *Z. Phys.*, vol. C74, pp. 687–697, 1997.

[23] A. B. Kaidalov, "Diffractive Production Mechanisms," *Phys. Rept.*, vol. 50, pp. 157–226, 1979.

[24] M. L. Good and W. D. Walker, "Diffraction disssociation of beam particles," *Phys. Rev.*, vol. 120, pp. 1857–1860, 1960.

[25] T. Sjöstrand, "A model for initial state parton showers," *Phys. Lett.*, vol. B157, p. 321, 1985.

[26] T. Sjostrand, S. Mrenna, and P. Skands, "PYTHIA 6.4 physics and manual," *JHEP*, vol. 05, p. 026, 2006.

[27] R. Engel, J. Ranft, and S. Roesler, "Hard diffraction in hadron hadron interactions and in photoproduction," *Phys. Rev.*, vol. D52, pp. 1459–1468, 1995.

[28] R. Engel and J. Ranft, "Hard diffraction and central diffraction in hadron hadron and photon hadron collisions," 1997. Proceedings of The Int. Symposium on Near Beam Physics, Fermilab, Sept. 22-24, 1997, eds. R. Carrigan and N. Mokhov, p. 12. (hep-ph/9711383).

[29] G. Ingelman and P. Schlein, "Jet Structure in High Mass Diffractive Scattering," *Phys. Lett.*, vol. B152, p. 256, 1985.

[30] B. E. Cox and J. R. Forshaw, Comput. Phys. Commun. **144** (2002) 104

[31] `http://www.pomwig.com`

[32] A. Aktas *et al.* [H1 Collaboration], Eur. Phys. J. C **48** (2006) 715

[33] S. Chatrchyan *et al.* [CMS Collaboration], Phys. Rev. D **87** (2013) 012006

[34] P. Bruni and G. Ingelman, Conf. Proc. C **930722** (1993) 595.

[35] T. Sjostrand, S. Mrenna and P. Z. Skands, Comput. Phys. Commun. **178** (2008) 852 [arXiv:0710.3820 [hep-ph]].

[36] A. Donnachie and P. V. Landshoff, Phys. Lett. B **296** (1992) 227 [hep-ph/9209205].

[37] G. A. Schuler and T. Sjostrand, Nucl. Phys. B **407** (1993) 539.
[38] G. A. Schuler and T. Sjostrand, Phys. Rev. D **49** (1994) 2257.
[39] S. Navin, arXiv:1005.3894 [hep-ph].
[40] G. Antchev *et al.* [TOTEM Collaboration], Europhys. Lett. **101** (2013) 21004.
[41] G. Antchev *et al.* [TOTEM Collaboration], Phys. Rev. Lett. **111** (2013) 1, 012001.
[42] A. Donnachie and P. V. Landshoff, Phys. Lett. B **727** (2013) 500 [arXiv:1309.1292 [hep-ph]].
[43] J. R. Cudell, K. Kang and S. K. Kim, Phys. Lett. B **395** (1997) 311 [hep-ph/9601336].
[44] R. Ciesielski and K. Goulianos, PoS ICHEP **2012** (2013) 301 [arXiv:1205.1446 [hep-ph]].
[45] M. L. Mangano, M. Moretti, F. Piccinini, R. Pittau and A. D. Polosa, JHEP **0307** (2003) 001 [hep-ph/0206293].
[46] J. Alwall, M. Herquet, F. Maltoni, O. Mattelaer and T. Stelzer, JHEP **1106** (2011) 128 [arXiv:1106.0522 [hep-ph]].
[47] T. Sjostrand and M. van Zijl, Phys. Rev. D **36** (1987) 2019.
[48] B. Andersson, Camb. Monogr. Part. Phys. Nucl. Phys. Cosmol. **7** (1997) 1.
[49] P. Skands, S. Carrazza and J. Rojo, arXiv:1404.5630 [hep-ph].
[50] H. Schulz and P. Z. Skands, Eur. Phys. J. C **71** (2011) 1644 [arXiv:1103.3649 [hep-ph]].
[51] T. Sjöstrand, arXiv:1310.8073 [hep-ph].
[52] J. R. Christiansen, T. Sjostrand and P. Z. Skands (2014)
[53] P. Z. Skands and D. Wicke, Eur. Phys. J. C **52** (2007) 133 [hep-ph/0703081 [HEP-PH]].
[54] J. Rathsman, Phys. Lett. B **452** (1999) 364 [hep-ph/9812423].
[55] R. Corke and T. Sjostrand, JHEP **1105** (2011) 009 [arXiv:1101.5953 [hep-ph]].
[56] R. Corke and T. Sjostrand, JHEP **1103** (2011) 032 [arXiv:1011.1759 [hep-ph]].
[57] T. Sjostrand, Phys. Lett. B **157** (1985) 321.
[58] M. Bengtsson and T. Sjostrand, Phys. Lett. B **185** (1987) 435.
[59] M. Bengtsson and T. Sjostrand, Nucl. Phys. B **289** (1987) 810.
[60] T. Sjostrand and P. Z. Skands, Eur. Phys. J. C **39** (2005) 129 [hep-ph/0408302].
[61] T. Sjostrand and P. Z. Skands, JHEP **0403** (2004) 053 [hep-ph/0402078].
[62] P. Z. Skands, Phys. Rev. D **82** (2010) 074018 [arXiv:1005.3457 [hep-ph]].
[63] R. Corke and T. Sjostrand, JHEP **1001** (2010) 035 [arXiv:0911.1909 [hep-ph]].
[64] A. Edin, G. Ingelman and J. Rathsman, Phys. Lett. B **366** (1996) 371 [hep-ph/9508386].
[65] S. Ostapchenko, AIP Conf. Proc. **928** (2007) 118 [arXiv:0706.3784 [hep-ph]].
[66] S. Ostapchenko, EPJ Web Conf. **52** (2013) 02001.
[67] V. N. Gribov, Sov. Phys. JETP **26** (1968) 414 [Zh. Eksp. Teor. Fiz. **53** (1967) 654].
[68] H. J. Drescher, M. Hladik, S. Ostapchenko and K. Werner, J. Phys. G **25** (1999) L91 [hep-ph/9903296].
[69] F. M. Liu, H. J. Drescher, S. Ostapchenko, T. Pierog and K. Werner, J. Phys. G **28** (2002) 2597 [hep-ph/0109104].
[70] M. Baker and K. A. Ter-Martirosian, Phys. Rept. **28** (1976) 1.
[71] O. V. Kancheli, Pisma Zh. Eksp. Teor. Fiz. **18** (1973) 465 [JETP Lett. **18** (1973) 274].
[72] J. L. Cardy, Nucl. Phys. B **75** (1974) 413.
[73] A. B. Kaidalov, L. A. Ponomarev and K. A. Ter-Martirosian, Yad. Fiz. **44** (1986) 722 [Sov. J. Nucl. Phys. **44** (1986) 468].

[74] S. Ostapchenko, Phys. Lett. B **636** (2006) 40 [hep-ph/0602139].
[75] S. Ostapchenko, Phys. Rev. D **77** (2008) 034009 [hep-ph/0612175].
[76] S. Ostapchenko, Phys. Rev. D **81** (2010) 114028 [arXiv:1003.0196 [hep-ph]].
[77] S. Ostapchenko, Phys. Lett. B **703** (2011) 588 [arXiv:1103.5684 [hep-ph]].
[78] S. Ostapchenko, Phys. Rev. D **89** (2014) 7, 074009 [arXiv:1402.5084 [hep-ph]].
[79] G. Antchev *et al.* [TOTEM Collaboration], Europhys. Lett. **101** (2013) 21003.
[80] F. Oljemark for the TOTEM Collaboration, *TOTEM Results on soft diffraction and forward multiplicities*, talk at the 15th Int. Conf. on Elastic and Diffractive Scattering (Saariselkä), September 9-13, 2013.
[81] M. G. Ryskin, A. D. Martin and V. A. Khoze, Eur. Phys. J. C **60** (2009) 249 [arXiv:0812.2407 [hep-ph]].
[82] M. G. Ryskin, A. D. Martin and V. A. Khoze, Eur. Phys. J. C **60** (2009) 265 [arXiv:0812.2413 [hep-ph]].
[83] G. Gustafson, Phys. Lett. B **718** (2013) 1054 [arXiv:1206.1733 [hep-ph]].
[84] T. Gleisberg, S. Hoeche, F. Krauss, A. Schalicke, S. Schumann and J. -C. Winter, JHEP **0402** (2004) 056 [hep-ph/0311263].
[85] T. Gleisberg, S. Hoeche, F. Krauss, M. Schonherr, S. Schumann, F. Siegert and J. Winter, JHEP **0902** (2009) 007 [arXiv:0811.4622 [hep-ph]].
[86] Z. Nagy and D. E. Soper, hep-ph/0601021.
[87] S. Schumann and F. Krauss, JHEP **0803** (2008) 038 [arXiv:0709.1027 [hep-ph]].
[88] J. -C. Winter, F. Krauss and G. Soff, Eur. Phys. J. C **36** (2004) 381 [hep-ph/0311085].
[89] K. Nakamura *et al.* [Particle Data Group Collaboration], J. Phys. G **37** (2010) 075021.
[90] G. Antchev, P. Aspell, I. Atanassov, V. Avati, J. Baechler, V. Berardi, M. Berretti and E. Bossini *et al.*, Europhys. Lett. **96** (2011) 21002 [arXiv:1110.1395 [hep-ex]].
[91] G. Aad *et al.* [ATLAS Collaboration], Nature Commun. **2** (2011) 463 [arXiv:1104.0326 [hep-ex]].
[92] S. Chatrchyan *et al.* [CMS Collaboration], Phys. Lett. B **722** (2013) 5 [arXiv:1210.6718 [hep-ex]].
[93] M. G. Poghosyan, J. Phys. G **38** (2011) 124044 [arXiv:1109.4510 [hep-ex]].
[94] G. Antchev *et al.* [TOTEM Collaboration], Europhys. Lett. **95** (2011) 41001 [arXiv:1110.1385 [hep-ex]].
[95] G. Antchev *et al.* [TOTEM Collaboration], Europhys. Lett. **101** (2013) 21002.
[96] N. A. Amos, M. M. Block, G. J. Bobbink, M. Botje, D. Favart, C. Leroy, F. Linde and P. Lipnik *et al.*, Nucl. Phys. B **262** (1985) 689.
[97] N. Kwak, E. Lohrmann, E. Nagy, M. Regler, W. Schmidt-Parzefall, K. R. Schubert, K. Winter and A. Brandt *et al.*, Phys. Lett. B **58** (1975) 233.
[98] D. Bernard *et al.* [UA4 Collaboration], Phys. Lett. B **198** (1987) 583.
[99] M. Bozzo *et al.* [UA4 Collaboration], Phys. Lett. B **155** (1985) 197.
[100] R. Battiston *et al.* [UA4 Collaboration], Phys. Lett. B **127** (1983) 472.
[101] F. Abe *et al.* [CDF Collaboration], Phys. Rev. D **50** (1994) 5518.
[102] N. A. Amos *et al.* [E-710 Collaboration], Phys. Lett. B **247** (1990) 127.
[103] G. Aad *et al.* [ATLAS Collaboration], New J. Phys. **13** (2011) 053033 [arXiv:1012.5104 [hep-ex]].
[104] G. Aad *et al.* [ATLAS Collaboration], Phys. Rev. D **83** (2011) 112001 [arXiv:1012.0791

[hep-ex]].

[105] M. G. Ryskin, A. D. Martin and V. A. Khoze, Eur. Phys. J. C **71** (2011) 1617 [arXiv:1102.2844 [hep-ph]].

[106] L. A. Harland-Lang, V. A. Khoze and M. G. Ryskin, Eur. Phys. J. C **74** (2014) 2848 [arXiv:1312.4553 [hep-ph]].

[107] Y. I. Azimov, V. A. Khoze, E. M. Levin and M. G. Ryskin, Sov. J. Nucl. Phys. **21** (1975) 215 [Yad. Fiz. **21** (1975) 413].

[108] J. Pumplin and F. Henyey, Nucl. Phys. B **117** (1976) 377.

[109] P. Lebiedowicz, R. Pasechnik and A. Szczurek, Phys. Lett. B **701** (2011) 434 [arXiv:1103.5642 [hep-ph]].

[110] V. A. Khoze, A. D. Martin and M. G. Ryskin, Eur. Phys. J. C **73** (2013) 2503 [arXiv:1306.2149 [hep-ph]].

[111] A. Breakstone *et al.* [Ames-Bologna-CERN-Dortmund-Heidelberg-Warsaw Collaboration], Z. Phys. C **48** (1990) 569.

[112] J. Monk and A. Pilkington, Comput. Phys. Commun. **175** (2006) 232 [hep-ph/0502077].

[113] V. A. Khoze, A. D. Martin and M. G. Ryskin, Eur. Phys. J. C **23** (2002) 311 [hep-ph/0111078].

[114] L. A. Harland-Lang, V. A. Khoze, M. G. Ryskin and W. J. Stirling, Eur. Phys. J. C **69** (2010) 179 [arXiv:1005.0695 [hep-ph]].

[115] L. A. Harland-Lang, V. A. Khoze, M. G. Ryskin and W. J. Stirling, Eur. Phys. J. C **65** (2010) 433 [arXiv:0909.4748 [hep-ph]].

[116] V. M. Budnev, I. F. Ginzburg, G. V. Meledin and V. G. Serbo, Phys. Rept. **15** (1974) 181.

[117] C. Royon, L. Schoeffel, S. Sapeta, R. B. Peschanski and E. Sauvan, Nucl. Phys. B **781** (2007) 1 [arXiv:hep-ph/0609291].

[118] V. A. Khoze, A. D. Martin and M. G. Ryskin, Eur. Phys. J. C **18** (2000) 167 [arXiv:hep-ph/0007359].

[119] C. Marquet, C. Royon, M. Trzebinski, R. Zlebcik, Phys.Rev. D**87** (2013) 3, 034010; O. Kepka, C. Marquet, C. Royon, Phys. Rev. D**83** (2011) 034036.

[120] http://starlight.hepforge.org/

[121] C. A. Bertulani, S. R. Klein and J. Nystrand, Ann. Rev. Nucl. Part. Sci. **55** (2005) 271 [nucl-ex/0502005].

[122] A. J. Baltz, G. Baur, D. d'Enterria, L. Frankfurt, F. Gelis, V. Guzey, K. Hencken and Y. Kharlov *et al.*, Phys. Rept. **458** (2008) 1 [arXiv:0706.3356 [nucl-ex]].

[123] S. Klein and J. Nystrand, Phys. Rev. C **60** (1999) 014903 [hep-ph/9902259].

[124] S. R. Klein and J. Nystrand, Phys. Rev. Lett. **84** (2000) 2330 [hep-ph/9909237].

[125] A. J. Baltz, Y. Gorbunov, S. R. Klein and J. Nystrand, Phys. Rev. C **80** (2009) 044902 [arXiv:0907.1214 [nucl-ex]].

[126] A. J. Baltz, S. R. Klein and J. Nystrand, Phys. Rev. Lett. **89** (2002) 012301 [nucl-th/0205031].

[127] O. Djuvsland and J. Nystrand, Phys. Rev. C **83** (2011) 041901 [arXiv:1011.4908 [hep-ph]].

[128] J. Adams *et al.* [STAR Collaboration], Phys. Rev. C **70** (2004) 031902 [nucl-ex/0404012].

[129] S. Afanasiev *et al.* [PHENIX Collaboration], Phys. Lett. B **679** (2009) 321 [arXiv:0903.2041 [nucl-ex]].

[130] E. Abbas *et al.* [ALICE Collaboration], Eur. Phys. J. C **73** (2013) 11, 2617 [arXiv:1305.1467 [nucl-ex]].

[131] J. Nystrand [ALICE Collaboration], Nucl. Phys. A **931** (2014) 298 [arXiv:1408.0811 [nucl-ex]].

[132] B. I. Abelev *et al.* [STAR Collaboration], Phys. Rev. C **77** (2008) 034910 [arXiv:0712.3320 [nucl-ex]].

[133] C. Adler *et al.* [STAR Collaboration], Phys. Rev. Lett. **89** (2002) 272302 [nucl-ex/0206004].

[134] T. Aaltonen *et al.* [CDF Collaboration], Phys. Rev. Lett. **102** (2009) 242001 [arXiv:0902.1271 [hep-ex]].

[135] R. Aaij *et al.* [LHCb Collaboration], J. Phys. G **41** (2014) 055002 [arXiv:1401.3288 [hep-ex]].

[136] L. A. Harland-Lang, V. A. Khoze and M. G. Ryskin, arXiv:1310.2759 [hep-ph].

[137] L. A. Harland-Lang, V. A. Khoze, M. G. Ryskin and W. J. Stirling, Eur. Phys. J. C **71** (2011) 1714 [arXiv:1105.1626 [hep-ph]].

[138] A. Aktas *et al.* [H1 Collaboration], Eur. Phys. J. C **46** (2006) 585 [hep-ex/0510016].

[139] L. Motyka and G. Watt, Phys. Rev. D **78** (2008) 014023 [arXiv:0805.2113 [hep-ph]].

[140] C. Adloff *et al.* [H1 Collaboration], Phys. Lett. B **541** (2002) 251 [hep-ex/0205107].

[141] M. G. Albrow *et al.* [FP420 R and D Collaboration], JINST **4** (2009) T10001 [arXiv:0806.0302 [hep-ex]].

[142] W. Schafer and A. Szczurek, Phys. Rev. D **76** (2007) 094014 [arXiv:0705.2887 [hep-ph]].

[143] M. G. Ryskin, Z. Phys. C **57** (1993) 89.

[144] A. D. Martin, W. J. Stirling, R. S. Thorne and G. Watt, Eur. Phys. J. C **63** (2009) 189 [arXiv:0901.0002 [hep-ph]].

[145] J. Pumplin, D. R. Stump, J. Huston, H. L. Lai, P. M. Nadolsky and W. K. Tung, JHEP **0207** (2002) 012 [hep-ph/0201195].

[146] A. Karneyeu, L. Mijovic, S. Prestel and P. Z. Skands, Eur. Phys. J. C **74** (2014) 2714 [arXiv:1306.3436 [hep-ph]].

[147] G. Aad *et al.* [ATLAS Collaboration], Eur. Phys. J. C **72** (2012) 1926 [arXiv:1201.2808 [hep-ex]].

[148] B. Abelev *et al.* [ALICE Collaboration], Eur. Phys. J. C **73** (2013) 2456 [arXiv:1208.4968 [hep-ex]].

Chapter 3

Soft Diffraction and Total Cross section

Conveners and Editors: V. Avati, T. Martin
Internal Reviewers: P. Grafstrom, V. Khoze

3.1 Introduction

High energy elastic proton-proton scattering is an important fundamental reaction, which provides information on the $pp \to pp$ strong interaction amplitude, and - via unitarity, about the sum of all inelastic processes as well. The LHC reaches sufficiently high energies that data should be able to distinguish between the different asymptotic scenarios for high energy interactions.

The t-slope of the elastic amplitude determines the value of the interaction radius. Moreover, after transformation into the impact parameter (b_t) representation, the elastic scattering amplitude (together with the total cross section) allows us to trace how the strong interaction at high energies approaches the black disk limit. In turn, proton diffractive dissociation is driven by the probability of parton elastic scattering. Therefore its mass- and t-dependences provide (integrated) information about the proton's partonic wave function; that is, about the k_t and rapidity distributions of the partons inside a proton.

On the other hand, the survival probability of Large Rapidity Gaps (which are an essential feature of diffractive dissociation events, and arise from the exchange of a colour singlet) reflects the probability of an additional inelastic soft interaction in the multi-particle process.

In high energy pp collisions about 40% of the total cross section comes from diffractive processes, like elastic scattering and single and double diffractive dissociation. We need to study these soft interactions to understand the structure of the total cross section, and the nature of the underlying events which accompany the rare hard sub-processes. Indeed, the hope is that a detailed study of these elastic and quasi-elastic soft processes will allow the construction of a Monte Carlo simulation which merges the soft and hard high energy interactions in a reliable and consistent way.

This chapter outlines the probability of detecting a proton in the forward detectors for high cross section elastic and inelastic proton interactions, and investigates details of the modelling in MC.

Past studies of large rapidity gaps in soft events are summarised and future prospects are listed, including the use of forward and very forward detectors to increase the acceptance of the LHC experiments to diffractive signatures.

Results on the total, elastic and inelastic cross section measurements are also summarised along with the outlook for Run-II.

3.2 Detecting soft diffraction with Forward Detectors

Forward detectors offer a unique opportunity to combine information about the centrally produced system and the intact protons. This additional information will be used to significantly increase the purity of diffractive samples and, in some cases, make the measurement possi-

ble, e.g. for some exclusive production channels. One can also construct dedicated diffractive triggers utilising the coincidences between forward and central detectors.

Protons were generated using PYTHIA 8 [1] with MBR tune[1] [2] and assuming $\sqrt{s} =$ 14 TeV. The following processes were taken into account: minimum-bias (PYTHIA process code = 101), elastic scattering (102), single diffraction (103 and 104), double diffraction (105) and central diffraction (106). Generated protons were then transported using FPTRACK [3] to the forward detector position. The vertex position was smeared accordingly to values from Table 1.1 and the momentum spread (*cf.* Table 1.1) was applied, tables are in Section 1.1.

All probabilities are for single interactions, including both elastic scattering and inelastic collisions. The interpretation of these data is in terms of tagging probabilities for high cross section processes. By multiplying this probability by an average pile-up value, the probability of a tag from a soft interaction forming a background to other hard processes is obtained.

Under real experimental conditions, a single-sided horizontal detector such as AFP will not be able to reconstruct elastically scattered protons unless their p_{T} is large enough. Moreover, such detector will never reconstruct both elastic protons since one of them will be deflected in the un-instrumented direction.

3.2.1 Per Interaction Probability of Single and Double Tag

The probability of observing a scattered proton in a forward detector depends on the distance between the detector active area and the beam centre – *cf.* Fig. 3.1. In this figure the solid black lines mark the results for the $\beta^* = 0.55$ m optics, dashed red ones for $\beta^* = 90$ m and the dotted blue – for $\beta^* = 1000$ m. Due to the fact that the beam size depends on the optics used (see Table 1.2), for each setting the distance in σ is marked with vertical lines. The additional distance of 0.3 mm represents the so-called 'dead edge' – the area between the edge and active part of the detector.

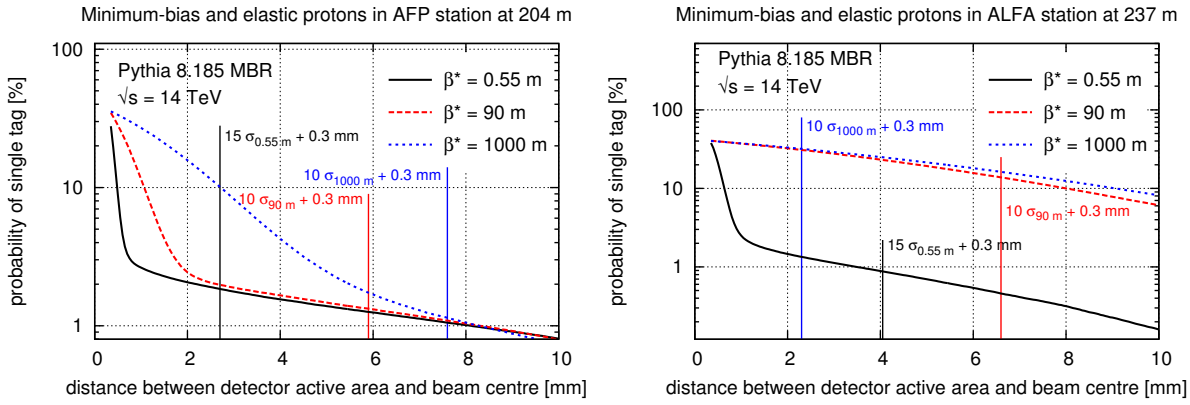
Minimum-bias and elastic protons in AFP station at 204 m
Pythia 8.185 MBR
√s = 14 TeV
β* = 0.55 m
β* = 90 m
β* = 1000 m
15 σ0.55 m + 0.3 mm
10 σ1000 m + 0.3 mm
10 σ90 m + 0.3 mm
probability of single tag [%]
distance between detector active area and beam centre [mm]
Minimum-bias and elastic protons in ALFA station at 237 m
Pythia 8.185 MBR
√s = 14 TeV
β* = 0.55 m
β* = 90 m
β* = 1000 m
10 σ1000 m + 0.3 mm
10 σ90 m + 0.3 mm
15 σ0.55 m + 0.3 mm
probability of single tag [%]
distance between detector active area and beam centre [mm]

Fig. 3.1: Probability per soft interaction of observing elastic or minimum-bias proton in one of the forward detector for the AFP (**left**) and ALFA (**right**) detectors. The solid black lines are for the $\beta^* =$ 0.55 m optics, dashed red ones for $\beta^* = 90$ m and the dotted blue – for $\beta^* = 1000$ m. The vertical lines mark the distance for each setting.

The AFP detectors are expected[2] to operate at 15 σ during the runs with the collision optics and at 10 σ during the high β^* ones. As can be seen from Fig. 3.1 (left) this translates

[1] It should be noted that the differences between various MC generators are known to be significant and even a factor of 2 in the predicted cross sections can be expected.

[2] The exact value depends obviously on the real beam intensity and will be fixed during the run.

to $1-2\%$ chance of observing scattered proton in the detector. These protons originate mainly from single diffractive events. There is also a contribution from double diffraction and non-diffractive events, which starts to be important at larger distances (higher ξ). For the $\beta^* = 90$ m and, especially, $\beta^* = 1000$ m a contribution of the elastics scattering is also visible, but as it decreases rapidly with increasing detector distance from the beam. Note that the elastic contribution also cannot be reconstructed in AFP as the other scattered proton is lost due to the single-sided horizontal acceptance.

For the ALFA detectors and $\beta^* = 0.55$ m, the situation is similar to one for AFP, except that the expected probability of observing a scattered proton at 15 σ distance is about two times smaller. For the *high-*β^* optics the situation changes drastically, as the contribution of the elastic scattering is dominant for all considered distances.

The probability of registering protons on both sides of the IP (so-called double tag) is shown in Fig. 3.2. Similarly to the single tag case the solid black lines marks results for the $\beta^* = 0.55$ m optics, dashed red ones for $\beta^* = 90$ m, the dotted blue – for $\beta^* = 1000$ m and the relevant beam smearing were considered.

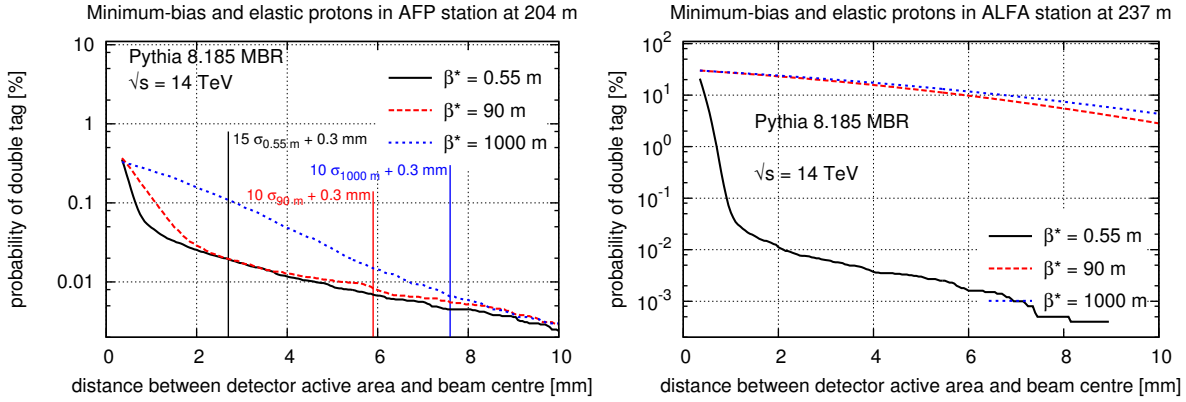
Minimum-bias and elastic protons in AFP station at 204 m
Pythia 8.185 MBR
√s = 14 TeV
β* = 0.55 m
β* = 90 m
β* = 1000 m
15 σ0.55 m + 0.3 mm
10 σ1000 m + 0.3 mm
10 σ90 m + 0.3 mm
probability of double tag [%]
distance between detector active area and beam centre [mm]
Minimum-bias and elastic protons in ALFA station at 237 m
Pythia 8.185 MBR
√s = 14 TeV
β* = 0.55 m
β* = 90 m
β* = 1000 m
probability of double tag [%]
distance between detector active area and beam centre [mm]

Fig. 3.2: Probability per soft interaction of observing double tagged event in the forward detector for the AFP (**left**) and ALFA (**right**) detectors. The solid black lines are for the $\beta^* = 0.55$ m optics, dashed red ones for $\beta^* = 90$ m and the dotted blue – for $\beta^* = 1000$ m. The vertical lines on the left figure mark the distance for each setting, they are at the same distances for the right hand figure.

For $\beta^* = 0.55$ m and 15 σ distance between the AFP detector and the beam centre the probability of observing a double tag event is about $2 \cdot 10^{-4}$. The main contribution comes from central diffraction. For *high-*β^* optics and 10 σ distance this probability is about $8 \cdot 10^{-5}$. For the distances larger than 10 σ the main contribution comes from double and central diffractive processes. The single diffraction process plays a secondary role.

In the case of the ALFA detectors and collision optics, the probability of observing a double tagged event at 10 σ distance is about $3 \cdot 10^{-5}$. These protons come mainly from central diffraction. For the *high-*β^* optics and 10 σ distance the probability of observing a double tag event is very high: 0.1 for $\beta^* = 90$ m and 0.2 for $\beta^* = 1000$ m. This is not surprising, since these events are in $\sim 95\%$ of cases due to the elastic scattering.

3.2.2 Soft Vertex Reconstruction

In hard diffractive analyses the background is mainly due to hard non-diffractive events. Proton tagging allows us to eliminate some of these events. However, due to pile-up, there could be the situation where a hard event is produced together with a soft one which contains forward

proton(s). Requiring exactly one vertex reconstructed in the central detector allows further background reduction. Apart from knowing how often the vertex originating from soft event (hereafter referred to as the 'soft vertex') is reconstructed when there is a diffractive proton in the forward detector, one needs also take into account that there are cases in which soft vertices are not visible. There are two main sources of vertex reconstruction inefficiency:

- the soft event is produced too close to a hard one; due to finite detector resolution and reconstruction algorithms the vertices are merged,
- there are not enough tracks pointing to the soft vertex.

In the presented studies, the vertex was assumed to be reconstructed if there are at least four charged particles within the ATLAS tracker ($|\eta| < 2.5$). In order to account for the detector efficiency, each particle had a certain probability of being registered. The thresholds were set to:

- 50% for particles with $100 < p_{\mathrm{T}} < 500$ MeV and
- 90% for particles with $p_{\mathrm{T}} > 500$ MeV.

These values are reflecting the behaviour of ATLAS inner detector [4], but are also similar for the CMS experiment. The minimal distance below which vertices are merged was set to 1.5 mm.

The probabilities should be multiplied by an average pile-up to yield the prediction of soft vertex reconstruction for the running conditions in question.

The vertex reconstruction probability under the condition that the proton is tagged in the forward detector as a function of the distance between detector active area and the beam centre is shown in Fig. 3.3. For $\beta^* = 0.55$ m it ranges between 0.6 and 0.7. In the case of the AFP (left) and *high-*β^* optics, this probability at the 10 σ distance is on average smaller by 0.1 than that for the collision optics. This situation is a bit different for the ALFA detectors (right) – due to the fact that the elastic scattering plays an important role in the wide range of distances, the probability to have a vertex in the event is much smaller. The shapes of the presented distributions are a consequence of a non-trivial interplay between the kinematics of forward proton and central system multiplicity.

The probability to reconstruct the soft vertex under the condition that there is a double tag in the AFP detector is shown in Fig. 3.4. One concludes that the shapes of the presented dependences are qualitatively very similar to those in the single tag case.

3.2.3 Proton and Vertex reconstruction Conclusion

Studies are presented which quantify the probability of reconstructing single and double proton-tagged events using the AFP and ALFA forward detectors (CT-PPS, TOTEM results are expected to be broadly similar). The results are presented for combined elastic, inelastic and MBR diffractive interactions at different LHC optics settings as a function of the detector-beam separation.

The probability of also reconstructing the soft vertex within the central tracking volume is subsequently investigated in conjunction with the forward proton tag. These studies together indicate an approximate (MC dependent) rate of proton tags from soft interactions which may be used in one of two ways. It quantifies the expected statistics to be gained from a minimum bias data taking campaign for studies on soft interactions with forward proton tags. Or by multiplying the probability by an average pileup value, it yields the chance that a hard interaction

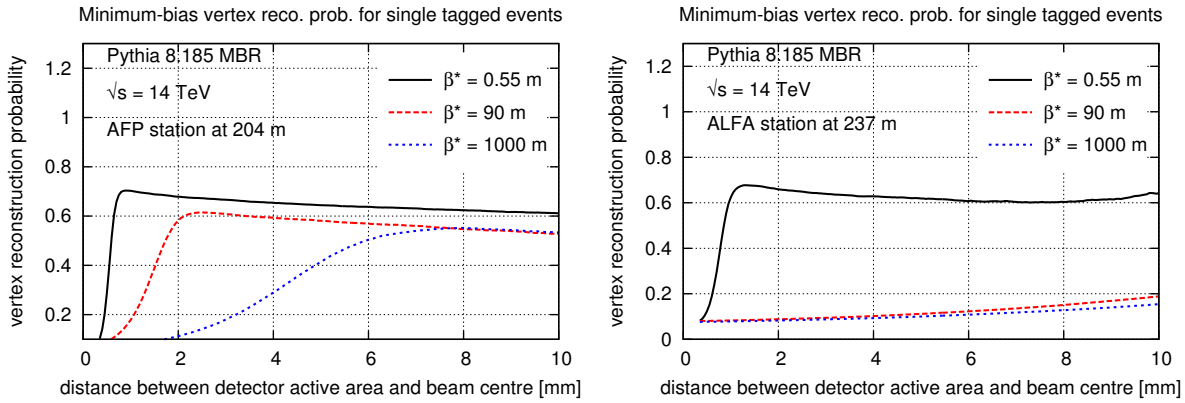
Minimum-bias vertex reco. prob. for single tagged events
Pythia 8 185 MBR
√s = 14 TeV
AFP station at 204 m
β* = 0.55 m
β* = 90 m
β* = 1000 m
vertex reconstruction probability
distance between detector active area and beam centre [mm]
Minimum-bias vertex reco. prob. for single tagged events
Pythia 8 185 MBR
√s = 14 TeV
ALFA station at 237 m
β* = 0.55 m
β* = 90 m
β* = 1000 m
vertex reconstruction probability
distance between detector active area and beam centre [mm]

Fig. 3.3: Soft vertex reconstruction probability for single tagged events tagged in the AFP (**left**) and ALFA (**right**) detectors. The solid black lines are for the $\beta^* = 0.55$ m optics, dashed red ones for $\beta^* = 90$ m and the dotted blue – for $\beta^* = 1000$ m. The vertex is assumed to be reconstructed if there are at least four charged particles in the ATLAS tracker ($|\eta| < 2.5$). Particles with $100 < p_{\mathrm{T}} < 500$ MeV have 0.5 chance to be detected whereas the probability for the ones with $p_{\mathrm{T}} > 500$ MeV was set to 0.9.

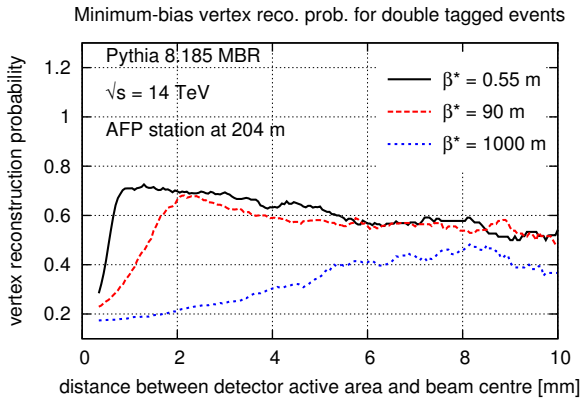
Minimum-bias vertex reco. prob. for double tagged events
Pythia 8 185 MBR
√s = 14 TeV
AFP station at 204 m
β* = 0.55 m
β* = 90 m
β* = 1000 m
vertex reconstruction probability
distance between detector active area and beam centre [mm]

Fig. 3.4: Soft vertex reconstruction probability for double tagged events tagged in the AFP detector. The solid black lines are for the $\beta^* = 0.55$ m optics, dashed red ones for $\beta^* = 90$ m and the dotted blue – for $\beta^* = 1000$ m. The vertex is assumed to be reconstructed if there are at least four charged particles in the ATLAS tracker ($|\eta| < 2.5$). Particles with $100 < p_{\mathrm{T}} < 500$ MeV have 0.5 chance to be detected whereas the probability for the ones with $p_{\mathrm{T}} > 500$ MeV was set to 0.9.

will overlap with a pileup event with forward proton tags - a possible source of background to smaller cross section hard diffractive processes, as investigated in Section 4.2.

3.3 Physics sources and properties of forward protons from inelastic interactions

Forward proton detectors such as AFP, ALFA and TOTEM reconstruct protons from elastic scattering, single-diffractive interactions and double-Pomeron exchange. Other physics mechanisms may exist however which produce protons within the acceptance of forward proton detectors, these too are explored in this section and with the aim of allowing for greater discrimination between soft physics models.

Soft pseudorapidity gaps, devoid of any final state particles above a low threshold (typically a few hundred MeV) have long been used as a probe of diffractive interactions [5–9]. At the LHC, the diffractive kinematics are such that for a single diffractive interaction to leave a

rapidity gap within the acceptance of the main detectors (here taken as $|\eta| < 5$), the scattered proton must be in the interval $-6 < \log_{10}(\xi_X) < -2$. Smaller diffractive masses escape down the beam-line, where specialist forward detectors are needed to measure them, while larger diffractive masses span the full η range of the central detector and hence do not leave a reconstructible pseudorapidity gap within.

The lowest ξ for which a single diffractive event will start to leave a pseudorapidity gap in the central detector is two times smaller than the lowest ξ reconstructible by AFP. Therefore if we wish to probe pseudorapidity gaps in a soft diffractive enriched data sample, we must explore other mechanisms by which a forward proton tag may be obtained.

Diffraction in the `Pythia 8` generator is described in Section 2.5, of key interest to this study is the modelling of double dissociative interactions where the mass of the smaller diffractive system (denoted M_Y) is of the order of the proton mass. For $M_Y < m_p + 1$ GeV (where m_p is the proton mass), the system is decayed isotropically by `Pythia` into a two body system while for masses up to 10 GeV the system is hadronised from a string with the quantum numbers of the originating proton. Only higher mass resolved systems (with a probabilistic turn on, starting from a diffractive mass of 10 GeV) are subjected to a perturbative modelling with [10] proton-Pomeron PDF from H1 and the full `Pythia` machinery for parton showers and MPI employed within the diffractive system[3].

These low mass diffractive excitations are predicted to often result in the beam baryon number being retained by a proton, but one with a significantly lower energy due to the two body decay or low mass string fragmentation. This is illustrated in Fig. 3.5a where the hadronisation of four independent low mass diffractive systems in `Pythia 8` are visualised with `MCViz` [11]. In each case, the forward proton (highlighted in magenta) was found to be produced within the kinematic acceptance of the AFP detector, assuming collision optics. The cross section prediction by `Pythia 8` of double diffractive interactions which produce a forward proton within AFP acceptance is 0.3 mb (3.3 % of the total double dissociative prediction, see Table 3.1). For all but the highest mass diffractive systems, there is very little correlation between the size of the two diffractive dissociations M_X and M_Y.

This high cross section process will allow for these protons, produced through low mass forward M_Y systems, to be used as independent tags to study the dynamics of the larger M_X system in minimum bias interactions and will be exploited in generator feasibility studies reported in this document (see Sections 3.4, 6.3 and 6.4).

Other MC generators considered are `EPOS` and `Herwig++`. `EPOS` uses a parton based Gribov-Regge model and is described in Section 2.2, `EPOS` interactions resulting in a forward proton within AFP acceptance are illustrated in Fig. 3.5b for two independent systems, one of low mass and one of high mass.

`Herwig++` is discussed in Section 2.4, events are generated using the `Herwig++` underlying event model where the hard scatter matrix element is set to the unit matrix and particle production is generated solely from the simulation of h semi-hard (containing object with $p_T > 3.36$ GeV) and n soft scatters where h and n are each chosen per event via the sampling of Poisson distributions. For the case $h = 0$ and $n = 0$, only the beam remnants are present. Although not explicitly modelling soft diffractive interaction here, `Herwig++` is also capable of generating protons within the acceptance of AFP and additionally uses the cluster hadronisation model. An example of a `Herwig++` event with a forward proton tag is illustrated in Fig. 3.6.

[3]Note that this is fully contained within the proton-Pomeron interaction and cannot interfere with or destroy the rapidity gap generated via the Pomeron exchange.

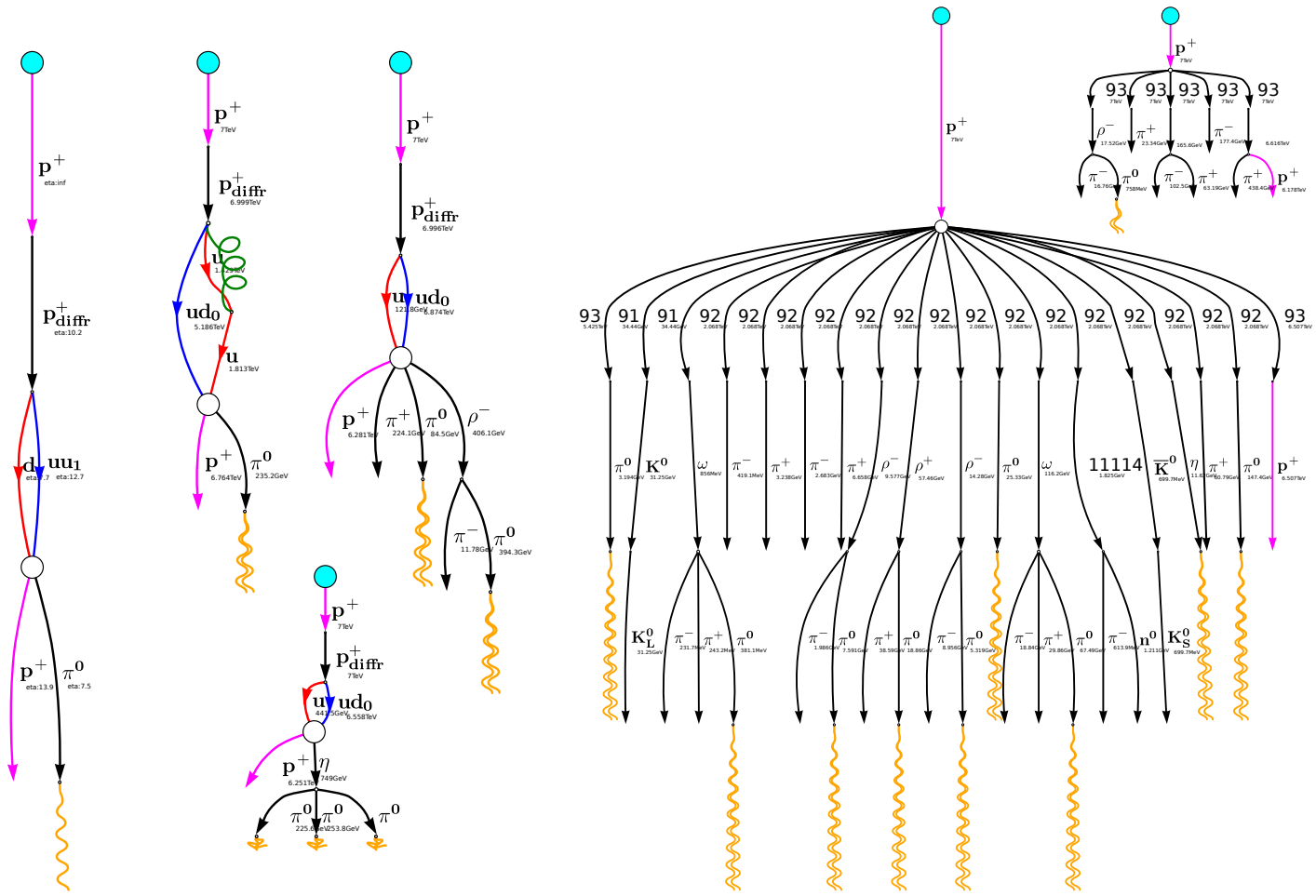

(a) (b)

Fig. 3.5: Example low mass dissociative systems from four independent `Pythia 8` interactions (a) which result in a forward proton within AFP acceptance. Equivalent example for decay products from two independent inelastic proton interactions simulated by `EPOS` (b) which result in a high and low mass system. In all cases the forward protons are highlighted in magenta.

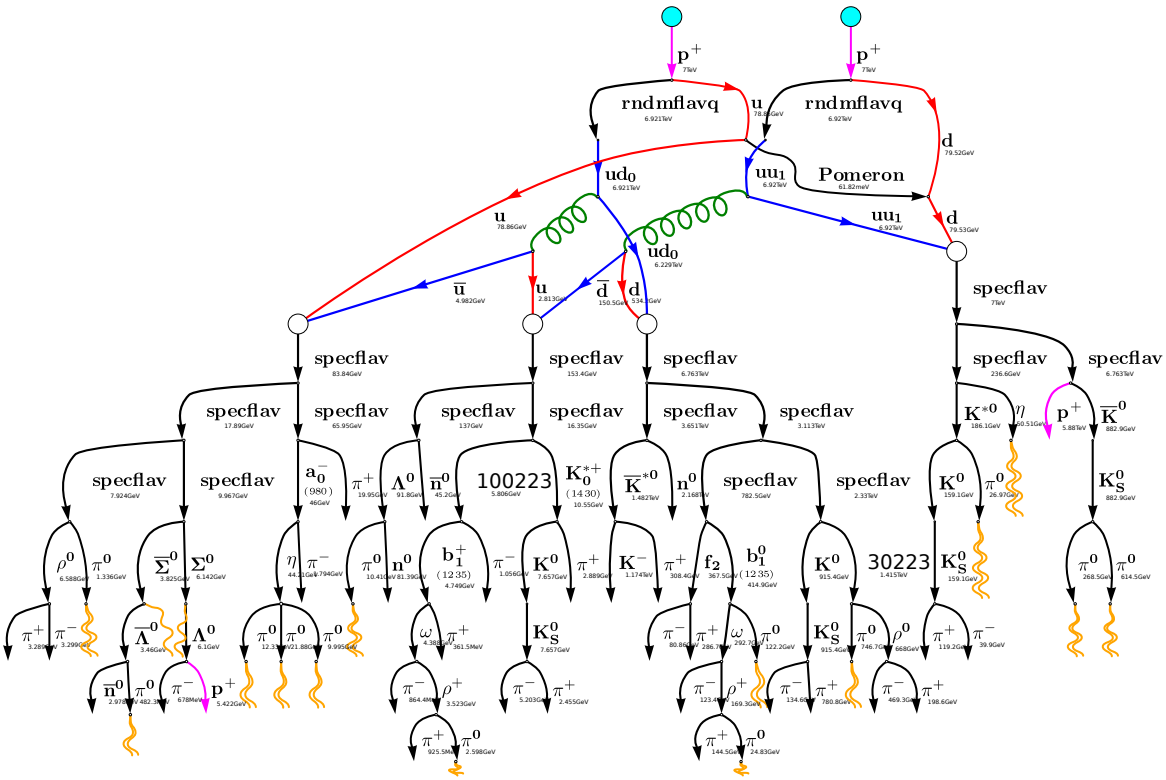

Fig. 3.6: Example inelastic interaction from the `Herwig++` underlying event model. Two protons are produced in the final state (highlighted in magenta). The proton on the right hand side of the diagram is within AFP acceptance.

3.3.1 MC versions and tagged proton selection for inelastic studies

The subsequent studies on the rapidity gap spectra, Section 3.4, transverse energy density, Section 6.3 and charged particle multiplicities, Section 6.4 use the following generators. `Pythia 8` version 8.176 with the option `Tune:pp=8` (ATLAS MB Tune A2 with the MSTW 2008 LO PDF) [12], `EPOS` version `1.99.crmc.v3200` with the tune `EPOS-LHC` and `Herwig++` version 2.7.0 with the `LHC-UE-EE-4.in` run card using the `CTEQ6L1` PDF, modified to increase $\sqrt{s}$ to 14 TeV. For event selections including a forward proton tag, acceptance efficiency and resolution maps for AFP and ALFA were provided by [13] binned in $p_{\mathrm{T},p}$ and $\xi_p = E_{\mathrm{beam}} - E_p/E_{\mathrm{beam}}$, see Section 1.1. Final state protons produced by the MC are checked against these maps and a forward proton tag is generated if $P(p_{\mathrm{T},p}, \xi_p) \geq r$ where $P(p_{\mathrm{T},p}, \xi_p)$ is the probability of detection for the given proton kinematics and r is a uniformly distributed random number over the range 0–1.

Primary considered scenarios were AFP tracking detectors at a distance of 2.0 mm (10σ) from the beam and collision optics, $\beta^* = 0.55$ m, this gives access to a large range of $p_{\mathrm{T},p}$ for $\xi_p > 0.01$. For ALFA a distance of 4.5 mm (5σ) was used with $\beta^* = 90$ m optics which accesses $\xi_p < 0.2$ for $p_{\mathrm{T},p} > 0.1$ GeV. See Section 9 for additional details on the current and future forward detectors at ATLAS and CMS. These settings are optimistic regarding how close the detectors will be able to approach the beam, however increasing the distance to $20(10)\sigma$ for AFP(ALFA) results only in a small increase in the minimum reconstructible $\xi_p(p_{\mathrm{T},p})$ in AFP(ALFA) and does not change the conclusions due to the large (millibarn) cross sections.

$\beta^* = 0.55$ collision optics were also investigated for the ALFA detector. It was found that

the MC predictions were in good agreement with the AFP predictions in terms of shape, however due to the reduced acceptance (ALFA does not posses horizontal detectors) the predicted number of diffractive events is further reduced from the AFP estimates by around a factor of 4 (~ 0.4 mb for single and double diffraction combined).

The cross sections and overall probabilities of acquiring exactly one forward proton tag per inelastic interaction are listed for the considered MC and forward detector arrangements in Table 3.1.

Table 3.1: MC predictions for the inelastic cross section at $\sqrt{s} = 14$ TeV, including a breakdown of `Pythia 8` into the diffractive and non-diffractive sub components. Also listed is the probability per event that exactly one proton is reconstructed in the forward detectors, based on the probabilistic acceptance as a function of ξ_p and $p_{\mathrm{T},p}$.

	Cross Section $\sqrt{s} = 14$ TeV (mb)	AFP Tag Prob. $\beta^* = 0.55$ m (%)	ALFA Tag Prob. $\beta^* = 90$ m (%)	ALFA Tag Prob. $\beta^* = 0.55$ m (%)
`Herwig++` UE-EE-4	78.0	0.7	0.3	0.2
`EPOS` LHC	80.1	4.6	1.7	1.1
`Pythia 8` A2	79.3	2.5	0.8	0.6
`Pythia 8` A2 SD	12.9 (16%)	11.5	3.9	2.7
`Pythia 8` A2 DD	8.9 (11%)	3.3	0.6	0.8
`Pythia 8` A2 ND	57.5 (73%)	0.4	0.2	0.1

Sources of background, such as discussed in Section 1.2, and the effects of pileup are not included in these studies.

3.3.2 Kinematics of tagged proton samples

Of the `Pythia 8`, `EPOS` and `Herwig++` interactions with exactly one forward proton tag in AFP for the $\beta^* = 0.55$ collision optics, a double-diffractive enhanced sample is selected by requiring a pseudorapidity gap $\Delta\eta > 4$ between any pair of neighbouring final state particles in the event. Single diffractive events are rejected by requiring the smaller system's mass to be greater than the proton mass.

All final state particles from either side of the largest pseudorapidity gap in the event are combined into two systems which are identified as M_{X} and M_{Y} (where $M_{\mathrm{X}} > M_{\mathrm{Y}}$). The correlations of the two systems are plotted in Fig. 3.7. The mechanism of forward protons generated through low mass dissociation in `Pythia 8` from Section 3.3 is observed as the excess of events with $\log_{10}(\xi_{\mathrm{Y}}) = -7$. `EPOS` also shows this independence of the variables, but it only holds for $\log_{10}(\xi_{\mathrm{X}}) < -4$. For larger M_{X}, `EPOS` and `Herwig++` display a less prominent anti-correlation between M_{X} and M_{Y}.

3.4 Soft pseudorapidity gaps

3.4.1 Previous measurements

Large pseudorapidity gaps devoid of all final state particles above a lower experimental cut off (typically of order a few hundreds of MeV) are a characteristic signature of diffractive interactions.

The soft pseudorapidity gap cross section was measured at $\sqrt{s} = 7$ TeV by ATLAS [8] and CMS [9]. Gaps size are expressed here in terms of the event variable $\Delta\eta^{\mathrm{F}}$, this is defined as the largest of the two forward rapidity regions extending to (at least) $\eta = \pm 4.9$ which contain no

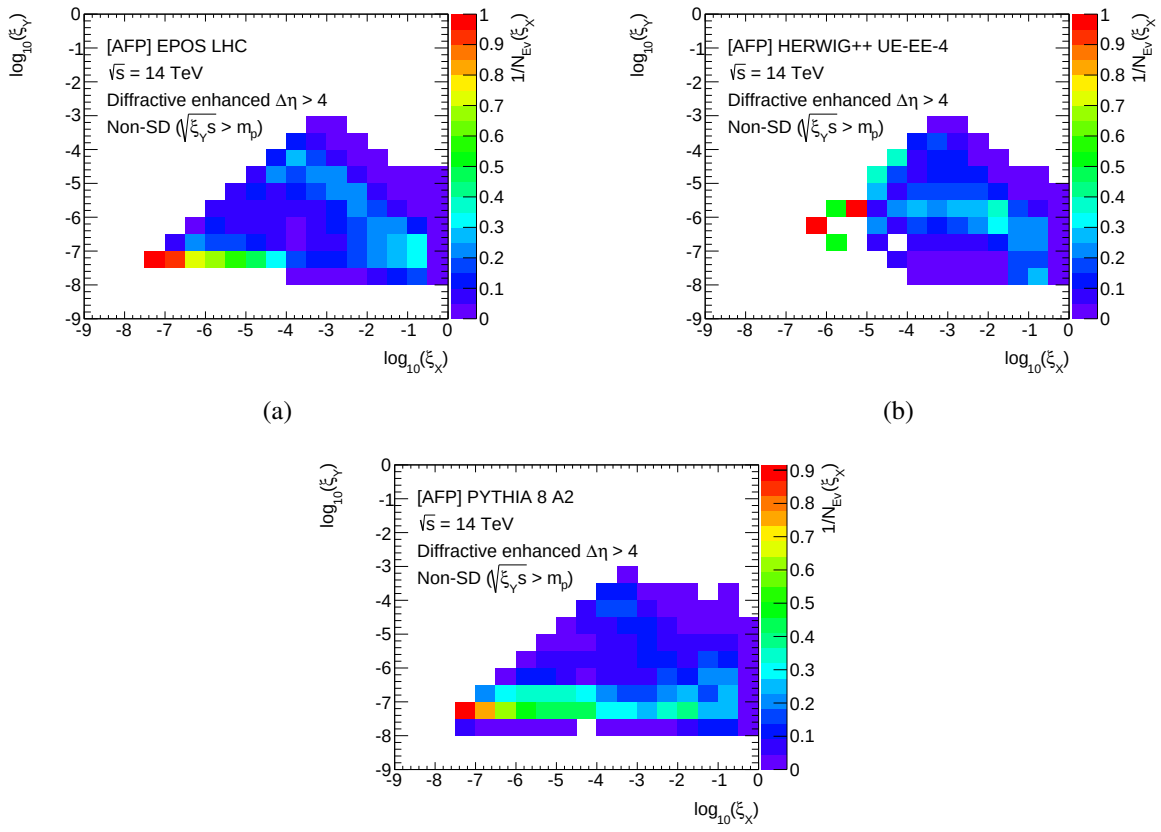

Fig. 3.7: Correlations of invariant masses of systems either side of the largest pseudorapidity gap for `EPOS` (a), `Herwig++` (b) and `Pythia 8` (c) generators using a double-diffractive enhancing selection of $\Delta\eta > 4$ and $M_{\mathrm{Y}} > m_p$. Distributions are normalised to unity in columns of $\log_{10}(\xi_{\mathrm{X}})$.

final state particles above a threshold $p_{\mathrm{T}} > p_{\mathrm{T}}^{\mathtt{Cut}}$. The value of $p_{\mathrm{T}}^{\mathtt{Cut}}$ is varied in the range[4] 200–800 MeV and as $p_{\mathrm{T}}^{\mathtt{Cut}}$ increases the modelling of hadronisation in the MC is tested, especially for small values of $\Delta\eta^{\mathrm{F}}$ where gap fluctuations from hadronisation effects dominate.

CMS in addition measures the cross section for single and double dissociation as a function of $\xi = M_X^2/s$, where M_X^2 is the mass of the larger (in the case of double diffraction) diffractive system [14].

TOTEM has measured the DD cross section in the forward rapidity range [15] using the T1 and T2 telescopes, and the SD cross section using the T1 and T2 telescopes and the forward proton [16]. An estimate of the low-mass diffractive events ($M_X < 3.4$ GeV/c^2) with no charged particles in the $|\eta| < 6.5$ range has been obtained by estimating the difference between the total inelastic cross section determined using elastic scattering and the optical theorem and the inelastic cross section measured using the T1 and T2 telescopes (see Section 3.6.3).

These data, along with other measurements including data from TOTEM and CDF, are being employed to test theoretical modelling which aims to globally describe LHC elastic and diffractive data. An example is shown in Fig. 3.8. See Section 2.7 and [17–20] for additional details.

[4]Note that for $p_{\mathrm{T}}^{\mathtt{Cut}} \geq 400$ MeV, the starting hemisphere of the rapidity gap as calculated at $p_{\mathrm{T}}^{\mathtt{Cut}} = 200$ MeV is used to fix the side of the detector from which $\Delta\eta^{\mathrm{F}}$ is measured.

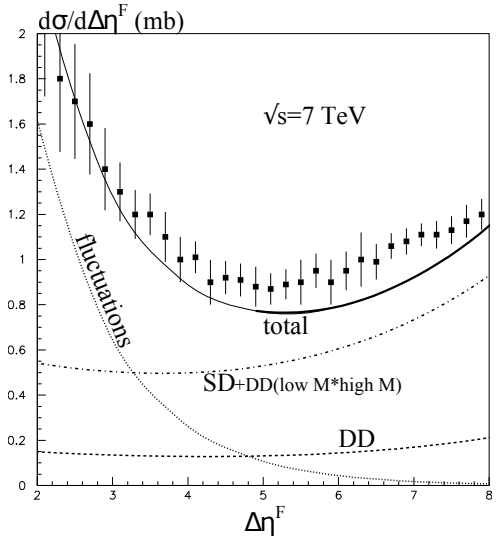

Fig. 3.8: Figure from [18] of the forward pseudorapidity gap size as measured by ATLAS [8] versus the proposed global description.

The ALICE collaboration used minimum bias data at 0.9, 2.76 and 7 TeV to calculate the single (SD) and double (DD) diffraction cross sections at these three energies [21]. In Run-I the data were triggered using the VZERO detector and the two innermost layers of the Inner Tracking System, with a combined pseudorapidity coverage $-3.7 \leq \eta \leq 5.1$. Offline selections were based on the largest forward and central pseudorapidity gaps between tracks at forward and central pseudorapidity, and on the ratio between these two gaps. These are used to define two samples which are strongly enhanced in SD and DD events. These were compared to distributions from two different event generators (PYTHIA 6 [Perugia-0, tune 320] [22] and PHOJET [23]) and the diffractive fractions were obtained from an adjustment of the fractions assumed in these two generators (see paper for details). For SD, an extrapolation was performed to estimate the rate for unobserved low-mass diffractive events according to the parametrisation of Kaidalov and Poghosyan [24]. The resulting SD and DD cross sections are shown as a function of energy in Fig. 3.9. The inelastic cross-sections derived from these measurements are discussed in Section 3.5. In Run-II the measurement will be repeated using essentially the same method, but with increased pseudorapidity coverage (to $-7 \leq \eta \leq 6.3$) using the new AD counters described in Section 9.6.1.

3.4.2 Future soft pseudorapidity gaps studies with a proton tag

By correlating pseudorapidity gaps with forward proton tags, we present an analysis which has the potential to offer enhanced sensitivity to the modelling of $\mathrm{d}\sigma/\mathrm{d}\xi$ over four orders of magnitude in ξ.

For the proton tagged event selection, the near side of the detector to the proton tag is defined as where the gap starts.

Diffractive topologies are isolated at large gap sizes, the distribution is truncated at $\Delta\eta^{\mathrm{F}} = 8$ due to experimental trigger inefficiencies for larger gaps (CMS are able to trigger events up to $\Delta\eta^{\mathrm{F}} = 8.4$). The `Pythia 8` decomposition of the inelastic cross section is explored in Fig. 3.10 (see Section 3.3.1 for forward proton selection and MC details). Here we observe an exponential fall both for the strongly suppressed non-diffractive events and the single diffractive events. The exponential fall of the single diffractive events is expected because only high mass single

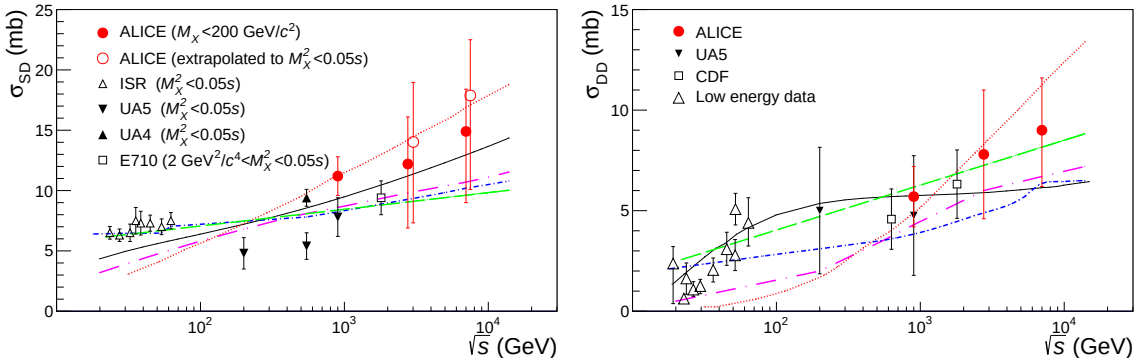

Fig. 3.9: Single diffractive cross section as a function of centre-of-mass energy (left) and for the double diffractive cross section (right) where $\Delta\eta > 3$. SD data from other experiments are for $M_X^2 < 0.05s$. ALICE measured SD points are shown with full red circles, in order to compare with data from other experiments these were extrapolated to $M_X^2 < 0.05s$ (open red circles), when needed. Theoretical model predictions, shown as lines, all correspond to $M_X^2 < 0.05s$.

diffractive events result in a large enough fractional momentum loss to enter the acceptance of AFP. These high mass systems span all of ATLAS and only contain rapidity gaps from hadronisation fluctuations.

The hypothesis that for double dissociation in `Pythia 8`, the low mass system decaying to a forward proton provides an independent tag is illustrated in the flatter behaviour of the double diffractive cross section, this follows from the relation $\ln(\xi_X) \propto \Delta\eta^F$. The small exponential slope is likely due to the residual effect of hadronisation from large diffractive masses.

The key conclusions is that a high purity diffractive sample is predicted where single diffraction is dominant at small gap sizes and double diffraction is dominant at large gap sizes.

When requiring an 90 m optics ALFA tag as in Fig. 3.10b, the non-diffractive component is observed to be even more suppressed than for the 0.55 m optics AFP case. However the lack of any large acceptance at high ξ_p also results in the large suppression of the diffractive components, with the double diffractive being much more heavily suppressed than the single diffractive.

In Fig. 3.11a, the inelastic cross section predictions of `Pythia 8`, `Herwig++` and `EPOS` are plotted differential in $\Delta\eta^F$ at $\sqrt{s} = 14$ TeV for an inclusive sample and for a sample requiring exactly one forward proton tag from AFP. For the inclusive selection, `EPOS` and `Pythia 8` are in rough agreement regarding the relative flatness of the diffractive tail, disagreeing at the 30% level regarding the normalisation. `Herwig++` generates an excess of events with $\Delta\eta^F = 6$ which is a known by-product of the cluster hadronisation of beam remnants.

Upon requiring a forward proton tag from AFP, the overall cross section predictions fall significantly and inline with the acceptances from Table 3.1. All three generators do however still predict a long tail, with the difference in normalisation between `EPOS` and `Pythia 8` now around a factor of 7.5. `Herwig++` also retains its excess of events at $\Delta\eta^F = 6$. The MC all remain sufficiently separated to allow for good model discrimination power given sufficiently precise data.

It is concluded from Fig. 3.10a that the AFP selection greatly suppresses non-diffractive interactions in `Pythia 8` allowing for a higher purity probe of the fragmentation of the *p–IP* system.

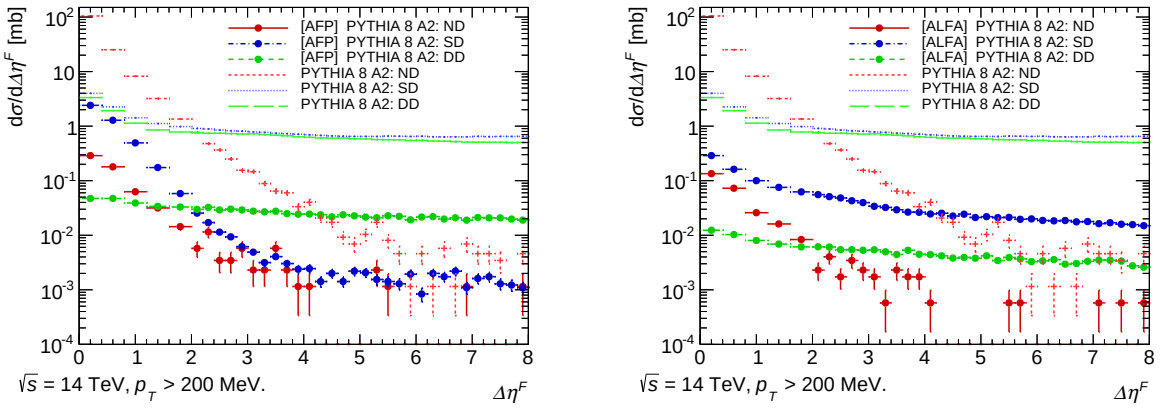
dσ/dΔη^F [mb]
[AFP] PYTHIA 8 A2: ND
[AFP] PYTHIA 8 A2: SD
[AFP] PYTHIA 8 A2: DD
PYTHIA 8 A2: ND
PYTHIA 8 A2: SD
PYTHIA 8 A2: DD
√s = 14 TeV, p_T > 200 MeV.
Δη^F
[ALFA] PYTHIA 8 A2: ND
[ALFA] PYTHIA 8 A2: SD
[ALFA] PYTHIA 8 A2: DD

(a) (b)

Fig. 3.10: Forward rapidity gap cross sections in the range $\Delta\eta^{\mathrm{F}} < 8$ compared between single-diffractive, double-diffractive and non-diffractive components of the inelastic cross section from `Pythia 8`, (a) for the inclusive and AFP selections and (b) for the inclusive and ALFA selections (see text).

One method used is to gradually increase $p_{\mathrm{T}}^{\mathrm{Cut}}$, allowing for hadronisation fluctuations to create larger pseudorapidity gaps and hence studying the p_{T} and η dependences of soft particle production. This is presented in Fig. 3.11, where the $p_{\mathrm{T}}^{\mathrm{Cut}}$ cut is varied over 200–800 MeV.

This scan in the $p_{\mathrm{T}}^{\mathrm{Cut}}$ defining the gap was originally motivated by [25] to study the differences in pseudorapidity gap fluctuations possible between different hadronisation models, see Fig. 3.12.

3.4.3 Soft pseudorapidity gap studies with CASTOR

The CASTOR calorimeter provides a unique detector at LHC to measure charged and neutral energy deposits in the very forward phase space. The detector extends the CMS acceptance to a pseudorapidity of -6.6. In this location of phase space, CASTOR is very sensitive to the production of medium- and low-mass excited states and can thus be used to study diffractive dissociation.

It was shown that CASTOR is well suited to distinguish double diffraction from single diffraction, and that it can contribute to studies of soft diffraction [9]. The RMS noise level per calorimeter cell is of the order of 100–300 MeV, which provides a very good environment to search for rapidity gaps under the condition that the luminosity and subsequently pileup levels are not high. Since CASTOR has no segmentation in pseudorapidity, only gaps larger than the acceptance of CASTOR can be observed.

The use of CASTOR allows for the soft pseudorapidity gap spectrum to be investigated over a larger range. As seen in Fig. 3.13a, very little integrated luminosity is required, around 10 nb^{-1} with low pileup ($\mu < 0.05$) is sufficient for many studies. Here rapidity gaps in CASTOR are defined as being events for which there was less than 10 GeV total energy deposit in the acceptance of CASTOR. The impact of out-of-time pileup events destroying any gap is highlighted for different bunch configurations in Fig. 3.13b.

Such data will contribute complementary information to other soft diffractive measurements that will be performed e.g. by the TOTEM Collaboration. The CASTOR data can be studied together with the TOTEM T2 tracking station data. In this way, rapidity gaps within the acceptance of CASTOR are resolved and correlation measurements of M_{X} vs. $\Delta\eta$ in this very

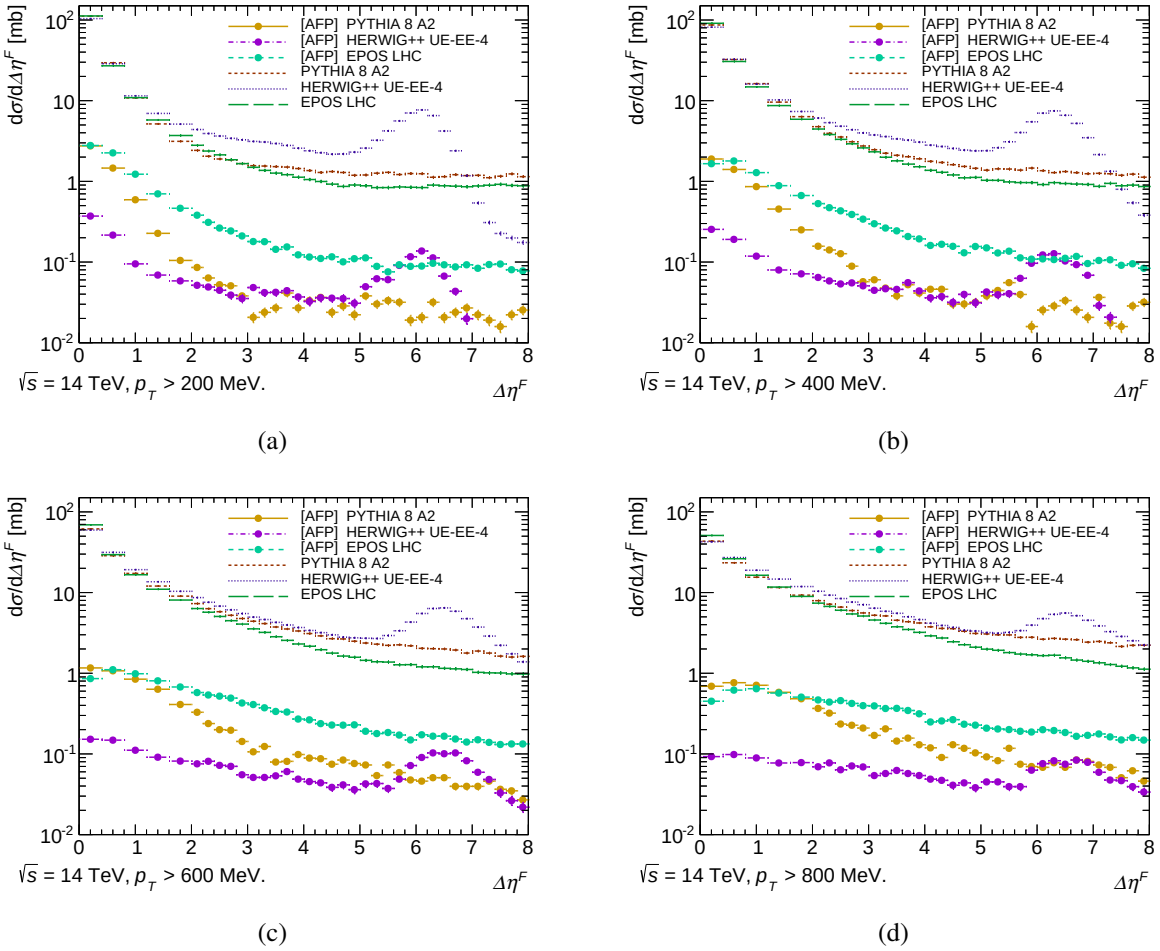

Fig. 3.11: Forward rapidity gap cross sections in the range $\Delta\eta^{\mathrm{F}} < 8$ compared between MC models for the inclusive and AFP selections for $p_{\mathrm{T}}^{\mathrm{Cut}} = 200$ (a), 400 (b), 600 (c) and 800 (d) MeV(see text). The rise in cross section with `Herwig++` at $\Delta\eta^{\mathrm{F}} = 6$ is a issue known to the authors which is due to clustering of beam remnants.

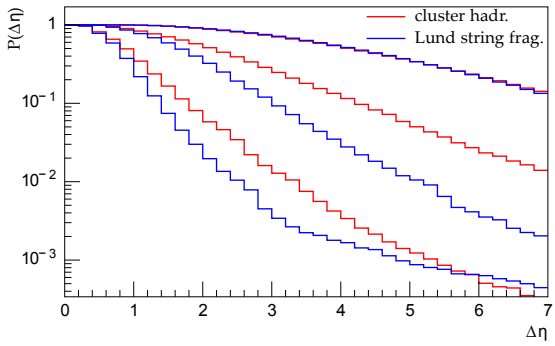

Fig. 3.12: Plot from [25] illustrating the probability of finding a hadron level pseudorapidity gap within $|\eta| < 5$ for different choices of $p_{\mathrm{T}}^{\mathrm{Cut}}$, shown for Sherpa 2.2.1 with the default cluster hadronisation and when instead using Lund string fragmentation from Pythia. From top to bottom the values of $p_{\mathrm{T}}^{\mathrm{Cut}}$ are 1.0, 0.5 and 0.1 GeV.

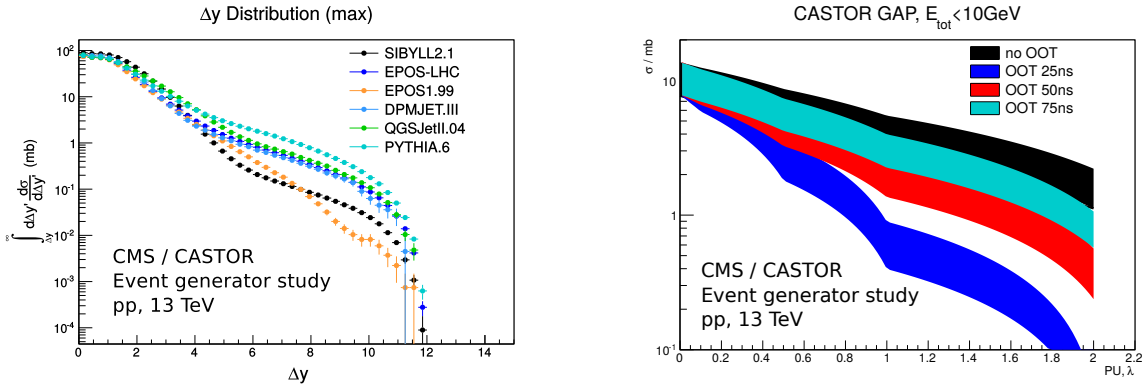

(a) (b)

Fig. 3.13: CASTOR/CMS event generator level distributions at $\sqrt{s} = 13$ TeV of (a) the distribution of rapidity gaps sizes in 13 TeV proton-proton collisions. The transition to low-mass diffraction for rapidity gaps larger then 10 is only accessible with the CASTOR detector and T2. (b) The dependence of detection efficiency of rapidity gaps ($E_{\mathrm{CASTOR}} < 10$ GeV) on pileup for different bunch spacing scenarios.

forward phase space interval can be performed. These are unique measurement opportunities at LHC in respect to soft diffraction. Firstly, to measure soft diffractive cross sections in differential bins of mass as well as rapidity gaps and, secondly, to measure single diffractive mass distributions, if possible correlated to the momentum loss of the surviving proton.

3.4.4 Extending pseudorapidity gaps with forward shower counters

As described in Section 9.7, the ALICE, CMS and LHCb collaborations have installed forward scintillator shower counters (FSC) which surround the beam pipe at large distances from the central detectors and provide a veto on very forward activity such as is found with low mass diffractive dissociations.

Although with lower granularity in η, such detectors will allow rapidity gap measurements to extend out yet further from the coverage of the central detectors to (in the case of CMS) $|\eta| = 9$ [26, 27] hence allowing rapidity gaps up to $|\Delta\eta| = 18$ to be measured.

Another primary use of FSC is motivated by LHCb. As the LHC beam is defocused at the LHCb IP to provide low-pileup conditions. The LHCb FSC will be of use in determining the exclusivity of central production events by vetoing on low mass dissociation.

Signals in forward scintialltor counters may also be used to measure low mass diffractive states and the data will also be of use for luminosity and beam condition motoring.

3.4.5 Soft rapidity gap conclusion

Rapidity gaps in soft events have been shown in Run-I to be sensitive probes of the physics of diffraction and hadronisation. Giving us a greater phenomenological understanding of the proton. This is made possible with small samples of data take at very low pileup in combination with the forward detectors.

In Run-II, the addition of proton tags is shown in MC to provide an event sample which is strongly diffractive-enhanced. Allowing for greater sensitivity to differences between proton-proton and Pomeron-proton interactions. Moreover it is predicted that the soft pseudorapidity gap spectrum will isolate the contributions from single diffractive dissociation at small gap sizes and double diffractive dissociation at large gap sizes.

The continued use of the CMS CASTOR detector, along with the TOTEM T1 and T2 telescopes and the range of Forward Shower Counters being installed at LHC experiments will fill the forward aperture, allowing for a much larger span of reconstructible pseudorapidity gap sizes and hence access to lower diffractive masses.

3.5 Measurements of the Inelastic Cross-Section

Measures of the total inelastic cross section during Run-I were performed by ALICE, ATLAS, CMS and LHCb central detectors and by TOTEM. Such studies rely on measuring the cross section from charged particle production within the kinematic and fiducial acceptance of the detectors and subsequently performing a model dependent extrapolation to the total inelastic cross section.

The ALICE collaboration made a measurement of σ_{inel} which makes use of the determination of the single diffractive and double diffractive cross sections (see Section 3.4.1) to determine the inelastic cross section. Measurements were made at three energies (0.9, 2.76 and 7 TeV). The 7 TeV measurement is shown in Fig. 3.14, and all the values can be found in reference [21].

ATLAS measured the cross section [28] corrected to the acceptance of the Minimum Bias Trigger Scintillators, this corresponds to all non-diffractive events along with diffractive events with mass $M_X^2/s > 5 \times 10^{-6}$.

CMS also corrects to this mass range using data from the forward calorimeters ($3 < |\eta| < 5$) and, as an independent method, CMS measures the cross section for events containing two or more charged particles with $p_T > 0.2$ GeV within $|\eta| < 2.4$ [29].

LHCb measures [30] the cross section for one or more charged particles with $p_T > 0.2$ GeV within $2 < \eta < 4.5$.

TOTEM measured directly the inelastic cross sections using the T1 and T2 telescopes with a $3.1 < |\eta| < 4.7$ and $5.3 < |\eta| < 6.5$ coverage at $\sqrt{s} = 7$ TeV (see Section 3.6.3) [31]. In addition higher precision on the inelastic measurement has been achieved by deriving σ_{inel} from the total cross section measurements based either on the luminosity independent method (TOTEM) or on the elastic scattering measurement (TOTEM and ALFA). See next Sections for details.

All results are in agreement to within experimental uncertainty, see Fig. 3.14. However the measurement based on larger pseudorapidity coverage like ALICE and TOTEM tend to give larger inelastic cross section values that in addition are better in agreement with the precision measurements of the inelastic cross-section using elastic scattering and the optical theorem. This points to a lack of the models to predict the cross section of low-mass diffraction in the 3.4 – 26 GeV/c^2 mass range. After model uncertainties due to extrapolation are included, the typical precision of these measurements is 5 – 11%.

3.6 Measurements of the Total, Elastic and Inelastic Cross-Section with the TOTEM detectors

The TOTEM experiment [32] has measured the total, elastic and inelastic proton-proton cross-section during LHC Run-I, at $\sqrt{s} = 7$ and 8 TeV. The data samples collected at different centre-of-mass energy have all been obtained in dedicated runs (most with special beam optics) with Roman Pots approaching the beam close enough to detect elastic events with squared four-momentum transfer $|t|$ as low as possible. The available data samples, $|t|$ ranges, event statistics and analysis status/publication reference are listed in Table 3.2. All the published total, elastic

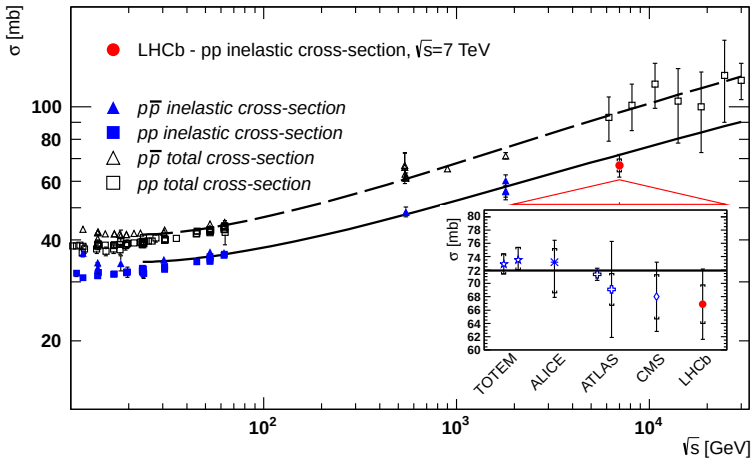

Fig. 3.14: Comparison of model-extrapolated total inelastic cross section measurements by ALICE, ATLAS, CMS and LHCb (discussed above) along with precision measurements by ATLAS (ALFA) and TOTEM (discussed below). Figure from LHCb [30].

and inelastic cross-section results by TOTEM are summarised and put in context of earlier measurements in Fig. 3.15.

Table 3.2: List of available data samples. The LHC optics is characterised by the betatron function value at the IP, β^*. The RP approach to the beam is given in multiples of the transverse beam size, σ. The number of elastic events corresponds to both diagonals after the proton tagging.

β^* (m)	RP approach	$\lvert t\rvert$ range (GeV^2)	elastic events	inelastic events	Results
$\sqrt{s}$ = 7 TeV					
90	10 σ	0.02 to 0.4	15 k		σ_{tot} [33]
90	4.8 to 6.5 σ	0.005 to 0.4	1 M	5.54 M	σ_{tot}, σ_{inel}, σ_{el}, $(d\sigma/dt)_{\text{el}}$ [34] [31] [35]
3.5	7 σ	0.4 to 2.5	66 k		$(d\sigma/dt)_{\text{el}}$ [36]
3.5	18 σ	2 to 3.5	10 k		$(d\sigma/dt)_{\text{el}}$ in progress
$\sqrt{s}$ = 8 TeV					
1000	3 – 10 σ	0.0006 to 0.2	352 k		ρ, $(d\sigma/dt)_{\text{el}}$ in progress
90	6 – 9.5 σ	0.01 to 0.3	0.65 M	4 M	σ_{tot}, σ_{inel},σ_{el} [37]
90	9.5 σ	0.03 to 1.4	7.2 M		$(d\sigma/dt)_{\text{el}}$ in progress
$\sqrt{s}$= 2.76 TeV					
11	5 – 13 σ	$\approx$ 0.06 to 0.5	45 k	1.5M	σ_{tot}, σ_{inel}, σ_{el}, $(d\sigma/dt)_{\text{el}}$ in progress

3.6.1 Total cross-section

Three complementary methods have been used to determine the total cross-section. The methods, having very different systematic dependences, give results in excellent agreement.

– The first method exploits only elastic scattering measurement. By applying the optical theorem the following formula for the total cross-section σ_{tot} is obtained:

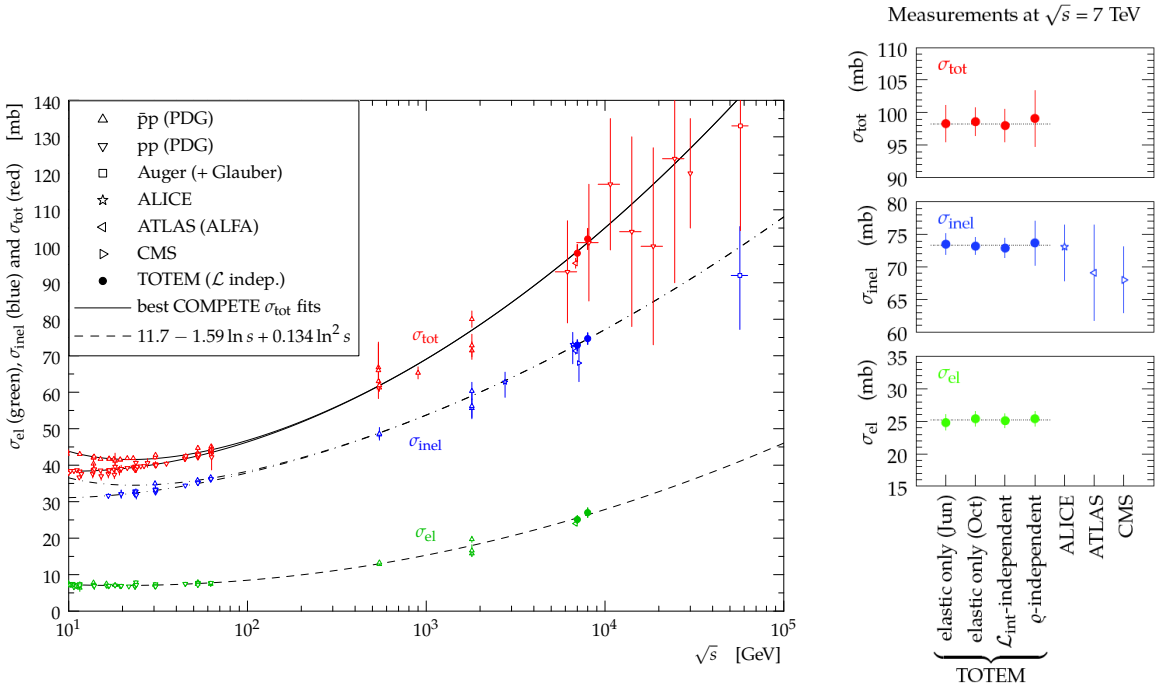

Fig. 3.15: *Left*: compilation [35,37–42] of total, inelastic and elastic cross-sections plotted as a function of the centre-of-mass energy $\sqrt{s}$. The continuous black lines (lower for pp, upper for $\bar{p}p$) represent the best fits of the total cross-section data by the COMPETE collaboration [43]. The dashed line results from a fit of the elastic scattering data. The dash-dotted curves correspond to the inelastic cross-section and is obtained as the difference between the continuous and dashed fits. *Right*: detail of the measurements of total, inelastic and elastic cross-sections at $\sqrt{s} = 7\,\text{TeV}$. The circles represent the four TOTEM measurements, the other points show the measurements of other LHC collaborations.

$$\sigma_{tot}^2 = \frac{16\pi}{1+\rho^2} \frac{1}{\mathscr{L}} \frac{dN_{el}}{dt}\bigg|_{t=0} , \tag{3.1}$$

where $\mathscr{L}$ stands for the integrated luminosity and $dN_{el}/dt|_{t=0}$ is the elastic differential rate extrapolated to $t = 0$. For the ρ parameter the COMPETE [43] preferred-model extrapolation has been used (0.141 ± 0.007 at 7 TeV).

– The second method relies on summing the elastic event rate N_{el} (obtained by integrating and extrapolating the differential rate) and the inelastic event rate N_{inel} (measured by the inelastic telescopes T1 and T2):

$$\sigma_{tot} = \frac{1}{\mathscr{L}} (N_{el} + N_{inel}) . \tag{3.2}$$

This method does not require the value of ρ as input from external sources and it doesn't rely on the Optical Theorem, but in addition it proofs its validity (at 3.5% level).

– The third method is luminosity-independent. The method requires the simultaneous measurements of the inelastic and elastic rates, as well as the extrapolation of the latter in the invisible region down to $t = 0$. Moreover, the value of the integrated luminosity can be determined as well:

$$\sigma_{tot} = \frac{16\pi}{1+\rho^2} \frac{dN_{el}/dt|_{t=0}}{N_{el} + N_{inel}} , \qquad \mathscr{L} = \frac{1+\rho^2}{16\pi} \frac{(N_{el} + N_{inel})^2}{dN_{el}/dt|_{t=0}} . \tag{3.3}$$

At $\sqrt{s} = 7\,\text{TeV}$, all three methods have been used, all exploiting the $\beta^* = 90\,\text{m}$ optics. The method based on elastic inputs only, Eq. (3.1), is described in [33] while in [35] all the three methods are described (second row from top in Table 3.2). Fig. 3.15 (right) shows the consistency of all four total cross-section results.

At $\sqrt{s} = 8\,\text{TeV}$ only the luminosity-independent results on elastic, inelastic and total cross-section have been published [37]. Moreover, the analysis of the $\beta^* = 1000\,\text{m}$ data is in progress: the separation of Coulomb and nuclear effects is at reach, thus yielding methodically more accurate results.

3.6.2 Elastic scattering

At the centre-of-mass energy $\sqrt{s} = 7\,\text{TeV}$ the differential cross-section of elastic scattering, $\text{d}\sigma/dt$, has been measured by TOTEM in the range $0.005 < |t| < 2.5$ GeV^2 (see Fig. 3.16), extending from the almost exponential forward peak ($\text{d}\sigma/dt \propto \exp(-Bt)$ with B = 19.9 ± 0.3 GeV^{-2}) [34] through the dip-bump region (with the minimum observed at 0.53 ± 0.01 GeV^2) to the large-$|t|$ domain exhibiting a power-law behaviour, $\propto |t|^{-7.8}$ [36] . The $|t|$-range analysed so far has been covered by two data sets and will be extended at its upper bound to about 3.5 GeV^2 with a third data set already under analysis (see Table 3.2).

The direct measurement of the cross section, based on the observation of 91% of the elastic events, gives $\sigma_{el} = (25.43 \pm 1.07)$ mb. The direct and indirect[5] evaluation of the elastic cross section is summarised in Table 3.2 and Fig. 3.15.

At the centre-of-mass energy $\sqrt{s} = 8\,\text{TeV}$ a first data set ($0.01 < |t| < 0.3\,\text{GeV}^2$) has been analysed and used for the luminosity independent measurement of the total cross section [37]. The elastic cross-section has been derived independently from the luminosity ($\sigma_{el} = (27.1 \pm 1.4)$ mb). Details of the analyses can be found in [34, 37].

More analyses with two different machine optics are in progress:

- With β^* = 1000m optics, $|t|$ values from $6 \cdot 10^{-4}\,\text{GeV}^2$ to 0.2 GeV^2 have been reached, and the interference between electromagnetic (Coulomb) and strong (nuclear) interactions has been observed for the first time at the LHC.
  This interference gives some sensitivity to the phase of the nuclear amplitude mainly at t = 0 and allows to separate the Coulomb and nuclear effects (beneficial for determinations of the *nuclear* total cross-section). However, the precise functional form of the scattering amplitude in the interference region is not known from first principles and thus is model dependent.
  The preliminary results for ρ are conditional to the functional form of modulus and phase of the nuclear amplitude, and to the choice of the interference formula.
- The second set at β^*= 90m is characterised by very high statistics (7 M events) in the range $0.03 < |t| < 1.4\,\text{GeV}^2$. Its strong statistical power enables an in depth analysis of the exponential slope $B(t)$.

The ratio $\sigma_{\text{el}}/\sigma_{\text{tot}}$ can give some insights into the shape and the opacity of the proton, subject to model-dependent theoretical interpretations. The steady rise of this ratio with energy (Fig. 3.17) is often interpreted as the increase of proton size and opacity with energy.

[5] From the luminosity and ρ independent method

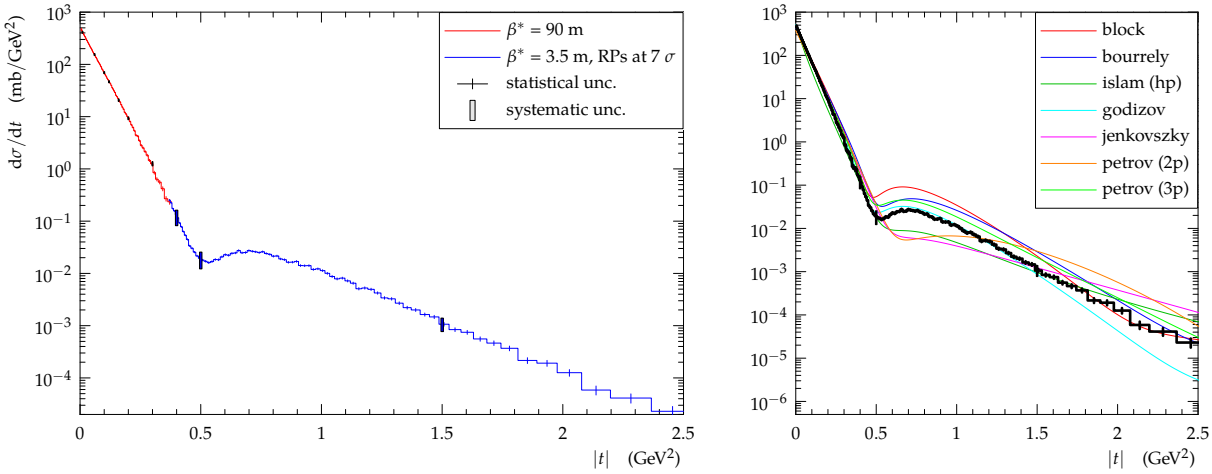

Fig. 3.16: Left: The elastic differential cross-section measurements by TOTEM at $\sqrt{s} = 7\,\text{TeV}$. Right: The measured $d\sigma/dt$ compared to the predictions of several models [44–48]

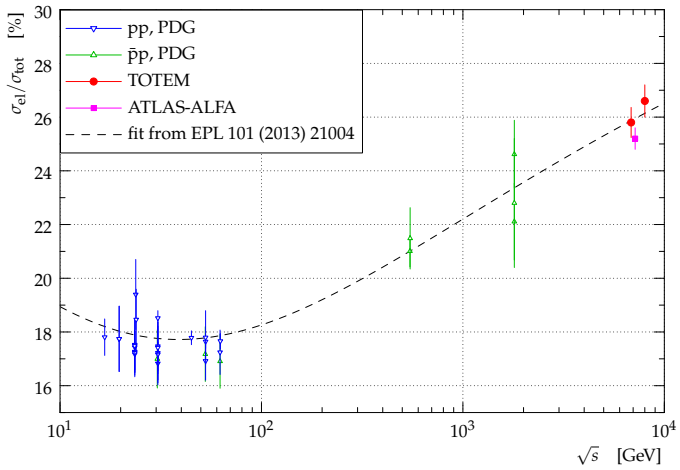

Fig. 3.17: The ratio of the elastic to total cross-section as a function of energy [35, 37, 38]. The dashed line shows the ratio of the $\sigma_{el}, \sigma_{tot}$ fits from Fig. 3.15

3.6.3 Inelastic scattering

At the centre-of-mass energy $\sqrt{s} = 7\,\text{TeV}$ the inelastic cross-section has been directly measured by TOTEM using inelastic events triggered by the T2 telescope [31]. The T2-visible inelastic cross section, in the pseudorapidity range $5.3 < |\eta| < 6.5$, has been measured to be (69.73 ± 2.88) mb.

After including the contributions of events with tracks measured only in T1 telescope ($3.1 < |\eta| < 4.7$), the contribution of diffractive events with no tracks in T1 and a rapidity gap covering T2, and the contribution of low mass diffraction with all final particles at $|\eta| > 6.5$, the total inelastic cross-section has been determined to be (73.7 ± 3.4) mb. The T1+T2 telescopes are sensitive to diffractive masses larger than 3.4 GeV. Although the extrapolation range is very small compared to other LHC experiments, low mass contribution is the second largest uncertainty of the inelastic cross-section measurement (after the luminosity).

An estimate of the contribution of low mass diffraction can be obtained by comparing the inelastic cross section measurement obtained from elastic scattering [34] with with the direct measurements as described before. From their difference,

$$\sigma_{\text{tot}}^{\text{RP}} - \sigma_{\text{el}}^{\text{RP}} - \sigma_{\text{inel},|\eta|<6.5}^{\text{T2}} = 2.62 \pm 2.17\,\text{mb}$$

, an upper limit of 6.31 mb at 95% confidence level on the cross-section for events with diffractive masses below 3.4 GeV has been deduced.

At the centre-of-mass energy $\sqrt{s} = 8\,\text{TeV}$, the inelastic cross-section has been derived independently from the luminosity, $\sigma_{inel} = (74.7 \pm 1.7)$ mb.

3.6.4 TOTEM Plans at $\sqrt{s} = 13\,\text{TeV}$

During LHC Run-II, TOTEM plans to perform the measurement of the total, elastic and inelastic cross-section at the energy $\sqrt{s} = 13\,\text{TeV}$ based on the methods described above. The high-beta optics ($\beta^* \leq 90\,\text{m}$) is expected to have the same performance as at lower energies: the lower acceptance limit in $|t|$ is roughly $|t|_{min,13TeV} \approx 2|t|_{min,7TeV}$, still allowing a good extrapolation of the differential elastic cross section to $t = 0$ at $\beta^* = 90\,\text{m}$ but not enough to acces the Coulomb interference region. A higher beta optics ($\beta^* = 2.5\,\text{km}$) is foreseen in order to access the required $|t|$-range. Moreover the differential elastic cross section will be measured, up to the high $|t|$ values, and further studies of the exponential behaviour at low-$|t|$ are envisaged. The full menu of diffractive measurements is described elsewhere in this document.

3.7 Measurement Total and Elastic cross-section with ALFA

The ATLAS precision measure of the total pp cross section was performed with the ALFA detector using the luminosity dependent parametrisation of the optical theorem in Equation 3.1 during a dedicated $\sqrt{s} = 7$ TeV run with $\beta^* = 90$ m optics.

ALFA uses parallel-to-point focusing optics in the vertical plane to translate the scattering angle θ at the interaction point to a vertical displacement at the detector. This angle was reconstructed from the impact points and beam transport matrix using the so called 'subtraction method' by exploiting that elastic protons will be reconstructed back-to-back in the forward and backward instrumentation.

Both background and efficiency determination were data driven and ALFA fits the $-t$ spectrum (Fig. 3.18) in the range of $> 10\%$ acceptance, $0.01 < -t < 0.1$ GeV^2, which yields fits to the B slope $B = 19.73 \pm 0.14(\text{stat.}) \pm 0.26(\text{syst.})$ GeV^{-2} and total cross section of $\sigma_{\text{tot}} = 95.35 \pm 0.38(\text{stat.}) \pm 1.25(\text{exp.}) \pm 0.37(\text{extr.})$ mb [40]. The 'extra.' uncertainty covers the extrapolation to the optical point $|t| \to 0$ and the dominant uncertainty comes from the luminosity and beam energy.

3.7.1 ALFA Plans at $\sqrt{s} = 13\,\text{TeV}$

For the upcoming Run-II period of the LHC, dedicated periods for special fills with high β^* are envisaged. The ALFA approved physics programme at the energy $\sqrt{s}$ = 13 TeV will initially focus on total and elastic cross-section and diffractive measurements at β^* = 90 m.

During the Long Shutdown 1 (2014) several upgrades have been performed on the ALFA detector to ensure good performance during Run-II. Most notably, a RF-protection system has been installed and the distance between stations has been increased to 8 m improving the local angle resolution by factor of 2 which will improve the final precision.

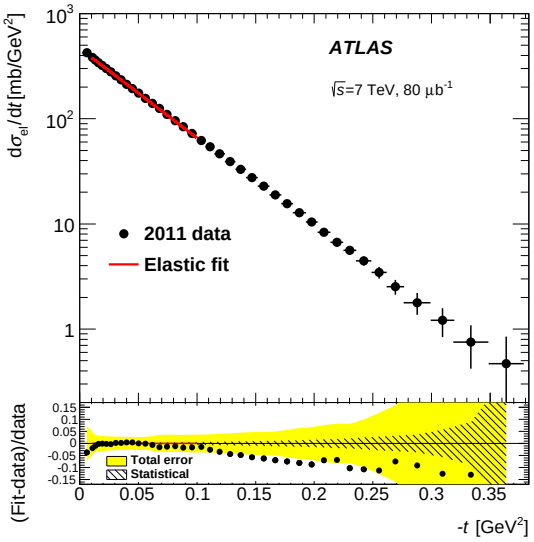

Fig. 3.18: Left: A fit of a parametrised form of the differential elastic cross section, reconstructed with the subtraction method.

For the shutdown 2015–2016 it is foreseen to install a new set of cables to power separately Q4 and Q7, allowing higher values in β^* and therefore giving access to lower $|t|$ values. The ultimate long term goal of ALFA is to run at very high β^* (2.5 km) optics to study the Coulomb interference region and to obtain a calibration of the absolute luminosity.

3.8 Conclusions & Running Conditions

The current Roman pot based detectors at the LHC are well located to make precision measurements of elastically scattered protons and will continue their program at higher energies which will be obtained in future runs. In addition, we have shown how joint analysis of forward tagged protons correlated with activity in the central detectors will allow for much greater soft physics model discrimination with very little integrated luminosity. Requiring a forward proton is expected to be a very good way of suppressing the non-diffractive component of the cross section while different LHC optics configurations will be used to enhance either the single or double diffractive components of the diffractive proton cross section. This will allow for a better handle on soft hadronisation effects originating from a Pomeron-proton vertex.

References

[1] T. Sjöstrand, S. Mrenna and P. Skands, JHEP05 (2006) 026, Comput. Phys. Comm. 178 (2008) 852.

[2] R. Ciesielski and K. Goulianos, PoS ICHEP2012 (2013) 301, arXiv:1205.1446

[3] P. Bussey, *FPTrack Program*, http://ppewww.physics.gla.ac.uk/~bussey/FPTRACK

[4] ATLAS Collaboration, ATL-COM-PHYS-2010-880, 2010.

[5] UA5 Collaboration. *Z. Phys. C*, 33(BONN-HE-86-19):175–185. 21 p, 1986.

[6] UA4 Collaboration. *Phys. Lett.*, B186:227, 1987.

[7] CDF Collaboration. *Phys. Rev. Lett.*, 87:141802, 2001.

[8] ATLAS Collaboration. *Eur.Phys.J.*, C72:1926, 2012.

[9] CMS Collaboration. CMS-PAS-FSQ-12-005 2013.

[10] A. Capella, A. Kaidalov, C. Merino, D. Pertermann, and J. Tran Thanh Van. *Phys. Rev.*, D53:2309–2316, 1996.

[11] Johannes Ebke, Peter Waller, and Tim Brooks. MCViz. Version used 2011.09.15.

[12] ATLAS Collaboration. Summary of ATLAS Pythia 8 tunes. ATL-PHYS-PUB-2012-003, CERN, Geneva, Aug 2012.

[13] M Trzebinski, Janusz Chwastowski, and Christophe Royon. *Study of QCD and Diffraction with the ATLAS detector at the LHC*. PhD thesis, Cracow, INP and U. Paris-Sud 11, Dept. Phys., Orsay, 2013. Presented 20 Sep 2013.

[14] The CMS Collaboration, "Measurement of diffraction dissociation cross sections at $\sqrt{s}$=7 TeV at the LHC", CMS-PAS-FSQ-12-005.

[15] The TOTEM Collaboration, *Phys. Rev. Lett.* **111** 262001 (2013)

[16] F. Oljemark, and K. Österberg, "Soft single diffraction with TOTEM at 7 TeV", LHC students poster session, 13 March 2013.

[17] V. A. Khoze, A. D. Martin and M. G. Ryskin, Int. J. Mod. Phys. A **30** (2015) 08, 1542004 [arXiv:1402.2778 [hep-ph]].

[18] V. A. Khoze, A. D. Martin and M. G. Ryskin, Eur. Phys. J. C **74** (2014) 2, 2756 [arXiv:1312.3851 [hep-ph]].

[19] A. D. Martin, V. A. Khoze and M. G. Ryskin, AIP Conf. Proc. **1654** (2015) 050002 [arXiv:1410.3261 [hep-ph]].

[20] M. G. Ryskin, A. D. Martin and V. A. Khoze, Eur. Phys. J. C **71**, 1617 (2011) [arXiv:1102.2844 [hep-ph]].

[21] B. Abelev *et al.* [ALICE Collaboration], Eur. Phys. J. C **73** (2013) 6, 2456 [arXiv:1208.4968 [hep-ex]].

[22] T. Sjöstrand, Comput. Phys. Commun. **82**, 74 (1994); T. Sjöstrand, S. Mrenna and P. Skands, JHEP **05**, 026 (2006). In this analysis Perugia-0 (320) tune is used: P.Z. Skands, Multi-Parton Interaction Workshop, Perugia, Italy, 28-31 Oct. 2008, arXiv:0905.3418 [hep-ph] (2009)

[23] R. Engel, J. Ranft, S. Roesler, Phys. Rev. **D52**, 1459 (1995)

[24] A.B. Kaidalov, M.G. Poghosyan, in *Proc. of the 13th Int. Conf. on Elastic and Diffractive Scattering ("Blois Workshop")*, June 2009, CERN, 91, (2010); arXiv:0909.5156 [hep-ph]

[25] V. A. Khoze, F. Krauss, A. D. Martin, M. G. Ryskin and K. C. Zapp, Eur. Phys. J. C **69**, 85 (2010) [arXiv:1005.4839 [hep-ph]].

[26] M. Albrow *et al.* [CMS Collaboration], JINST **4**, P10001 (2009) [arXiv:0811.0120 [hep-ex]].

[27] M. Albrow, P. Collins and A. Penzo, Int. J. Mod. Phys. A **29**, no. 28, 1446018 (2014).

[28] G. Aad *et al.* [ATLAS Collaboration], Nature Commun. **2** (2011) 463 [arXiv:1104.0326 [hep-ex]].

[29] S. Chatrchyan *et al.* [CMS Collaboration], Phys. Lett. B **722** (2013) 5 [arXiv:1210.6718 [hep-ex]].

[30] R. Aaij *et al.* [LHCb Collaboration], arXiv:1412.2500 [hep-ex].

[31] The TOTEM Collaboration, *Europhys. Lett.* **101** 21003 (2013)

[32] The TOTEM Collaboration, *JINST* **3** S08007 (2008)

[33] The TOTEM Collaboration, *Europhys. Lett.* **96** 21002 (2011)

[34] The TOTEM Collaboration, *Europhys. Lett.* **101** 21002 (2013)

[35] The TOTEM Collaboration, *Europhys. Lett.* **101** 21004 (2013)
[36] The TOTEM Collaboration, *Europhys. Lett.* **95** 41001 (2011)
[37] The TOTEM Collaboration, *Phys. Rev. Lett.* **111** 012001 (2013)
[38] Nakamura, K. et al. (Particle Data Group), *J. Phys. G* **37** 075021 (2010)
[39] ALICE Collaboration, *Eur. Phys. J. C* **73** 2456 (2013)
[40] ATLAS Collaboration, *Nuclear Physics, Section B* **889** 486-548 (2014)
[41] CMS Collaboration, Report No. CMS-PAS-FWD-11-001;
CMS Collaboration, *Phys. Lett. B* **722** 5 (2013)
[42] Abreu, P. et al. (Pierre Auger Collaboration), *Phys. Rev. Lett.* **109** 062002 (2012)
[43] Cudell, J. R., Ezhela, V., Gauron, P., Kang, K., Kuyanov, Yu., Lugovsky, S., Martynov, E., Nicolescu, B., Razuvaev, E. and Tkachenko, N. (COMPETE Collaboration), *Phys. Rev. Lett.* **89** 201801 (2002)
[44] Block M. M. et al., *Phys. Rept.* **36** 71-215 (2006)
[45] Bourrely C. et al., *Eur. Phys. J.* **C28** 97-105 (2003)
[46] Islam M. et al., *Int. J. Mod. Phys.* **A21** 1-42 (2006), *Mod. Phys. Lett.* **A24** 485-496 (2009)
[47] Jenkovszky L. et al., *Int. J. Mod. Phys.* **A 26** 4755 (2011)
[48] Petrov V. et al., *Eur. Phys. J.* **C23** 135-143 (2002)

Chapter 4

Inclusive Hard Diffraction

Conveners and Editors: M. Ruspa, M. Trzebiński
Internal Reviewers: P. Bussey, T. Martin, M. Obertino

4.1 Introduction

Hard diffractive processes are important part of the studies performed in a high energy physics since their discovery in the UA8 experiment [1, 2]. Data collected by HERA and Tevatron detectors allowed to significantly increase this knowledge. Nevertheless, at the LHC era, many questions still remain open.

The definition of diffraction is connected to the exchange of a colourless object (the Pomeron). Such exchange does not only leave the interacting proton intact, but also creates a region in rapidity devoid of particles – a large rapidity gap (LRG). Such signature is often a requirement in the diffractive event selection. However, as the gap is created between the scattered proton and the Pomeron remnants, *i.e.* in the very forward direction, it is sometimes beyond the detector acceptance. Moreover, a gap could be created also in the non-diffractive events as a result of a fluctuation of the final state particles. Alternatively to requiring the LRG, the intact proton can be directly tagged, provided the adequate instrumentation is available.

During Run I a number of diffractive measurements were done at the LHC by the ATLAS [3–6], CMS [7–9, 11, 21], TOTEM [12–16], ALICE [17, 18] and LHCb [19, 20] experiments. These analyses, preformed at $\sqrt{s}$ of 7 or 8 TeV will be continued also at Run II, when the centre-of-mass energy will be increased to 13 TeV.

This chapter describes the foreseen hard diffractive programme of the CMS/TOTEM and ATLAS experiments, with special attention paid to measurements utilising forward proton tagging techniques (see Chapter 1 for details on the instrumentation). These results include experimental motivation as well as an estimation of the obtainable significances along with the technical requirements for the collection of suitable datasets. In particular, the possibilities of measuring various single diffractive and double Pomeron exchange events will be discussed.

4.2 Backgrounds

In measurements using a forward tagging technique in a non-zero pile-up environment a variety of backgrounds are present. They may originate from events in which a non-diffractive system is produced together with a forward proton coming from a different interaction in the same bunch crossing. For example, a hard single diffractive production process might be mimicked by a hard non-diffractive interaction overlaid with an intact proton coming from the minimum-bias events. In case of double Pomeron exchange (DPE) production, the background may come from non-diffractive or single diffractive events (see Fig. 4.1).

In addition to pile-up events, other particles circulating with the LHC beam (the so-called beam halo) can be detected in the forward detectors and act as a background. The realistic way of simulating such events is not yet known. Fortunately, at low luminosities (low pile-up values) they can be sufficiently suppressed by data driven approaches based on the correlations between

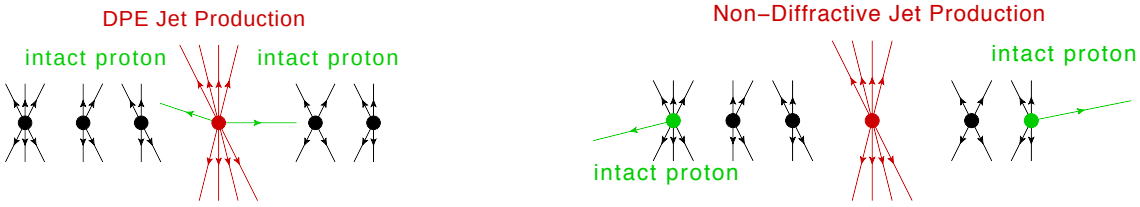

Fig. 4.1: An example of diffractive signal (**left**) and non-diffractive background (**right**) in non-zero pile-up environment. The non-diffractive event is overlaid with minimum-bias protons visible in the forward detectors.

the central system and the forward protons. In order to reduce these backgrounds, the following selection criteria can be applied:

- proton tag,
- one vertex reconstructed in central detector,
- correlation between kinematics of proton(s) and central system.

Since the mentioned backgrounds are similar for all measurements described in this Chapter, their treatment is discussed commonly in this Section.

4.2.1 Proton Tag

The presence of the forward proton(s) is a natural requirement in the following analyses. In order to mimic a diffractive event, there has to be a proton visible in the forward detector.

The probability of having intact protons originating from soft events depends on various factors, such as the LHC optics settings and the acceptance of the forward detectors. These issues are discussed in details in Section 1.1.

4.2.2 One Vertex Requirement

Another constraint that may suppress pile-up backgrounds comes from the single vertex requirement. Unfortunately, this rejection is not 100% effective due to:

- finite resolution of the central trackers which may result in the merging of nearby vertices,
- too few tracks originating from the soft pile-up vertex.

In the ATLAS feasibility studies presented in this Chapter, the vertex is assumed to be reconstructed if there are at least four charged particles in the tracker ($|\eta| < 2.5$). In order to account for the detector efficiency, each particle was assigned a probability of being reconstructed. The thresholds were set to:

- 50% for the particles with $100 < p_T < 500$ MeV and
- 90% for the ones with $p_T > 500$ MeV.

These values reflect the performance of the ATLAS inner detector [23], but are also similar for the CMS experiment [24]. The minimal distance below which vertices are merged was set to 1.5 mm.

4.2.3 Relative Energy Loss Difference

In order to suppress pile-up and beam-halo backgrounds a data driven approach based on the correlations between the central system and the forward protons can be used. For example, in a CMS-TOTEM analysis of single diffractive dijet production with Run I data, beam halo and pile-up backgrounds were subtracted by comparing the longitudinal momentum loss of the proton reconstructed with CMS (ξ_{CMS}, obtained summing up the energies and longitudinal momenta of all final state particles) and that reconstructed with the TOTEM Roman Pots (RP) (ξ_{TOTEM}) [25]. The difference $\xi_{\mathrm{CMS}} - \xi_{\mathrm{TOTEM}}$ is shown in Fig. 4.2 (left).

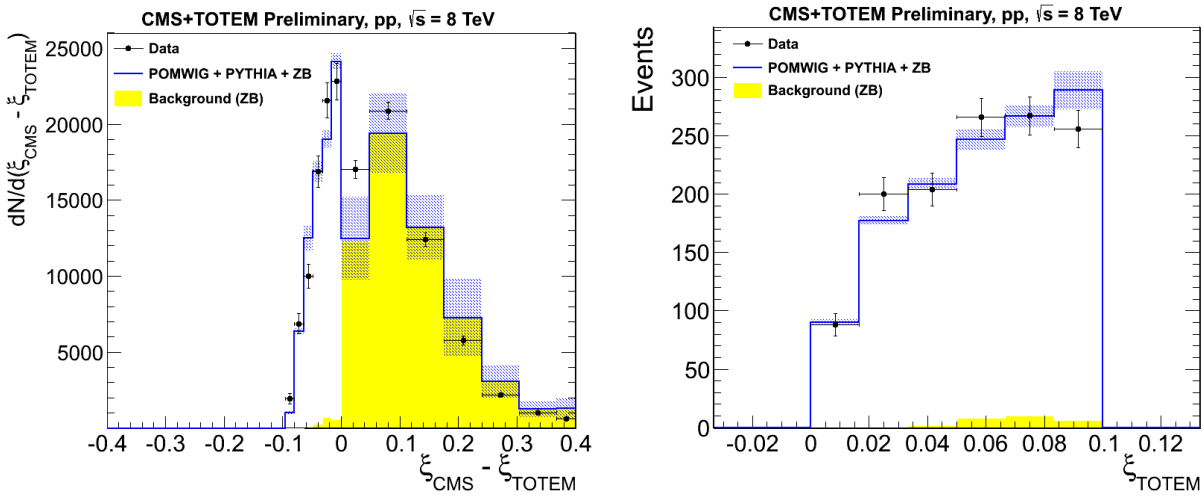

Fig. 4.2: **Left:** difference between the longitudinal momentum loss of the proton reconstructed with CMS and with TOTEM in the single diffractive dijet production process. The data points (full circles) are compared to a mixture of MC and ZB events. **Right:** longitudinal momentum loss of the proton reconstructed with TOTEM after application of the background subtraction condition $\xi_{\mathrm{CMS}} - \xi_{\mathrm{TOTEM}} > 0$.

The data in Fig. 4.2 are compared to a mixture of MC (containing signal and non-diffractive background) and zero bias data events. These data were collected with the CMS and TOTEM detectors in proton-proton collisions at $\sqrt{s} = 8$ TeV during a dedicated run with $\beta^* = 90$ m (and therefore include events with protons originating from pile-up and particles from beam halo). It is worth stressing that such conditions are similar to those expected for the low-luminosity, low-pile-up scenarios during the LHC Run II.

Background events populate the kinematically forbidden region of $\xi_{\mathrm{CMS}} - \xi_{\mathrm{TOTEM}} > 0$. The requirement $\xi_{\mathrm{CMS}} - \xi_{\mathrm{TOTEM}} < 0$, applied in Fig. 4.2 (right) where ξ_{TOTEM} is shown, selects mostly signal events. The remaining contamination of background was found to be $\sim 4\%$.

4.2.4 Running Conditions

As run conditions are not fixed and the optimal data-taking conditions differ process by process studied, it is useful to discuss the measurements as a function of the average number of interactions per bunch crossing μ (so-called pile-up).

The integrated luminosity as a function of μ is shown in Fig. 4.3. The lines represent the product of the number of colliding bunches n_{bunch} and run time, t, in hours. For example, the collection of a 5 pb^{-1} data sample at $\mu = 0.1$, requires $n_{\mathrm{bunch}} \times t(\mathrm{h}) = 10^5$ equivalent to 100 h (1 week) of running with $n_{\mathrm{bunch}} = 1000$ colliding bunches.

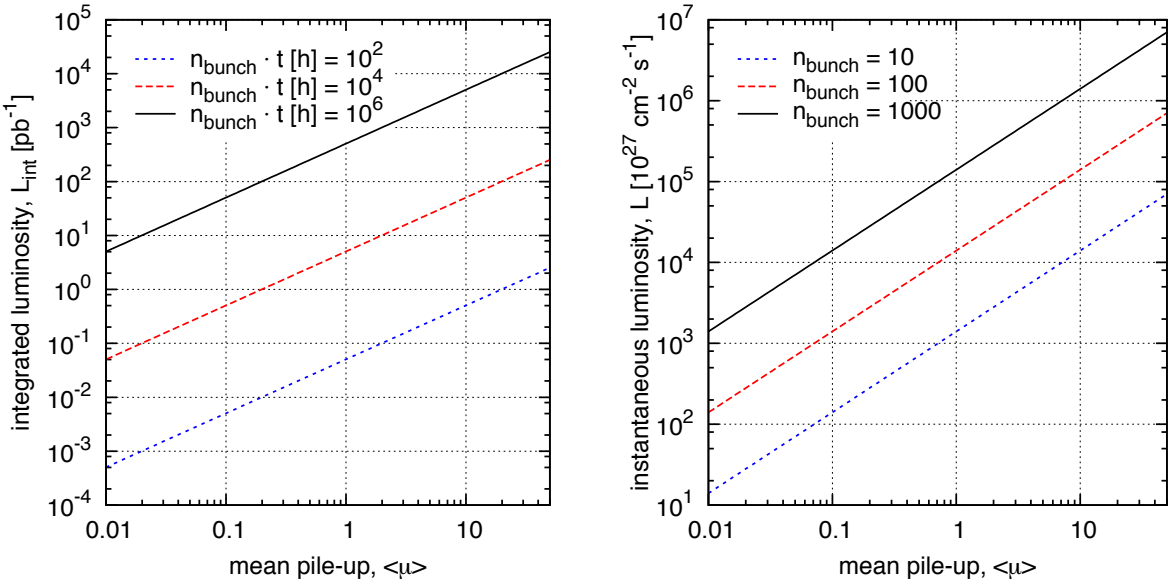
integrated luminosity, L_{int} [pb^{-1}]
$n_{bunch} \cdot t$ [h] = 10^2
$n_{bunch} \cdot t$ [h] = 10^4
$n_{bunch} \cdot t$ [h] = 10^6
mean pile-up, <μ>
instantaneous luminosity, L [10^{27} cm^{-2} s^{-1}]
n_{bunch} = 10
n_{bunch} = 100
n_{bunch} = 1000
mean pile-up, <μ>

Fig. 4.3: Integrated (**left**) and instantaneous (**right**) luminosity as a function of pile-up. The lines represent three different bunch configurations. The tick marks on the vertical scale are at multipliers 2, 5, and 8.

4.3 Factorisation Tests

A key physics issue in diffractive processes is whether the diffractive Parton Distributions Functions (DPDFs) are universal, *i.e.* whether the collinear factorisation [36] holds or not. DPDFs were extracted from high precision HERA data by performing perturbative QCD fits at next-to-leading order accuracy and include a full experimental and theoretical error estimation [37, 38]. Support to the factorisation theorem was provided by analyses of diffractive dijet cross sections in DIS. These results, despite large theoretical errors, are well described by next-to-leading order predictions based on DPDFs extracted from the inclusive diffractive DIS data [39–41]. However, the hard scattering factorisation was proven to fail in $p\bar{p}$ collisions at the Tevatron [42, 43], where the single diffractive production cross sections of dijet and the electro-weak bosons were overestimated by an order of magnitude w.r.t. predictions based on HERA DPDFs. In Ref. [44], it was shown that this breakdown can be explained by screening effects quantified by the so-called rapidity gap survival probability. In photoproduction at HERA ($Q^2 \simeq 0$), the exchanged photon, which is real or quasi-real, can either interact directly with the proton (so-called direct photoproduction) or behave like a hadron, first dissolving into partonic constituents that then scatter off the target (so-called resolved photoproduction). For the latter process, the factorisation is expected to fail like in the hadron-hadron case. Whether H1 and ZEUS dijet phoproduction data show a suppression, as predicted by theory [44, 45], has been a dilemma for the last decade [39, 41, 42].

The factorisation theorem is at the heart of modern QCD phenomenology at hadron colliders. It provides a crucial predictivity to the theory and, so far, has been tested and verified by all phenomenological analyses. Understanding the mechanism, responsible for the striking breaking of factorisation in hard diffraction, would unveil the non-perturbative phenomena behind it. Single diffractive production processes, like Drell-Yan and vector boson production, are among the best tools to look for such effects in proton-proton collisions at the LHC energies. Moreover the concept of photoproduction of diffractive dijets at HERA can be revisited at the LHC with the flux of quasi-real photons in ultraperipheral collisions (UPS) [46, 47], relying on

the notation of equivalent photon approximation. In order to get a full quantitative prediction for the diffractive photoproduction of two and three jets, one needs both the $\gamma \to q\bar{q}g$ impact factor at leading order [48] and the virtual corrections to the $\gamma \to q\bar{q}$ impact factor [49].

4.3.1 Predictions

The single diffractive cross sections for Z^0, γ^* (diffractive DY) and $W^\pm$ bosons production, calculated for $\sqrt{s} = 14$ TeV according to the model [50–52], are presented in Fig. 4.4. The cross section is shown differentially in the dilepton mass squared (left plot) and in the longitudinal momentum fraction (right plot). These plots do not reflect particular detector constraints. The M^2 distributions were integrated over the *ad hoc* interval of fractional boson momentum of $0.3 < x_1 < 1$, corresponding to the forward rapidity region (at not extremely large masses). Then the mass distribution is integrated over the potentially interesting invariant mass interval of $5 < M^2 < 10^5$ GeV^2.

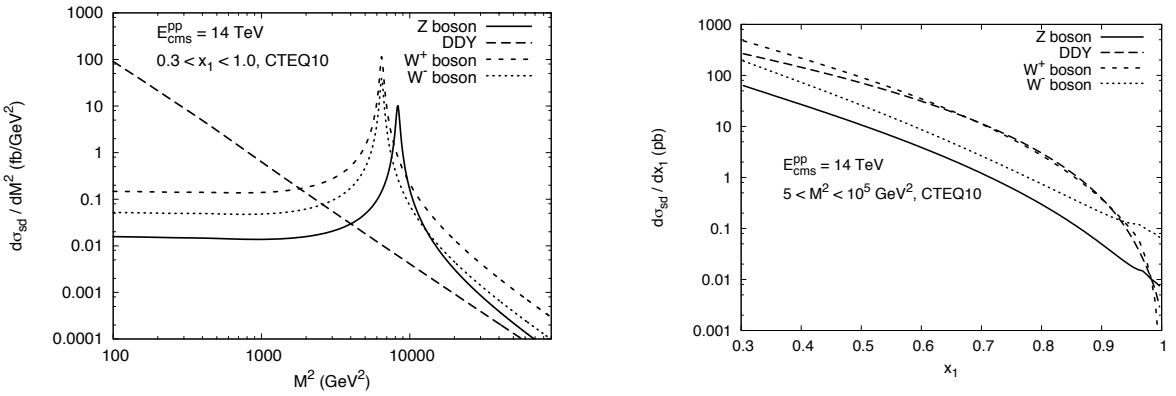

Fig. 4.4: Diffractive gauge boson production cross section as a function of boson invariant mass squared M^2 (**left**) and boson fractional light-cone momentum x_1 (**right**) in pp collisions at $\sqrt{s} = 14$ TeV. Solid, long-dashed, dashed and dotted curves correspond to Z, γ^*, W^+ and W^- bosons, respectively. The CTEQ10 PDF parametrization [53] was used.

The M^2 distributions of the Z^0 and $W^\pm$ bosons clearly demonstrate their resonant behaviour: in the resonant region it significantly exceeds the corresponding diffractive Drell-Yan component. Only for very low masses the γ^* contribution becomes important. For x_1 distribution, when integrated over the low mass and resonant regions, the diffractive W^+ and γ^* components become comparable to each other, both in shapes and values, whereas the W^- and, especially, Z-boson production cross section are noticeably lower. The W^- cross section is smaller than the W^+ one due to differences in valence u- and d-quark densities (dominating over sea quarks at large x_q) in the proton. The precise measurement of differences in the forward diffractive W^+ and W^- rates would allow to constrain the quark content of the proton at large values of $x_q \equiv x_1/\alpha$.

From the phenomenological point of view, the distribution of the forward diffractive cross section in the dilepton transverse momentum $q_\perp$ could also be of major importance. In Fig. 4.5 (left) the dilepton transverse momentum $q_\perp$ distribution of the double-differential diffractive cross section at $\sqrt{s} = 14$ TeV is shown for the dilepton invariant mass fixed at a corresponding resonance value – the Z or W mass. The shapes turned out to be smooth and the same for different gauge bosons, whereas the normalisation is different. The longitudinal-to-transverse gauge boson polarisations ratio, σ^L/σ^T, shown in Fig. 4.5 (right), does not strongly vary for

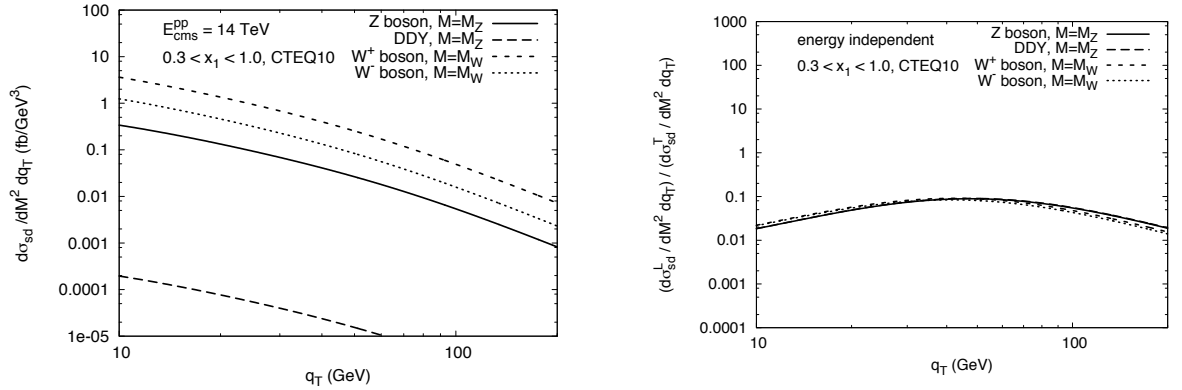

Fig. 4.5: **Left**: double-differential diffractive gauge boson production cross section as function of the di-lepton transverse momentum $q_\perp$ in pp collisions at $\sqrt{s} = 14$ TeV. **Right**: longitudinal-to-transverse gauge bosons polarisations ratio as a function of the di-lepton transverse momentum $q_\perp$. In both plots, the invariant mass is fixed as $M = M_Z$ in the Z^0, γ^* production case and as $M = M_W$ in the $W^\pm$ production case.

different bosons. It is peaked at about the half of the resonance mass, and uniformly decreases to smaller/larger $q_\perp$ values.

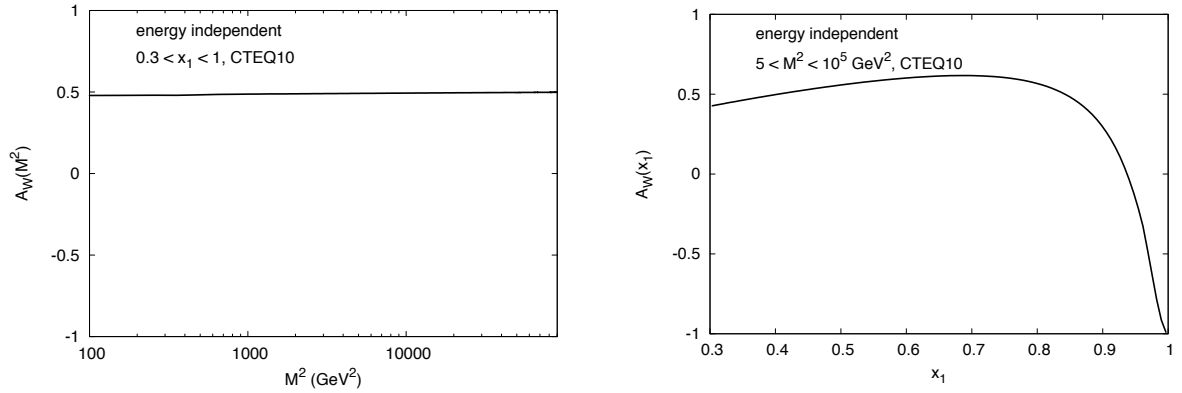

Fig. 4.6: Charge asymmetry in the single diffractive W^+ and W^- cross sections as a function of M^2, at fixed $x_1 = 0.5$ (**left**), and as a function of x_1, at fixed $M^2 = M_W^2$ (**right**). The solid lines correspond to $\sqrt{s} = 14$ TeV, the dashed lines to the RHIC energy $\sqrt{s} = 500$ GeV.

Due to its sensitivity to the difference between u- and d-quark PDFs at large x, the $W^\pm$ charge asymmetry, A_W, is a crucial observable. It is shown in differentially as a function of the dilepton invariant mass squared M^2 and integrated over the $0.3 < x_1 < 1.0$ interval in Fig. 4.6 (left) and as a function of the boson momentum fraction x_1 and integrated over the $5 < M^2 < 10^5$ GeV^2 interval in Fig. 4.6 (right). A_W turns out to be independent on both the hard scale M^2 and the center of mass energy. One concludes that, due to different x-shapes of valence u, d quark PDFs, at small x_1 the diffractive W^+ bosons' rate dominates over W^- one. However, when $x_1 \to 1$ the W^- boson cross section becomes increasingly important and strongly dominates over the W^+ one.

The diffractive to inclusive ratio, $\sigma_{sd}/\sigma_{incl}$, shown in Fig. 4.7, is independent on the type of the gauge boson, its polarisation or quark PDFs. In this respect, it is the most convenient and model independent observable. The ratio decreases with energy, but increases with the hard

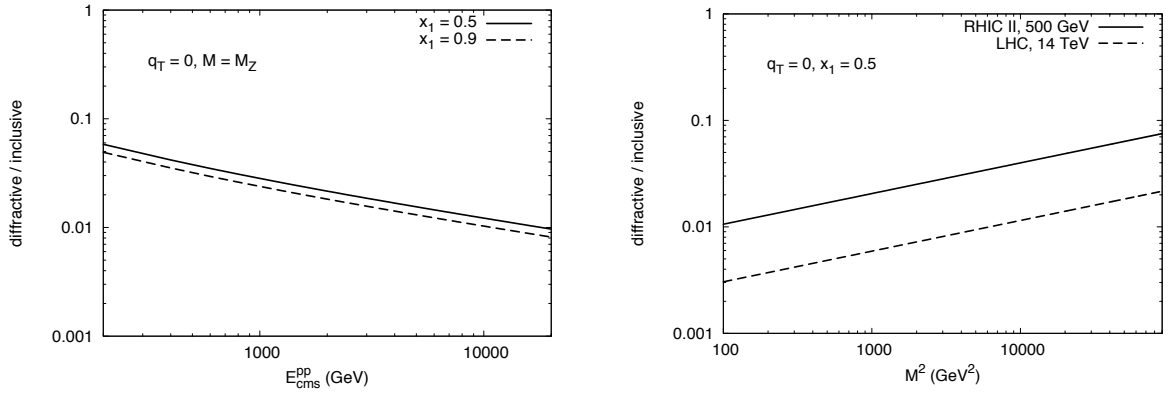

Fig. 4.7: The diffractive-to-inclusive ratio of the gauge bosons production cross sections in pp collisions as a function of the center of mass energy (**left**) and the dilepton invariant mass M^2 (**right**). It does not depend on the type of the gauge boson and quark PDFs.

scale, thus it behaves opposite to what is expected according to the diffractive factorisation-based approaches. Therefore, measurements of the single diffractive gauge boson production cross section, at least at two different energies, would provide an important information about the interplay between soft and hard interactions in QCD, and their role in the formation of diffractive excitations and colour-screening effects.

4.4 Single Diffractive Jet Production

In the single diffractive jet production process (Fig. 4.8 left) a jet system is produced in the central region and one of the protons emits a Pomeron, stays intact and is scattered at very high pseudorapidity. Depending on the momentum lost in the interaction, the intact proton may be detected by proton taggers. Unfortunately, not all such protons will survive. This is due to the additional soft interactions between the diffracted proton and the rest of the final state. Such effect will be hereafter quantified by the so called gap survival probability factor. For hard single diffractive processes at $\sqrt{s} = 13$ TeV such probability is estimated to be of about 0.1 [26].

It is informative to compare the single diffractive jet production to the non-diffractive one (Fig. 4.8 right). In the latter process, both interacting protons are destroyed and two jets are produced; low-p_T particles populate the pseudorapidity region between the two jets and the proton remnants.

By studying single diffractive jet production, the universality of the Pomeron in ep and pp collision can be probed [27]. Moreover, the gap survival probability can be quantified: a good experimental precision will allow for comparison to theoretical predictions and differential measurements of the dependence of the survival factor on (for example) the mass of the central system. Finally, the QCD evolution of the gluon and quark densities in the Pomeron can be tested and compared with the HERA measurements.

It must be pointed out that going from the HERA to the LHC kinematics means extrapolating the diffractive parton distribution functions well beyond the region in which they have been measured. The HERA coverage in photon virtualities, Q^2, reaches typically several hundred GeV^2, at least one order of magnitude below that of the LHC data, where in single diffractive dijet production the scale corresponds roughly to the transverse momentum of the outgoing parton. Figure 4.9 shows the distribution of Q^2 and the momentum fraction of the parton initiating the hard scattering in single diffractive dijet events. The simulation was performed with

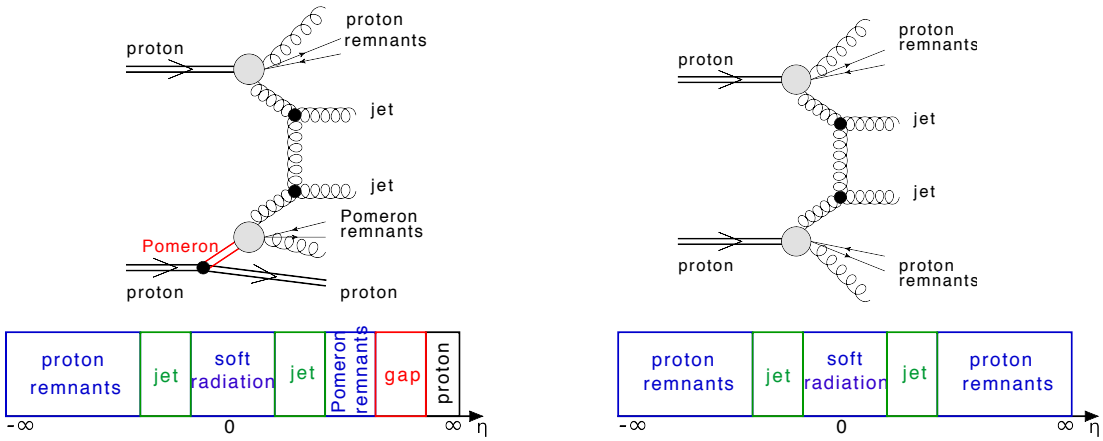

Fig. 4.8: **Left:** single diffractive jet production – one interacting proton stays intact, the second one is destroyed and two jets are produced. **Right:** non-diffractive jet production – the interacting protons are destroyed and two jets are produced.

POMWIG, version 2.0 beta [55]. The outgoing proton is scattered in the positive z direction and the outgoing parton has transverse momentum $p_T > 30$ GeV. The NLO H1 2006 Fit B [37] was used for the diffractive PDF (DPDF) and the Pomeron flux calculation. This is one of several DPDF fits performed with the HERA data (see Sect. 4.3). Figure 4.10 shows the distribution of Q^2 and β, the fractional momentum of the diffractive exchange carried by the struck quark. The coverage in β extends at the LHC down to 10^{-3}, below that of the HERA data. One may note that $x = \beta\xi$, where ξ (or x_{IP}) is the longitudinal momentum loss of the proton in such events and x the momentum fraction of the parton initiating the hard scattering. Also shown is the HERA measurement region used to extract the diffractive parton distribution functions in Ref. [37]; the regions corresponding to values of x_{IP} from 0.0003 to 0.003 (low-x_{IP}) and from 0.01 to 0.03 (high-x_{IP}) are shown separately. The Q^2 values range from $Q^2 = 8.5$ GeV^2 up to a maximum of $Q^2 = 1600$ GeV^2, while β has a maximum value of 0.8. It should be noted that decreasing the transverse momentum requirement to values of 20 GeV or lower could substantially reduce the extrapolation with respect to the HERA measurement region.

4.4.1 ATLAS Feasibility Studies for $\sqrt{s} = 13$ TeV

In the following studies the FPMC generator [30] was used to generate diffractive jet samples. Non-diffractive jets were generated by PYTHIA8 [31]. Pile-up was generated using PYTHIA8 with the MBR tune [32] and the following processes were included: non-diffractive production, elastic scattering, single diffraction, double diffraction and central diffraction. The vertex position was smeared according to values from tables in Section 1.1.

In order to calculate the proton transport through the LHC structures between the ATLAS Interaction Point (IP) and the forward detectors, the FPTRACK [33] program was used. For a given distance between the forward detector and the beam, diffractive protons were checked to be within the detector acceptance. The proton energy was reconstructed based on the procedure described in [34].

Jets were reconstructed using the FASTJET package with the anti-k_T ($R = 0.4$) algorithm [35]. A particle was considered visible in the tracker if the criteria described in Section 4.2 were fulfilled. Three thresholds for the transverse momentum of the leading jet were considered: p_T^{jet1} of 20 GeV, 50 GeV and 100 GeV. The sub-leading jet was required to have $p_T^{\text{jet2}} > 20$ GeV. In order to assure reconstruction of a hard vertex, both leading jets were required to be

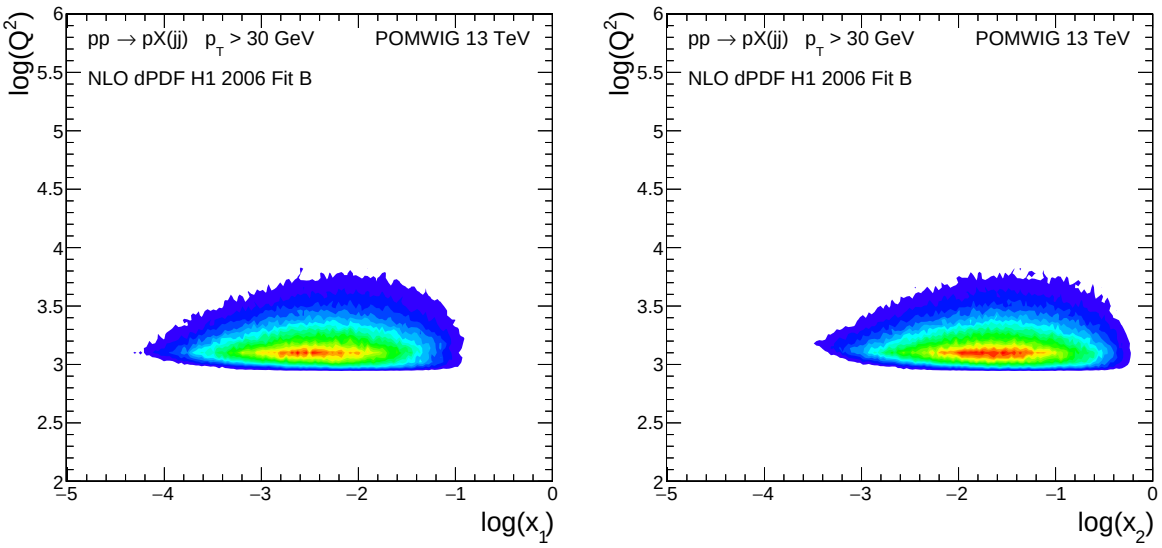

Fig. 4.9: Distribution of the hard scale Q^2 for single diffractive dijet production simulated with POMWIG and the momentum fraction of the parton initiating the hard scattering in the outgoing proton direction (**left**), and in the opposite direction (**right**).

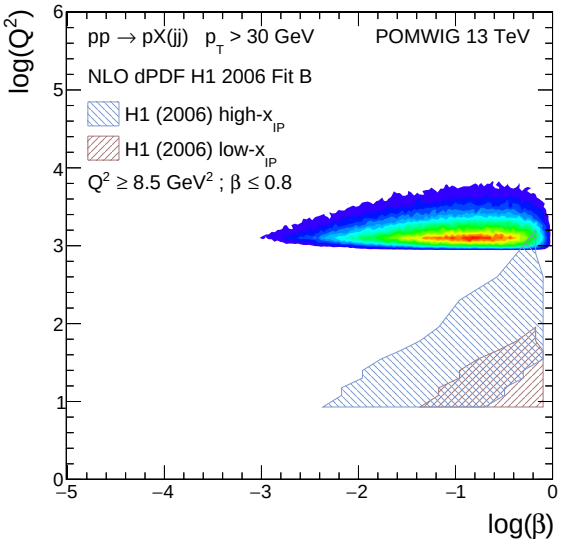

Fig. 4.10: Distribution of the hard scale Q^2 and β, the momentum fraction at which the diffractive PDF is probed, for single diffractive dijet production simulated with POMWIG. The region covered by the H1 data used to extract the NLO H1 2006 Fit B [37] is also shown.

inside the acceptance of the ATLAS tracker ($|\eta| < 2.5$).

The results for the AFP detector and $\beta^* = 0.55$ m optics are shown in Fig. 4.11. In the left plot the purity, hereafter defined as the ratio of the signal to the sum of signal and background events, is presented as a function of the mean pile-up, μ. In this figure, the black solid line is for events with proton tag in the AFP detector whereas the red dashed line is for those with a tag and exactly one reconstructed vertex. Purity greater than 50% was obtained for $\mu \sim 0.5$. Moreover, it grows rapidly to values greater than 80% for $\mu < 0.1$. This plot was done for jets with $p_T > 50$ GeV, but the purity is not significantly different for the other considered p_T thresholds (*cf.* Tab. 4.A.1).

In Fig. 4.11 (right) the statistical significance, hereafter defined as the number of collected signal events over the square root of the sum of the accepted signal and background events, is presented as a function of the mean pile-up for jets with $p_T > 50$ GeV. To compute the statistical significance, a certain integrated luminosity must be assumed. For the presented results this was done by setting the number of bunches (n_b) multiplied by the data collecting time (t_{data}, in hours) to be $n_b \cdot t_{data} = 1000$. This can be interpreted as one hour of data-taking with 1000 bunches, or 10 hours with 100 bunches, (*cf.* Fig. 4.3).

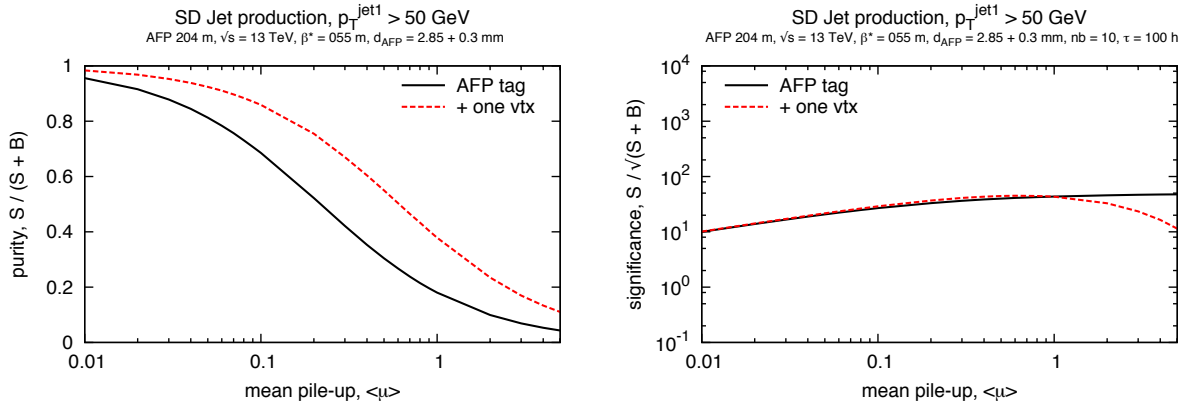
SD Jet production, p_T^jet1 > 50 GeV
AFP 204 m, √s = 13 TeV, β* = 055 m, d_AFP = 2.85 + 0.3 mm
AFP tag
+ one vtx
purity, S / (S + B)
mean pile-up, <μ>
SD Jet production, p_T^jet1 > 50 GeV
AFP 204 m, √s = 13 TeV, β* = 055 m, d_AFP = 2.85 + 0.3 mm, nb = 10, τ = 100 h
AFP tag
+ one vtx
significance, S / √(S + B)
mean pile-up, <μ>

Fig. 4.11: Single diffractive jet production with protons tagged in the AFP detectors for $\sqrt{s} = 13$ TeV and $\beta^* = 0.55$ m: purity (**left**) and significance (**right**) for jets with $p_T > 50$ GeV as a function of average pile-up. The number of bunches multiplied by data collecting time (in hours) was assumed to be 1000. In the analysis the following cuts were considered: proton tag in the AFP detector (black solid line) and tag + exactly one reconstructed vertex (red dashed line).

Studies for the AFP detector and $\beta^* = 90$ m optics are shown in Fig. 4.12. For such an optics configuration and for a 10 σ distance from the beam, the purity and significance are similar to the case discussed above. The same conclusions were obtained in the case of the ALFA detector and $\beta^* = 0.55$ m optics (*cf.* Fig. 4.13).

The situation changes dramatically when ALFA detectors and $\beta^* = 90$ m optics are considered (see Fig. 4.14). Due to the acceptance for the elastic scattering, the purity is only higher than 50% for the mean pile-up smaller than 0.02. Filtering out the elastic events (blue dotted line) increases the purity. However, an average pile-up of less than 0.05 is still needed. In conclusion, the optimal data taking conditions for such configuration are for $\mu \sim 0.01$.

The summary of these feasibility studies is presented in Table 4.A.1. The rate was calculated for 100 bunches.

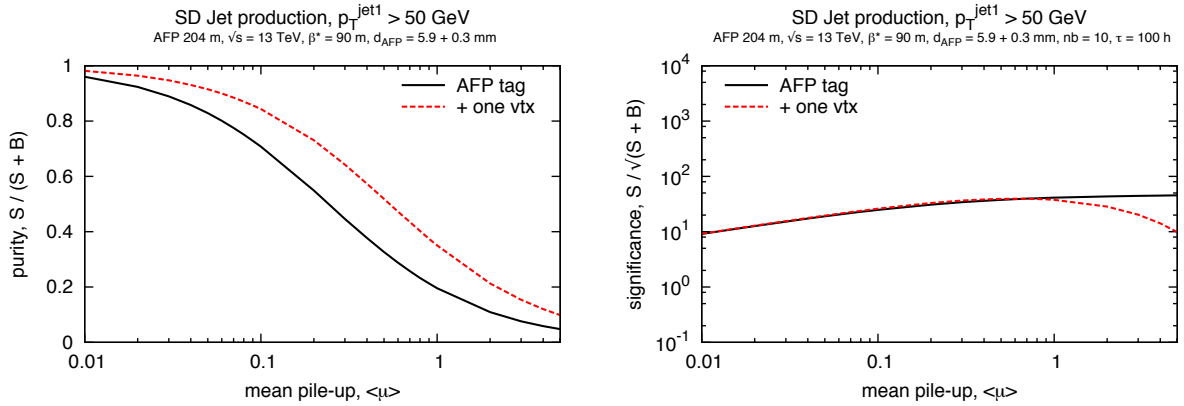
SD Jet production, $p_T^{jet1} > 50$ GeV
AFP 204 m, √s = 13 TeV, β* = 90 m, d_{AFP} = 5.9 + 0.3 mm
AFP tag
+ one vtx
purity, S / (S + B)
mean pile-up, <μ>
SD Jet production, $p_T^{jet1} > 50$ GeV
AFP 204 m, √s = 13 TeV, β* = 90 m, d_{AFP} = 5.9 + 0.3 mm, nb = 10, τ = 100 h
AFP tag
+ one vtx
significance, S / √(S + B)
mean pile-up, <μ>

Fig. 4.12: Single diffractive jet production with protons tagged in the AFP detectors for $\sqrt{s} = 13$ TeV and $\beta^* = 90$ m: purity (**left**) and significance (**right**) for jets with $p_T > 50$ GeV as a function of average pile-up. The number of bunches multiplied by the data collecting time (in hours) was assumed to be 1000. In the analysis the following cuts were considered: proton tag in the AFP detector (black solid line) and tag + exactly one reconstructed vertex (red dashed line).

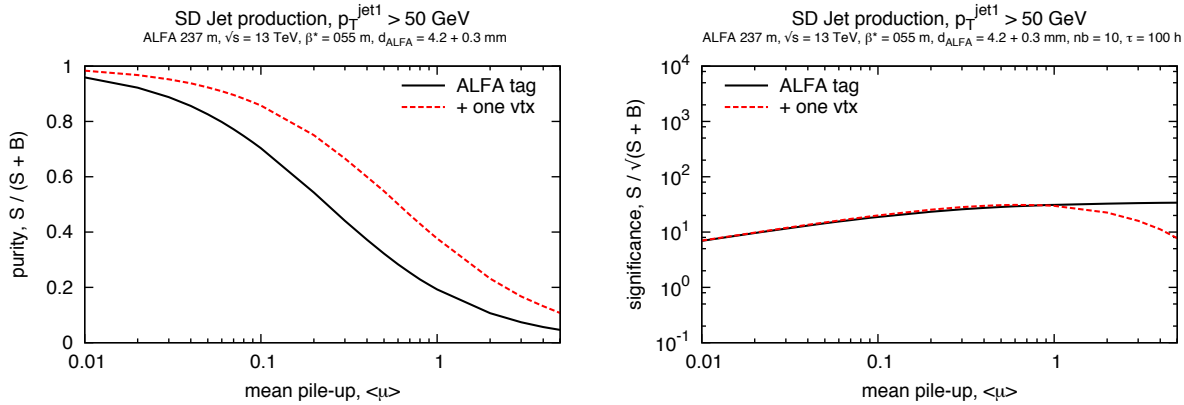
SD Jet production, $p_T^{jet1} > 50$ GeV
ALFA 237 m, √s = 13 TeV, β* = 055 m, d_{ALFA} = 4.2 + 0.3 mm
ALFA tag
+ one vtx
purity, S / (S + B)
mean pile-up, <μ>
SD Jet production, $p_T^{jet1} > 50$ GeV
ALFA 237 m, √s = 13 TeV, β* = 055 m, d_{ALFA} = 4.2 + 0.3 mm, nb = 10, τ = 100 h
ALFA tag
+ one vtx
significance, S / √(S + B)
mean pile-up, <μ>

Fig. 4.13: Single diffractive jet production with protons tagged in the ALFA detectors for $\sqrt{s} = 13$ TeV and $\beta^* = 0.55$ m: purity (**left**) and significance (**right**) for jets with $p_T > 50$ GeV as a function of average pile-up. The number of bunches multiplied by the data collecting time (in hours) was assumed to be 1000. In the analysis the following cuts were considered: proton tag in the ALFA detector (black solid line) and tag + exactly one reconstructed vertex (red dashed line).

4.5 Single Diffractive Z, W and J/Ψ Production

The leading order diagram for single-diffractive Z, W boson, or J/ψ meson production is shown in Fig. 4.15. The two final-state particles originating on either side of the colour-singlet are, in general, well separated by a rapidity gap.

The single-diffractive production of W/Z bosons and J/ψ meson is sensitive to the diffractive structure function of the proton, notably to its quark component, since many of the observed production modes can originate from quark fusion. Moreover, as in case of the single diffractive dijet production, the diffractive boson production can help quantifying the gap survival probability.

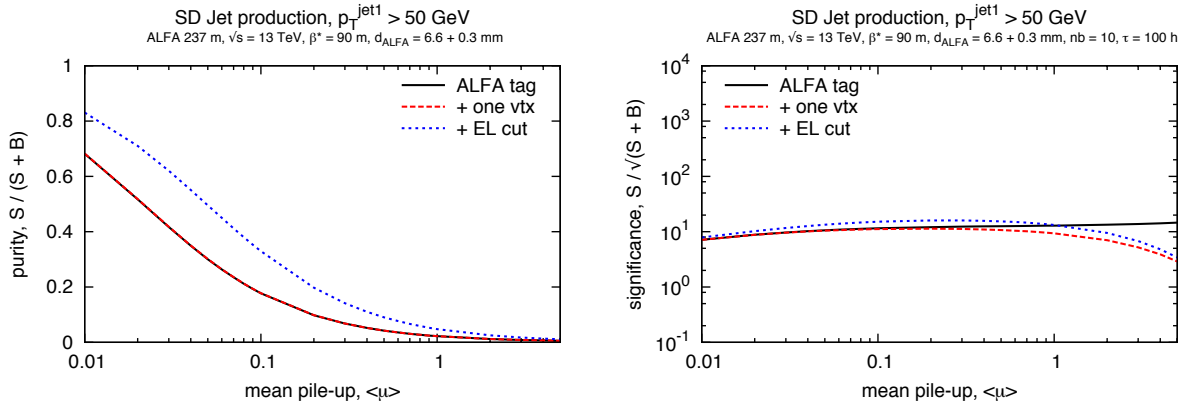
SD Jet production, $p_T^{jet1} > 50$ GeV
ALFA 237 m, √s = 13 TeV, β* = 90 m, d_{ALFA} = 6.6 + 0.3 mm
ALFA tag
+ one vtx
+ EL cut
purity, S / (S + B)
mean pile-up, <μ>
SD Jet production, $p_T^{jet1} > 50$ GeV
ALFA 237 m, √s = 13 TeV, β* = 90 m, d_{ALFA} = 6.6 + 0.3 mm, nb = 10, τ = 100 h
ALFA tag
+ one vtx
+ EL cut
significance, S / √(S + B)
mean pile-up, <μ>

Fig. 4.14: Single diffractive jet production with protons tagged in the ALFA detectors for $\sqrt{s} = 13$ TeV and $\beta^* = 90$ m: purity (**left**) and significance (**right**) for jets with $p_T > 50$ GeV as a function of average pile-up. The number of bunches multiplied by the data collecting time (in hours) was assumed to be 1000. In the analysis the following cuts were considered: proton tag in the ALFA detector (black solid line), tag + exactly one reconstructed vertex (red dashed line) and tag + one vertex + elastic veto (blue dotted line).

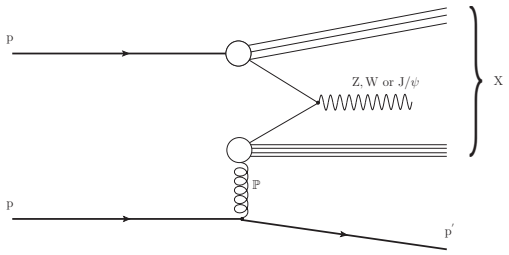

Fig. 4.15: Single diffractive Z, W and J/ψ production.

4.5.1 CMS-TOTEM Feasibility Studies for $\sqrt{s} = 13$ TeV

The results presented in this Section are based on a Monte Carlo study presented in Ref. [54]. These studies were done for the low-luminosity, low-pile-up LHC runs and illustrate the potential for physics measurements with the CMS and TOTEM experiments at the beginning of Run II.

4.5.1.1 Signal and Background Simulation

Single-diffractive Z and W boson production was simulated with POMWIG [55] in the electron and muon decay channels. Single-diffractive J/ψ production was generated with POMPYT [56]. Pile-up events were simulated using the PYTHIA8 Monte Carlo event generator [31] with A2 tune. Pile-up events were added to the signal with a probability $p(n;\mu)$, where n is the number of pile-up events given by a Poisson distribution with an average of $\mu = 1$.

The presented predictions include a rapidity gap survival probability of 0.1, which provides a good description of CMS diffractive dijet data [21]. According to POMWIG, the cross-section for the lepton decay of the Z boson is 12.1 pb. For the W boson decaying into lepton and (anti)neutrino, the predicted cross-section is of about 131 pb. The POMPYT cross-section for diffractive $J/\psi \to \mu\mu$ production is 2.5 nb.

4.5.1.2 *Trigger Strategy*

The trigger strategy in Run II will be similar to the one in Run I: the signal accepted by CMS (TOTEM) will be sent to TOTEM (CMS) to trigger the readout. In Run I, with 112 bunches and a pile-up of $\mu \sim 0.07$, the detector trigger selections and corresponding rates were:

- for single-diffractive Z or W selection:
  - at least one muon (electron) with $p_{\mathrm{T}} > 7$ GeV (57 Hz) or
  - at least two muons (electrons) with $p_{\mathrm{T}} > 3$ GeV (22 Hz),
- for single-diffractive J/ψ selection at least two muons with non-zero p_T and $|\eta| < 2.45$ (45 Hz).

4.5.1.3 *Event Selection*

The simulation and reconstruction software used in this study did not include the description of the forward proton detectors. Instead, an acceptance table was used to quantify the probability that a proton is measured. This table was determined on the basis of a parametrisation of the proton propagation in the LHC beam line [58].

The Z or W boson and J/ψ meson final states were selected using the central CMS detector in the range $|\eta| < 2.5$. The detailed MC simulation of the CMS detector response was based on GEANT4 [59]. All events were required to be within the acceptance of the TOTEM Roman pots on either side of the interaction point and to have exactly one reconstructed vertex. For the specific samples the following additional criteria were applied:

- $\mathrm{Z} \to \mathrm{e}^+\mathrm{e}^-$ and $\mathrm{Z} \to \mu^+\mu^-$:
  - both leading leptons were required to have $p_{\mathrm{T}} > 20$ GeV and to fulfil the isolation criteria described in Ref. [60];
  - the dilepton system invariant mass was required to be within the range of $60 < \mathrm{M}_{ll} < 110$ GeV;
- $\mathrm{W}^{\pm} \to \mathrm{e}^{\pm}\nu_e$ and $\mathrm{W}^{\pm} \to \mu^{\pm}\nu_\mu$:
  - the leading lepton was required to have $p_{\mathrm{T}} > 20$ GeV and to fulfil the isolation criteria [60];
  - events with an additional lepton with $p_{\mathrm{T}} > 10$ GeV were rejected;
  - the transverse mass of the lepton-neutrino system, $\mathrm{M}_{\mathrm{T}} = \sqrt{2\mathrm{E}_{\mathrm{T,l}} \cdot \mathrm{E}_{\mathrm{T},\nu}[1 - \cos(\phi_l - \phi_\nu)]}$, was required to be in the range $60 < \mathrm{M}_{\mathrm{T}} < 110$ GeV;
- $\mathrm{J}/\psi \to \mu^+\mu^-$:
  - at least two muons were required with opposite charge, with $|\eta| < 2.45$;
  - the dimuon system invariant mass was required to be in the range $3.05 < \mathrm{M}_{\mu^-\mu^+} < 3.15$ GeV.

The distributions of pseudorapidity, η, and relative energy loss, ξ, of the protons tagged in the forward detectors in $\mathrm{Z} \to \mathrm{e}^+\mathrm{e}^-$ events are shown in Fig. 4.16. Figure 4.17 shows the distributions of t and ξ of protons tagged in $\mathrm{J}/\psi \to \mu^+\mu^-$ events. Figure 4.18 shows the distributions of the transverse mass and the leading lepton pseudorapidity in $\mathrm{W}^{\pm} \to \mathrm{e}^{\pm}\nu_e$ events.

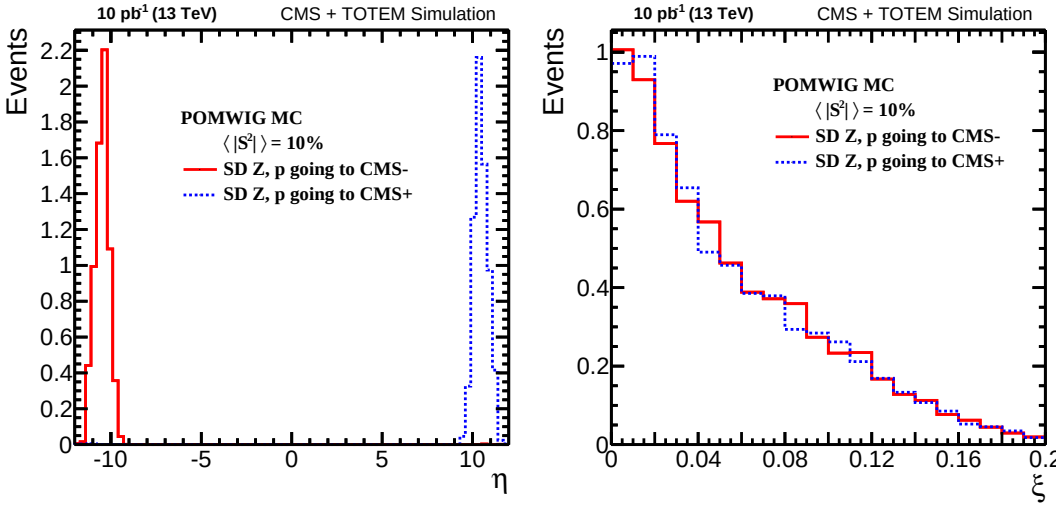

Fig. 4.16: Distributions of the pseudorapidity η (**left**) and of ξ (**right**) of the protons tagged in the TOTEM RP detector stations in $Z \to e^+e^-$ events. Outgoing protons in the CMS z-negative direction are shown in red (solid line) and protons in the z-positive direction in blue (dashed line). Events were simulated with the POMWIG MC and normalized to an integrated luminosity of 10 pb^{-1}. A gap survival probability of 0.1 was used.

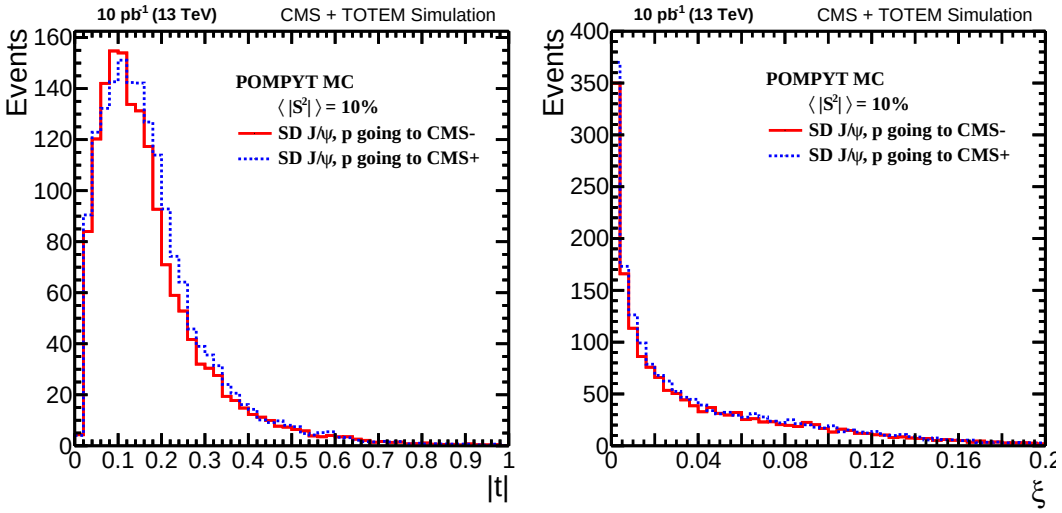

Fig. 4.17: Distributions of t (**left**) and ξ (**right**) of protons tagged in the TOTEM RP detector stations in $J/\psi(\mu^+\mu^-)$ events. Outgoing protons in the CMS z-negative direction are shown in red (solid line) and protons in the CMS z-positive direction in blue (dashed line). Events were simulated with the POMPYT MC and normalized to an integrated luminosity of 10 pb^{-1}. A gap survival probability of 0.1 was used.

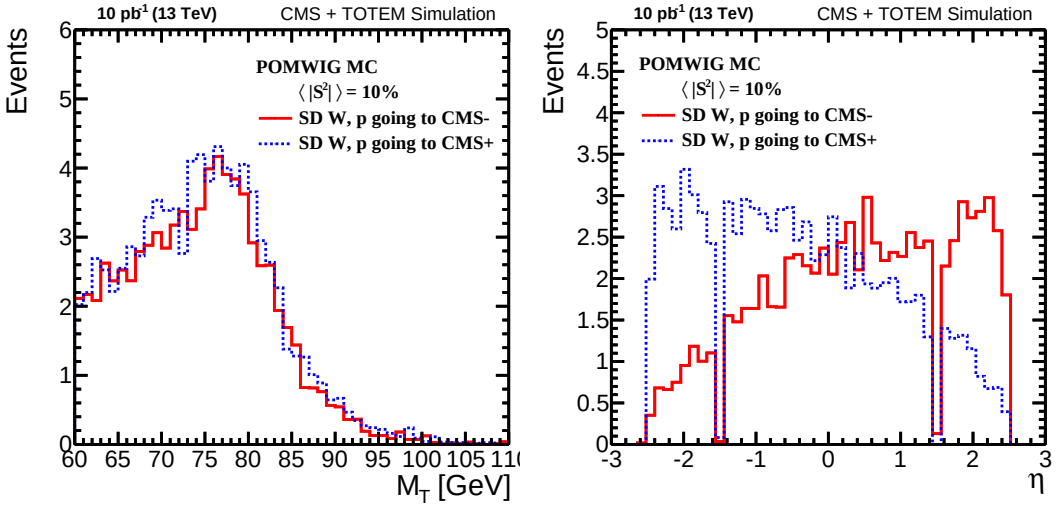

Fig. 4.18: Distributions of the transverse mass M_T (**left**) and the leading lepton pseudorapidity (**right**) in $W^{\pm} \to e^{\pm}\nu_e$ events. Events with a proton detected by TOTEM RP detector stations in the CMS z-negative (positive) direction are shown in solid red (dashed blue) line. Events were simulated with the POMWIG MC and normalized to an integrated luminosity of 10 pb^{-1}. A gap survival probability of 0.1 was used.

4.5.1.4 Results

Table 4.1 summarizes the results of the visible cross-section (σ_{vis}) for the electron and muon channels for the considered production channels. The obtained visible cross-section summed over all considered channels are:

- 3.38 ± 0.03 pb for SD Z,
- 36.7 ± 0.3 pb for SD W,
- 332.5 ± 2.9 pb for J/ψ.

Table 4.2 gives an overview of the expected event yields assuming an integrated luminosity of 10 pb^{-1}. The results shown are further corrected by the TOTEM proton reconstruction efficiency of $92.5 \pm 2.5\%$ [61].

Table 4.1: Overview of the visible cross-section values obtained in the SD $Z \to e^+e^-$, $Z \to \mu^+\mu^-$, $W \to e\nu_e$, $W \to \mu\nu_\mu$ and $J/\psi \to \mu^+\mu^-$ production channels, shown for events with a proton detected in the CMS z-negative or z-positive directions. The uncertainties shown are statistical.

	$Z \to e^+e^-$	$Z \to \mu^+\mu^-$	$W^+ \to e^+\nu_e$ $W^- \to e^-\bar{\nu}_e$	$W^+ \to \mu^+\nu_\mu$ $W^- \to \mu^-\bar{\nu}_\mu$	$J/\psi(\mu^+\mu^-)$
σ_{vis} [pb]	1.34 ± 0.02	2.04 ± 0.02	16.37 ± 0.21	20.30 ± 0.23	332.5 ± 2.9

4.5.2 ATLAS Feasibility Studies for $\sqrt{s} = 13$ TeV

In this Section the possibility of observing single diffractive W and Z events using proton tagging technique and the ATLAS detector is discussed. The single diffractive W/Z events were generated by FPMC with a gap survival factor of 0.1 [62], whereas the non-diffractive samples

Table 4.2: Overview of the expected event yields with the statistical uncertainty, for an integrated luminosity of 10 pb^{-1} in the SD Z or W and J/ψ production channels.

LHC Scenario	SD Boson Z	SD Boson W	SD J/ψ
10 pb^{-1}	30 ± 1	340 ± 10	3080 ± 90

were obtained using PYTHIA8. The visible cross-section, distance between forward detector and LHC beam and probability of having a minimum-bias tag were taken analogously as in Section 4.4. In the following, only results for $W \to l\nu$ (where l means an electron or muon) are shown, since the shapes of the distributions in the case of $Z \to ll$ are similar.

The purity and significance for the AFP detector and $\beta^* = 0.55$ m optics is shown in Fig. 4.19. In this figure the black solid line is for events with a proton tag in the AFP detector whereas the red dashed line is for events with a proton tag and exactly one reconstructed vertex. A purity greater that 50% is obtained for $\mu \sim 0.2$ and grows to values greater than 80% for $\mu < 0.06$. The number of bunches multiplied by the data collecting time[1] was assumed to be 10000, which is the minimal value for observing such events. Similar conclusions can be driven for the cases of AFP runs with $\beta^* = 90$ m and ALFA with $\beta^* = 0.55$ m optics.

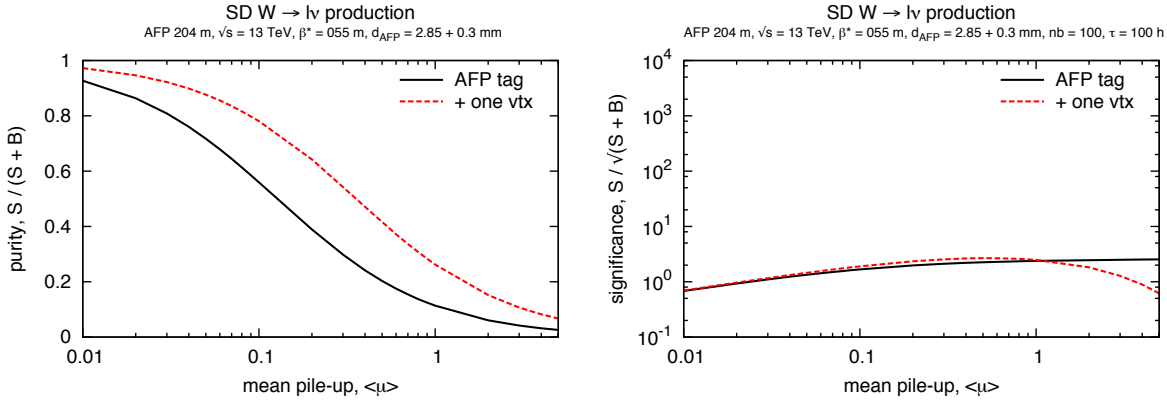
SD W → lν production
AFP 204 m, √s = 13 TeV, β* = 055 m, d_AFP = 2.85 + 0.3 mm
purity, S / (S + B)
mean pile-up, <μ>
AFP tag
+ one vtx
SD W → lν production
AFP 204 m, √s = 13 TeV, β* = 055 m, d_AFP = 2.85 + 0.3 mm, nb = 100, τ = 100 h
significance, S / √(S + B)
mean pile-up, <μ>
AFP tag
+ one vtx

Fig. 4.19: Single diffractive $W \to l\nu$ production with protons tagged in the AFP detectors for $\sqrt{s} = 13$ TeV and $\beta^* = 0.55$ m: purity (**left**) and significance (**right**) as a function of average pile-up. The number of bunches multiplied by the data collecting time (in hours) was assumed to be 10000. In the analysis the following cuts were considered: proton tag in the AFP detector (black solid line) and tag + exactly one reconstructed vertex (red dashed line).

The situation worsens for the ALFA run with $\beta^* = 90$ m optics. As can be observed in Fig. 4.20, even after the rejection of double-tagged events from the elastic background, the purity is greater than 50% only for $\mu < 0.02$.

From the presented studies it is clear that a significant measurement of diffractive W and Z boson production cannot be achieved unless the data-taking conditions are as follows:

- pile-up not larger than 0.1,
- number of bunches greater than couple of hundreds,
- data collecting time of at least 100 hours.

[1] For the reference see Section 4.4.1 and Fig. 4.3.

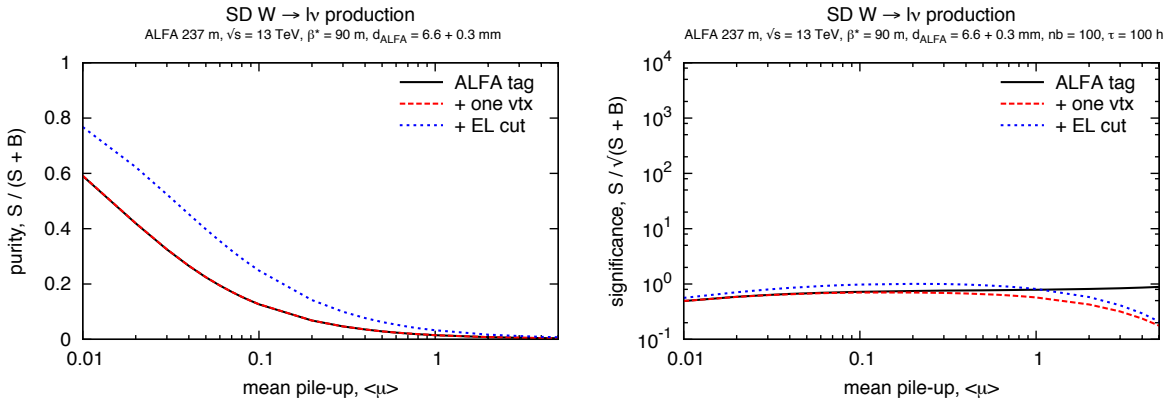
SD W → lν production
ALFA 237 m, √s = 13 TeV, β* = 90 m, d_ALFA = 6.6 + 0.3 mm
purity, S / (S + B)
mean pile-up, <μ>
ALFA tag
+ one vtx
+ EL cut
SD W → lν production
ALFA 237 m, √s = 13 TeV, β* = 90 m, d_ALFA = 6.6 + 0.3 mm, nb = 100, τ = 100 h
significance, S / √(S + B)
mean pile-up, <μ>
ALFA tag
+ one vtx
+ EL cut

Fig. 4.20: Single diffractive $W \to l\nu$ production with protons tagged in the ALFA detectors for $\sqrt{s} = 13$ TeV and $\beta^* = 90$ m: purity (**left**) and significance (**right**) as a function of average pile-up. The number of bunches multiplied by the data collecting time (in hours) was assumed to be 10000. In the analysis the following cuts were considered: proton tag in the ALFA detector (black solid line), tag + exactly one reconstructed vertex (red dashed line) and tag + one vertex + elastic veto (blue dotted line).

4.6 Double Pomeron Exchange Jet Production

In double Pomeron exchange (DPE) jet production, shown in Fig. 4.21, two jets are created and a colourless object is emitted from both interacting protons. As discussed in Section 4.4, the additional soft interactions can break the two protons. At $\sqrt{s} = 13$ TeV the rapidity gap survival probability is estimated to be 0.03 [62]. In case of double Pomeron exchange this factors is expected to be smaller than in SD cases. Nevertheless, it is worth stressing that since the theoretical uncertainties are quite large, the determination of the gap survival probability using data is a very important measurement.

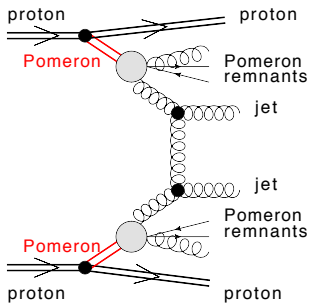

Fig. 4.21: Double Pomeron exchange jet production – both interacting protons stays intact and two jets are produced centrally.

The DPE jet production is sensitive to the gluon density in the Pomeron [27]. This is shown in Fig. 4.22, where the gluon density is modified by $(1-x)^{\nu}$. The central black line displays the cross-section value for the gluon density of the Pomeron as measured at HERA and including an additional survival probability of 0.03 [62]. The yellow band shows the effect of a 20% error on the gluon density, taking into account the normalisation uncertainties. The dashed curves display the expected cross-section sensitivities at the LHC to the gluon density distribution.

Unfortunately, due to the constant ratio between the curves for various gluons densities, it will be difficult to distinguish if observed changes in the absolute gluonic parton cross-section

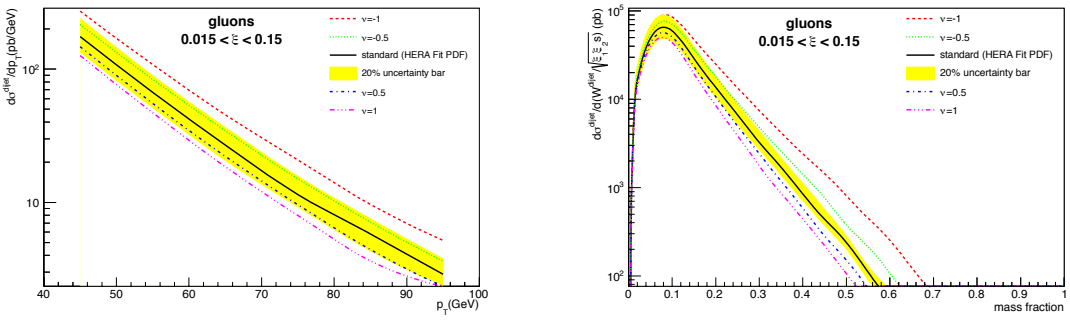

Fig. 4.22: Cross-section of DPE jet production as a function of leading jet p_T (**left**) and mass fraction (**right**). The different curves correspond to different modifications of the Pomeron gluon density extracted from HERA data (see text).

are due to the gluon density or to the survival probability. Hence the so-called mass fraction, defined as the ratio of the dijet mass to the total diffractive mass[2], is introduced. As can be observed in Fig. 4.22 (right), the curves corresponding to the different values of ν diverge faster at high values of the dijet mass fraction.

4.6.1 ATLAS Feasibility Studies for $\sqrt{s} = 13$ TeV

The results presented in this Section were obtained analogously as the ones in Section 4.4: after the event generation the protons were transported to the forward detector location, their energy was reconstructed taking into account various experimental effects, the jets were obtained using the anti-k_t algorithm and tracks were required to fulfil the reconstruction criteria. The distance between forward detectors and beam centre was set to 15 σ and 10 σ in case of $\beta^* = 0.55$ m and $\beta^* = 90$ m optics, respectively.

The results for the the AFP detector and $\beta^* = 0.55$ m optics are shown in Fig. 4.23. In these figures, the red line shows events with a double proton tag in the AFP detectors, the green line events with a double tag and exactly one reconstructed vertex, the blue line events with a double tag and finally the black line represents all these cuts. Since in DPE events there are two outgoing protons, their time-of-flight can be calculated and compared to the position of the hard vertex. The resolution of the AFP timing detectors was assumed to be 20 ps and the cut was done at 2σ. These values were taken similarly as in exclusive jet analyses (see the next Chapter for details).

The statistical significance is maximised for $\mu \sim 1$. For such pile-up values the purity is of about 80%. Data taken at smaller pile-up result in a smaller statistical significance, however with a very high purity ($> 95\%$). Assuming the number of bunches multiplied by the data collecting time of 1000 and $\mu \sim 1$, jets with p_T up to 100 GeV could be measured. Similar conclusions are drawn in case of the AFP detector and $\beta^* = 90$ m optics (see Fig 4.24).

The results for the ALFA detector and $\beta^* = 0.55$ m optics are shown in Fig. 4.25. Since at present there is no plan to install timing detectors in ALFA, only two constraints were considered: double proton tag (red line) an exactly one reconstructed vertex (green line). At the maximal significance ($\mu \sim 1$) the purity is of about 60%. Going to smaller pile-up values increases the purity, but reduces the statistical significance.

[2]The diffractive mass was computed as $\sqrt{s\xi_1\xi_2}$, where $\xi_{1,2}$ are the proton fractional momentum carried by each Pomeron and $\sqrt{s}$ the center-of-mass energy.

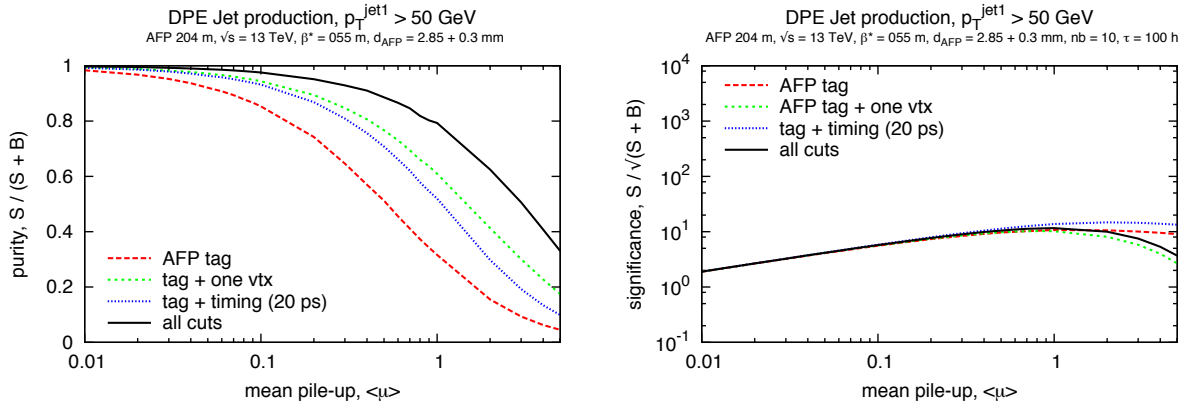
DPE Jet production, $p_T^{jet1} > 50$ GeV
AFP 204 m, √s = 13 TeV, β* = 055 m, d_{AFP} = 2.85 + 0.3 mm
purity, S / (S + B)
mean pile-up, <μ>
AFP tag
tag + one vtx
tag + timing (20 ps)
all cuts
DPE Jet production, $p_T^{jet1} > 50$ GeV
AFP 204 m, √s = 13 TeV, β* = 055 m, d_{AFP} = 2.85 + 0.3 mm, nb = 10, τ = 100 h
significance, S / √(S + B)
mean pile-up, <μ>
AFP tag
AFP tag + one vtx
tag + timing (20 ps)
all cuts

Fig. 4.23: Double Pomeron exchange jet production with both protons tagged in the AFP detectors for $\sqrt{s} = 13$ TeV and $\beta^* = 0.55$ m: purity (**left**) and significance for jets with $p_T > 50$ GeV (**right**) as a function of average pile-up. The number of bunches multiplied by the data collecting time (in hours) was assumed to be 1000. In the analysis the following cuts were considered: double proton tag in the AFP detector (red line), tag + exactly one reconstructed vertex (green line), tag + timing requirement (20 ps, blue line) and all cuts (black line).

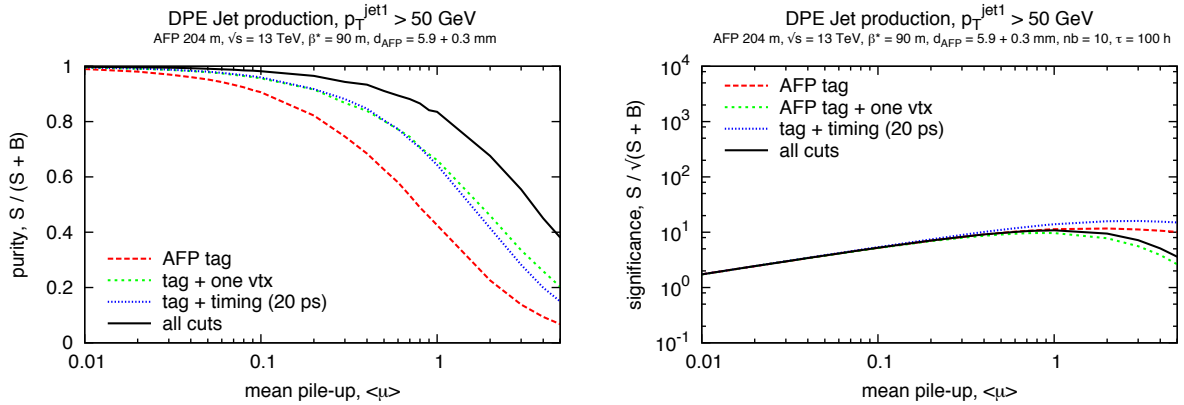
DPE Jet production, $p_T^{jet1} > 50$ GeV
AFP 204 m, √s = 13 TeV, β* = 90 m, d_{AFP} = 5.9 + 0.3 mm
purity, S / (S + B)
mean pile-up, <μ>
AFP tag
tag + one vtx
tag + timing (20 ps)
all cuts
DPE Jet production, $p_T^{jet1} > 50$ GeV
AFP 204 m, √s = 13 TeV, β* = 90 m, d_{AFP} = 5.9 + 0.3 mm, nb = 10, τ = 100 h
significance, S / √(S + B)
mean pile-up, <μ>
AFP tag
AFP tag + one vtx
tag + timing (20 ps)
all cuts

Fig. 4.24: Double Pomeron exchange jet production with both protons tagged in the AFP detectors for $\sqrt{s} = 13$ TeV and $\beta^* = 90$ m: purity (**left**) and significance for jets with $p_T > 50$ GeV (**right**) as a function of average pile-up. The number of bunches multiplied by the data collecting time (in hours) was assumed to be 1000. In the analysis the following cuts were considered: double proton tag in the AFP (red line), tag + exactly one reconstructed vertex (green line), tag + timing requirement (20 ps, blue line) and all cuts (black line).

Similarly as in the case of SD jet production, the measurement worsens dramatically when $\beta^* = 90$ m optics is considered (see Fig. 4.26). This is due to the fact that this optics was designed to measure the elastic scattering with ALFA, thus such events are well within the acceptance and contribute as a background. Fortunately, the elastic signature is relatively easy to filter out by using kinematic constraints. In the following studies, the filtering efficiency was assumed to be 100%, *i.e.* all generated elastic events were removed. Unfortunately, even after such selection the purity is greater than 60% only for $\mu < 0.02$. This is due to high acceptance for the soft central exclusive processes. This means that even for jets with $p_T \sim 50$ GeV a significant measurement is possible only in long runs (~ 100 h) with hundreds of bunches.

A summary of the studies presented above is presented in Tab. 4.B.1. Moreover, in this

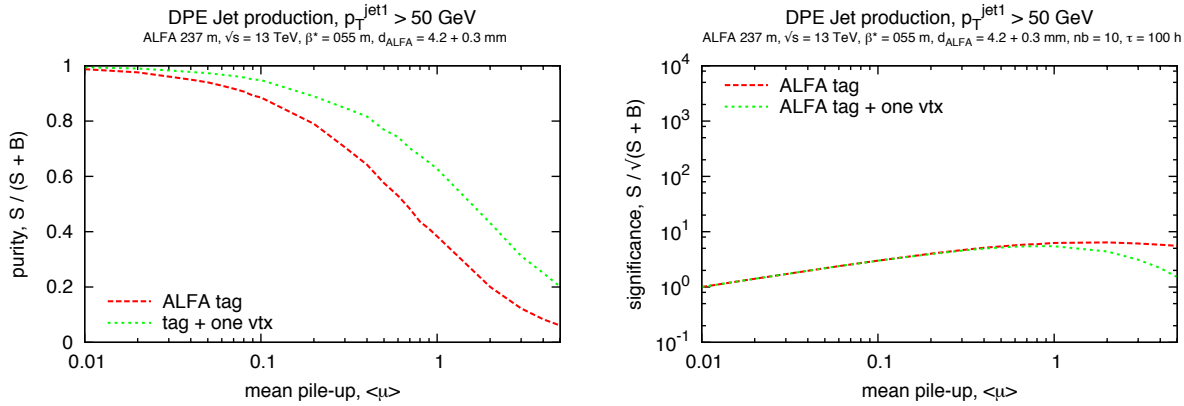
DPE Jet production, p_T^jet1 > 50 GeV
ALFA 237 m, √s = 13 TeV, β* = 055 m, d_ALFA = 4.2 + 0.3 mm
purity, S / (S + B)
mean pile-up, <μ>
ALFA tag
tag + one vtx
DPE Jet production, p_T^jet1 > 50 GeV
ALFA 237 m, √s = 13 TeV, β* = 055 m, d_ALFA = 4.2 + 0.3 mm, nb = 10, τ = 100 h
significance, S / √(S + B)
mean pile-up, <μ>
ALFA tag
ALFA tag + one vtx

Fig. 4.25: Double Pomeron exchange jet production with both protons tagged in the ALFA detectors for $\sqrt{s} = 13$ TeV and $\beta^* = 0.55$ m: purity (**left**) and significance for jets with $p_T > 50$ GeV (**right**) as a function of average pile-up. The number of bunches multiplied by the data collecting time (in hours) was assumed to be 1000. In the analysis the following cuts were considered: double proton tag in the ALFA detector (red line) and tag + exactly one reconstructed vertex (green line).

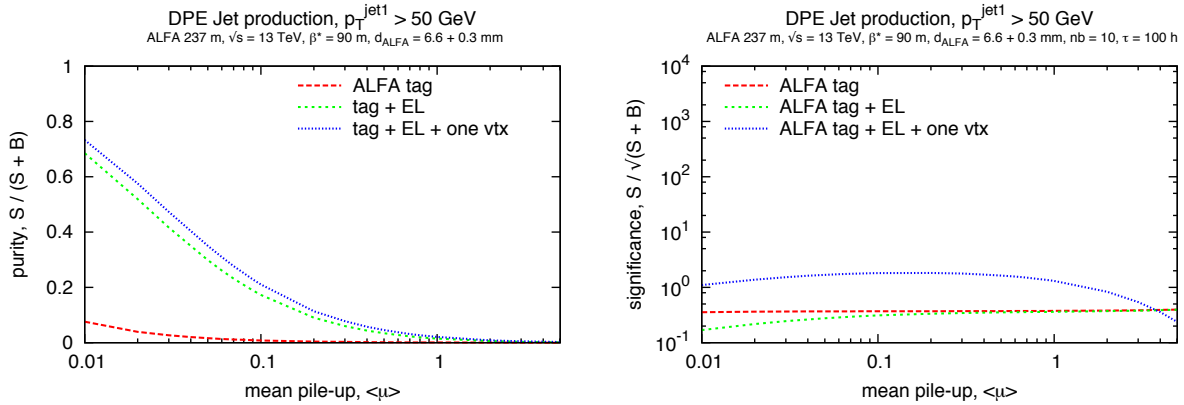
DPE Jet production, p_T^jet1 > 50 GeV
ALFA 237 m, √s = 13 TeV, β* = 90 m, d_ALFA = 6.6 + 0.3 mm
purity, S / (S + B)
mean pile-up, <μ>
ALFA tag
tag + EL
tag + EL + one vtx
DPE Jet production, p_T^jet1 > 50 GeV
ALFA 237 m, √s = 13 TeV, β* = 90 m, d_ALFA = 6.6 + 0.3 mm, nb = 10, τ = 100 h
significance, S / √(S + B)
mean pile-up, <μ>
ALFA tag
ALFA tag + EL
ALFA tag + EL + one vtx

Fig. 4.26: Double Pomeron exchange jet production with both protons tagged in the ALFA detectors for $\sqrt{s} = 13$ TeV and $\beta^* = 90$ m: purity (**left**) and significance for jets with $p_T > 50$ GeV (**right**) as a function of average pile-up. The number of bunches multiplied by the data collecting time (in hours) was assumed to be 1000. In the analysis the following cuts were considered: double proton tag in the ALFA detector (red line), tag + elastic veto (green line) and tag + elastic veto + exactly one reconstructed vertex (blue line).

table the purity and statistical significance for other considered jet p_T thresholds are given. The rate was calculated assuming 100 colliding bunches.

4.7 Double Pomeron Exchange Photon+Jet Production

In double Pomeron exchange mode also events containing a (quark) jet and a photon could be produced. In such case one Pomeron emits a gluon, whereas from the other one a quark is taken. A diagram for such production is presented in Fig. 4.27.

A measurement of photon+jet events produced in DPE mode can be used to test the Pomeron universality between HERA and LHC. Moreover, the Pomeron quark content can be probed: the QCD diffractive fits performed at HERA assumed that $u = d = s = \bar{u} = \bar{d} = \bar{s}$, since data were not sensitive to the difference between the different quark component in the

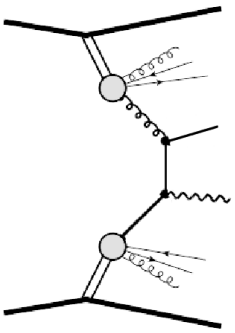

Fig. 4.27: Double Pomeron exchange photon+jet production – both interacting protons stays intact and a (quark) jet and a photon are produced centrally.

Pomeron. As will be shown, the LHC data would allow to check if this assumption was correct. For example, if a value of $d/u \neq 1$ will be favoured by data, the HERA QCD diffractive fits will have to be modified.

Observables that can probe the quark content in the Pomeron at the LHC are the transverse momentum of the leading jet (p_T) and the diffractive (missing) mass $M = \sqrt{s\xi_1\xi_2}$. They are shown in Fig. 4.28 for different assumptions, namely d/u varying between 0.25 and 4. For comparison the predictions of the Soft Colour Interaction (SCI) model [63] are presented.

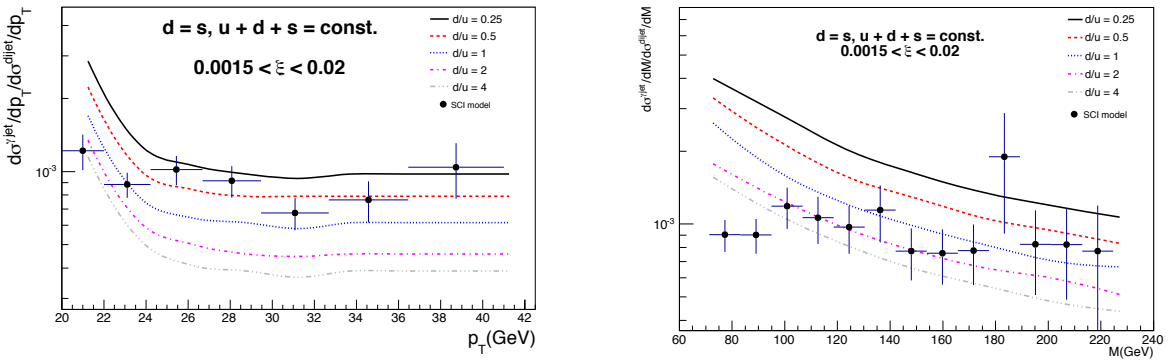

Fig. 4.28: **Left:** ratio of γ+jet over dijet differential cross-section as a function of the leading jet p_T. **Right:** ratio of γ+jet over dijet differential cross-section as a function of the diffractive mass $M = \sqrt{s\xi_1\xi_2}$. The different curves correspond to different ratios d/u inside the Pomeron. Proton-proton collisions at $\sqrt{s} = 14$ TeV are assumed.

4.7.1 ATLAS Feasibility Studies for $\sqrt{s} = 14$ TeV

Results, based on Ref. [64], for the AFP detectors and $\beta^* = 0.55$ m are shown in Fig. 4.29. In this plot the differential cross-section ratio of the DPE γ+jet events to the non-diffractive dijets is presented as a function of the diffractive mass. Most of the systematic uncertainties cancel since the mass distributions for γ+jet and dijet events are similar. Taking into account that the typical mass resolution is of the order of 2 to 3%, a significant measurement can be done with an integrated luminosity of 300 pb^{-1}.

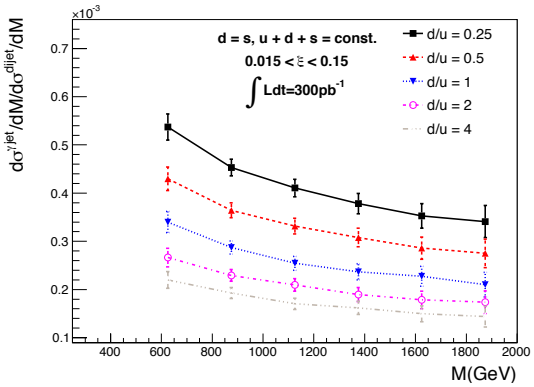

Fig. 4.29: DPE γ+jet to dijet differential cross-section ratio as a function of the diffractive mass $M = \sqrt{\xi_1 \xi_2 s}$ for different values of d/u within the acceptance of the 210 m proton detectors.

4.8 Double Pomeron Exchange Jet-Gap-Jet Production

A jet-gap-jet event features a large rapidity gap with a high-p_T jet on each side. Across the gap, the object exchanged in the t-channel is a colour singlet and carries a large momentum transfer. When the rapidity gap is sufficiently large, the perturbative QCD description of jet-gap-jet events is performed in terms of a Balitsky-Fadin-Kuraev-Lipatov (BFKL) Pomeron [65]. The jet-gap-jet topology is also produced in the single diffractive and the double Pomeron exchange processes. In such events, a colour singlet is exchanged between the protons and in the t-channel between the jets. The signature, shown in Fig. 4.30, is two intact protons scattered in the forward regions and a gap in rapidity between the jets.

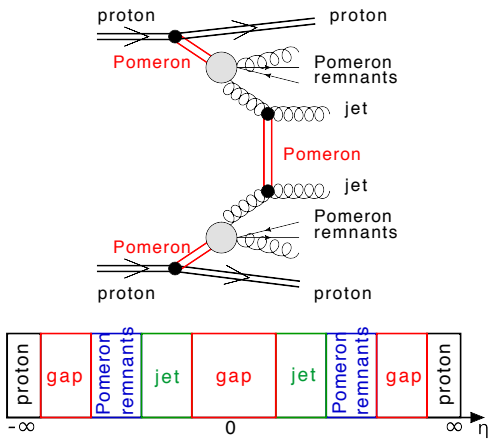

Fig. 4.30: Double Pomeron exchange jet-gap-jet production: both interacting protons stay intact and two jets are produced. In both cases the object exchanged in the t channel is colour singlet and there is a gap in rapidity between the two jets.

The process of double Pomeron exchange jet-gap-jet production was never measured experimentally. By studying its properties, the BFKL model can be tested, *e.g.* by comparing the fraction of DPE JGJ to all DPE jet events. In case of DPE such ratio is larger than the corresponding fraction in "standard" JGJ production, since in DPE events the penalty of the gap survival probability applies to both the DPE JGJ and the total DPE cross-sections [66].

4.8.1 ATLAS Feasibility Studies for $\sqrt{s} = 14$ TeV

In order to simulate the DPE jet-gap-jet production the FPMC program was employed. The used version contained an implementation for summing over non-conformal spins in the leading logarithm (LL) and next-to-leading logarithm (NLL) approximations [66].

A crucial element of the DPE jet-gap-jet measurement is the probability to tag the protons with forward detectors. In the presented analysis, ATLAS and AFP were taken as central and forward detectors, respectively. The leading jet was required to have a transverse momentum greater than 40 GeV. The transverse momentum of the sub-leading jet was required to be greater than 20 GeV.

In the following studies, a gap is defined as a rapidity interval devoid of final state particles with a transverse momentum greater than 200 MeV. The two leading jets were required to be on the opposite pseudo-rapidity hemispheres and the rapidity gap (η_g) was requested to be symmetric around zero. These requirements are somewhat arbitrary and were introduced due to the simplicity – the central tracker region has the highest efficiency for reconstructing low-p_T tracks. Obviously, this analysis can be extended to events with non-symmetric gaps which will increase the visible cross-section.

Since both protons need to be tagged in the AFP stations, not all events can be recorded. As illustrated in Fig. 4.31 (left), the visible cross-section depends on the distance between the AFP active detector edge and the beam centre. For this analysis, a distance of 3.5 mm was assumed. This results in a visible cross-section of about 1 nb.

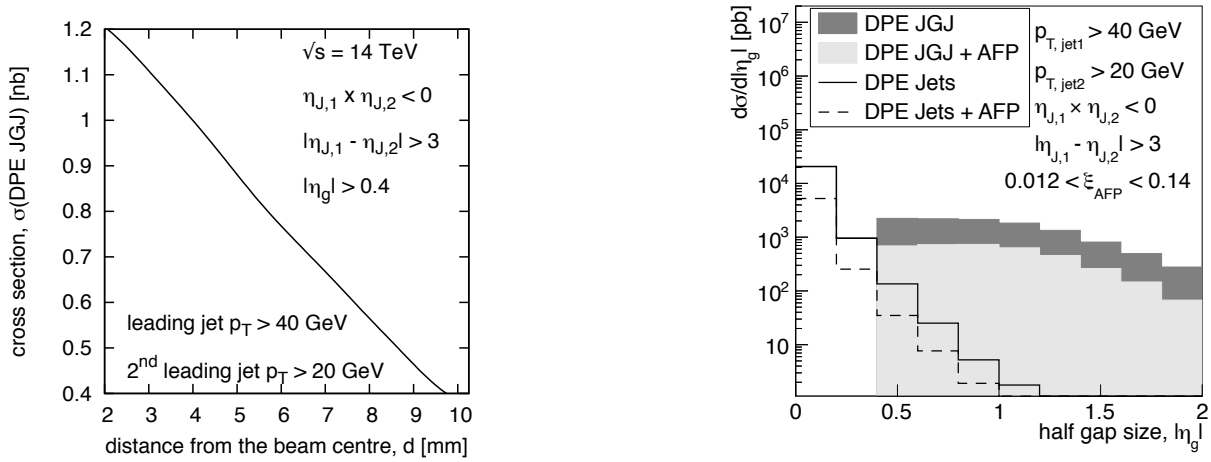
cross section, σ(DPE JGJ) [nb]
√s = 14 TeV
η_J,1 x η_J,2 < 0
|η_J,1 - η_J,2| > 3
|η_g| > 0.4
leading jet p_T > 40 GeV
2nd leading jet p_T > 20 GeV
distance from the beam centre, d [mm]
dσ/d|η_g| [pb]
DPE JGJ
DPE JGJ + AFP
DPE Jets
DPE Jets + AFP
p_T, jet1 > 40 GeV
p_T, jet2 > 20 GeV
η_J,1 × η_J,2 < 0
|η_J,1 - η_J,2| > 3
0.012 < ξ_AFP < 0.14
half gap size, |η_g|

Fig. 4.31: **Left:** visible cross-section as a function of the distance between the detector and the beam centre. **Right:** gap size distribution for DPE jets and DPE jet-gap-jet events with and without the AFP tag requirement. For large enough gaps $\Delta\eta_g > 0.5$, the gap-between-jets events are not dominated by fluctuations of dijets events.

The main background to the DPE jet-gap-jet production will be the DPE jet production. For such processes a gap between the jets may be due to the fluctuations in hadronisation, but this background is significantly reduced by requiring large gap sizes. This is illustrated in Fig. 4.31 (right), where the DPE background is shown as a continuous and dashed lines whereas the DPE JGJ signal is plotted as a grey area. The probability of having a gap due to a fluctuation falls exponentially with the increase of the gap size. For example, if $|\eta_g| > 0.5$, the background will mimic the signal in less than 5% of cases.

Larger gap sizes are increasingly dominated by the jet-gap-jet process. However, the cross-section also falls steeply with an increase of the gap size. Assuming both protons tagged

in AFP, a good balance between the signal to background ratio and the visible cross-section was found for a gap of $|\eta_g| \sim 0.5$.

The DPE jet-gap-jet event ratio is plotted in Fig. 4.32 as a function of the transverse momentum of the leading jet and as a function of the pseudorapidity difference between the two jets with the highest transverse momentum, $\Delta\eta_J$. To take into account the NLO QCD effects, absent in the FPMC program, the LO ratio was corrected by the cross-section ratio σ(DPE LO Jet++)/σ(DPE NLO Jet++) obtained with the NLO JET++ program [67]. The detailed description of this procedure can be found in Ref. [66]. To verify the statistical power of this measurement, statistical errors corresponding to 300 pb^{-1} of integrated luminosity were computed.

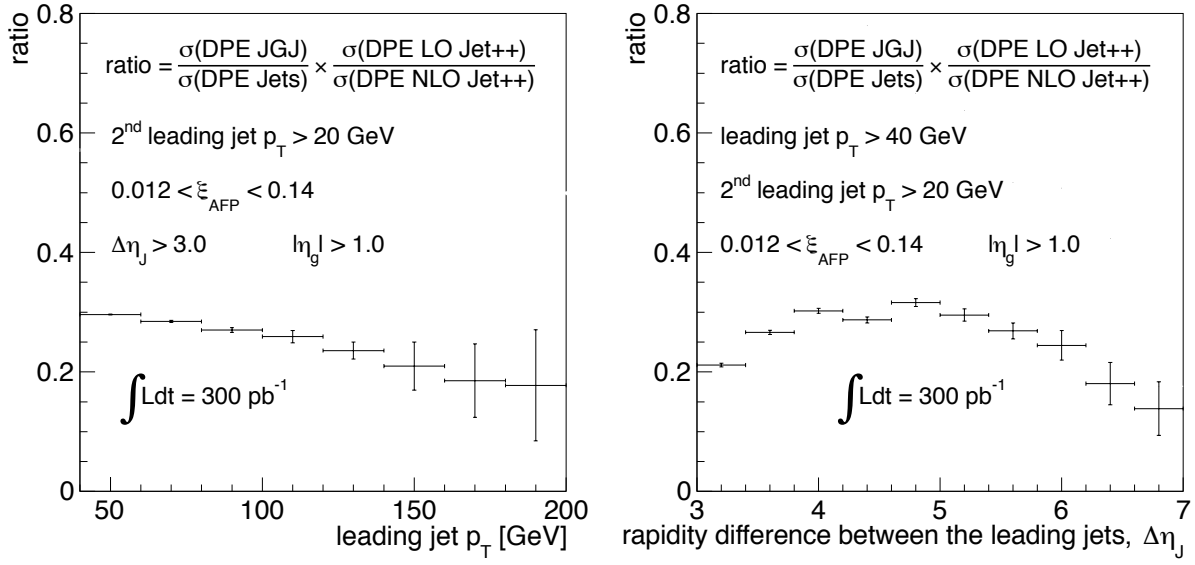
ratio
ratio = σ(DPE JGJ)/σ(DPE Jets) × σ(DPE LO Jet++)/σ(DPE NLO Jet++)
2nd leading jet p_T > 20 GeV
0.012 < ξ_AFP < 0.14
Δη_J > 3.0
|η_g| > 1.0
∫Ldt = 300 pb^-1
leading jet p_T [GeV]
leading jet p_T > 40 GeV
rapidity difference between the leading jets, Δη_J

Fig. 4.32: Predictions for the DPE jet-gap-jet to DPE jet cross-section ratio at the LHC, as a function of the leading jet transverse momentum p_T (**left**), and of the rapidity difference between the two leading jets $\Delta\eta_J$ (**right**). For both plots, an integrated luminosity of 300 pb^{-1} was assumed.

4.9 Conclusions

CMS and ATLAS have a dense program of hard diffractive measurements. Several of them are feasible with moderate integrated luminosities and/or benefitting from the special low luminosity runs foreseen in 2015. Studies described in this Chapter were done under the assumption that protons are tagged in forward detectors: AFP or ALFA in case of the ATLAS experiment or TOTEM Roman pots for CMS. The analyses assumed either collision ($\beta^* = 0.55$ m) or special, high-β^*, optics.

The measurements of single diffractive J/ψ, W and Z bosons were shown to be possible with with 10 pb^{-1} of integrated luminosity. The amount of data needed to be collected for single diffractive or double Pomeron exchange studies depend strongly on the jet p_T threshold. Nevertheless, the low p_T jets could be measured already with few inverse picobarns collected. In order to study the double Pomeron exchange γ+jet and jet-gap-jet productions more data is needed. In particular, it was shown that the measurement of later two processes is possible with O(300) pb^{-1}.

By studying diffractive production a number of QCD tests can be performed. For example, such measurements may shed a light on the problem of the Pomeron universality in ep and

pp collision. Moreover, the gap survival probability can be quantified and the QCD evolution of the gluon and quark densities in the Pomeron can be tested and compared with the HERA measurements. Some of the diffractive processes, like double Pomeron exchange jet-gap-jet production, were never measured experimentally. Moreover, by studying the properties of JGJ events QCD models, like BFKL, can be tested.

Acknowledgments

Pieces of this chapter has been supported in part by Polish National Science Centre grant number 2012/05/B/ST2/02480.

Appendix

4.A Expected Statistics of Single Diffractive Jet Measurement

Table 4.A.1: Purity, statistical significance, number of events and rate for single diffractive jet production for various optics settings and ATLAS forward detectors. The sub-leading jet was required to have $p_T > 20$ GeV. The number of bunches multiplied by the data collecting time (in hours) was assumed to be 1000. The rate was calculated for 100 bunches.

Leading jet p_T threshold	**Purity**	**Significance**	**Number of events**	**rate [Hz]**
AFP 204 m, β^* = 0.55 m, μ = 0.1				
$p_T > 20$ GeV	0.7	64	10000	5
$p_T > 50$ GeV	0.85	21	1000	0.3
$p_T > 100$ GeV	0.8	7	100	0.02
AFP 204 m, β^* = 90 m, μ = 0.1				
$p_T > 20$ GeV	0.65	56	8000	3
$p_T > 50$ GeV	0.85	19	800	0.3
$p_T > 100$ GeV	0.8	5	50	0.01
ALFA 237 m, β^* = 0.55 m, μ = 0.1				
$p_T > 20$ GeV	0.7	45	5000	3
$p_T > 50$ GeV	0.85	15	500	0.2
$p_T > 100$ GeV	0.85	3	20	0.01
ALFA 237 m, β^* = 90 m, μ = 0.01				
$p_T > 20$ GeV	0.65	20	1000	5
$p_T > 50$ GeV	0.8	7	100	0.3
$p_T > 100$ GeV	0.8	1	5	0.02

4.B Expected Statistics of Double Pomeron Exchange Jet Measurement

Table 4.B.1: Purity, statistical significance, number of events and rate for double Pomeron exchange jet production for various optics settings and ATLAS forward detectors. The sub-leading jet was required to have $p_T > 20$ GeV. The number of bunches multiplied by the data collecting time (in hours) was assumed to be 1000. The rate was calculated for 100 bunches.

Leading jet p_T threshold	**Purity**	**Significance**	**Number of events**	**rate [Hz]**
AFP 204 m, β^* = 0.55 m, μ = 0.1				
$p_T > 20$ GeV	0.95	49	5000	0.2
$p_T > 50$ GeV	0.95	16	500	0.01
$p_T > 100$ GeV	0.95	2	10	0.0004
AFP 204 m, β^* = 90 m, μ = 0.1				
$p_T > 20$ GeV	0.95	38	3000	0.1
$p_T > 50$ GeV	0.95	12	300	0.01
$p_T > 100$ GeV	0.95	3	20	0.0005
ALFA 237 m, β^* = 0.55 m, μ = 0.1				
$p_T > 20$ GeV	0.9	22	1000	0.05
$p_T > 50$ GeV	0.95	7	100	0.003
$p_T > 100$ GeV	0.95	2	5	0.0001
ALFA 237 m, β^* = 90 m, μ = 0.01				
$p_T > 20$ GeV	0.6	11	300	2
$p_T > 50$ GeV	0.7	1	2	0.05
$p_T > 100$ GeV	0.6	0	0.2	0.003

References

[1] UA8 Collaboration (A. Brandt *et. al*). *Evidence for Transverse Jets in High Mass Diffraction*. Phys. Lett. B **211** (1988) 239.

[2] UA8 Collaboration (A. Brandt *et. al*). *Cross-section measurements of hard diffraction at the SPS collider*. Phys. Lett. B **421** (1998) 395.

[3] ATLAS Collaboration. *Measurement of the total cross section from elastic scattering in pp collisions at $\sqrt{s}$=7 TeV with the ATLAS detector*. NP B **889**, 486 (2014).

[4] ATLAS Collaboration. *Rapidity gap cross sections measured with the ATLAS detector in pp collisions at sqrt(s) = 7 TeV*. EPJ C **72**, 1926 (2012).

[5] ATLAS Collaboration. *Measurements of jet vetoes and azimuthal decorrelations in dijet events produced in pp collisions at $\sqrt{s}$ = 7 TeV using the ATLAS detector*. EPJ C **74**, 3117 (2014).

[6] ATLAS Collaboration. *Measurement of dijet production with a veto on additional central jet activity in pp collisions at $\sqrt{s}$=7 TeV using the ATLAS detector*. JHEP 1109, 053.

[7] CMS Collaboration. *Forward Energy Flow, Central Charged-Particle Multiplicities, and Pseudorapidity Gaps in W and Z Boson Events from pp Collisions at $\sqrt{s}$=7 TeV*. Eur. Phys. J. C **72** (2012) 1839.

[8] CMS Collaboration. *Exclusive $\gamma\gamma \to \mu^+\mu^-$ production in proton-proton collisions at $\sqrt{s}$=7 TeV*. J. High Energy Phys. **01** (2012) 052.

[9] CMS Collaboration. *Search for exclusive or semi-exclusive $\gamma\gamma$ production and observation*

of exclusive and semi-exclusive e+eâĹŠ production in pp collisions at $\sqrt{s}$=7 TeV. J. High Energy Phys. **11** (2012) 080.

[10] CMS Collaboration. *Observation of a diffractive contribution to dijet production in proton-proton collisions at $\sqrt{s}$=7 TeV*. Phys. Rev. D **87** (2013) 012006.

[11] CMS Collaboration. *Measurement of diffractive dissociation cross sections in pp collisions at $\sqrt{s}$=7 TeV*. arXiv:1503.08689.

[12] TOTEM Collaboration. *First measurements of the total proton-proton cross section at the LHC energy of sqrt $\sqrt{s}$=7 TeV*. EPL **96** (2011) 21002.

[13] TOTEM Collaboration. *Measurement of the forward charged particle pseudorapidity density in pp collisions at sqrt $\sqrt{s}$=7 TeV with the TOTEM experiment*. EPL **98** (2012) 31002.

[14] TOTEM Collaboration. *Double diffractive cross-section measurement in the forward region at LHC*. Rev. Lett. **111** (2013) 262001.

[15] TOTEM Collaboration. *Measurement of pseudorapidity distributions of charged particles in proton-proton collisions at sqrt(s) = 8 TeV by the CMS and TOTEM experiments*. EPJC **74** (2014) 3053.

[16] TOTEM Collaboration. *Measurement of the forward charged particle pseudorapidity density in pp collisions at sqrt(s) = 8 TeV using a displaced interaction point*. CERN-PH-EP-2014-260.

[17] ALICE Collaboration. *Measurement of inelastic, single- and double-diffraction cross sections in proton-proton collisions at the LHC with ALICE*. Eur. Phys. J. C **73** (2013) 2456.

[18] ALICE Collaboration. *Exclusive J/ψ photoproduction off protons in ultra-peripheral p-Pb collisions at $\sqrt{s_{\rm NN}} = 5.02$ TeV*. Phys. Rev. Lett. **113** (2014) 232504.

[19] LHCb Collaboration. *Measurement of the forward energy flow in pp collisions at $\sqrt{s}$=7 TeV*. Eur. Phys. J. **C** 73 (2013) 2421.

[20] LHCb Collaboration. *Observation of charmonium pairs produced exclusively in pp collisions*. J. Phys. G **41** (2014) 115002.

[21] Serguei Chatrchyan et al. Observation of a diffractive contribution to dijet production in proton-proton collisions at $\sqrt{s} = 7$ TeV. *Phys.Rev.*, D87(1):012006, 2013.

[22] Serguei Chatrchyan et al. Forward Energy Flow, Central Charged-Particle Multiplicities, and Pseudorapidity Gaps in W and Z Boson Events from pp Collisions at $\sqrt{s}$ = 7 TeV. *Eur.Phys.J.*, C72:1839, 2012.

[23] ATLAS Collaboration. *Charged-particle multiplicities in pp interactions at $\sqrt{s}$ = 7 TeV and 900 GeV measured from pT > 100 MeV: Supporting the MinBias 2nd Publication*. ATL-COM-PHYS-2010-880, 2010.

[24] CMS Collaboration. *Charged particle multiplicities in pp interactions at $\sqrt{s} = 0.9$, 2.36, and 7 TeV*. JHEP **1101** (2011) 079.

[25] TOTEM Collaboration. Development of a (beam halo + pileup) background rejection procedure for diffractive analyses in low-pileup runs based on totem roman pot tagging, 2015.

[26] A. B. Kaidalov, V. A. Khoze, A. D. Martin, and M. G. Ryskin. *Probabilities of rapidity gaps in high energy interactions*. Eur. Phys. J. C **21** (2001) 521-529.

[27] C. Royon. *Forward physics with tagged protons at the LHC: QCD and anomalous couplings*. Proceedings of the Low x 2013 workshop, May 30 - June 4 2013, Rehovot and Eilat, Israel.

[28] Brian E. Cox and Jeffrey R. Forshaw. POMWIG: HERWIG for diffractive interactions. *Comput.Phys.Commun.*, 144:104–110, 2002.

[29] A. Aktas et al. Measurement and QCD analysis of the diffractive deep-inelastic scattering cross-section at HERA. *Eur.Phys.J.*, C48:715–748, 2006.

[30] M. Boonekamp *et al.* *FPMC: a generator for forward physics*. http://project-fpmc.web.cern.ch/project-fpmc/.

[31] T. Sjostrand, S. Mrenna, and P. Skands. *A Brief Introduction to PYTHIA 8.1*. Comput. Phys. Commun. **178** (2008).

[32] R. Ciesielski and K. Goulianos. *MBR Monte Carlo Simulation in PYTHIA8*. PoS ICHEP2012 (2013) 301, arXiv:1205.1446.

[33] P. Bussey. *FPTrack Programme*.

[34] M. Trzebinski, R. Staszewski, and J. Chwastowski. *LHC High Beta* Runs: Transport and Unfolding Methods* . ISRN High Energy Physics, vol. 2012 (2012) 491460.

[35] M. Cacciari, G.P. Salam, and G. Soyez. *FastJet user manual*. Eur. Phys. J. **C72** (2012) 1896.

[36] John C. Collins. Proof of factorization for diffractive hard scattering. *Phys.Rev.*, D57:3051–3056, 1998.

[37] H1 Collaboration (A. Aktas *et al.*) *Eur. Phys. J.* **C48**. 715 . 2006.

[38] *Nucl. Phys.* **B831** ZEUS Collaboration (S. Chekanov *et al.*). 1 . 2010.

[39] A. Aktas et al. Dijet Cross Sections and Parton Densities in Diffractive DIS at HERA. *JHEP*, 0710:042, 2007.

[40] F.D. Aaron et al. Diffractive Dijet Photoproduction in ep Collisions at HERA. *Eur.Phys.J.*, C70:15–37, 2010.

[41] S. Chekanov et al. Dijet production in diffractive deep inelastic scattering at HERA. *Eur.Phys.J.*, C52:813–832, 2007.

[42] T. Aaltonen et al. Diffractive Dijet Production in $\bar{p}p$ Collisions at $\sqrt{s} = 1.96$ TeV. *Phys.Rev.*, D86:032009, 2012.

[43] T. Aaltonen et al. Diffractive W and Z Production at the Fermilab Tevatron. *Phys.Rev.*, D82:112004, 2010.

[44] A.B. Kaidalov, Valery A. Khoze, Alan D. Martin, and M.G. Ryskin. Probabilities of rapidity gaps in high-energy interactions. *Eur.Phys.J.*, C21:521–529, 2001.

[45] A.B. Kaidalov, V.A. Khoze, A.D. Martin, and M.G. Ryskin. Unitarity effects in hard diffraction at HERA. *Phys.Lett.*, B567:61–68, 2003.

[46] A.J. Baltz, G. Baur, D. d'Enterria, L. Frankfurt, F. Gelis, et al. The Physics of Ultraperipheral Collisions at the LHC. *Phys.Rept.*, 458:1–171, 2008.

[47] Gerhard Baur, Kai Hencken, Dirk Trautmann, Serguei Sadovsky, and Yuri Kharlov. Coherent gamma gamma and gamma-A interactions in very peripheral collisions at relativistic ion colliders. *Phys.Rept.*, 364:359–450, 2002.

[48] L. Szymanowski R. Boussarie, A. Grabovsky and S. Wallon. Impact factor for high-energy two and three jets diffractive production. *JHEP*, 1409 (2014) 026, [arXiv:1405.7676].

[49] L. Szymanowski R. Boussarie, A. Grabovsky and S. Wallon. In preparation.

[50] B.Z. Kopeliovich, I.K. Potashnikova, I. Schmidt, and A.V. Tarasov. Unusual features of Drell-Yan diffraction. *Phys.Rev.*, D74:114024, 2006.

[51] R.S. Pasechnik and B.Z. Kopeliovich. Drell-Yan diffraction: Breakdown of QCD factorisation. *Eur.Phys.J.*, C71:1827, 2011.

[52] Roman Pasechnik, Boris Kopeliovich, and Irina Potashnikova. Diffractive Gauge Bosons Production beyond QCD Factorisation. *Phys.Rev.*, D86:114039, 2012.

[53] Hung-Liang Lai, Marco Guzzi, Joey Huston, Zhao Li, Pavel M. Nadolsky, et al. New parton distributions for collider physics. *Phys.Rev.*, D82:074024, 2010.

[54] CMS/TOTEM Collaboration. Cms-totem feasibility studies for single diffractive z, w, $j\psi$ production and central esclusive dijet production in pp collisions at $\sqrt{(s)}$ = 13 tev. `http://cds.cern.csh/record/1954682?ln=en`, 2014.

[55] Brian E. Cox and Jeffrey R. Forshaw. Pomwig: Herwig for diffractive interactions. *Comput. Phys. Commun.*, 144:104–110, 2002.

[56] P. Bruni and G. Ingelman. Diffractive hard scattering at ep and p anti-p colliders. DESY REPORT DESY 93-187, CERN, 1993.

[57] Serguei Chatrchyan et al. Observation of a diffractive contribution to dijet production in proton-proton collisions at $\sqrt{s} = 7$ TeV. *Phys. Rev.*, D87:012006, 2013.

[58] Hubert Niewiadomski, Valentina Avati, Cinzia Da Via, and Karsten Eggert. *Reconstruction of Protons in the TOTEM Roman Pot Detectors at the LHC*. PhD thesis, Manchester U., Manchester, 2008. Presented on 11 Sep 2008.

[59] S. Agostinelli et al. GEANT4: A simulation toolkit. *Nucl. Instrum. Meth.*, A506:250–303, 2003.

[60] Vardan Khachatryan et al. Measurements of inclusive w and z cross sections in pp collisions at $\sqrt{s} = 7$ TeV. *JHEP*, 01:080, 2011.

[61] G. Antchev et al. Performance of the TOTEM Detectors at the LHC. *Int. J. Mod. Phys.*, A28:1330046, 2013.

[62] V. A. Khoze, A. D. Martin, and M. G. Ryskin. *Diffraction at the LHC*. arXiv:1306.2149.

[63] A. Edin, G. Ingelman, and J. Rathsman. *Soft color interactions as the origin of rapidity gaps in DIS*. Phys. Lett. B **366**, 371 (1996); Z.Phys. C75, 57 (1997).

[64] C. Marquet, C. Royon, M. Saimpert, and D. Werder. *Probing the Pomeron structure using dijets and γ+jet events at the LHC*. arXiv:1306.4901.

[65] O. Kepka, C. Marquet, and C. Royon. *Gaps between jets in hadronic collisions*. Phys. Rev. D **83** (2011) 034036.

[66] C. Marquet, C. Royon, M. Trzebinski, and R. Zlebcik. *Gaps between jets in double-Pomeron-exchange processes at the LHC*. Phys. Rev. D **87**, (2013) 034010.

[67] Z. Nagy and Z. Trocsanyi. *Multi-jet cross sections in deep inelastic scattering at next-to-leading order*. Phys. Rev. Lett. **87**, 082001 (2001).

Chapter 5

Central Exclusive Production

Conveners and Editors: L. Harland-Lang, V. Khoze, M. Saimpert
Internal Reviewers: R. Mc Nulty, M. Rangel

5.1 Introduction

Central Exclusive Production (CEP) is the reaction

$$pp(\bar{p}) \to p + X + p(\bar{p}) \,,$$

where '+' signs are used to denote the presence of large rapidity gaps, separating the system X from the intact outgoing protons (anti–protons). Over the last decade there has been a steady rise of theoretical and experimental interest in studies of this process in high–energy hadronic collisions, see [1–3] for reviews. On the theoretical side, the study of CEP requires the development of a framework which is quite different from that used to describe the inclusive processes more commonly considered at hadron colliders. This requires an explicit account of both soft and hard QCD, and is therefore sensitive to both of these regimes. Moreover, the dynamics of the CEP process leads to unique predictions and effects which are not seen in the inclusive mode. Experimentally, CEP represents a very clean signal, with just the object X and no other hadronic activity seen in the central detector (in the absence of pile up).

In addition, in such reactions the outgoing hadrons can be measured by installing proton tagging detectors, situated far down the beam line from the central detector, which can provide information about the mass and quantum numbers of the centrally produced state; this is the aim of the CT-PPS and CMS-TOTEM detectors, and the ALFA and AFP detectors for ATLAS. This chapter will discuss the motivation and possibilities for performing measurements of exclusive processes both with and without tagged protons at low to medium luminosity, as part of special high β^* runs with ATLAS and CMS, or during general LHCb and ALICE running, and at higher luminosity with tagged protons, where tools such as precision timing detectors will be fundamental to control pile up effects.

The CEP process requires the t–channel exchange of a color–singlet object, so that the outgoing protons can remain intact. More generally, in order for the cross section not to vanish with rising rapidity gaps between the final state particles, the t–channel exchanges cannot transfer charge, isospin, or color. One possibility to achieve this is the two–photon fusion process $\gamma\gamma \to X$, where the radiated quasi–real photons couple to the electromagnetic charge of the whole protons. Another possibility is to consider so–called Double Pomeron Exchange (DPE), where both protons interact strongly, 'emitting' pomerons, which then 'fuse' to create the object $I\!P I\!P \to X$. Provided the object X mass is large enough, this process can be considered in the framework of pQCD, that is by considering gluon rather than pomeron interactions. Finally it is possible for 'photoproduction' reactions to occur, where both photon and pomeron (gluon) emission take place, i.e. $I\!P\gamma \to X$. All three processes will be considered in this chapter; the label 'CEP' will be used in all cases.

The outline of this chapter is as follows. In Section 5.2, the methods of selecting exclusive events, namely through proton tagging or rapidity gap based techniques, are discussed, and the

relevant features of the LHC experiments for performing CEP measurements are summarised. Theoretical details, as well as the experimental results and outlook are presented in Sections 5.3 and 5.4 for a range of QCD and photon exchange/photoproduction exclusive processes, respectively. Finally, in Section 5.5, the possibility for performing exploratory searches, and probing BSM physics are discussed.

5.2 Analysis techniques and detectors to study exclusive processes at the LHC

In this Section, we start by presenting the two methods for selecting exclusive events in collision data applied so far in analyses: proton tagging and rapidity gap detection, see Section 5.2.1. Then, we summarise briefly the advantages and challenges of the different detectors at the LHC when measuring CEP processes: in Section 5.2.2 the LHCb and ALICE detectors and in Section 5.2.3, the CMS and ATLAS detectors, are discussed. The reader is referred to Chapter 9 for further details of the relevant detectors.

5.2.1 Analysis techniques

Proton tagging is both a very challenging and powerful technique. For a CEP process, by detecting the intact protons in addition to the system produced in the central detector the full event kinematics are reconstructed, which is generally not possible in a hadron–hadron collider. Detecting the outgoing protons is the only way to get a pure sample of exclusive events experimentally: indeed, the kinematic variables reconstructed from the forward and the central detectors can be compared in order to reject a very large fraction of the traditional backgrounds encountered in CEP measurements (e.g. quasi-exclusive, dissociated proton events). That is, a comparison between the central mass, M_{central}, computed from the centrally produced particles, and M_X, computed from the outgoing protons, can be performed. More specifically, the transverse (p_T) and longitudinal (p_z) momentum of the central state and the two protons may also be compared, and the rapidity gaps predicted by the proton fractional momentum loss ξ measurements can be verified. In all cases consistency between the central and proton systems is expected in the case of CEP, but not in general for background events. Furthermore, the full kinematics reconstruction has recently been shown to make various CEP measurements competitive in searches for BSM physics in the nominal LHC high luminosity running, compared to standard LHC searches using the central detector only (see Section 5.5). This presents completely new possibilities for forward physics and CEP measurements. As well as serving as the most effective way to select exclusive events experimentally, proton tagging is also of great interest theoretically, as a means to measure the momenta of the outgoing intact protons in the CEP reactions, see Sections 5.3.2 and 5.4.2.

Without tagging the outgoing protons it is still possible to select events which are dominantly due to CEP, by using rapidity gap methods, i.e. demanding that there is no additional hadronic activity associated with the event in a large enough region of rapidity. In order to veto quasi-exclusive interactions containing low mass proton dissociation, a wide rapidity coverage of veto detectors is advantageous. This technique is most readily applied to higher cross section processes, for example exclusive J/ψ photoproduction where one may require (excluding the decay of the central system) no reconstructed tracks, no central calorimeter energy deposits above noise, and no activity in forward scintillators or calorimeters. The exact requirements vary between experiments due to different detector technologies covering differing solid angles. Such techniques require the probability of more than one proton interaction per bunch crossing to be small. However, for smaller cross section processes other techniques to select dominantly exclusive events, in the presence of pile–up, can be still applied, for example vetoing on any additional tracks associated with the interaction vertex.

5.2.2 Central exclusive production at LHCb and ALICE

No proton tagging detectors are currently installed at LHCb, and so the determination of the exclusivity of an event depends on no activity being seen in an active detection region that extends over as large a pseudorapidity range as possible. The LHCb detector is fully instrumented

for pseudorapidities $2 < \eta < 4.5$, and includes a high-precision tracking system consisting of a silicon-strip vertex detector (VELO) surrounding the pp interaction region, which has sensitivity to charged particles in the backwards region ($-3.5 < \eta < -1.5$), as well as extending the sensitivity in the forward region to $1.5 < \eta < 5$. Thus the Run–I rapidity coverage sums to roughly 5.5 units in rapidity. During Run–II, the newly installed HERSCHEL forward scintillation detectors will allow vetoes on additional particle production up to $|\eta| \approx 8$ extending the detection of a rapidity gap to up to about 12 units, see Section 9.6.1. The triggering capability of the LHCb detector, being designed for low mass objects, is well suited to CEP. It consists of a two-stage system, a fast hardware trigger followed by a software trigger that applies a full event reconstruction. For CEP, the hardware stage triggers on muons with transverse momentum above 400 MeV, or electromagnetic or hadronic energy above 1000 MeV, all of which are placed in coincidence with a charged multiplicity of less than 10 deposits in the scintillating-pads (SPD). The software trigger is configured to select concidence with a low charged particle multiplicity requirement. The data-taking conditions at LHCb are advantageous for the selection of CEP events. Unlike ATLAS and CMS, where there were typically 20 interactions per beam-crossing in the 2012 data-taking, the beams are defocused at LHCb, resulting in an average of about 1.5 proton-proton interactions per beam-crossing. Consequently, about 20% of the total luminosity has a single interaction and is usable for CEP. During high–luminosity Run–II conditions, LHCb intend to run with an average of 1.1 proton–proton interactions per collision.

Due to specific detector restrictions, ALICE requires a reduced luminosity in pp interactions at IP2, therefore the instantaneous luminosity delivered to ALICE for pp collisions is adjusted accordingly. The experiment aims to collect pp data for CEP studies during dedicated runs for diffractive studies, as well as during runs dedicated for minimum-bias studies. Another advantage of the ALICE experiment for performing CEP and diffractive studies is its low-p_T reach. It has very good track reconstruction and particle identification efficiency starting from $p_T \simeq 150$ MeV. MC simulations show that the invariant mass and transverse momentum resolution for the two-track system is better than 0.5% and that the systematic shifts are negligible. In order to enhance the ALICE capabilities for diffractive studies, two new scintillator counters have been installed during LS1 in both sides of the interaction region, covering pseudorapidities up to $|\eta| \simeq 7$, see Section 9.7 for further details. In addition, ALICE is currently introducing a dedicated online trigger to be used during Run-II for selecting a sample with an enhanced CEP contribution. It will require an activity in the central barrel and no activity up to pseudorapidities $|\eta| \simeq 7$.

5.2.3 Central exclusive production at CMS and ATLAS

In the case of ATLAS or CMS, the tracker is of particular importance. In both cases it is designed for efficient and precise reconstruction of the trajectories of charged particles with transverse momentum above 1 GeV in the pseudorapidity range $|\eta| < 2.5$. Special tracking algorithms extend the tracking capabilities down to $p_T \sim 0.1$ GeV, essential for CEP studies.

The CMS detector already includes proton taggers associated with the Interaction Point (IP), with both the existing TOTEM experiment and the CMS-TOTEM Precision Proton Spectrometer (CT-PPS) upgrade soon to start data taking, see Section 9.2 and 9.4. For the ATLAS collaboration, the existing ALFA detectors allow intact protons to be detected at high β^*, similarly to TOTEM, and the properties of the future AFP detectors are similar to the CT-PPS upgrade, see Sections 9.1 and 9.5. In the following some further details are given in the case of CMS-TOTEM, but it should be emphasised that much of this discussion also applies in the ATLAS-ALFA-AFP case.

The combination of the CMS and TOTEM experiments gives an exceptionally large pseudorapidity coverage for tracking and calorimetry that is well suited for studies of diffractive processes like CEP. The addition of proton timing detectors with ~ 50 ps timing resolution in the vertical Roman Pots (RPs) allows access to CEP processes with O(pb) cross sections. The Forward Shower Counters (FSC), covering $6 \lesssim |\eta| \lesssim 8$ in rapidity, can be used to veto proton diffractive dissociation and extend rapidity gap measurements. Since protons with any fractional momentum loss ξ can be detected in the vertical RPs with low pile–up $\beta^* = 90$ m optics (see Chapter 1), the mass coverage in CEP and photon exchange reactions extends to any central system mass M_X, as long as the $|t|$ of both scattered protons is larger than ~ 0.04 GeV^2. This is therefore complementary to the reach of the CMS-TOTEM precision proton spectrometer (CT-PPS) discussed below. Already, data has been taken during a common CMS-TOTEM $\beta^* = 90$ m run at $\sqrt{s} = 8$ TeV in July 2012, showing the feasibility of CEP measurements. The available double-arm RP jet (jet or lepton) triggered sample corresponds to an integrated luminosity of ~ 0.003 (~ 0.1) pb^{-1}.

The CT-PPS (equivalent in ATLAS to the AFP project) adds precision proton tracking and timing detectors in the very forward region on both sides of CMS at about 220–240m from the IP, to study CEP in proton-proton collisions. At $\sqrt{s} = 13$ TeV and in normal high-luminosity conditions, with the CT-PPS detectors at 15σ from the beam, values of the central system mass $M_X \gtrsim 300$ GeV will be accessible. Even with an average of 50 pile up events, the backgrounds can be suppressed by matching the reconstructed values of $M_{central}$ (in the central detector) and M_X (in the CT-PPS), by requiring small charged multiplicity associated to the di-lepton vertex for the case of leptonic final states (i.e. $X = e^+e^-, \mu^+\mu^-, \tau^+\tau^-$ and W^+W^-), and by exploiting the proton timing constraint on the z-vertex position.

Finally, it should be noted that complementary measurements of rapidity gaps during special runs at low luminosity without proton tagging are also possible with ATLAS and CMS detectors alone.

5.3 QCD processes

In this Section, theoretical discussion of CEP processes that proceed via the strong interaction, and motivations for future measurements, are presented.

5.3.1 Introduction

The CEP process may be mediated purely by the strong interaction, in the language of Regge theory proceeding via double Pomeron exchange. In this case, and when the mass of the system, X, produced in the CEP reaction is sufficiently large, a perturbative QCD approach becomes applicable [1,2,4,5], and we may consider the two–gluon exchange diagram shown in Fig. 5.1. This approach, often referred to as the 'Durham model', was developed in papers such as [5,6] and has undergone much development in subsequent years; see [2] for a review and [7–10, 12, 79] for some examples of further theoretical and phenomenological work. It represents a novel application of perturbative QCD, as well as requiring an account of soft diffractive physics. For such processes it is found that a dynamical selection rule operates [2, 13], where $J_z^{PC} = 0^{++}$ quantum number states (here J_z is the projection of the produced object angular momentum on the beam axis) are dominantly produced; this simple fact leads to many interesting and non–trivial implications for CEP processes, which are not seen in the inclusive case.

Within this approach, the perturbative CEP amplitude is written as [2,5]

$$T = \pi^2 \int \frac{d^2\mathbf{Q}_\perp \mathscr{M}}{\mathbf{Q}_\perp^2 (\mathbf{Q}_\perp - \mathbf{p}_{1\perp})^2 (\mathbf{Q}_\perp + \mathbf{p}_{2\perp})^2} f_g(x_1, x_1', Q_1^2, \mu^2; t_1) f_g(x_2, x_2', Q_2^2, \mu^2; t_2) \,, \qquad (5.1)$$

where $\mathscr{M}$ is the color-averaged, normalised sub-amplitude for the $gg \to X$ process:

$$\mathscr{M} \equiv \frac{2}{M_X^2} \frac{1}{N_C^2 - 1} \sum_{a,b} \delta^{ab} q_{1_\perp}^\mu q_{2_\perp}^\nu V_{\mu\nu}^{ab} \,. \tag{5.2}$$

Here a and b are color indices, M_X is the central object mass, $V_{\mu\nu}^{ab}$ is the $gg \to X$ vertex, $q_{i_\perp}$ and x_i are the transverse momenta and momentum fractions of the incoming gluons, respectively, and x_i' are the momentum fractions of the screening gluon, which does not couple to the hard subprocess. The f_g's in (5.1) are the skewed unintegrated gluon densities of the proton. These correspond to the distribution of gluons in transverse momentum $Q_\perp$, which are evolved in energy up to the hard scale $\mu \sim M_X$, such that they are accompanied by no additional radiation, as is essential for exclusive production. In the $x' \sim Q_\perp^2/s \ll x \sim M_X/\sqrt{s}$ region relevant to CEP, these can be expressed in terms of the conventional gluon PDFs, and a 'Sudakov factor', T_g, which resums the logarithmically enhanced higher–order corrections, and corresponds to the (Poissonian) probability of no extra parton emission from each fusing gluon. This factor is essential in ensuring a perturbatively stable result [2, 9].

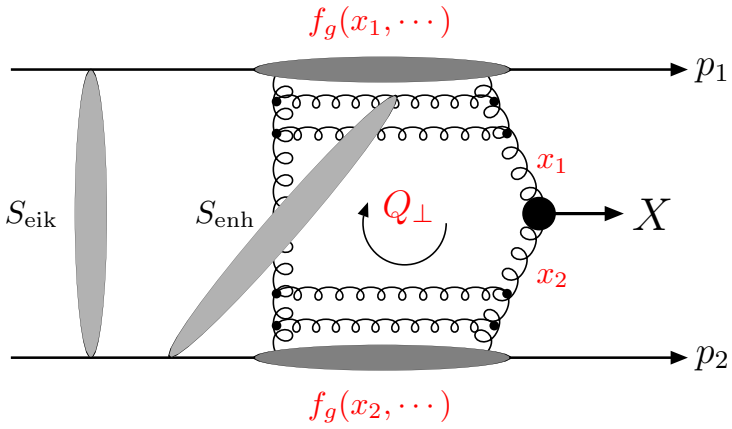

Fig. 5.1: The perturbative mechanism for the exclusive process $pp \to p + X + p$, with the eikonal and enhanced survival factors shown symbolically.

In addition to this amplitude (5.1) for the exclusive production of an object X in a short–distance interaction, it is also necessary to include the probability that extra particles are not produced in additional soft proton–proton interactions ('rescatterings'), independent of the hard process, i.e. as a result of underlying event activity. This probability is encoded in the so–called 'eikonal survival factor' [14–18], $S_{\rm elk}^2$: while this is a soft quantity which cannot be calculated using pQCD, it may be extracted from hadronic data. Although there is some uncertainty in the precise level of suppression (in particular in its dependence on the c.m.s. energy $\sqrt{s}$), it is found to be a sizeable effect, reducing the CEP cross section by about two orders of magnitude. It is in addition expected that there may be some suppression due to rescatterings of the protons with the intermediate partons in the hard process. This is encoded in the so–called 'enhanced' survival factor [15, 18, 19]: while this is expected to have a much less significant effect than the eikonal survival factor, the precise level of suppression remains uncertain and may be clarified by future CEP measurements.

It is in principle possible to consider the CEP of any C–even particle which couples to gluons within this mechanism, and an important advantage of these reactions is that they provide an especially clean environment in which to investigate in detail the properties of a wide range of

SM and BSM states [2, 5, 7, 20, 21]. In addition, as described above, the theoretical framework is sensitive to both hard and, through the survival factors, soft aspects of QCD, as well as depending sensitively on the gluon PDF in the low x and Q^2 region, where it is currently quite poorly determined from global fits. This process therefore provides a very promising framework within which to study various aspects of QCD, both perturbative and non–perturbative, as well as new physics at the LHC.

Finally, we note that in the past other approaches have been taken to modelling the QCD–mediated CEP process discussed above. Most notably, the 'Saclay' model [22], an implementation of the calculation of [23], did not include a Sudakov factor in the amplitude (5.1) but rather the low–$Q_\perp$ infrared–unsafe region was suppressed by the introduction of 'non–perturbative' gluon propagators, the parameters of which were fitted to total and elastic cross section data (see e.g. [24] for further discussion). This favours much lower average gluon $Q_\perp$ than in the Durham approach so that, it turns out, the $J_z = 0$ selection rule discussed above would not necessarily hold, and in addition leads to a much gentler fall in the cross section with M_X, as well as generally much larger predicted cross sections. These latter predictions were found to be in strong disagreement with the CDF measurement of exclusive jet production [25] (which was on the other hand in good agreement with the Durham model predictions); moreover, from a theoretical point of view the omission of the Sudakov factor, a crucial element in the perturbative calculation, lacks clear justification. For these reasons, such models are generally less used in current phenomenological work.

5.3.2 Forward proton tagging: phenomenological insight and advantages

In an exclusive reaction any transverse momentum $p_\perp = |\mathbf{p}_\perp|$ of the outgoing protons is transferred to the central object X. For this reason a measurement of the distributions with respect to such variables as the magnitude of the proton $p_\perp$ and the angle ϕ between the proton $p_\perp$ vectors (which is only possible with proton tagging detectors) is sensitive to the structure of the $gg \to X$ vertex, and the spin–parity of the produced object. Moreover, it is found that additional soft interactions, which generate the soft survival factor $S^2_{\rm eik}$, can have a very strong and model–dependent effect on these distributions.

In general, we can write down an expression for the CEP cross section at X rapidity y_X as [21]

$$\frac{\mathrm{d}\sigma}{\mathrm{d}y_X} = \langle S^2_{\rm enh} \rangle \int \mathrm{d}^2\mathbf{p}_{1_\perp} \mathrm{d}^2\mathbf{p}_{2_\perp} \frac{|T(\mathbf{p}_{1_\perp}, \mathbf{p}_{2_\perp})|^2}{16^2\pi^5} S^2_{\rm eik}(\mathbf{p}_{1_\perp}, \mathbf{p}_{2_\perp}) \,, \tag{5.3}$$

where T is given by (5.1), and $\langle S^2_{\rm enh} \rangle$ is the averaged 'enhanced' survival factor discussed above, which is expected to depend very weakly on the proton $p_\perp$, and is therefore not relevant to the current considerations [15, 19]. As mentioned above, the $\mathbf{p}_\perp$ dependence of the hard amplitude T is strongly sensitive to the quantum numbers of the produced state. For example, for small $p_\perp$ it can be shown that we expect the squared amplitudes for the CEP of an object of spin–parity J^P to behave as [13]

$$|T_{0^+}|^2 \sim \text{const.} \,, \tag{5.4}$$

$$|T_{1^+}|^2 \sim (\mathbf{p}_{1_\perp} - \mathbf{p}_{2_\perp})^2 \,, \tag{5.5}$$

$$|T_{0^-}|^2 \sim \mathbf{p}^2_{1_\perp} \mathbf{p}^2_{2_\perp} \sin^2\phi \,. \tag{5.6}$$

Such a behaviour is seen in Fig. 5.2, which shows distributions with respect to the azimuthal angle ϕ at $\sqrt{s} = 14$ TeV, for the case of χ_c and η_c CEP within the Durham approach (very similar distributions are expected for the higher mass χ_b, η_b): this effect is driven by the different

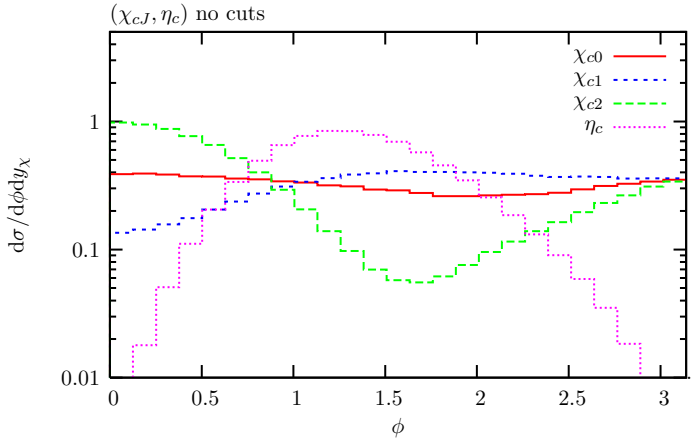

Fig. 5.2: Distribution [26] (in arbitrary units) within the perturbative framework of the difference in azimuthal angle of the outgoing protons for the CEP of different J^P $c\bar{c}$ states at $\sqrt{s} = 14$ TeV and rapidity $y_X = 0$.

Lorentz forms of the $gg \to X$ couplings, depending on the J^P of the state X. A measurement of this distribution is therefore directly sensitive to the nature of the produced state, as well as more generally the structure of the production subprocess. It is moreover the case that the $J^{PC} = 0^{++}$ selection rule discussed in Section 5.3 is exact in the limit of exactly forward protons (i.e. $p_\perp = 0$), and becomes weaker as the proton $p_\perp$ is increased. Within the Durham approach, it is found that

$$\frac{|T(|J_z| = 2)|^2}{|T(J_z = 0)|^2} \sim \frac{\langle p_\perp^2 \rangle^2}{\langle Q_\perp^2 \rangle^2}\,, \tag{5.7}$$

where $\langle p_\perp^2 \rangle$ is the average squared proton transverse momentum, and $\langle Q_\perp^2 \rangle \sim$ a few GeV^2 is the average squared transverse momentum going round the gluon loop. Thus by selecting events with higher or lower proton $p_\perp$, the relative fraction of non–$J_z^P = 0^+$ states can be enhanced or suppressed, respectively.

In addition, it can be seen from (5.3) that the eikonal survival factor depends on the proton $\mathbf{p}_\perp$ vectors. Physically, this is to be expected, as the survival factor cannot be a simple multiplicative constant, but will rather depend on the impact parameter of the colliding protons. Loosely speaking, as the protons become more separated in impact parameter, we should expect there to be less additional particle production, and so for the survival factor to be larger (consequently, the average survival factor is much larger in the case of photon–mediated processes, where larger impact parameters are favoured, when compared to QCD processes). As the transverse momenta $\mathbf{p}_{i_\perp}$ of the scattered protons are nothing other than the Fourier conjugates of the proton impact parameters, $\mathbf{b}_{it}$, this leads to the $\mathbf{p}_{i_\perp}$ dependence seen in (5.3).

In Fig. 5.3 the ϕ distribution at the LHC ($\sqrt{s} = 13$ TeV) for $\pi^+\pi^-$ CEP is shown, with four different models for the eikonal survival factor, as described in [27]. A very distinct 'diffractive' dip structure is observed, with the distributions reaching a minimum at a particular value of ϕ. This destructive interference is completely driven by the effect of these additional 'screening' corrections which generate the soft survival factor. In particular, to account for soft survival effects the CEP amplitude including rescattering effects, T^{res}, should be calculated, by integrating over the transverse momentum $\mathbf{k}_\perp$ carried round the Pomeron loop (represented by the grey oval labeled 'S^2_{eik}' in Fig 5.1). The amplitude including rescattering corrections is given in the

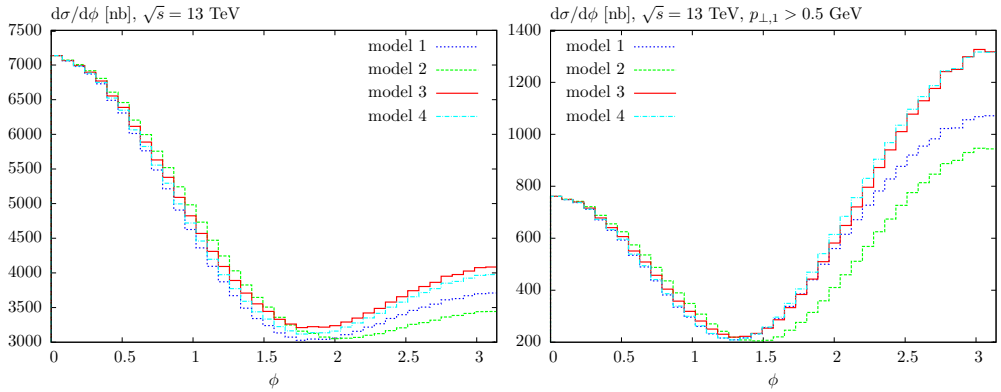

Fig. 5.3: Differential cross section $\mathrm{d}\sigma/\mathrm{d}\phi$ for the process $pp \to p + \pi^+\pi^- + p$, where ϕ is the azimuthal angle between the outgoing proton $p_\perp$ vectors, at the $\sqrt{s} = 13$ TeV LHC, for the four soft models of [27]. In the left plot the proton $p_\perp$ is unconstrained, while in the right plot an additional cut of $p_\perp > 0.5$ GeV is placed on one proton. In both cases, a cut of $|y_\pi| < 2$ on the centrally produced pions is placed. For display purposes the predictions are normalized in the first ϕ bin, to the model 1 predictions. Plots from [28] are made using `Dime` MC [30].

simplest approach by

$$\mathscr{M}^{\mathrm{res}}(s, \mathbf{p}_{1_\perp}, \mathbf{p}_{2_\perp}) = \frac{i}{s} \int \frac{\mathrm{d}^2\mathbf{k}_\perp}{8\pi^2}\, \mathscr{M}_{\mathrm{el}}(s, \mathbf{k}_\perp^2)\, \mathscr{M}(s, \mathbf{p'}_{1_\perp}, \mathbf{p'}_{2_\perp})\,, \tag{5.8}$$

where $\mathbf{p'}_{1_\perp} = (\mathbf{p}_{1_\perp} - \mathbf{k}_\perp)$ and $\mathbf{p'}_{2_\perp} = (\mathbf{p}_{2_\perp} + \mathbf{k}_\perp)$, while $\mathscr{M}^{\mathrm{el}}(s, \mathbf{k}_\perp^2)$ is the elastic pp scattering amplitude in transverse momentum space, see for example [2, 29] for more details. The 'bare' amplitude excluding rescattering effects must be added to this to give the full result: it is the interference between this screened and the unscreened amplitude which generates these clear diffractive dips seen in Fig. 5.3. For a particular value of ϕ this interference is strongest, resulting in the observed minimum in the ϕ distribution. As the form of the screened amplitude depends on the particular soft model, we may expect the position and depth of this minimum to be sensitive to this, as well as depending on the particular cuts imposed on the proton $p_\perp$. In fact, it appears from Figs. 5.3 that the position of the minimum does not depend too strongly on the choice of model, but nonetheless the overall shape of the ϕ distribution does show some variation. Thus a measurement of distributions with respect to ϕ (or the magnitude of the proton $p_\perp$, where similar dipping structure may be seen) could help differentiate between the available models of soft physics which are needed to calculate the survival factors. Although the case of $\pi^+\pi^-$ CEP is considered here, such diffractive dip structure is expected to be observable in any CEP process, such as exclusive jet or quarkonium production, see e.g. [26].

5.3.3 Conventional quarkonium production

Motivation and theory

The exclusive production of heavy quarkonium [10, 21, 31–37] provides a valuable test of the QCD physics of bound states, with the predictions for the range of available J^{PC} states exhibiting distinct features in the exclusive mode. The direct production channel can be easily selected, that is without feed–down contributions, and only the 'core' color–singlet component of the state is probed, due to the requirement that no additional hadronic particles are present.

Exclusive χ_{cJ} production has been observed by both CDF at the Tevatron [45] and LHCb [39]

at the LHC (see the following section for further details), and quite high production cross sections are expected: the Durham framework predicts total cross sections for the χ_{c0}, χ_{c1} and χ_{c2} at $\sqrt{s}$ = 13 TeV of $\sim$ 340 nb, $\sim$ 8.0 nb and $\sim$ 4.4 nb, respectively [21], with an uncertainty of about a factor 2–3. It is clear from these results that the cross sections for the three different spin states are predicted to follow a strong hierarchy: due to the $J^{PC} = 0^{++}$ selection rule described above for the χ_{c2} (within the non–relativistic approximation), and due to the Landau–Yang theorem [40,41] for the χ_{c1}, the cross sections for these higher spin states are expected to be at the level of a few percent of the χ_{c0} cross section. Such a suppression is not expected or seen in the inclusive mode [42], where all three spin states are observed to give comparable contributions before branching. In the $\chi_c \to J/\psi\gamma$ decay channel, for which the $\chi_{c(1,2)}$ branching ratios are much higher, we should expect to see non–negligible contributions from all three states. Crucially, in the case of the LHCb data, it was possible to distinguish between the three different spin states, with results that were found qualitatively to support this expectation.

However, there remain some open questions related to the χ_{c2}, for which an apparent enhancement relative to theory expectations is seen by LHCb. As discussed in more detail in [2], this may be due to proton dissociation not seen in the LHCb detector acceptance; while this is quite poorly understood theoretically, it is expected to preferentially enhance the higher spin states, in particular the χ_{c2}. Alternatively, such an enhancement may be due to additional 'non–perturbative' corrections in the theory calculation, as the mass scale of the χ_c may be too low to allow a purely perturbative approach, which assumes that $M_X \sim M_\chi \gg Q_\perp$, as well as to relativistic corrections to the χ_c wave function. This issue can only be fully clarified with further higher statistics data from the LHC, with for example the HERSCHEL system (see Chapter 9), not used in any existing measurements, being a particularly effectively way to reduce the effect of proton dissociation at LHCb. Measurements with the CMS-TOTEM and ALFA in runs at high β^*, for which the proton tagging detectors can effectively eliminate the effect of proton dissociation, would also be very useful. Such data would give a much cleaner comparison with theory, and could be sensitive to any transition to a non–perturbative regime for these lower χ_c masses, where a Regge theory based approach can be taken.

An observation of the higher mass bottomonium χ_b states, for which the mass scale is safely in the perturbative regime, would provide a more stringent test of the theory. The predicted χ_{b0} cross is $\sim$ 100 pb at $\sqrt{s} = 14$ TeV [21], and a similar hierarchy in spin states to the χ_c case is predicted, but with a negligible χ_{b1} cross section due to the higher mass. It is also worth noting that the spin assignments of the P–wave χ_{bJ} states still need experimental confirmation [43], and so this is an issue which the spin–parity selecting properties of CEP could shed light on.

Other observables of interest include the χ_c states via two body ($\pi\pi$, KK...) decays, for which the exclusive continuum background is expected to be manageable [44,45]. The CEP of the odd–parity $\eta_{c,b}$ states, for which the cross sections are predicted to be similarly suppressed to the higher spin $\chi_{c,b}$ states, would also represent a further potential observable. As discussed in Section 5.3.2, the distributions of the outgoing protons are expected to be highly sensitive to the spin–parity of the produced quarkonium state, as well as to the soft survival factors. Finally, exclusive photoproduction of C–odd quarkonia (J/ψ, $\psi(2S)$, Υ...) is of much interest; this is discussed in more detail in Section 5.4.

Experimental results and outlook

A favourable decay mode of the χ_c meson is to $J/\psi\gamma$, with the only significant experimental background being contamination from $\psi(2S) \to J/\psi\pi^0\pi^0$ where only one photon is identified

from the subsequent pion decays.

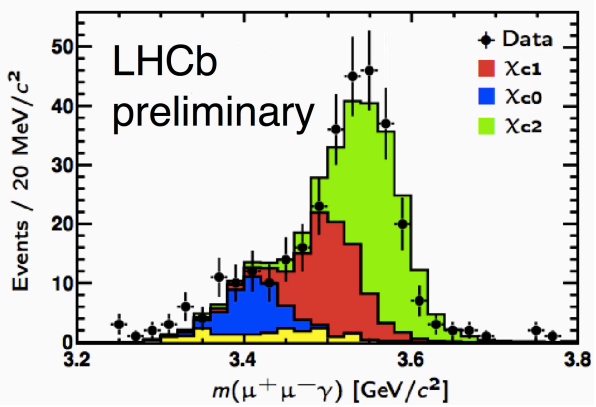

Fig. 5.4: Invariant mass of the di-muon plus photon system in events having no other activity inside LHCb.

LHCb has made preliminary measurements [39] of the production of χ_c mesons with 37 pb^{-1} of data. The selection of events proceeds as for the J/ψ selection in Sec. 5.4.4 but now one (rather than no) photon candidate is required. The invariant mass of the di-muon plus photon system is shown in Fig. 5.4 fitted to expectations from the SuperChic simulation [31, 46] for $\chi_{c0}, \chi_{c1}.\chi_{c2}$ signal contributions and the $\psi(2S)$ background. The CDF collaboration made the first observation [45] of CEP of χ_c mesons but because of the limited mass resolution, assumed it all to consist of χ_{c0} mesons. The mass resolution of LHCb is sufficiently good to distinguish the three states. In this decay mode, the contribution from χ_{c2} dominates although much of that is due to the higher branching fraction for this state to decay to $J/\psi\gamma$. Unfortunately, the resolution is not good enough to separate the three states completely and so the fraction of the sample that is exclusively produced is determined for the whole sample and is estimated to be 0.39 ± 0.13 using the p_T of the reconstructed meson. The cross sections times branching fractions are measured to be $9 \pm 5, 16 \pm 9, 28 \pm 12$ pb for $\chi_{c0}, \chi_{c1}, \chi_{c2}$, respectively, slightly higher but in reasonable agreement with the theoretical predictions of 4, 10, 3 pb for purely exclusive production. Only the relative cross sections for χ_{c2} to χ_{c0} of 3 ± 1 appears to be somewhat higher in the data than the theory expectation that they are roughly equal. This is consistent with the CDF measurement of $\pi^+\pi^-$ CEP [47], where a limit on the $\chi_{c0} \to \pi^+\pi^-$ cross section is set which indicates that less than $\sim 50\%$ of the previously observed $\chi_c \to J/\psi\gamma$ events at the Tevatron [45] are due to the χ_{c0}. As discussed above, one possible reason for this discrepancy is that the fraction of elastic exclusive events in the sample differs for each of the three resonances. With greater statistics, a more sophisticated fit can be performed in order to estimate the fraction of exclusive events separately for each χ_c state.

Further discrimination of the χ_c states is possible by considering different decay modes. Of particular interest are the decays to two pions or two kaons, which are not possible for χ_{c1} and are about four times higher for χ_{c0} than for χ_{c2}. In addition, the mass resolution in this channel is about a factor of three better than in the $\mu\mu\gamma$ channel. Making use of their ability to trigger on hadronic objects with low transverse momentum during the $\sqrt{s}$ =7 and 8 TeV running, LHCb has collected a large sample of low-multiplicity data in single proton-proton interactions (without pile-up) corresponding to an integrated luminosity of about 600 pb^{-1}. Consequently, the observation of χ_c states in the $\pi\pi$ and KK modes ought to be possible, so long as the backgrounds from the double pomeron exchange production of pairs of pseudo-scalar mesons is not too large.

In addition to this rapidity gap based analysis there are also possibilities for future LHC measurements with tagged forward protons. With CMS-TOTEM and ALFA, the different χ_c states can be easily separated in charged-particle-only final states, and the proton dissociation background can be eliminated using proton tagging. A preliminary analysis has been performed on the data of the common CMS-TOTEM $\beta^* = 90$ m run at $\sqrt{s} = 8$ TeV in July 2012. The available data set contains a few χ_c exclusive candidates, consistent with the CDF and LHCb measurements. In the case that the χ_c decays to two- or three-$\pi^+\pi^-$ pairs or to $K^+K^-\pi^+\pi^-$, the tracker dE/dx can be used to confirm the pion or kaon hypothesis. This combined with higher branching ratios compared to the $\pi^+\pi^-$ and K^+K^- final states, where no particle identification is possible, makes these three decay modes the most promising in terms of signal-to-background ratio. In 5 pb^{-1} of integrated luminosity, more than 1000 χ_{c0} candidates are expected in each of the decay modes ($2(\pi^+\pi^-)$, $3(\pi^+\pi^-)$, $K^+K^-\pi^+\pi^-$). This will allow a good determination of the cross section$\times$branching ratio as well as a detailed study of the azimuthal angular difference $\Delta\phi$ of the outgoing protons for each decay mode separately. According to the predictions of [21], 5 pb^{-1} does not seem be sufficient to be able to study exclusive χ_{c1} and χ_{c2} production. However, given the possible discrepancy regarding exclusive χ_{c2} production between the LHCb measurement discussed above, it might well be that the exclusive χ_{c2} production cross section at $\sqrt{s} = 13$ TeV is almost an order of magnitude higher than predicted and hence feasible to study even with an integrated $\beta^* = 90$ m luminosity of ~ 5 pb^{-1}. Such an observation (or the absence of it) would provide valuable information about the model of [2], and its application to $c\bar{c}$ systems.

5.3.4 'Exotic' quarkonium production

Motivation and theory

In addition to conventional quarkonia states, there are possibilities for the observation and study of 'exotic' charmonium–like states, which have been discovered over the past 10 years [48]. In some cases, the J^{PC} quantum numbers of these states have not been determined experimentally and often a range of interpretations are available: a $D^0\overline{D}^{*0}$ molecule, tetraquarks, $c\bar{c}g$ hybrids, the conventional $c\bar{c}$ charmonium assignment, and more generally a mixture of these different possibilities. Considering the CEP of such objects, then the effect of the $J^P_z = 0^+$ selection rule, as well as a measurement of the distribution of the outgoing proton momenta, may help to fix the quantum numbers of the centrally produced system.

One possibility is the CEP of the $Y(3940)$, in particular via the $J/\psi\omega$ channel, which could help to resolve current uncertainties [49,50] in the interpretation of this state. Another particularly topical example is the $X(3872)$, for which the quantum numbers are determined [51] to be $J^{PC} = 1^{++}$, but a concrete interpretation remains elusive. In the case of a dominantly $D^0\overline{D}^{*0}$ interpretation, the hadroproduction of such a state with the size of cross section observed [52] in the $X(3872)$ case, if possible at all, should in general take place in an environment where additional particles are emitted [53,54], so that the initially produced short–distance $c\bar{c}$ pair can form the loosely–bound $D^0\overline{D}^{*0}$ state. The observation of the $X(3872)$ in the exclusive mode, via for example the $X(3872) \to J/\psi\pi^+\pi^-$ decay channel, where any additional hadronic activity is vetoed on, would therefore strongly disfavor such a dominantly molecular $D^0\overline{D}^{*0}$ interpretation. The $X(3872)$ may instead be dominantly a conventional $\chi_{c1}(2^3P_1)$ state, in which case the cross section is expected to be of a comparable size to the ground–state χ_{c1}, which has already been observed by LHCb. If, as may be more realistic [55], it is a mixture of a $\chi_{c1}(2P)$ and a molecular $D^0\overline{D}^{*0}$ state, then the size of this ratio will also be driven by the probability weight of the purely $c\bar{c}$ component; if this is small, that is the molecular component is dominant, then

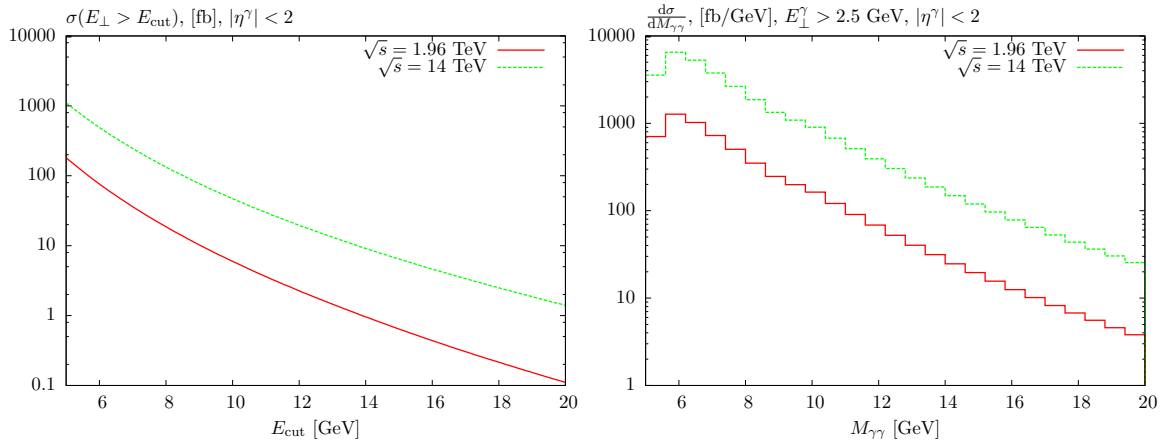

Fig. 5.5: Cross sections for $\gamma\gamma$ CEP at $\sqrt{s} = 1.96$ and 14 TeV [2], calculated using MSTW08LO PDFs [26] as a function of the cut on the photon transverse energy $E_\perp > E_{\rm cut}$ and invariant mass distribution $\mathrm{d}\sigma/\mathrm{d}M_{\gamma\gamma}$ for $E_\perp > 2.5$ GeV. In both cases the photon pseudorapidity is required to lie within $|\eta^\gamma| < 2$. Predictions made using the `SuperChic` [46] MC.

the $X(3872)$ cross section will be suppressed relative to the $\chi_{c1}(1P)$.

Experimental results and outlook

LHCb is well positioned to observe exotic states with J/ψ mesons in the final state. About 600 pb^{-1} of data without pile-up was taken in Run–I, and 1.5 fb^{-1} is expected in Run–II. High efficiency triggering and reconstruction of J/ψ mesons has been demonstrated [47], and the reconstruction of other final state particles, including π^0, can be performed provided the transverse momentum of the final state charged and neutral objects is greater than about 100 MeV. This measurement will be complementary to the ones performed at low diffractive masses by the CMS-TOTEM and ALFA experiments.

5.3.5 Photon pair production

Motivation and theory

The CEP of a pair of photons ($\gamma\gamma$) produced via an intermediate quark loop represents an experimentally clean test of the perturbative CEP mechanism and is less sensitive to some of the theoretical uncertainties which are present, for example, in the case of χ_c CEP, due to the higher invariant masses, $M_X = M_{\gamma\gamma}$, which are accessible here. A measurement of the differential cross section with respect to $M_{\gamma\gamma}$ is a particularly useful observable, sensitive to the effect of the Sudakov factor, as well as the gluon PDF and the theoretically challenging 'enhanced' survival factor $S^2_{\rm enh}$.

In Fig. 5.5 some representative predictions for $\gamma\gamma$ CEP at the LHC and Tevatron are shown. Already exclusive $\gamma\gamma$ data have been taken: the 2011 CDF observation [58] of 43 $\gamma\gamma$ events in $|\eta(\gamma)| < 1.0$ with no other particles detected in $-7.4 < \eta < 7.4$ was found to be in reasonable agreement with the Durham prediction. As can be seen from Fig. 5.5 the predicted cross sections are somewhat larger at the LHC, due to the larger gluon density at the lower x values probed. Further tests at the higher $\sqrt{s}$ of the LHC would be very useful: by considering for example the ratio of cross sections at different $\sqrt{s}$ values various theoretical uncertainties decrease, and the energy dependence of the cross section, driven primarily by the survival factors and the x dependence of the gluon density, are probed.

Experimental results and outlook

As discussed above, exclusive $\gamma\gamma$ data has been taken by the CDF collaboration at the Tevatron. More recently, at the LHC, CMS [59] has presented a search for exclusive $\gamma\gamma$ events using 36 pb^{-1} of data collected at $\sqrt{s} = 7$ TeV. The trigger and analysis methods were identical to the CMS $\gamma\gamma \to ee$ measurement, apart from the selection of two photons instead of two electrons. While no candidate diphoton events were observed, the corresponding limits were close to the theoretical predictions, providing a strong motivation for further searches at the LHC in the future. LHCb will be able to measure $\gamma\gamma$ CEP for $E(\gamma) > 2$ GeV with about 1.5 fb^{-1} of Run–II data, using a new di-photon trigger that builds on the experience of the low multiplicity triggers used in Run–I.

Such a measurement could also be performed during Run–II during dedicated high β^* runs by ALFA or CMS-TOTEM [80]. Due to the low instantaneous luminosity of those special runs it should be possible to implement a dedicated di-photon trigger with p_T thresholds as low as $p_{T1,2} > 5$ GeV, in which case we can expect $\sim$ 10s of events, for a typical integrated luminosity of 0.1 fb^{-1}.

5.3.6 Light meson pair production

Motivation and theory

Another interesting CEP process is the production of light meson pairs [61, 62] ($X = \pi\pi, KK, \rho\rho, \eta(')\eta(')$). At sufficiently high meson transverse momentum $k_\perp$, a perturbative approach combining the Durham model with the 'hard exclusive' formalism [63, 64] to evaluate the meson production subprocess may be taken. The basic idea of the latter approach is that the hadron–level amplitude can be written as a convolution of a (perturbatively calculable) parton–level amplitude, T, and a 'distribution amplitude' ϕ, which contains all the (non–perturbative) information about the binding of the partons in the meson. It has been shown that within this approach the distinct features of the relevant parton–level helicity amplitudes $gg \to q\bar{q}q\bar{q}$, $q\bar{q}gg$, $gggg$ lead to some highly non–trivial predictions.

In particular, in the case of flavour non–singlet mesons ($\pi\pi, KK$...), it is found that there is a strong suppression in the CEP cross section, due to the vanishing of the parton–level production amplitudes for $J_z = 0$ incoming gluons and the $J_z = 0$ CEP selection rule [61]. In the case of flavour–singlet mesons ($\eta(')\eta(')$...) a different configuration of the outgoing partons can enter, with the effect that the $J_z = 0$ amplitudes do not vanish, and so the corresponding CEP cross sections are expected to be much larger. The flavour–singlet cross sections may even be sensitive to the size of the gluonic component of the η' (and, through mixing, η), via the valence gg contributions to the $gg \to \eta(')\eta(')$ amplitudes [65]. Currently the long–standing issue concerning the extraction of the gluon content of the η' (and η) remains uncertain, in particular due to non–trivial theory assumptions and approximations that must be made, as well as the current experimental uncertainties and limitations [66, 67]. It has in particular been shown that even a small gluonic component could lead to a sizeable increase in the predicted $\eta(')\eta(')$ CEP cross sections [65]. A representative invariant mass distribution, for typical central LHC cuts (the results are similar for forward production, as in the case of LHCb), are shown in Fig. 5.6, and the expected enhancement in the $\eta'\eta'$ cross section is clear. Also shown are predictions for the vector $\rho\rho$ case.

As the meson transverse momentum $k_\perp$ and/or meson pair invariant mass decreases, we will expect to enter a regime where a Regge–theory inspired approach is more applicable [28, 68]. This mechanism of production is shown in Fig. 5.7 for the case of non-resonant $\pi^+\pi^-$ production. In this case, it has been shown that for example $\pi^+\pi^-$ CEP can serve as a probe

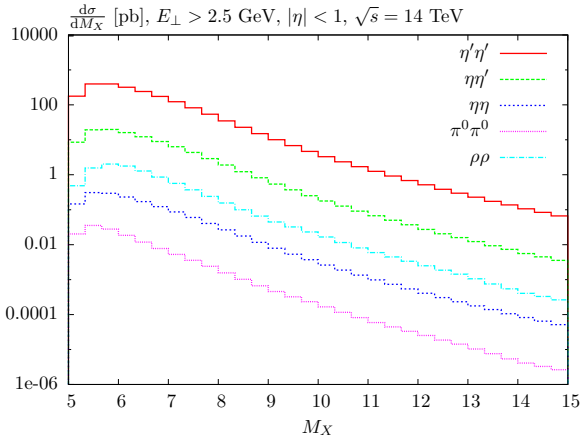

Fig. 5.6: Differential cross section $\mathrm{d}\sigma/\mathrm{d}M_X$ for the CEP of meson pairs, for meson transverse energy $E_\perp > 2.5$ GeV and pseudorapidity $|\eta| < 1$. Predictions made using `SuperChic` MC [46].

of the tools of Regge theory, and of the uncertain question of the transition to the perturbative regime discussed above. In addition, the observation of light meson pairs with tagged protons can serve as a detailed probe of the models of soft physics which are used to calculate the soft survival factors (see Section 5.3.2).

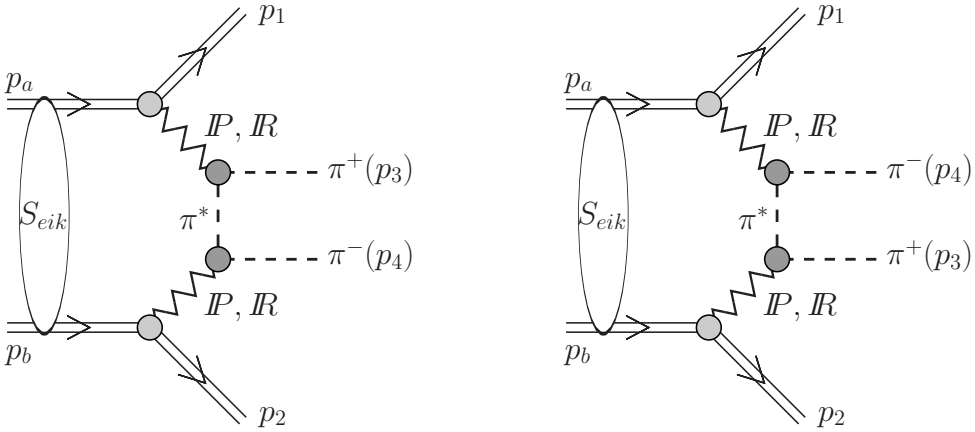

Fig. 5.7: The 'non–perturbative' mechanism for the CEP of $\pi^+\pi^-$ pairs.

Experimental results and outlook

An important possible background to the $\gamma\gamma$ CEP process discussed in Section 5.3.5 is the exclusive production of a pair of π^0 mesons, with one photon from each π^0 decay undetected or the two photons merging. At first sight it would appear that the cross section for this purely QCD process may be much larger than the $\gamma\gamma$ cross section and so would constitute an appreciable background. In the CDF measurement [58] of $\gamma\gamma$ CEP, despite previous hints of a non–negligible $\pi^0\pi^0$ contribution in earlier data [69], of the 43 candidate $\gamma\gamma$ events, the contamination caused by $\pi^0\pi^0$ CEP was observed to be very small (< 15 events, corresponding to a ratio $N(\pi^0\pi^0)/N(\gamma\gamma) < 0.35$, at 95% CL). This supports the prediction discussed in the previous section, namely that there is a strong dynamical suppression in the production cross section for pairs of flavour–non–singlet mesons such as $\pi^0\pi^0$; without this dynamical suppression the

expected cross section would be ~ 2 orders of magnitude higher. Nonetheless, this prediction, and in particular the expected hierarchy in production cross sections between flavour–non–singlet and singlet meson pairs has yet to be confirmed or disproved experimentally, by a direct observation safely in the perturbative region; this would represent a very interesting observation to be made at the LHC.

On the other hand, in the region of lower system invariant masses and (more significantly) meson transverse momenta, where the tools of Regge theory should be applied, a variety of data exist at RHIC, the Tevatron and LHC. CDF data on $\pi^+\pi^-$ production at $\sqrt{s} = 900$ and 1960 GeV have been presented in [47], and a preliminary measurement of $\pi^+\pi^-$ and K^+K^- production has been performed by CMS [70].

ALICE has taken data on central diffractive pion and kaon pair production [71]. During Run–I, candidate CEP events were selected offline from data taken with a minimum-bias trigger (at least one charged particle anywhere in 8 units of pseudorapidity) by requiring an activity in the central barrel ($|\eta| < 0.9$) surrounded with large gaps (up to $|\eta| \simeq 4.5$) on both sides. While the statistics were quite low, qualitatively quite pronounced resonant structures were observed for masses below 2 GeV in both the $\pi\pi$ and KK channels. Some preliminary results can be found in [72]. In addition, in the four–track event sample an indication of interesting features is observed, relating to the fragmentation of produced system into the 4π and $2\pi 2K$ final states.

LHCb has triggered on low multiplicity $\pi\pi$ and KK systems when the transverse momentum of the hadrons was greater than about 500 MeV. In Run–II, the trigger threshold will be lowered, allowing an investigation of the region around the $f_0(980)$. Studies are ongoing on $\rho\rho$ and $\eta(')\eta(')$ states using Run–I data, and these will allow dedicated triggers to be installed during Run–II in order to collect high statistics samples.

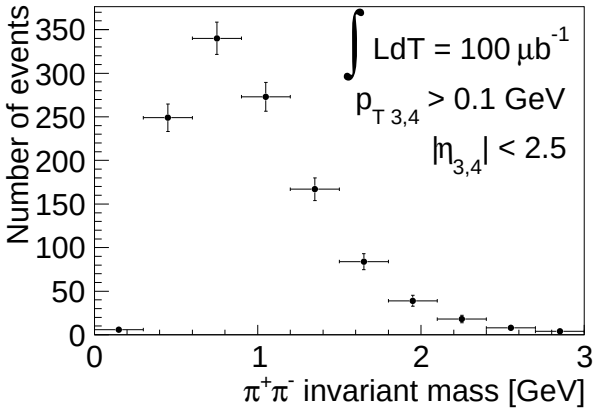

Fig. 5.8: Simulated measurement of the $\pi^+\pi^-$ invariant mass distribution. The pions are measured with the ATLAS tracking detector and protons with the ALFA stations. An integrated luminosity of 100 μb^{-1} is assumed and only the statistical errors are plotted.

In addition to these measurements, selected with rapidity gap based techniques, the possibility of observing exclusive meson pair production with tagged protons is of much interest and has been the subject of detailed studies. The STAR collaboration at RHIC [73] have reported a preliminary measurement of $\pi^+\pi^-$ CEP with tagged protons, in broad agreement with Regge expectations. At the LHC, in [74] the case of exclusive $\pi^+\pi^-$ is considered within the context of the ATLAS + ALFA detectors (similar possibilities exist with the CMS + TOTEM detectors). While a value of $\sqrt{s} = 7$ TeV is taken in this study, these results give a very good indication of the measurement possibilities at the higher $\sqrt{s}$ values relevant to Run-II. Fig. 5.8, taken from [74], presents a possible measurement of the $\pi^+\pi^-$ invariant mass that could be

performed with 100 μb^{-1} of integrated luminosity (30 hours of data acquisition time assuming the luminosity value of 10^{27} $cm^{-2}s^{-1}$) for the experimental conditions assumed above. This corresponds to the non–resonant model depicted in Fig. 5.7: there will be a range of resonance (ρ_0, f_0, f_2) structure in addition to this continuum contribution.

5.3.7 Production of low mass resonances and glueballs

Motivation and theory

The CEP process effectively turns the LHC into a gluon-gluon collider and provides an excellent opportunity to study gluon systems with a longitudinal momentum fraction $x \sim 10^{-4}$ and, in particular, to search for glueball candidates[1]. Glueballs are predicted by QCD as gluon bound states with no valence quark content. The absence of valence quarks, in combination with the $J_z^{PC} = 0^{++}$ selection rule [13], makes CEP reactions an ideal place to search for them. QCD lattice calculations foresee a $J^{PC} = 0^{++}$ ground state and a 2^{++} state followed by a spectrum of excited states [75,76]. The $f_0(1500)$ or the $f_0(1710)$ are generally regarded as potential glueball 0^{++} states since one of them is in excess to the meson $SU(3)$ multiplet and both are compatible with a glueball in terms of mass, spin, parity, and decay channels (having e.g. a suppressed $\gamma\gamma$ mode). Recent unified lattice calculations [76, 77] predict the 0^{++} glueball at $\sim$ 1700 MeV within $\sim$ 100 MeV overall uncertainty (statistical and systematic), thus favouring the $f_0(1710)$ as a glueball candidate. Formerly proposed meson–glueball mixings [78–80] relied on an incorrect mass hierarchy ($u\bar{u}$, $d\bar{d}$, gg, $s\bar{s}$) and have been made obsolete by further calculations [81,82] based on the correct ($u\bar{u}$, $d\bar{d}$, $s\bar{s}$, gg) mass hierarchy giving a $\gtrsim 95\,\%$ glueball purity at $\sim$ 1700 MeV. Measuring the CEP of a resonance as well as its decay branching ratios [75, 83] could help to establish its glueball nature.

The WA102 experiment [78–80] reported that the $f_0(1710)$ branching ratio into K^+K^- exceeded its branching ratio to $\pi^+\pi^-$, contrary to the case of the $f_0(1500)$, disfavouring a glueball interpretation of the $f_0(1710)$. This measurement leads to the conclusion that the coupling of the $f_0(1710)$ to s–quarks must be larger than the u,d-quark couplings, a result which is not expected for a glueball state (although in [84] a possible coupling to quark mass for the decays of pure gluonic states is noted). Moreover, the predicted decay mode into $\rho\rho$ has not been observed so far. An observation of the $f_0(1710) \to \rho\rho$ decay at the LHC would, in addition to being the first observation of this mode, alter the $K\bar{K}$ vs 'pionic' branching ratios and therefore change the expected couplings to u,d-quarks vs s-quark to values more consistent with those expected for glueballs. In relation to the measurement of the decay to K^+K^-, it would also bring additional knowledge about the coupling to quark masses.

The $f_0(1710)$ mass measurements (consistently pointing to a 1700–1710 MeV mean value within uncertainties) do not allow the Particle Data Group (PDG) to do a reliable average due to the systematically shifted measurements by BELLE and BES. Currently, the most precise existing measurement gives 1701 MeV from ZEUS [85]. A high precision measurement at the LHC could give the decisive word about the $f_0(1710)$ mass. The $f_0(1710)$ has been interpreted in the past as an f_2 by several experiments, although it has been consistently found to be an f_0 by modern experiments and the issue is considered solved [43]. However a thorough spin analysis is mandatory for any $f_0(1710)$ measurement to confirm the quantum numbers of the measured resonance, as well as to cross-calibrate the purity of the event selection with the mass measurement. While for the $f_0(1500)$ the yields, decay channels and branching ratios have been extensively measured, the $f_0(1710)$ branching ratios are controversial in the literature, being

[1] It should be noted that the final–states for the processes considered in this section are often the same as those discussed in Section 5.3.6, where the case of non–resonant light meson pair production is considered.

largely unknown, and the main decay channels are described as 'seen' by the PDG [43]. As already mentioned, allowed decay modes such as $\rho\rho$ have never been observed. A systematic and quantitative study of the decay modes and other properties of the $f_0(1710)$ can be performed at the LHC via CEP.

Former experiments (ISR, SPS, WestArea,...) did not have sensitivity to the $\rho\rho$ decay, due to their limited reach in invariant mass ($\lesssim$ 1.5 GeV) and/or to the 4π final state, and those few that had the sensitivity e.g. [86], had the analysis faked by the old assumption that the $f(1710)$ was an f_2 (as wrongly measured by several previous experiments at that time and also reported by the PDG). Attempts from modern experiments (FNAL, LHC, RHIC) lacked either the purity due to the absence of double proton tagging or the mass resolution for the two charged particles final states. The unique characteristics of the LHC are a $\sqrt{s}$ such that $\sim$ 1–10 GeV invariant masses can be produced diffractively with $\xi_{1,2} \sim 10^{-3}$–10^{-4}, ensuring purely gluonic exchanges.

While the quantum numbers of glueballs that can be *singly* produced in exclusive double pomeron exchange are dominantly J^{PC} = (even)$^{++}$, many other quantum numbers are allowed in theory, see e.g. [77]. Any glueballs can be pair produced in CEP, and this is a promising channel since the pomeron is dominated by gluons, especially at the low–Q^2 values relevant here. One potential strategy is to select single interaction events with central mass $M_X \sim$ 4 - 10 GeV between two large rapidity gaps (detecting one or both protons would be beneficial, but may not be essential), and then to require the state X to have zero charge, strangeness, etc., and finally, dividing the central event into two neutral clusters, to select cases where their masses are consistent with being equal and plot their average mass. The decays of the two clusters may be different, e.g. $(\pi^+\pi^-\pi^+\pi^-)$ and $(\pi^+\pi^-K^+K^-)$, possibly containing meson resonances such as ρ^0 and ϕ, etc. Unfortunately the branching fractions of these states are not well predicted, so this would largely be a data–driven search. It would probably require large statistics, e.g. 10^5–10^6 events with no pile up in that M_X range, but the CEP cross sections are not expected to be small ($\sim$ nb) and with an optimised trigger high statistics could be collected in a dedicated period of a few days.

Especially interesting would be the discovery of "oddballs" [87], which have quantum numbers such as $J^{PC} = 0^{--}$ (a G_{0-}), and which cannot be composed of two gluons (by C–parity) or $q\bar{q}$, so that they do not mix with conventional mesons. The mass of G_{0-} has been estimated to be about 3.8 GeV, and it should be relatively narrow; a possible decay mode is $G_{0-} \to \gamma + f_1(1285) \to \gamma + 4\pi$. Exclusive production of G_{0-} pairs at the LHC could be an excellent discovery mechanism, and it would open a new chapter in non–perturbative QCD. A more speculative glueball topology in the string model is a barred-loop with two 3-string junctions (there are no quarks, which would be the ends of open strings). The most likely decay would be through triple-string-breaking to two baryons.

Experimental results and outlook

A preliminary analysis of low mass resonance production has been performed on the data of the common CMS-TOTEM β^* = 90 m run at $\sqrt{s}$ = 8 TeV in July 2012. There is excellent mass resolution ($\sim$ 20-30 MeV) with the tracker for charged-particle-only final states, allowing the produced resonances to be clearly identified, without further steps like model- and parameter-dependent partial-wave analysis. Events with two RP protons and only two or four charged particles in the tracker with zero total charge are selected in the double arm RP triggered sample [88]. The background has been shown to be low by selecting events with the same criteria but with a non-zero net charge for the charged particles. In the analyzed data sample of $\sim$ 3

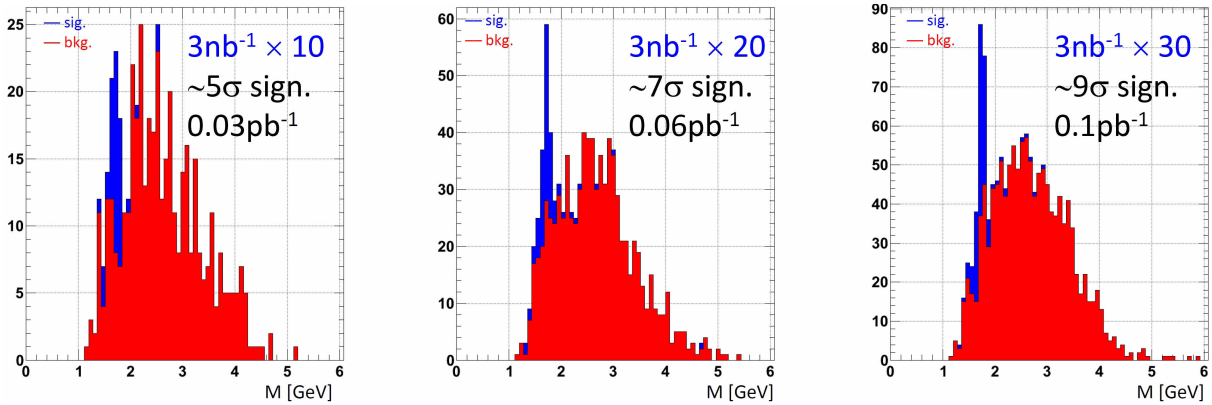

Fig. 5.9: Simulated signal and background mass distributions for exclusive $f_0(1710) \to \rho^0\rho^0 \to 2(\pi^+\pi^-)$ production in CMS-TOTEM. Three different integrated luminosities are given: $0.03\,\mathrm{pb}^{-1}$, $0.06\,\mathrm{pb}^{-1}$ and $0.1\,\mathrm{pb}^{-1}$ together with the local peak significance. The background estimate from non-resonant exclusive $\rho^0\rho^0$ production is based on the `Dime MC` [28]. Other backgrounds like exclusive $2(\pi^+\pi^-)$ and $\pi^+\pi^-\rho^0$ production as well as exclusive production of adjacent f_2 states are not taken into account.

nb^{-1}, $\sim$ 1000 $\pi^+\pi^-$ and a few tens of $\rho^0\rho^0$ exclusive candidates were found, where for the latter two $\pi^+\pi^-$ combinations are required to be compatible with the ρ^0.

A preliminary analysis of the common CMS-TOTEM data reveals sensitivity to events showing the possible decay of $f_0(1710) \to \rho^0\rho^0 \to 2(\pi^+\pi^-)$. Due to the limited amount of data, the background due to non-resonant exclusive $\rho^0\rho^0$ production is estimated with the DIME Monte Carlo [28] event generator. Fig. 5.9 shows simulated signal distributions of $f_0(1710) \to \rho^0\rho^0 \to 2(\pi^+\pi^-)$ together with background due to non-resonant exclusive $\rho^0\rho^0$ production with their local significance, for three different integrated luminosity scenarios. According to the simulation, at least $0.06\,\mathrm{pb}^{-1}$ is required to observe the resonance. A similar integrated luminosity is needed for the measurement of $f_0(1500) \to K^+K^-$.

A precise measurement of the branching ratios of the f_0 resonances is essential in the context of identifying the resonances as glueball candidates. As the branching ratios for low mass resonances may easily differ by an order of magnitude (e.g. for $f_0(1500)$: Br $(K\bar{K}) \approx 9\,\%$, Br $(\eta\eta) \approx 5\,\%$ and Br $(4\pi) \approx 50\,\%$) and assuming a similar range for $f_0(1710)$, a factor of ten of integrated luminosity higher than that estimated for observing $f_0(1710) \to \rho^0\rho^0 \to 2(\pi^+\pi^-)$, would be required in order to precisely measure the $\pi^+\pi^-$, $\mathrm{K}^+\mathrm{K}^-$ and $2(\pi^+\pi^-)$ decay modes. As the backgrounds from exclusive $2(\pi^+\pi^-)$ and $\pi^+\pi^-\rho^0$ production as well as the adjacent f_2 states were not taken into account in the above analysis, a detailed measurement of the $f_0(1500)$ and the $f_0(1710)$ branching ratios will in reality require slightly more i.e. an integrated $\beta^* = 90$ m luminosity of $\sim 1\,\mathrm{pb}^{-1}$.

Finally, a study to estimate the required luminosity for a detailed angular momentum analysis, based on the $f_J \to \rho^0\rho^0 \to 2(\pi^+\pi^-)$ decay is summarised below; such an analysis is of high importance to give full confidence that the measured branching ratios of the potential low mass glueball candidates are correct. The study [88] is carried out with a simplified detector acceptance model and in addition no background is assumed. The integrated luminosity requirements for an angular momentum study are illustrated in Fig. 5.10 (left) that shows the sensitivity of the spin J determination allowed by the distribution of the polar angle θ_{π^+} of the π^+ from the decay of the ρ^0 with $\eta > 0$, produced in the reaction $f_J \to \rho^0\rho^0 \to 2(\pi^+\pi^-)$. The rejection of an incorrect $J = 2$ hypothesis is possible with at least 300 events, corresponding

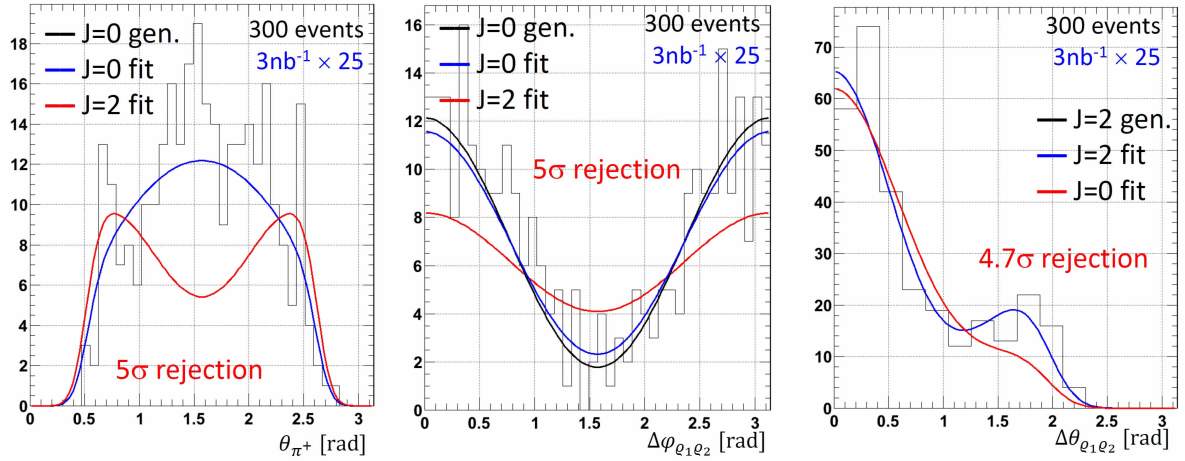

Fig. 5.10: Simulated spin analysis in exclusive $f_J \to \rho^0\rho^0 \to 2(\pi^+\pi^-)$ production. Left: Distribution of the polar angle θ_{π^+} of the π^+ from the decay of the ρ^0 with $\eta > 0$. Center: Distribution of the azimuthal angle difference $\Delta\varphi_{\rho_1\rho_2}$ between the two $\pi^+\pi^-$ pairs. Right: Distribution of the polar angle difference $\Delta\theta_{\rho_1\rho_2}$ between the two $\pi^+\pi^-$ pairs produced. All plots correspond to an integrated luminosity of $\sim 75\,\mathrm{nb}^{-1}$. The histograms represent the simulated samples assuming either $J = 0$ (left and center) or $J = 2$ (right). The blue (red) curves are the fits to the simulated data for the (in)correct hypothesis. The significance quoted in the histograms refers to the incompatibility to data of the fit with the incorrect hypothesis. No contributions from backgrounds have been included in the simulated samples.

to an integrated luminosity of $\sim 75\,\mathrm{nb}^{-1}$. A similar integrated luminosity requirement is imposed by the spin determination from the azimuthal and polar angle difference $(\Delta\varphi_{\rho_1\rho_2}, \Delta\theta_{\rho_1\rho_2})$ between the $\pi^+\pi^-$ pairs, as illustrated in Figs. 5.10 (middle) and 5.10 (right). The angular correlations between the leading protons will also have sensitivity to the spin of the centrally produced exclusive state, see Section 5.3.2.

However, the considerations illustrated by Fig. 5.10 can be considered only as rough estimates since they do not take into account the background from exclusive $2(\pi^+\pi^-)$, $\pi^+\pi^-\rho^0$ and $\rho^0\rho^0$ production. Moreover, in the vicinity of the $f_0(1710)$ there are other resonances, such as the $f_2(1640)$ or $f_2(1810)$, which partially overlap in the invariant mass spectrum. The decay amplitude coupling constants of a given resonance may differ as a function of the invariant mass M. Finally the $\rho^0\rho^0$ angular momentum $L_{\rho^0\rho^0}$ needs to be properly determined. A realistic spin-parity analysis therefore requires a study of the angular amplitudes as a function of the invariant mass in a wider interval than the resonance width itself, to make the deconvolution of the overlapping contributions coming from adjacent resonances and background possible. Similar approaches were already successfully employed in low mass resonance studies, see e.g. [89].

The spin-parity analysis therefore has to be performed in mass steps ΔM. The smallest step size ΔM is limited by the mass reconstruction resolution $\sigma(M) \approx$ 20-30 MeV. The largest possible step size could be a fraction of the resonance width ($\sim$ 100 MeV) but nevertheless should not exceed $\sim$ 40 MeV. Taking all the above into account, a full spin-parity analysis of the exclusive production of f_0 states will need to be made in mass bins with a size $\Delta M =$ 30-40 MeV and when requiring sufficient statistics in each ΔM bin, it is strictly only fully feasible with a integrated β^* = 90 m luminosity of $\sim$ 4-5 pb^{-1}. A similar analysis will be possible in ATLAS-ALFA but will suffer more from contamination at large rapidities since the forward coverage in ATLAS is worse than in CMS-TOTEM.

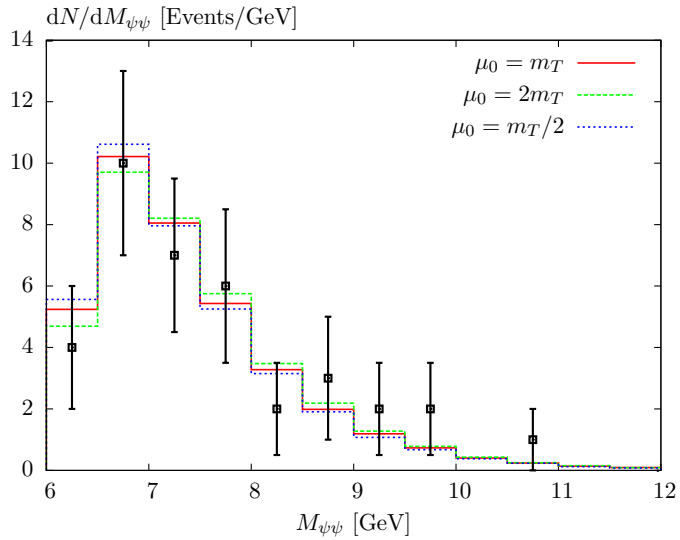

Fig. 5.11: Comparison of LHCb measurement [90] of $J/\psi J/\psi$ invariant mass distribution with theory prediction, calculated as described in the text. In all cases the result is normalized to the data.

5.3.8 Quarkonium Pair Production

Motivation and theory

Motivated by the LHCb measurement of exclusive double J/ψ and $J/\psi\psi(2S)$ production [90], see below, the first calculation of exclusive double J/ψ production in hadronic collisions was presented in [91]. After an analysis of the Born–level $gg \to J/\psi J/\psi$ amplitudes within the non–relativistic quarkonium approximation, the predicted exclusive cross sections were found to be suppressed by the CEP dynamical $J_z = 0$ selection rule, although still of a reasonable size: depending on the choice of gluon PDF and model of soft survival factor the predicted cross sections were found to lie in the $\sim 2-7$ pb range, in reasonable agreement (considering other theoretical uncertainties, such as the variation of the renormalization/factorization scale) although somewhat lower than the LHCb measurement of 24 ± 9 pb. It is worth emphasising that without the effect of the $J_z = 0$ selection rule, the predicted cross section would be ~ 2 orders of magnitude higher.

The shape of the invariant mass distribution, which has a much smaller theoretical uncertainty than the absolute cross section, is shown in Fig. 5.11, normalised to the data, and is seen to describe the LHCb measurement well, within the (quite large) experimental errors. Further higher statistics measurements would clearly allow a closer comparison with theory. Other observables such as the J/ψ transverse momentum and the rapidity difference $\Delta(y)$ between the mesons, are also of interest; in the latter case, the predicted distribution is found to be broader than in the inclusive process, an effect which is driven by the CEP selection rule, which enhances the amplitudes with $J_z = 0$ incoming gluons, for which the $\Delta(y)$ distribution is much broader. In inclusive production, some broadening is also expected (and observed [92]), but here it is generated by the 'double parton scattering' production mechanism [93], where each J/ψ is produced in independent scatters. In [91], this contribution was found to be very small in exclusive production, and thus the pure, single–parton scattering (and colour–singlet) contribution is probed. These reactions are also in principle quite sensitive to additional particles which might be produced in decay chains that involve exotic particles.

Finally, it is possible to estimate the expected cross sections for $J/\psi\psi(2S)$ and $\psi(2S)\psi(2S)$

production, giving

$$\sigma^{J/\psi J/\psi} : \sigma^{J/\psi\psi(2S)} : \sigma^{\psi(2S)\psi(2S)} = 1 : 0.40 : 0.044\,, \tag{5.9}$$

to be compared with the LHCb measurement of

$$\frac{\sigma(J/\psi\psi(2S))}{\sigma(J/\psi J/\psi)} = 1.1^{+0.5}_{-0.4}\,, \tag{5.10}$$

assuming the same exclusive fraction in both cases. There is clearly reasonable agreement, but with further data it will be possible to make a more precise statement about this. The cross sections involving χ_c mesons are estimated to be much smaller, although this needs to be confirmed by a full calculation. On the other hand, as the formation amplitude of the pseudoscalar η_c meson is proportional to the same value of the wave function at the origin as in the J/ψ case, and the CEP pair production mechanism may also be produced by additional so–called 'ladder' diagram (similar to the case of $\eta(')\eta(')$ production discussed in Section 5.3.6), we may expect the cross section for double η_c production to be of the same size or even bigger than for the J/ψ.

It is worth emphasising that the work of [91] represents the first calculation of exclusive double J/ψ production, while the LHCb data [90] is the first ever measurement of this process. This therefore represents a very new topic of investigation, and there is a great deal of further theory work to be pursued: for example, the effect of relativistic corrections, in particular in the case of the $\psi(2S)$, the calculation of higher–order contributions and a full calculation for the case of χ_c and η_c final states has not yet been fully considered. Further measurements of these processes, and more differential tests of the theory, will be essential in pursuing such a programme.

Experimental results and outlook

LHCb has recently made measurements, using a data sample corresponding to 3 pb^{-1}, of double charmonia [90], $J/\psi J/\psi, J\psi\psi(2S), \psi(2S)\psi(2S)$, $\chi_{c0}\chi_{c0}$, $\chi_{c1}\chi_{c1}, \chi_{c2}\chi_{c2}$. The selection proceeds in a similar fashion to that described in Sec. 5.4.4, although now four charged tracks (at least three of which are identified muons) and no other activity are required to select pairs of S-wave states, while one or more photons are required to select pairs of P-wave states. Very few low multiplicity events have three or more identified muons. The invariant mass distribution of the two pairwise combinations is given in the left plot of Fig. 5.12 and shows an accumulation of events at the J/ψ and $\psi(2S)$ masses in a region of phase space that is otherwise empty. The right plot in Fig. 5.12 shows the higher mass combination when asking that the lower mass combination is consistent with the J/ψ meson. There are 37 $J/\psi J/\psi$, 5 $J/\psi\psi(2S)$ and no $\psi(2S)\psi(2S)$ candidates. The only substantial background to the $J/\psi J/\psi$ signal comes from $J/\psi\psi(2S)$ where $\psi(2S) \to J/\psi X$ with X unreconstructed. After correcting for detector acceptance and efficiencies, the measured cross sections for pairs of S-wave mesons with $2 < y < 4.5$, which are exclusive *within the LHCb acceptance*, are $\sigma^{J/\psi J/\psi} = 58 \pm 10 \pm 6$ pb, $\sigma^{J\psi\psi(2S)} = 63^{+27}_{-18} \pm 10$ pb, and $\sigma^{\psi(2S)\psi(2S)} < 237$ pb at the 90% confidence level. The search for P-wave pairs has a single candidate for $\chi_{c0}\chi_{c0}$ that is also consistent with $J/\psi\psi(2S)$ production, and so upper limits at the 90% confidence level are set on the production of χ_{c0}, χ_{c1} and χ_{c2} pairs at 69, 45 and 141 pb, respectively.

The numbers quoted above are for di-mesons detected in the absence of any other activity inside the LHCb acceptance. In order to compare with theory predictions, a correction needs to be made for events which are not truly exclusive. This is determined to be $(42 \pm 13)\%$

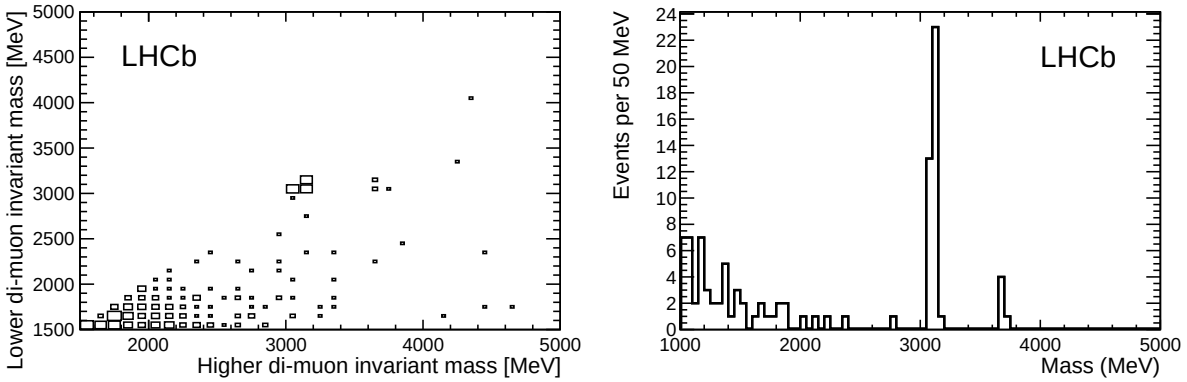

Fig. 5.12: (Left) Invariant masses of the two di-muon candidates. (Right) The higher mass di-muon candidate having required the lower mass candidate to be consistent with the J/ψ mass.

with a large uncertainty due to the low number of $J/\psi J/\psi$ events observed, and leads to a measurement of elastic CEP $J/\psi J/\psi$ with $2 < y < 4.5$, at an average $\sqrt{s} = 7.6$ TeV, of 24 ± 9 pb. This is in fair agreement with the predictions of [91], see Section 5.3.8. There is a sizeable uncertainty on the theoretical prediction, due in large part to the poorly understood low-x gluon PDF that enters with the fourth power in the theoretical calculation. More data, both to pin down the gluon PDF (as described in Sec. 5.4.4) and to improve the $J/\psi J/\psi$ CEP measurement will enable a more precise comparison.

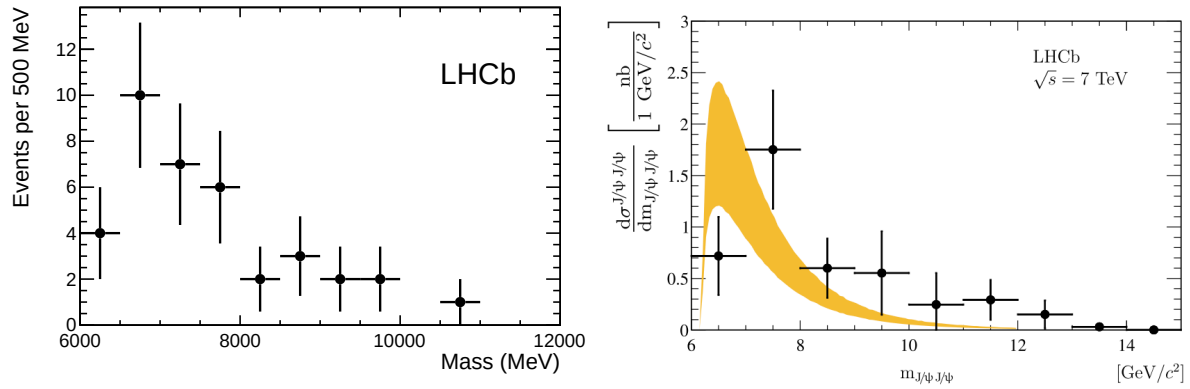

Fig. 5.13: Invariant mass of the $J/\psi J/\psi$ system in (left) exclusive and (right) inclusive events. The shaded area is the theoretical prediction of [95].

In Fig. 5.13, the invariant mass of the exclusive signal is compared to that of an inclusive measurement of double J/ψ production, performed by LHCb [94]; both have a similar shape. The data in the inclusive measurement are shifted to slightly higher masses than the theory, and this has been discussed as possible evidence for double parton scattering [93] or tetraquark states [95]. The former is negligible in CEP due to the ultra-peripheral nature of the collision (see [91] for further discussion), and thus with more statistics, the exclusive measurement will become sensitive to the presence of higher mass resonances. Similar complementary measurements will be possible with proton tagging at high β^* in CMS-TOTEM and ATLAS-ALFA.

5.3.9 Jet production

Motivation and theory

Exclusive jet production [96, 97], in particular of a 2–jet system (jj), has been of great importance in testing the underlying perturbative CEP formalism. Moreover, as discussed below, there is much potential to measure this process at the LHC, in particular with both protons tagged using the installed and proposed forward proton spectrometers: the expected production cross sections can be as high as the nanobarn level, depending on the precise event selection and in particular the M_X range probed. Indeed, as discussed below, already a sample of 'exclusive–like' 2–jet and 3–jet events has been collected in a combined CMS+TOTEM run at 8 TeV. Most events with two scattered protons and central jets will correspond to central diffractive (CD) jet production, i.e they will not be exclusive, but will have additional particle production from the Pomeron remnants. Exclusive production may be regarded as a particular case of CD jet production with only the jets in the final state, and no Pomeron remnants. It proceeds through the mechanism shown in Fig. 5.1, via the $gg \to gg, q\bar{q}$ and $gg \to ggg, gq\bar{q}$ subprocesses for 2– and 3–jet production, respectively.

The different behaviour of the parton–level helicity amplitudes relevant to exclusive jet production leads to some highly non–trivial predictions. For example, considering quark jets, the $gg \to q\bar{q}$ amplitudes are given by

$$\mathscr{M}\left((g(\pm)g(\pm) \to q_h \bar{q}_{\bar{h}}\right) = \frac{\delta^{cd}}{N_c} \frac{16\pi\alpha_s}{(1-\beta^2\cos^2\theta)} \frac{m_q}{M_X} (\beta h \pm 1)\delta_{h,\bar{h}}\,, \tag{5.11}$$

$$\mathscr{M}\left((g(\pm)g(\mp) \to q_h \bar{q}_{\bar{h}}\right) = \pm h \frac{\delta^{cd}}{2N_c} 8\pi\alpha_s \left(\frac{1 \pm h\cos\theta}{1 \mp h\cos\theta}\right)^{1/2} \delta_{h,-\bar{h}}\,, \tag{5.12}$$

for gluons of '$\pm$' helicity and quarks of helicity h, while c, d are the outgoing quark color labels, and $\beta = (1-4m_q^2/M_X^2)^{1/2}$. We can see that the $J_z = 0$ amplitude involves a helicity flip along the quark line, and vanishes as the quark mass $m_q \to 0$. Thus we expect a strong suppression in the CEP cross section for quark di-jets, relative to the gg case, for which the $gg \to gg$ amplitudes with $J_z = 0$ incoming gluons display no such suppression. In this way the exclusive mode offers the possibility to study almost purely (over 99% for typical event selections) gluonic and, crucially, isolated jets [6] (produced by the collision of a color–singlet gg state), shedding light on the underlying properties of these jets (such as multiplicity, particle correlations etc) in a well–defined and comparatively clean exclusive environment. In Table 5.1, some representative predictions for exclusive two and three jet production are shown and this $gg/q\bar{q}$ hierarchy is clear. The quite large predicted cross sections are also evident.

M_X(min)	gg	$q\bar{q}$	$b\bar{b}$	ggg	$gq\bar{q}$
75	120	0.073	0.12	6.0	0.14
150	4.0	1.4×10^{-3}	1.7×10^{-3}	0.78	0.02
250	0.13	5.2×10^{-5}	5.2×10^{-5}	0.018	5.0×10^{-4}

Table 5.1: Parton–level predictions for exclusive two and three jet production cross sections (in pb) at the LHC for different cuts on the minimum central system invariant mass M_X at $\sqrt{s} = 13$ TeV. The jets are required to have transverse momentum $p_\perp > 20$ GeV for $M_X(\text{min}) = 75, 100$ GeV and $p_\perp > 40$ GeV for $M_X(\text{min}) = 250$ GeV and pseudorapidity $|\eta| < 2.5$. The Anti–k_t algorithm with $R = 0.6$ is used in the three jet case and the $q\bar{q}$ cross sections correspond to one quark flavour. Predictions made using the `SuperChic 2` MC [98].

In the case of three jet production, that is $q\bar{q}g$ and ggg jets, this suppression in the $q\bar{q}$ exclusive di-jet cross section also leads to some interesting predictions [99, 100]. In particular, we expect the behaviour of the $q\bar{q}g$ amplitude as the radiated gluon becomes soft to be governed by the corresponding Born–level, $q\bar{q}$, amplitude. This is expected to lead to an enhancement of 'Mercedes–like' configurations for the $q\bar{q}g$ case, where all three partons carry roughly equal energies and are well separated. More generally, it would be of much interest to investigate the difference in the predicted event shape variables, which may be quite different between the experimentally distinguishable $b\bar{b}g$[2] and ggg cases, as well as to the corresponding inclusive cases.

In addition, in [101] so–called 'planar radiation zeros' were shown in [101] to be present in 5–parton QCD amplitudes, that is, a complete vanishing of the Born–level amplitudes, independent of the particle polarisations, when their momenta lie in a plane and satisfy certain additional conditions on their rapidity differences. These were seen in particular to occur in the $gg \to ggg$ and, in certain cases, the $gg \to q\bar{q}g$ amplitudes, when the initial–state gluons were in a colour–singlet configuration. This is precisely the situation for exclusive 3–jet production, and so the presence of such zeros may be detectable in the CEP process.

Experimental results and outlook

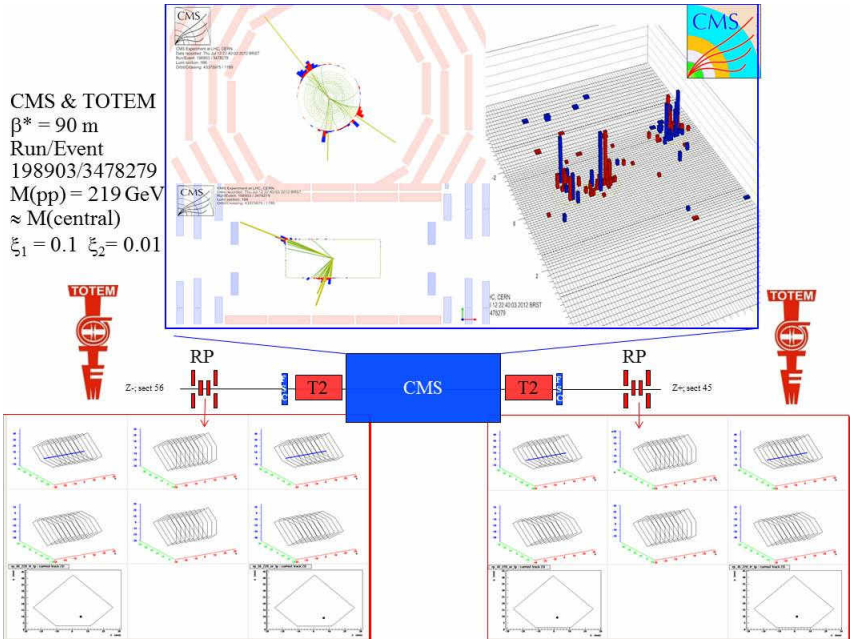

Fig. 5.14: A central diffractive three-jet event recorded by TOTEM and CMS in a $\beta^* = 90$m run at $\sqrt{s} = 8$ TeV. The upper part of the figure displays the central part of the event, as seen in CMS; the lower part displays the proton information in the TOTEM Roman Pots.

In 2008, the CDF collaboration reported [25] the observation and cross section measurement of exclusive jet production using a data sample of 310 pb^{-1}, at $\sqrt{s} = 1.96$ TeV and for $E_\perp^{\rm jet} > 10$ GeV, selected by tagging the outgoing anti–proton and requiring a rapidity gap in the proton direction (which was not tagged). They presented both dijet invariant mass M_{jj} and jet transverse momenta $E_\perp^{\rm jet}$ distributions, out to quite high $M_{jj} \sim 130$ GeV, and $E_\perp^{\rm jet} \sim 35$ GeV, and

[2]Predictions are presented in Table 5.1 for $gq\bar{q}$ production with massless quarks, however the corresponding cross sections with b–quarks are expected to be similar.

it was found that the perturbative approach of the Durham model described the data well. This observation was later supported by the measurement of the D0 collaboration [102], which found evidence for exclusive dijet production with $M_{jj} > 100$ GeV. The first study of di-jet production at $\sqrt{s} = 7$ TeV is presented in [103], which however is limited to single-diffractive (SD) di-jet production and has no measurement of the scattered proton. An older study also exists with Tevatron data, presented in [104].

In high β^* runs, CMS-TOTEM and ATLAS-ALFA can study CD dijets with $E_T > 20$ GeV at any M_X. Some two- and three-jet events, though not truly exclusive since $M(jj, jjj) < < M(pp)$, were already seen by CMS and TOTEM during the short high-β^* run in July 2012. Common data were recorded with a CMS trigger on two jets with $E_T > 20$ GeV. Selecting events with a proton in each direction in the TOTEM RPs, extremely clean events with jets were found, as shown in Fig. 5.14. With 100 pb^{-1} of high β^* running, a sample of about 10,000 CEP jet events with $M_X > 60$ GeV is expected, since the expected visible cross section for CMS-TOTEM is about 100 pb [2]. The expected number of background events is significantly lower [88]. The obtained sample will enable studies of the azimuthal difference ϕ between the scattered protons, the shape of the proton t-distribution and the overall cross section behaviour with M_X, providing a good test of different models [2, 105, 106].

Such high β^* measurements are complementary to the possibilities with the CT-PPS and AFP detectors, in standard LHC running, which only have access to $M_X \gtrsim 300$ GeV , but with much higher integrated luminosities. Measurement feasibilities in this scenario have been the subject of detailed studies, in the case of both detector set–ups: these are summarised in the following sections.

5.3.10 Jet production: ATLAS feasibility study

In this section, a feasibility study for exclusive jet production, performed for $\sqrt{s} = 14$ TeV, and using the ATLAS detector equipped with the AFP stations is summarised. The full analysis is described in [108].

Exclusive dijet events were generated using the FPMC generator [107]. Further details of the tools used for generating non–diffrative dijet and single/double Pomeron exchange events, as well as additional proton–proton interactions are given in [108]. In order to simulate the detector response, all events were reconstructed using the ATLAS full simulation chain [109].

Due to the distance from the beam assumed in this analysis, the minimal energy loss visible in the AFP detectors is $\xi_{min} \approx 0.02$, which translates to a jet momentum of about 140–150 GeV. One proton is required in each AFP station, reducing the ND background by an order of magnitude. The difference between the primary vertex z position reconstructed by the ATLAS main detector and the one reconstructed from the AFP time measurement, Δz, is required to be less than 3.5 mm.

The Δz distribution for signal and background events is shown in Figure 5.15. The broad distributions for ND and SD jet production are due to the size of the beamspot, as in these cases protons are coming from pile-up interactions. The tails in the case of DPE jet production are due to the events in which one 'hard' proton was not seen in the AFP, but there was an additional pile-up proton. For DPE jets with $p_T > 150$ GeV such a situation is quite probable as protons are expected to lose a lot of their initial energy. The exclusive signal was generated with both protons in the AFP acceptance; here, the width is mainly due to the AFP timing resolution. When more than one proton was observed in a given station, all combinatoric possibilities were considered and the one with the smallest Δz was taken.

For signal events, the kinematics of the central dijet system can be estimated from the

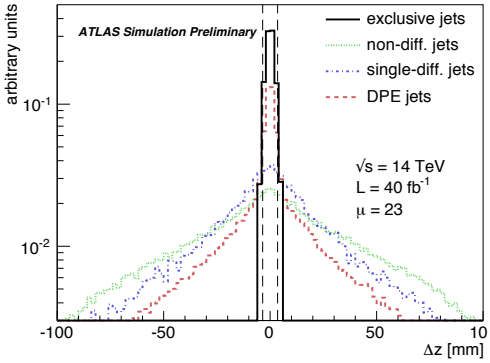

Fig. 5.15: The difference of the vertex z-coordinate as reconstructed by the ATLAS main detector and the one reconstructed from the AFP time measurement. The integral of the distribution is normalised to 1. The AFP time resolution of 10 ps has been assumed for background rejection. The exclusive signal is plotted as a solid black line, whereas the backgrounds are a dotted green (non-diffractive jet production), dashed-dotted blue (single diffractive jet production) and dashed red (double Pomeron exchange jet production) lines. The black dashed line represents the value of the applied cut.

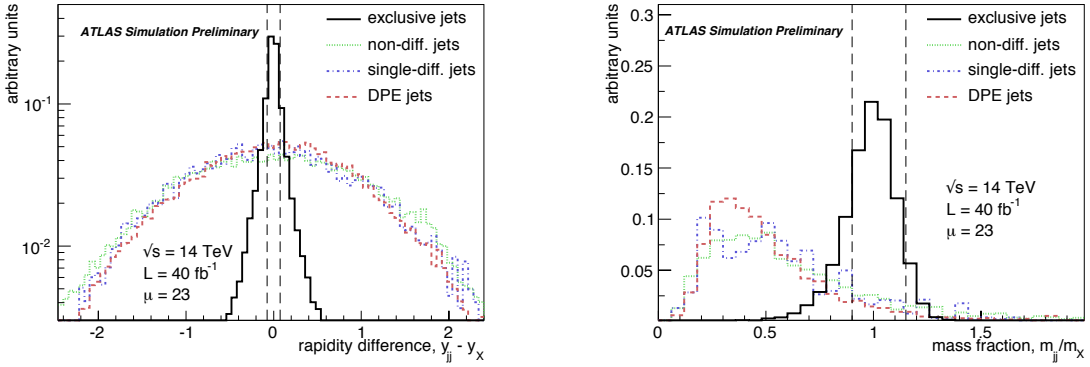

Fig. 5.16: **Left:** Difference, $y_{jj} - y_X$, of the rapidity of the jet system (y_{jj}) and the rapidity of the proton system $y_X = 0.5 \cdot \ln\left(\frac{\xi_1}{\xi_2}\right)$. **Right:** Ratio of the jet system mass to the missing mass $m_X = \sqrt{s \cdot \xi_1 \cdot \xi_2}$. The ξ_1 and ξ_2 are relative energy losses of protons tagged in the AFP stations. The integral of the distribution is normalised to 1. The black dashed line represents the value of the applied cut.

forward proton measurements, and correlated with the kinematics reconstructed from the jet four-momenta. Fig. 5.16 (left) shows the ratio of the dijet mass reconstructed from the jet four-vectors to that obtained from the proton kinematics. The exclusive signal can be enhanced with respect to the background by the following cuts: $|y_{jj} - y_X| < 0.075$ and $0.9 < \frac{m_{jj}}{m_X} < 1.15$. These requirements provide further background reduction by about three orders of magnitude.

The lack of both underlying event activity and proton/Pomeron remnants provides another handle with which to improve the signal purity. A track with $\eta > 0$ is considered to be outside the jet system if $\eta_{trk} > \eta_{jet} + 0.7$ and $\eta_{trk} > \eta_{jet} + w_{jet} + 0.2$, where w_{jet} is the reconstructed jet width [110], with a similar condition if $\eta < 0$. A track is considered as perpendicular in ϕ to the leading jet if $\frac{\pi}{3} < \Delta\phi < \frac{2\pi}{3}$ or $\frac{4\pi}{3} < \Delta\phi < \frac{5\pi}{3}$, where $\Delta\phi$ is the azimuthal angle between the track and the leading jet. Then, by cutting on the number of tracks perpendicular in ϕ to the leading jet and outside the jet system in η (required to be less than or equal to 2 and 5, respectively), the background can be reduced by almost two orders of magnitude.

In addition, three further selection criteria were applied in this analysis: the azimuthal

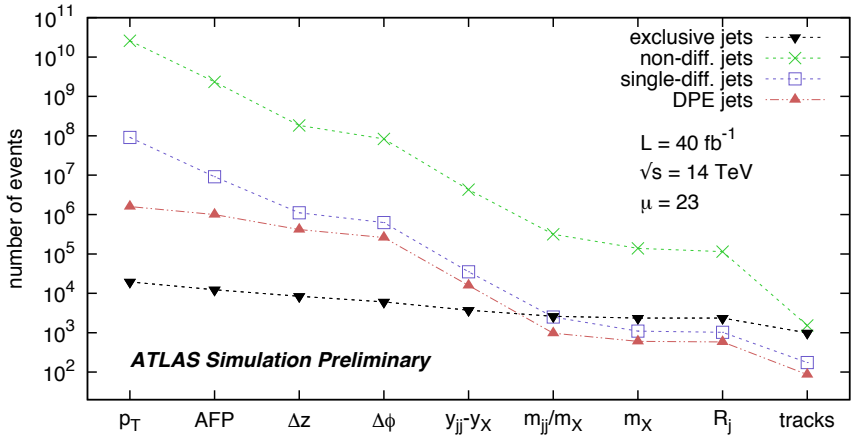

Fig. 5.17: Number of events accepted after a given cut for signal (exclusive jet production) and background (double Pomeron exchange (DPE), single diffractive (SD) and non-diffractive (ND) jet production) processes for an integrated luminosity of 40 fb^{-1} and an average number of interactions of $\mu = 23$ as a function of the applied consecutive cuts. The AFP time resolution of 10 ps has been assumed for background rejection.

angle between the two leading jets must satisfy $2.9 < \Delta\phi < 3.3$ – exclusive jets are expected to be produced back-to-back; the missing mass must satisfy $m_X < 550$ GeV – the ξ distribution falls much more steeply for exclusive jets production; the mass fraction is required to be $0.9 < m_{jj}/m_X < 1.3$ – this variable was proposed in [97] to reduce the effects of hard state radiation and is strongly correlated with mass ratio and rapidity difference requirements. The change in the fiducial cross section for signal and background processes after each selection requirement for an integrated luminosity of 40 fb^{-1} and average number of interactions of $\mu = 23$ is shown in Fig. 5.17. The dominant background is due to non-diffractive jet production overlaid with protons from pile-up interactions. After all selection requirements the signal to background ratio is increased from 10^{-6} to ~ 0.57.

The analysis was repeated for the average number of interactions of $\mu = 46$ and an integrated luminosity of 300 fb^{-1}. The selection criteria for these conditions are similar to the ones used in the $\mu = 23$ analysis. The dominant background from ND dijet events overlaid with protons from minimum bias events increases with respect to the signal, as the probability of producing this combinatorial background increases quadratically with the number of interactions per beam bunch crossing.

The leading jet transverse momentum above a given threshold for an integrated luminosity $L = 40\,(300)$ fb^{-1} and an average number of interactions of $\mu = 23\,(46)$ are presented in the upper (lower) panels of Fig. 5.18. Although the statistical significance is roughly the same in both scenarios, the impact of statistical and background uncertainties is much larger in the latter situation. Improvements in the AFP timing detector resolution and/or the analysis method are needed in order to control the background modelling uncertainties. For example, if the background is measured in control regions to an accuracy of $\sim 1\%$ then the accuracy of the cross section measurement would be similar to that for $\mu = 23$.

In summary, while the initial signal to background ratio for exclusive jet production in AFP is about 10^{-6}, after dedicated signal selection cuts have been applied, this reduces to about 0.57 (0.16) for $\mu = 23$ (46). In both cases the statistical errors are considerably smaller. The biggest uncertainty is associated with the modelling of the background from ND dijet events overlapping with two protons from pile-up events. The impact of the ND background on the

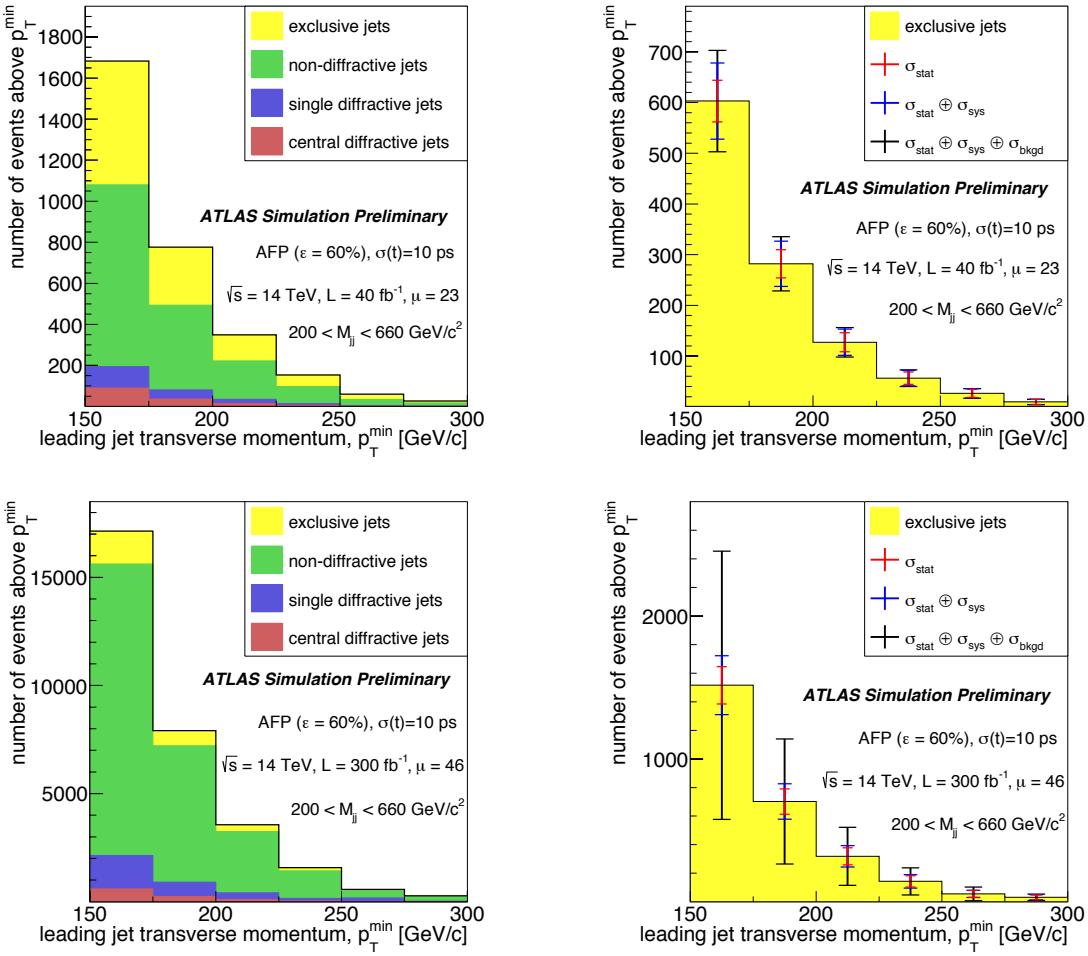
exclusive jets
non-diffractive jets
single diffractive jets
central diffractive jets
ATLAS Simulation Preliminary
AFP (ε = 60%), σ(t)=10 ps
√s = 14 TeV, L = 40 fb-1, μ = 23
200 < Mjj < 660 GeV/c2
number of events above pTmin
leading jet transverse momentum, pTmin [GeV/c]
σstat
σstat ⊕ σsys
σstat ⊕ σsys ⊕ σbkgd
√s = 14 TeV, L = 300 fb-1, μ = 46

Fig. 5.18: **Left:** Number of accepted events as a function of the leading jet p_T threshold. The background consists of the production of double Pomeron exchange (red), single diffractive (blue) and non-diffractive (green) jets. **Right:** Number of signal events, marked as yellow bar, with statistical (σ_{stat}), systematic (σ_{sys}) and background (σ_{bkgd}) uncertainties. The $\oplus$ sign indicates that the corresponding errors are added in quadrature. The upper (lower) plots correspond to an integrated luminosity of $L = 40\,(300)$ fb^{-1} and average number of interactions of $\mu = 23\,(46)$

measurement ultimately depends on the success of data–driven methods using dedicated control regions. In case of $L = 40$ fb^{-1} and $\mu = 23$, the measurement will be challenging, but potentially feasible. On the other hand, in order to make such a measurement in a higher pile-up environment, much better control of systematic effects is needed.

5.3.11 Jet production: CT–PPS feasibility study

In this section, a detailed study of the measurement possibilities for exclusive jet production with the CT-PPS detectors, based on the experimental techniques developed in Refs. [25, 103], is summarised.

Events are selected by requiring a time coincidence in both arms of the CT-PPS. Leading protons are required to be in the CT-PPS fiducial region, and the arrival time difference at the CT-PPS location depends on the z-vertex position, z_{PPS}, and must be consistent with the vertex position of the central di-jet system, z_{vertex}. An expected time resolution of 10 ps (30 ps) is assumed. Two jets with reconstructed transverse momenta $p_T > 100(150)$ GeV in the

central ($|\eta| < 2.0$) detector are required. Jets are reconstructed using the anti-k_T jet clustering algorithm with a distance parameter of 0.5 [110]. Finally, the instrumental background in the CT–PPS from additional sources is accounted for, as discussed in Chapter 1. The main physics backgrounds are from minimum bias events –including SD and DPE events– in coincidence with either two jets in the central detector or another leading proton within the PPS detector acceptance. A cut on the time-of-flight difference Δt that varies according to the z-vertex position, which keeps approximately 60% (50%) of signal events while reducing the inclusive di-jet background by a factor 33 (18), for a 10 (30) ps timing resolution, is chosen.

Fig. 5.19 (left) shows the di-jet mass fraction, $R_{jj} = M_{jj}/M_X$, and the rapidity difference (right) of the jet system (y_{jj}) and the proton system, $y_X = 0.5 \cdot \ln(\xi_1/\xi_2)$. Consistency is required between the values of the jet mass system measured in the central detector (M_{jj}) and in the CT–PPS (M_X), and the requirement $0.70 < R_{jj} < 1.15$ is applied. A selection cut of $|(y_{jj} - y_X)| < 0.1$ is also required.

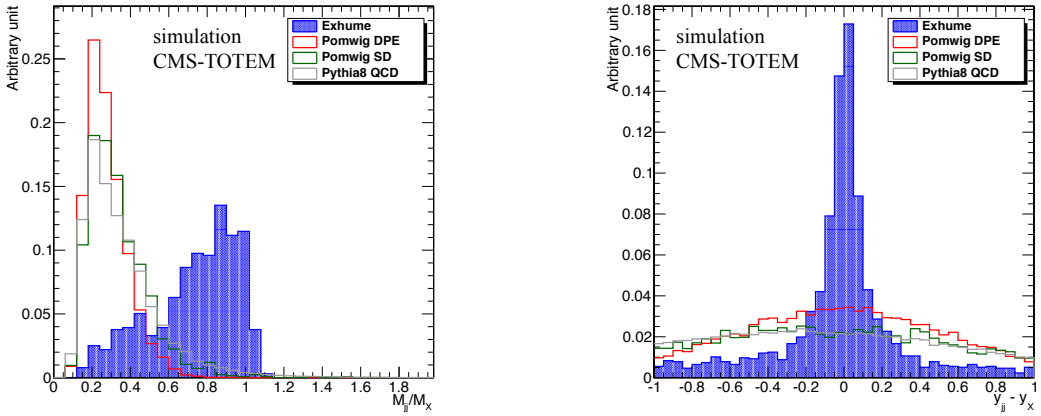

Fig. 5.19: *Left:* Dijet mass fraction $R_{jj} = M_{jj}/M_X$ (left). *Right:* Rapidity difference of jet (y_{jj}) and proton (y_X) systems. Distributions are shown for exclusive di-jet signal (ExHuME) and for background (SD, DPE, inclusive dijets) events and are normalized to unit area.

The track multiplicity associated to the di-jet vertex is used to discriminate exclusive signal events against backgrounds. In particular, techniques developed in [111] are exploited. Two variables that account for the "exclusivity" of the event by counting the number of extra tracks between the jets, both in ϕ and η, are built, denoted by N^{ϕ}_{tracks} and N^{η}_{tracks}. All tracks from the primary vertex are considered and the area of -1.0 ($+1.0$) away from the minimum (maximum) jet η coordinates is defined, η_{min} and η_{max}. Then, the number of extra tracks that are below (above) the η_{min} (η_{max}) position are counted. Similarly, the N^{ϕ}_{tracks} variable is built. In this case, the number of tracks that are perpendicular to the plane formed by the two-jet system are counted, in the region $0.54 < \phi < 2.60$. The track multiplicity variables after the timing selection cuts are shown in Fig. 5.20. Exclusive signal events tend to have significantly lower track multiplicity than inclusive di-jet events in either ϕ and η. The tracking multiplicity separation in η helps in further rejecting SD and DPE events. Events are kept if the conditions $N^{\phi}_{\text{tracks}} \leq 9$ and $N^{\eta}_{\text{tracks}} \leq 2$ are satisfied. Fig. 5.21 illustrates the evolution of the event yields as a function of the cuts applied for a time resolution of 10 ps. The cross section for signal events (given by ExHuME) is multiplied by a factor of 5/3 to simulate a gap survival probability of 5% (i.e. the same used for DPE di-jet event processes in POMWIG), instead of the gap survival probability given by ExHuME of 3%.

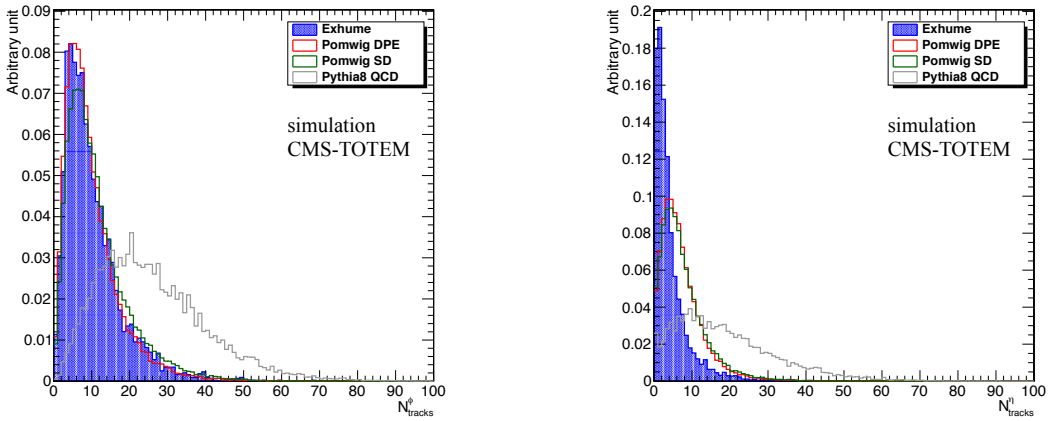

Fig. 5.20: Number of extra tracks outside the jet system in ϕ (left) and in η (right), associated to the di-jet vertex for exclusive dijet and background processes. Distributions are shown after the leading proton time-of-flight correlation requirements (with a 10 ps resolution). Event yields are normalized to unit area.

Table 5.2: Number of expected signal and background (SD, DPE, and inclusive dijets) events (after the N_{tracks} cut), for separate bins of missing mass M_X. Yields normalized to an integrated luminosity of 1 fb^{-1} are shown for average pile up multiplicities of $\mu = 25$ and $\mu = 50$. Statistical uncertainties are shown. A timing resolution of 10 ps is assumed.

	Exclusive di-jets	DPE	SD	Inclusive dijets	S:B
pile up $\mu = 25$					
$M_X \leq 500$ GeV	4.0±0.2	0.2±0.1	0±1	1 ± 1	3:1
$500 < M_X \leq 800$ GeV	3.1±0.2	0.3±0.1	0±1	15 ± 1	1:5
$M_X > 800$ GeV	0.3±0.1	0.3±0.1	1±1	4 ± 1	1:18
pile up $\mu = 50$					
$M_X \leq 500$ GeV	2.8±0.2	0.6±0.2	0±1	5 ± 1	1:2
$500 < M_X \leq 800$ GeV	2.3±0.2	0.7±0.3	1.3±1.0	26 ± 1	1:12
$M_X > 800$ GeV	0.3±0.1	0±1	0±1	9 ± 1	1:30

The study demonstrates the feasibility of measuring exclusive di-jet production in Run 2 with CT–PPS with an average pile up of $\mu = 50$. A signal-to-background ratio of S:B$\simeq$1:8 can be achieved (after the "N_{tracks}" cut), with the signal events appearing as an enhancement of the M_{jj}/M_X distribution around $M_{jj}/M_X = 1$. The case of a lower average number of pile up interactions, $\mu = 25$, has also been studied. A signal-to-background ratio of S:B$\simeq$1:3 can be achieved in the less harsh condition with pile up of $\mu = 25$ (after the "N_{tracks}" cut). Fig. 5.21 (right) illustrates the evolution of the event yields as a function of the cuts applied for a time resolution of 10 ps. Table 5.2 summarises the yields of signal and background events (after the N_{tracks} cut) estimated in bins of separate missing mass regions, $M_X < 500$ GeV (where most of the signal is expected), $500 < M_X < 800$ GeV, and $M_X > 800$ GeV. Yields normalized to an integrated luminosity of 1 fb^{-1} are shown for average pile up multiplicities of $\mu = 25$ and $\mu = 50$, and a timing resolution of 10 ps is assumed.

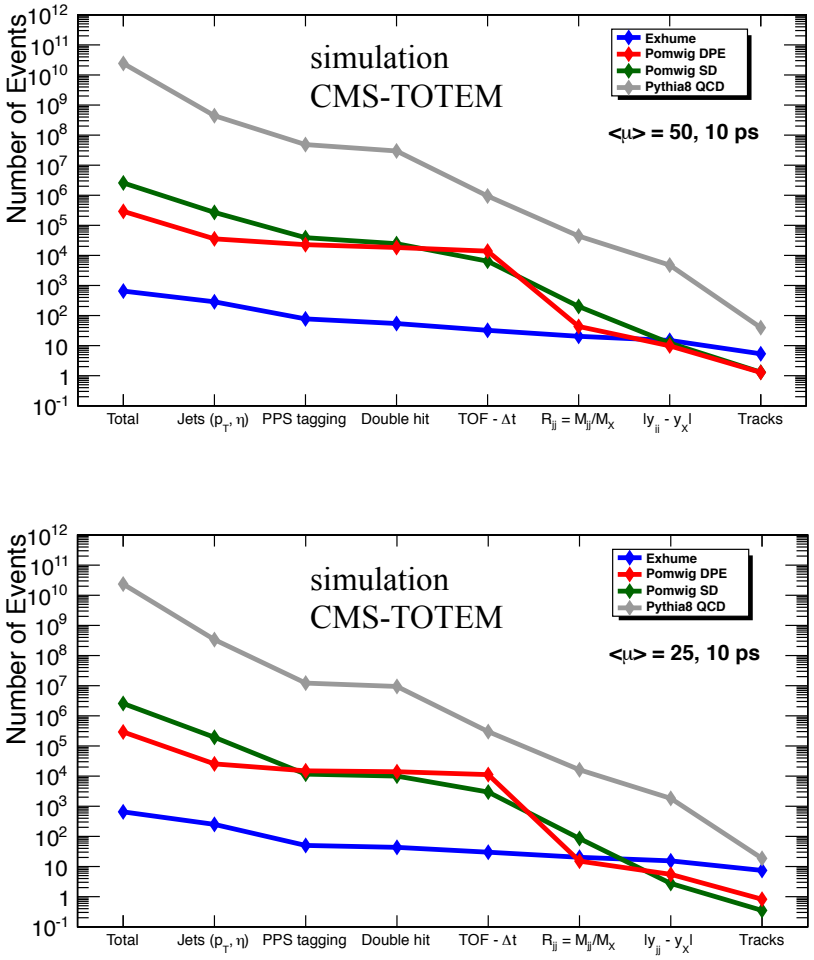

Fig. 5.21: Graphical illustration of the event yields for signal and background processes as a function of the cuts applied. A time resolution of 10 ps is assumed, and an average pile up multiplicity of $\mu = 50$ (25) is taken in the left (right) figure. Yields are normalized to an integrated luminosity of 1 fb^{-1}.

5.4 Photon–induced and photoproduction processes

In this Section, theoretical discussion of two–photon induced and photoproduction processes, and motivations for future measurements, are presented.

5.4.1 Introduction

High energy charged particles are a source of a flux of Weizsäcker-Williams (WW) photons [112, 113]. At the LHC, this opens the possibility to study photon–hadron interactions at unprecedented energies. Such reactions may be observed in ultraperipheral heavy ions collisions, where the WW flux ($\propto Z^2$) is enhanced by the large charge Z of the ion, as well as proton-proton (and proton-antiproton) collisions.

In this section the two–photon collision and photoproduction processes described in the introduction are discussed. The former proceeds via the $\gamma\gamma \to X$ subprocess and is a theoretically well–understood purely QED process, up to small corrections due to additional soft

proton–proton interactions, while in the latter case one proton interacts strongly while the other interacts via photon exchange (in the language of Regge theory, via photon–pomeron fusion, $\gamma I\!P \to X$).

Due to the well understood production mechanism in the initial state, two–photon collision processes provide a valuable handle on the electroweak sector, can in principle serve as an effective luminosity monitor, and as a tool for BSM particle discovery (see Section 5.5), while studies of such processes with dissociating outgoing protons can provide information about the soft survival factors introduced in Section 5.3.1.

The photoproduction of vector mesons, $pp \to p+V+p$, has been the focus of much theoretical study, see for example [16, 115–118, 123]. The virtuality of equivalent photons is controlled by the electromagnetic form factors of the proton, for which quasi–real photon exchanges are dominant, so that the dominant momentum transfers are deeply in the non–perturbative region. On the other hand, a hard scale necessary for the application of perturbative QCD may be supplied by the quark mass. Therefore, among the possible final states, heavy $c\bar{c}$, $b\bar{b}$ quarkonium for which a pQCD approach may be considered, stand out as being of special interest; for heavy vector mesons ($J/\psi, \Upsilon$) it serves as a probe of the small–x (unintegrated) gluon distribution, see for example [118], as well as of models of gluon saturation. In addition, it has long been speculated that besides the C-even predominantly imaginary Pomeron exchange, the Regge-phenomenology of strong interactions at high energies would feature a C–odd, dominantly real, trajectory, known as the Odderon (see for example [124–126]). This exchange is experimentally very elusive, and as of yet no firm evidence for it exists, but it should in general contribute to the vector meson CEP cross section (via $OI\!P \to X$); thus measurements of exclusive vector meson production could constitute the first clear experimental evidence for the Odderon. A further process that may be studied is the photoproduction of Z boson: this would represent a completely new observation and can provide a test of the pQCD model of the production mechanism. Further details of all of the topics discussed above can be found in the following sections.

5.4.2 Forward proton tagging: phenomenological insight and advantages

One process discussed in e.g. [127], for which proton tagging is particularly beneficial, is the exclusive production of lepton pairs. This purely QED cross section is known theoretically to very high, sub 1% level, precision, and so represents a potential luminosity monitor. Achieving this level of theoretical precision, and in particular the high insensitivity to the effect of additional proton–proton soft rescatterings, relies crucially on the fact that the interaction is truly exclusive, that is the protons remain intact after the collision. Proton tagging is the only way to select such purely exclusive events. On the other hand, achieving this level of precision in the experimental measurement may be challenging due to the effect of systematic errors, and the relatively low cross sections within the invariant mass acceptance of the tagging detectors during high luminosity running.

Proton tagging can also provide an additional handle regarding the Odderon, the C–odd partner of the Pomeron, discussed above. It has been shown [128] that any contribution of the Odderon to the vector meson photoproduction cross section suffers from important uncertainties and may be hard to disentangle from the photon–exchange contribution. On the other hand, a firm prediction is that the distribution with respect to the proton (or meson) transverse momentum $p_\perp$ should be much harder in the Odderon case, and so a measurement of this distribution, in particular at larger $p_\perp$ values, could provide evidence for the Odderon. However, at large $p_\perp$ the probability that the interacting proton will dissociate rapidly increases, and so such a mea-

surement would be very challenging using rapidity gap based selection techniques. By tagging the protons, this dissociative contribution can be effectively eliminated, and a clean probe of the Odderon provided. In addition, as discussed in [74], by measuring the proton $p_\perp$ distribution it may be possible to distinguish between models with and without gluon saturation effects. In particular, as a result of unitarity features of the colour dipole amplitude in the saturation regime, there is expected to be a pronounced dip (or multiple dips) in the higher $p_\perp$ region. The observation of these dips, for which proton tagging is clearly essential, would represent clear evidence in favour of such models.

5.4.3 Two-photon collisions

Motivation and theory

Two–photon production in pp collisions is described in the framework of Equivalent Photon Approximation (EPA) [112, 113, 130]. The almost real photons (with low photon virtuality $Q^2 = -q^2$) are emitted by the incoming protons, producing an object X in the $pp \to pXp$ process, through two–photon exchange $\gamma\gamma \to X$. The photon spectrum of virtuality Q^2 and energy E_γ is proportional to the Sommerfeld fine–structure constant α and reads (in the lab frame)

$$\mathrm{d}N = \frac{\alpha}{\pi}\frac{\mathrm{d}E_\gamma}{E}\frac{\mathrm{d}Q^2}{Q^2}\left[\left(1-\frac{E_\gamma}{E}\right)\left(1-\frac{Q^2_{min}}{Q^2}\right)F_E + \frac{E_\gamma^2}{2E^2}F_M\right], \tag{5.13}$$

where E is the energy of the incoming proton of mass m_p, $Q^2_{min} \equiv m_p^2 E_\gamma^2/[E(E-E_\gamma)]$ is the photon minimum virtuality allowed by kinematics and F_E and F_M are functions of the electric and magnetic form factors. They read in the dipole approximation [130]

$$F_M = G_M^2 \qquad F_E = (4m_p^2 G_E^2 + Q^2 G_M^2)/(4m_p^2 + Q^2) \qquad G_E^2 = G_M^2/\mu_p^2 = (1+Q^2/Q_0^2)^{-4}\,. \tag{5.14}$$

The magnetic moment of the proton is $\mu_p^2 = 7.78$ and the fitted scale $Q_0^2 = 0.71$ GeV^2. The electromagnetic form factors are steeply falling functions of Q^2: for this reason the two–photon cross section can be factorized into a sub–matrix element and two photon fluxes.

The theoretical framework described above is firmly established, and in principle allows pure QED two–photon collision processes to be described to a high degree ($\lesssim 0.1\%$) of accuracy. As discussed in Section 5.4.2, this presents the possibility of using exclusive di-lepton production, which proceeds via this mechanism, as a luminosity monitor at the LHC if the systematics are low enough. Alternatively, this accurate knowledge of the two–photon initial state allows such processes to be used as effective probes of BSM physics. In particular, as discussed in Section 5.5.3, this can provide by far the most stringent probe that is currently possible of triple and quartic anomalous gauge boson couplings, as well as providing a complementary measurement of SM gauge boson pair production.

Finally, as discussed in [44], while, due to the peripheral nature of the interaction, the probability of additional soft proton–proton interactions, which generate the soft survival factor, is very small, this is only the case provided proton dissociation can be effectively eliminated. Conversely, if proton dissociation is allowed in the event selection then such processes can provide a differential probe of the soft survival factor, for example by measuring the region of higher $p_\perp(l^+l^-)$ in quasi–exclusive lepton pair production. Here, the deviation of the observed cross section from simulations including proton dissociation, but which do not include soft survival effects, can be evaluated. Such deviation has already been seen in the CMS measurement [131] of $\gamma\gamma \to \mu\mu$, performed in the context of a $\gamma\gamma \to WW$ analysis.

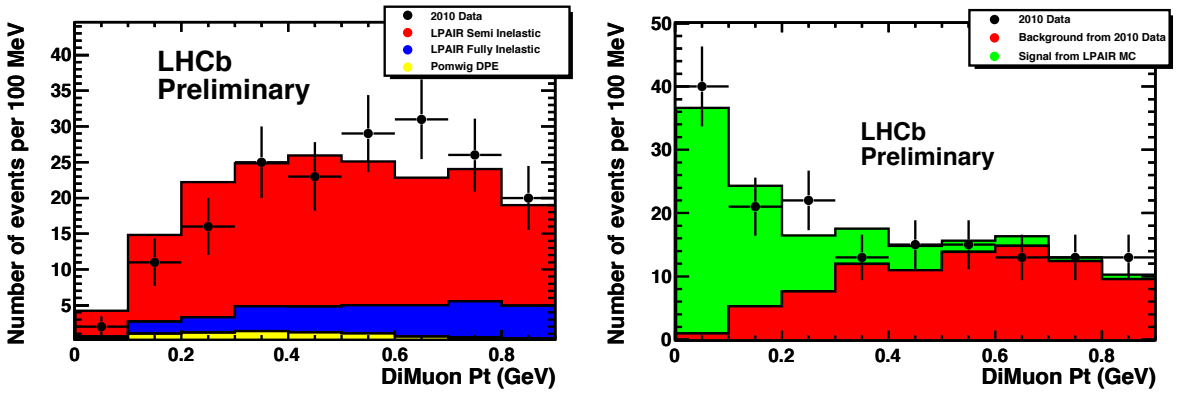

Fig. 5.1: Transverse momentum of di-muons that have an invariant mass above 2.5 GeV and are not consistent with vector meson production. The plot on the left shows events with more than two tracks compared to expectations for inelastic di-muon production. The plot on the right shows events with exactly two tracks and no other activity inside the LHCb detector. The shape of the signal is taken from LPAIR. The background shape is taken from the data in the left-hand plot.

A preliminary measurement of the cross section for muon pairs produced through two-photon fusion has been made by the LHCb collaboration [39] using the small 2010 data sample of 37 pb^{-1}. The selection is as described in Sec. 5.4.4 and the candidate events are those in Fig. 5.11, with masses above 2.5 GeV but outside mass windows around the vector meson resonances. To determine the elastic CEP component, a fit to the transverse momentum distribution is made, using a template shape from the LPAIR simulation [133, 134] to describe the elastic signal events and using data, (low multiplicity di-muon candidates that have additional tracks) to describe the background. A comparison of this data-driven background estimate to the simulation of inelastic di-muon production, where one or both protons dissociate, shows good agreement (see the left plot in Fig. 5.1,) albeit with rather large uncertainties due to the limited statistics. The fit to the signal candidates in the right plot of Fig. 5.1 also shows good agreement and an almost pure sample of di-muons from elastic di-photon fusion is obtained when requiring the p_T of the pair to be below 100 MeV. A cross section times branching fraction estimate of 67 ± 19 pb for both muons produced inside the LHCb acceptance is in agreement with the theoretical prediction of 42 pb, but is a long way from the aim of a few-percent measurement.

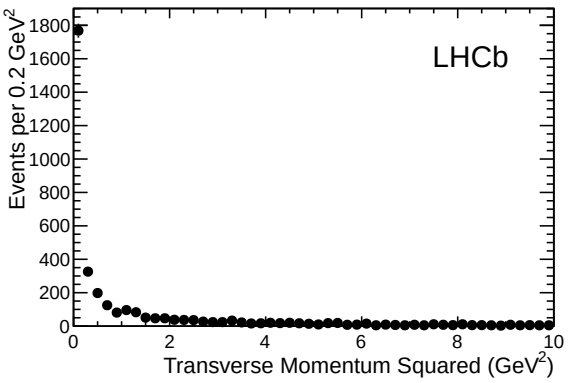

Fig. 5.2: Transverse momentum squared of di-muons with an invariant mass between 6 and 9 GeV.

There are only 40 candidates with $p_T < 100$ MeV in the analysis of 37 pb^{-1} of data, but

improvements to the trigger and a reduction in the average number of proton-proton interactions per beam crossing suggest that about 10,000 candidates are available in the 3 fb^{-1} of data taken in 2011 and 2012, sufficient for a 1% statistical measurement. Fig. 5.2 shows the p_T^2 distribution for di-muon candidates with an invariant mass between 6 and 9 GeV in about 3 fb^{-1} of data taken at $\sqrt{s} = 7$ and 8 TeV. The strong peak below 0.2 GeV^2 is characteristic of the QED process. Note that the distribution falls off much more rapidly than the $\approx \exp(-6p_T^2)$ dependence for the J/ψ in Fig. 5.13. An estimate of how much signal there is in the first bin requires a complete description of the spectrum.

Measurements of $\gamma\gamma \to \mu\mu$ [135] and $\gamma\gamma \to ee$ [59] production at $\sqrt{s} = 7$ TeV were also performed by CMS using 40 pb^{-1} and 36 pb^{-1} of data, respectively[3] In the e^+e^- channel events were selected by requiring two electrons with $E_T > 5.5$ GeV, no additional charged tracks, and no unassociated activity in the calorimeters above the noise threshold. A dedicated trigger was employed to maintain a low electron threshold throughout the data-taking period. The background, extrapolated from the sideband region in the calorimeter tower and track multiplicities, was determined to be 0.85 ± 0.28 events. In the data 17 events were observed, in agreement with the LPAIR prediction of 16.3 ± 1.3 events from the sum of elastic and proton dissociation production. In the $\mu^+\mu^-$ channel events were selected by requiring two muons with $p_T > 4$ GeV, $|\eta| < 2.1$, and $m(\mu\mu) > 11.5$ GeV, with no other charged tracks associated to the dimuon vertex. This selection method allowed for a much higher efficiency in the presence of pile up, compared to the CMS e^+e^- analysis. A template fit to the $p_T(\mu\mu)$ distribution was then performed, to extract the elastic component of the cross section. The resulting fiducial cross section was $3.38^{+0.58}_{-0.55}(\text{stat.}) \pm 0.16(\text{syst.}) \pm 0.14(\text{lumi.})$ pb, consistent at the $\sim 1\sigma$ level with the LPAIR prediction. In both the e^+e^- and $\mu^+\mu^-$ channels, the shapes of the single lepton and pair distributions were observed to be in good agreement with the predictions. In the context of the CMS $\gamma\gamma \to WW$ analysis, high-mass $\gamma\gamma \to \mu\mu$ events were also analyzed using a much larger sample of 5 fb^{-1} in order to study the proton dissociation contribution, as well as the effects of pile up on the selection [131].

Finally, one should note that exclusive processes in the $\gamma\gamma$ channel are very promising to reveal the elusive Odderon discussed above. Indeed, consider the exclusive production of two $\pi^+\pi^-$ pairs. Since the $C-$parity of the amplitude describing this process is not fixed, both the Odderon and the Pomeron exchanges contributes. Considering charge asymmetries, one can therefore build an observable which involves the interference of Odderon and Pomeron, and thus linear in the tiny Odderon contribution [132].

5.4.4 Diffractive photoproduction $\gamma p \to V p$

Motivation and theory: available models

Two largely equivalent approaches to modelling the exclusive photoproduction of a vector meson of mass M_V at a γp center-of-mass energy W, applicable at small values of $x = M_V^2/W^2$, are the color-dipole approach and k_T-factorization. Within the color-dipole framework (see e.g. [19, 117, 137] and references therein), the amplitude depicted in Fig. 5.3 takes the form

$$A_T^{\gamma p \to E+p}(x,\vec{\Delta}) = \mathrm{i} \int \mathrm{d}^2\vec{r} \int_0^1 \frac{\mathrm{d}z}{4\pi} \int \mathrm{d}^2\vec{b}\, (\Psi_E^*\Psi_\gamma)_T\, \mathrm{e}^{-\mathrm{i}[\vec{b}-(1-z)\vec{r}]\cdot\vec{\Delta}}\, \frac{\mathrm{d}\sigma_{q\bar{q}}}{\mathrm{d}^2\vec{b}}\, \sqrt{(1+\beta^2)}, \qquad (5.15)$$

where z $(1-z)$ is the longitudinal momentum fraction of the quark (anti–quark), Δ denotes the transverse momentum lost by the outgoing proton ($t = -\Delta^2$) and x is the Bjorken variable.

[3] In the final stages of the preparation of this report, ATLAS have reported the measurement of exclusive e^+e^- and $\mu^+\mu^-$ production at $\sqrt{s} = 7$ TeV, where the muons (electrons) are required to have $p_\perp > 10(12)$ GeV, and in both cases $|\eta^l| < 2.4$. See [136] for details.

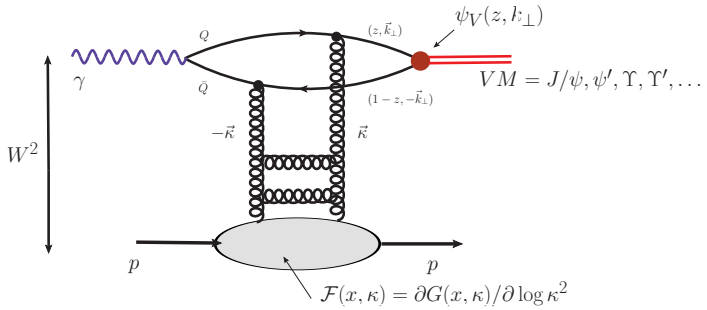

Fig. 5.3: Representative diagram for the exclusive $\gamma p \to V p$ production of a vector meson V.

The variable b is the transverse distance from the center of the target to the center of mass of the $q\bar{q}$ dipole and the factor in the exponential arises when one takes into account non-forward corrections to the wave functions [33]. The factor of $\sqrt{1+\beta^2}$ in (5.15) is a correction to account for the real part of the S-matrix element for dipole–proton scattering. A common ansatz for the differential dipole cross section for the $q\bar{q}$ pair to scatter elastically off the proton is given by [41]

$$\frac{\mathrm{d}\sigma_{q\bar{q}}}{\mathrm{d}^2\vec{b}} = 2\left[1 - \exp\left(-\frac{\pi^2}{2N_c} r^2 \alpha_S(\mu^2) R_g x g(x,\mu^2) T(b)\right)\right], \tag{5.16}$$

where the factor R_g relates the generalized gluon PDF (the same object introduced in (5.1)) that is relevant in this situation to the standard diagonal gluon PDF, see [12, 32]. The scale μ^2 is related to the dipole size r by $\mu^2 = 4/r^2 + \mu_0^2$. In the case of exclusive production in pp, pA or AA collisions the photoproduction regime $Q^2 \approx 0$ prevails, so that for example for J/ψ photoproduction the hard scale is $\sim 2.4\,\mathrm{GeV}^2$. It is worth noting that such a scale is quite close to what one may expect for a saturation scale, e.g. in the case of a heavy nucleus. These saturation effects manifest themselves in the small-x behaviour of the (unintegrated) gluon and therefore mainly affect the energy dependence of the photoproduction cross section. Finally, other approaches to modelling the dipole cross section exist in the literature, see e.g. [19] for phenomenological studies.

A related approach is given by the k_T-factorization representation of the forward amplitude, see [142] for a detailed discussion and references . The imaginary part of the amplitude for the $\gamma p \to V p$ process, for vanishing transverse momentum transfer $\Delta = 0$, can then be written as a convolution of an impact factor for the $\gamma \to V$ transition and the unintegrated gluon distribution of the target:

$$\begin{aligned}\Im m\, \mathscr{M}_{\lambda_\gamma,\lambda_V}(W,\Delta^2=0) = W^2 \frac{c_\Upsilon \sqrt{4\pi\alpha_{em}}}{4\pi^2} \int \frac{d^2\kappa}{\kappa^4} \alpha_S(q^2) f_g(x_1,x_2,\kappa) \\ \times \int \frac{dz d^2k}{z(1-z)} \psi_V(z,k)\, I_{\lambda_\gamma,\lambda_V}(z,k,\kappa)\,,\end{aligned} \tag{5.17}$$

Here, the unintegrated gluon distribution $f_g(x_1,x_2,\kappa_1)$ is again the same off-diagonal ("skewed") object introduced in (5.1), which as above can be reconstructed from the diagonal one. The explicit expressions for $I_{\lambda_\gamma,\lambda_V}$ can be found in [142]. For heavy vector mesons, helicity–flip transitions may be neglected, so that one can safely take $\lambda_\gamma = \lambda_V$.

Besides the unintegrated gluon distribution the second important non–perturbative input, in both the colour dipole and $k_\perp$ factorisation approaches, is the ("radial") light-cone wave

function $\psi_V(z,k)$ of the vector meson. The relativistic vertex $V \to Q\bar{Q}$ for an S–wave vector meson is [118, 143, 144]:

$$\varepsilon_\mu \, \bar{u}(p_Q)\Gamma^\mu v(p_{\bar{Q}}) = [M^2 - M_V^2] \, \psi_V(z,k^2) \, \bar{u}(p_Q)\Big(\gamma^\mu - \frac{p_Q^\mu - p_{\bar{Q}}^\mu}{M+2m_Q}\Big)v(p_{\bar{Q}})\,\varepsilon_\mu \,, \tag{5.18}$$

where ε_μ is the polarization vector of the vector meson. and $p^\mu_{Q,\bar{Q}}$ are the on-shell four–momenta of the $Q,\bar{Q}$ quarks, $p^2_{Q,\bar{Q}} = m_Q^2$. The invariant mass of the $Q\bar{Q}$ pair is given in terms of light-cone variables as

$$M^2 = \frac{k^2 + m_Q^2}{z(1-z)} \,. \tag{5.19}$$

The radial wave–function $\psi_V(z,k^2)$ can be regarded as a function not of z and k independently, but rather of the three–momentum $\vec{p}$ of, say, the quark in the rest frame of the $Q\bar{Q}$ system of invariant mass M, $\vec{p} = (k, (2z-1)M/2)$. Then,

$$\psi_V(z,k^2) \to \psi_V(p^2) \,, \frac{dz d^2k}{z(1-z)} \to \frac{4\,d^3\vec{p}}{M} \,, p^2 = \frac{M^2 - 4m_Q^2}{4} \,. \tag{5.20}$$

It is assumed that the Fock–space components of the V–states are exhausted by the two-body $Q\bar{Q}$ components. In the absence of first-principles calculations of the light-cone wave function, different phenomenological models are available [142]. For example, the Gaussian, harmonic–oscillator–like wave functions:

$$\psi_{1S}(p^2) = C_1 \exp\left(-\frac{p^2 a_1^2}{2}\right) \,, \psi_{2S}(p^2) = C_2(\xi_0 - p^2 a_2^2)\exp\left(-\frac{p^2 a_2^2}{2}\right) \,, \tag{5.21}$$

and the Coulomb–like wave functions, with a slowly decaying power–like tail:

$$\psi_{1S}(p^2) = \frac{C_1}{\sqrt{M}} \frac{1}{(1+a_1^2 p^2)^2} \,, \psi_{2S}(p^2) = \frac{C_2}{\sqrt{M}} \frac{\xi_0 - a_2^2 p^2}{(1+a_2^2 p^2)^3} \,. \tag{5.22}$$

The parameters a_i^2 are obtained from fitting to the e^+e^- decay widths, whereas ξ_0, and therefore the position of the node of the $2S$ wave function, is obtained from the orthogonality of the $2S$ and $1S$ states.

While (5.17) is written for the case of zero momentum transfer Δ, the full amplitude, at finite momentum transfer within the diffraction cone, is given by

$$\mathscr{M}(W,\Delta^2) = (i+\beta)\,\Im m\mathscr{M}(W,\Delta^2=0)\exp(-B(W)\Delta^2/2) \,, \tag{5.23}$$

where β accounts for the real part of the scattering amplitude, as in (5.15), while $B(W)$ is the energy–dependent slope parameter:

$$B(W) = B_0 + 2\alpha'_{eff}\log\left(\frac{W^2}{W_0^2}\right) \,, \tag{5.24}$$

where B_0 depends on the vector meson in question, whereas α'_{eff} can be taken as universal in the present applications.

In going from γp to pp collisions (see Fig. 5.4), there are two complications. Firstly, either of the colliding protons can emit the photon, and the amplitudes for these two processes

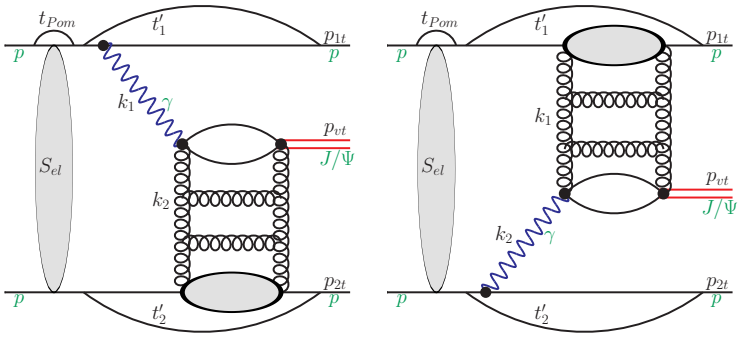

Fig. 5.4: Diagrams representing the two interfering amplitudes for the $pp \to ppJ/\psi$ process, including absorptive corrections.

interfere. This interference mainly affects the transverse momentum distributions. In the Born approximation, the interference contribution will cancel after azimuthal integration but in the presence of absorption, a small effect of the interference can remain. Secondly, as for all central exclusive diffractive processes, the fact that protons may also interact strongly must be taken into account, i.e. the gap survival probability [14–18] discussed in Section 5.3.1. The effects of gap survival are however expected to be much weaker than for the purely QCD process, due to the peripheral nature of the photon exchange. See [5, 115, 116] for further discussion of these points.

Motivation and theory: predictions

A selection of results for the rapidity spectrum of exclusive vector mesons at Tevatron and LHC energies are now presented. At Tevatron energies and at central rapidities, the subprocess energies for $\gamma p \to Vp$ or $\gamma\bar{p} \to V\bar{p}$ cover the known HERA domain. At LHC energies, it is possible to extend the energy range beyond the one already studied at HERA. For example, for J/ψ production at central rapidity $y = 0$, we have $W_{\gamma p} \sim 140\,\text{GeV}$, whereas at $y = 4$ this extends to $W_{\gamma p} \sim 1\,\text{TeV}$.

Considering first numerical results from a recent work [145–148] based on the k_T-factorization formalism, in Fig. 5.5 the predicted vector meson rapidity distributions at the Tevatron and LHC are shown. The first measurement of exclusive J/ψ production was made by the CDF collaboration at the Tevatron [45], and this data point is also shown. At the LHC, data for exclusive $J/\psi, \psi'(2S)$ have been obtained by the LHCb collaboration [47, 149]. In Fig. 5.6, the predicted rapidity distributions of J/ψ compared to these data [47] are shown. In the first two panels from the left, the results for two different unintegrated gluon distributions are shown. In the first panel, the gluon from [150] is used while in the second panel one of the distributions from [115] is used. Both these distributions describe the HERA data for F_2 well, but the latter is obtained from a nonlinear evolution equation which accounts for the physics of gluon saturation at small x. The former, Ivanov-Nikolaev, gluon does not include explicit saturation effects. We observe that the data appear to prefer the gluon distribution including saturation effects. On the other hand in the rightmost panel, a calculation using a fit to the vector meson production amplitude by the H1-collaboration, used in [115], and simply extrapolated to LHC energies, is shown. It describes the data quite well, and being an effective Pomeron-pole approximation casts some doubt on the saturation interpretation.

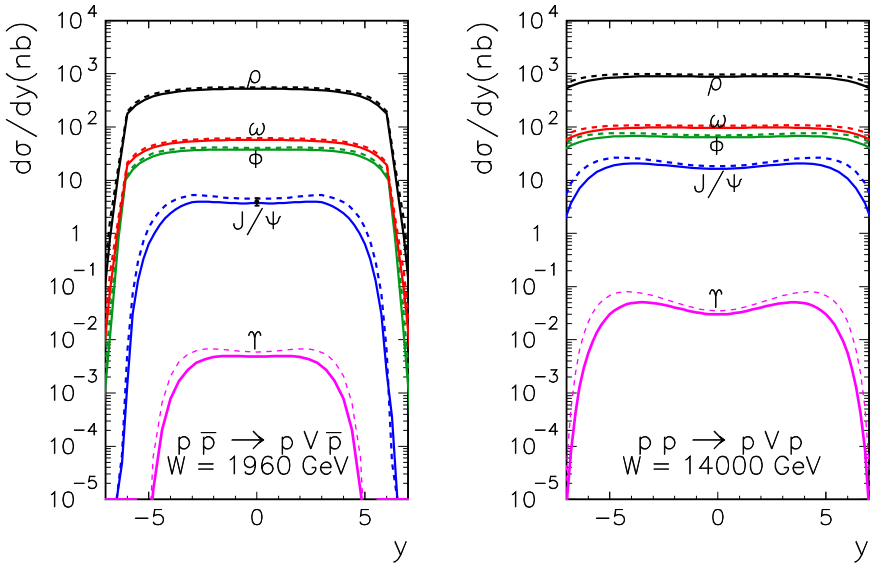

Fig. 5.5: Rapidity dependence of central exclusive vector meson production in proton-(anti)proton collisions. Left panel: proton-antiproton collisions at $\sqrt{s}$ =W=1960 GeV. Right panel: proton-proton collisions at $\sqrt{s}$ =W=14 TeV. The left panel also shows the data point from the CDF collaboration. Dashed lines are without absorptive corrections, while solid lines include them.

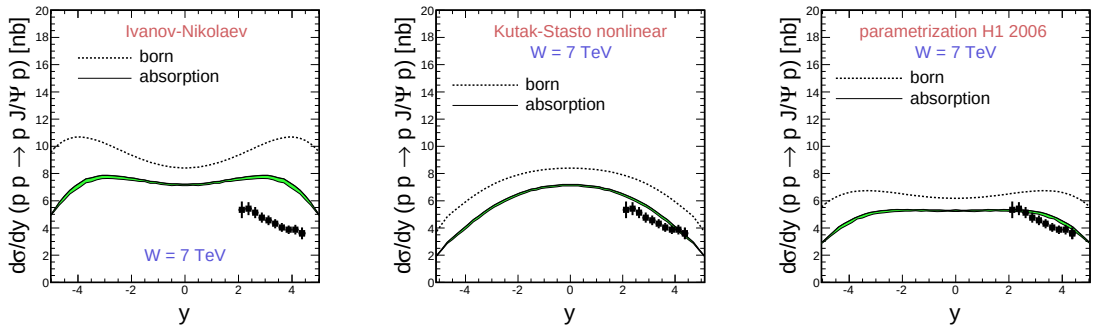

Fig. 5.6: J/ψ rapidity distribution calculated with the inclusion of absorption effects (solid line), compared to the Born result (dashed line) for $\sqrt{s}$ = 7 TeV. The LHCb data points from [47] are shown for comparison.

In Fig. 5.7 the predicted rapidity distribution for the $\psi'(2S)$ production is shown. Again it is seen that the gluon from [115] gives a very good description of the data. It should be added that these calculations use the Gaussian-type wave function of the vector meson, which is strongly favoured by the $\psi'(2S)$ data. It should be emphasised that only the k_T-factorization or color dipole approaches make reliable predictions for the production of excited vector meson states. Such predictions cannot be obtained in the collinear approach, and it is worth stressing that the convolution of impact factor with unintegrated gluon cannot be simply reduced to a choice of the scale in the collinear gluon distribution.

In the future it will be important to include proton dissociative processes in theoretical models, which generally concentrate on the exclusive case. On the γ-side one can proceed

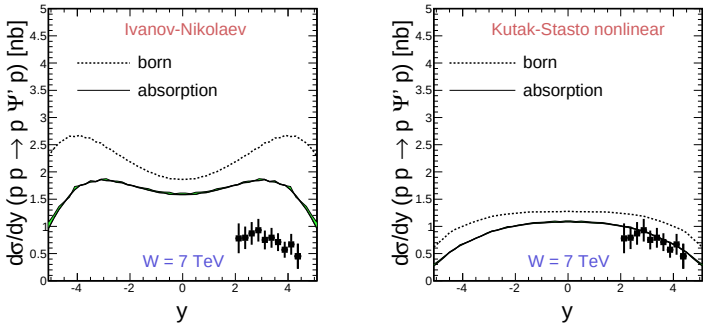

Fig. 5.7: ψ' rapidity distribution calculated including absorption effects (solid line), compared with the result when absorption effects are ignored (dotted line) for $\sqrt{s} = 7$ TeV. The LHCb data points from [47] are shown for comparison.

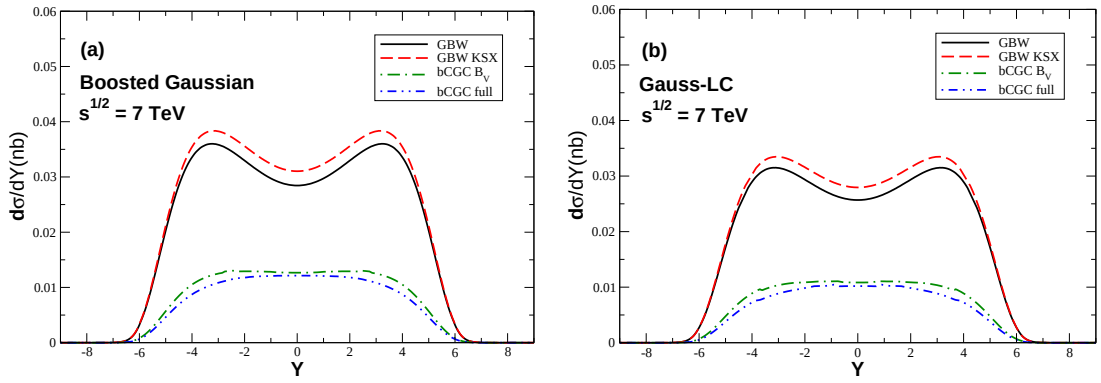

Fig. 5.8: (Color online) Exclusive Υ photoproduction in pp collisions at $\sqrt{s} = 7$ TeV.

analogously to [152] (the $p \to \gamma\Delta^+$ transition has recently been included in [123]). A treatment of the Pomeron side requires a better understanding of the quasi-diffractive $\gamma p \to J/\psi X$ process, as well as a coupled channel treatment of absorptive corrections.

As previously noted, the results presented above are from the recent work of [145–148], based on the k_T-factorization formalism. However, it is also possible to model the photoproduction process using the color dipole approach, see for example [19, 60, 117]. In Figs. 5.8 and 5.9 the predicted rapidity distributions for exclusive Υ photoproduction at $\sqrt{s} = 7$ TeV and $\sqrt{s} = 14$ TeV, respectively, are shown using the colour dipole approach (see [154]). Here 'bCGC' and 'GBW' correspond to two alternative phenomenological models for the dipole cross section introduced in (5.15). In addition the results from approximate and more precise evaluations of the t–dependence of the cross section are given, and for two different forms of the meson wave functions ('Boosted Gauss' and 'Gauss-LC'), defined in [19]. While there is some difference between the choices of wave functions, the variation between the different models of the dipole cross section are dramatic. The 'bCGC' is mildly disfavoured by (low statistics) HERA measurements but LHC data on Υ photoproduction can greatly clarify this.

A complementary approach, using the same $k_\perp$ factorisation formalism described in the previous sections, but differing in some elements, is described in [118, 144]. Simple parametric forms for the low–x gluon PDF fitted to the existing data from HERA and LHCb, and both a LO and a NLO–type fit are considered; in the latter case this is not the result of a full NLO

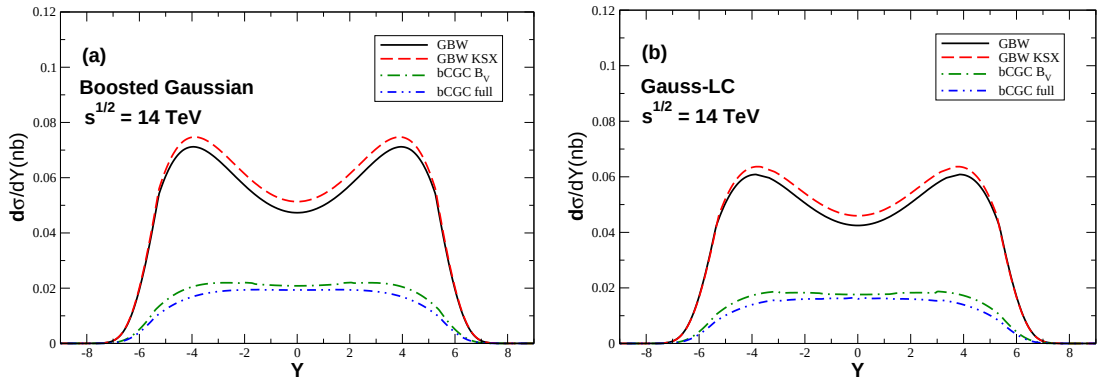

Fig. 5.9: (Color online) Exclusive Υ photoproduction in pp collisions at $\sqrt{s} = 14$ TeV.

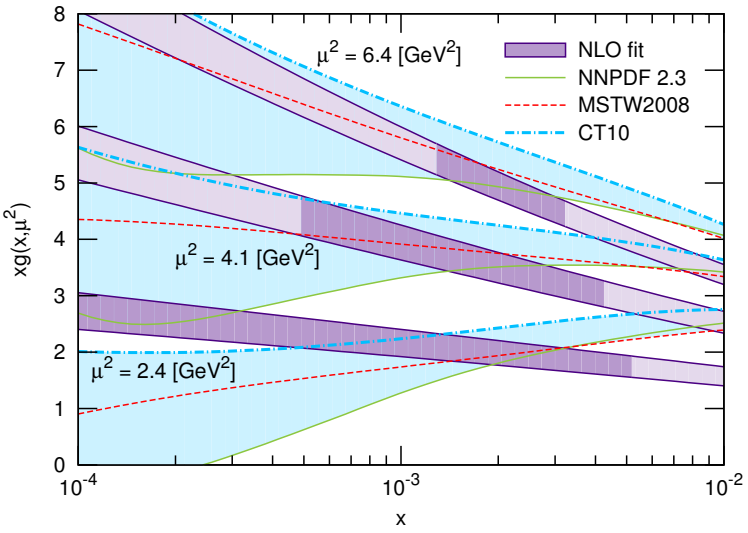

Fig. 5.10: NLO gluon resulting from a fit to the available HERA and LHCb data on J/ψ photoproduction, taken from [118].

calculation, but rather the form of the gluon is chosen so as to reproduce the effect of NLO DGLAP evolution. Such an approach is motivated by the large uncertainty in the low–x, low–Q^2 gluon that results from global parton analyses, and conversely highlights the way in which such processes can help reduce this uncertainty, as is shown in Fig. 5.10. This fit then allows predictions for the cross sections and rapidity distributions at higher energies, and for other processes such as exclusive Υ and $\psi(2S)$ photoproduction, to be given. In all cases a full treatment of soft survival effects, and in particular the rapidity (i.e. W) dependence of the survival factor is given, which as seen above, must be included for a precise comparison to data in hadronic collisions. Finally, it should be noted that a proper inclusion of the 'skewedness', i.e. the relation between the off-diagonal gluon in 5.17 and the standard gluon PDF, for the case that the gluon is unintegrated over the parton transverse momentum, as in the $k_\perp$–factorization approach, may be of some importance in future high–precision theoretical work [12]. It is worth emphasising that measurements of the ratios of these cross sections at different $\sqrt{s}$ values would be particularly sensitive to the gluon PDF in this low$-x$ and Q^2 region, with other uncertainties due to e.g. soft survival effects, largely cancelling in this ratio.

Finally, in the case of photoproduction processes with the momentum transfer square

playing the role of the hard scale, one can perform a systematic analysis of this process based on the twist expansion of meson distribution amplitude in an analogous way as it was done in [119, 120] for meson hard electroproduction at HERA. One should note that such a twist expansion can be done in the color dipole picture [121], offering a natural way for including saturation effects [122].

In addition to these lighter vector mesons states, exclusive Z-boson photoproduction is also accessible at the LHC, but only in high luminosity running. This proceeds via an interesting "vertex", actually a loop diagram, with electromagnetic, strong and weak lines together. The process $\gamma\gamma \to Z$ is forbidden by the Landau-Yang theorem, and so this photoproduction process naturally dominates. The central $e^+e^-, \mu^+\mu^-$ or $\tau^+\tau^-$ pairs have $p_T \lesssim 2$ GeV and so $(\Delta\phi(\ell^+\ell^-) - 180^\circ) < 1^\circ$, with no other tracks associated with the vertex.

The Z photoproduction cross section at the LHC in both pp and heavy ion collisions has been calculated in [117, 155]. The virtual photon fluctuates into a $q\bar{q}$ pair (a colour dipole), which scatters off the proton diffractively by two-gluon exchange and recombines as a Z. The wave functions and the dipole-proton cross sections are reasonably well known from HERA photoproduction data, and consequently Z-photoproduction can be considered as a good test of pQCD (due to the high Z-mass scale). The largest uncertainty is the gap survival probability; such measurements would therefore be sensitive to such soft survival effects. The prediction of [117] is, for Z production at the LHC, $\frac{d\sigma}{dy}(y = 2.5) = 1.7$ fb, and 1.4 fb at $y = 0$. The prediction of [155] is in agreement; for $\sqrt{s} = 14$ TeV it is 11 fb for all $y(Z)$, and $\frac{d\sigma}{dy}$ peaks at $|y| = 3$.

Measuring the process with both protons detected requires forward proton detectors at 420 m, but with CT-PPS Stage 1 or AFP at $z \sim 220$ m, and a Z boosted to $2 \lesssim |y_Z| \lesssim 3$ one proton can be measured. If the event is really exclusive the proton momentum is well known from $p_z(Z)$, even if the other proton dissociates. However, allowing for the Z branching fractions of only 3.63% for each of the e^+e^- and $\mu^+\mu^-$ channels, an observation of this process is challenging, but could be possible in a large enough data sample. For example, assuming an efficient trigger, which should include a proton tag, the prediction gives $24 \times A \times f$ events in 100 fb^{-1} of integrated luminosity, where A is the acceptance and efficiency, and $f \sim 1.5 - 2$ is a factor allowing the other proton to dissociate. A control of the background is provided by considering $W \to e/\mu + \not{E}_T$ candidates, which cannot occur exclusively.

Experimental results and outlook

The LHCb collaboration has made two measurements of J/ψ and $\psi(2S)$ production at $\sqrt{s} = 7$ TeV, one with an integrated luminosity of 37 pb^{-1} (2010 data) [149], and one with 930 pb^{-1} (2011 data) [47][4]. The selection starts by triggering on low multiplicity events containing two muons. The events are then selected as exclusive inside the LHCb acceptance by requiring no additional charged tracks or neutral deposits in the detector. The invariant mass of the two muons after the trigger and after the selection is shown in Fig. 5.11 for the 37 pb^{-1} sample. Within a falling continuum, there are clear signals after the trigger requirements for several vector mesons: $\phi, J/\psi, \psi(2S), \Upsilon(1S), \Upsilon(2S)$. With the additional exclusivity requirements, only charmonia signals remain visible in this limited data sample. Candidate events for J/ψ and $\psi(2S)$ mesons in the larger 930 pb^{-1} sample can be seen in Fig. 5.12.

Three backgrounds are considered in extracting the elastic signal: non-resonant di-muon production, feed-down from other mesons and inelastic J/ψ production. The non-resonant background is determined from the fit shown in Fig. 5.12. Feed-down is only considered for the

[4] In the final stages of the preparation of this report, LHCb have reported a measurement of exclusive $\Upsilon \to \mu + \mu^-$ production at $\sqrt{s} = 7$ and 8 TeV, see [156] for details.

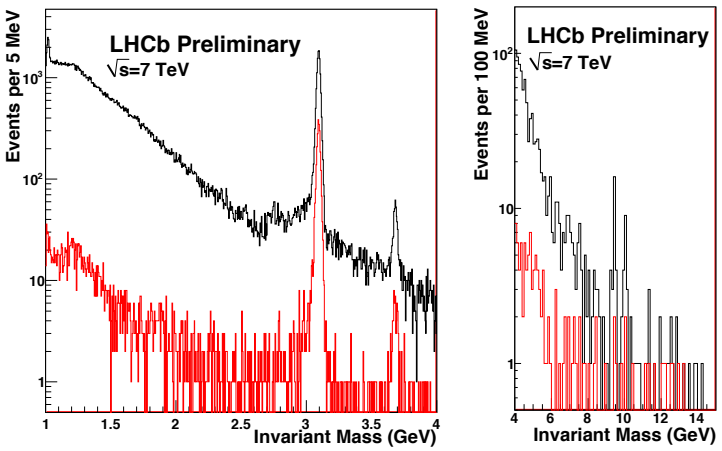

Fig. 5.11: Invariant mass of di-muons in 37 pb^{-1} of data after the low-multiplicity di-muon trigger (black) and after requiring no other activity inside LHCb (red). The discontinuity at 2.5 GeV is due to a trigger threshold.

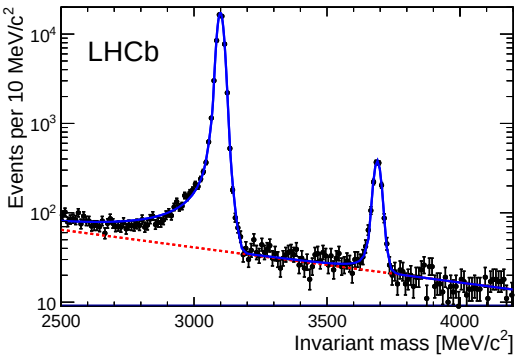

Fig. 5.12: Invariant mass of selected di-muon candidates in 930 pb^{-1} of data.

J/ψ selection and can come from $\chi_{c0}, \chi_{c1}, \chi_{c2}$ or $\psi(2S)$ decays, with the other decay products being below the threshold for detection or outside the LHCb acceptance. Feed-down from $\chi_c \to J/\psi\gamma$ is evaluated to be $(7.6 \pm 0.9)\%$ by selecting events in which the photon is seen and using the simulation to estimate the number of events in which it would be undetected. Feed-down from the decays $\psi(2S) \to J/\psi X$ is estimated from the simulation, which has been normalised to the observed number of events from the decay $\psi(2S) \to \mu\mu$, and contributes $(2.5 \pm 0.2)\%$ of the J/ψ sample.

The third background source is the largest and is also the most poorly determined for this analysis and all other analyses of the same kind that LHCb has performed. This consists of centrally produced J/ψ or $\psi(2S)$ mesons that appear exclusive inside the LHCb acceptance, but have activity outside of the active area of the detector, originating either from additional gluon radiations or low mass diffractive dissociation of one or both protons. Assuming that the p_T^2 distribution for both the elastic and inelastic components can be described by exponential functions, $\exp(-bp_T^2)$, a fit to the data is performed to determine the b values and the relative sizes of both components. The results are shown in Fig. 5.13 and an overall purity of 0.592 ± 0.012 is obtained for the J/ψ sample and 0.52 ± 0.07 for the $\psi(2S)$ sample. It is also worth noting that the fitted b values are consistent with the photoproduction results from the H1 collabora-

tion [44], once the difference in the centre-of-mass of the photon-proton system has been taken into account.

The ALICE collaboration have reported in [46] a measurement of coherent J/ψ photoproduction in ultra peripheral p–Pb collisions at $\sqrt{s_{NN}} = 5.02$ TeV. Results are selected with a dimuon pair produced either in the rapidity interval, in the laboratory frame, $2.5 < y < 4$ (p–Pb) or $-3.6 < y < -2.6$ (Pb–p), and with no other particles observed in the ALICE acceptance. The data were found to be consistent with a power law dependence of the J/ψ photoproduction cross section in γp energies from $W_{\gamma p} \sim 20 - 700$ GeV, and with results that are consistent with the LHCb measurement.

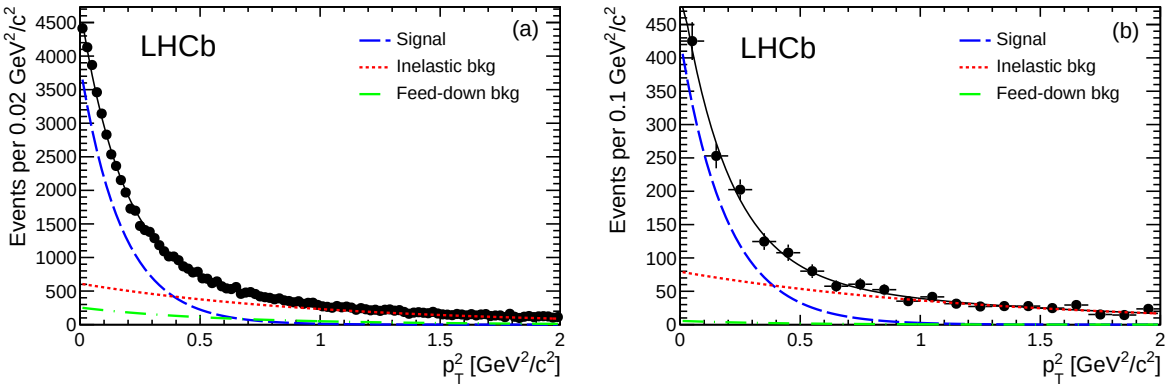

Fig. 5.13: Transverse momentum squared of (a) J/ψ and (b) $\psi(2S)$ candidates. The fitted contributions from the CEP signal, the inelastic and feed-down backgrounds are indicated in the legend.

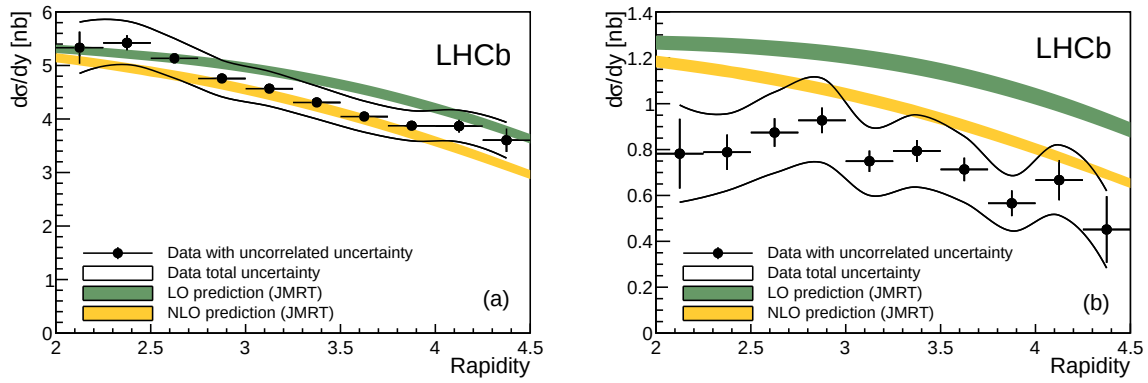

Fig. 5.14: Differential cross section for (a) J/ψ and (b) $\psi(2S)$ compared to LO and NLO predictions.

After correcting for the LHCb data for detector efficiency and acceptance, the differential cross section as a function of rapidity, y, is calculated and is shown in Fig. 5.14 compared to predictions at LO and 'NLO' from Refs. [118,144], see also Fig. 5.10. The 'NLO' calculation is not a full next-to-leading-order calculation but includes the dominant effects. The experimental points are plotted with their statistical and total uncertainties. Most of the total uncertainty is correlated bin-to-bin and so the overall shape is well determined by the data, which fits the 'NLO' predictions better than LO, for both the J/ψ and $\psi(2S)$ mesons.

The difference between the 'NLO' and 'LO' predictions becomes more pronounced in Υ production [118]. Analyses are ongoing at LHCb, using about 600 pb^{-1} of pile-up free Run–I data, to measure the CEP of Υ as well as other vector mesons such as ϕ and ω. Measurements

of the CEP of J/ψ and Υ mesons will be repeated at $\sqrt{s} = 13$ TeV and the ratio of these to measurements at $\sqrt{s} = 7$ TeV will provide important constraints on the gluon PDF at parton fractional momenta around $x \sim 10^{-5}$.

In addition to this rapidity gap based analysis there are also possibilities for future LHC measurements with tagged forward protons. It is worth emphasising that all of the existing measurements in hadronic collisions suffer from proton dissociation backgrounds; such a background can only be fully eliminated by tagging the outgoing protons. The possibility of such a measurement with CMS-TOTEM joint data taking is being actively pursued (the ATLAS–ALFA detector shows similar potential). To overcome efficiency losses in the muon reconstruction and triggering at low muon p_T's, the exclusive J/ψ analysis will be done on two charged-particle-only final states using the double arm RP triggered event sample without any muon identification requirement. In 5 pb^{-1} of integrated luminosity at high β^*, more than 1000 J/ψ candidates are expected in the $\mu^+\mu^-$ decay mode with little background. This will allow a detailed study of the azimuthal angular difference ϕ of the outgoing protons and for the p_T spectrum of the produced J/ψ meson to be determined, essentially without background, even at larger p_T's, where proton dissociation events dominate the existing measurements. As discussed in Section 5.4.2, the Odderon, the C-odd partner of the Pomeron, is predicted to significantly modify the large p_T part of the spectrum [128], which a CMS-TOTEM or ATLAS-ALFA measurement could test. Up to now there is no compelling experimental evidence for the existence of Odderon exchange, despite it being predicted by QCD.

5.5 Exploratory physics

The study of BSM signatures in the CEP channel, which usually have very low cross sections and signal to background ratios, can be very competitive with and complementary compared to standard LHC searches. In this section, some examples of such processes are given.

5.5.1 Search for invisible objects via the missing mass and momentum methods

Motivation and theory

CEP processes provide a possibility for simultaneous and precise measurements of the initial and final state kinematics, which can be used to search for events with missing mass or missing momentum signatures, see e.g. [159]. This opens up ways to search for new physics that might have escaped the searches of the general purpose detectors, CMS and ATLAS, e.g. in scenarios where the new physics couples dominantly or only to gluons.

Experimental results and outlook

A preliminary analysis has been performed on the data of the common CMS-TOTEM $\beta^* =$ 90 m run at $\sqrt{s} = 8$ TeV in July 2012, with a search for missing mass or missing momentum events performed on the existing data samples of double arm RP triggered and jet triggered events [160]. Only CEP events with a central mass, $M_{central}$, $\lesssim M_X$ are examined to avoid contamination from pile up events. $M_{central}$ is reconstructed from the sum of the CMS particle flow objects and the missing momentum, $\not{p}$, is reconstructed from the difference of the sum of the proton momenta and the sum of the momenta of the particle flow objects. The rapidity gaps, $\Delta\eta = -\ln \xi$, predicted by the proton ξ measurements (momentum loss fraction) are verified using the T2 detector with a rapidity coverage of $5.3 < |\eta| < 6.5$. To probe O(pb) cross sections for the two signal topologies described below, a statistics of double-arm RP-triggered and of jet-triggered events corresponding to an integrated luminosity of ~ 100 pb^{-1} is needed.

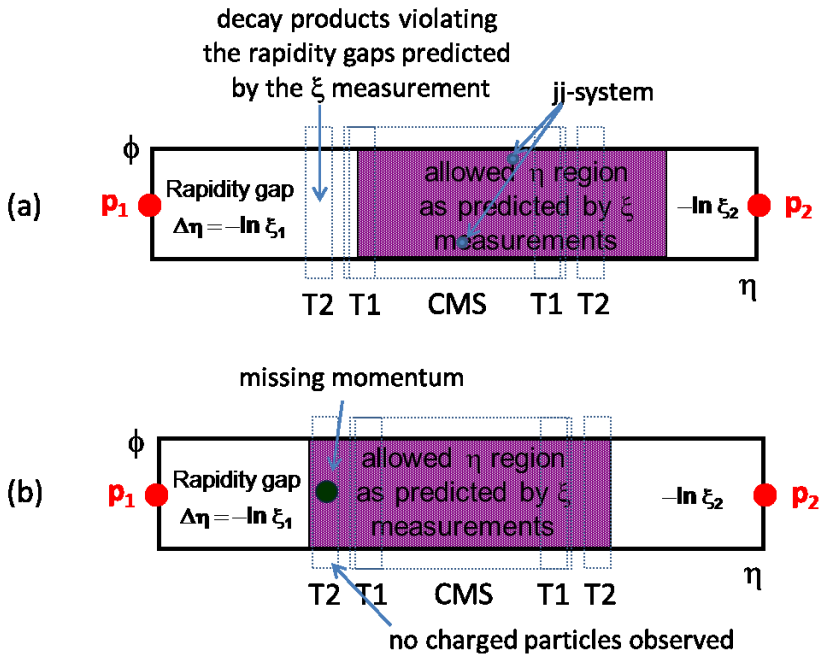

Fig. 5.1: Schematical drawings of the two event topologies used in the search for missing mass and momentum signatures in CEP events. (a) Events with charged particles in T2, violating the rapidity gaps predicted by the ξ measurement, from e.g. the decay of a CEP-produced particle. (b) Events with high missing momentum, pointing towards an η region with good CMS-TOTEM instrumentation and no charged particles or energy deposits observed in the η region where the missing momentum points. T2 η region is given as example; this could be due to a CEP-produced particle escaping undetected.

To verify the performance and the search methodology, control samples of events were selected both in double arm RP triggered and in the jet triggered samples with the following requirements: the presence of charged particles in T2, when allowed by the rapidity gaps predicted by the ξ measurements, and no charged particles in T2, when not allowed by the rapidity gaps predicted by the ξ measurements. Many such events, corresponding to standard CEP events, were found in both the double arm RP triggered and jet triggered data samples and these will be used for a determination of the inclusive CEP event and CEP jet cross sections, respectively. One such candidate in the jet sample with $M_{central} \approx M_X$ is shown in Fig. 5.14.

A first signal topology, depicted schematically in Fig. 5.1(a), are events with charged particles in T2 violating the ξ-predicted rapidity gaps. This could happen if a particle is created in the CEP reaction and some of its decay products go into the T2 η acceptance region. Such events would be used to search for the production of new particles by studying the M_X (and $M_X - M_{central}$) distributions. No candidate events were found in the available jet sample. Remaining single diffractive pile up and beam halo background makes the double-arm RP triggered sample unusable for such searches.

An even more striking signature is events with high missing momentum pointing towards the region with good CMS-TOTEM instrumentation ($|\eta| < 6.5$) and no charged particles or energy deposits in the η region close to where the missing momentum points. Fig. 5.1(b) depicts the case where the missing momentum points towards T2. This could happen if a particle is created in the CEP reaction and escapes the experimental apparatus, undetected in the T2 acceptance region. Events are rejected if more forward rapidity gaps than T2 ($|\eta| > 6.5$) would be allowed by the ξ measurements. This confines the search to the mass region between

a few times the combined resolution of the $M_{central}$ and M_X measurements and the maximal central mass allowed by the T2 acceptance. For $\sqrt{s}$ = 13 TeV, this implies a 150-600 GeV mass range. Events with missing mass up to 400 GeV were found in both the double arm RP and jet triggered data set at $\sqrt{s}$ = 8 TeV with background events expected from neutral particles escaping detection in the T2 acceptance region, due to "acceptance gaps" between the forward detectors as well as from $p+p \to N^* + X + p$ or $p + X + N^*$ reactions. In the latter case, one of the observed protons would come from a decay of a nucleon resonance, N^*, and the other decay products of the N^* would escape detection. With increased statistics, it is expected that these backgrounds will be modelled sufficiently well.

5.5.2 Searching for magnetic monopoles with forward proton detectors

Motivation and theory

One theoretical possibility which could produce the signal described in the previous section is the exclusive production of magnetic monopoles. The existence of magnetic monopoles has been discussed since the discovery of magnetism, although it is well established that all magnetic and electromagnetic phenomena surrounding us can be explained with electric charges and electric currents. However, while the existence of magnetic monopoles is not required, it is also not excluded. Our current understanding of electromagnetism is formulated in terms of Maxwell's equations. These are in fact a special case of more general relations, which contain additional terms connected to magnetic charges (ρ_{m}) and currents ($\mathbf{j}_{\mathrm{m}}$):

$$\nabla \cdot \mathbf{E} = 4\pi\rho_{\mathrm{e}} \,, \qquad \nabla \cdot \mathbf{B} = 4\pi\rho_{\mathrm{m}} \,,$$
$$-\nabla \times \mathbf{E} = \frac{1}{c}\frac{\partial \mathbf{B}}{\partial t} + \frac{4\pi}{c}\mathbf{j}_{\mathrm{m}} \,, \qquad \nabla \times \mathbf{B} = \frac{1}{c}\frac{\partial \mathbf{E}}{\partial t} + \frac{4\pi}{c}\mathbf{j}_{\mathrm{e}} \,.$$

The existence of magnetic monopoles are therefore not mathematically inconsistent with Maxwell's equations; it is simply that in their usual form they assume their absence in Nature. In the theory of quantum mechanics, the electromagnetic field is described in terms of the vector potential. It has been shown by Dirac [161] that it is possible to incorporate magnetic monopoles into this description: a vector potential singular along an infinite line starting at some point $\vec{x}$ describes the field of a magnetic monopole placed at $\vec{x}$. This is equivalent to a solenoid of an infinitely small radius starting at $\vec{x}$ and ending at infinity. Such a description is called the Dirac string. Naturally, such a picture can only describe a particle (the monopole) if the string is unobservable. This leads to a constraint on the possible values of the magnetic charge, known as Dirac's quantisation:

$$eg = \frac{n}{2}\hbar c, \quad n = 0, \pm 1, \pm 2, \ldots$$

where e is the elementary electric charge and g is a possible value of magnetic charge. This result has a significant implication – if magnetic monopoles exist, electric charge is quantised; the existence of magnetic monopoles would therefore predicts electric charge quantisation, the origin of which is one of the biggest questions in particle physics. In addition, the relation between the electric and magnetic elementary charges allows the former to be calculated as

$$g = \frac{ne}{2\alpha} \approx e \cdot 68.5n \,,$$

where α is the fine-structure constant. This high value of the magnetic charge means that a magnetic monopole would interact with electromagnetic field like a heavy nucleus.

Many searches for magnetic monopoles have been performed over the years [162]. Two of them [163, 164] observed signals consistent with a magnetic monopole passing through su-

perconducting coils (manifesting as a sudden change of the magnetic flux, see Fig. 5.2). While no alternative explanations for these signals have been found, each of the experiments only observed a single such event; moreover, each pointed towards a different value of the magnetic charge. Magnetic monopoles have also been searched for at particle colliders. Typical methods include searches for highly ionizing particles, see for example the ATLAS result [165].

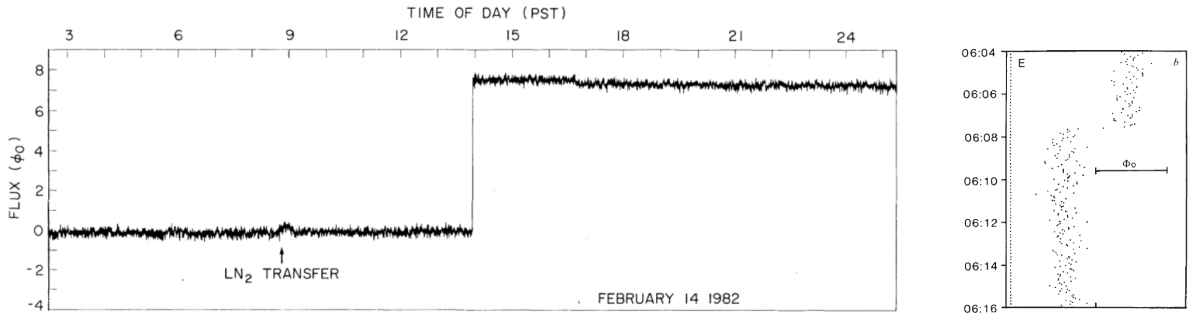

(a) (b)

Fig. 5.2: Two magnetic monopole candidate events: (a) from [163], (b) from [164].

However, it is possible that magnetic monopoles would not be observed by the main LHC detectors, even if they are produced in collisions. For example, if monopoles are heavy, their velocity will be low and they can miss the trigger window. Another possibility is that the monopoles could be trapped inside dead material, such as the beam pipe. This leads to another widely used search method – scanning the exposed beam pipe with very sensitive magnetometers [166, 167]. MoEDAL [168, 169] is a dedicated experiment at the LHC, devoted to magnetic monopole searches. Its aim is to address the typical drawbacks of general purpose detectors, and it consists of trapping detectors, which can capture magnetic monopoles for further study with magnetometers, and plastic tracking detectors, which are sensitive to highly ionising particles and do not suffer from the trigger issue described above.

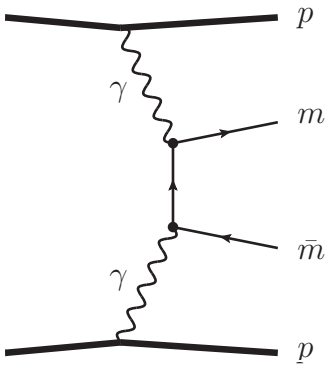

Fig. 5.3: Exclusive magnetic monopole production mechanism.

Experimental results and outlook

In assessing the measurement feasibility for magnetic monopole searches with tagged forward protons, one of the main issues is the lack of a reliable model for magnetic monopole production. Although one can as usual draw a Feynman diagram for the production process, the very high value of coupling (magnetic charge) invalidates perturbative calculations. It is therefore not possible to predict the expected cross section value using current calculation tools. On the other

hand, it is possible to consider the potential sources of backgrounds to assess the cross section sensitivity. Most simply, an analysis could be performed in a low pile-up environment, in which case the signature will consist of two forward protons tagged in the forward detectors and an empty central detector.

Two types of background can be considered. First, the two measured protons may not directly originate from the same collision, i.e. they can be produced by two separate soft single diffractive events, or they can be two halo particles (or a combination of these two cases). For diffractive protons, a lack of particles in the central detector means that the proton could have lost only a tiny part of its momentum. Therefore, these types of background will be important for measurements with high-β^* optics. On the other hand, the background from two halo particles is relevant for all optics scenarios. Moreover, such a background cannot be accurately predicted and can change from run to run, or even during the run. However, since the two particles are independently produced, the probability of such an event should be equal to the product of probabilities of having protons on each side. In addition, halo protons are expected to be close to the beam in low β^* optics, so they should have a sizable impact on the sensitivity of the search mainly in the low mass monopole region.

For high mass monopoles searches, where the cross sections are expected to be lower, low β^* optics are necessary. Here, the main background is expected to originate from soft double diffractive processes, where the central detector is empty, and the forward protons can then be present in the dissociated state as a simple consequence of baryon number conservation (i.e. the dissociated state will always contain either a proton or a neutron). Usually, the energy of such protons is too small to reach the forward detectors, however the high cross section of the process means that the resulting background is non-negligible.

In Fig. 5.4 the particle flow for double diffractive events with the signature of invisible particles production is presented, i.e. empty central detectors and two forward protons with $0.02 < \xi < 0.12$ (measurements with low-β^* optics). It has been assumed that the central detector can measure particles with $|\eta| < 5$ and $p_T > 200$ MeV (both charged and neutral), and Pythia 8 has been used here and in the results which follow. The very thin parabolic shape at $10 < |\eta| < 14$ corresponds to the forward protons. One can clearly see that the majority of particles have $6 < |\eta| < 9$, and thus vetoing on activity in this regions will suppress a significant part of the background.

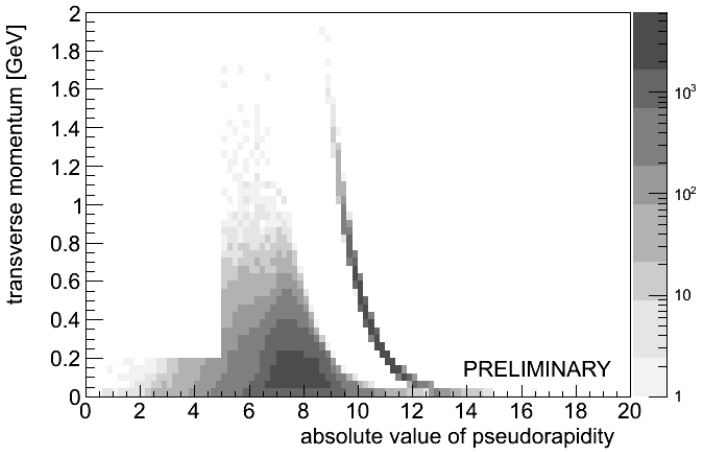

Fig. 5.4: Particle flow for double diffractive events consistent with the signature of invisible particle production (empty central detectors and two forward protons with $0.02 < \xi < 0.12$).

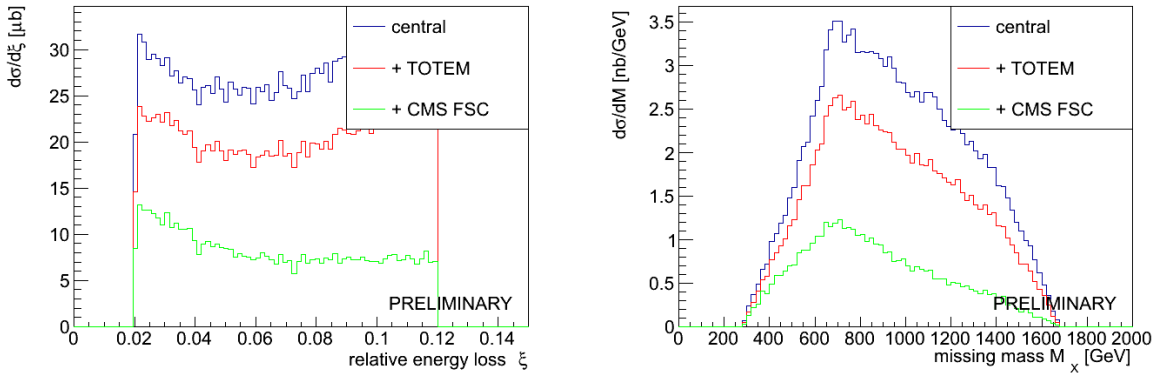

(a) (b)

Fig. 5.5: Distributions of (a) relative momentum loss and (b) missing mass for events with the signature of invisible particle production (empty central detectors and two forward protons with $0.02 < \xi < 0.12$). The effect of an additional veto from the TOTEM tracker and CMS FSCs is presented.

It is interesting to consider the relative momentum loss and missing mass distributions for these background events. These are presented in Figs. 5.5 (a) and 5.5 (b), respectively, where in addition the effects of a veto with the TOTEM T2 detectors and CMS FSCs are presented.

Even with the most stringent selection, the background cross section remains at the mb level. However, one must remember that for the case of magnetic monopoles, the electromagnetic coupling is very large, and the signal cross section may therefore be significant. Although it is not possible to reliably predict the expected cross section, one can compare the obtained value to the most recent limits. ATLAS put limits on the cross section of 145 – 16 fb for monopole masses of 200 – 1200 GeV. It is therefore clear that the forward proton method described above will not be competitive with these general monopole searches. However, it will remain useful for scenarios in which the monopoles are not visible in the standard ways, in which case these may be missed by standard searches.

5.5.3 Standard Model exclusive production of $\gamma\gamma$, WW and ZZ via photon induced processes

Motivation and theory

In the SM, the couplings of fermions and gauge bosons are constrained by the gauge symmetries of the Lagrangian. Therefore, the measurement of W, Z boson and γ pair production via the

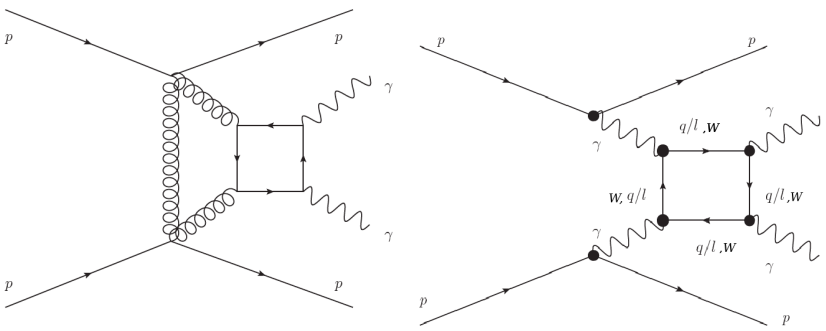

Fig. 5.6: Di-photon exclusive Standard Model production via QCD (left) and photon induced (right) processes at the lowest order of perturbation theory.

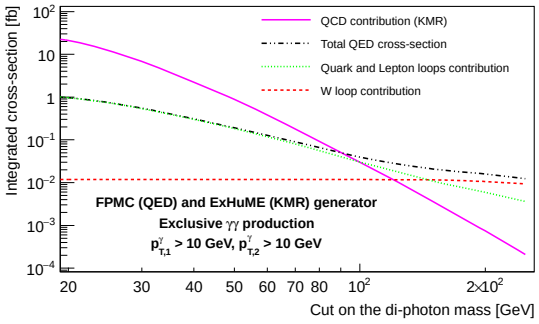
QCD contribution (KMR)
Total QED cross-section
Quark and Lepton loops contribution
W loop contribution
FPMC (QED) and ExHuME (KMR) generator
Exclusive γγ production
$p_{T,1}^{\gamma}$ > 10 GeV, $p_{T,2}^{\gamma}$ > 10 GeV
Integrated cross-section [fb]
Cut on the di-photon mass [GeV]

Fig. 5.7: Integrated di-photon production cross section as a function of the minimum di-photon mass requirement. In addition, both photons must have a transverse momentum $p_{\perp} > 10$ GeV. The QCD exclusive (Durham) processes, solid line, dominates at low masses while QED di-photon production dominates at higher masses (dashed lines). The QED production corresponds to di-photon production via lepton/fermion loops (dotted line) and W boson loops (dashed-dotted line).

Cut / Process	QCD Exclusive (KMR)	QED Fermion loop	W loop
$m_{\gamma\gamma} > 10$ GeV,$p_{T1,2} > 5$ GeV	372.1 fb	5.5 fb	0.01 fb
$m_{\gamma\gamma} > 20$ GeV,$p_{T1,2} > 10$ GeV	20.4 fb	1. fb	0.012 fb
$m_{\gamma\gamma} > 50$ GeV,$p_{T1,2} > 10$ GeV	0.87 fb	0.18 fb	0.012 fb
$m_{\gamma\gamma} > 100$ GeV,$p_{T1,2} > 10$ GeV	0.030 fb	0.03 fb	0.012 fb
$m_{\gamma\gamma} > 200$ GeV,$p_{T1,2} > 10$ GeV	$7.4{\cdot}10^{-4}$ fb	$5.{\cdot}10^{-3}$ fb	0.010 fb
$m_{\gamma\gamma} > 500$ GeV,$p_{T1,2} > 10$ GeV	$3.2{\cdot}10^{-6}$ fb	$3.{\cdot}10^{-4}$ fb	0.004 fb

Table 5.1: Integrated cross sections of the different SM exclusive di-photon production processes at the LHC at $\sqrt{s} = 14$ TeV for various requirements on the di-photon mass ($m_{\gamma\gamma}$) and photon transverse momenta ($p_{T1,2}$).

exchange of two photons can directly provide stringent tests of one of the most important and least understood mechanism in particle physics, namely electroweak symmetry breaking.

Considering first W pair production induced by the exchange of two photons [170], this is a pure electroweak process in which the decay products of the W bosons are measured in the central detector and the scattered protons may remain intact. This process, as well as the different diffractive backgrounds, are all implemented in the FPMC Monte Carlo [107] and Herwig++. After simple cuts to select exclusive W pairs decaying into leptons, such as a cut on the proton momentum loss ($0.0015 < \xi < 0.15$) — assuming that the protons are tagged in AFP or CT-PPS at 210 and 420 m — on the transverse momentum of the leading and second leading leptons at 25 and 10 GeV respectively, on $E_{\mathrm{T}}^{\mathrm{miss}} > 20$ GeV, $\Delta\phi > 2.7$ between leading leptons, and $160 < M_X < 500$ GeV, the diffractive mass reconstructed using the forward detectors, the background is found to be less than 1.7 event for 30 fb^{-1} for a SM signal of 51 events [171].

Considering the $\gamma\gamma$ final state, in Fig. 5.6, the leading processes that produce two photons and two intact protons in the final state are shown. Fig. 5.6 (left) corresponds to exclusive QCD di-photon production, while Fig. 5.6 (right) correspond to photon–induced production, which is of interest here. It is worth noticing that quark, lepton and W loops need to be considered in order to get the correct SM cross section for di-photon production, as shown in Fig 5.7. The QCD induced process, discussed in Section 5.3.5, is dominant at low masses whereas the photon induced process dominates at higher di-photon masses [5]. It should be emphasised that the W

loop contribution dominates at high di-photon masses [79, 80, 172, 173]; all of these terms have been implemented for the first time in a single generator in FPMC [107]. In Table 5.1, some selected values of the cross sections from Fig. 5.7 discussed above are shown. The threshold where the W-loop contribution becomes dominant is for a di-photon mass slightly above 100 GeV.

While, as can be seen in Table 5.1, and discussed further in Section 5.3.5, the expected cross sections for the QCD production mechanism are sufficient for measurements at the LHC, including during special luminosity runs, there appears to be limited sensitivity to the SM photon–induced mechanism. On the other hand, it may be possible to study di-photon production via quark, lepton and even W loops at the LHC in the heavy ion mode [79].

Experimental results and outlook

An initial study of $\gamma\gamma \to WW$ [131] was performed at CMS using 5 fb^{-1} of data collected at $\sqrt{s} = 7$ TeV, based on the final state consisting of an electron, a muon, and undetected neutrinos. Events were selected by requiring the presence of a $\mu^{\pm}e^{\mp}$ vertex with zero additional charged tracks associated, and $p_T(\mu^{\pm}e^{\mp}) > 30$ GeV. The first requirement was used to suppress inclusive backgrounds, while the $p_T(\mu^{\pm}e^{\mp})$ requirement also suppressed backgrounds from $\gamma\gamma \to \tau\tau$. As the outgoing protons could not be tagged, the selected sample also contained a large fraction of proton dissociation, which was estimated from data using control samples of high-mass $\gamma\gamma \to \mu\mu$ events. The backgrounds were estimated using simulation and control regions in the data. In the signal region two events were observed in the data, compared to an expectation of 2.2 ± 0.4 signal events and 0.84 ± 0.15 background. The event properties such as the $\mu^{\pm}e^{\mp}$ invariant mass and acoplanarity, and the missing transverse energy, were compatible with Standard Model expectations.

5.5.4 Anomalous gauge couplings: $\gamma\gamma\gamma\gamma$

Motivation and theory

Assuming that the new physics mass scale Λ is heavier than the experimentally accessible energy E, all new physics manifestations can be described using an effective Lagrangian valid for $\Lambda \gg E$. Among these operators, the pure photon dimension-eight operators

$$\mathscr{L}_{4\gamma} = \zeta_1^{\gamma} F_{\mu\nu}F^{\mu\nu}F_{\rho\sigma}F^{\rho\sigma} + \zeta_2^{\gamma} F_{\mu\nu}F^{\nu\rho}F_{\rho\lambda}F^{\lambda\mu} \tag{5.25}$$

can induce the $\gamma\gamma\gamma\gamma$ process, highly suppressed in the SM [172, 174]. Different new physics processes can contribute to $\zeta_{1,2}^{\gamma}$. For example, loops of heavy charged particles contribute to the 4γ couplings [172, 174] as $\zeta_i^{\gamma} = \alpha_{\text{em}}^2 Q^4 m^{-4} N c_{i,s}$, where $c_{1,s}$ is related to the spin of the heavy particle of mass m running in the loop and Q its electric charge. The factor N counts all additional multiplicities such as color or flavor. These couplings scale as $\sim Q^4$ and are enhanced in the presence of particles with large charges. For example, certain light composite fermions, characteristic of composite Higgs models, have typical electric charges of several units. For a 500 GeV vector (fermion) resonance with $Q = 3\,(4)$, large couplings ζ_i^{γ} of the order of $10^{-13} - 10^{-14}$ GeV^{-4} can be reached. The difference of sensitivity between vector and fermions comes from the $c_{i,s}$ factors. Beyond perturbative contributions to ζ_i^{γ} from charged particles, non-renormalizable interactions of neutral particles are also present in common extensions of the SM. Such theories can contain scalar, pseudo-scalar and spin-2 resonances that couple to the photon and generate the 4γ couplings by tree-level exchange as $\zeta_i^{\gamma} = (f_s m)^{-2} d_{i,s}$, where $d_{1,s}$ is related to the spin of the particle. Strongly-coupled conformal extensions of the SM

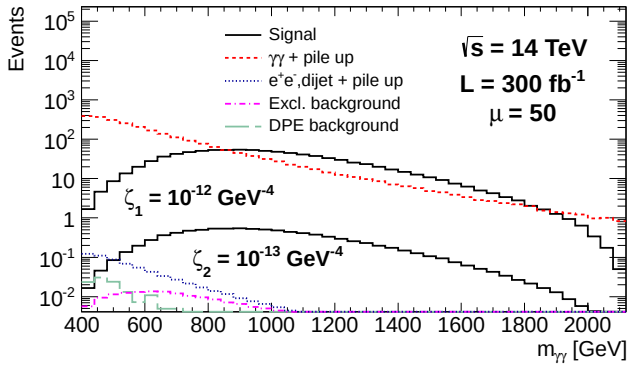

Fig. 5.8: Di-photon invariant mass distribution for the signal ($\zeta_1 = 10^{-12},\ 10^{-13}$ GeV^{-4}, see Eq. 5.25) and for the backgrounds (dominated by $\gamma\gamma$ with protons from pile up), requesting two protons in the forward detectors and two photons of $p_T > 200$ (100) GeV for the leading (subleading) photon with at least one converted photon in the central detector, for a luminosity of 300 fb^{-1} and an average pile up of $\mu = 50$.

contain a scalar particle ($s = 0^+$), the dilaton. Even a dilaton of mass 2 TeV can produce a sizeable effective photon interaction, $\zeta_1^\gamma \sim 10^{-13}$GeV^{-4}. These features are reproduced for a large number of colors by the gauge-gravity correspondence in warped extra dimensions. Warped-extra dimensions also feature Kaluza-Klein (KK) gravitons [175], that can induce anomalous couplings [174]

$$\zeta_i^\gamma = \frac{\kappa^2}{8\tilde{k}^4} d_{i,2} \tag{5.26}$$

where $\tilde{k}$ is the IR scale that determines the first KK graviton mass and κ is a parameter that can be taken $\mathcal{O}(1)$. For $\kappa \sim 1$, and $m_2 \lesssim 6$ TeV, the photon vertex can easily exceed $\zeta_2^\gamma \sim 10^{-14}$ GeV^{-4}.

Table 5.2: Number of signal (for a baseline coupling of 2.10^{-13} GeV^{-4}) and background events after various selections for an integrated luminosity of 300 fb^{-1} and $\mu = 50$ at $\sqrt{s} = 14$ TeV. At least one converted photon is required. The standard cuts correspond to the AFP or CT-PPS acceptance ($0.015 < \xi < 0.15$) and the request of the photon p_T to be above 50 GeV

Cut / Process	Signal	Excl.	DPE	e^+e^-, di-jet + pile up	$\gamma\gamma$ + pile up
standard	20.8	3.7	48.2	$2.8 \cdot 10^4$	$1.0 \cdot 10^5$
$p_{T1} > 200$GeV, $p_{T2} > 100$ GeV	17.6	0.2	0.2	1.6	2968
$m_{\gamma\gamma} > 600$ GeV	16.6	0.2	0	0.2	1023
$p_{T2}/p_{T1} > 0.95$, $\lvert\Delta\phi\rvert > \pi - 0.01$	16.2	0.1	0	0	80.2
$\sqrt{\xi_1\xi_2 s} = m_{\gamma\gamma} \pm 3\%$	15.7	0.1	0	0	2.8
$\lvert y_{\gamma\gamma} - y_{pp}\rvert < 0.03$	15.1	0.1	0	0	0

Experimental results and outlook

The $\gamma\gamma\gamma\gamma$ process (Fig. 5.6) can be probed via the detection of two intact protons in the forward proton detectors and two energetic photons in the corresponding electromagnetic calorimeters.

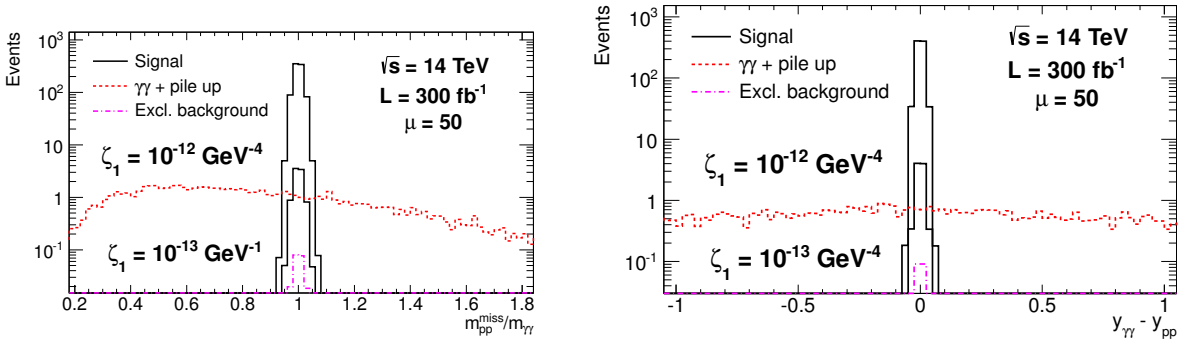

Fig. 5.9: Di-photon to missing proton mass ratio (left) and rapidity difference (right) distributions for signal considering two different coupling values (10^{-12} and 10^{-13}GeV^{-4}, see Eq. 5.25) and for backgrounds after requirements on photon p_T, di-photon invariant mass, p_T ratio between the two photons and on the angle between the two photons. At least one converted photon is required. The integrated luminosity is 300 fb^{-1} and the average pile up is $\mu = 50$.

The SM cross section for exclusive di-photon production is dominated by the QED process at high di-photon mass — and not by gluon exchanges — and is thus very well known. The photon identification efficiency is expected to be around 75% for $p_T > 100$ GeV, with jet rejection factors exceeding 4000 even at high pile up (>100) [176]. In addition, about 1% of the electrons are mis-identified as photons. These numbers are used in the phenomenological study presented below. As in the previous studies, the anomalous $\gamma\gamma\gamma\gamma$ process has been implemented in the FPMC generator [107]. The FPMC generator was also used to simulate the background processes giving rise to two intact protons accompanied by two photons, electrons or jets that can mimic the photon signal. These include exclusive SM production of $\gamma\gamma\gamma\gamma$ via lepton and quark boxes and $\gamma\gamma \to e^+e^-$. The CEP of $\gamma\gamma$ via two-gluon exchange, not present in FPMC, was simulated using ExHuME [177]. More details on those Monte Carlo generators can be found in Chapter 2. This series of backgrounds is called “Exclusive" in Table 5.2 and Figs. 5.8 and 5.9. FPMC was also used to produce $\gamma\gamma$, Higgs to $\gamma\gamma$ and di-jet productions via double pomeron exchange (‘DPE’ in Table 5.2 and Fig. 5.8). Such backgrounds tend to be softer than the signal and can be suppressed with requirements on the transverse momenta of the photons and the di-photon invariant mass. In addition, the final-state photons for the signal are typically back-to-back and have about the same transverse momenta. Requiring a large azimuthal angle $|\Delta\phi| > \pi - 0.01$ between the two photons and a ratio $p_{T,2}/p_{T,1} > 0.95$ greatly reduces the contribution of non-exclusive processes. Additional background processes include the quark and gluon-initiated production of two photons, two jets and Drell-Yan processes leading to two electrons. The two intact protons arise from pile up interactions (these backgrounds are called $\gamma\gamma$ + pile up and e^+e^-, di-jet + pile up in Table 5.2). These events were produced using HERWIG [178] and PYTHIA [179]. The pile up background is further suppressed by requiring the proton missing mass to match the di-photon invariant mass within the expected resolution and the di-photon system rapidity and the rapidity of the two protons to be similar.

The number of expected signal and background events passing respective selections is shown in Table 5.2 for an integrated luminosity of 300 fb^{-1} for a center-of-mass energy of 14 TeV. Exploiting the full event kinematics with the forward proton detectors allows the background to be suppressed with a signal selection efficiency after the acceptance cuts exceeding 70%. Tagging the protons is essential to suppress the $\gamma\gamma$ + pile up events. Further background reduction is possible by requiring the photons and the protons to originate from the same vertex, providing an additional rejection factor of 40 for 50 pile up interactions. A similar study

Luminosity	300 fb^{-1}	300 fb^{-1}	300 fb^{-1}	300 fb^{-1}	3000 fb^{-1}
pile up (μ)	50	50	50	50	200
coupling (GeV^{-4})	≥ 1 conv. γ 5 σ	≥ 1 conv. γ 95% CL	all γ 5 σ	all γ 95% CL	all γ 95% CL
ζ_1 f.f.	$8 \cdot 10^{-14}$	$5 \cdot 10^{-14}$	$4.5 \cdot 10^{-14}$	$3 \cdot 10^{-14}$	$2.5 \cdot 10^{-14}$
ζ_1 no f.f.	$2.5 \cdot 10^{-14}$	$1.5 \cdot 10^{-14}$	$1.5 \cdot 10^{-14}$	$9 \cdot 10^{-15}$	$7 \cdot 10^{-15}$
ζ_2 f.f.	$2 \cdot 10^{-13}$	$1 \cdot 10^{-13}$	$9 \cdot 10^{-14}$	$6 \cdot 10^{-14}$	$4.5 \cdot 10^{-14}$
ζ_2 no f.f.	$5 \cdot 10^{-14}$	$4 \cdot 10^{-14}$	$3 \cdot 10^{-14}$	$2 \cdot 10^{-14}$	$1.5 \cdot 10^{-14}$

Table 5.3: 5 σ discovery and 95% CL exclusion limits on ζ_1 and ζ_2 couplings in GeV^{-4} (see Eq. 5.25) with and without form factor (f.f.), requesting at least one converted photon ($\geq$ 1 conv. γ) or not (all γ). All sensitivities are given for 300 fb^{-1} and $\mu = 50$ pile up events (medium luminosity LHC) except for the numbers of the last column which are given for 3000 fb^{-1} and $\mu = 200$ pile up events (high luminosity LHC).

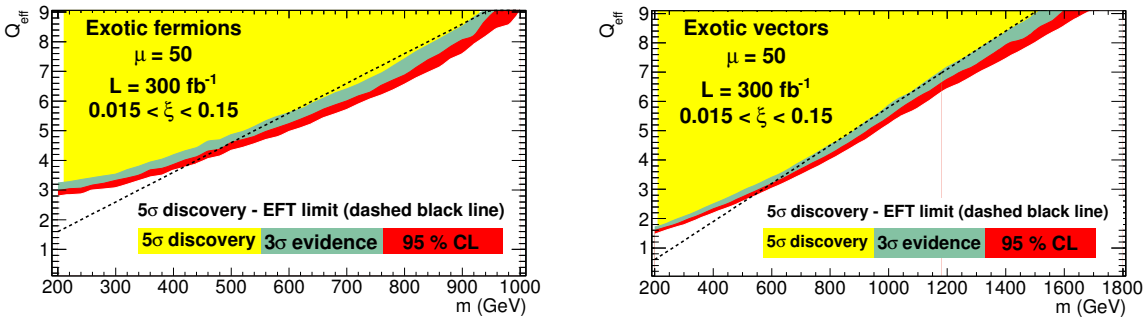

Fig. 5.10: Exclusion plane in terms of mass and effective charge of generic fermions and vectors. in the case of no requirement of photon conversion at the analysis stage and full integrated luminosity of the LHC (300 fb^{-1}, $\mu = 50$).

at a higher pile up of 200 was performed and led to a very small background (< 5 expected background events for 300 fb^{-1} without re-optimizing the event selection) . The sensitivities on photon quartic anomalous couplings are given in Table 5.3. The sensitivity extends up to $7 \cdot 10^{-15}$ GeV^{-4}, allowing the models of new physics described above to be probed further.

A more recent study has been performed using a full amplitude calculation in the case of BSM contributions from generic new heavy charged particles [80]. Here, the cross section is fully determined by the particle spin (vectors or fermions), mass, charge and multiplicity, which allows an effective charge of the new particles, $Q_{\text{eff}} = Q \cdot N^{1/4}$, to be defined. In Fig. 5.10 the mass-effective charge exclusion plane with 300 fb^{-1} at the 14 TeV LHC with a comparison with the effective field theory study results is shown, while Tab. 5.4 gives the 5 σ discovery limits for various mass scenarios. More details can be found in [80].

5.5.5 Anomalous gauge couplings: $\gamma\gamma WW$ and $\gamma\gamma ZZ$

Motivation and theory

As well as altering the 4γ coupling from SM expectations, BSM physics such as the scenarios described in the previous section can also effect the couplings to electroweak bosons, namely $\gamma\gamma WW$ and $\gamma\gamma ZZ$. The parameterization of [180] can be adopted for the quartic anomalous

Mass (GeV)	300	600	900	1200	1500
Q_{eff} (vector)	2.2	3.4	4.9	7.2	8.9
Q_{eff} (fermion)	3.6	5.7	8.6	-	-

Table 5.4: 5 σ discovery limits on the effective charge of new generic charged fermions and vectors for various masses scenarios in the case of no requirement of photon conversion at the analysis stage and full integrated luminosity at the LHC (300 fb^{-1}, $\mu = 50$).

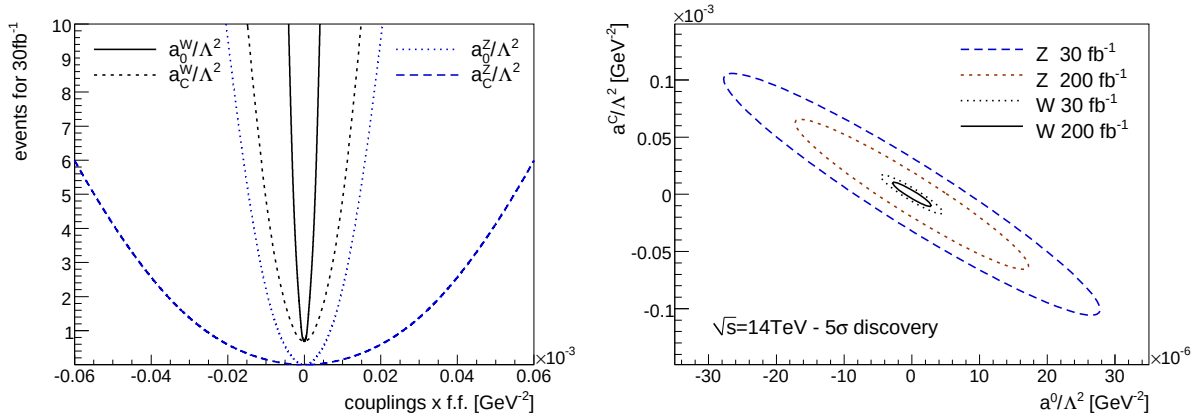

Fig. 5.11: (left) Number of events for signal due to different values of anomalous couplings after all cuts (see text) for a luminosity of 30 fb^{-1} and (right) 5σ discovery contours for all the WW and ZZ quartic couplings at $\sqrt{s} = 14$ TeV for a luminosity of 30 fb^{-1} and 200 fb^{-1}.

gauge couplings. The cuts to select the anomalous WW events are similar to the ones mentioned in the Section 5.5.3, namely $0.0015 < \xi < 0.15$ for the tagged protons corresponding to the AFP or CT-PPS detector at 210 and 420 m, $E_{\text{T}}^{\text{miss}} > 20$ GeV, $\Delta\phi < 3.13$ between the two leptons. In addition, a cut on the p_T of the leading lepton $p_T > 160$ GeV and on the diffractive mass $W > 800$ GeV are requested since anomalous coupling events appear at high mass. After these requirements, about 0.7 background events for a signal of 17 events are expected, for a luminosity of 30 fb^{-1}, if the anomalous coupling is about four orders of magnitude lower than the present LEP limit [181] ($|a_0^W/\Lambda^2| = 5.4 \cdot 10^{-6}$) or two orders of magnitude lower with respect to the D0 and CDF limits [131, 182], or CMS measurement at $\sqrt{s} = 7$ TeV [131] mentioned above. The strategy to select anomalous coupling ZZ events is similar and the presence of three leptons or two like sign leptons are requested. Table 5.5 summarizes the reach on anomalous couplings at the LHC for luminosities of 30 and 200 fb^{-1} compared to the present OPAL limits from the LEP accelerator [181]. Fig. 5.11 shows the expected number of signal events as a function of the anomalous coupling value (left) and the 5σ discovery contours for all WW and ZZ anomalous couplings for 30 and 200 fb^{-1} (right); sensitivity to values expected in extra dimension models [80, 172] is demonstrated. Proton tagging is the only method at present to test quartic anomalous couplings down to such small values.

Finally, we note that the LHC sensitivity to triple gauge anomalous couplings at the LHC has been studied in [171], however in this case the limits obtained in the context of proton tagging based analyses are comparable to the inclusive ones, and therefore do not appear to be particularly competitive.

Couplings	OPAL limits [GeV^{-2}]	Sensitivity @ $\mathscr{L} = 30$ (200) fb^{-1}	
		5σ	95% CL
a_0^W/Λ^2	[-0.020, 0.020]	$5.4 \cdot 10^{-6}$ ($2.7 \cdot 10^{-6}$)	$2.6 \cdot 10^{-6}$ ($1.4 \cdot 10^{-6}$)
a_C^W/Λ^2	[-0.052, 0.037]	$2.0 \cdot 10^{-5}$ ($9.6 \cdot 10^{-6}$)	$9.4 \cdot 10^{-6}$ ($5.2 \cdot 10^{-6}$)
a_0^Z/Λ^2	[-0.007, 0.023]	$1.4 \cdot 10^{-5}$ ($5.5 \cdot 10^{-6}$)	$6.4 \cdot 10^{-6}$ ($2.5 \cdot 10^{-6}$)
a_C^Z/Λ^2	[-0.029, 0.029]	$5.2 \cdot 10^{-5}$ ($2.0 \cdot 10^{-5}$)	$2.4 \cdot 10^{-5}$ ($9.2 \cdot 10^{-6}$)

Table 5.5: Reach on anomalous couplings obtained in γ induced processes after tagging the protons in AFP or CT-PPS compared to the present OPAL limits. The 5σ discovery and 95% C.L. limits are given for a luminosity of 30 and 200 fb^{-1} [170].

Experimental results and outlook

Measurements of two-photon production of W boson pairs, in the process $pp \to p\mathrm{W}^+\mathrm{W}^-p$, were performed in the $\mu^\pm\mathrm{e}^\mp$ final state, using 5.05 fb^{-1} of data collected in proton-proton collisions at $\sqrt{s} = 7$ TeV with the CMS detector at the LHC in 2011, but without proton tagging [131]. Model-independent upper limits were extracted and compared to predictions involving anomalous quartic gauge couplings (AQGCs). This resulted in limits of $|a_0^W/\Lambda^2| < 0.00015$ GeV^{-2} and $|a_C^W/\Lambda^2| < 0.0005$ GeV^{-2} at 95% CL on the dimension-six AQGC operators, including a dipole form factor with $\Lambda_{\text{cutoff}} = 500$ GeV to preserve unitarity.

The prospects of sensitivities to quartic $\gamma\gamma WW$ couplings, using a full detector simulation, have been studied in detail within the context of the AFP and CT-PPS detectors, following the phenomenological study presented above. As these studies and anomalous coupling searches represent an important part of the high–luminosity AFP and CT–PPS programs, these are described in more detail in Section 5.5.6.

5.5.6 Anomalous $\gamma\gamma WW$ couplings: detailed studies

As discussed in Section 5.5.5, the prospects of sensitivities to quartic $\gamma\gamma WW$ couplings, using a full detector simulation, have been studied in detail within the context of AFP and CT-PPS. The first study was presented in the Letter of Intent of Phase-I ATLAS upgrade [183], confirming that results from phenomenological studies can be obtained with realistic detector setup. As these studies and anomalous coupling searches represent an important part of the high–luminosity AFP and CT–PPS programs, these are described in some detail below. This ATLAS study is summarized first, followed by a more detailed discussion of the more recent CMS analysis, performed for this report, and based on the experimental techniques developed in [131]. While these studies differ in selections, they give similar overall obtainable sensitivity. Before this, some more general aspects of the studies and processes under consideration are described.

With the integrated luminosity expected to be collected during Run II and with the AFP and CT-PPS detectors, the experimental reach on the anomalous quartic coupling $\gamma\gamma WW$ can be extended by several orders of magnitude with respect to the best limits obtained so far. In the process $pp \to p\mathrm{WW}p$, both forward-scattered protons are detected in the CT-PPS, depending on the acceptance on the mass of the WW central system produced. The AFP and CT-PPS detectors were assumed to be operating at 10 and 15 σ from the beam, respectively. The process is

characterized by a primary vertex from the two leptons $\ell^{\pm}\ell'^{\mp}$ (where $\ell = e, \mu$) from the W boson pair decays, no other tracks, a large transverse momentum of the dilepton system, $p_{\mathrm{T}}(\ell^{\pm}\ell'^{\mp})$, and a large invariant mass, $M(\ell^{\pm}\ell'^{\mp})$. A simulated sample of SM exclusive $pp \to p\mathrm{WW}p$ signal events is used, in conjunction with samples in which anomalous quartic gauge couplings (AQGC) are assumed.

Considering first the ATLAS study, the full list of background processes used for the ATLAS measurement of Standard Model WW cross section was simulated, namely $t\bar{t}$, WW, WZ, ZZ, W+jets, Drell-Yan and single top events. In addition, processes having two forward protons denoted as 'diffractive backgrounds' were simulated. They include two-photon and double pomeron exchange production of dileptons and WW. In addition, single diffractive production of dileptons, W and WW was simulated. Inclusive and single diffractive events have zero or one forward proton in the final state, however, due to significant amount of multiple proton-proton interaction rate in Run–II, similar final state signatures may emerge as for the signal due to coincidences with soft diffractive events. The requirement of the presence of at least one proton on each side of AFP within a time window of 10 ps allows the background to be reduced by a factor of about 200 (50) for $\mu = 23$ (46), by matching the vertex position reconstructed inside ATLAS with that calculated from time arrival of the protons. The p_T of the leading lepton originating from the leptonic decay of the W bosons is required to be $p_T >$ 150 GeV, and that of the next-to-leading lepton $p_T > 20$ GeV. An additional requirement of the dilepton mass to be above 300 GeV allows most of the diboson events to be removed. Since only leptonic decays of the W bosons are considered, in addition less than 3 tracks associated to the primary vertex are required, which allows a large fraction of the non-diffractive backgrounds (e.g. $t\bar{t}$, diboson productions, W+jet, etc.) to be rejected. This is illustrated in Fig. 5.12 (left) where signal events clearly peak at low track multiplicities. The remaining Drell-Yan and QED backgrounds are suppressed by requiring the difference in azimuthal angle between the two leptons to satisfy $\Delta\phi < 3.1$.

Fig. 5.12 (right) displays the reconstructed missing mass m_X in AFP for the irreducible QED WW background and for signal events produced with three values of anomalous coupling. Anomalous coupling events are seen to appear at high W-pair invariant masses. The requirement that $m_X > 800\,\mathrm{GeV}$, reconstructed using the two scattered protons in the AFP, allows the backgrounds to be rejected by an additional factor of four.

With the above event selection, a similar sensitivity with respect to fast simulation without pile up was obtained. The 95% C.L. limits are $a_0^W/\Lambda^2 = 2.4 \cdot 10^{-6}(1.3 \cdot 10^{-6})\mathrm{GeV}^{-2}$ for the assumed collected integrated luminosity of 40 (300) fb^{-1} with μ =23(46) mean number of interactions per bunch crossing.

Considering now the CMS-TOTEM study, experience from the CMS measurement [131] discussed above was used and only the significant backgrounds have been considered. The dominant SM backgrounds come from inclusive $\mathrm{W}^+\mathrm{W}^-$ and exclusive $\tau^+\tau^-$ pair production. Drell-Yan (DY) production of $\tau^+\tau^-$, where one τ decays via the electron channel and the other one via the muon channel, in combination with pile up protons, may lead to a similar event configuration as the exclusive WW signal. A selection cut on the transverse momentum of the dilepton pair $p_T(\ell^{\pm}\ell'^{\mp}) > 30$ GeV was used in [131] to reject the DY background almost completely. A further rejection of the other SM backgrounds, and a reduction of signal events by approximately 20% is expected. In this study, only the eμ final state is selected. The simulated samples for the signal process are compared to the SM background expectations, and the tails of the M_X distribution ($M_X = \sqrt{s \cdot \xi_1 \cdot \xi_2} > 1$ TeV), where the SM $\gamma\gamma \to \mathrm{W}^+\mathrm{W}^-$ contribution is expected to be small, are investigated to look for AQGCs. Events are selected by requiring

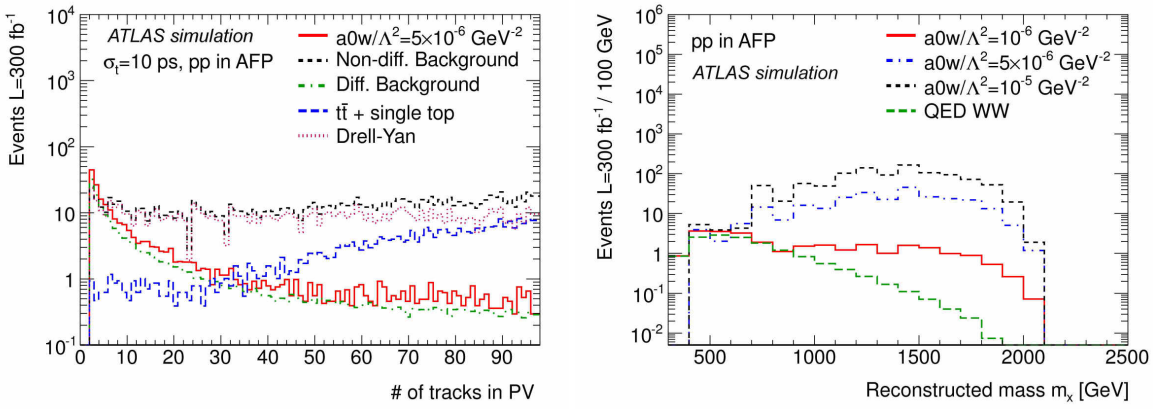

Fig. 5.12: Distribution of the number of tracks fitted to the primary vertex (left) and of the reconstructed missing mass in the forward detectors (right) for signal and the different backgrounds. Those results were obtained using a full simulation of the ATLAS detector.

two central ($|\eta| < 2.4$) leptons with a minimum transverse momentum $p_T > 20$ GeV. In order to reduce the contamination from the W+jet (or other non-prompt lepton) background, "tight" lepton identification criteria are imposed (as in [131]). Leptons are also required to have charges of opposite sign and to come from the same primary vertex. For signal events (either SM or AQGC), the scattered protons are in the region covered by CT-PPS, and the presence of hits in both tracking and timing detectors is therefore required: a large background suppression is expected. A source of inefficiency comes from high detector occupancy, as hits are required not to overlap in the timing detector cells.

Signal events from SM exclusive WW events are correlated in time with the leading protons detected in the CT-PPS detectors, whereas inclusive WW events -superimposed with additional pile up events- are not. Therefore, the information of the proton time-of-flight arrival at the CT-PPS detector location can be used as an additional background rejection. After requiring the coincidence of hits in both tracking and timing detector stations, the time-of-flight difference between the two leading protons arriving at the CT-PPS detector location on opposite sides of the IP is shown in Fig. 5.13 as a function of the z-vertex position of the leading central lepton, for signal (left) and background (right) events. For each event, if there is more than one pp combination in the CT-PPS detector, only the one with the closest match between the time-of-flight Δt and the lepton vertex position in z is kept ("vertex matching" in Table 5.6). The background is shown for inclusive WW events in coincidence with pile up events. Distributions corresponding to a timing resolution of 10 ps are shown for signal and background events.

The distance (in z) of the vertex positions measured from the CT-PPS timing detectors and from the leading lepton in the central detector, $\Delta z = z_{\text{PPS}} - z_{\text{lead lep}}$, is shown in Fig. 5.14 (left) for SM exclusive WW/$\tau\tau$ and inclusive WW events, and for AQGC exclusive WW events, after all cuts, except for the time-of-flight information requirement. Time-of-flight requirements may help reduce the inclusive WW background by a factor of 10 (5), for a timing resolution of 10 ps (30 ps). The track multiplicity associated to the dilepton vertex after the timing selection cuts is shown in Fig. 5.14 (right) for SM signal and backgrounds, after all cuts, except for the track multiplicity cut. The number of extra tracks associated to the dilepton vertex is significantly larger for inclusive WW events, and a selection of $N_{\text{tracks}} < 10$ is expected to suppress the inclusive background by 90%, while retaining approximately 90% of the exclusive events. A signal-to-background ratio of 1:1 can be achieved for the standard model production after applying a cut on the maximum number of reconstructed tracks in the central detector (except

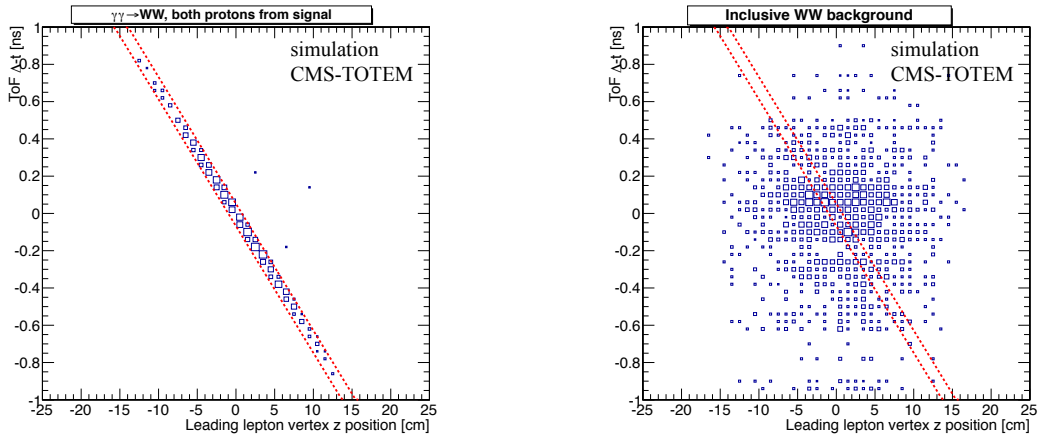

Fig. 5.13: Time-of-flight difference between the two leading protons arriving at the CT-PPS detector location on opposite sides of the IP as a function of the z-vertex position of the leading central lepton for exclusive signal (left) and background inclusive WW (right) events. A timing resolutions of 10 ps is assumed. Distributions are shown for events where both leading protons are within the CT-PPS detector acceptance (after selecting the closest match of the vertices of the dilepton system and of the leading protons), and before the time-of-flight difference requirement. The dotted lines show an ideal window retaining close to 100% of signal events. An arbitrary normalization is used in the distributions.

the two selected leptons).

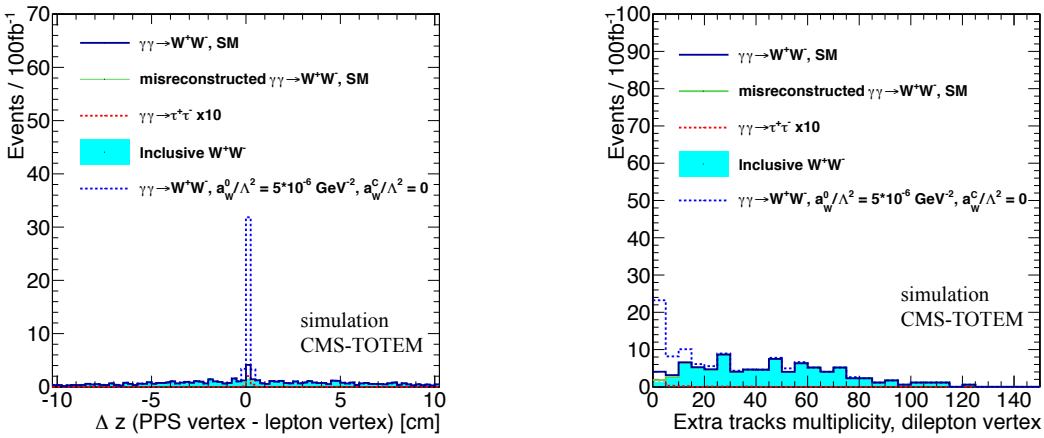

Fig. 5.14: *Left:* Distance along the z-axis (in cm) of the vertex positions as measured from the CT-PPS timing detectors and from the leading lepton in the central detector, $\Delta z = z_{\text{PPS}} - z_{\text{lead lepton}}$. Distribution is shown after all cuts, except for the time-of-flight information requirement. *Right:* Number of extra tracks associated to the dilepton vertex for exclusive (WW and $\tau\tau$) and inclusive (WW) events. Distribution is shown after all cuts, except for the track multiplicity cut. Distributions are shown for SM exclusive WW/$\tau\tau$, inclusive WW events, and AQGC exclusive WW events, and a timing resolutions of 10 ps is assumed. Event yields are normalized to an integrated luminosity of 100fb^{-1} and a timing resolution of 10 ps. Histograms are stacked, except for that of the exclusive $\tau\tau$ background, which is not stacked and is multiplied by a factor of 10.

Kinematic distributions after the full event selections are shown in Fig. 5.15. The transverse momentum of the dilepton system, the azimuthal angle difference between the two leading

muons, and the missing mass distributions are shown for signal and for the background exclusive $\tau\tau$ event yields. The missing mass $M_X = \sqrt{s \cdot \xi_1 \cdot \xi_2}$ (also indicated as $W_{\gamma\gamma}$ in Fig. 5.15) is estimated from the reconstructed values of the two leading protons, ξ_1 and ξ_2. The yields of exclusive $\tau\tau$ background events are multiplied by a factor of 10, in order to allow comparison of the shapes.

Table 5.6 summarizes the cross sections (in fb) after each selection cut, while Table 5.7 summarizes the cross sections (in fb) for the expected exclusive WW events due to AQGC for two different values of the coupling parameters, a_0^W and a_C^W. Cross sections include the branching fractions and are given for the dominant SM processes within the geometrical and detector acceptance. A small contribution from incorrectly reconstructed exclusive WW signal events, where at least one of the leading protons comes from a pile up or SD/DPE event, is also estimated separately.

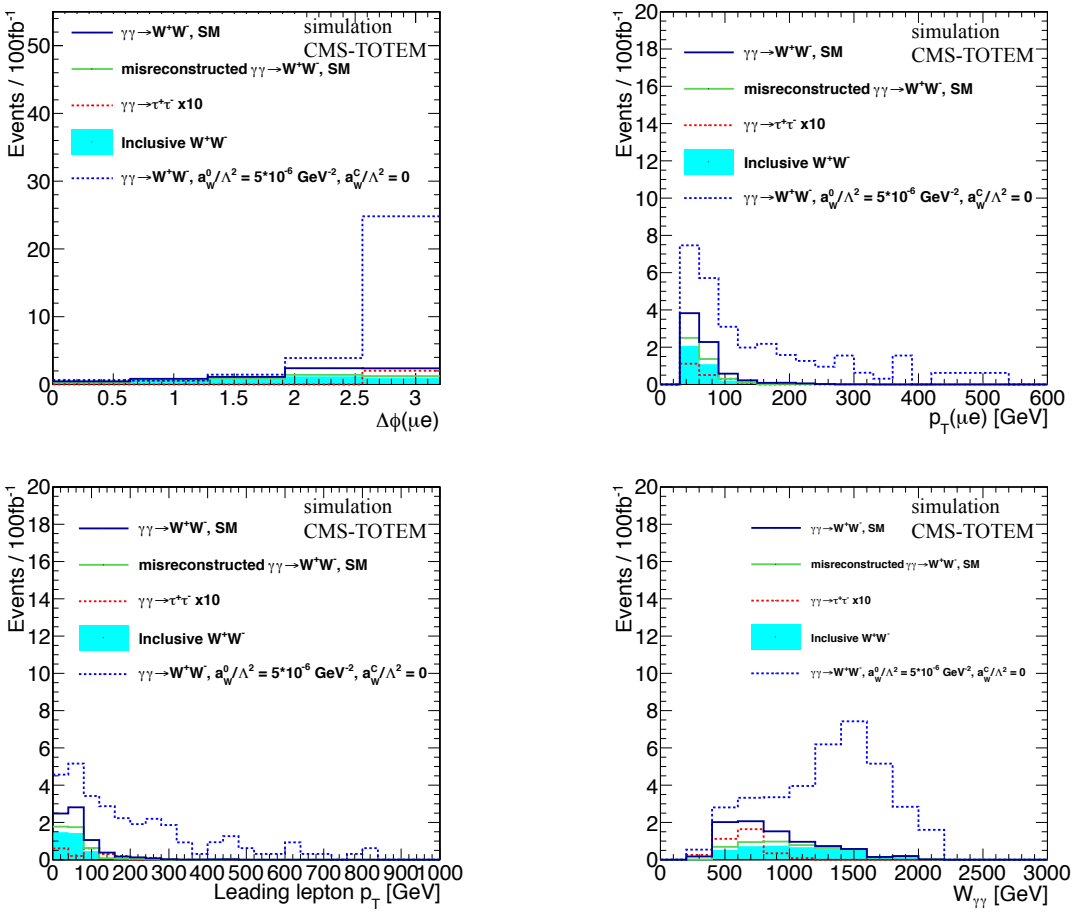

Fig. 5.15: Azimuthal angle difference between the two leading leptons (top, left), transverse momentum of the dilepton pair (top, right), leading lepton transverse momentum (bottom, left), and missing mass (bottom, right) for signal and background events, and in the presence of exclusive WW events due to AQGC processes. Distributions are shown after the full event selection, for an integrated luminosity of 100 fb^{-1}. Histograms are stacked, except for that of the exclusive $\tau\tau$ background, which is not stacked and is multiplied by a factor of 10.

The cross section times the acceptance for SM exclusive WW events is already sizeable at small reconstructed values of the missing mass ($M_X \simeq 300 \div 400$ GeV), and a close approach to the beam can provide a rapid increase of SM signal event yield. The variation of the acceptance

Table 5.6: Cross section (in fb) for the expected SM processes, exclusive and inclusive WW, and exclusive $\tau\tau$ events, after each selection cut (for a timing resolution of 10 ps). In case of different values, numbers in parentheses are for a timing resolution of 30 ps. Only the eμ final state is considered. Statistical uncertainties are shown.

Selection	Cross section (fb)			
	exclusive WW	exclusive WW (incorrectly reconstructed)	inclusive WW	exclusive $\tau\tau$
generated $\sigma \times \mathscr{B}(WW \to e\mu\ \nu\bar{\nu})$	0.86±0.01	N/A	2537	1.78±0.01
≥ 2 leptons ($p_T > 20$ GeV, $\eta < 2.4$)	0.47±0.01	N/A	1140±3	0.087±0.003
opposite sign leptons, "tight" ID	0.33±0.01	N/A	776±2	0.060±0.002
dilepton pair $p_T > 30$ GeV	0.25±0.01	N/A	534±2	0.018±0.001
protons in both PPS arms (ToF and TRK)	0.055 (0.054)±0.002	0.044 (0.085)±0.003	11 (22)±0.3	0.004±0.001
no overlapping hits in ToF + vertex matching	0.033 (0.030)±0.002	0.022 (0.043)±0.002	8 (16)±0.2	0.003 (0.002)±0.001
ToF difference, $\Delta t = (t_1 - t_2)$	0.033 (0.029)±0.002	0.011 (0.024)±0.001	0.9 (3.3)±0.1	0.003 (0.002)±0.001
$N_{\text{tracks}} < 10$	0.028 (0.025)±0.002	0.009 (0.020)±0.001	0.03 (0.14)±0.01	0.002±0.001

Table 5.7: Cross section (in fb) for the expected exclusive WW events due to anomalous quartic gauge couplings, for different values of anomalous coupling parameters (a_0^W and a_C^W) after each selection cut (for a timing resolution of 10 ps). In case of different values, numbers in parentheses are for a timing resolution of 30 ps. Only the eμ final state is considered. Statistical uncertainties are shown.

Selection	Cross section (fb)	
	$a_0^W/\Lambda^2 = 5 \cdot 10^{-6}\text{GeV}^{-2}$ ($a_C^W = 0$)	$a_C^W/\Lambda^2 = 5 \times 10^{-6}\text{GeV}^{-2}$ ($a_0^W = 0$)
generated $\sigma \times \mathscr{B}(WW \to e\mu\ \nu\bar{\nu})$	3.10±0.14	1.53±0.07
≥ 2 leptons ($p_T > 20$ GeV, $\eta < 2.4$)	2.33±0.08	1.00±0.04
opposite sign leptons, "tight" ID	1.82±0.08	0.78±0.03
dilepton pair $p_T > 30$ GeV	1.69±0.07	0.68±0.03
protons in both PPS arms (ToF and TRK)	0.52 (0.50)±0.04	0.18 (0.17)±0.02
no overlapping hits in ToF detectors	0.35 (0.32)±0.03	0.12 (0.11)±0.01
ToF difference, $\Delta t = (t_1 - t_2)$	0.35 (0.32)±0.03	0.12 (0.11)±0.01
$N_{\text{tracks}} < 10$	0.27 (0.24)±0.03	0.11 (0.10)±0.01

as a function of the detector distance from the beam has been evaluated. In particular, the visible cross section for signal exclusive WW events increases by a factor of two when the detector distance from the beam decreases from 15 σ to 10 σ [184]. The selected events are used to set limits on the AQGC parameters, a_0^W/Λ^2 and a_C^W/Λ^2. The resulting limit values are of the order of $a_0^W/\Lambda^2 = 2 \times 10^{-6}$ (3×10^{-6}), and $a_C^W/\Lambda^2 = 7 \times 10^{-6}$ (10×10^{-6}), in case of a 10 ps (30 ps) time resolution. Approximate 95% CL limits expected with 10 ps and 30 ps timing resolutions (Fig. 5.16, left) are compared to the 2011 CMS results [131] from exclusive WW events (Fig. 5.16, right). Expected limits for Run 2 are estimated for an integrated luminosity of 100 fb^{-1}. The areas outside the contours are excluded at 95% CL.

The study demonstrates the feasibility of measuring exclusive WW production in Run 2. With an integrated luminosity of 100 fb^{-1}, approximately 3 SM exclusive WW signal events are expected and a similar number of background events, even when looking at the eμ channel alone. Anomalous quartic gauge couplings would produce a striking, very visible signal. Approximately 30 (10) events would be visible in the presence of AQGC, with coupling parameters $a_0^W\,(a_C^W)/\Lambda^2 = 5 \cdot 10^{-6}\text{GeV}^{-2}$.

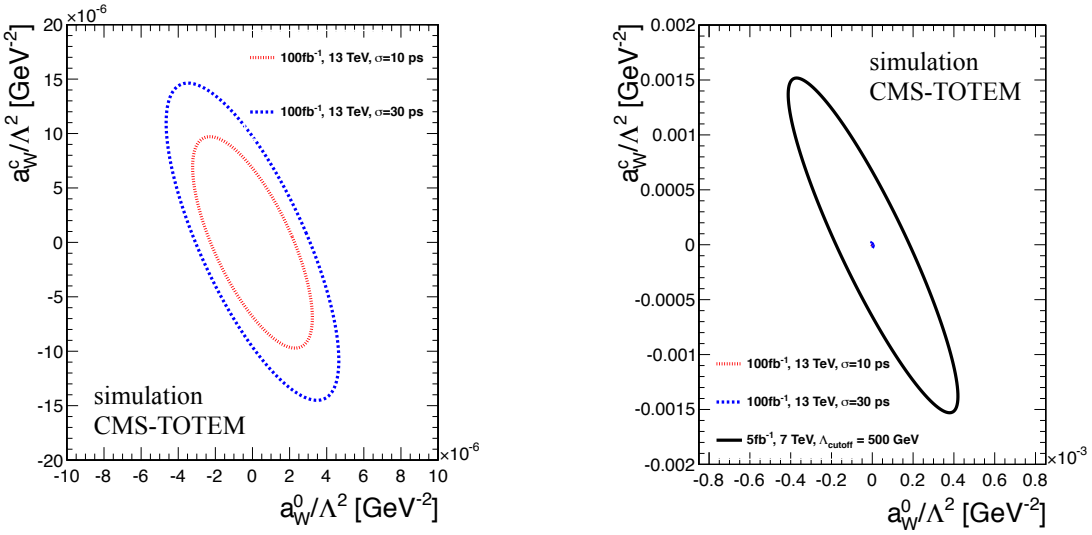

Fig. 5.16: Excluded values of the anomalous coupling parameters a_0^W/Λ^2 and a_C^W/Λ^2. The areas outside the contours are excluded at 95% CL. Approximate limits expected with 10 ps and 30 ps timing resolutions (left) compared to the current 2011 CMS limits from exclusive WW events (right).

5.5.7 New strong dynamics in exclusive processes

After the recent discovery of the Higgs boson [185, 186] at the LHC and follow-up precision studies of its interactions with SM particles, a rough picture of consistency with the SM has begun to emerge. This consistency, however, does not yet mean that the nature of the Higgs boson and electroweak symmetry breaking (EWSB) is completely understood [187]. An immediate question that challenges our current understanding of symmetries in Nature is what initiates EWSB in the SM.

One of the major questions to be answered in the ongoing search for New Physics at the LHC is whether a fine structure of the Higgs-like signal exists in the low invariant mass interval $110 - 140$ GeV, predominantly in $\gamma\gamma$, $W\gamma$ and $Z\gamma$ channels, or not. There exists a possibility that yet unknown resonances which decay into two photons could be very difficult to identify in inclusive measurements. As indicated by for example the CMS data [186] on Higgs boson production, such a fine structure is not yet completely excluded, and this is being explored theoretically in various BSM scenarios. It is therefore interesting to study such a structure in the $\gamma\gamma$ and $Z\gamma$ decay channels, both in QCD and VBF-initiated exclusive production mechanisms. An exclusive measurement has the advantage that $\gamma\gamma$-resonance signals could be enhanced relative to the two-photon background. This offers important advantages compared to searches of new $\gamma\gamma$-resonances in inclusive reactions.

New strongly-coupled dynamics at the TeV energy scale is one possible cause for EWSB in the SM [188, 189]. This initiates EW symmetry breaking dynamically by means of confined techniquark condensation at low energy scales. Such new dynamics unavoidably predicts a variety of new states; most importantly, composite Higgs-like particles [190] whose properties depend on the group-theoretical structure of underlying theory and its ultraviolet (UV) completion. The discovery of such a family of new (pseudo)scalar states with invariant masses not exceeding 200 GeV in these channels is of high priority for strongly-coupled dynamics searches at the LHC.

A number of realisations of such new dynamics at the TeV scale, known as "Techni-

color" (TC) or "compositeness" scenarios, have been proposed in the literature (for a review, see e.g. [191, 192]). However, these have been strongly restricted by electroweak (EW) precision tests and recent SM Higgs-like particle observations. At present, among the most appealing scenarios for dynamical EWSB consistent with current constraints is a class of TC models with vector-like (Dirac) UV completion – vector-like Technicolor (VLTC). The simplest realisation of a VLTC scenario with two vector-like or Dirac techniflavors and a SM-like Higgs boson has been studied for the first time in [193, 194] and very recently has emerged in composite Higgs scenarios with confined $SU(2)_{\rm TC}$ [195, 196].

Here an important case of light exotic resonances is considered, namely the pseudo-Goldstone T-pions, commonly predicted by Technicolor extensions of the Standard Model. Since T-pions in the consistent VLTC scenario do not couple directly to SM fermions and gluons, the only way to produce them is in vector-boson ($\gamma\gamma$, γZ, ZZ) fusion. At Born level, the pseudoscalar T-pions can only be pair-produced in $\gamma\gamma$ and VBF reactions. At one-loop level, T-pions are coupled to photon and vector bosons via either a T-quark triangle or box diagrams, depending on the number of T-colors. In a QCD-like scenario with $N_{\rm TC} = 3$ and a degenerate T-quark doublet, the T-pion decays into two gauge bosons V_1 and V_2, while in the case of $N_{\rm TC} = 2$ the T-pion can only decay into three gauge bosons via a T-quark box diagram. Thus, in the former case one expects single T-pion $\tilde{\pi}^0$ production, predominantly, in $\gamma\gamma$-fusion via the T-quark triangle, whereas in the latter case a single T-pion will be produced in V_1V_2-fusion in association with an extra gauge boson V_3. Then, each produced T-pion should further decay either into two or three gauge bosons, depending on $N_{\rm TC}$, or into a pair of Higgs bosons $\tilde{\pi} \to hh$.

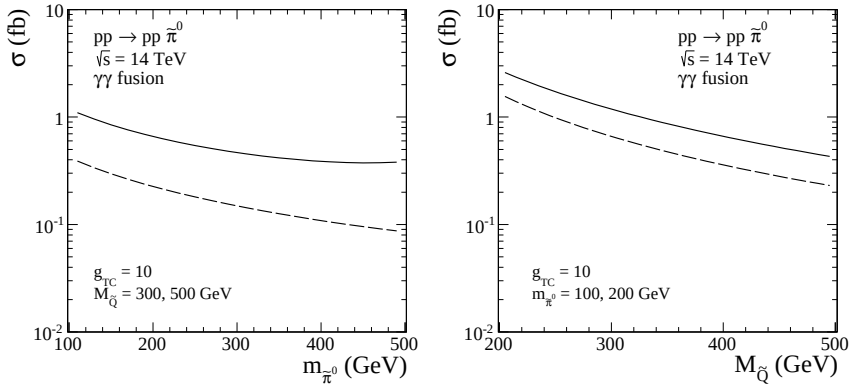

Fig. 5.17: Integrated cross section of central exclusive T-pion as a function of T-pion mass (left) and T-quark mass (right) for fixed model parameters. For more details, see [194].

The central exclusive $pp \to p\tilde{\pi}^0 p$ reaction dominated by the $\gamma^*\gamma^* \to \tilde{\pi}^0 \to \gamma\gamma$ hard subprocess is of special interest for the $N_{\rm TC} = 3$ scenario (the $N_{\rm TC} = 2$ case is much more challenging). As can be seen in Fig. 5.17, the predicted central exclusive $\tilde{\pi}^0$ production cross section in the $\gamma\gamma$ channel can be of the same order or even exceed the traditional Higgs boson CEP cross section, making the considered proposal particularly relevant for the forward physics program at the LHC [1, 5]; see also [197] for a study of the CEP of a BSM dilaton, which is for example predicted within a range of techicolour scenarios.

In order to estimate the feasibility of such an exclusive T-pion measurement the exclusive $\gamma\gamma$ background must be considered. There are two basic non-resonant leading order box-induced contributions – the QCD mechanism via $gg \to \gamma\gamma$ and the QED (light-by-light) scattering mechanism ($\gamma\gamma \to \gamma\gamma$), depicted in Fig. 5.7. At relatively low masses, the QCD mechanism domi-

nates, however above $M_{\gamma\gamma} > O(100)$ GeV, the photon-photon mechanism takes over. The latter is therefore the most important potential background for the T-pion signal in the $\gamma\gamma$ channel. After inclusion of the ATLAS detector resolution, the S/B ratio for the T-pion CEP is significantly better than for the inclusive case as well as for Higgs boson CEP in the $b\bar{b}$ channel. This analysis demonstrates that the exclusive reaction $pp \to pp\gamma\gamma$ is probably the best suited in searches for T-pions at the LHC; see [194] for further details.

In general, this indicates that the exclusive production of two photons in pp collisions can be an especially attractive channel for the search of new heavy resonances that predominantly couple to photons. This process is interesting by itself and rather unique due to relatively well understood QED mechanism. Any deviation from the Standard Model prediction here may be a signal of New Physics contributions. This motivates the search for both continuum and resonance $\gamma\gamma$ signals of New Physics in exclusive processes, via the ATLAS and CMS forward proton tagging detectors.

5.6 Conclusion

In this chapter, the central exclusive production (CEP) process has been considered, where a system X is produced in the central detector while the outgoing protons remain intact after the collision. This may be mediated purely by the strong interaction, in the language of Regge theory by double pomeron exchange, as well as by two–photon and photon–Pomeron collisions (that is, in photoproduction reactions). Theoretically, these require the development of a framework which is sensitive to both the hard and soft QCD regimes, and lead to predictions and effects which are not seen in the more common inclusive modes. Experimentally, CEP represents a very clean signal (in the absence of pile–up), while the outgoing protons can be measured by proton tagging detectors situated far from the interaction point. This is the aim of the installed CMS–TOTEM, CT–PPS and ALFA and planned AFP detectors at the LHC. This chapter has discussed the motivation and possibilities for performing exclusive measurements both with and without tagged protons at low to medium luminosity, as part of special high β^* runs with ATLAS and CMS, or during general LHCb and ALICE running, and at higher luminosity with tagged protons, where tools such as precision timing detectors will be fundamental to control pile up effects. A wide range of final–states has been considered, and it has been shown how the exclusive mode can provide additional insight and information about physics both within and beyond the SM, which is complementary to and can extend beyond the possibilities with more conventional inclusive measurements.

Acknowledgments

Pieces of this chapter has been supported in part by Polish Nation Science Centre grants number: 2013/08/M/ST2/00320, DEC-2011/01/B/ST2/04535 and 2012/05/B/ST2/02480. Some of the results presented here come from a fruitful collaboration with Emilien Chapon, Sylvain Fichet, Gero von Gersdorff, Oldřich Kepka, Bruno Lenzi.

References

[1] M. G. Albrow, T. D. Coughlin and J. R. Forshaw, Prog. Part. Nucl. Phys. **65** (2010) 149 [arXiv:1006.1289 [hep-ph]].

[2] L. A. Harland-Lang, V. A. Khoze, M. G. Ryskin and W. J. Stirling, Int. J. Mod. Phys. A **29** (2014) 1430031 [arXiv:1405.0018 [hep-ph]].

[3] L. A. Harland-Lang, V. A. Khoze and M. G. Ryskin, Int. J. Mod. Phys. A **29**, 1446004 (2014).

[4] L. A. Harland-Lang, V. A. Khoze and M. G. Ryskin, Int. J. Mod. Phys. A **30**, 1542013 (2015).

[5] V. A. Khoze, A. D. Martin and M. G. Ryskin, Eur. Phys. J. C **23** (2002) 311 [hep-ph/0111078].

[6] V. A. Khoze, A. D. Martin and M. G. Ryskin, Eur. Phys. J. C **19** (2001) 477 [Erratum-ibid. C **20** (2001) 599] [hep-ph/0011393].

[7] S. Heinemeyer, V. A. Khoze, M. G. Ryskin, W. J. Stirling, M. Tasevsky and G. Weiglein, Eur. Phys. J. C **53** (2008) 231 [arXiv:0708.3052 [hep-ph]].

[8] R. S. Pasechnik, A. Szczurek and O. V. Teryaev, Phys. Rev. D **78** (2008) 014007 [arXiv:0709.0857 [hep-ph]].

[9] T. D. Coughlin and J. R. Forshaw, JHEP **1001** (2010) 121 [arXiv:0912.3280 [hep-ph]].

[10] R. S. Pasechnik, A. Szczurek and O. V. Teryaev, Phys. Rev. D **81** (2010) 034024 [arXiv:0912.4251 [hep-ph]].

[11] D. d'Enterria and G. G. da Silveira, Phys. Rev. Lett. **111** (2013) 080405 [arXiv:1305.7142 [hep-ph]].

[12] L. A. Harland-Lang, Phys. Rev. D **88** (2013) 3, 034029 [arXiv:1306.6661 [hep-ph]].

[13] A. B. Kaidalov, V. A. Khoze, A. D. Martin and M. G. Ryskin, Eur. Phys. J. C **31** (2003) 387 [hep-ph/0307064].

[14] J. D. Bjorken, Phys. Rev. D **47** (1993) 101.

[15] M. G. Ryskin, A. D. Martin and V. A. Khoze, Eur. Phys. J. C **60** (2009) 265 [arXiv:0812.2413 [hep-ph]].

[16] S. Ostapchenko, Phys. Rev. D **81** (2010) 114028 [arXiv:1003.0196 [hep-ph]].

[17] V. A. Khoze, A. D. Martin and M. G. Ryskin, arXiv:1402.2778 [hep-ph].

[18] E. Gotsman, E. Levin and U. Maor, arXiv:1403.4531 [hep-ph].

[19] A. D. Martin, M. G. Ryskin and V. A. Khoze, Acta Phys. Polon. B **40** (2009) 1841 [arXiv:0903.2980 [hep-ph]].

[20] A. B. Kaidalov, V. A. Khoze, A. D. Martin and M. G. Ryskin, Eur. Phys. J. C **33** (2004) 261 [hep-ph/0311023].

[21] L. A. Harland-Lang, V. A. Khoze, M. G. Ryskin and W. J. Stirling, Eur. Phys. J. C **69** (2010) 179 [arXiv:1005.0695 [hep-ph]].

[22] M. Boonekamp, R. B. Peschanski and C. Royon, Nucl. Phys. B **669** (2003) 277 [Erratum-ibid. B **676** (2004) 493] [hep-ph/0301244].

[23] A. Bialas and P. V. Landshoff, Phys. Lett. B **256** (1991) 540.

[24] J. R. Forshaw, hep-ph/0508274.

[25] T. Aaltonen *et al.* [CDF Collaboration], Phys. Rev. D **77** (2008) 052004 [arXiv:0712.0604 [hep-ex]].

[26] L. A. Harland-Lang, V. A. Khoze, M. G. Ryskin and W. J. Stirling, Eur. Phys. J. C **71** (2011) 1545 [arXiv:1011.0680 [hep-ph]].

[27] V. A. Khoze, A. D. Martin and M. G. Ryskin, Eur. Phys. J. C **73** (2013) 2503 [arXiv:1306.2149 [hep-ph]].

[28] L. A. Harland-Lang, V. A. Khoze and M. G. Ryskin, Eur. Phys. J. C **74** (2014) 2848 [arXiv:1312.4553 [hep-ph]].

[29] V. A. Khoze, A. D. Martin and M. G. Ryskin, Eur. Phys. J. C **24** (2002) 581 [hep-ph/0203122].

[30] The `Dime` code and documentation are available at `http://projects.hepforge.org/dimemc/`

[31] L. A. Harland-Lang, V. A. Khoze, M. G. Ryskin and W. J. Stirling, Eur. Phys. J. C **65** (2010) 433 [arXiv:0909.4748 [hep-ph]].

[32] V. A. Khoze, A. D. Martin, M. G. Ryskin and W. J. Stirling, Eur. Phys. J. C **35** (2004) 211 [hep-ph/0403218].

[33] R. S. Pasechnik, A. Szczurek and O. V. Teryaev, Phys. Lett. B **680** (2009) 62 [arXiv:0901.4187 [hep-ph]].

[34] F. Yuan, Phys. Lett. B **510** (2001) 155 [hep-ph/0103213].

[35] V. A. Petrov and R. A. Ryutin, JHEP **0408** (2004) 013 [hep-ph/0403189].

[36] A. Bzdak, Phys. Lett. B **619** (2005) 288 [hep-ph/0506101].

[37] M. Rangel, C. Royon, G. Alves, J. Barreto and R. B. Peschanski, Nucl. Phys. B **774** (2007) 53 [hep-ph/0612297].

[38] T. Aaltonen *et al.* [CDF Collaboration], Phys. Rev. Lett. **102** (2009) 242001 [arXiv:0902.1271 [hep-ex]].

[39] [LHCb Collaboration], LHCb-CONF-2011-022, CERN-LHCb-CONF-2011-022.

[40] L. D. Landau, Dokl. Akad. Nauk Ser. Fiz. **60** (1948) 207.

[41] C. -N. Yang, Phys. Rev. **77** (1950) 242.

[42] R. Aaij *et al.* [LHCb Collaboration], JHEP **1310** (2013) 115 [arXiv:1307.4285 [hep-ex]].

[43] K. A. Olive *et al.* [Particle Data Group Collaboration], Chin. Phys. C **38**, 090001 (2014).

[44] L. A. Harland-Lang, V. A. Khoze, M. G. Ryskin and W. J. Stirling, Eur. Phys. J. C **72** (2012) 2110 [arXiv:1204.4803 [hep-ph]].

[45] P. Lebiedowicz, R. Pasechnik and A. Szczurek, Nucl. Phys. Proc. Suppl. **219-220** (2011) 284 [arXiv:1108.2522 [hep-ph]].

[46] The `SuperChic` code and documentation are available at `http://projects.hepforge.org/superchic/`

[47] T. Aaltonen *et al.* [CDF Collaboration], arXiv:1502.01391 [hep-ex].

[48] N. Brambilla, S. Eidelman, B. K. Heltsley, R. Vogt, G. T. Bodwin, E. Eichten, A. D. Frawley and A. B. Meyer *et al.*, Eur. Phys. J. C **71** (2011) 1534 [arXiv:1010.5827 [hep-ph]].

[49] R. M. Albuquerque, J. M. Dias, M. Nielsen and C. M. Zanetti, Phys. Rev. D **89** (2014) 076007 [arXiv:1311.6411 [hep-ph]].

[50] W. Sreethawong, K. Xu and Y. Yan, arXiv:1306.2780 [hep-ph].

[51] R. Aaij *et al.* [LHCb Collaboration], Phys. Rev. Lett. **110** (2013) 22, 222001 [arXiv:1302.6269 [hep-ex]].

[52] S. Chatrchyan *et al.* [CMS Collaboration], JHEP **1304** (2013) 154 [arXiv:1302.3968 [hep-ex]].

[53] P. Artoisenet and E. Braaten, Phys. Rev. D **81** (2010) 114018 [arXiv:0911.2016 [hep-ph]].

[54] C. Bignamini, B. Grinstein, F. Piccinini, A. D. Polosa and C. Sabelli, Phys. Rev. Lett. **103** (2009) 162001 [arXiv:0906.0882 [hep-ph]].

[55] M. B. Voloshin, Prog. Part. Nucl. Phys. **61** (2008) 455 [arXiv:0711.4556 [hep-ph]].

[56] R. Aaij *et al.* [LHCb Collaboration], J. Phys. G **41** (2014) 055002 [arXiv:1401.3288 [hep-ex]].

[57] A. D. Martin, W. J. Stirling, R. S. Thorne and G. Watt, Eur. Phys. J. C **63** (2009) 189 [arXiv:0901.0002 [hep-ph]].

[58] T. Aaltonen *et al.* [CDF Collaboration], Phys. Rev. Lett. **108** (2012) 081801 [arXiv:1112.0858 [hep-ex]].

[59] S. Chatrchyan *et al.* [CMS Collaboration], JHEP **1211**, 080 (2012) [arXiv:1209.1666 [hep-ex]].

[60] S. Fichet, G. von Gersdorff, B. Lenzi, C. Royon and M. Saimpert, arXiv:1411.6629 [hep-ph].

[61] L. A. Harland-Lang, V. A. Khoze, M. G. Ryskin and W. J. Stirling, Eur. Phys. J. C **71** (2011) 1714 [arXiv:1105.1626 [hep-ph]].

[62] L. A. Harland-Lang, V. A. Khoze, M. G. Ryskin and W. J. Stirling, Phys. Lett. B **725** (2013) 316 [arXiv:1304.4262 [hep-ph]].

[63] S. J. Brodsky and G. P. Lepage, Phys. Rev. D **24** (1981) 1808.

[64] M. Benayoun and V. L. Chernyak, Nucl. Phys. B **329** (1990) 285.

[65] L. A. Harland-Lang, V. A. Khoze, M. G. Ryskin and W. J. Stirling, Eur. Phys. J. C **73** (2013) 2429 [arXiv:1302.2004 [hep-ph]].

[66] C. E. Thomas, JHEP **0710** (2007) 026 [arXiv:0705.1500 [hep-ph]].

[67] C. Di Donato, G. Ricciardi and I. Bigi, Phys. Rev. D **85** (2012) 013016 [arXiv:1105.3557 [hep-ph]].

[68] P. Lebiedowicz and A. Szczurek, AIP Conf. Proc. **1523** (2012) 132 [arXiv:1212.0166 [hep-ph]].

[69] T. Aaltonen *et al.* [CDF Collaboration], Phys. Rev. Lett. **99** (2007) 242002 [arXiv:0707.2374 [hep-ex]].

[70] David d'Enterria, private communication.

[71] R. Schicker, Int. J. Mod. Phys. A **29** (2014) 1446015 [arXiv:1411.1283 [hep-ex]].

[72] F. Reidt, *Analysis of Double-Gap Events in Proton-Proton Collisions at* $\sqrt{s} = 7$ *TeV with the ALICE Experiment at the LHC*, Master thesis, Heidelberg, 2012

[73] L. Adamczyk, W. Guryn and J. Turnau, Int. J. Mod. Phys. A **29** (2014) 28, 1446010 [arXiv:1410.5752 [hep-ex]].

[74] R. Staszewski, P. Lebiedowicz, M. Trzebinski, J. Chwastowski and A. Szczurek, *"Exclusive* $\pi^+\pi^-$ *Production at the LHC with Forward Proton Tagging,"* Acta Phys. Polon. B **42**, 1861 (2011).

[75] V. Mathieu, N. Kochelev and V. Vento, Int. J. Mod. Phys. E **18** (2009) 1 [arXiv:0810.4453 [hep-ph]].

[76] Y. Chen, A. Alexandru, S. J. Dong, T. Draper, I. Horvath, F. X. Lee, K. F. Liu and

N. Mathur *et al.*, Phys. Rev. D **73** (2006) 014516 [hep-lat/0510074].
[77] C. J. Morningstar and M. J. Peardon, Phys. Rev. D **60** (1999) 034509 [hep-lat/9901004].
[78] A. Kirk, Phys. Lett. B **489** (2000) 29 [hep-ph/0008053].
[79] A. Kirk [WA102 Collaboration], In *Frascati 1999, Hadron spectroscopy* 29-36 [hep-ph/9904314].
[80] A. Kirk [WA102 Collaboration], Nucl. Phys. A **663** (2000) 608 [hep-ph/9907302].
[81] W. J. Lee and D. Weingarten, Phys. Rev. D **61** (2000) 014015 [hep-lat/9910008].
[82] H. Y. Cheng, C. K. Chua and K. F. Liu, Phys. Rev. D **74** (2006) 094005 [hep-ph/0607206].
[83] W. Ochs, J. Phys. G **40** (2013) 043001 [arXiv:1301.5183 [hep-ph]].
[84] M. Chanowitz, Phys. Rev. Lett. **95** (2005) 172001 [hep-ph/0506125].
[85] S. Chekanov *et al.* [ZEUS Collaboration], Phys. Rev. Lett. **101** (2008) 112003 [arXiv:0806.0807 [hep-ex]].
[86] A. Breakstone *et al.* [Ames-Bologna-CERN-Dortmund-Heidelberg-Warsaw Collaboration], Z. Phys. C **58** (1993) 251.
[87] C. F. Qiao and L. Tang, Phys. Rev. Lett. **113** (2014) 22, 221601 [arXiv:1408.3995 [hep-ph]].
[88] TOTEM Collaboration, Timing Measurements in the Vertical Roman Pots of the TOTEM Experiment, CERN-LHCC-2014-020 TOTEM-TDR-002 (2014); TOTEM Collaboration, TOTEM upgrade proposal, CERN-LHCC-2013-009 / LHCCP-007 (2013). Timing Measurements in the Vertical Roman Pots of the TOTEM Experiment LHCC document CERN-LHCC-2014-020, CERN-LHCC-2014-024 ; TOTEM-TDR-002-ADD-1 (2014)
[89] D. Barberis *et al.* [WA102 Collaboration], Phys. Lett. B **462** (1999) 462 [hep-ex/9907055].
[90] R. Aaij *et al.* [LHCb Collaboration], J. Phys. G **41** (2014) 115002 [arXiv:1407.5973 [hep-ex]].
[91] L. A. Harland-Lang, V. A. Khoze and M. G. Ryskin, J. Phys. G **42** (2015) 5, 055001 [arXiv:1409.4785 [hep-ph]].
[92] V. M. Abazov *et al.* [D0 Collaboration], arXiv:1406.2380 [hep-ex].
[93] C. H. Kom, A. Kulesza and W. J. Stirling, Phys. Rev. Lett. **107** (2011) 082002 [arXiv:1105.4186 [hep-ph]].
[94] R. Aaij *et al.* [LHCb Collaboration], Phys. Lett. B **707** (2012) 52 [arXiv:1109.0963 [hep-ex]].
[95] A. V. Berezhnoy, A. K. Likhoded, A. V. Luchinsky and A. A. Novoselov, Phys. Rev. D **84** (2011) 094023 [arXiv:1101.5881 [hep-ph]].
[96] A. D. Martin, M. G. Ryskin and V. A. Khoze, Phys. Rev. D **56** (1997) 5867 [hep-ph/9705258].
[97] V. A. Khoze, A. D. Martin and M. G. Ryskin, Eur. Phys. J. C **48** (2006) 467 [hep-ph/0605113].
[98] L. A. Harland-Lang, V. A. Khoze and M. G. Ryskin, future publication.
[99] V. A. Khoze, M. G. Ryskin and W. J. Stirling, Eur. Phys. J. C **48** (2006) 477 [hep-ph/0607134].
[100] V. A. Khoze, M. G. Ryskin and A. D. Martin, Eur. Phys. J. C **64** (2009) 361 [arXiv:0907.0966 [hep-ph]].
[101] L. A. Harland-Lang, JHEP **1505** (2015) 146 [arXiv:1503.06798 [hep-ph]].
[102] V. M. Abazov *et al.* [D0 Collaboration], Phys. Lett. B **705** (2011) 193 [arXiv:1009.2444 [hep-ex]].

[103] S. Chatrchyan *et al.* [CMS Collaboration], "Observation of a diffractive contribution to di-jet production in proton-proton collisions at $\sqrt{s} = 7$ TeV", Phys. Rev. D 87, 012006 (2013), [arXiv:1209.1805 [hep-ex]].

[104] O. Kepka and C. Royon, Phys. Rev. D **76**, 034012 (2007) [arXiv:0704.1956 [hep-ph]].

[105] V. A. Petrov and R. A. Ryutin, J. Phys. G **35** (2008) 065004 [arXiv:0711.2370 [hep-ph]].

[106] R. A. Ryutin, Eur. Phys. J. C **73** (2013) 2443 [arXiv:1211.2105 [hep-ph]].

[107] M. Boonekamp, A. Dechambre, V. Juranek, O. Kepka, M. Rangel, C. Royon, R. Staszewski, e-Print: arXiv:1102.2531; M. Boonekamp, V. Juranek, O. Kepka, C. Royon "Forward Physics Monte Carlo", "Proceedings of the workshop: HERA and the LHC workshop series on the implications of HERA for LHC physics," arXiv:0903.3861 [hep-ph].

[108] ATLAS Collaboration, *Exclusive Jet Production with Forward Proton Tagging*, ATL-PHYS-PUB-2015-003.

[109] ATLAS Collaboration, *The ATLAS Simulation Infrastructure*, Eur. Phys. J. **C 70** (2010) 823.

[110] M. Cacciari, G. P. Salam and G. Soyez, "The anti-k_T jet clustering algorithm", JHEP 0804 (2008) 063 [arXiv:0802.1189 [hep-ph]].

[111] M. Trzebinski, "Study of QCD and Diffraction with the ATLAS detector at the LHC", CERN-THESIS-2013-166.

[112] C. F. von Weizsacker, Z. Phys. **88**, 612 (1934).

[113] E. J. Williams, Phys. Rev. **45**, 729 (1934).

[114] S. R. Klein and J. Nystrand, Phys. Rev. Lett. **92** (2004) 142003 [hep-ph/0311164].

[115] W. Schäfer and A. Szczurek, Phys. Rev. D **76** (2007) 094014 [arXiv:0705.2887 [hep-ph]].

[116] V. A. Khoze, A. D. Martin and M. G. Ryskin, Eur. Phys. J. C **55**, 363 (2008) [arXiv:0802.0177 [hep-ph]].

[117] L. Motyka and G. Watt, Phys. Rev. D **78** (2008) 014023 [arXiv:0805.2113 [hep-ph]].

[118] S. P. Jones, A. D. Martin, M. G. Ryskin and T. Teubner, JHEP **1311** (2013) 085 [arXiv:1307.7099].

[119] I. V. Anikin, D. Y. Ivanov, B. Pire, L. Szymanowski and S. Wallon, Phys. Lett. B **682** (2010) 413-418 [arXiv:0903.4797 [hep-ph]]; Nucl. Phys. B **828**, (2010) 1-68 [arXiv:0909.4090 [hep-ph]].

[120] I. V. Anikin, A. Besse, D. Y. Ivanov, B. Pire, L. Szymanowski and S. Wallon, Phys. Rev. D **84** (2011) 054004 [arXiv:1105.1761 [hep-ph]].

[121] A. Besse, L. Szymanowski and S. Wallon, Nucl. Phys. B **867**, (2013) 19-60 [arXiv:1204.2281 [hep-ph]].

[122] A. Besse, L. Szymanowski and S. Wallon, JHEP **1311** (2013) 062 [arXiv:1302.1766 [hep-ph]].

[123] V. Guzey and M. Zhalov, arXiv:1405.7529 [hep-ph].

[124] V. Barone and E. Predazzi, *High-energy particle diffraction* (Springer, Berlin 2002); S. Donnachie, H. G. Dosch, O. Nachtmann and P. Landshoff, Camb. Monogr. Part. Phys. Nucl. Phys. Cosmol. **19** (2002) 1.

[125] S. Donnachie, H. G. Dosch, O. Nachtmann and P. Landshoff, Camb. Monogr. Part. Phys. Nucl. Phys. Cosmol. **19** (2002) 1.

[126] C. Ewerz, "The Odderon in quantum chromodynamics," hep-ph/0306137.

[127] V. A. Khoze, A. D. Martin, R. Orava and M. G. Ryskin, Eur. Phys. J. C **19** (2001) 313

[hep-ph/0010163].
[128] L. Motyka, arXiv:0808.2216 [hep-ph].
[129] N. Armesto and A. H. Rezaeian, Phys. Rev. D **90** (2014) 054003 [arXiv:1402.4831 [hep-ph]].
[130] V. M. Budnev, I. F. Ginzburg, G. V. Meledin and V. G. Serbo, Phys. Rept. **15** (1975) 181.
[131] S. Chatrchyan *et al.* [CMS Collaboration], JHEP **1307**, 116 (2013) [arXiv:1305.5596 [hep-ex]].
[132] B. Pire, F. Schwennsen, L. Szymanowski and S. Wallon, "Hard Pomeron-Odderon interference effects in the production of $\pi + \pi$ pairs in high energy gamma-gamma collisions at the LHC", Phys. Rev. D **78** (2008) 094009
[133] J. A. M. Vermaseren, Nucl. Phys. B **229** (1983) 347.
[134] S. P. Baranov, O. Duenger, H. Shooshtari and J. A. M. Vermaseren, In *Hamburg 1991, Proceedings, Physics at HERA, vol. 3* 1478-1482. (see HIGH ENERGY PHYSICS INDEX 30 (1992) No. 12988)
[135] S. Chatrchyan *et al.* [CMS Collaboration], JHEP **1201**, 052 (2012) [arXiv:1111.5536 [hep-ex]].
[136] G. Aad *et al.* [ATLAS Collaboration], arXiv:1506.07098 [hep-ex].
[137] B. E. Cox, J. R. Forshaw and R. Sandapen, JHEP **0906** (2009) 034 [arXiv:0905.0102 [hep-ph]].
[138] V. P. Goncalves and M. V. T. Machado, Phys. Rev. C **84**, 011902 (2011).
[139] J. Bartels, K. J. Golec-Biernat and K. Peters, Acta Phys. Polon. B **34** (2003) 3051 [hep-ph/0301192].
[140] H. Kowalski, L. Motyka and G. Watt, Phys. Rev. D **74** (2006) 074016 [hep-ph/0606272].
[141] A. G. Shuvaev, K. J. Golec-Biernat, A. D. Martin and M. G. Ryskin, Phys. Rev. D **60** (1999) 014015.
[142] I. P. Ivanov, N. N. Nikolaev and A. A. Savin, Phys. Part. Nucl. **37** (2006) 1.
[143] I. P. Ivanov and N. N. Nikolaev, JETP Lett. **69**, 294 (1999). Phys. Rev. D **47** (1993) 101.
[144] S. P. Jones, A. D. Martin, M. G. Ryskin and T. Teubner, J. Phys. G **41** (2014) 055009 [arXiv:1312.6795 [hep-ph]].
[145] A. Rybarska, W. Schäfer and A. Szczurek, Phys. Lett. B **668** (2008) 126.
[146] A. Cisek, W. Schäfer and A. Szczurek, Phys. Lett. B **690** (2010) 168.
[147] A. Cisek, P. Lebiedowicz, W. Schäfer and A. Szczurek, Phys. Rev. D **83** (2011) 114004.
[148] A. Cisek, W. Schäfer and A. Szczurek, arXiv:1405.2253 [hep-ph].
[149] R. Aaij *et al.* [LHCb Collaboration], J. Phys. G **40** (2013) 045001 [arXiv:1301.7084 [hep-ex]].
[150] I. P. Ivanov and N. N. Nikolaev, Phys. Rev. D **65** (2002) 054004 [hep-ph/0004206].
[151] K. Kutak and A. M. Staśto, Eur. Phys. J. C **41** (2005) 343
[152] G. G. da Silveira, L. Forthomme, K. Piotrzkowski, W. Schäfer and A. Szczurek, arXiv:1409.1541 [hep-ph].
[153] M. B. Gay Ducati, M. T. Griep and M. V. T. Machado, Phys. Rev. D **88**, 017504 (2013).
[154] V. P. Goncalves, B. D. Moreira and F. S. Navarra, Phys. Lett. B **742** (2015) 172 [arXiv:1408.1344 [hep-ph]].
[155] V. P. Goncalves and M. V. T. Machado, Eur. Phys. J. C **56** (2008) 33 [Erratum-ibid. C **61** (2009) 351] [arXiv:0710.4287 [hep-ph]].

[156] R. Aaij *et al.* [LHCb Collaboration], arXiv:1505.08139 [hep-ex].

[157] C. Alexa *et al.* [H1 Collaboration], Eur. Phys. J. C **73** (2013) 2466 [arXiv:1304.5162 [hep-ex]].

[158] B. B. Abelev *et al.* [ALICE Collaboration], Phys. Rev. Lett. **113** (2014) 23, 232504 [arXiv:1406.7819 [nucl-ex]].

[159] V. A. Khoze, A. D. Martin, M. G. Ryskin and A. G. Shuvaev, Eur. Phys. J. C **68**, 125 (2010) [arXiv:1002.2857 [hep-ph]].

[160] H. Niewiadomski on behalf of TOTEM Collaboration, TOTEM Physics program, analysis and results, LHC seminar 29 January 2013, `http://indico.cern.ch/event/230889/`.

[161] P. A. M. Dirac, *Quantised Singularities in the Electromagnetic Field*, Proc. R. Soc. Lond. A September 1, 1931, vol 133, no. 821, 60 – 72.

[162] K. A. Milton, *Theoretical and experimental status of magnetic monopoles*, Rept. Prog. Phys. **69**, 1637 (2006).

[163] B. Cabrera, *First Results from a Superconductive Detector for Moving Magnetic Monopoles*, Phys. Rev. Lett. **48** (1982) 1378.

[164] A. D. Caplin, M. Hardiman, M. Koratzinos and J. C. Schouten, *Observation of an Unexplained Event From a Magnetic Monopole Detector,* Nature **321** (1986) 402.

[165] G. Aad *et al.* [ATLAS Collaboration], *Search for magnetic monopoles in* $\sqrt{s} = 7$ *TeV pp collisions with the ATLAS detector,* Phys. Rev. Lett. **109** (2012) 261803.

[166] G. R. Kalbfleisch, W. Luo, K. A. Milton, E. H. Smith and M. G. Strauss, *Limits on production of magnetic monopoles utilizing samples from the D0 and CDF detectors at the Tevatron*, Phys. Rev. D **69**, 052002 (2004).

[167] A. Aktas *et al.* [H1 Collaboration], *A Direct search for stable magnetic monopoles produced in positron-proton collisions at HERA," Eur. Phys. J. C* **41** *(2005) 133.*

[168] MoEDAL Collaboration (J. L. Pinfold *et al.*), *Technical Design Report of the MoEDAL Experiment*, CERN-LHCC-2009-006. MoEDAL-TDR-001, 2009.

[169] B. Acharya *et al.* [MoEDAL Collaboration], *The Physics Programme Of The MoEDAL Experiment At The LHC,* Int. J. Mod. Phys. A **29** (2014) 1430050.

[170] J. de Favereau de Jeneret, V. Lemaitre, Y. Liu, S. Ovyn, T. Pierzchala, K. Piotrzkowski, X. Rouby and N. Schul *et al.*, arXiv:0908.2020 [hep-ph].

[171] O. Kepka and C. Royon, Phys. Rev. D **78** (2008) 073005 [arXiv:0808.0322 [hep-ph]].

[172] S. Fichet, G. von Gersdorff, O. Kepka, B. Lenzi, C. Royon and M. Saimpert, Phys. Rev. D **89**, 114004 (2014) [arXiv:1312.5153 [hep-ph]].

[173] H. Sun, Eur. Phys. J. C **74** (2014) 8, 2977 [arXiv:1406.3897 [hep-ph]].

[174] S. Fichet and G. von Gersdorff, JHEP **1403** (2014) 102 [arXiv:1311.6815 [hep-ph]].

[175] L. Randall and R. Sundrum, Phys. Rev. Lett. **83** (1999) 3370.

[176] G. Aad *et al.* [ATLAS Collaboration], JINST **3** (2008) S08003.

[177] J. Monk and A. Pilkington, Comput. Phys. Commun. **175** (2006) 232

[178] G. Corcella, I. G. Knowles, G. Marchesini, S. Moretti, K. Odagiri, P. Richardson, M. H. Seymour and B. R. Webber, hep-ph/0210213.

[179] T. Sjostrand, S. Mrenna and P. Z. Skands, Comput. Phys. Commun. **178** (2008) 852 [arXiv:0710.3820 [hep-ph]].

[180] G. Belanger and F. Boudjema, Phys. Lett. B **288** (1992) 201.

[181] G. Abbiendi *et al.* [OPAL Collaboration], Phys. Rev. D **70** (2004) 032005 [hep-

ex/0402021].

[182] V. M. Abazov *et al.* [D0 Collaboration], Phys. Rev. D **88** (2013) 012005 [arXiv:1305.1258 [hep-ex]].

[183] ATLAS Collaboration, Letter of Intent for the Phase-I Upgrade of the ATLAS Experiment, CERN-LHCC-2011-012 / LHCC-I-020 (2011).

[184] M. Albrow *et al.* [CMS and TOTEM Collaborations], "CMS-TOTEM Precision Proton Spectrometer", CERN-LHCC-2014-021. TOTEM-TDR-003. CMS-TDR-13, Sept. 2014.

[185] G. Aad *et al.* [ATLAS Collaboration], Phys. Lett. B **716** (2012) 1 [arXiv:1207.7214 [hep-ex]].

[186] S. Chatrchyan *et al.* [CMS Collaboration], JHEP **1306**, 081 (2013) [arXiv:1303.4571 [hep-ex]].

[187] J. Ellis, arXiv:1501.05418 [hep-ph].

[188] S. Weinberg, Phys. Rev. D **13** (1976) 974.

[189] L. Susskind, Phys. Rev. D **20** (1979) 2619.

[190] D. Barducci, A. Belyaev, M. S. Brown, S. De Curtis, S. Moretti and G. M. Pruna, JHEP **1309**, 047 (2013) [arXiv:1302.2371 [hep-ph]].

[191] C. T. Hill and E. H. Simmons, Phys. Rept. **381**, 235 (2003) [Erratum-ibid. **390**, 553 (2004)] [hep-ph/0203079].

[192] F. Sannino, Acta Phys. Polon. B **40** (2009) 3533 [arXiv:0911.0931 [hep-ph]].

[193] R. Pasechnik, V. Beylin, V. Kuksa and G. Vereshkov, Phys. Rev. D **88**, 075009 (2013) [arXiv:1304.2081 [hep-ph]].

[194] P. Lebiedowicz, R. Pasechnik and A. Szczurek, Nucl. Phys. B **881**, 288 (2014) [arXiv:1309.7300 [hep-ph]].

[195] A. Hietanen, R. Lewis, C. Pica and F. Sannino, arXiv:1404.2794 [hep-lat].

[196] G. Cacciapaglia and F. Sannino, arXiv:1402.0233 [hep-ph].

[197] V. P. Goncalves and W. K. Sauter, Phys. Rev. D **91** (2015) 035004 [arXiv:1501.06354 [hep-ph]].

Chapter 6

Cosmic Ray Physics, Particle multiplicities, correlations and spectra

Convener and Editor: T. Pierog
Internal Reviewers: D. D'Enterria, T. Sako, D. Salek

In this chapter, measurements needed for the simulation of cosmic ray air showers are reported. A general overview of the air-shower measurements is presented in Section 6.1, followed by a brief overview of the air-shower simulations in Section 6.2. Sections 6.3-6.5 give an overview of the past and future planned measurements that are relevant to understand and fine-tune hadronic models used for air shower simulations. Finally, a proposal for a dedicated beam conditions for min-bias analyses in Run-2 is outlined in Section 6.6.

6.1 Introduction

Understanding the sources and the propagation of cosmic rays are central questions of astroparticle physics. While there is increasing evidence that supernova remnants accelerate cosmic rays up to energies of $\sim Z \times 10^{14}$ eV (with Z being the charge of the cosmic ray nucleus), the sources of the particles of energies up to 10^{20} eV are not known [1]. Accelerating particles to such energies requires exceptional astrophysical objects [2]. Using the LHC technology of superconducting magnets one would have to build the ring of an LHC-like accelerator as big as the orbit of the planet Mercury to be able to accelerate protons up to 10^{20} eV. Ultra-high energy cosmic rays are not only messengers from the extreme Universe, they also allow us to study the laws of physics under extreme conditions (for example, to search for violation of Lorentz invariance or extra dimensions) and provide a window to particle physics at energies up to $\sqrt{s} \sim 400$ TeV. Therefore it is not surprising that the physics of ultra-high energy cosmic rays is subject of very intensive research.

The study of cosmic rays of energies higher than about 10^{14} eV is hampered by the low flux of the particles arriving at Earth. With the flux being too low for direct particle detection one has to resort to the observation of extensive air showers produced by cosmic rays entering the atmosphere [3]. Although being very efficient for large aperture measurements, the drawback of this approach is the need of detailed air shower simulations for deriving the primary particle energy, and more importantly, the particle type and its mass number from the measured air shower observables.

An overview of recent measurements of the flux of cosmic rays is given in Fig. 6.1 [4]. Both the lab. energy measured in cosmic ray experiments and the equivalent c.m.s. energy, assuming the primary particles are protons, are shown. LHC measurements allow us to access, for the first time, energies beyond the *knee* in the cosmic ray spectrum, a break of the power law of the flux at about 3×10^{15} eV, which is not yet understood. In a number of models this break has been attributed to an unexpected change of particle physics above $\sqrt{s} \sim 2$ TeV, which could be ruled out by the first LHC measurements (see [5] and references therein). Furthermore the cosmic ray flux exhibits an ankle at about 3×10^{18} eV (probably related to the transition between galactic and extragalactic cosmic rays [6, 7]) and a very strong suppression at energies above 7×10^{19} eV.

To understand the sources of cosmic particles at energies above 10^{15} eV and the astro-

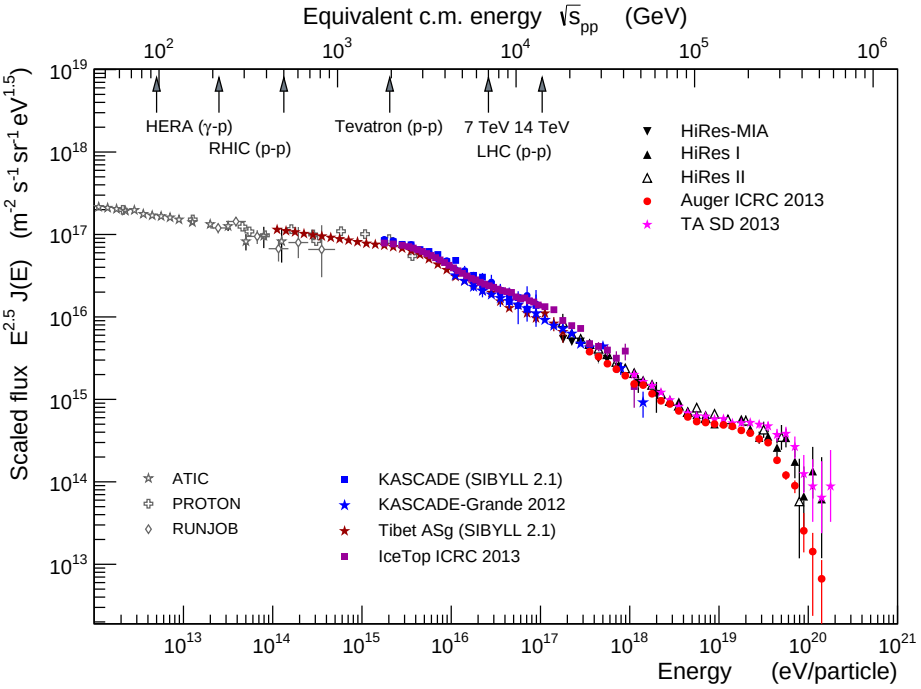

Fig. 6.1: Compilation of representative measurements of the flux of cosmic rays at Earth (from [4], updated). All data sets shown in color are derived from air shower measurements. The gray (open) symbols show direct measurements covering the energy range below the knee. The equivalent energies of LHC proton-proton collisions at different c.m.s. energies are shown at the upper axis.

physical origin of the striking features in the cosmic ray flux it is needed to derive the mass composition of cosmic rays. A good example is the flux suppression at the highest energies, which was expected due to energy loss effects in the CMB first described by Greisen [8] and Zatsepin and Kuzmin [9] (GZK). However, recent data of the Auger Observatory on the mass composition indicate that the upper end of the energy spectrum is more likely related to the maximum injection energy of the particles at the sources [10–12].

Being able to derive reliably the mass composition of cosmic rays from air shower measurements is of fundamental importance and is currently hampered mainly by the large uncertainties in predicting hadronic multiparticle production at high energy [4, 13]. Due to not being able to calculate corresponding predictions within QCD, performing further measurements at accelerators is the only way to make progress.

The relation between the characteristics of hadronic interactions at high energy and air shower observables has been reviewed in [4] and recent numerical studies can be found in [14–16]. In each hadronic interaction a number of π^0 are produced that decay immediately, feeding the electromagnetic shower component with high-energy photons. Already after less than 5 generations of hadronic interactions more than 80% of the primary particle energy is transferred to the em. shower component. In contrast, the production of muons, which are mainly coming from the decay of low energy pions, takes place only after $8-12$ consecutive hadronic interactions. Only then the energy of the produced charged pions is low enough ($E_{\pi^\pm} \sim 30$ GeV) that they decay instead of interacting again [17]. While muons are most directly linked to the hadronic shower component, interactions of a very wide range of energies are important for

understanding the properties of the muonic shower component.

Understanding the energy transfer from the hadronic to the electromagnetic and muonic shower components is of key importance for reliably predicting shower observables. This means that both secondary particle multiplicities as well as the energy given to different particle types are of direct relevance to air shower physics. In particular, knowing the number of baryons, charged and neutral pions as well as kaons at large Feynman-x are of outstanding importance. In addition, the interaction cross sections of the different particles are needed to estimate the depth at which different stages of showers develop. On the other hand, transverse momentum distributions of particles are only of secondary importance for cosmic ray interactions. Due to the large Lorentz boost needed to transfer $\sqrt{s} \sim 14$ TeV collisions to the lab. frame, in which these interactions take place in an air shower, even rather large transverse momenta lead to very small angles of the particles relative to the shower axis.

The interaction models used in cosmic ray physics have been tuned to describe not only particular data sets at certain collider energies but also the energy dependence of multiparticle production. While cosmic ray models were developed before LHC was turned on, their predictions bracket many distributions measured in minimum-bias mode at LHC, as shown section 6.2.1 and in [5]. This is a great success of the phenomenology developed for soft hadronic interactions. On the other hand, the predictions can be improved considerably by tuning the models to match the LHC data, as it will be illustrated in section 6.2.2. In the following we will discuss LHC measurements that can further improve the understanding of hadronic multiparticle production with direct relevance to cosmic ray physics and air shower simulations.

6.2 LHC and air showers

There are two categories of LHC measurements that are important for improving predictions for extensive air showers. First of all, the measurement of the multiplicities and energy fractions given to the different secondary particles, and their production cross sections can be used directly in shower simulations. However, due to the limited phase space covered by collider experiments such data can cover only a small part of the relevant phase space and will always be restricted to certain interaction energies. The second category of measurements is closely related to theoretical and phenomenological concepts implemented in interaction models. While these measurements can be limited to phase space regions that are, in general, not of direct relevance to air showers, they test fundamental concepts of the models and, thanks to energy-momentum and quantum number conservation as well as inherent correlations, allow us to make predictions on particle production in phase space regions or at energies not accessible.

However, the particle production, which carries the majority of the primary energy, is what drives the development of extensive air showers and, thus, determines all the relevant features necessary for the analysis of cosmic ray data. It is a problem for the reliability of hadronic interaction models in extensive air showers, when they are tuned to central particle production ($|\eta| < 3$) only, since this only explains about 5% of the resulting observed air shower particles as shown on Fig. 6.1 (for a primary proton at $E_0 = 10^{17}$ eV the corresponding energy of the primary interaction is $\sqrt{s_{NN}} = 14$ TeV). Crucial observables, as the location of the air shower maximum or also the muon fraction at ground level cannot be reliably predicted in this situation. Considering forward acceptance up to $\eta \sim 7$ allow to reach about 50% of the observed particles in such extensive air showers.

Of course, the better the forward direction is covered in the measurements the smaller are the model extrapolations. But it will always be necessary to use hadronic interaction models as tool to link LHC data, and accelerator measurements in general, to air shower physics.

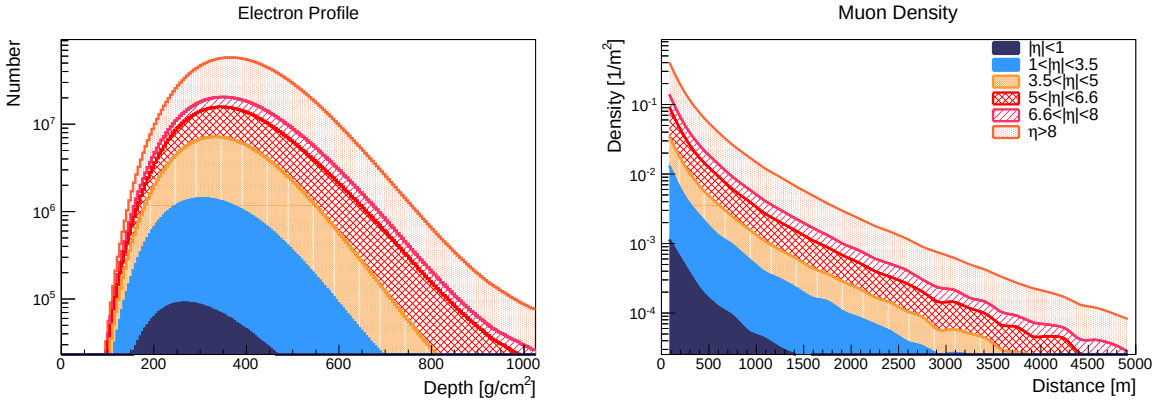

Fig. 6.1: Fraction of the air shower development for one proton induced air shower at 10^{17}eV primary energy, which is determined by the hadronic particle production in the initial inelastic p-air collision in different acceptance regions for electrons in longitudinal profile (left hand-side and muons in lateral distribution at ground (right hand-side). The acceptance is calculated in the center-of-mass frame of the collision, and the shown values are related to typical LHC detectors. The major part of the air shower is determined by particle production in the forward region.

The LHC data on total, elastic and diffractive cross sections and other measurements related to soft diffraction (rapidity gaps, energy loss, ...) are examples of the first category, while mean particle multiplicities, multiplicity distributions, jet cross sections at low $p_\perp$, particle spectra and correlations between observables belong to the second one.

6.2.1 LHC data and hadronic interaction models

For instance, measurement of the pseudorapidity dependence of the transverse energy flow and charged particle multiplicity distributions in proton-proton collisions are sensitive to the modeling of soft fragmentation effects, MPI and diffractive interactions. As well as allowing for a deeper understanding of these effects in their own right, the tuning of MC models yields more accurate simulations of the "underlying event" - comprising MPI and additional soft interactions between the primary partons in events with a hard perturbative scatter. The dynamics of soft interactions are also important to understand at the LHC due to the large number of soft interactions (pile-up) which occur during every event. An example of how models can be retuned using these data is shown on Fig. 6.2. On the left-hand side, predictions of pre-LHC models used for air shower simulations (EPOS 1.99 [18,19] (solid line), QGSJETII-03 [21,22] (dashed line), QGSJET01 [23, 24] (dash-dotted line) and SIBYLL 2.1 [25–27] (dotted line)) are compared to ALICE data [28], while on the right-hand side results are presented for the two models (EPOS LHC [29] (solid line) and QGSJETII-04 [30] (dashed line)) which where retuned using first LHC data.

By requiring a forward proton to be tagged in a LHC Roman pot based detector, a subset of inelastic interactions are probed which will allow diffraction to be investigated in more detail. This in turn will lead to more accurate tunes and possibly highlight areas of tension where the current phenomenological models are unable to describe the data and would therefore need revisiting. Such samples are especially sensitive to the modeling of the forward regions and will be of use to constrain cosmic-ray air shower physics.

The CASTOR (CMS) calorimeter provides the unique possibility to minimize the gap in the forward coverage of detectors at LHC. While other forward charged particle detectors reach up to $|\eta| < 5$, this is extended by CASTOR up to 6.6. For the physics in extensive air showers

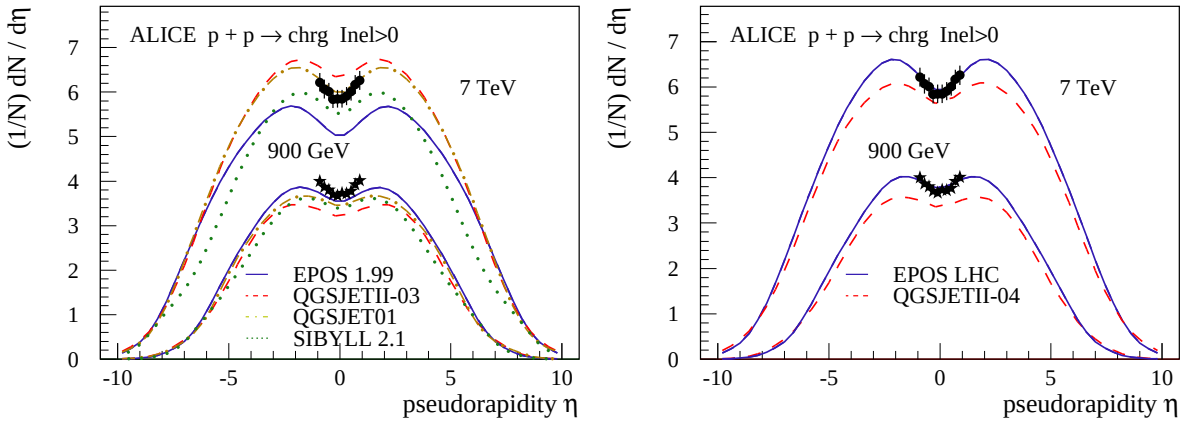

Fig. 6.2: Pseudorapidity distribution $dN/d\eta$ of charged particles for events with at least one charged particle with $|\eta| < 1$ for p-p interactions at 900 GeV and 7 TeV. Simulations with EPOS 1.99 (solid line), QGSJETII-03 (dashed line), QGSJET01 (dash-dotted line) and SIBYLL 2.1 (dotted line) on left panel, and EPOS LHC (solid line) and QGSJETII-04 (dashed line) on right panel, are compared to data points from ALICE experiment [28].

this is very important, since the vast majority of primary energy is directed in the very forward phase space. Even more forward, the LHCf experiment can measure the neutral particle spectra for the highest pseudorapidities.

Other measurements like the various cross-sections by TOTEM [31] or the rapidity gap distributions [32] and many other distributions from CMS, ATLAS, ALICE or LHCb experiments were taken into account to improve the models used for air shower simulations (see [29] for EPOS LHC).

6.2.2 Hadronic interaction models and air showers

Since min-bias measurement of antiproton-proton interactions at Tevatron had large uncertainties, LHC data provided the first high quality data useable for cosmic ray MC since the RHIC measurements at 510 GeV, thus a gain by about a factor 15 in center-of-mass energy. As a consequence the modifications of the models due to LHC data have a strong impact on air shower observables.

One of the most important measurement of air shower property is the depth of shower maximum which is sensitive to the mass composition of primary cosmic rays. As shown on Fig. 6.3 left-hand side, the simulations before LHC were such that at the highest energy the difference between model predictions was almost as large as the maximum range expected between the lightest (proton) and the heaviest (iron) element, making any mass composition measurement very difficult. Furthermore the slope of the mean X_{max} as function of the primary energy, the elongation rate, was very different between the models. So even a change in composition (change in the slope) could be interpreted very differently depending on the simulation used.

Using the post-LHC models EPOS LHC and QGSJETII-04, Fig. 6.3 right-hand side, there is still some remaining difference of about 20 g/cm^{-2} (same order than the experimental systematic error) due to the different predictions of the models for nuclear and pion interaction (see section 6.2.3) but the elongation rates are now very similar leading to the same interpretation of the break in the slope of the mean X_{max}.

Looking at the muon production at ground on Fig. 6.4, the situation really improved a

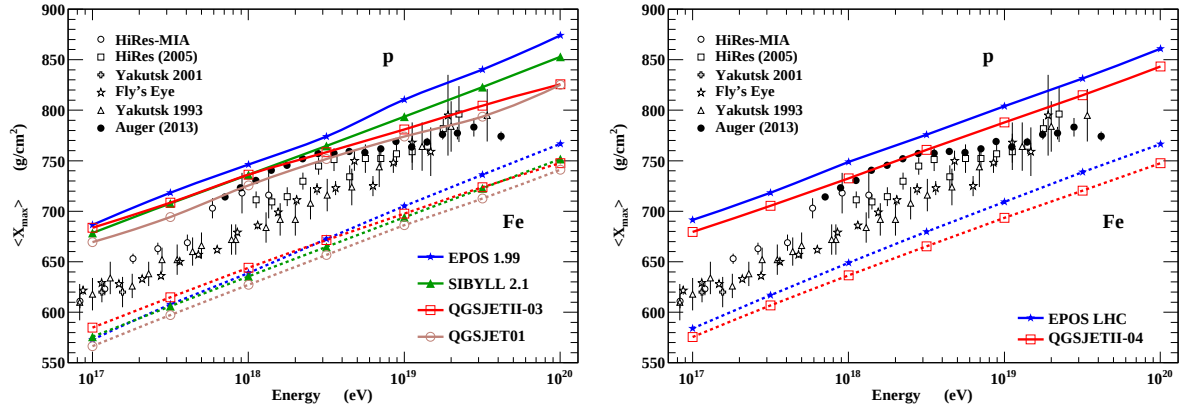

Fig. 6.3: Mean X_{max} for proton and iron induced showers as a function of the primary energy. Predictions of different high-energy hadronic interaction models, full lines for proton and dashed lines for iron with full stars for EPOS 1.99, open squares for QGSJETII-03, open circles for QGSJET01, and full triangles for SIBYLL 2.1 on top panel and full stars for EPOS LHC, open squares for QGSJETII-04 on bottom panel, are compared to data. Refs. to the data can be found in [3] and [33].

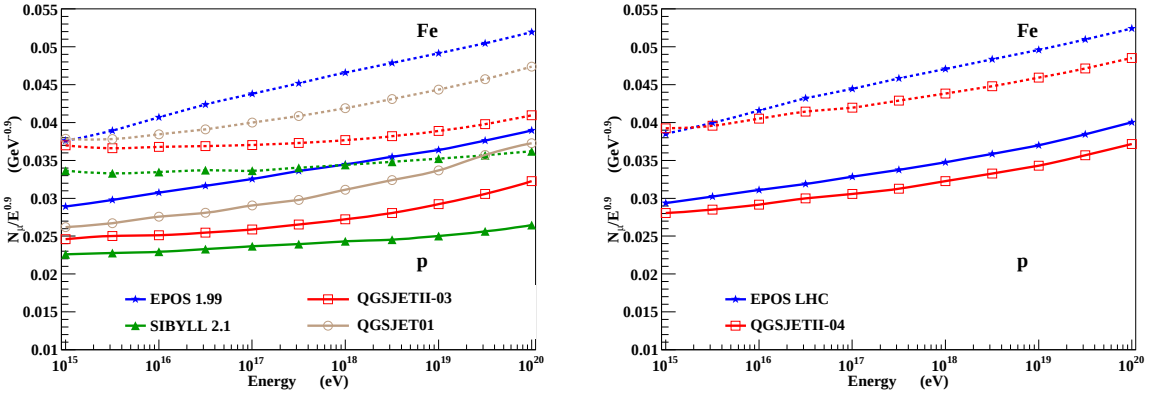

Fig. 6.4: Mean number of muons at ground divided by the primary energy to the power 0.9 for proton and iron induced showers as a function of the primary energy. Predictions of different high-energy hadronic interaction models are presented: full lines for proton and dashed lines for iron with full stars for EPOS 1.99, open squares for QGSJETII-03, open circles for QGSJET01, and full triangles for SIBYLL 2.1 on left panel and full stars for EPOS LHC, open squares for QGSJETII-04 on right panel.

lot from a confusing overlap between proton prediction from EPOS LHC and SIBYLL 2.1 for instance to an almost constant shift of about 7% between the two post LHC models.

6.2.3 Need for measuring proton-oxygen interactions

In air showers, all hadronic interactions are with nuclei of air as target particles. While there are many measurements available and planned for proton-proton interactions, only a few fixed-target measurements exist for interactions of protons or pion/kaons with light nuclei [34]. This means that, even if we had an arbitrary good understanding of p-p interactions, still a model-dependent extrapolation is needed to apply this knowledge in simulations of cosmic ray interactions in the atmosphere.

The data on interactions of heavier nuclei (p-Pb and Pb-Pb) can be used to improve and

tune hadronic interaction models. However, there are a number of collective effects that are of central importance in heavy ion collisions and much less of relevance for proton interactions with light ions, in which typically only 3 nucleons participate on average. This means that the modeling of most of the heavy ion data involves additional effects that will not help much to understand cosmic ray interactions. The most promising way could be, perhaps, to select peripheral p-Pb collisions with the same mean number of interaction nucleons as expected for air. This would allow us to compare inclusive cross sections or other quantities that do not depend on event-by-event fluctuations. The key point of such a measurement would be that the number of interacting nucleons should not be determined by any quantity related to secondary particle production (such as transverse energy, for example) but by the number of spectator nucleons.

Given the lack of heavy ion data selected by the number of spectator nucleons and its limited applicability to average quantities, the most promising way to reduce the uncertainties of describing interactions with light nuclei is the direct measurement of p-O interactions at LHC. (O is preferred over N only because it is used already as carrier ion for accelerating Pb and it is hoped it can be injected without too high an effort of re-tuning the accelerator.)

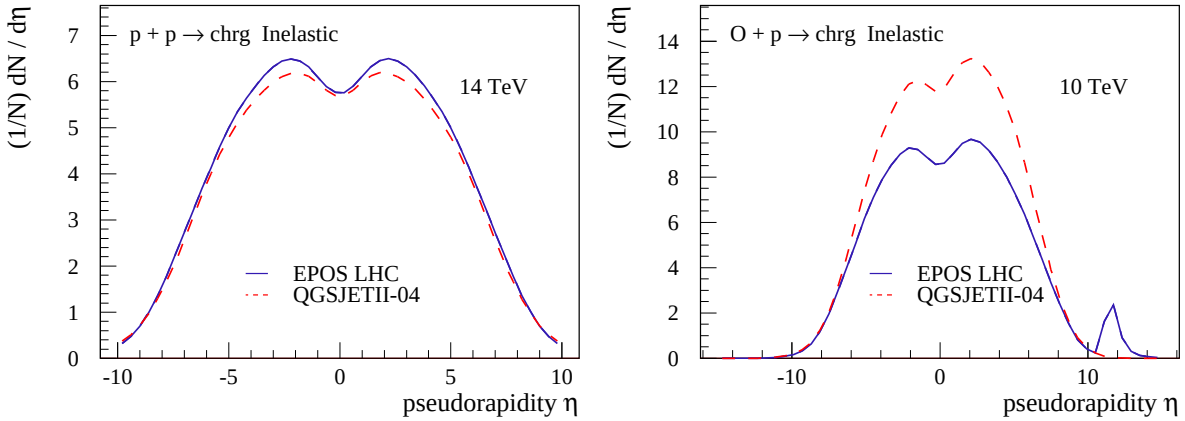

Fig. 6.5: Pseudorapidity distribution $dN/d\eta$ of charged particles for inelastic events for *p-p* interactions at 14 TeV on left panel and *O-p* interactions at 10 TeV on right panel. Predictions are from EPOS LHC (solid line) and QGSJETII-04 (dashed line). The difference at very large pseudorapidity is related to spectator nucleons that are not treated in QGSJET.

To illustrate the potential gain in accuracy of air shower predictions we first compare the pseudorapidity distributions of charged particles in p-p interactions with that predicted for p-O collisions, see Fig. 6.5. Only models already tuned to the new p-p data from LHC are shown. Still there is a difference of $20-30\%$ between the predictions for, for example, the charged particle multiplicity of p-O interactions.

These differences in modeling p-O interactions lead to corresponding uncertainties in the predictions of important air shower observables. This is shown in Fig. 6.6 considering the mean depth of shower maximum, one of the observables typically used to determine the mass composition of cosmic rays. The curves give the change in the predicted $X_{\rm max}$ as function of the relative difference between the nominal model prediction at LHC energy and a potential measurement. The largest dependence is found for the p-O cross section for particle production. If this cross section were 10% smaller than current expectations the predicted depth of shower maximum would shift by $\sim 30\,{\rm g/cm^2}$, more than the difference between proton and helium primaries. Similarly deviation of the particle multiplicity by 30% would correspond to a change

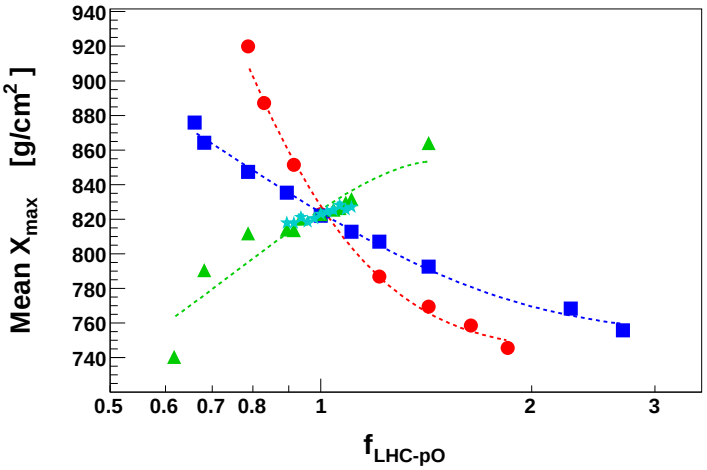

Fig. 6.6: Change of the predicted mean depth of shower maximum, X_{max}, as a function of the relative difference between the expected and measured quantity for p-O at LHC, $f_{\mathrm{LHC-pO}}$. The observables are particle production cross section – red circles, charged particle multiplicity – blue squares, energy fraction carried by the most energetic secondary particle (elasticity) – green triangles, and ratio between charged and neutral particles – green stars. The curves have been obtained in the same way as those in [15].

equivalent to going from proton to helium as primary cosmic ray particles.

Whereas the LHC data from Run-1 have made it possible to distinguish more reliably between proton and iron primaries, see Figs. 6.3 and 6.4, the direct measurement of p-O interactions could improve the separation power to the level of the proton-helium difference.

6.3 Energy Flow

The energy flow of hadronic interactions is one of the most important component of air shower simulations. The whole cascade development depends on the way the energy is transferred from one generation to the other. For air showers the total energy flow is important while in some cases only the transverse energy flow has been measured by LHC experiment. Nevertheless this measurement is important to understand the energy transfer in the hadronic interaction models which are used for air shower simulations.

6.3.1 Past Measurements of Energy Flow

Measurements of the transverse energy flow in minimum bias interactions have been performed by the ATLAS [35], CMS [36], and LHCb [37] experiments, in all cases without the use of forward proton tags. Instead, based on event triggers requiring minimal activity in the rather central regions covered by the detectors, calorimeters are used to measure the energy flow in inelastic proton interactions over a large angular range. The contributions from neutral particles are in all cases included.

The ATLAS measurement at $\sqrt{s} = 7$ TeV used an event selection based on the number of charged particles $N_{\mathrm{Ch}} \geq 2$ with $p_{\mathrm{T}} > 200$ MeV and $|\eta| < 2.5$. The measured differential transverse energy flow was corrected to a particle level definition based on the transverse energy of all stable charged (neutral) final state particles with $p > 500(200)$ MeV and $|\eta| < 4.8$.

The CMS measurement was performed on events with at least four tracks ($p_{\mathrm{T}} > 75$ MeV) associated to a primary vertex and with signals in the forward and backward BSC ($3.9 < |\eta| < 4.4$). The data were corrected to a particle level definition of all charged and neutral stable final state particles within $3.15 < |\eta| < 4.9$, excluding muons and neutrinos. Additionally one or more charged particles were required within the forward and backward acceptance of the BSC to replicate the detector-level definition.

The LHC beauty experiment (LHCb) has measured the energy flow in the pseudorapidity range $1.9 < \eta < 4.9$ with data collected by the LHCb experiment in pp collisions at $\sqrt{s} =$ 7 TeV for inclusive minimum-bias interactions, hard scattering processes and events with enhanced or suppressed diffractive contribution [37]. In this study, the primary measurement is the energy flow carried by charged particles. For the measurement of the total energy flow, a data-constrained MC estimate of the neutral component is used. The energy flow is found to increase with the momentum transfer in an underlying pp inelastic interaction. The evolution of the energy flow as a function of pseudorapidity is reasonably well reproduced by the PYTHIA-based and cosmic-ray interaction models. Nevertheless, the majority of the PYTHIA tunes underestimate the measurements at large pseudorapidity, while most of the cosmic-ray interaction models overestimate them, except for diffractive enriched interactions. For inclusive and non-diffractive enriched events, the best description of the data at large η is given by the SIBYLL 2.1 and PYTHIA 8.135 generators. The latter also provides a good description of the energy flow measured with diffractive enriched events, especially at large η. The comparison shows that the absence of hard diffractive processes moderates the amount of the forward energy flow meaning that their inclusion is vital for a more precise description of partonic interactions. It also demonstrates that higher-order QCD effects as contained in the Pomeron phenomenology play an important role in the forward region. None of the event generators used in this analysis are able to describe the energy flow measurements for all event classes that have been studied.

All experiments applied subsequently harder selection criteria, such as additionally requiring a high-p_{T} particle or di-jet event. This allow a better understanding of the underlying physics in the models.

6.3.2 Future Measurements of Energy Flow

Future measurements of the energy flow in ATLAS will include a forward proton tag. MC predictions for the pseudorapidity differential transverse energy density at $\sqrt{s} = 14$ TeV are presented for the ATLAS inclusive selection ($N_{\mathrm{Ch}} \geq 2$ with $p_{\mathrm{T}} > 200$ MeV, $|\eta| < 2.5$) and for a sample of events where the only event selection is exactly one tagged forward proton in either the AFP or ALFA detectors (see Section 3.3.1 for forward proton selection and MC details). In both cases, the event averaged transverse energy density is calculated from all charged (neutral) final state particles with $p > 500(200)$ MeV. In order to preserve any asymmetry which may be modeled in the energy flow, the tagged proton in the AFP and ALFA triggered samples is required to be at $+z$. Events where the tag is at $-z$ are therefore inverted along the z axis.

In Fig. 6.1, the transverse energy density from the ATLAS inclusive selection is compared to an event selection requiring exactly one tagged forward proton in either AFP or ALFA. The model spread for ATLAS central event selection is shown to be relatively small, 15% at central-pseudorapidity and 20% at forward-pseudorapidity. The dip at central-pseudorapidity is predominantly driven by the exclusion of very low momentum particles which make up a larger fraction of the energy flow in this region where $p \approx p_{\mathrm{T}}$. EPOS consistently predicts the largest average energy density while Herwig++ predicts the lowest.

Upon requiring a forward proton tag, the situation changes dramatically. For an AFP

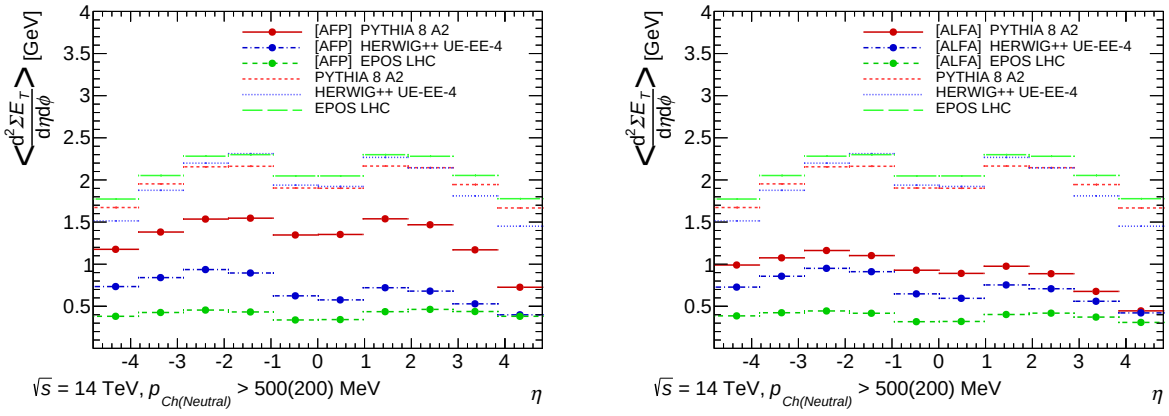

(a) (b)

Fig. 6.1: Transverse energy density in the range $|\eta| < 4.8$ compared between MC models, (a) for the inclusive and AFP selections and (b) for the inclusive and ALFA selections (see text).

tag, the predicted energy density from all models is significantly lower, with EPOS now predicting the lowest average energy density, Pythia 8 predicting the highest - and differing from EPOS by a factor of 4.2. The distributions are also of interest for their asymmetry – it was explored above (Section 3.3) that a fraction of these proton tags from Pythia 8 originate from low mass double dissociation giving an independent probe of the dissociation of the proton traveling in the $-z$ direction over a wide range of possible diffractive masses. Such topologies are expected to deposit more energy at negative pseudorapidity due to the presence of the pseudorapidity gap between the two diffractive systems. In Pythia 8 this results in the transverse energy density in the $-4.80 < \eta < -3.84$ region being 70% greater than the opposite $3.84 < \eta < 4.80$ region. Although with less overall activity, Herwig++ also predicts a 75% increase in the transverse energy density between the two forward regions while EPOS predicts zero asymmetry in events with an AFP tag, probably because in EPOS the independent remnant scheme [38] imply a different proton spectrum and the AFP tag might select different kind of diffractive events (like central diffraction which is symmetric).

When the proton tag is required to be within ALFA acceptance, both Herwig++ and EPOS change relatively little - with EPOS developing a small asymmetry of around a 30% increase in the $-z$ direction (Herwig++ remains the same at a 75% increase). The predicted activity from Pythia 8 is substantially reduced with the average central transverse energy density falling from 1.35 to 0.4 GeV. The predicted asymmetry is also increased to a factor of 2.4 difference between the edge bins.

Pythia 8 generates samples of pure single-, double- and non-diffractive interactions. Using these, the generator's proposed mechanisms which drive these changes are explored in more detail. Figure 6.2 illustrates that the dramatic overall drop in the predicted transverse energy density is driven by the single diffractive component. AFP has good acceptance for high mass single diffractive events whereas in ALFA all masses are accessible but are suppressed by the small but non-zero requirement on $p_{\mathrm{T},p}$. In both cases it is indeed the double-diffractive events which display the largest asymmetry, with a factor of 7 increase in the transverse energy density at $-z$ compared to $+z$. It must be noted however that double dissociation measured to make up only around 5% (see TOTEM references [39, 40]) of the inelastic cross section and hence the asymmetries observed in single dissociation (increase of 50%) and in non-diffractive events (increase of 60%) are also of importance when comparing the inclusive distributions.

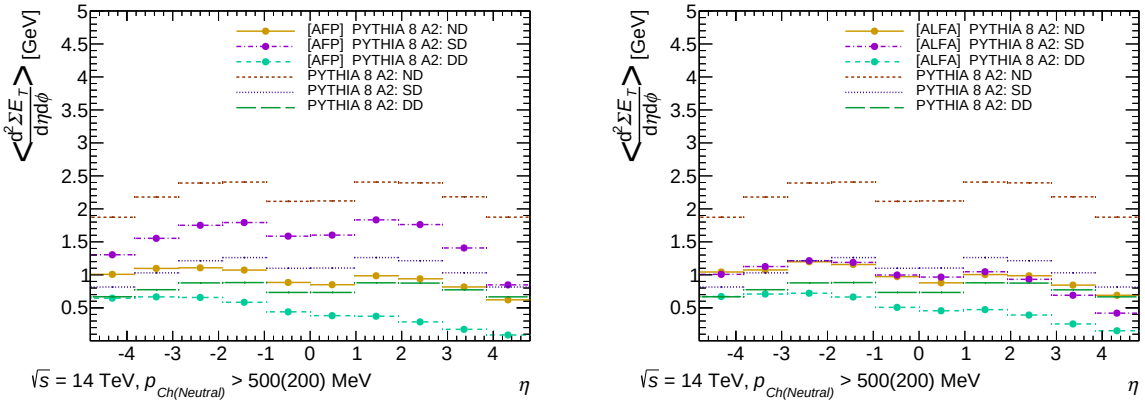
[AFP] PYTHIA 8 A2: ND
[AFP] PYTHIA 8 A2: SD
[AFP] PYTHIA 8 A2: DD
PYTHIA 8 A2: ND
PYTHIA 8 A2: SD
PYTHIA 8 A2: DD
[GeV]
√s = 14 TeV, p Ch(Neutral) > 500(200) MeV
η
[ALFA] PYTHIA 8 A2: ND
[ALFA] PYTHIA 8 A2: SD
[ALFA] PYTHIA 8 A2: DD

(a) (b)

Fig. 6.2: Transverse energy density in the range $|\eta| < 4.8$ compared between single-, double- and non-diffractive components of the inelastic cross section from `Pythia 8`, (a) for the inclusive and AFP selections and (b) for the inclusive and ALFA selections (see text).

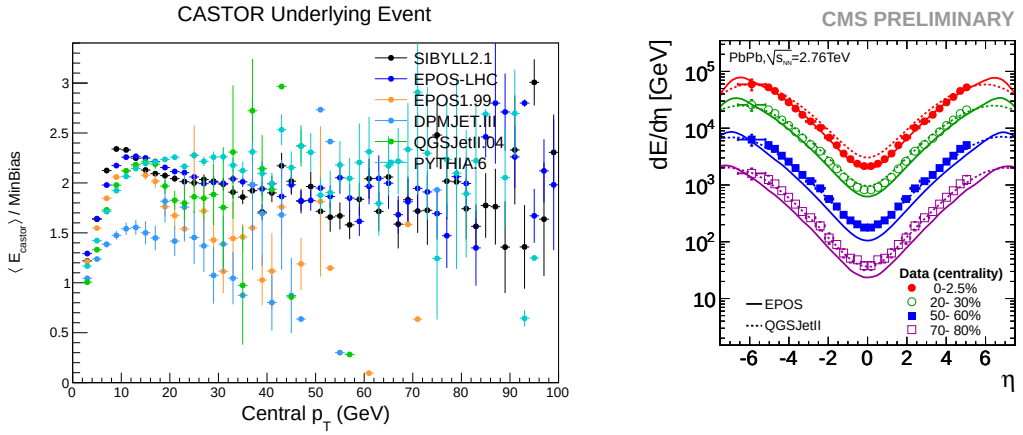

Fig. 6.3: Left panel: Expected CASTOR underlying event measurement at 13 TeV. Shown is the average CASTOR response normalized to the inclusive minimum bias response as a function of central jet p_T. Right panel: Measured dE/dη over the full CMS phase space, from -6.6 to +5 in PbPb data at $\sqrt{s_{NN}}$ of 2.76 TeV [42]

Having larger differences between models thanks to the proton tagging means that it is easier to identify the sources of discrepancy between them and hence to improve our understanding of the underlying physics. As a consequence, the predictive power of such model can be really improved and reduce uncertainties in air shower simulations.

For CASTOR experiment, one of the first measurements of Run-2 may be the underlying event in very forward direction [125]. The model predictions for this measurement at 13 TeV are shown in Fig. 6.3 (left). For this analysis data on the order of 2 nb^{-1} at a pileup of μ<0.05 are needed. Furthermore, after a full high statistics halo muon intercalibration of all channels of CASTOR, which can be done using the scraping runs before the first technical stop of LHC (TS1), also an absolute energy measurement will be possible and dE/dη over the full acceptance of CMS $-6.6 < \eta < +5$, can be performed, see an example of this in Fig. 6.3 (right).

The full dE/dη distribution measured in p-p interaction at 13 TeVwill be of primary im-

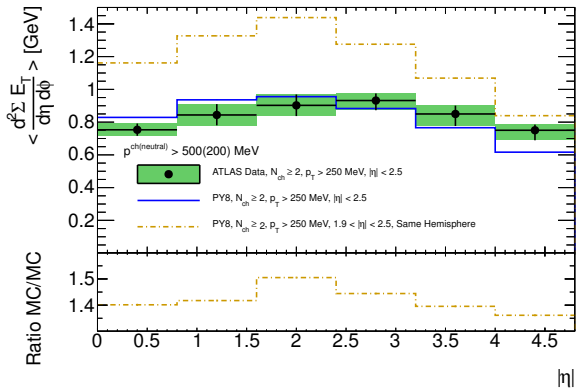

Fig. 6.4: The differential transverse energy flow as measured by ATLAS at $\sqrt{s} = 7$ TeV compared to `Pythia 8` tune 4C. The dashed line denotes the prediction of `Pythia 8` 4C using the new common selection as proposed in the text.

portance to test and improve models used for air shower simulation.

Common Fiducial Definition for Energy Flow Measurement

The current $\sqrt{s} = 7$ TeV measurement of the differential energy flow performed by LHC experiments are not directly comparable due to the different choices in event and kinematic selections detailed above. A common definition accessible to ATLAS, CMS and LHCb for use in future analyzes in addition to the experiment's preferred selection will allow for direct comparisons in the regions of overlapping pseudorapidity between the experiments. The proposed common selection is as follows:

- For each event, treat the $+z$ and $-z$ hemispheres separately (does not apply to LHCb).
- Per hemisphere, require $N_{\mathrm{Ch}} \geq 2$ with $p_{\mathrm{T}} > 250$ MeV and $\pm 1.9 < \eta < \pm 2.5$.
- Measure hemisphere transverse energy flow differential in pseudorapidity.
- Unfold measured transverse energy flow to a hadron level definition of all charged (neutral) stable particles with $p > 500(200)$ MeV.

An example of this new definition is presented in Fig. 6.4, here ATLAS experimental data from reference [35] and the corresponding prediction from `Pythia 8` 4C are shown along side the `Pythia 8` 4C prediction for this proposed common selection. The mean energy flow for $|\eta| < 4.8$ is predicted to be approximately 40% larger by MC, peaking in the region of the new common event selection requirement. With this new selection, events with a very central activity and low transverse energy flow are excluded.

6.4 Particle multiplicities

After the energy flow, the particle multiplicity is a very important ingredient of air shower development since it impacts directly the speed at which the cascade grows in the atmosphere having a direct influence on the position of the shower maximum. To improve the model prediction not only the measurement at higher energy is important but the separation between diffractive and non-diffractive events with an extended η coverage is fundamental to reduce significantly the model uncertainties.

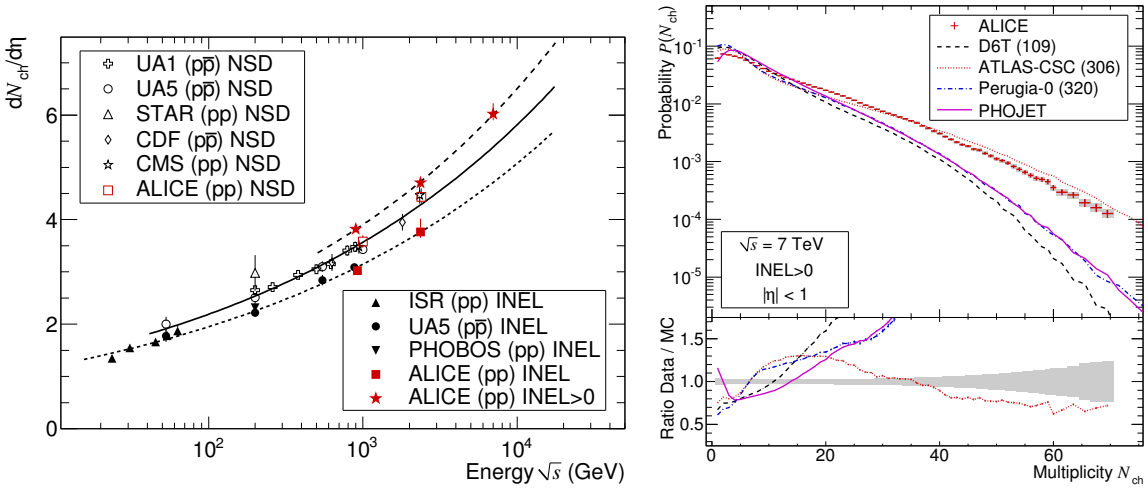

Fig. 6.1: Left: The charged-particle density as a function of center-of-mass energy as measured by ALICE is compared to results from other experiments. Right: The multiplicity distribution of charged particles at mid-rapidity measured by ALICE at $\sqrt{s} = 7$ TeV is compared to several MC models. Figures from [28]

6.4.1 Past measurements of charged particle multiplicities

The LHC collaborations have published charged particle multiplicity spectra at various center of mass energies spanning the range $\sqrt{s} =$ 900–7000 GeV [28, 43–46]. Complimentary acceptances of the different LHC experiments allow for the charged particle multiplicity to be investigated over the ranges $|\eta| < 2.5$ (ALICE (partial), ATLAS and CMS), $2.0 < \eta < 4.5$ (LHCb), $3.1 < |\eta| < 4.7$ and $5.3 < |\eta| < 6.5$ (TOTEM, telescopes $T1$ and $T2$). In addition, the definition of common selection requirements decided by the minimum bias and underlying event LPCC working group have allowed direct comparisons between the experiments.

The ALICE Collaboration has measured the density of charged particles at mid-rapidity and the multiplicity distribution in pp collisions at 0.9 TeV, 2.36 TeV [47, 48] and 7 TeV [28]. The results are presented for non-single diffractive and for inelastic processes. The charged-particle density is presented as a function of energy in the left panel of Figure 6.1. ALICE measurements for the inelastic case with at least one charged particle in the pseudo rapidity range $|\eta| < 1$ are compared to those of several other collaborations. The measurements are well described by a power-law increase with energy and reach up to 6 charged particles per unit of pseudo rapidity at mid rapidity for the highest energies. The left panel of the same figure shows the multiplicity distribution measured at 7 TeV for inelastic events and compares it to predictions of different MC models. Data are reasonably well described by a Negative Binomial Distribution, which slightly under(over) estimates data at small (large) multiplicities.

The CMS and TOTEM experiments have measured the charged particle multiplicity as function of $|\eta|$ at a center-of-mass energy of $\sqrt{s} = 8$ TeV in three different event samples based on the T2 event topology: an inclusive pp interaction sample that includes more than 90 % of all inelastic pp collisions, one sample depleted and one sample enhanced in single diffractive pp interactions [49, 50]. The measurement is performed in $|\eta| < 2.2$ for $p_T > 100$ MeV/c and in $5.3 < |\eta| < 6.4$ for $p_T > 40$ MeV/c with at least one charged particle per event required in $5.3 < |\eta| < 6.5$ range and then corrected down to $p_T = 0$ MeV/c. The measurement is compared to several models used to describe high-energy hadronic interactions. None of the models considered provide a consistent description of the measured distributions.

By using the full spectrometer information, the previous LHCb results [45] have been extended to include momentum dependent measurements. The LHCb experiment has measured charged particle multiplicities and mean particle densities as functions of p_T and η in inclusive pp interactions at a center-of-mass energy of $\sqrt{s} = 7$ TeV [51]. The measurement is performed in the kinematic range $p > 2$ GeV/c, $p_T > 0.2$ GeV/c and $2.0 < \eta < 4.8$, in which at least one charged particle per event is required. The comparison of data with predictions from PYTHIA-based and Herwig-based event generators shows that predictions from recent generators, tuned to LHC measurements in the central rapidity region, are in better agreement than predictions from older generators. While the phenomenology in some kinematic regions is well described by recent PYTHIA and Herwig++ simulations, the data in the higher p_T and small η ranges of the probed kinematic region are still underestimated. None of the event generators considered in this study are able to describe the entire range of measurements.

Such data on the charged particle multiplicity spectrum and pseudorapidity dependence, charged particle p_T spectrum, and correlation between the average charged particle p_T and the charged particle multiplicity continue to be used in the tuning of soft inelastic MC models.

6.4.2 Future measurements of charged particle multiplicities

The effect of requiring a forward proton tag on the charged particle multiplicity spectra is investigated in $\sqrt{s} = 14$ TeV MC for an ATLAS inclusive selection ($N_{Ch} \geq 2$, $p_T > 100$ MeV, $|\eta| < 2.5$) and for an event selection requiring exactly one forward proton tag in either AFP or ALFA (see Section 3.3.1 for proton tagging and MC details).

The event normalized charged particle spectra is plotted in Fig. 6.2. For larger N_{Ch}, the tails of the distributions are observed to fall more sharply with AFP or ALFA tags than for the inclusive selection. EPOS in particular has a very low probability of generating events with $N_{Ch} > 50$ and a forward proton while the tail in Herwig++ and Pythia 8 forward-tagged events extends to $N_{Ch} = 100$ for the same number of events.

For the region at low multiplicity, where diffractive signatures may be expected due to lower particle production in rapidity gap events, a large spread of predictions is observed. EPOS and Herwig++ both support this hypothesis and predict an enhancement for $2 < N_{Ch} < 20$ with regards to their inclusive distributions, as does Pythia 8 for the ALFA selection. For the AFP selection however, the opposite is true and fewer events are expected in this region. This is understood by examining the breakdown of Pythia 8 into its diffractive and non-diffractive components in Fig. 6.3. The AFP selection is biased to a harder spectrum than for the inclusive distribution in the region $20 < N_{Ch} < 70$ by high-mass single diffractive events within AFP acceptance, the final state particles from the dissociated proton in such events fully span the $|\eta| < 2.5$ acceptance of the central tracking detectors. The tail is still observed to fall faster than for the inclusive case as very high multiplicity events ($N_{Ch} > 100$) are predicted to be dominated by low impact-parameter non-diffractive interactions which are suppressed by requiring an AFP or ALFA tag. For low N_{Ch}, only the double-diffractive sample (which as discussed in Section 3.3 may cause large rapidity gaps) retains the enhancement in the tagged sample, but with a smaller fractional cross section, see Table 3.1.

In addition to the multiplicity spectrum, the charged particle p_T spectra are investigated for just the inclusive and AFP selections in Fig. 6.4. The corresponding ALFA distributions were noted to be very similar to the AFP ones for these selections (see section 3.3.1) are hence not reproduced here. In Fig. 6.4a, the charged particle multiplicity is plotted versus the mean particle p_T summed over all tracks in all events of a given multiplicity. All the AFP tagged distributions suffer from statistical fluctuations in their respective tails from Fig. 6.2. The Pythia

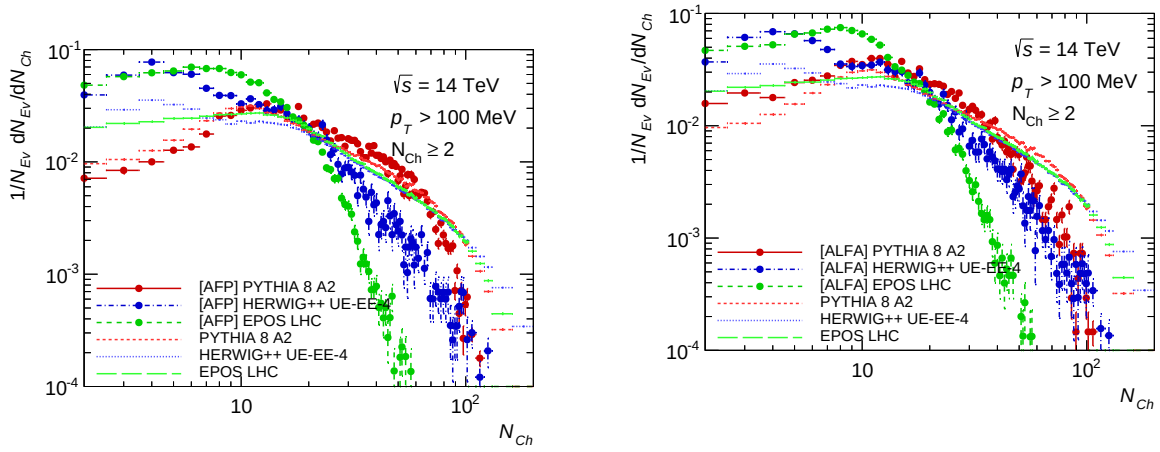

(a) (b)

Fig. 6.2: Event normalized charged particle multiplicities compared between MC models for inclusive and AFP selections (a) and inclusive and ALFA selections (b).

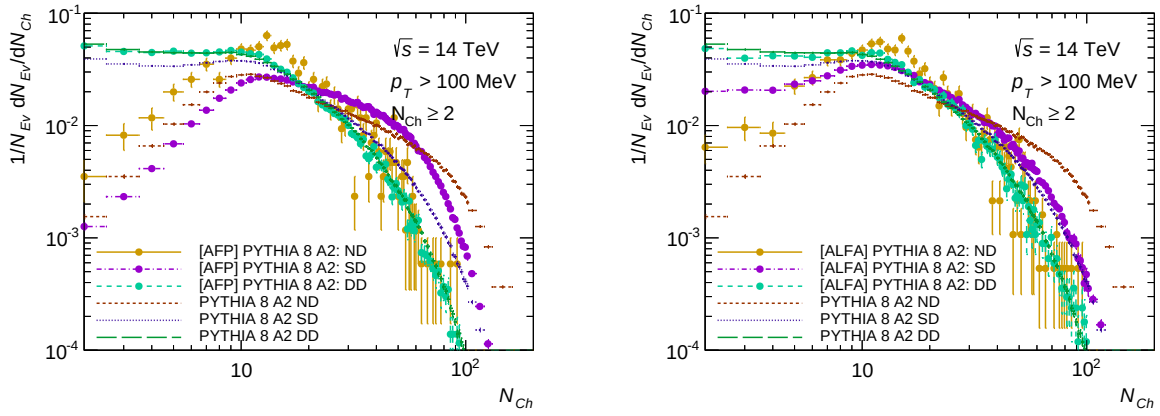
√s = 14 TeV
p_T > 100 MeV
N_Ch ≥ 2
[AFP] PYTHIA 8 A2: ND
[AFP] PYTHIA 8 A2: SD
[AFP] PYTHIA 8 A2: DD
PYTHIA 8 A2 ND
PYTHIA 8 A2 SD
PYTHIA 8 A2 DD
[ALFA] PYTHIA 8 A2: ND
[ALFA] PYTHIA 8 A2: SD
[ALFA] PYTHIA 8 A2: DD
PYTHIA 8 A2 ND
PYTHIA 8 A2 SD
PYTHIA 8 A2 DD
1/N_Ev dN_Ev/dN_Ch
N_Ch

(a) (b)

Fig. 6.3: Event normalized charged particle multiplicities compared with single-, double- and non-diffractive components of the inelastic cross section from `Pythia 8` for inclusive and AFP selections (a) and inclusive and ALFA selections (b).

`8` prediction is very similar for the inclusive and AFP tagged distributions over the range which is comparable with the available statistics. With `EPOS`, the shape of the distributions agree, however the particle spectrum is on average softer for the tagged distribution. Unlike the other MCs, `Herwig++` predicts a $< p_{\mathrm{T}} >$ distribution which is roughly invariant in N_{Ch} for the inclusive distribution. The tagged `Herwig++` sample becomes increasingly soft at higher multiplicities indicating that for this class of event, there are kinematic constraints imposed by the generator limiting the energy available to perform the cluster hadronization of the final state.

Figure 6.4b shows the charged particle p_{T} spectra. The above observations are conformed in the normalizations of the AFP tagged samples. Some differences in slope are also visible, most notably for `Herwig++`.

The large η coverage ($|\eta| < 6.5$) of the combined CMS and TOTEM tracking will enable interesting charged multiplicity measurement at $\sqrt{s}$ = 13 and 14 TeV. In addition to straight

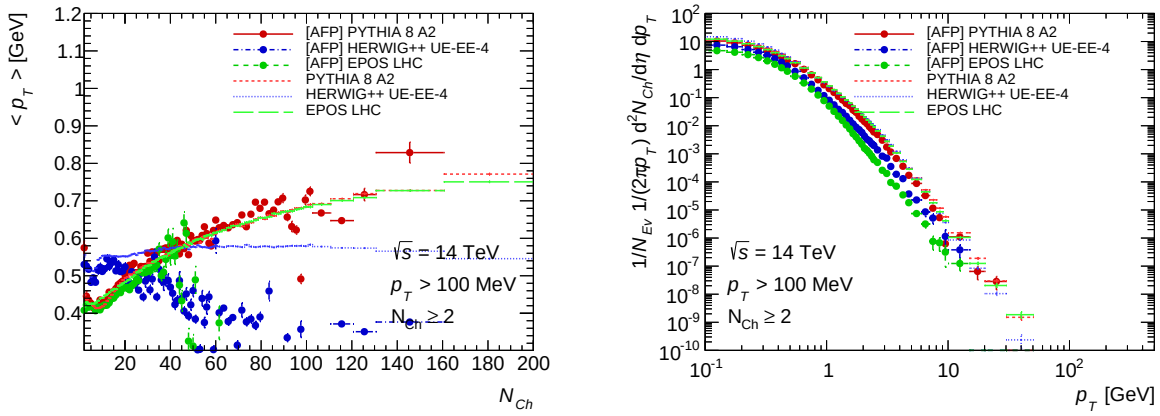

(a) (b)

Fig. 6.4: Event normalized charged particle η and p_{T} distributions compared between MC models for inclusive and AFP selections using log-log axes.

forward multiplicity measurements are also charged multiplicity correlation (e.g. forward vs backward, forward vs central) measurements envisaged. The capability to deplete or enhance the event sample in single diffractive interactions either based on the forward event topology (using T2) or the detection of the diffractive proton in the Roman Pots even further enhances the sensitivity of these measurements.

Having new type of correlations, in particular with a proton tagging, greatly enhance the possibility to distinguish between diffractive and non-diffractive events and hence increase the visible difference between models. It will first of all allow a better understanding of diffractive event as such, but furthermore the tuning of the hadronic interaction models will be improve being based on almost pure samples of diffractive and/or non-diffractive while until now it was always a mixing.

6.5 Spectra

Identified particle spectra are a key component of model tuning for air shower simulations since the muon production depends on the relative abundance of π^0, strangeness and baryon production in the total multiplicity. With the new LHC run not only larger energies will be reached but special triggers can be developed to better understand the particle production mechanisms and then improve model extrapolations.

6.5.1 Measurement of identified charged particle spectra in pp and p-Pb collisions with ALICE

Recent measurements of identified particle spectra in proton-lead and lead-lead collisions show relatively large discrepancies with standard hadronic model predictions in particular for strange baryons. Presenting the results according to event multiplicity and centrality, respectively, have shown interesting signs of hadrochemistry changes and of modifications to transverse momentum distributions of identified particles. Even if these analysis are based on rare particles and at midrapidity which are not so relevant for direct air shower physics, knowing the correct hadronization scheme is of primary importance for the modelisation of hadronic interactions in particular for air shower simulations which require large extrapolations to unexplored energies and phase space. An interesting goal to constrain hadronic interaction models would be thus to perform extensive identified particle spectra measurements according to multiplicity also in

proton-proton collisions. Existing data allows for these studies only for the more abundantly produced particles, but the more exotic hyperons such as the Ω essentially require very large statistics that are currently unavailable. Performing such a measurement is particularly important for hyperons, as this may help in understanding the mechanisms behind the strangeness enhancement already observed in nuclear collisions [52]. In particular, this may further constrain or discriminate some aspects of thermal models such as non-equilibrium, the use of γ_S and canonical strangeness production. Furthermore, the high mass of the hyperons makes them particularly susceptible to the presence of collective effects in high multiplicity proton-proton collisions, further underlining the need for such a measurement.

6.5.1.1 Past measurements of charged particle spectra

The ALICE collaboration has systematically measured the production of identified particle spectra in pp collisions at mid-rapidity ($|\eta| < 0.5$)for a variety of light flavour particle species, ranging from the more abundant $\pi^{\pm}$, $K^{\pm}$, p and $\bar{p}$, the multi-strange Ξ and Ω and resonances such as $K^*(892)^0$, $\phi(1020)$, $\Sigma(1385)^{\pm}$ and $\Xi(1530)^0$.

The more abundant of the light flavour species, $\pi^{\pm}$, $K^{\pm}$, p and $\bar{p}$, have been studied at energies of 900 GeV, 2760 GeV and 7 TeV [53–55]. These analyses employ several different particle identification techniques, such as specific energy loss in both Time Projection Chamber and Inner Silicon tracker as well as time of flight measurements, to cover a broad range of transverse momentum. The measured spectra have been compared to QCD-based models such as PYTHIA in various tunes as well as PHOJET, and none of the event generators have been able to reproduce all spectra simultaneously with a precision better than 30%. These serve as important reference data for modelling efforts as well as benchmarks for comparisons to other systems such as p-Pb and Pb-Pb.

Furthermore, multi-strange baryon measurements in pp collisions at 7 TeV [56] over a wide range in momentum are made possible by exploiting the weak decay topology and employing particle identification via energy loss in the Time Projection Chamber on the daughter tracks. The resulting measurements can be seen in Figure 6.1 together with predictions from the PYTHIA6 event generator using its Perugia-2011 tune. The Monte Carlo simulations are unable to reproduce the measured yields, underpredicting the Ξ spectra by up to a factor 2 and the Ω spectra by up to a factor 4-5, although better agreement can be observed for Ξ for larger momenta of around 6-7 GeV/c.

Further identified particle spectra measured by ALICE in pp collisions include the $K^*(892)^0$ and $\phi(1020)$ [57] as well as the $\Sigma(1385)^{\pm}$ and $\Xi(1530)^0$ resonances [58]. Since for those resonances the measured decay daughters originate from the primary vertex, one cannot exploit the decay topology to isolate their signals. Instead, methods such as event mixing and like-sign background estimation have to be used in order to compute the combinatorial background to be subtracted from the measured invariant mass distributions, which then results in invariant mass peaks that are suitable for signal extraction.

The transverse momentum spectra obtained in these analyses can be seen in Figures 6.3 and 6.4. Also in those cases, PYTHIA fails to correctly reproduce the measured yields by up to a factor 2. Other models, such as PHOJET, have also been tested but also fail at reproducing both integrated yields as well as spectral shapes. These various measurements serve as reference for better understanding of particle production mechanisms in pp collisions and introduce further constraints on future modelling efforts.

In addition to the more elementary pp collisions, ALICE has been performing systematic measurements of identified particle spectra also in the p-Pb colliding system. Measurements

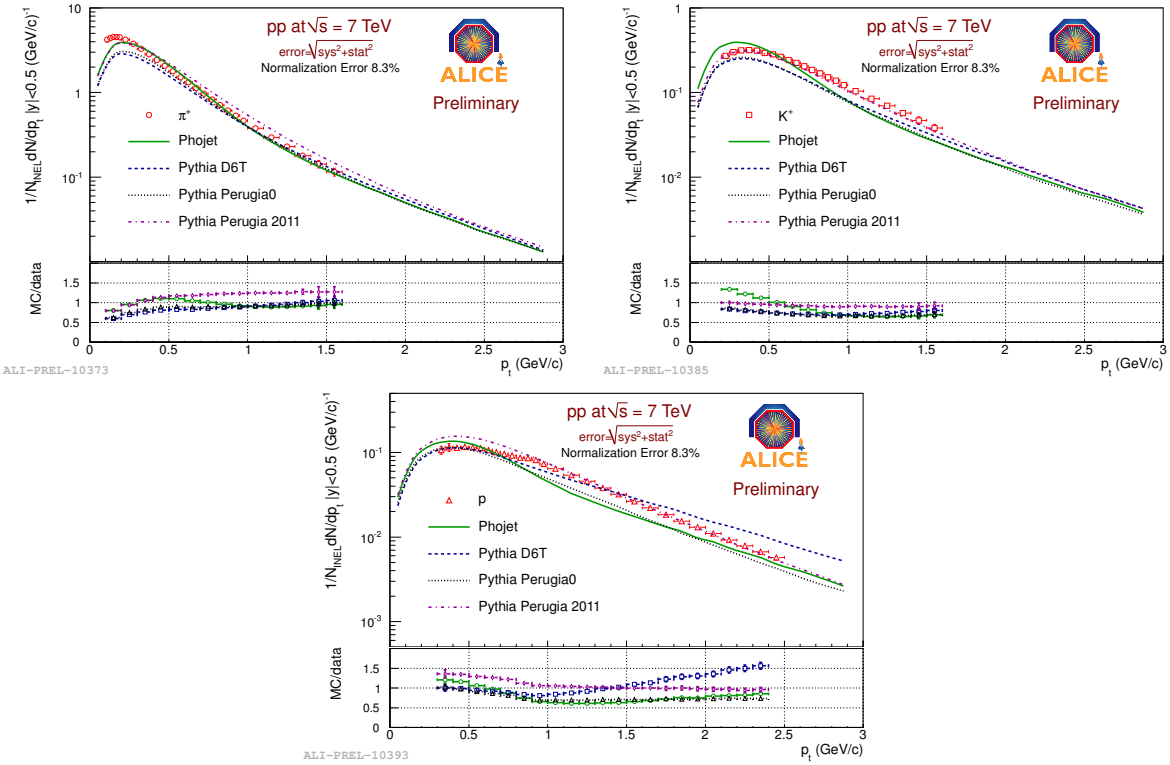

Fig. 6.1: π^+ (top left), K^+ (top right) and p (bottom) spectra in pp collisions at $\sqrt{s} = 7$ TeV. The corresponding antiparticles are not drawn since they are identical within uncertainties. Figures from [55].

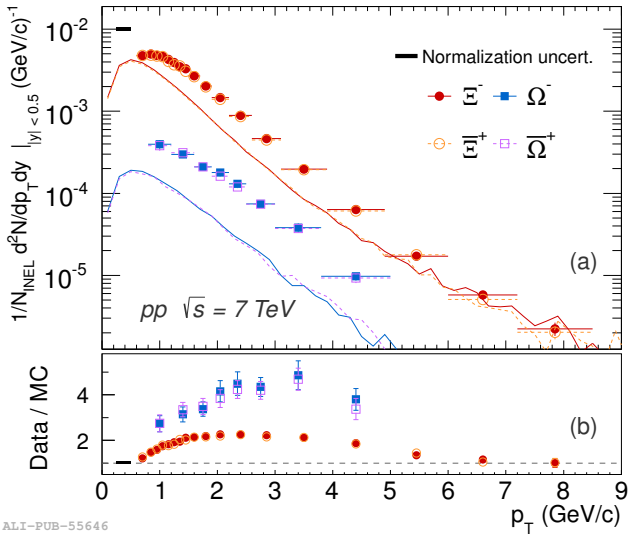

Fig. 6.2: Ξ^-, $\bar{\Xi}^+$, Ω^- and $\bar{\Omega}^+$ transverse momentum spectra in pp collisions at $\sqrt{s} = 7$ TeV measured by ALICE compared with predictions from PYTHIA6 using tune Perugia-2011. Figure from [56].

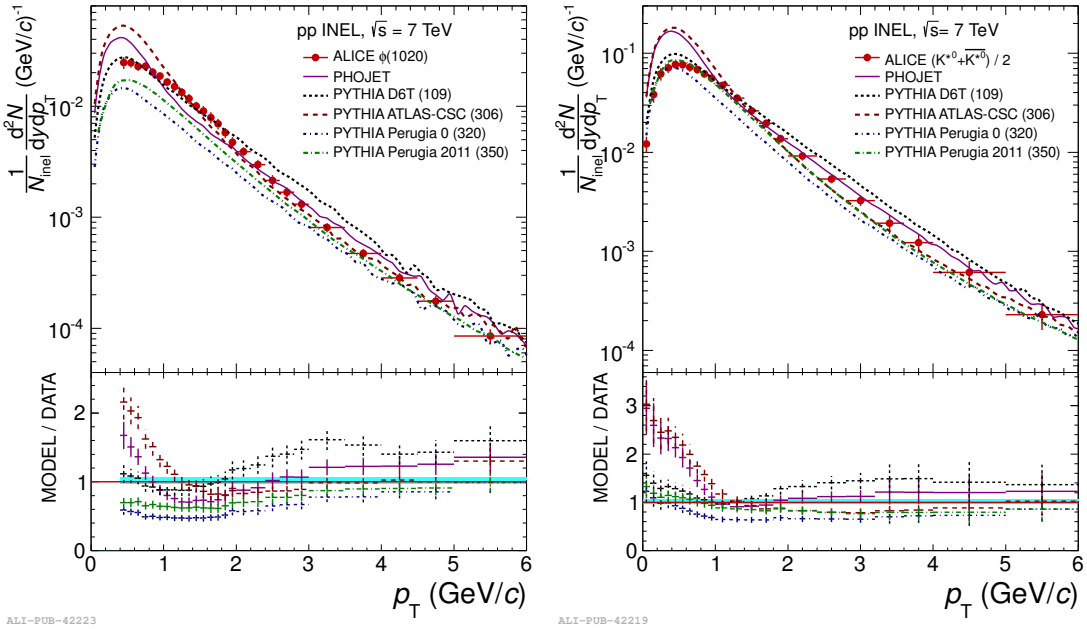

Fig. 6.3: $\phi(1020)$ (left) and $K^*(892)^0$ (right) transverse momentum spectra at mid-rapidity in pp collisions at $\sqrt{s} = 5.02$ TeV. Figures from [57].

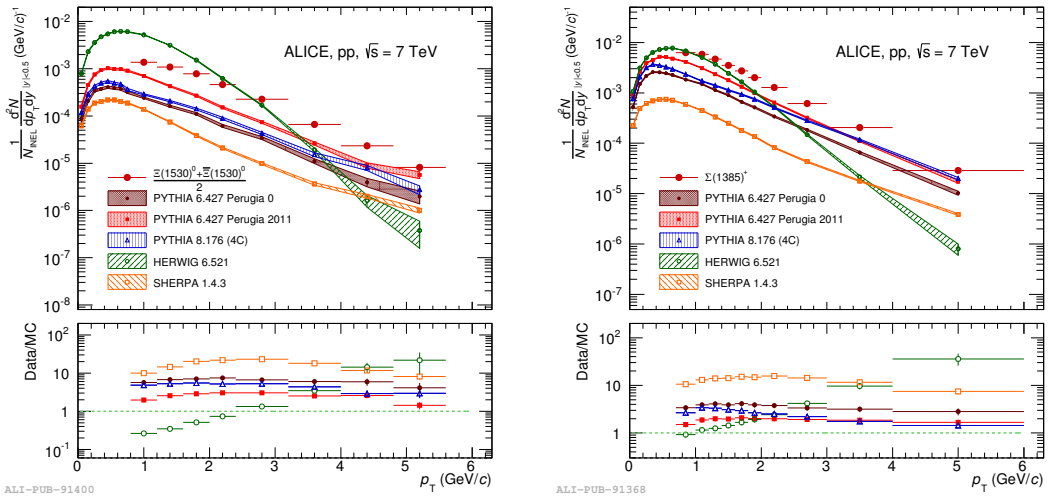

Fig. 6.4: $\Sigma(1385)^{\pm}$ (left) and $\Xi(1530)^0$ (right) transverse momentum spectra at mid-rapidity in pp collisions at $\sqrt{s} = 5.02$ TeV. Figures from [58].

of p_T-differential yields of $\pi^{\pm}$, $K^{\pm}$, K^0_S, p, $\bar{p}$, Λ and $\bar{\Lambda}$ have been performed as a function of charged particle multiplicity [59]. These measurements also employ the same techniques as used for the pp observations, such as energy loss in the Time Projection Chamber, time of flight measurements and reconstruction by decay topology for weakly decaying hadrons. The observed spectra show a clear evolution with multiplicity, as can be seen in Figure 6.5, similar to what occurs in high energy pp and Pb-Pb collisions. They have been compared to predictions from DPMJet, a QCD-inspired event generator based on the Gribov-Glauber approach which is not able to reproduce spectral shapes. Other models, such as EPOS which include a phase of collective hadronization, are significantly better at describing the measured spectra shapes.

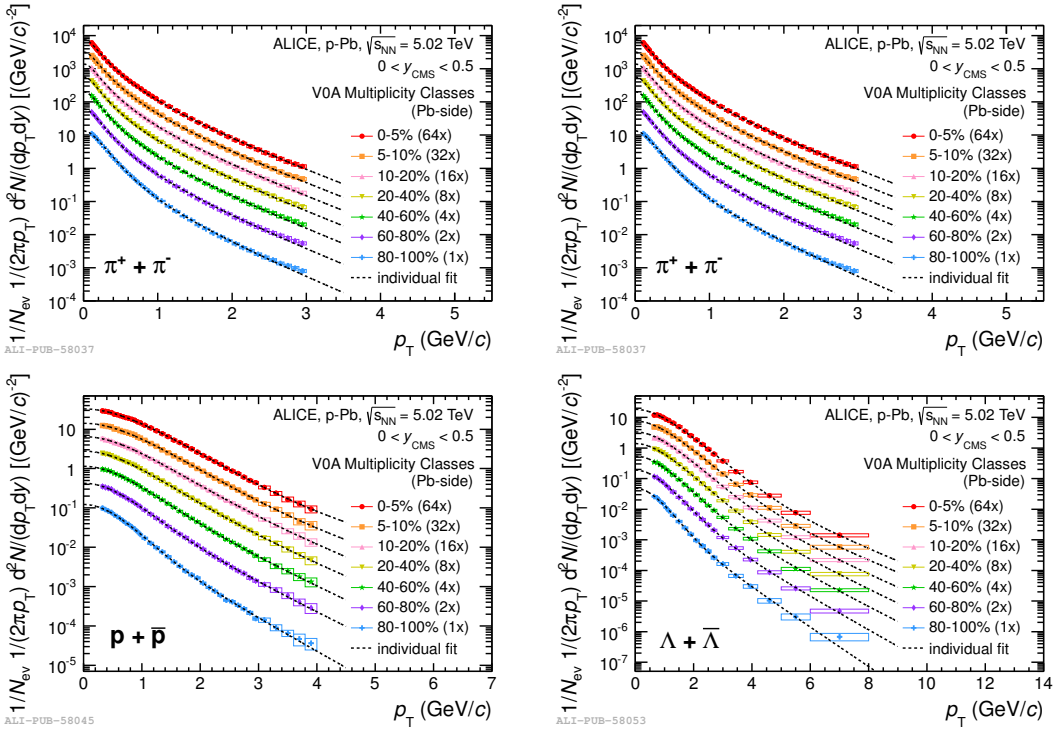

Fig. 6.5: $\pi^{\pm}$ (top left), $K^{\pm}$ (top right), $p+\bar{p}$ (bottom left) and $\Lambda+\bar{\Lambda}$ (bottom right) transverse momentum spectra as a function of event multiplicity in p-Pb collisions at $\sqrt{s} = 5.02$ TeV. Figures from [59]

Identified particle spectra according to multiplicity Currently existing data enables particle spectra measurements according to multiplicity for $\pi^{\pm}$, $K^{\pm}$, p, $\bar{p}$ [60], Λ, $\bar{\Lambda}$ and even Ξ^- and Ξ^+, albeit with limited momentum and multiplicity reach for the Ξ baryons. An ongoing analysis has shown that the spectra for all particles except the Ξ can be computed according to mid-rapidity track counts reaching a charged particle density of up to approximately a factor 6 higher than the minimum-bias value using a sample of approximately 150×10^6 minimum-bias proton-proton collisions at 7 TeV. For the Ξ, the multiplicity distribution is such that another factor 10 in statistics would be required to reach the same multiplicity. These analyzes used runs for which operational conditions were such that the interaction probability $\mu < 0.1$, and standard inner tracking system (ITS) pileup tagging methods revealed no more than an average 5% pileup rate for the largest multiplicity bin[1], as can be seen in Fig. 6.6 . This would represent an acceptable rate of pileup for which systematic uncertainties would still be under control, and it is an important consideration since simply collecting data with large luminosities will incur in prohibitively large pileup rates for the high-multiplicity event classes.

Assuming that one wishes to perform a similar measurement for the Ω baryon under the same conditions and having the same reach in multiples of minimum-bias charged particle density, two components need to be considered:

– The Ω/Ξ ratio, which, while being one of the goals of such a measurement, can be estimated to be of in the range of the published minimum-bias Ω/Ξ ratio or more and is of approximately 0.085 (see Ref. [56]);
– The fact that Ω has a lower reconstruction efficiency than Ξ, which is mostly a con-

[1] though note that these methods have been estimated to only successfully tag half of the piled up events, and so the real pileup rates could be as much as twice these values.

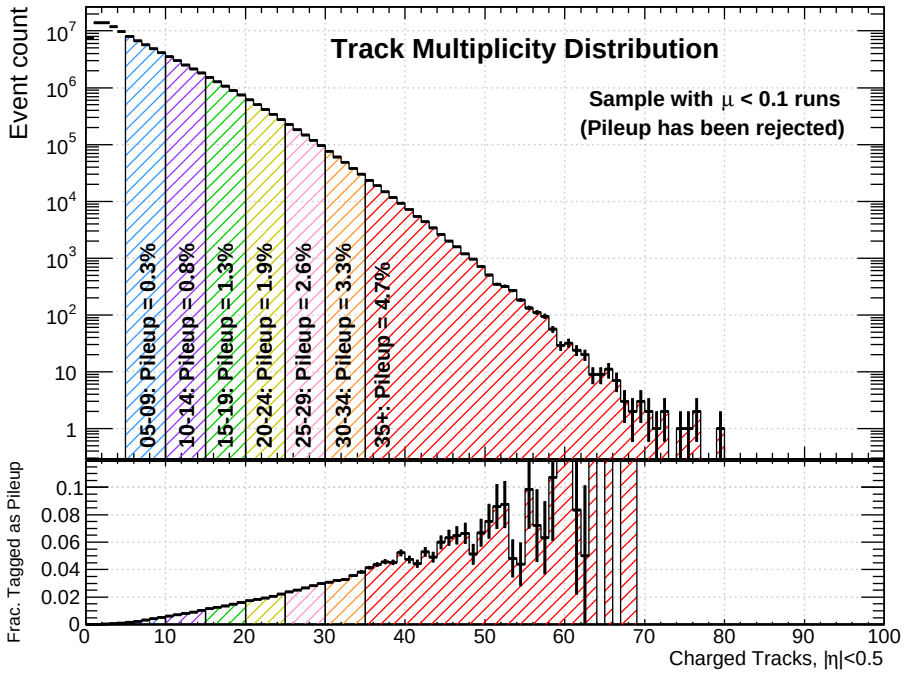

Fig. 6.6: Reconstructed charged particle density distribution in proton-proton collisions at 7 TeV (top pad) and fraction of events thereof that have been tagged as pileup (bottom plot).

sequence of the fact that the measured Ω channel has a lower branching ratio than the measured Ξ channel, in addition to different decay kinematics. The resulting difference is of about a factor 2.

Having these considerations in mind, the number of minimum-bias events required for the Ω analysis according to charged particle multiplicity would be of approximately 5.0×10^{10} detected events. Assuming a worst-case scenario trigger efficiency and analysis selection event loss, this would require a delivered integrated luminosity of at least 1.0 pb^{-1} or more and ensuring $\mu < 0.1$. Operationally, it will also be important to consider high-multiplicity triggering during such data taking.

6.5.1.2 Future measurements of charged particle spectra : dedicated triggering

If selecting large multiplicity events, a much smaller sample of triggered events would be sufficient to perform an Ω analysis according to multiplicity. The triggering can be performed based on a charged particle density estimate acquired either in mid-pseudorapidity, such as a counting tracks in $|\eta| < 0.5$ or $|\eta| < 0.8$, where ALICE has full central barrel detector coverage, or in forward pseudorapidity, as would be the case if using the amplitudes measured by the VZEROA and VZEROC scintillators, located in $2.8 < \eta < 5.1$ and $-3.7 < \eta < -1.7$, respectively. It would be of interest to study the possibility to trigger on either one, since it is known that using mid-rapidity multiplicity estimators adds biases to the measurements of primary charged particle yields with respect to weakly decaying particles such as the V0 and cascade decays. Having two trigger strategies will provide a tool to study such biases.

Furthermore, in order to study the multiplicity dependence of identified particle production, it will be important to also set up different multiplicity triggers with different downscalings to compensate for the steeply falling multiplicity distribution. In any case, this special triggering

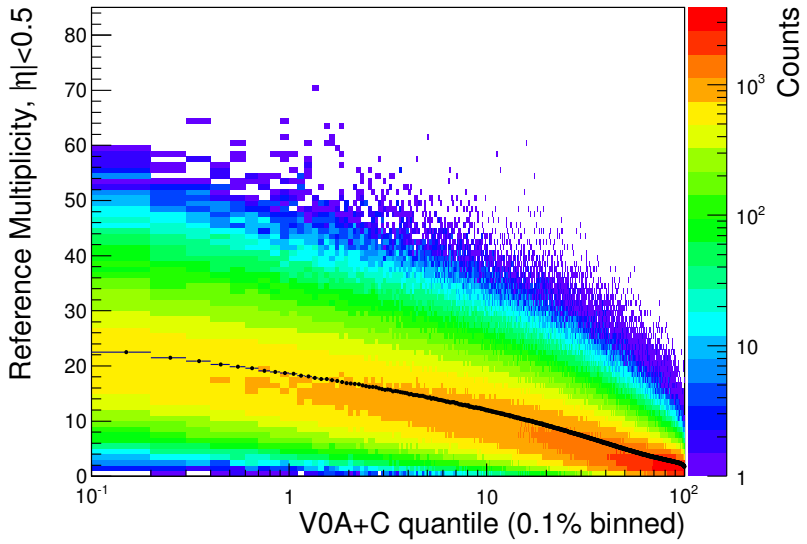

Fig. 6.7: Mid-rapidity raw multiplicity estimator according to VZERO cross-section quantiles.

would have to be accompanied by a short min-bias data taking period to calibrate and determine proper normalization.

- Triggering on mid-rapidity track density: One of the simplest possibilities to study high multiplicity proton-proton events is to classify events based on the number of charged particle tracks at mid-pseudorapidity as reconstructed by the ALICE ITS and TPC. By doing so, one can reach relatively high multiplicities, as can be seen Fig. 6.6, where the highest multiplicity class corresponds to 0.1% of the measured cross-section. Triggering using a similar criterion would thus ensure a recorded data reduction of a factor 10^3.
- Triggering on VZERO amplitudes: The effects of selecting on the VZERO amplitudes for reaching high mid-rapidity charged particle densities can be seen in Fig. 6.7, where the mid-rapidity raw multiplicity is drawn as a function of the VZERO quantile. It is also noteworthy that, for the minimum-bias data sample, the mid-rapidity multiplicity estimator returns an average multiplicity of approximately 6. Thus, for instance, selecting on the 1% of events with highest VZERO amplitudes would yield a sample with approximately $4 \times (dN_{ch}/d\eta)_{MB}$ and one would need only 5×10^8 recorded events in that case.

6.5.2 Neutral particle spectra

The ALICE Collaboration has measured the production of the neutral pion and the η meson in pp collisions at $\sqrt{s} = 0.9$ TeV and $\sqrt{s} = 7$ TeV [62]. The production of the neutral pion has also been measured at $\sqrt{s} = 2.76$ TeV [63]. The measurements were performed using the two-photon decay channel and cover the mid-rapidity region and a large range in transverse momentum. The spectra are compared to NLO calculations using a variety of fragmentation functions. Data is well described at the lowest energy, while the predictions are not so successful at the largest energies. Nonetheless, the ratio η/π^0 is well described over the full energy range.

The LHCf detector [64] is purpose made for measurements in the very forward direction. It is installed on both sides of the ATLAS interaction point behind the inner beam separation dipoles that sweep the charged particles from the collisions aside. Therefore only neutral particles reach the detector and are measured by LHCf.

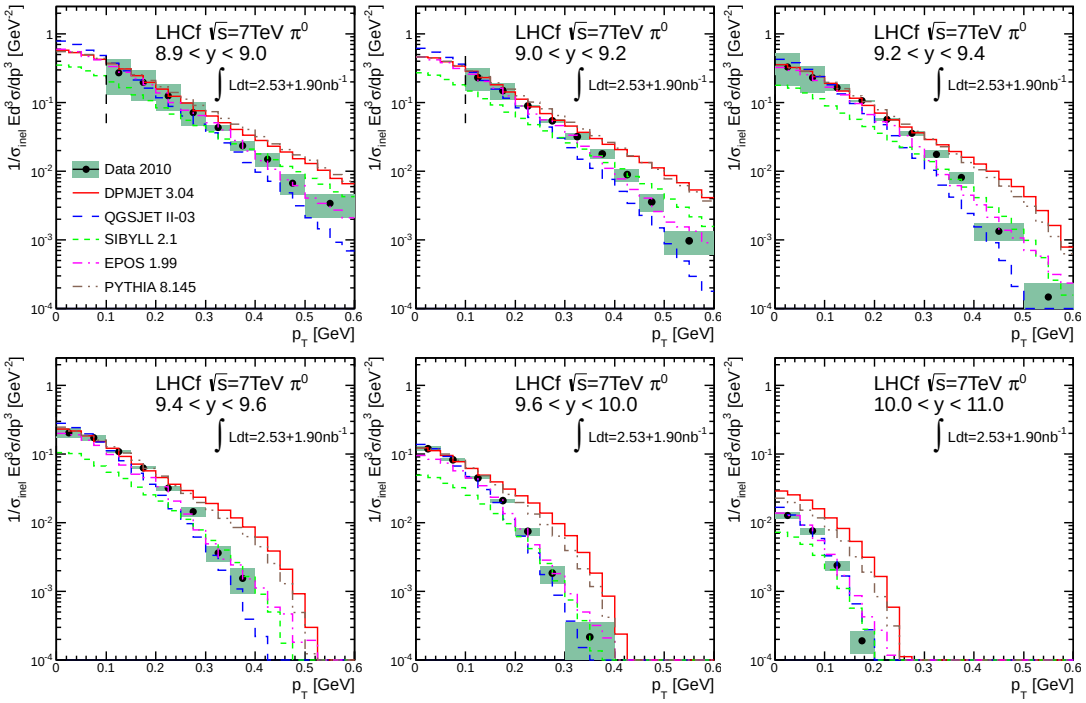

Fig. 6.8: Transverse momentum spectra of π^0 observed at LHC 7 TeV p-p collision. Experimental results are presented in six rapidity ranges together with the model predictions.

LHCf has so far operated at the LHC 900 GeV and 7 TeV p-p collisions in 2009–2010 [65] and 5.02 TeV p-Pb collisions and 2.76 TeV p-p collisions in 2013. During the 2013 operation, only the Arm2 detector was installed. To operate at the 13 TeV p-p collisions in 2015 under a high radiation dose, the LHCf detectors were upgraded by replacing plastic scintillators to Gd_2SiO_5 (GSO) scintillators [66, 67].

6.5.2.1 Past measurements of neutral particle spectra

Single photon spectra from 900 GeV and 7 TeV p-p collisions LHCf published photon spectra at $8.81 < \eta < 8.99$ and $10.94 < \eta < \infty$ from the 7 TeV p-p collision data [68]. Similar analysis was also performed from the 900 GeV data for $8.77 < \eta < 9.46$ and $10.15 < \eta < \infty$ [69]. Experimental results were compared with the model predictions, but no model could perfectly reproduce the experimental results. On the other hand, the experimental results were well between the variation of model predictions.

π^0 spectra from 7 TeV p-p collisions Transverse momentum (p_T) spectra of π^0 for 6 different rapidity (y) ranges were obtained from the 7 TeV p-p collision data as shown in Fig.6.8 [70]. Again no model could explain the experimental data but EPOS 1.99 [18, 19] had a better agreement than the other models. Mean p_T measurements, $< p_T >$, were obtained from 6 rapidity bins by fitting the observed spectra using empirical functions. When plotting $< p_T >$ as a function of y_{beam}–y together with the UA7 results [71] from Sp$\bar{p}$S 630 GeV p-$\bar{p}$ collisions, data points were found to be smoothly connected.

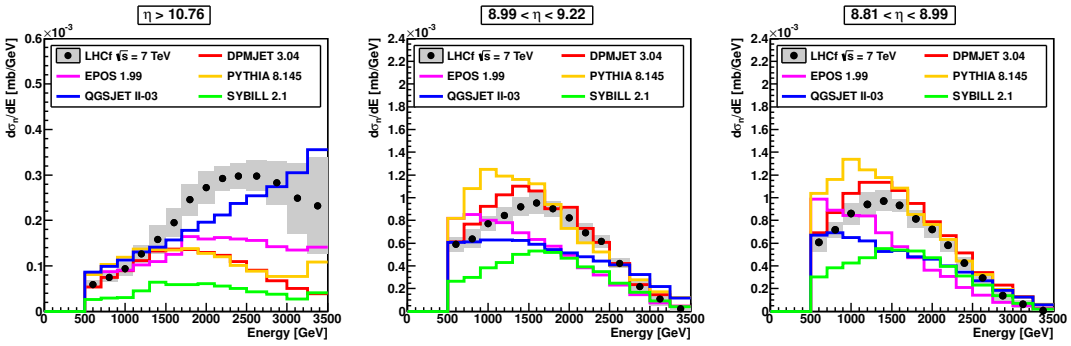

Fig. 6.9: Forward neutron spectra measured at η >10.76, 8.99< η <9.22 and 8.81< η <8.99 in LHC 7 TeV p-p collision. Spectra are corrected for the detector efficiency and resolution, then compared with the model predictions [20].

π^0 spectra from 5 TeV p-Pb collisions and nuclear effect p_T spectra of π^0 were also obtained from the $\sqrt{s_{NN}}$=5.02 TeV p-Pb collision data [72] at the direction of the proton beam. A characteristic shoulder structure was observed and it was identified to be a result of Ultra-Peripheral Collisions between a proton and electro-magnetic field around the Pb nuclei. After subtracting this UPC effect based on a calculation, π^0 from QCD interaction were extracted. The π^0 spectra in p-p collisions at the corresponding collision energy were estimated by interpolating the p-p data at 2.76 TeV and 7 TeV. Dividing the π^0 spectra in p-Pb collisions by those in p-p collisions and theoretical number of binary collisions, the nuclear modification factors were calculated. Large factors around 0.1 were observed and these values were explained by existing models.

Neutron spectra from 7 TeV p-p collisions Although the LHCf calorimeters were optimized for the electro-magnetic shower measurements, they have a sensitivity to the hadronic showers. Hadronic shower events, predominantly neutrons, were analyzed from the 7 TeV p-p collision data [20]. In both folded and unfolded spectra, energy spectra were compared between the data and MC predictions. The unfolded spectra obtained for η >10.76, 8.99< η <9.22 and 8.81< η <8.99 are shown in Fig.6.9. At the most forward direction including the zero degree, a very hard spectrum was obtained and that was similar to the prediction by the QGSJETII-03 model [21, 74] both in the shape and absolute cross section. At the smaller rapidities, the data were close to the models predicting a high neutron yield. When comparing the number of neutrons over number of photons with energy larger than 100 GeV, the experimental data showed a larger neutron yield than the models.

6.5.2.2 Future measurements of neutral particle spectra

13 TeV p-p in 2015 The original goal of the LHCf was to take data at the highest accelerator energy possible. The 14 (13) TeV p-p collisions to be achieved at the LHC correspond to 1.0 (0.9)$\times 10^{17}$ eV in the laboratory frame. This is an important energy in the cosmic-ray physics because the transition from the galactic to the extra-galactic cosmic ray is expected at this energy. Because of a high radiation dose at the TAN location, LHCf cannot survive for a long time even though using radiation-hard GSO scintillators. LHCf will take the highest energy data soon after the start of RUN2 and the target collisions energy is 13 TeV.

6.5.3 Heavy flavor particle spectra

The measurement of inclusive very forward electrons in proton-proton collisions is a challenging opportunity with a potential to provide unique insights into the very low-x quark structure of hadrons which is very important for the forward physics leading air shower development. This specifically includes the heavy quark content which are also of particular interest because it is a background for astrophysical neutrino detection.

6.5.3.1 Past measurements of heavy flavor particle spectra

The ALICE Collaboration has measured the production of heavy flavour in pp collisions at 2.76 and 7 TeV both at mid and at forward rapidity using semi-leptonic decays [75–80]. The measurements at forward rapidity are performed with the MUON spectrometer, which covers the rapidity range $2.5 < y < 4$ and transverse momenta from around 2 to 15 GeV/c. The dependence on these two variables is well described by theoretical models. In particular, FONLL pQCD is in good agreement with data within experimental and theoretical uncertainties, although the data are close to the upper limit of the model calculations.

The results in the mid-rapidity region are obtained measuring the electrons from the semi-leptonic decays of hadrons containing heavy quarks. These analyses use the particle-identification capabilities of ALICE. The electrons are identified using their energy loss when traversing the Time Projection Chamber (TPC) complemented with the information from the Time-Of-Flight system and the Transition Radiation Detector. Another complementary technique is to use the TPC in conjunction with the Electromagnetic Calorimeter. The spectra are measured for the rapidity interval $|y| < 0.5$ and the transverse momentum is measured from 0.5 to 8 GeV/c. To separate the electrons originating from the decay of beauty hadrons, the impact parameter of the lepton tracks with respect to the main interaction vertex is used. With this technique the contribution from charm and from beauty can be separated and measured independently. In both cases perturbative QCD calculations agree with the measured cross section within the experimental and theoretical uncertainties.

In addition the ALICE collaboration has measured the production of charmed mesons such as the D^0, D^+ and D^{*+} in pp collisions at 7 TeV [81] at mid-rapidity ($|\eta| < 0.5$). The weakly decaying D^0 and D^+ have decay vertices which are typically displaced by a few hundreds of μm from the primary vertex. This displacement is such that, given the high resolution of ALICE tracking, topological selections are able to discern between decay daughters of these mesons and primary particles. Furthermore, the strongly decaying D^{*+} will have decay positions indistinguishable from the primary vertex but can measured in its $D^0\pi^+$ decay channel, whereas topological selections can again be used for the D^0 daughters. The resulting measurements are shown in Figure 6.10 and are reproduced within uncertainties by theoretical calculations based on QCD such as FONLL and GM-VFNS.

6.5.3.2 Future measurements of heavy flavor particle spectra

As explained in section 6.3.2, the CASTOR experiment is ideally placed to study forward energy flow relevant for air shower physics. However the complexity of the very forward detectors is much reduced with respect to the central detectors, firstly, due to a more extensive amount of dead material in front as well as other geometrical limitations, and, secondly, because of the missing magnetic bending power to precisely measure particle momenta and particle identification.

The combination of the TOTEM T2 tracking station with the CMS CASTOR calorimeter can to some extend overcome some of these limitations. While T2 can precisely measure and

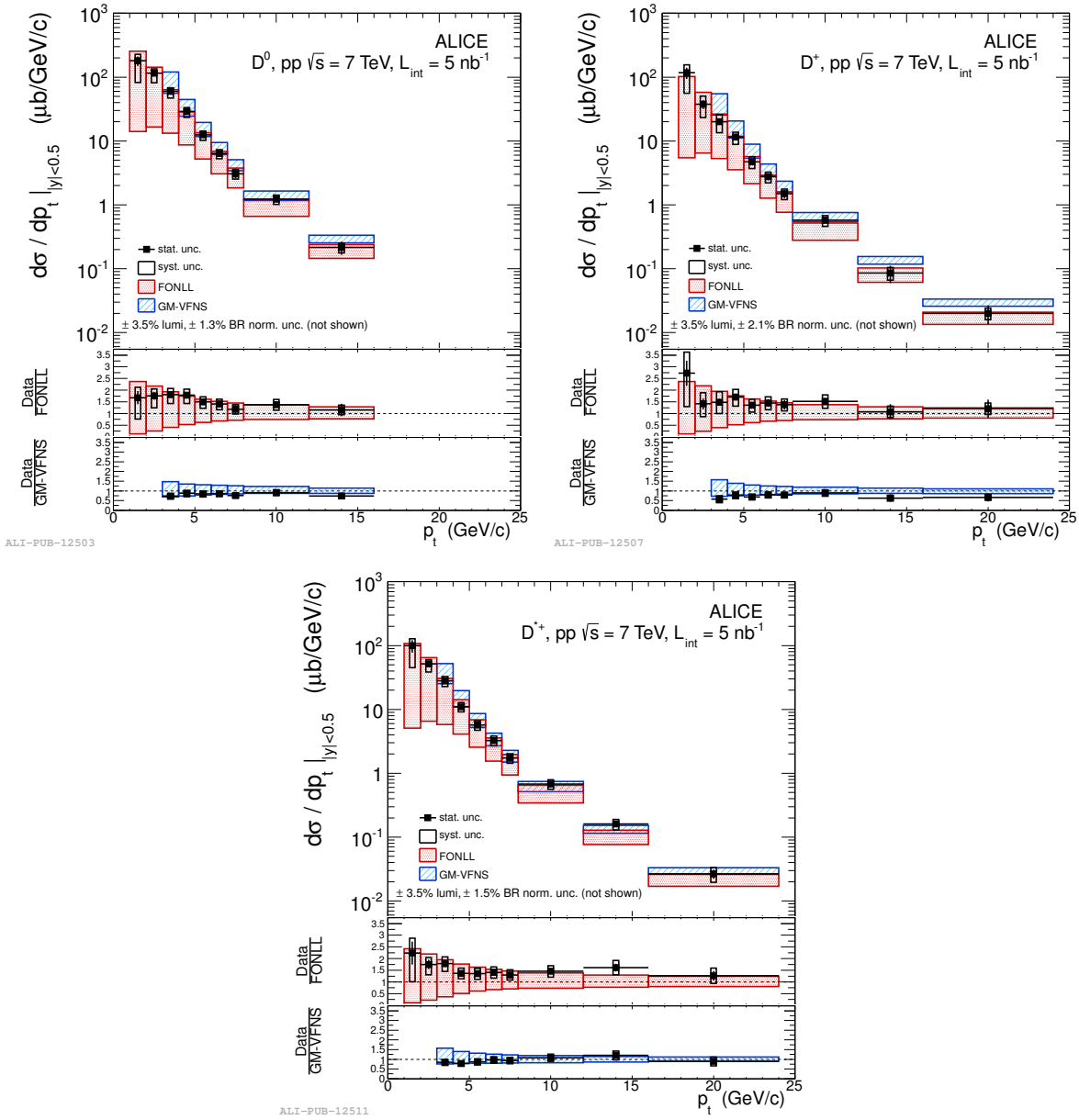
ALICE
D⁰, pp √s = 7 TeV, L_int = 5 nb⁻¹
dσ / dp_t |_|y|<0.5 (μb/GeV/c)
stat. unc.
syst. unc.
FONLL
GM-VFNS
± 3.5% lumi, ± 1.3% BR norm. unc. (not shown)
Data / FONLL
Data / GM-VFNS
p_t (GeV/c)
ALI-PUB-12503
ALICE
D⁺, pp √s = 7 TeV, L_int = 5 nb⁻¹
± 3.5% lumi, ± 2.1% BR norm. unc. (not shown)
ALI-PUB-12507
ALICE
D*⁺, pp √s = 7 TeV, L_int = 5 nb⁻¹
± 3.5% lumi, ± 1.5% BR norm. unc. (not shown)
ALI-PUB-12511

Fig. 6.10: D^0 (top left), D^+ (top right) and D^{*0} (bottom) inclusive p_T-differential cross-sections in pp collisions at 7 TeV. Figure from [81]

tag charged particles, CASTOR can identify electromagnetic from hadronic particles and also perform energy measurements. For the example of electrons this allows a full reconstruction, since the particle identification can be performed very reliably and, thus, also the particle four-vector can be measured precisely. For other particles further assumptions are necessary, which is in general in the very forward phase space not a major limitation. In particular the measurement of very forward scattered partons, which fragmented into jets, may provide unique insight into the low-x structure of gluons in hadrons. The measurement of inclusive very forward electrons will provide information on the Drell-Yan process, and thus the quark content at low-x, but also on the heavy quark content at very low-x via the decay of heavy hadrons into electrons. Forward Charm production, being very poorly known until now, could provide a very interesting input for high energy muon production in air showers.

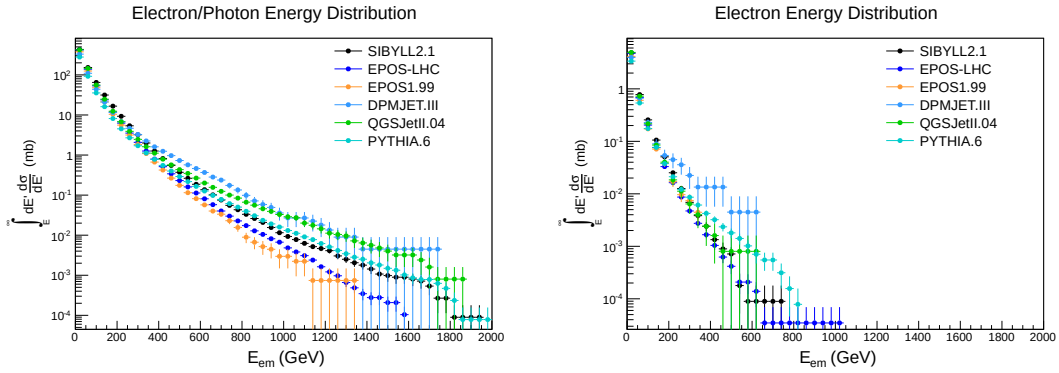

Fig. 6.11: Left panel: Integrated inclusive production of very forward electron and photons in 13 TeV pp collisions. Right panel: same only for very forward electrons. The cross sections drops rapidly as a function of the energy.

In order to reach to very high energy electrons in the CMS experiment, and thus very low-x physics, an integrated luminosity of about 100 nb^{-1} is necessary and 1 pb^{-1} will be useful, where the average pileup should be small since at $\mu \sim 0.07$ the average underlying event contribution per event is on the level of 10% for a 500 GeV electron, which is the case for $\mu \sim 0.15$ for 1 TeV electrons. The best performance of this data analysis will be achieved, when a dedicated trigger menu with an isolated very forward electron trigger is used. However, it is not possible to perform a geometric matching of TOTEM T2 tracks with electromagnetic clusters in proton-proton collisions, thus, photons cannot be distinguished from electrons at trigger level with CASTOR. Fig. 6.11 indicates that only about 1% of all electromagnetic particles are in fact electrons. This situation requires to record the triggered events without any prescale and do an offline event separation of electrons from photons in a dedicated data analysis. At the same time this will set the allowed lower energy threshold for the trigger very high, in order to keep the trigger rates low. The details depend on the luminosity and the pileup of the data taking.

6.6 Beam

6.6.1 Proton-proton collisions

For inclusive inelastic studies, a data sample of 10 million events is required to sufficiently populate the tails at large charged particle multiplicity and p_{T}. Previous experience from ATLAS at $\sqrt{s} = 8$ TeV during LHC fill number 2470 indicates that such a sample is obtainable with approximately three hours data taking with an output rate of 1 kHz from ten colliding bunches and an average number of interactions per bunch-crossing $< \mu >= 0.003$. Low $< \mu >$ ($\sim 1\%$) is important to allow for the correlation of the central and forward detectors and to preserve any large rapidity gaps.

MC predictions (Table 3.1) indicate that a forward tag rate of the order 1% should be expected. Therefore three hours with $\sim$1000 bunches or 30 hours with $\sim$100 bunches is sufficient to collate a forward-tagged data sample of equivalent size for a given optics arrangement. To avoid collision pileup, an operation at low luminosity, L$\sim 10^{29}$ $\text{cm}^{-2}\text{s}^{-1}$, is required.

For LHCf experiment, in addition an angle of individual particle β^* larger than 10 m is necessary. To cope with a slow data acquisition, number of collision bunches below 40 are also required. Because these requests can be shared with those of the van der Meer scan, the dedicated operation of LHCf will be carried out with the vdM scan campaign in May 2015.

Beam parameters for this operation are summarized as follows.

- Instantaneous luminosity; 1.5×10^{29} cm^{-2}s^{-1}
- Integrated luminosity 15 nb^{-1}
- Number of collision bunch pair; 40, a few non-collision pairs
- Maximum crossing angle (half angle 145 μrad)
- β^*=19 m as defined from vdM scan

These beam conditions will allow most of the analysis needed to tune the hadronic interactions models for air shower simulations presented in this chapter.

LHCf is also planning to take data with ATLAS. LHCf will send its trigger signal to ATLAS and ATLAS will record the data after prescaling this trigger. By tagging the forward events using the central detector, classification of diffractive and non-diffractive events at the event-by-event basis will be available.

Models for extensive air-showers constrained by the collider data rely on extreme extrapolations to high energies. These extrapolations depend on the underlying assumptions in the models, related to particular types of interactions and their properties. The LHCf experiment has provided useful information on the forward energy flow from neutral particles. However, without knowing the true nature of the pp interaction, the production mechanism cannot be fully understood. Therefore, a combined LHCf+ATLAS pp run would help to classify the interactions and further tune the air-shower models. We propose the following two measurements:

- Measure the energy flow of photons, π^0 and neutrons in LHCf in the case of an activity in the central ATLAS detector (non-diffractive events) and in the case of no activity in central ATLAS detector (low mass single diffractive or double-diffractive events).
- Measure $dN/d\eta$, multiplicity, dN/dp_t and $<p_t>$ vs. multiplicity in ATLAS for the events triggered by LHCf.

Such measurements would complement possible outcomes of the analysis of the p+Pb data taken in early 2013 where a common LHCf trigger was defined in the ATLAS trigger menu. Nuclear effects need to be taken into account in order to understand diffractive p+Pb interactions and pp can be used as a reference here. For the cosmic air-shower models, it is the p-Air processes that matter in the end.

6.6.2 Light ion collisions

Due to its SMOG system, which allows injection of noble gases into the interaction point, the LHCb detector is able to perform fixed target physics with beam-gas interactions [82]. In particular, during the 2012 proton-ion pilot run, the neon gas has been injected into the LHCb interaction region that has increased the beam-gas interaction rate by two orders of magnitude. It allows accurate measurements of the beam profile for a precise determination of the absolute luminosity. In this particular case the nucleon-nucleon center-of-mass energy was $\sqrt{s_{NN}} =$ 87 GeV and the whole system was boosted by $\Delta y \approx 4.5$ units in the direction of the proton beam. The rate of beam-gas interactions between the proton beam and the injected gas was sufficient to measure light quark and strangeness production. In particular, clear signals have been observed for different strange hadrons [82]. Studies of light quark and strangeness production in these collisions provide unique input to cosmic-ray interaction models and will be conducted by the LHCb experiment although the center-of-mass energy is still very low compared to nominal LHC data.

As a consequence, to get full advantage of the LHC beam and reach a center-of-mass energy per nucleon of $\sqrt{s_{NN}} = 10$ TeV, LHCf is discussing a future possibility of light-ion collisions at LHC. This is ultimate goal for the cosmic-ray physics to simulate CR-atmosphere interactions as explained in 6.2.3. A technical feasibility was presented in [83]. From the detector point of view, even with light ion A-A collisions a multiplicity around zero degree is significantly higher than the case of p-p collisions. Even using a LHCf-like small calorimeter, more than one particle enter a single calorimeter in 80% of events. To reconstruct the energies of these 'multi-hit' particles, energy measurement with a higher granularity is required. Silicon-pad detectors having a pad size of $\sim$mm are thought to fit this request. (Note that the Molière unit of Tungsten is 9 mm and any very fine structure is not useful.) A basic R&D to design a future light-ion collision experiment is started.

Such a light ion beam could be used by all other experiments for measurements presented in this section and will be of great help to further constrain the MC generator necessary for air shower simulation and to reduce uncertainties in cosmic ray measurements as explained in 6.2.3.

References

[1] K. Kotera and A. V. Olinto, "The Astrophysics of Ultrahigh Energy Cosmic Rays," *Ann. Rev. Astron. Astrophys.*, vol. 49, pp. 119–153, 2011.

[2] A. M. Hillas, "The Origin of Ultrahigh-Energy Cosmic Rays," *Ann. Rev. Astron. Astrophys.*, vol. 22, pp. 425–444, 1984.

[3] J. Blümer, R. Engel, and J. R. Hörandel, "Cosmic Rays from the Knee to the Highest Energies," *Prog. Part. Nucl. Phys.*, vol. 63, pp. 293–338, 2009.

[4] R. Engel, D. Heck, and T. Pierog, "Extensive air showers and hadronic interactions at high energy," *Ann.Rev.Nucl.Part.Sci.*, vol. 61, pp. 467–489, 2011.

[5] D. d'Enterria, R. Engel, T. Pierog, S. Ostapchenko, and K. Werner, "Constraints from the first LHC data on hadronic event generators for ultra-high energy cosmic-ray physics," *Astropart. Phys.*, vol. 35, pp. 98–113, 2011.

[6] V. Berezinsky, A. Z. Gazizov, and S. I. Grigorieva, "On astrophysical solution to ultra high energy cosmic rays," *Phys. Rev.*, vol. D74, p. 043005, 2006.

[7] D. Allard, E. Parizot, E. Khan, S. Goriely, and A. V. Olinto, "Uhe nuclei propagation and the interpretation of the ankle in the cosmic-ray spectrum," *Astron. Astrophys.*, vol. 443, pp. L29–L32, 2005.

[8] K. Greisen, "End to the cosmic ray spectrum?," *Phys. Rev. Lett.*, vol. 16, pp. 748–750, 1966.

[9] G. T. Zatsepin and V. A. Kuzmin *J. Exp. Theor. Phys. Lett.*, vol. 4, p. 78, 1966.

[10] J. Abraham, "Measurement of the Depth of Maximum of Extensive Air Showers above 10^{18} eV," *Phys. Rev. Lett.*, vol. 104, p. 091101, 2010.

[11] D. Allard, "Extragalactic propagation of ultrahigh energy cosmic-rays," *Astropart. Phys.*, vol. 39-40, pp. 33–43, 2012.

[12] P. Abreu *et al.*, "Interpretation of the Depths of Maximum of Extensive Air Showers Measured by the Pierre Auger Observatory," *JCAP*, vol. 1302, p. 026, 2013.

[13] K.-H. Kampert and M. Unger, "Measurements of the Cosmic Ray Composition with Air Shower Experiments," *Astropart.Phys.*, vol. 35, pp. 660–678, 2012.

[14] H.-J. Drescher, "Remnant break-up and muon production in cosmic ray air showers," *Phys. Rev.*, vol. D77, p. 056003, 2007.

[15] R. Ulrich, R. Engel, and M. Unger, "Hadronic Multiparticle Production at Ultra-High Energies and Extensive Air Showers," 2010.

[16] T. Pierog and K. Werner, "Muon production in extended air shower simulations," *Phys. Rev. Lett.*, vol. 101, p. 171101, 2008.

[17] C. Meurer, J. Blümer, R. Engel, A. Haungs, and M. Roth, "Muon production in extensive air showers and its relation to hadronic interactions," *Czech. J. Phys.*, vol. 56, p. A211, 2006.

[18] K. Werner, F.-M. Liu, and T. Pierog, "Parton ladder splitting and the rapidity dependence of transverse momentum spectra in deuteron gold collisions at rhic," *Phys. Rev.*, vol. C74, p. 044902, 2006.

[19] T. Pierog and K. Werner, "EPOS Model and Ultra High Energy Cosmic Rays," *Nucl.Phys.Proc.Suppl.*, vol. 196, pp. 102–105, 2009.

[20] O. Adriani, et al", "Measurement of very forward neutron energy spectra for 7 TeV proton–proton collisions at the Large Hadron Collider", arXiv hep-ex 1503.03505, 2015.

[21] S. Ostapchenko, "Non-linear screening effects in high energy hadronic interactions," *Phys. Rev.*, vol. D74, p. 014026, 2006.

[22] S. Ostapchenko, "On the re-summation of enhanced pomeron diagrams," *Phys. Lett.*, vol. B636, pp. 40–45, 2006.

[23] N. N. Kalmykov, S. S. Ostapchenko, and A. I. Pavlov, "Quark-gluon string model and eas simulation problems at ultra-high energies," *Nucl. Phys. Proc. Suppl.*, vol. 52B, pp. 17–28, 1997.

[24] N. N. Kalmykov and S. S. Ostapchenko, "The nucleus-nucleus interaction, nuclear fragmentation, and fluctuations of extensive air showers," *Phys. Atom. Nucl.*, vol. 56, pp. 346–353, 1993.

[25] J. Engel, T. K. Gaisser, T. Stanev, and P. Lipari, "Nucleus-nucleus collisions and interpretation of cosmic ray cascades," *Phys. Rev.*, vol. D46, pp. 5013–5025, 1992.

[26] R. S. Fletcher, T. K. Gaisser, P. Lipari, and T. Stanev, "Sibyll: An event generator for simulation of high-energy cosmic ray cascades," *Phys. Rev.*, vol. D50, pp. 5710–5731, 1994.

[27] E.-J. Ahn, R. Engel, T. K. Gaisser, P. Lipari, and T. Stanev, "Cosmic ray interaction event generator SIBYLL 2.1," *Phys. Rev. D*, vol. 80, p. 094003, 2009.

[28] K. Aamodt *et al.*, "Charged-particle multiplicity measurement in proton-proton collisions at $\sqrt{s} = 7$ TeV with ALICE at LHC," *Eur.Phys.J.*, vol. C68, pp. 345–354, 2010.

[29] T. Pierog, I. Karpenko, J. Katzy, E. Yatsenko, and K. Werner, "EPOS LHC : test of collective hadronization with LHC data," 2013.

[30] S. Ostapchenko, "Monte Carlo treatment of hadronic interactions in enhanced Pomeron scheme: I. QGSJET-II model," *Phys.Rev.*, vol. D83, p. 014018, 2011.

[31] T. Csörgö *et al.*, "Elastic Scattering and Total Cross-Section in $p+p$ reactions measured by the LHC Experiment TOTEM at $\sqrt{s} = 7$ TeV," *Prog.Theor.Phys.Suppl.*, vol. 193, pp. 180–183, 2012.

[32] G. Aad *et al.*, "Rapidity gap cross sections measured with the ATLAS detector in pp collisions at $\sqrt{s} = 7$ TeV," *Eur.Phys.J.*, vol. C72, p. 1926, 2012.

[33] A. Aab *et al.*, "Highlights from the Pierre Auger Observatory," 2013.

[34] R. Engel, T. K. Gaisser, and T. Stanev, "Pion production in proton collisions with light nuclei: Implications for atmospheric neutrinos," *Phys. Lett.*, vol. B472, pp. 113–118, 2000.

[35] G. Aad *et al.*, "Measurements of the pseudorapidity dependence of the total transverse

energy in proton-proton collisions at $\sqrt{s} = 7$ TeV with ATLAS," *JHEP*, vol. 1211, p. 033, 2012.

[36] S. Chatrchyan *et al.*, "Measurement of energy flow at large pseudorapidities in pp collisions at $\sqrt{s} = 0.9$ and 7 TeV," *JHEP*, vol. 1111, p. 148, 2011.

[37] R. Aaij *et al.*, "Measurement of the forward energy flow in pp collisions at $\sqrt{s} = 7$ TeV," *Eur.Phys.J.*, vol. C73, p. 2421, 2013.

[38] F. Liu, J. Aichelin, M. Bleicher, H. Drescher, S. Ostapchenko, *et al.*, "Constraints on models for proton proton scattering from multistrange baryon data," *Phys.Rev.*, vol. D67, p. 034011, 2003.

[39] G. Antchev *et al.*, "Double diffractive cross-section measurement in the forward region at LHC," *Phys.Rev.Lett.*, vol. 111, p. 262001, 2013.

[40] G. Antchev *et al.*, "Luminosity-independent measurements of total, elastic and inelastic cross-sections at $\sqrt{s} = 7$ TeV," *Europhys.Lett.*, vol. 101, p. 21004, 2013.

[41] S. Chatrchyan *et al.*, "Study of the underlying event at forward rapidity in pp collisions at $\sqrt{s}$ = 0.9, 2.76, and 7 TeV," *JHEP*, vol. 1304, p. 072, 2013.

[42] H. Wöhrmann, "Studies of the nuclear stopping power in PbPb collisions at 2.76 TeV with CMS," *Nucl.Phys.*, vol. A904-905, pp. 787c–790c, 2013.

[43] G. Aad *et al.*, "Charged-particle multiplicities in pp interactions measured with the ATLAS detector at the LHC," *New J.Phys.*, vol. 13, p. 053033, 2011.

[44] V. Khachatryan *et al.*, "Charged particle multiplicities in pp interactions at $\sqrt{s} = 0.9$, 2.36, and 7 TeV," *JHEP*, vol. 1101, p. 079, 2011.

[45] R. Aaij *et al.*, "Measurement of charged particle multiplicities in pp collisions at $\sqrt{s} = 7$ TeV in the forward region," *Eur.Phys.J.*, vol. C72, p. 1947, 2012.

[46] G. Antchev *et al.*, "Measurement of the forward charged particle pseudorapidity density in pp collisions at $\sqrt{s} = 7$ TeV with the TOTEM experiment," *Europhys.Lett.*, vol. 98, p. 31002, 2012.

[47] K. Aamodt *et al.*, "First proton-proton collisions at the LHC as observed with the ALICE detector: Measurement of the charged particle pseudorapidity density at s**(1/2) = 900-GeV," *Eur.Phys.J.*, vol. C65, pp. 111–125, 2010.

[48] K. Aamodt *et al.*, "Charged-particle multiplicity measurement in proton-proton collisions at sqrt(s) = 0.9 and 2.36 TeV with ALICE at LHC," 2010.

[49] S. Chatrchyan *et al.*, "Measurement of pseudorapidity distributions of charged particles in proton-proton collisions at $\sqrt{s}$ = 8 TeV by the CMS and TOTEM experiments," *Eur.Phys.J.*, vol. C74, no. 10, p. 3053, 2014.

[50] G. Antchev *et al.*, "Measurement of the forward charged particle pseudorapidity density in pp collisions at $\sqrt{s}$ = 8 TeV using a displaced interaction point," 2014.

[51] R. Aaij *et al.*, "Measurement of charged particle multiplicities and densities in pp collisions at $\sqrt{s} = 7$ TeV in the forward region," *Eur.Phys.J.*, vol. C74, p. 2888, 2014.

[52] B. B. Abelev *et al.*, "Multi-strange baryon production at mid-rapidity in Pb-Pb collisions at $\sqrt{s_{NN}}$ = 2.76 TeV," *Phys.Lett.*, vol. B728, pp. 216–227, 2014.

[53] K. Aamodt *et al.*, "Production of pions, kaons and protons in pp collisions at $\sqrt{s} = 900$ GeV with ALICE at the LHC," *Eur.Phys.J.*, vol. C71, p. 1655, 2011.

[54] B. B. Abelev *et al.*, "Production of charged pions, kaons and protons at large transverse momenta in pp and Pb-Pb collisions at $\sqrt{s_{\rm NN}}$ =2.76 TeV," *Phys.Lett.*, vol. B736, pp. 196–207, 2014.

[55] M. Chojnacki, "Measurement of π, K, p transverse momentum spectra with ALICE in

proton-proton collisions at $\sqrt{s} = 0.9$ and 7 TeV," *J.Phys.*, vol. G38, p. 124074, 2011.

[56] B. Abelev *et al.*, "Multi-strange baryon production in pp collisions at (s)$^{1/2}$ = 7 TeV with ALICE," *Phys.Lett.*, vol. B712, pp. 309–318, 2012.

[57] B. Abelev *et al.*, "Production of $K^*(892)^0$ and $\phi(1020)$ in pp collisions at $\sqrt{s} = 7$ TeV," *Eur.Phys.J.*, vol. C72, p. 2183, 2012.

[58] B. B. Abelev *et al.*, "Production of $\Sigma(1385)^{\pm}$ and $\Xi(1530)^0$ in proton-proton collisions at $\sqrt{s} = 7$ TeV," *Eur.Phys.J.*, vol. C75, no. 1, p. 1, 2015.

[59] B. B. Abelev *et al.*, "Multiplicity Dependence of Pion, Kaon, Proton and Lambda Production in p-Pb Collisions at $\sqrt{s_{NN}}$ = 5.02 TeV," *Phys.Lett.*, vol. B728, pp. 25–38, 2014.

[60] C. Andrei,"Light flavor hadron spectra at low p_T and search for collective phenomena in high multiplicity pp, pPb and PbPb collisions measured with the ALICE experiment", *Nucl.Phys.*, vol. A931, pp. 888–892, 2014.

[61] C. A. for the ALICE Collaboration, "," *To Appear in the Proceedings of QM2014*, 2014.

[62] B. Abelev *et al.*, "Neutral pion and η meson production in proton-proton collisions at $\sqrt{s} = 0.9$ TeV and $\sqrt{s} = 7$ TeV," *Phys.Lett.*, vol. B717, pp. 162–172, 2012.

[63] B. B. Abelev *et al.*, "Neutral pion production at midrapidity in pp and Pb-Pb collisions at $\sqrt{s_{\rm NN}} = 2.76$ TeV," *Eur.Phys.J.*, vol. C74, no. 10, p. 3108, 2014.

[64] O. Adriani *et al.*, "The LHCf detector at the CERN Large Hadron Collider," *JINST*, vol. 3, p. S08006, 2008.

[65] O. Adriani *et al.*, "LHCf Detector Performance during the 2009-2010 LHC RUN," *Int.J.Mod.Phys.*, vol. A28, p. 1330036, 2013.

[66] K. Kawade, K. Fukatsu, Y. Itow, K. Masuda, T. Murakami, *et al.*, "Study of radiation hardness of Gd(2)SiO(5) scintillator for heavy ion beam," *JINST*, vol. 6, p. T09004, 2011.

[67] T. Suzuki, K. Kasahara, K. Kawade, T. Murakami, K. Masuda, *et al.*, "Performance of very thin Gd(2)SiO(5) scintillator bars for the LHCf experiment," *JINST*, vol. 8, p. T01007, 2013.

[68] O. Adriani, L. Bonechi, M. Bongi, G. Castellini, R. D'Alessandro, *et al.*, "Measurement of zero degree single photon energy spectra for $\sqrt{s}$ = 7 TeV proton-proton collisions at LHC," *Phys.Lett.*, vol. B703, pp. 128–134, 2011.

[69] O. Adriani *et al.*, "Measurement of zero degree inclusive photon energy spectra for $\sqrt{s} =$ 900 GeV proton-proton collisions at LHC," *Phys.Lett.*, vol. B715, pp. 298–303, 2012.

[70] O. Adriani *et al.*, "Measurement of forward neutral pion transverse momentum spectra for $\sqrt{s}$ = 7 TeV proton-proton collisions at LHC," *Phys.Rev.*, vol. D86, p. 092001, 2012.

[71] E. Pare, T. Doke, M. Haguenauer, V. Innocente, K. Kasahara, *et al.*, "Inclusive Production of π^0s and Feynman Scaling Test in the Fragmentation Region at the S $\bar{\rm p}$p S Collider," *Phys.Lett.*, vol. B242, pp. 531–535, 1990.

[72] O. Adriani, E. Berti, L. Bonechi, M. Bongi, G. Castellini, *et al.*, "Transverse momentum distribution and nuclear modification factor of forward neutral pion in proton–lead collisions at $\sqrt{s_{NN}} = 5.02$ TeV," *Phys.Rev.*, vol. C89, p. 065209, 2014.

[73] O. *et al.*, "7 TeV neutron," *should be submitted before yellow report is ready*, 2014.

[74] S. Ostapchenko, "QGSJET-II: Results for extensive air showers," *Nucl. Phys. Proc. Suppl.*, vol. 151, pp. 147–150, 2006.

[75] B. Abelev *et al.*, "Heavy flavour decay muon production at forward rapidity in proton–proton collisions at $\sqrt{s} = 7$ TeV," *Phys.Lett.*, vol. B708, pp. 265–275, 2012.

[76] B. Abelev *et al.*, "Measurement of electrons from semileptonic heavy-flavour hadron de-

cays in pp collisions at $\sqrt{s} = 7$ TeV," *Phys.Rev.*, vol. D86, p. 112007, 2012.

[77] B. Abelev *et al.*, "Production of muons from heavy flavour decays at forward rapidity in pp and Pb-Pb collisions at $\sqrt{s_{NN}}$ = 2.76 TeV," *Phys.Rev.Lett.*, vol. 109, p. 112301, 2012.

[78] B. Abelev *et al.*, "Measurement of electrons from beauty hadron decays in pp collisions at $\sqrt{s} = 7$ TeV," *Phys.Lett.*, vol. B721, pp. 13–23, 2013.

[79] B. B. Abelev *et al.*, "Measurement of electrons from semileptonic heavy-flavor hadron decays in pp collisions at $\sqrt{s} = 2.76$ TeV," *Phys.Rev.*, vol. D91, no. 1, p. 012001, 2015.

[80] B. B. Abelev *et al.*, "Beauty production in pp collisions at $\sqrt{s}$ = 2.76 TeV measured via semi-electronic decays," *Phys.Lett.*, vol. B738, pp. 97–108, 2014.

[81] B. Abelev *et al.*, "Measurement of charm production at central rapidity in proton-proton collisions at $\sqrt{s} = 7$ TeV," *JHEP*, vol. 1201, p. 128, 2012.

[82] "First analysis of the pPb pilot run data with LHCb," Dec 2012.

[83] D.Manglunki, "Results and prospects of forward physics at the LHC," *presentation at workshop held at CERN in 11-12 Feb*, 2013.

Chapter 7

Heavy Ion Physics

Convener and Editor: D. Takaki
Internal Reviewers: V. Avati, M. Murray

7.1 Introduction

The LHC is not only the most powerful collider for proton-proton and heavy-ion collisions, but also for photon-photon and photon-hadron (γp and γPb) interactions, offering a unique opportunity to study fundamental aspects of QED and QCD via photon-induced processes. The protons and ions which are accelerated by the LHC themselves carry an electromagnetic field, which can be viewed as a source of photons [1–5]. That is, a photon generated by one of these hadrons can interact with another photon (or with a hadron) producing a wide variety of particles.

In recent years there has been an increasing interest in these physics processes that can be studied in ultra-peripheral collisions (UPC) in hadronic colliders [8, 9]. The relevant collisions typically occur at impact parameters of several tens (or even hundreds) of femtometres –cases when the incoming ions barely overlap, and well beyond the range of the strong force. This is because these reactions occur when the protons or ions pass by each other with impact parameters larger than the sum of their radii and are mediated by the exchange of virtual photons between the nuclei. The number of photons scales as the square of the nuclear charge while typical photon energies scale with the Lorentz contraction of the nuclei and so increase with beam energy.

The beam energies at the LHC are high enough to make the LHC the most energetic photon source ever built. In Pb-Pb collisions the LHC can reach $W_{\gamma\mathrm{Pb}}$ energies up to 500 GeV, while in p–Pb collisions it can reach $W_{\gamma\mathrm{p}}$ up to about 1500 GeV in γp interactions. Photon-induced processes have by far the largest cross sections in PbPb collisions at the LHC. The total cross section for breaking up one of the nuclei through a photonuclear process is over 200 barns. In most of these reactions the nucleus just breaks up without any particle production. However, the cross section for having at least one photoproduced charged particle at mid-rapidity is still substantial, about 4 b. But both these numbers are dwarfed by the total cross section for producing an e^+e^- pair from an interaction between two photons. This cross section is about 3 million times larger than that for normal hadronic pp collisions.

We discuss recent results on ultra-peripheral heavy-ion collisions measured at the LHC. Special emphasis is given to the measurements of exclusive photonuclear processes, as well as the prospects for future photon-induced measurements.

7.2 Exclusive photonuclear processes

A photonuclear interaction that has attracted a lot of interest is exclusive vector meson production. That is, a reaction where only a vector meson is produced in the final state, and nothing else. The large cross section of this process can be understood from what is known as Vector Meson Dominance. This means that the photon may fluctuate into a quark-anti-quark pair and,

since the photon has spin 1 and negative parity, the fluctuation will most likely be to a vector meson.

Exclusive vector meson production in heavy-ion collisions provides a way to probe the nuclear gluon density for which there is a considerable uncertainty at low values of Bjorken-x, where x is the fractional parton momentum $x = p_{\text{parton}}/p_{\text{hadron}}$. For example, a J/$\psi$ produced at rapidity y is sensitive to the gluon distribution at $x = \frac{M_{J/\psi}}{\sqrt{s}} e^{\pm y}$ at hard scales $Q^2 \sim \frac{M^2_{J/\psi}}{4}$.

Up to now, two types of UPC processes have bean measured at the LHC: (1) The photo-production of a vector meson in photo-nuclear interactions, where the vector meson is reconstructed from its decay products, and (2) the two-photon process decaying to a di-lepton pair ($\gamma\gamma \to l^+l^-$), where $l = e, \mu$. Studies to τ decays have not been performed so far. The experimental signature of these events is characterized by their very low transverse momenta. Apart from two tracks in the final state the detector is otherwise empty. Figure 7.1 shows an event display for a J/ψ candidate produced in an ultra-peripheral Pb–Pb collision at $\sqrt{s_{NN}} = 2.76$ TeV with CMS. The Feynman diagrams for these proceses are shown in Figure 7.2. These processes are further classified into the following classes of events

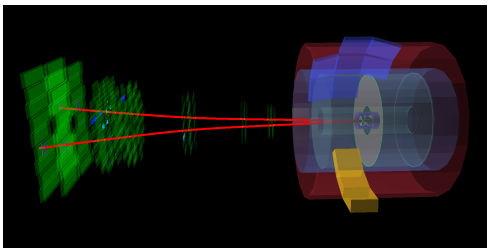

Fig. 7.1: Event display of J/ψ candidate produced in an ultra-peripheral Pb–Pb collision at $\sqrt{s_{NN}} = 2.76$ TeV.

- Photoproduction off nuclei in ultra-peripheral Pb–Pb collisions
  - **Coherent production:** The photon interacts coherently with the whole nucleus. The coherence condition, both in the emission of the photon and in the interaction with the nuclear target, constraints the transverse momentum of the produced di-lepton or vector meson to be of the order of $1/2R_{\text{Pb}}$ – where R_{Pb} is the radius of the lead nucleus – which corresponds to a $p_T \sim 60$ MeV/c.
  - **Coherent production with nuclear break up:** Owing to the intense electromagnetic fields of the lead nuclei it is possible to have independent electromagnetic interactions between the nuclei. These additional interactions may excite at least one of the nuclei, resulting in the emission of at least one neutron in the same direction to that of the emitting nucleus.
  - **Incoherent production**. In this case the photon interacts not with the whole nucleus, but rather with a single nucleon. There are two main differences with respect to the coherent case. First, as the radius of the nucleon is smaller than that of the nuclei, the transverse momentum of the produced system is larger, around 300 MeV/c. Second, in the incoherent case the interaction makes the nuclei to break up producing, in almost all cases, forward neutrons.
- Photoproduction off protons in ultra-peripheral p–Pb collisions
  - **Exclusive production:** The photon interacts with the proton without breaking it. The transverse momentum of the produced system is of the order of 300 MeV/c.

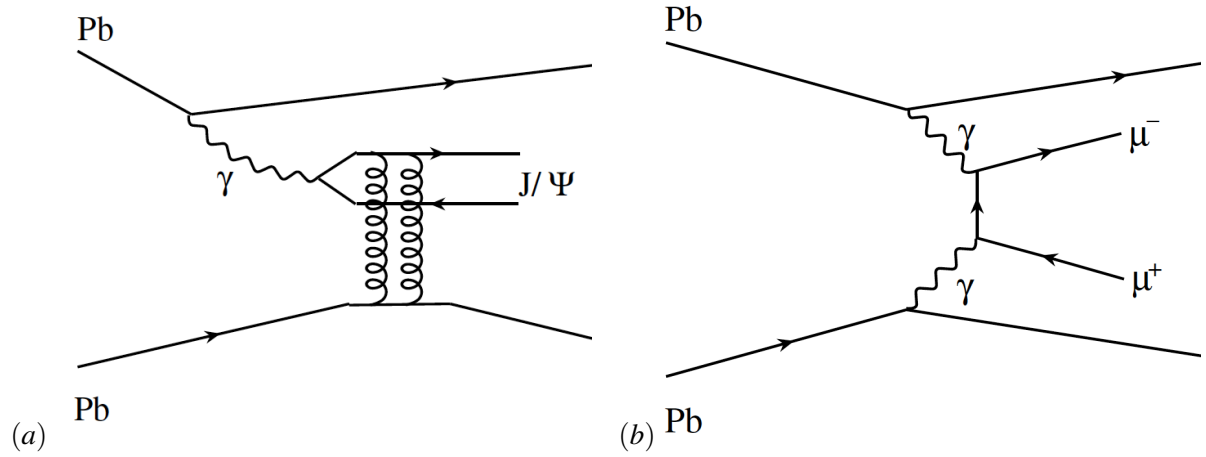

Fig. 7.2: Feynman diagrams for the photoproduction of vector messons (panel a) and the two-photon process (panel b) in ultra-peripheral Pb–Pb collisions.

- **Dissociative production:** The proton is excited by the interaction and dissociates. The transverse momenta of the produced di-lepton or vector meson extends to well above 1 GeV/c.

The cross section for the vector meson photoproduction in ultra-peripheral Pb–Pb collisions is given by

$$\frac{d\sigma_{\mathrm{PbPb}}(y)}{dy} = N_{\gamma/\mathrm{Pb}}(y,M)\sigma_{\gamma\mathrm{Pb}}(y) + N_{\gamma/\mathrm{Pb}}(-y,M)\sigma_{\gamma\mathrm{Pb}}(-y), \tag{7.1}$$

where M is the mass of the produced vector meson state, and y is the rapidity given by $y = \ln(2k/M)$, where k is the photon energy and $\sigma_{\gamma\mathrm{Pb}}(y)$ is the corresponding photoproduction cross section. $N_{\gamma/\mathrm{Pb}}$ is the photon flux. There are two terms because each of the incoming lead nuclei may act as the photon source.

A similar formula can be written for the production of vector mesons in ultra-peripheral p–Pb collisions. In this case, the term involving the photon emission by the proton is very small and the dominant contribution is given by

$$\frac{d\sigma_{\mathrm{pPb}}(y,M)}{dy} \approx N_{\gamma/\mathrm{Pb}}(y,M)\sigma_{\gamma\mathrm{p}}(y) \tag{7.2}$$

In a similar way, the two-photon cross section can be calculated. In this case two photon fluxes are convoluted with the corresponding photon-photon cross section.

The photon flux per unit area in the semi-classical description is given by (see for example [10])

$$n(k,\vec{b}) = \frac{\alpha Z^2}{\pi^2 b^2} x^2 \left[K_1^2(x) + \frac{1}{\gamma} K_0^2(x) \right], \tag{7.3}$$

where k is the photon energy in the nucleus frame with Lorentz factor γ, Z is the electric charge of the emitting heavy nuclei, K_0 and K_1 are Bessel functions and $x = kb/\gamma$. This formula is a good approximation for heavy nuclei and at impact parameters b larger than b_{min}, the sum

of the radii of the interacting particles. In this case, the photon flux $n(k) = \int d^2\vec{b}\, n(k,\vec{b})$ is given by

$$n(k) = \frac{2\alpha Z^2}{\pi}\left[\xi K_0(\xi)K_1(\xi) - \frac{\xi^2}{2}\left(K_1^2(\xi) - K_0^2(\xi)\right)\right], \tag{7.4}$$

where $\xi = kb_{\min}/\gamma$.

The photon flux from a lead nucleus is then obtained using the corresponding values of Z and γ and using rapidity instead of photon energy as the relevant variable:

$$N_{\gamma/\mathrm{Pb}}(y,M) \equiv k\frac{dn(k)}{dk}\bigg|_{\mathrm{Pb}}. \tag{7.5}$$

Figure 7.3 presents $N_{\gamma/\mathrm{Pb}}(y,M)$ as a function of rapidity for the masses of the J/ψ and the Υ for two different energies of the lead beam: 1.38 GeV –used during Run 1 in the Pb–Pb data taking periods of 2010 and 2011– and 2.76 TeV which will be possible in Run 2. The drop of the flux at large rapidities is given by the behaviour of the Bessel functions at large photon energies. Comparing the Run 1 and Run 2 scenarios, there is a significant increase in the acceptance at forward rapidities. According to STARLIGHT (see section on Monte Carlo generators for more details), this represents a 60% increase in statistics for J/ψ, 70% increase for ψ(2S) and a 200% increase for Υ(1S). This would allow differential studies using Run 2 data. The colliding system for nucleus-nucleus collisions to be taken from Run 3 onwards will be decided depending on the physics outcome from Run 2. Possibilities include not only p–Pb and Pb–Pb collisions, but also light ion colliding systems such as Ar–Ar.

7.3 Models for photonuclear production

The following models have predicted cross sections for photonuclear production at LHC energies will be discuss in this section:

AB-AN: Model by Adeluyi and Bertulani [11] and Adeluyi and Nguyen [12];

CSS: Model by Cisek, Schäfer and Szczurek [13];

KN: Model by Klein and Nystrand implemented in the STARLIGHT Monte Carlo program [14–16];

LM: Model by Lappi and Mantysaari [17, 18];

GM-GDGM: Model by Goncalves and Machado [19] and by Gay-Ducati, Griep and Machado [20];

RSZ: Model by Rebyakova, Strikman and Zhalov [21], and

IKS: Model by Ivanov, Kopeliovich and Schmidt [22].

All models are based on Equation (7.1) which has two ingredients: the photon flux and the photonuclear cross section. The first difference among the models is that some of them (CSS, LM, GM-GDGM) use the hard sphere approximation of the photon flux; i.e., equation (7.4), and other models (AB-AN, KN, RSZ-GZ) integrate the convolution of equation (7.3) with the probability of no hadronic interaction.

As for the photonuclear cross section the models contain the following ingredients: (*i*) the models have to assume a nuclear distribution in the transverse plane, (*ii*) the models also include implicitly or explicitly a prescription for the wave function of the vector meson and finally (*iii*) all models fix some of the parameters using data on exclusive photoproduction of charmonium

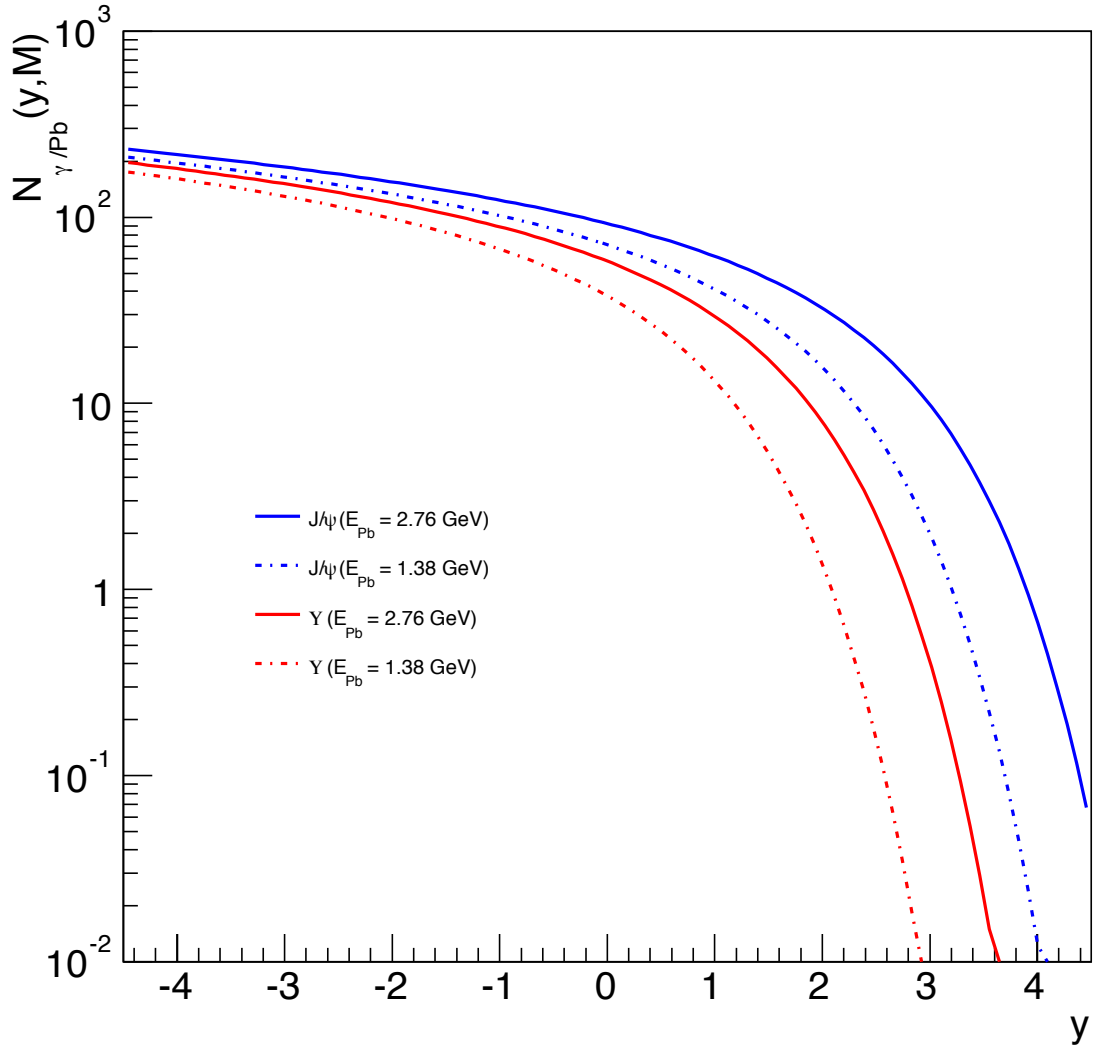

Fig. 7.3: Photon flux emitted by a lead nucleus at two different LHC energies as a function of rapidity for photon energies corresponding to the production of a J/ψ and a Υ vector meson at the corresponding rapidity.

off the proton and thus have to include a prescription to link the photoproduction off protons with that of the photonuclear interaction. For these reasons, the models can be grouped into three different groups: models based on the generalized vector dominance model (KN), on LO pQCD (AB-AN, RSZ) and on the color dipole model (CSS, LM, GM-GDGM).

7.3.1 Models based on the vector dominance model

The only model in this class is the KN model. The main ingredients of this model are three. The vector dominance model (VDM) relates both the γ+Pb $\rightarrow$ Pb + V and the γ+p $\rightarrow$ p + V processes to Pb + V $\rightarrow$ Pb + V and p + V $\rightarrow$ p + V, respectively. Here V represents a vector meson. The optical theorem relates these last processes to the total cross section. Finally a

classical Glauber model relates the total cross section on protons to that on nuclei. This can be expressed in the following way

$$\sigma_{\gamma\mathrm{Pb}}(y) \equiv \sigma(\gamma{+}\mathrm{Pb} \to \mathrm{V}+\mathrm{Pb}) = \left.\frac{d\sigma(\gamma{+}\mathrm{Pb} \to \mathrm{V}+\mathrm{Pb})}{dt}\right|_{t=0} \int_{t_{min}}^{\infty} dt|F(t)|^2, \tag{7.6}$$

where $F(t)$ is the nuclear form factor and t the momentum transferred to the nucleus. Using VDM and the optical theorem yields

$$\left.\frac{d\sigma(\gamma{+}\mathrm{Pb} \to \mathrm{V}+\mathrm{Pb})}{dt}\right|_{t=0} = \frac{\alpha\sigma^2_{\mathrm{TOT}}(\mathrm{Pb}+\mathrm{V})}{4f_V^2}, \tag{7.7}$$

where f_V is the vector meson photon coupling. A classical Glauber model produces

$$\sigma_{\mathrm{TOT}}(\mathrm{Pb}+\mathrm{V}) = \int d^2\vec{b}\left(1-\exp\left[-\sigma_{\mathrm{TOT}}(\mathrm{p}+\mathrm{V})T_{\mathrm{Pb}}(\vec{b})\right]\right), \tag{7.8}$$

where T_{Pb} is the nuclear thickness function and $\sigma_{\mathrm{TOT}}(\mathrm{p}+\mathrm{V})$ is obtained from the optical theorem, now applied at the nucleon level

$$\sigma^2_{\mathrm{TOT}}(\mathrm{p}+\mathrm{V}) = 16\pi \left.\frac{d\sigma(\mathrm{V}+\mathrm{p} \to \mathrm{V}+\mathrm{p})}{dt}\right|_{t=0}. \tag{7.9}$$

Using VDM leads to

$$\left.\frac{d\sigma(\mathrm{V}+\mathrm{p} \to \mathrm{V}+\mathrm{p})}{dt}\right|_{t=0} = \frac{f_V^2}{4\pi\alpha} \left.\frac{d\sigma(\gamma{+}\mathrm{p} \to \mathrm{V}+\mathrm{p})}{dt}\right|_{t=0}, \tag{7.10}$$

where the elementary cross section

$$\left.\frac{d\sigma(\gamma{+}\mathrm{p} \to \mathrm{V}+\mathrm{p})}{dt}\right|_{t=0} = b_V\left(XW^{\varepsilon}_{\gamma\mathrm{p}} + YW^{-\eta}_{\gamma\mathrm{p}}\right) \tag{7.11}$$

is fitted to experimental data to obtain the values for the X, Y, ε, η and b_V parameters.

7.3.2 Models based on LO pQCD

These models start from Equation 7.6 and use the LO pQCD calculation [23,24] for the forward cross section

$$\left.\frac{d\sigma(\gamma{+}\mathrm{Pb} \to \mathrm{V}+\mathrm{Pb})}{dt}\right|_{t=0} = \frac{16\pi^3\alpha_s^2\Gamma_{ee}}{3\alpha M^5}\left[xG_A(x,Q^2)\right]^2, \tag{7.12}$$

where Γ_{ee} is the decay width to electrons and G_A is the nuclear gluon density distribution at a scale Q^2, which for the models described below was chosen to be $Q^2 = M^2/4$, although other options are possible and may describe better the experimental data [25]. It is important to note that this equation contains implicitly a model for the wave function of the vector meson, but in the final result the only trace of it is the presence of Γ_{ee}.

The AB-AN model modifies equation 7.12 by adding a normalization parameter to the right side, which should take into account effects missing in the approximation. This factor is then fitted to reproduce HERA data using the same type of equation applied to the $\gamma{+}\mathrm{p} \to \mathrm{p}+J/\psi$ case. Nuclear effects are modelled as $G_A(x,Q^2) = g_p(x,Q^2)R_g^A(x,Q^2)$, where g_p is the gluon distribution in the proton and R_g^A is the nuclear modification factor of the gluon

distribution. MSTW08 [26] is used for the gluon distribution in the proton, while several different choices are made for R_g^A to estimate nuclear effects: EPS08 [27], EPS09 [28], HKN07 [29] and $R_g^A = 1$ to model the absence of nuclear effects.

The RSZ model computes R_g^A in the leading twist approach to nuclear shadowing [30]. The main ingredients are the factorization theorem for hard diffraction and the theory of inelastic shadowing by Gribov. The evolution is done using DGLAP equations. The experimental input to fix the parameters of the model is given by inclusive diffractive parton distribution functions of nucleons as measured at HERA. For the gluon distribution in the proton they use the LO distribution from [31].

7.3.3 Models based on the colour dipole approach

The basic idea of this formalism is that long before the interaction, the photon splits into a quark-antiquark pair, which forms a colour dipole. Long time afterwards, this dipole interacts with the target and after another long time the dipole creates a vector meson. The cross section in this formalism is given by

$$\frac{d\sigma(\gamma+\mathrm{Pb}\to J/\psi+\mathrm{Pb})}{dt} = \frac{R_g^2(1+\beta^2)}{16\pi}\left|A(x,Q^2,\vec{\Delta})\right|^2, \tag{7.13}$$

where the so called skewdness correction R_g^2 compensate for the fact that only one value of x is used, even thought the two gluons participating in the interaction have different x [32], while $(1+\beta^2)$ is the correction that takes into account the contribution from the real part of the amplitude. The amplitude is given by

$$A(x,Q^2,\vec{\Delta}) = i\int dz d^2\vec{r} d^2\vec{b} e^{-i(\vec{b}-(1-z)\vec{r})\cdot\vec{\Delta}}\left[\Psi^*_{J/\psi}\Psi\right] 2\left[1-\exp\left\{-\frac{1}{2}\sigma_{\mathrm{dip}}T_{\mathrm{Pb}}(b)\right\}\right], \tag{7.14}$$

where the integration variable $\vec{r}$ represents the distance between the quark and the antiquark in the plane transverse to the collision, z quantifies the fraction of the photon momentum carried by the quark and b is the distance between the centres of the target and the dipole; $\vec{\Delta}$ is the transverse momentum transferred to the nucleus; the virtuality of the incoming photon is denoted by Q^2 and for the case of photoproduction discussed here is zero; Ψ describes the splitting of the photon into the dipole and $\Psi_{J/\psi}$ is the wave function of the J/ψ; the term $i(1-z)\vec{r}\cdot\vec{\Delta}$ in the exponential is a third correction to take into account non-forward contributions to the wave function $\Psi_{J/\psi}$, which is modelled for the forward case [33]; and finally σ_{dip} is the universal cross section for the interaction of a colour dipole with a nuclear target. The models differ in the functional form of $\Psi_{J/\psi}$, in corrections they consider and in their formulation of the universal dipole cross section.

In the case of LM they do not consider the non-forward correction to the wave function. They use two different prescriptions for the wave function: the Gauss-LC [34] and the boosted Gaussian [35, 36]. They write σ_{dip} in terms of the cross section of a dipole and a proton, σ^p_{dip}; assuming a Gaussian profile in impact parameter for the proton, $\exp(-b^2/(2B_p))$ they arrive at

$$\frac{1}{2}\sigma_{\mathrm{dip}} = 2\pi B_p A N(r,x), \tag{7.15}$$

where $N(r,x)$ is the dipole target amplitude. They use two different models for $N(r,x)$: The IIM model [139] which is a parameterisation of the expected behaviour of the solution to the BK

equation [40, 118, 119] which includes a non-linear term for the evolution of $N(r,x)$; and the IPsat model [34,41] which uses DGLAP equations to evolved an eikonalized gluon distribution.

The GM-GDGM model uses the boosted Gaussian prescription for the wave function. The dipole cross section is given by $\sigma_{\rm dip} = R_g^A(x,Q^2)\sigma_{\rm dip}^{\rm p}$, where $\sigma_{\rm dip}^{\rm p}$ is given according to the IIM model and the leading twist approximation is used for $R_g^A(x,Q^2)$.

7.4 Experimental results on exclusive photonuclear processes

7.4.1 Exclusive J/ψ photoproduction off protons in ultra-peripheral p–Pb collisions

Exclusive J/ψ photoproduction has been studied in previous colliders at HERA [42–44] and the Tevatron [45]. Recently, both ALICE [46] and LHCb [47] reported results on exclusive J/ψ photoproduction. By studying photon-proton collisions one can get insights about one of the most interesting QCD discoveries from the last decade: the density of gluons carrying a small fraction of the momentum of hadrons grows extremely rapidly. The growth of the probability density function (PDF) for small-x gluons cannot continue forever. Gluon saturation [49,105] is the most straightforward mechanism to slow down the growth of the gluon PDF at small-x, and it would have important implications in the early stages of ultra-relativistic heavy-ion collisions at RHIC and LHC. Consequently, finding evidence for gluon saturation has become a central task for present experiments and for future projects that aim to study QCD. Although gluon saturation regime should manifest in terms of new physics in the strongly interacting sector, only hints for this QCD phenomena at HERA, RHIC, CEBAF and LHC have been found so far.

ALICE results on exclusive J/ψ in p–Pb collisions [46] provide a unique opportunity to study the proton gluon distribution over an unprecedented range in Bjorken-x, from 2×10^{-2} to $\times 10^{-5}$, and do not suffer from the ambiguities and assumptions that have to be made when studying symmetric systems such as in pp collisions. These results indicate no significant change in the behavior of the gluon density from HERA to LHC energies, extending by a factor five the x values previously explored. These findings thus substantially advance our understanding of the proton structure and set important constraints on gluon saturation.

The measurement of exclusive J/ψ production in ultra-peripheral heavy-ion collisions [14] is one of the key measurements for the future electron-ion collider such as the LHeC electron-proton and electron-ion collider [50]. Similar studies have been highlighted in the U.S. electron-ion collider design study reports [51, 52].

7.4.2 Coherent and incoherent J/ψ photoproduction from ultra-peripheral Pb–Pb collisions

One of the most important questions in relativistic heavy-ion physics is the nature of the initial state produced in high energy heavy-ion collisions. A common denominator in heavy-ion physics analyses is the need to distinguish between final states effects expected from the QGP from those inherent to the nuclei themselves. The competing Glauber and Color Glass Models are two well studied alternatives but both may be wrong. Uncertainty over the initial state is an impediment to measuring fundamental properties of the QGP such as viscosity. The photon-nuclear measurements at the LHC are putting important constraints on the initial state by measuring the nuclear effects on the parton distribution functions (PDFs). The modifications due to nuclear effects in the gluon PDF are called nuclear shadowing. This is related to the fact that nuclear parton distributions at small-x are suppressed compared to the case of a free proton. The degree of gluon shadowing effects for a $x < 0.01$ is poorly known. The study of photo-nuclear reactions at the LHC allows us to put important constraints on theoretical models that predict nuclear gluon shadowing. Although similar studies were performed by PHENIX [53], there studies were limited by their small sample size.

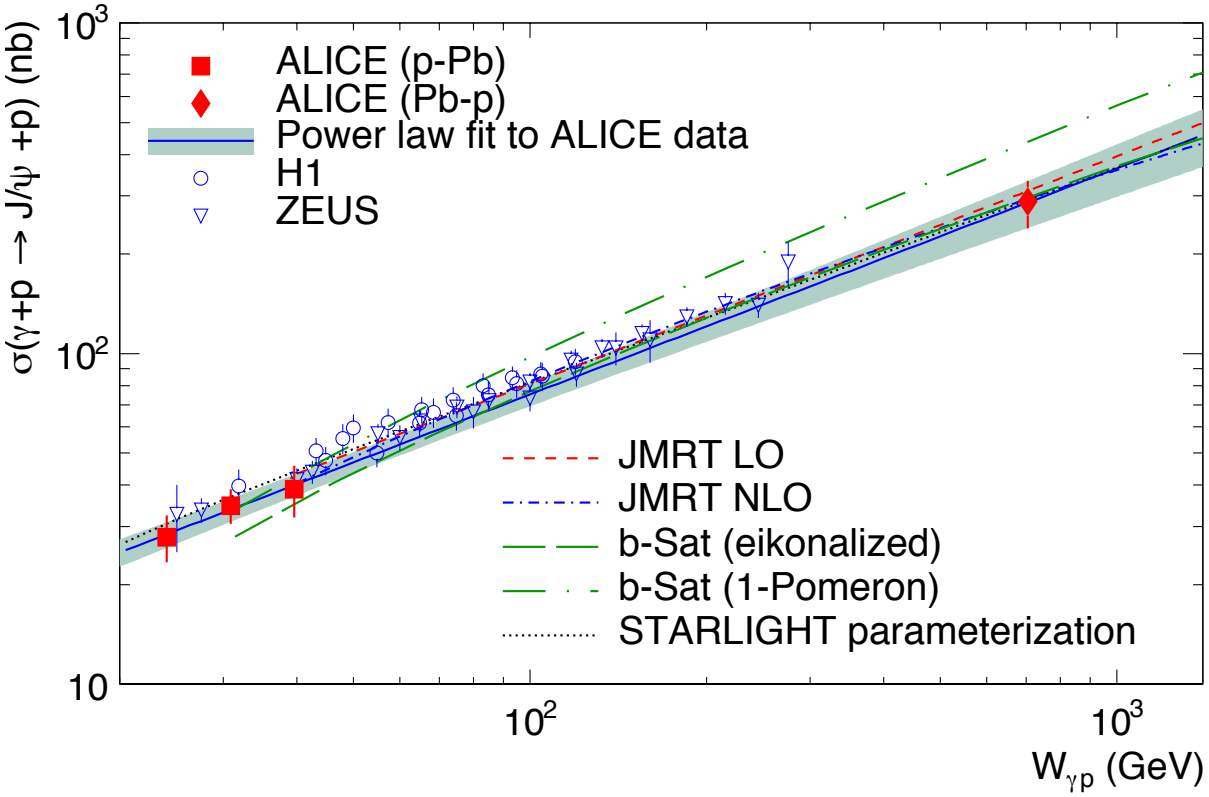

Fig. 7.1: Exclusive J/ψ photoproduction cross section off protons measured by ALICE and compared to HERA data [46]. Comparisons to STARLIGHT, JMRT and the b-Sat models are shown. The power law fit to ALICE data is also shown.

The coherent J/ψ measured by ALICE is detected through its dimuon decay in the muon spectrometer of the ALICE detector, which also provides the trigger for these events, or in its dielectron or dimuon decay in the central barrel. At the rapidities [54] (y around 3) studied in the muon arm, J/ψ photoproduction is sensitive mainly to the gluon distribution at values of Bjorken-x of about 10^{-2}, whereas at mid-rapidity on probes x $\sim 10^{-3}$ [55]. Preliminary CMS results on the measured cross section for coherent J/ψ were presented for the first time in Fall 2014 [56]. Figure 7.2 shows the comparison between the coherent J/ψ cross section in ultra-peripheral PbPb collisions at $\sqrt{s_{NN}} = 2.76$ TeV [54,55] and theoretical predictions [12,13, 18,20,25,57–61]. Models which do not include nuclear gluon shadowing are inconsistent with the measured ALICE results [11,14]. Best agreement is found for models that incorporate the EPS09 shadowing parameterization [11].

The ALICE measurements have provided the first direct experimental evidence [54,55] for nuclear gluon shadowing at small values of Bjorken-x [61]. In addition, the ALICE measurements have shown that certain models can be rejected [62]. The next step is to use these measurements to determine the nuclear parton distribution.

Incoherent production of J/ψ in Pb–Pb UPC has been measured at mid rapidities [55] using the same trigger and detectors as for the coherent case. The incoherent contribution was obtained from the distribution of transverse momentum. The centre of mass energy in the γ-Pb system are the same as for the coherent case. The measured cross section is $0.98\ ^{+0.19}_{-0.17}$ (stat+sys) mb.

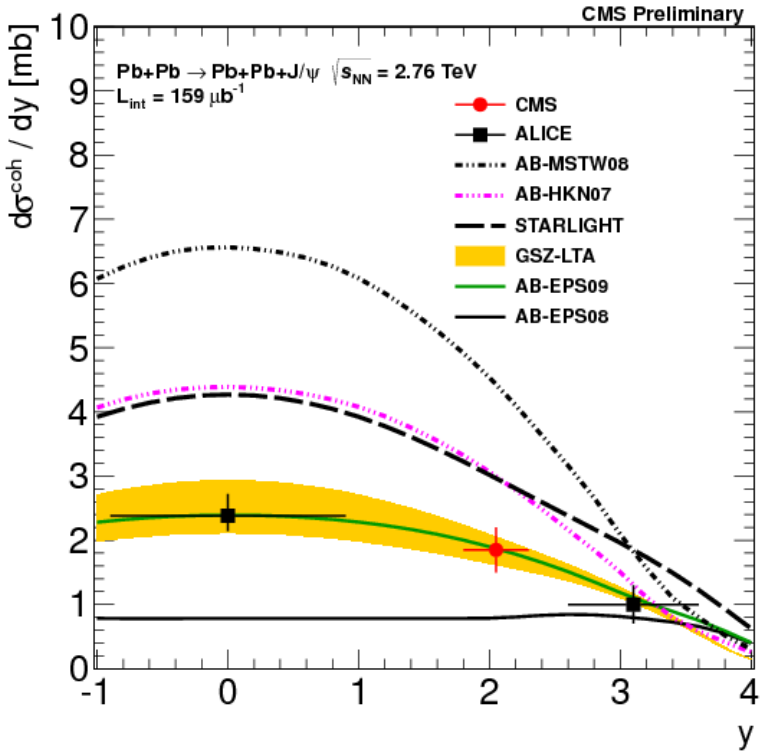

Fig. 7.2: Coherent J/ψ photoproduction cross section in ultra-peripheral Pb–Pb collisions at $\sqrt{s_{NN}}$ = 2.76 TeV measured by ALICE and CMS [54–56]. CMS results corresponds to preliminary results and have not been corrected for feed-down contributions from ψ(2S) decays. Data is compared to model calculations.

7.4.3 Coherent ψ(2S) photoproduction from ultra-peripheral Pb–Pb collisions

Preliminary results on coherent production of ψ' in ultra-peripheral Pb–Pb collisions at mid-rapidity have been reported. The ψ' has been identified in the following channels: to l^+l^- and to $J/\psi \to \pi^+\pi^-$, with $J/\psi \to l^+l^-$, where $l = e, \mu$. The measurement correspondeds to $W_{\gamma\mathrm{Pb}} \approx$ 100 GeV ($x \approx 1.3 \cdot 10^{-3}$). The coherent ψ(2S) is expected to be sensitive to nuclear gluon shadowing as for the J/ψ case. Despite the small sample size and the considerable uncertainty in the underlying $\gamma + \mathrm{p} \to \mathrm{V} + \mathrm{p}$ cross section, the ALICE measurement concludes that models with no nuclear effects or with a strong nuclear gluon shadowing are disfavored.

7.4.4 Coherent ρ^0 photoproduction from ultra-peripheral Pb–Pb collisions

ALICE has recently reported preliminary results on coherent ρ^0 photoproduction from ultra-peripheral Pb–Pb collisions at $\sqrt{s_{NN}}$ = 2.76. The measured cross section was found to be in agreement with both STARLIGHT [14] and the Goncalves and Machado (GM) model. The prediction by Glauber-Donnachie-Landshoff (GDL) is about a factor 2 larger than in data. This confirms the STAR findings [63]. However, it is surprising that the measured cross section agrees with the STARLIGHT that does not include the elastic component of the total cross section. It would be important to understand why the scaling of the γp cross section using the Glauber model [21, 64] overpredicts the measured cross section.

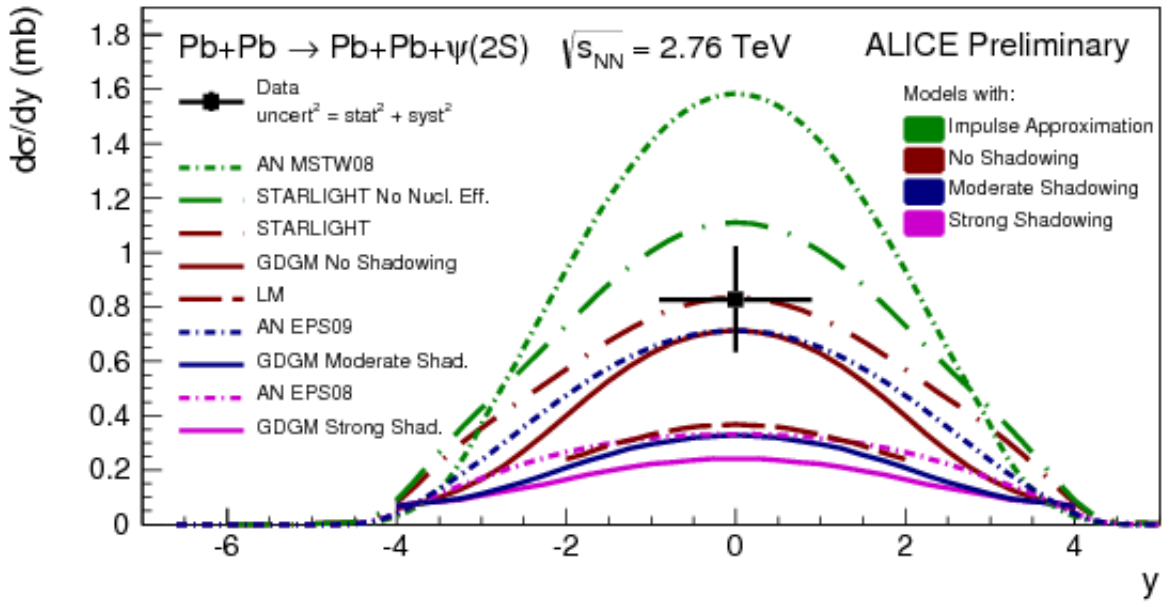

Fig. 7.3: Coherent ψ(2S) photoproduction cross section measured by the ALICE experiment (preliminary results) and compared to model calculations.

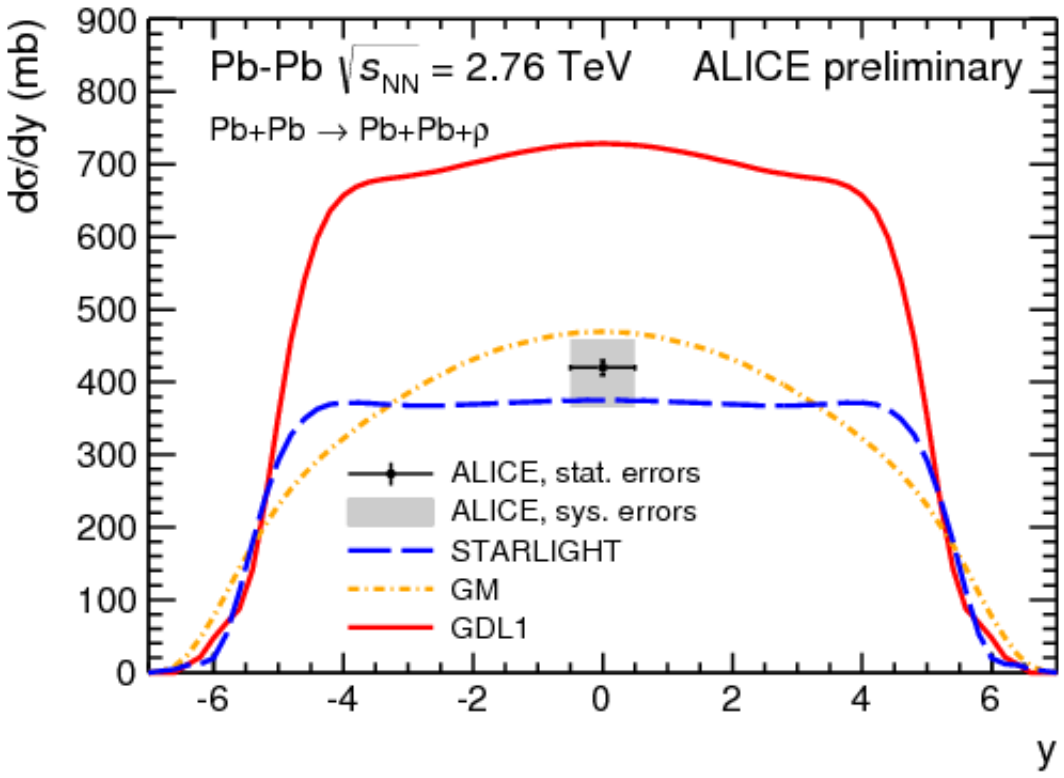

Fig. 7.4: Coherent ρ^0 photoproduction cross section in ultra-peripheral Pb–Pb collisions at $\sqrt{s_{NN}}$ = 2.76 TeV measured by the ALICE experiment and compared to model predictions.

7.4.5 Four-pion production in ultra-peripheral Pb–Pb collisions

It is interesting to look for excited states of photo-produced ρ^0 mesons. It is not clear how many excited states exist or their quantum numbers (see special PDG review [65]). STAR reported on four-pion production in UPC [66], albeit at much lower centre-of-mass energies. No HERA publications on photo-production of a ρ^0 excited states exist. Figure 4 in [67] shows the four-pion p_T distribution, where a clear coherent peak can be seen at low transverse momenta. This corresponds to data collected during the 2011 Pb-Pb run, where we have 10 times more statistics than those published by STAR. One of the current research interesest is understanding the possible production mechanics [68].

7.5 Two-photon physics

The two-photon process is governed by QED. Here, the coupling between the photon and the emitting nucleus is enhanced by a factor Z. Thus, higher order terms might be important. However, recent ALICE results on $\gamma\gamma \to e^+e^-$ are well described by STARLIGHT which only includes the leading QED order terms [55]. The published analysis [55] was carried out using data from the 2011 Pb–Pb run, a data that was recored using a topology trigger. This restricted the analysis to invariant masses $M_{e^+e^-} > 2.2$ GeV/c^2. A preliminary analysis of the 2010 Pb–Pb run was presented at Quark Matter and ICHEP 2014 [**?**, 69]. The 2011 data does not include a topology trigger and so the analysis can be performed to go down to $M_{e^+e^-} > 0.6$ GeV/c^2.

7.6 UPC lessons from LHC Run 1

The experimental challenge for such measurements consists in having dedicated UPC triggers that are often orthogonal to the general trigger strategy of the experiments. Moreover, validating an exclusive analysis requires a good understanding of the trigger efficiency for the exclusivity conditions imposed at the online and offline levels, for which control triggers are usually required. The main experimental challenges during Run 2 are threefold

- **Background suppression**. The detectors do not have a complete acceptance in rapidity. It is possible that some of the tracks of low multiplicity non-UPC processes are not detected and thus the events are included in the UPC sample. This has been dealt with data driven approaches to describe and subtract the remaining background. The situation will improved be in Run 2
  - There will be new detectors [71, 72] which will increase the capabilities to tag, and thus to veto the background events.
  - CMS and TOTEM will work together, which will allow, for some special beam optics, to tag the elastically scattered proton in p–Pb collisions and thus tag directly the exclusive photoproduction of vector mesons.
- **Triggering**. The vector mesons or low mass di-leptons produced in UPC produce few particles each with low transverse momenta. It is very difficult to trigger on these configurations, because the detectors where optimized to study hard processes and/or very high multiplicities. Nonetheless the experience gained during Run 1 will help improving both the purity and the efficiency of the triggers. Also the new detectors mentioned above will be key in this respect.
- **Statistics.** The low statistics collected in Run 2 is due to a combination of the problems related with triggering on these events and to the small production cross sections for some of these UPC processes. For Run 2, one expect the following improvements:

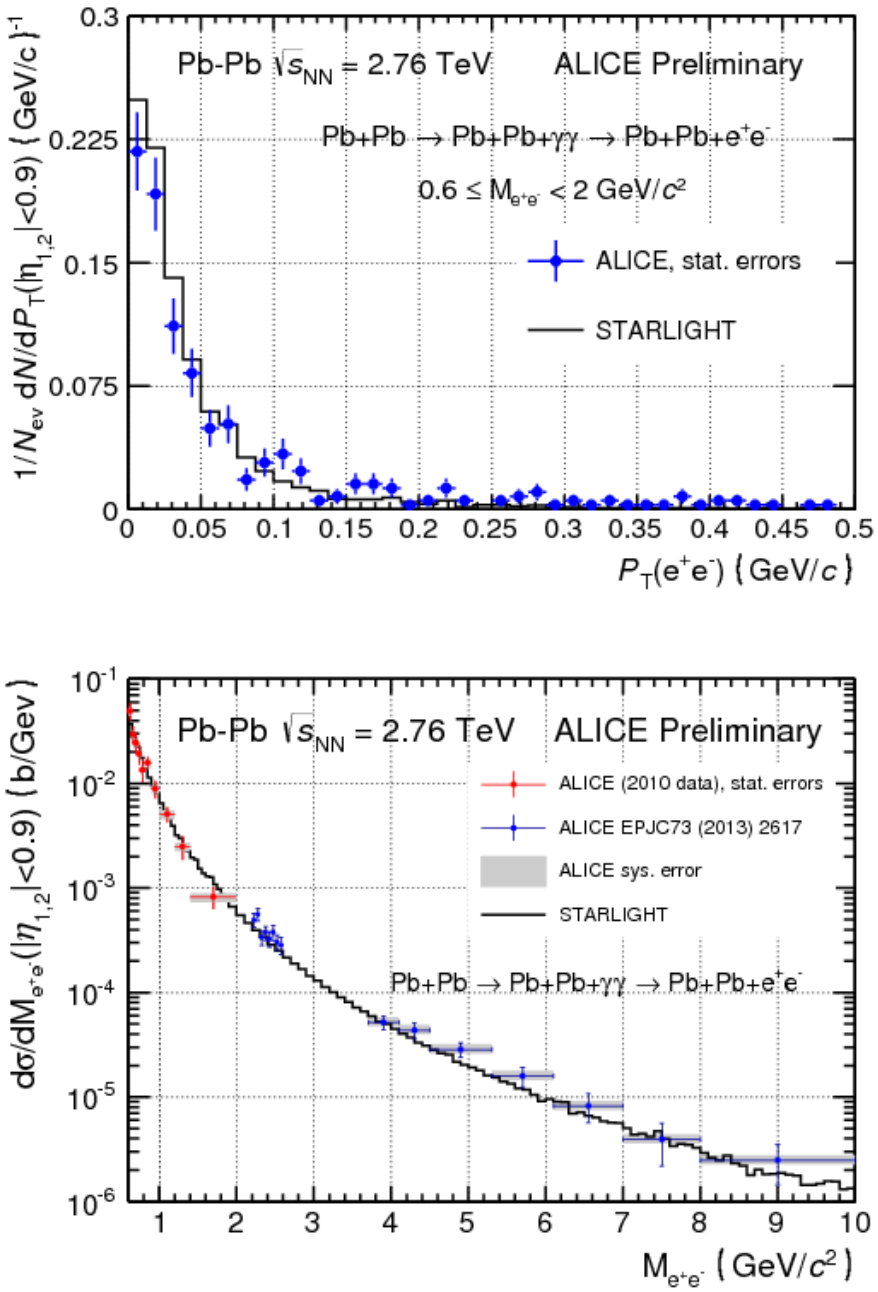

Fig. 7.1: Transverse momentum distribution of exclusive e^+e^- pairs measured by ALICE and compared to STARLIGHT (upper panel). Measured cross section for the exclusive two-photon process measured by ALICE and compared to STARLIGHT [55, 69].

- It is expected that the triggers will be more efficient as mentioned previously;
- It is expected that the luminosity will be a factor 50 larger in Pb–Pb, and
- It is expected that the energy will be larger in Pb–Pb, and the case of p–Pb is under discussion. For the UPC program a larger energy in p–Pb would allow to reach even lower values of Bjorken-x which could be crucial for finding the onset of gluon saturation in exclusive vector meson photoproduction.

7.7 Experimental prospects

Apart from expanding the program on exclusive photonuclear processes, the next LHC runs will open the possibility to study inclusive photonuclear processes. For example, the charm photoproduction through photon-gluon fusion [73]. Most of the attention has been put on small-x physics and in the determination of the nuclear parton distribution. However, it would be possible to study physics signatures sensitive to physics beyond the standard model [8].

During Run 1 the ALICE analyses were performed on a integrated luminosity of about 20 μb^{-1} for the mid-rapidity measurement and about 50 μb^{-1} for the muon arm analysis for 2.76 TeV Pb–Pb collisions. Note that the trigger efficiency for the muon analysis during the 2011 Pb–Pb was low. During Run 2, the plan is to collect about 1 nb^{-1} at 5.5 TeV Pb–Pb collisions. The factor 50 increase in luminosity represent a significant increase in the number of reconstructed events even assuming if the detector conditions will remain the same as for the 2011 Pb–Pb run.

The increase of statistics will allow us to perform differential studies in p_T and y for coherent and incoherent J/ψ and ψ(2S). Fourier transforms of the p_T distribution is thought to be sensitive to the spacial distribution of glue in the nucleus [74, 75]. The t distribution is expected to present a pronounced diffractive peak which can then be used to clearly discriminate between saturation and non-saturation models. Light vector mesons like the ϕ would be more sensitive to gluon saturation compared to the J/ψ. It would be very interesting to have UPC $\phi \to K^+K^-$ and $\omega \to \pi^+\pi^-\pi^0$ measurements at the LHC during Run 2, which might be possible with the ALICE detector.

By tagging the neutron in UPC J/ψ measurements one can disentangle the coherent and incoherent processes [76, 77]. This would also allow us to identify the low and high $W_{\gamma\mathrm{Pb}}$ contributions to the total cross section. This is very interesting as both contributions are sensitive to different values of Bjorken-x.

It would be possible to study exclusive J/ψ in p–Pb collisions during Run 2. The UPC program would benefit by having the largest possible energy. During Run 1, ALICE reported measurements at 5.02 TeV that reached Bjorken-x values of about 10^{-5}, while by colliding at 8.16 TeV we would be able to reach up to 10^{-6}.

Measurement the Υ(1S) would be performed for the first time during Run 2. CMS and ATLAS would be in an ideal position to collect these events which can be used to constraint nuclear shadowing models, although there is a significant large uncertainty on the corresponding γp cross section at present. Given the expected integrated luminosity of 1 nb^{-1} for the 5.1 TeV Pb–Pb run, CMS and ATLAS should be able to measure UPC dijets from γPb interactions over a wide rapidity and p_T range [6, 8]. Together with the UPC quarkonia measurements, these data can then be used to map the gluon distribution over a wide range of Bjorken-x. Apart from the study of four-pion photoproduction, other exotic quarkonium states can also be studied [8]. The UPC program at RHIC have also explored other measurements that can be

studied in the future [7], for example, the study of low transverse momentum vector mesons and interference [78].

The two-photon physics program would also benefit from the experimental conditions expected during Run 2. In the future it would be interested to study whether there is any asymmetries between the positive and negative lepton as this has been proposed as a possible signature for higher order terms [70]. It would be possible to study various $\gamma\gamma$ decay channels, namely, η_c, χ_{c0}(2P) and χ_{c2}(2P) in the decay channels $\pi^+\pi^-\pi^+\pi^-$, $K^+\pi^-K^-\pi^+$ and $K^+K^-K^+K^-$. It would also be possible to perform first studies on light-by-light scattering [79, 80]. Furthermore, the study of bound-free pair production e^+e^- originating from an electron bound to one of the ions [81, 82] will be possible. This study will provide useful information about the LHC accelerator performance for high luminosity heavy-ion collisions at the LHC.

7.8 Experimental Summary

In summary, we have reviewed recent experimental results on ultra-peripheral heavy-ion collisions at the LHC. The coherent J/ψ results provide the first direct experimental evidence for nuclear gluon shadowing. Results from coherent ρ^0 are also very interesting. The quantum Glauber calculation which works for low fixed-target energies does not work for RHIC and LHC energies. The two-photon QED process has also been measured and does not favour higher order terms.

Given the significant increase in energy and luminosity for Run 2 and the increase capabilities LHC detectors it is important to be open to unexpected phenomena. For example the production of open b or c quarks in ultra-peripheral collisions may reveal new insight into the initial state produced in high energy heavy-ion collisions. Photon-induced processes are also sensitive to physics beyond the standard model. To prepare for the unexpected it is important to spend considerable effort on developing clean and efficient UPC triggers since these will be the key for capturing new rare physics. Furthermore, the studies of photon-nuclear processes would allow us to gain insights that will be important as the electron-ion collider facilities are developed.

7.9 Theoretical proposals

Here we will focus on several promising directions of the UPC studies which emerged in the last few years after the review [8] was published.

7.9.1 Tracking fast small color dipoles through strong gluon fields at the LHC

It was discussed in a number of papers that the process of photon - proton scattering with production of a leading meson at $p_t \geq$ few GeV with a rapidity gap

$$\gamma + p \to J/\psi(\rho) + \text{rapidity gap} + Y, \tag{7.16}$$

is dominated by the scattering of the photon in a small transverse size configuration. The process is mediated by the elastic scattering of $q\bar{q}$ pair off a gluon (quark) of the target (with x_g expressed through the value of the rapidity gap interval). In the discussed kinematics one may expect that the elastic scattering is mediated by the perturbative gluon ladder. Hence such process provides a unique method to studying the BFKL dynamics by measuring the cross section at fixed $-t = p_t^2$ as a function of the rapidity gap for fixed t, M_Y^2:

$$\frac{d\sigma^{\gamma+p\to J/\psi+\text{gap + Y}}(t,y)}{dt} \propto \exp\left[2(\alpha_{I\!P}(t)-1)\Delta y\right], \tag{7.17}$$

see [84] and references therein. Such studies should be feasible in the pp scattering at the LHC in the low lumi runs. They may require detection of the leading proton to suppress the contributions of non UPC processes.

The analogous process in AA collisions provides a unique opportunity for studying interaction of small color dipoles propagating through the nuclear media [85]. In particular, it allows to study the onset of the novel perturbative QCD regime of strong absorption for the interaction of small dipoles at the collider energies. Such a study would be clearly complementary to the study of suppression of the forward hadron production discussed in Sec. 7.10. It appear that it would be feasible to probe in the forthcoming AA run interaction of $q\bar{q}$ dipoles of sizes ~ 0.2 fm with nuclear media down to $x = (m_V^2 - t)/s \sim 10^{-5}$. Two possible mechanisms of the deviation of the yield from linear in A regime are multiple interactions of the dipole with the media and the gluon leading twist shadowing. Since the first effect is primarily a function of $W_{\gamma N}$ while the second one is a function of x_g (the rapidity gap) these two effects can be easily separated for example by comparing $x_g \geq 0.01$ and $x_g \sim 10^{-3}$ cross sections. Study of the structure of hadronic system Y would provide an additional information on the mechanism of absorption and in particular dependence of the cross section on the centrality.

7.9.2 Studies of the color fluctuation phenomena

Dominance of large longitudinal distances in the hadron (photon) nucleus interactions at high energies implies that the quark- gluon configurations in which projectile interacts with the nucleus can be considered as frozen during the passage of the nucleus. At the same time different configurations in the projectile, h, are expected to interact with different strength - in particular due to the different area occupied by color in different configurations. This phenomenon is referred to as the color fluctuation phenomenon, for the recent discussion and references see [86]. It is characterized by the distribution over the strength of the interaction $P_h(\sigma)$ which satisfies normalization conditions: $\int P(\sigma)d\sigma = 1, \int \sigma P(\sigma)d\sigma = \sigma_{tot}$. Information about variance of $P(\sigma)$ - $\omega_\sigma = \int (\sigma/\sigma_{tot} - 1)P(\sigma)d\sigma$ can be extracted using Miettinen - Pumplin relation from diffractive data [87]. Color fluctuations lead to a significant broadening of the distribution over the number of the wounded nucleons, ν, as compared to the conventional Glauber model. Evidence for such an effect was reported in ref. [168]. Also, it was demonstrated recently [89] that the pattern of violation of the Glauber picture for centrality dependence of the rate of forward jet production observed in pA collisions at the LHC [90, 168] provides evidence that configurations in the proton containing a parton with large x_p interact with a signicantly smaller than average cross section and have smaller than average size.

UPC in AA collisions provide a complementary tool as compared to the t pA scattering for studies of the color fluctuations. Indeed, one expects a much broader distribution over σ in the case of the photon projectile. Such a pattern already in the vector dominance model approximation as the variance of the distribution over σ is larger in the the case of meson - nucleon interaction [91]. An additional broadening comes from the enhanced contribution of small size configurations which lead to $P_\gamma(\sigma \to 0) \propto 1/\sigma$ [92] as compared to $P_N(\sigma \to 0) \propto \sigma$.

In the UPC it would be possible to large extent to regulate the transverse size of the configuration by selecting final states with leading pions (ρ, ω - like configurations), kaons ($s\bar{s}$ configurations in the photon), and D-mesons (small size, $d \propto 1/m_c$, configurations). Another way to select small size dipoles would be triggering on the leading pion production and studying distribution over the number of wounded nucleons as a function of p_t. Moreover it would be possible to study effects of color fluctuations as a function of the collision energy $W_{\gamma N}$ in a wide interval of W

It is worth emphasizing that in the kinematics where the small dipole nucleon interaction is far from the BDR, but $x = 4p_t^2/s < 10^{-2}$ is small enough, we expect a significant suppression of the forward back to back pion production due to the leading twist gluon shadowing. For example for the pion transverse momenta ~ 1 GeV/c we expect shadowing comparable to that for the amplitude of the coherent J/ψ elastic photoproduction corresponding to the suppression of the yield by a factor of ~ 0.6 (0.5) for $x \sim 10^{-3}(10^{-4})$ and average number of wounded nucleons $\nu = 1.6(2)$ [30]. A much larger suppression is expected for the energy range where BDR is reached.

7.9.3 Multiparton interactions in the direct photon kinematics

In addition to the studies of the leading twist hard processes we mentioned in sec 7.1, UPC can be used to study multiparton interactions (MPI). A promising kinematics is the one dominated by the contribution of the direct photon mechanism. In this mechanism photon splits into $q\bar{q}$ pair with comparable light-cone fractions and which carries practically all momentum of the photon. Next, quark and antiquark experience hard collisions with a parton of the target with sufficiently larger rapidity gap between the quark (antiquark) and the balancing jet. In this kinematics one can suppress the leading twist mechanism by both choosing back-to-back kinematics and optimal distances in rapidity. The cleanest channel is the one where photon splits into charm – anticharm pair since in this case the photon wave function is purely perturbative with the final state being two dijets each containing charm (anticharm) quarks and carrying $x_1, x_2 > 0.2$ fractions of the photon momentum and two balancing jets. It was demonstrated in [93] that in this case cross section is more directly related to the nucleon (nucleus) generalized parton distribution than in the case of double parton interactions in the proton–proton (nucleus) collisions. A significant number of such double parton interactions should be produced in $p-Pb$ and $Pb-Pb$ collisions at the LHC in a 10^6 sec run: $\sim 6 \cdot 10^4$ for $Pb-Pb$, and $\sim 7 \cdot 10^3$ for p–Pb collisions for the same transverse momentum cutoff.

7.10 Propagation of partons through nucleons and nuclei at ultrahigh energies

7.10.1 Introduction

In perturbative QCD interaction of a small color dipole of size d with target grows rapidly with energy. In the leading log approximation the probability for a $q\bar{q}$ dipole to interact is at a given impact parameter is

$$\Gamma_{inel}(d,x,b) = \frac{\pi^2}{3}\alpha_s(Q^2_{eff})d^2\left[xG_T(x,Q^2_{eff},b) + \frac{2}{3}xS_N(x,Q^2_{eff},b)\right], \qquad (7.18)$$

where $Q^2_{eff} = \lambda/d^2, \lambda = 4 \div 10, x = Q^2_{eff}/s$ and G_T, S_T are generalized parton distributions in the target. In the case of a color octet dipole the gluon term is larger by a factor of 9/4 while the second term is missing. One can see from Eq. 7.18 that $\Gamma_{inel}(d,x,b)$ rather rapidly grows with increase of energy (this explains for example the energy dependence of the J/ψ exclusive photoproduction) and starts to approach black disk (unitarity limit) regime (BDR) of $\Gamma_{inel}(d,x,b) = 1$ for small b at sufficiently small x.

It can be argued that the pattern of interaction of a quark (gluon) of virtuality μ^2 through the target is similar to that of the $q\bar{q}$ (gg) dipole with $d^2 \propto 1/\mu^2$. Hence measurements in the very forward kinematics at the LHC allow to probe theBDR down to x_p, $x_A \sim 10^{-6}$ for virtualities of the order of few GeV^2.

In the BDR partons with virtuality $< \mu^2$ should interact with probability of the order one, acquire transverse momenta on the scale μ and also split into partons with virtualities $\sim \mu^2$.

The latter effect is manifested as effective *fractional* energy losses which explicitly breaks the QCD factorization for hard processes [94, 95].

As a result, one expects that for collisions at small impact parameters in pp and especially pA collisions the coherence of quarks in the proton should be completely destroyed. As a result in this limit all leading partons should fragment independently (if $z \geq 0.1 \div 0.2$(z is the fraction of the projectile momentum carried by produced hadron) at the LHC) leading to (a) a strong suppression of the leading hadron spectrum [96, 97] (see e.g. fig.1 from [97]):

$$d\sigma(p+T \to h+X)/dx_F \propto (1-x_F)^{n(p_t)}, n_N(p_t) \sim 5 \div 6, \tag{7.19}$$

with $n_h(p_t)$ decreasing with increase of p_t, (b) $\langle p_t \rangle$ broadening of the spectrum: $p_t \sim \mu$ [97,98], and dominance of the leading meson production as compared to that of baryons: $d\sigma(p+T \to \pi+X)/dz \gg d\sigma(p+T \to N+X)/dz$ for $z \geq 0.5$. Since for peripheral collisions distribution of nucleons in z is known to be practically flat for $z \leq 0.8$ and average $p_t \sim$ .5 GeV/c we expect a gross change of the spectrum in the central pA collisions. These predictions are based on very

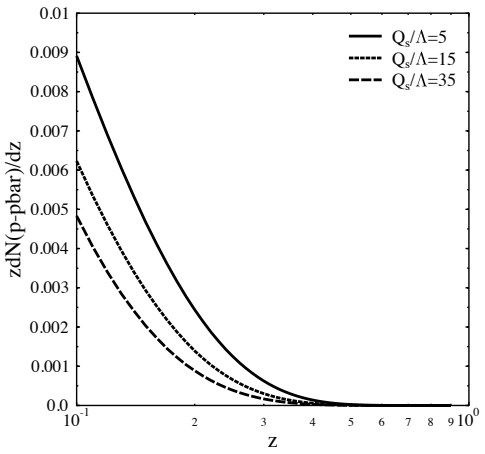

Fig. 7.1: Distribution of protons over z in central pA collisions for different p_t ranges of dominance of black disk dynamics. The neutron yields for large z are a factor of two smaller.

generic features of the interaction of leading quarks in the black disk regime. Hence the study of the leading hadron production would provide a critical test of the expectation that the BDR is reached at the LHC in the interactions with nuclei and nucleons for $p_t \leq$ few GeV/c.

Note here that the current calculations neglect effective fractional energy losses which further amplify the discussed effects. Measurement of these losses at the LHC would require observations of hard interactions with hard scale $\leq$5 GeV. Observation of the dijet production is hardly possible in this case. One would have to focus on the study of the leading hadron production. At RHIC a strong suppression of the pion spectrum was observed for $z \geq 0.3$ [99], and the observed regularities of the process (in particular the forward – central correlation) [100] are consistent with the effective energy loss scenario [95]. It would be desirable to study at the LHC centrality dependence of the leading pion (nucleon) spectrum in similar kinematics since for $x_F \leq 0.2$ effective fractional energy losses lead to a small reduction of the cross section which maybe compensated by p_t broadening.

In the case of large z measurements, of say the leading π^0, it would be desirable to study

also the centrality dependence of the production of the recoil hadrons in the $x_A \geq 0.01$ range where nuclear PDFs are close to the nucleon ones.

A warning: in the measurements one has to put a requirement that there is some activity at negative rapidities (towards the nucleus fragmentation region) - otherwise the processes of photon-proton interaction would give the dominant contribution.

Similar questions can be asked for pp collisions. One can study how the differential multiplicity of leading baryons depends on the centrality - for example one can investigate whether it is strongly suppressed for the high multiplicity events - say for $N/\langle N\rangle \geq 3$ where collisions are dominated by scattering at small impact parameters b$\leq$ 0.5 fm [101] . One can also investigate modification of the baryon spectrum at $x_F \geq 0.3$ for a moderate increase of the centrality using as a trigger p_t of a hadron / jet at central (or negative rapidities) – for sufficiently large p_t ($\geq 10 GeV/c$) as this selects significantly smaller b than average (0.7 fm vs 1.2 fm) [102]. Overall one expects that for such a trigger the neutron distribution would be softer but not change significantly with p_t of the trigger (similar to pattern observed for the underlying events for central rapidities). Modeling of the dependence of the nucleon spectrum on centrality was performed in [103] where it was suggested that combining several centrality triggers (including veto on the neutron production) may allow to probe high gluon densities in pp collisions at the LHC which are comparable to those present in the central pA collisions.

Use of two ZDC's in pp scattering would allow to study correlation between production of hadrons at the huge rapidity interval up to $\Delta y \sim 20$. If a forward neutron is detected it is likely to enhance the selection of large impact parameters and hence enhance the probability to have a neutron in the opposite ZDC. Calculations of [103] indicate that there should be also a correlation (though rather mild) between absences of signal in the ZDCs. However the model was pretty crude and it is easy to imagine models with a stronger correlation. An important issue here is how much the correlation is diluted by the acceptance of the ZDCs. Current versions of PYTHIA allow to look for such effects.

Acknowledgements

M.S.'s research was supported by the US Department of Energy Office of Science, Office of Nuclear Physics under Award No. DE-FG02-93ER40771.

References

[1] E. Fermi, Z. Phys. **29** (1924) 315.

[2] Enrico Fermi. On the theory of collisions between atoms and electrically charged particles. *Nuovo Cim.*, 2:143–158, 1925.

[3] C.F. von Weizsacker. Radiation emitted in collisions of very fast electrons. *Z.Phys.*, 88:612–625, 1934.

[4] E.J. Williams. Nature of the high-energy particles of penetrating radiation and status of ionization and radiation formulae. *Phys.Rev.*, 45:729–730, 1934.

[5] C. A. Bertulani, AIP Conf. Proc. **1645** (2015) 121 [arXiv:1409.6671 [nucl-th]].

[6] M. Strikman, R. Vogt and S. N. White, Phys. Rev. Lett. **96** (2006) 082001 [hep-ph/0508296].

[7] S. R. Klein, arXiv:1502.06662 [nucl-ex].

[8] A. J. Baltz, G. Baur, D. d'Enterria, L. Frankfurt, F. Gelis, V. Guzey, K. Hencken and Y. Kharlov *et al.*, Phys. Rept. **458** (2008) 1 [arXiv:0706.3356 [nucl-ex]].

[9] Carlos A. Bertulani, Spencer R. Klein, and Joakim Nystrand. Physics of ultra-peripheral nuclear collisions. *Ann.Rev.Nucl.Part.Sci.*, 55:271–310, 2005.

[10] Gerhard Baur, Kai Hencken, Dirk Trautmann, Serguei Sadovsky, and Yuri Kharlov. Coherent gamma gamma and gamma-A interactions in very peripheral collisions at relativistic ion colliders. *Phys.Rept.*, 364:359–450, 2002.

[11] A. Adeluyi and C. A. Bertulani, Phys. Rev. C **85** (2012) 044904 [arXiv:1201.0146 [nucl-th]].

[12] A. Adeluyi and T. Nguyen, Phys. Rev. C **87** (2013) 2, 027901 [arXiv:1302.4288 [nucl-th]].

[13] A. Cisek, W. Schafer and A. Szczurek, Phys. Rev. C **86** (2012) 014905 [arXiv:1204.5381 [hep-ph]].

[14] S. Klein and J. Nystrand, Phys. Rev. C **60** (1999) 014903 [hep-ph/9902259].

[15] A. J. Baltz, S. R. Klein and J. Nystrand, Phys. Rev. Lett. **89** (2002) 012301 [nucl-th/0205031].

[16] S. R. Klein and J. Nystrand, Phys. Rev. Lett. **92** (2004) 142003 [hep-ph/0311164].

[17] T. Lappi and H. Mantysaari, Phys. Rev. C **83** (2011) 065202 [arXiv:1011.1988 [hep-ph]].

[18] T. Lappi and H. Mantysaari, Phys. Rev. C **87** (2013) 3, 032201 [arXiv:1301.4095 [hep-ph]].

[19] V. P. Goncalves and M. V. T. Machado, Phys. Rev. C **84** (2011) 011902 [arXiv:1106.3036 [hep-ph]].

[20] M. B. G. Ducati, M. T. Griep and M. V. T. Machado, Phys. Rev. C **88** (2013) 014910 [arXiv:1305.2407 [hep-ph]].

[21] V. Rebyakova, M. Strikman and M. Zhalov, Phys. Lett. B **710** (2012) 647 [arXiv:1109.0737 [hep-ph]].

[22] Y. P. Ivanov, B. Z. Kopeliovich and I. Schmidt, arXiv:0706.1532 [hep-ph].

[23] M. G. Ryskin, Z. Phys. C **57** (1993) 89.

[24] S. J. Brodsky, L. Frankfurt, J. F. Gunion, A. H. Mueller and M. Strikman, Phys. Rev. D **50** (1994) 3134 [hep-ph/9402283].

[25] V. Guzey and M. Zhalov, JHEP **1310** (2013) 207 [arXiv:1307.4526 [hep-ph]].

[26] A. D. Martin, W. J. Stirling, R. S. Thorne and G. Watt, Eur. Phys. J. C **63** (2009) 189 [arXiv:0901.0002 [hep-ph]].

[27] K. J. Eskola, H. Paukkunen and C. A. Salgado, JHEP **0807** (2008) 102 [arXiv:0802.0139 [hep-ph]].

[28] K. J. Eskola, H. Paukkunen and C. A. Salgado, JHEP **0904** (2009) 065 [arXiv:0902.4154 [hep-ph]].

[29] M. Hirai, S. Kumano and T.-H. Nagai, Phys. Rev. C **70** (2004) 044905 [hep-ph/0404093].

[30] L. Frankfurt, V. Guzey and M. Strikman, Phys. Rept. **512** (2012) 255 [arXiv:1106.2091 [hep-ph]].

[31] A. D. Martin, C. Nockles, M. G. Ryskin and T. Teubner, Phys. Lett. B **662** (2008) 252 [arXiv:0709.4406 [hep-ph]].

[32] A. G. Shuvaev, K. J. Golec-Biernat, A. D. Martin and M. G. Ryskin, Phys. Rev. D **60** (1999) 014015 [hep-ph/9902410].

[33] J. Bartels, K. J. Golec-Biernat and K. Peters, Acta Phys. Polon. B **34** (2003) 3051 [hep-ph/0301192].

[34] H. Kowalski and D. Teaney, Phys. Rev. D **68** (2003) 114005 [hep-ph/0304189].

[35] J. Nemchik, N. N. Nikolaev and B. G. Zakharov, Phys. Lett. B **341** (1994) 228 [hep-

ph/9405355].
[36] J. Nemchik, N. N. Nikolaev, E. Predazzi and B. G. Zakharov, Z. Phys. C **75** (1997) 71 [hep-ph/9605231].
[37] E. Iancu, K. Itakura and S. Munier, Phys. Lett. B **590** (2004) 199 [hep-ph/0310338].
[38] I. Balitsky, Nucl. Phys. B **463** (1996) 99 [hep-ph/9509348].
[39] Y. V. Kovchegov, Phys. Rev. D **60** (1999) 034008 [hep-ph/9901281].
[40] Y. V. Kovchegov, Phys. Rev. D **61** (2000) 074018 [hep-ph/9905214].
[41] H. Kowalski, L. Motyka and G. Watt, Phys. Rev. D **74** (2006) 074016 [hep-ph/0606272].
[42] S. Chekanov *et al.* [ZEUS Collaboration], Eur. Phys. J. C **24** (2002) 345 [hep-ex/0201043].
[43] A. Aktas *et al.* [H1 Collaboration], Eur. Phys. J. C **46** (2006) 585 [hep-ex/0510016].
[44] C. Alexa *et al.* [H1 Collaboration], Eur. Phys. J. C **73** (2013) 6, 2466 [arXiv:1304.5162 [hep-ex]].
[45] T. Aaltonen *et al.* [CDF Collaboration], Phys. Rev. Lett. **102** (2009) 242001 [arXiv:0902.1271 [hep-ex]].
[46] B. B. Abelev *et al.* [ALICE Collaboration], Phys. Rev. Lett. **113** (2014) 23, 232504 [arXiv:1406.7819 [nucl-ex]].
[47] R. Aaij *et al.* [LHCb Collaboration], J. Phys. G **41** (2014) 055002 [arXiv:1401.3288 [hep-ex]].
[48] L. V. Gribov, E. M. Levin and M. G. Ryskin, Phys. Rept. **100** (1983) 1.
[49] A. H. Mueller, Nucl. Phys. B **335** (1990) 115.
[50] J. L. Abelleira Fernandez *et al.* [LHeC Study Group Collaboration], arXiv:1211.5102 [hep-ex].
[51] A. Accardi *et al.*, arXiv:1212.1701 [nucl-ex].
[52] E. C. Aschenauer *et al.*, arXiv:1409.1633 [physics.acc-ph].
[53] S. Afanasiev *et al.* [PHENIX Collaboration], Phys. Lett. B **679** (2009) 321 [arXiv:0903.2041 [nucl-ex]].
[54] B. Abelev *et al.* [ALICE Collaboration], Phys. Lett. B **718** (2013) 1273 [arXiv:1209.3715 [nucl-ex]].
[55] E. Abbas et al. Charmonium and e^+e^- pair photoproduction at mid-rapidity in ultra-peripheral Pb-Pb collisions at $\sqrt{s_{NN}}$ = 2.76 TeV. *Eur.Phys.J.*, C73:2617, 2013.
[56] CMS Collaboration [CMS Collaboration], CMS-PAS-HIN-12-009.
[57] G. S. d. Santos and M. V. T. Machado, Phys. Rev. C **89** (2014) 2, 025201 [arXiv:1312.0770 [hep-ph]].
[58] V. P. Goncalves and M. M. Machado, Eur. Phys. J. A **50** (2014) 72 [arXiv:1309.0664 [hep-ph]].
[59] V. Guzey and M. Zhalov, JHEP **1402** (2014) 046 [arXiv:1307.6689 [hep-ph]].
[60] M. B. Gay Ducati, M. T. Griep and M. V. T. Machado, Phys. Rev. D **88** (2013) 017504 [arXiv:1305.4611 [hep-ph]].
[61] V. Guzey, E. Kryshen, M. Strikman and M. Zhalov, Phys. Lett. B **726** (2013) 290 [arXiv:1305.1724 [hep-ph]].
[62] R. Vogt, J. Phys. Conf. Ser. **509** (2014) 012007.
[63] B. I. Abelev *et al.* [STAR Collaboration], Phys. Rev. C **77** (2008) 034910 [arXiv:0712.3320 [nucl-ex]].
[64] L. Frankfurt, M. Strikman and M. Zhalov, Phys. Lett. B **537** (2002) 51 [hep-ph/0204175].

[65] J. Beringer *et al.* [Particle Data Group Collaboration], Phys. Rev. D **86** (2012) 010001.
[66] B. I. Abelev *et al.* [STAR Collaboration], Phys. Rev. C **81** (2010) 044901 [arXiv:0912.0604 [nucl-ex]].
[67] J. D. Tapia Takaki, J. Phys. Conf. Ser. **509** (2014) 012107.
[68] M. KÅĆusek-Gawenda and A. Szczurek, Phys. Rev. C **89** (2014) 2, 024912 [arXiv:1309.2463 [nucl-th]].
[69] J. Nystrand [ALICE Collaboration], Nucl. Phys. A **931** (2014) 298 [arXiv:1408.0811 [nucl-ex]].
[70] S. J. Brodsky and J. Gillespie, Phys. Rev. **173** (1968) 1011.
[71] M. Albrow *et al.*, JINST **9** (2014) 10, C10032.
[72] G. Herrera-Corral [ALICE Collaboration], AIP Conf. Proc. **1350** (2011) 176.
[73] S. R. Klein, J. Nystrand and R. Vogt, Phys. Rev. C **66** (2002) 044906 [hep-ph/0206220].
[74] N. Armesto and A. H. Rezaeian, Phys. Rev. D **90** (2014) 5, 054003 [arXiv:1402.4831 [hep-ph]].
[75] T. Toll and T. Ullrich, Phys. Rev. C **87** (2013) 2, 024913 [arXiv:1211.3048 [hep-ph]].
[76] M. Strikman, M. Tverskoy and M. Zhalov, Phys. Lett. B **626** (2005) 72 [hep-ph/0505023].
[77] V. Guzey, M. Strikman and M. Zhalov, Eur. Phys. J. C **74** (2014) 7, 2942 [arXiv:1312.6486 [hep-ph]].
[78] B. I. Abelev *et al.* [STAR Collaboration], Phys. Rev. Lett. **102** (2009) 112301 [arXiv:0812.1063 [nucl-ex]].
[79] D. d'Enterria and G. G. da Silveira, Phys. Rev. Lett. **111** (2013) 080405 [arXiv:1305.7142 [hep-ph]].
[80] S. Fichet, G. von Gersdorff, B. Lenzi, C. Royon and M. Saimpert, JHEP **1502** (2015) 165 [arXiv:1411.6629 [hep-ph]].
[81] S. R. Klein, Nucl. Instrum. Meth. A **459** (2001) 51 [physics/0005032 [physics.acc-ph]].
[82] R. Bruce, J. M. Jowett, S. Gilardoni, A. Drees, W. Fischer, S. Tepikian and S. R. Klein, Phys. Rev. Lett. **99** (2007) 144801 [arXiv:0706.2292 [physics.acc-ph]].
[83] Anthony J. Baltz, Yuri Gorbunov, Spencer R. Klein, and Joakim Nystrand. Two-Photon Interactions with Nuclear Breakup in Relativistic Heavy Ion Collisions. *Phys.Rev.*, C80:044902, 2009.
[84] B. Blok, L. Frankfurt and M. Strikman, Eur. Phys. J. C **67** (2010) 99 [arXiv:1001.2469 [hep-ph]].
[85] L. Frankfurt, M. Strikman and M. Zhalov, Phys. Rev. Lett. **102** (2009) 232001 [arXiv:0811.0368 [hep-ph]].
[86] M. Alvioli, L. Frankfurt, V. Guzey and M. Strikman, Phys. Rev. C **90** (2014) 034914 [arXiv:1402.2868 [hep-ph]].
[87] H. I. Miettinen and J. Pumplin, Phys. Rev. D **18** (1978) 1696.
[88] Conference note ATLASCONF–096 (2013) https://cds.cern.ch/record/1599773
[89] M. Alvioli, B. Cole, L. Frankfurt and M. Strikman, arXiv:1409.7381 [hep-ph].
[90] S. Chatrchyan *et al.* [CMS Collaboration], Eur. Phys. J. C **74** (2014) 2951 [arXiv:1401.4433 [nucl-ex]].
[91] B. Blaettel, G. Baym, L. L. Frankfurt and M. Strikman, Phys. Rev. Lett. **70** (1993) 896.
[92] L. Frankfurt, V. Guzey and M. Strikman, Phys. Rev. D **58** (1998) 094039 [hep-ph/9712339].

[93] B. Blok and M. Strikman, arXiv:1410.5064 [hep-ph].

[94] L. Frankfurt, V. Guzey, M. McDermott and M. Strikman, Phys. Rev. Lett. **87**, 192301 (2001) [hep-ph/0104154].

[95] L. Frankfurt and M. Strikman, Phys. Lett. B **645** (2007) 412 [nucl-th/0603049].

[96] A. Berera, M. Strikman, W. S. Toothacker, W. D. Walker and J. J. Whitmore, Phys. Lett. B **403** (1997) 1 [hep-ph/9604299].

[97] A. Dumitru, L. Gerland and M. Strikman, Phys. Rev. Lett. **90**, 092301 (2003) [Erratum-ibid. **91**, 259901 (2003)] [hep-ph/0211324].

[98] F. Gelis, A. M. Stasto and R. Venugopalan, Eur. Phys. J. C **48** (2006) 489 [hep-ph/0605087].

[99] I. Arsene *et al.* [BRAHMS Collaboration], Phys. Rev. Lett. **93** (2004) 242303 [nucl-ex/0403005].

[100] J. Adams *et al.* [STAR Collaboration], Phys. Rev. Lett. **97** (2006) 152302 [nucl-ex/0602011].

[101] M. Y. Azarkin, I. M. Dremin and M. Strikman, Phys. Lett. B **735** (2014) 234, arXiv:1401.1973 [hep-ph].

[102] L. Frankfurt, M. Strikman and C. Weiss, Phys. Rev. D **83** (2011) 054012 [arXiv:1009.2559 [hep-ph]].

[103] H. J. Drescher and M. Strikman, Phys. Rev. Lett. **100**, 152002 (2008).

Chapter 8

BFKL and saturation

Conveners and Editors: J. Bartels, H. Jung, C. Marquet
Internal Reviewers: A. Sabio Vera, S. Wallon

8.1 Introduction

In this section we discuss jets in the forward region, as well as the production of Drell-Yan lepton pairs close to the beam axis (large η values). Such measurements will allow to analyze QCD beyond the collinear factorization, in particular BFKL dynamics [1–4], multiparton interactions, and saturation. In more detail:

- the cross section for di-jets with a large rapidity separation (forward-backward jets, Fig. 8.1 a, left) includes multi-parton (gluon) radiation in the rapidity interval between the jets and thus is sensitive to the BFKL Pomeron [5]: "Mueller-Navelet"-jets. For large rapidity separations and not too high transverse momenta of the jets multiparton interactions can play a significant role (Fig 8.1 a, right).
- the cross section of inclusive forward jets is sensitive to very small and very large values of the parton momentum fraction x and thus can be used to constrain the parton densities at very small or very large x (Fig 8.1 b, left). In particular, the measurement of multijets at very large rapidities allows to address unintegrated gluons densities, saturation, and contributions from multiparton interactions (MPI, see Fig 8.1 b, right).
- the observation of Drell-Yan lepton pairs close to the beam directions at large rapidities represents the outstanding possibility to study small-x dynamics at the LHC. In particular, inclusive forward DY production can be sensitive to saturation effects (Fig. 8.2 a) The study of Drell-Yan pairs near the forward direction, together with a jet in the backward direction is sensitive to multiparton radiation (higher order radiation, similar to the "Mueller Navelet" jets): see Fig. 8.2 b. In an alternative measurement, central DY production in association with jets in the forward or backward region, small-x resummation can be probed in a different region of phase space (Fig. 8.1 c).

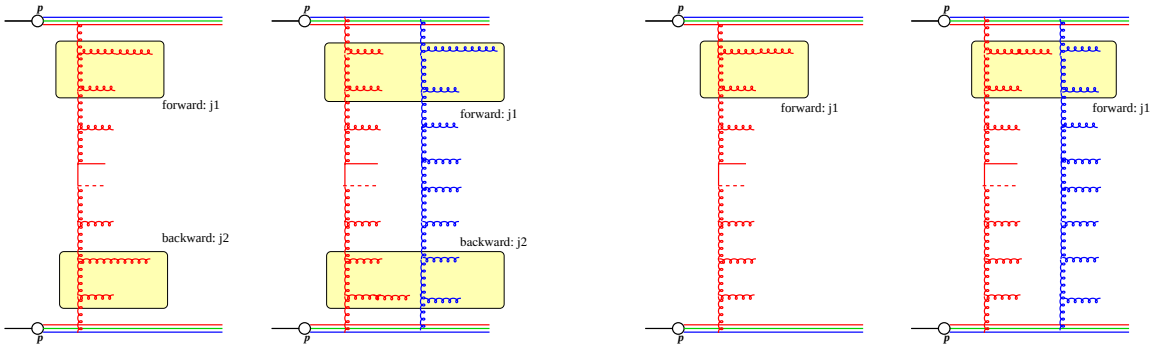

Fig. 8.1: Schematic view of (a) forward-backward jets and (b) inclusive forward jets

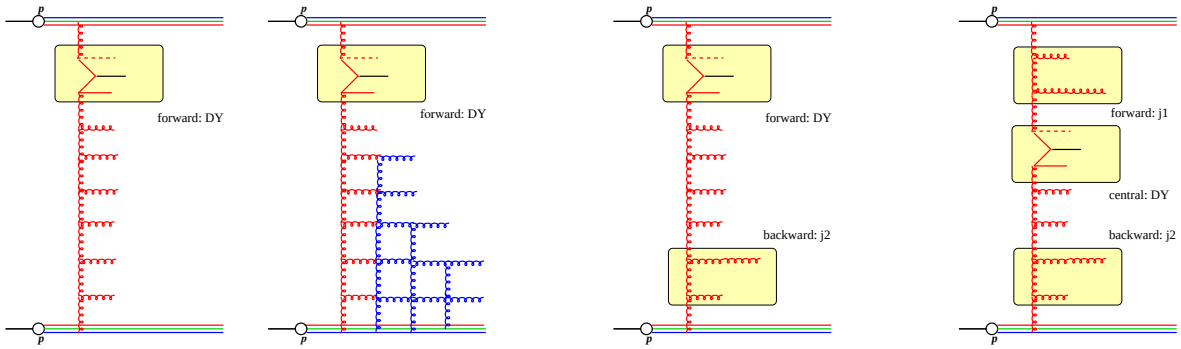

(a) (b) (c)

Fig. 8.2: Schematic view of (a) forward Drell-Yan production, (b) forward Drell-Yan + jet, (c) central DY + forward - backward jets

While the basic idea to investigate forward-backward jets (Fig 8.1 b) as a probe for BFKL dynamics is old (the first proposal was made by Mueller and Navelet [5] in 1986), the actual measurement and the interpretation is still very challenging, and there are questions and measurements which have not yet been addressed. Measurements performed until now required a lower p_t threshold for the jets and have been found to be compatible (within uncertainties) with predictions coming from simulations based on collinear parton distribution functions supplemented by parton showers and multi-parton interactions. In contrast, differential measurements requiring a p_t window for the forward-backward jets should be better suited for discriminating between predictions based on collinear factorisation and BFKL-based predictions. As to 'clean' BFKL signals, most attention has been given to azimuthal decorrelations. Different machine energies at the LHC provide the unique opportunity of looking also for the BFKL intercept: keeping the momentum fractions of the two parton densities fixed, a change of the machine energy directly translates into a variation of the size of the rapidity gap between the forward-backward jets. A new aspect is also the potential importance of multiparton contributions: first quantitative estimates indicates that, for highest LHC energies and moderate p_t of the jets, multiparton contributions can become sizable and hence should be taken into account when searching for BFKL signals.

In addition to the search for such 'clean' BFKL signals which result from the infinite sum of gluon emissions between the forward and backward jets, it will be useful to test BFKL predictions also in another way. With the state-of-the art calculations for multiple jet production allowing to access matrix elements with high parton multiplicity matched to parton showers, one is able to calculate to sufficiently high order in perturbation theory jet cross sections with full matrix-elements which include a large part of what is expected from a BFKL calculation in the high energy limit. However, a fixed order calculation cannot predict a stabilisation of the cross section in the high energy limit, which comes eventually only from a resummation to all orders. The search for BFKL thus is to identify regions of phase space, where a fixed order calculation (even at high orders) will be not sufficient and resummation effects become important. In this case BFKL provides an effective method to calculate the resummation. In this context it is extremely helpful to have a dedicated, purely BFKL-based Monte Carlo event generator (BFKLex): this allows to investigate final states with fixed numbers of jets (partons) with large rapidity separations.

Jet production at large rapidities probes the region of small and large x momentum fractions of the partons involved in the hard scattering. While jet production at central rapidities is rather well described by calculations based on collinear factorization and next-to-leading order

(NLO) partonic calculations, jet production at forward rapidities is well-suited to study unintegrated parton densities and is also sensitive to multiple parton radiation beyond NLO, which show up in systematic kinematic shifts (see for example [6]). Such effects come from multiple hard parton radiation, which becomes significant, when x is small, and eventually are sensitive to small x resummation treated in BFKL. The large-x region attracts interest since it allows to look for the "intrinsic" heavy quark content of the proton.

Saturation lies at the interface between hard scattering and nonperturbative strong interaction physics, and it is of particular importance for understanding the initial state in heavy ion collisions. In pp scattering at the LHC, a particularly promising observable is the Drell-Yan production of lepton pairs of low mass in the forward direction. This kinematic region probes the gluon density at very small x and thus could be sensitive to saturation effects. Several studies compare predictions based upon saturation models with the collinear approach and find significant differences.

Unfortunately, in pA collisions which are very interesting for saturation studies due to the higher gluon density, the measurement of Drell-Yan may not be feasible due to luminosity constraints. Here the measurement of real photons might provide a valuable alternative probe, which is more abundantly produced. However, such a measurement would require upgraded detectors at forward rapidity. In the following we discuss these questions in more detail. In the following we discuss these questions in more detail.

8.2 Forward backward jet production in $p\bar{p}$ and pp: the BFKL program

We discuss first new theoretical developments in forward-backward jet production, followed by a survey of measurements from Tevatron and LHC run1.

8.2.1 Theoretical remarks

We start with a brief theoretical introduction and a description of observables where the BFKL formalism is expected to apply. The BFKL approach identifies and calculates, for scattering amplitudes in the Regge limit, at each order of perturbation theory those contributions which have powers of $\ln s$ and thus grow with the center-of-mass energy. These terms are associated to final states extending over large rapidity intervals. Compared to other high energy calculations (e.g. hard scattering processes within the collinear factorization), the BFKL formalism exhibits new degrees of freedom: reggeized gluons and quarks. These reggeons are universal in the sense that they drive a large variety of cross sections with very different initial and final state configurations, and they are present in lepton-lepton, lepton-hadron and hadron-hadron induced scattering processes. Most prominent is the Pomeron which, in QCD, appears as a bound state of two reggeized gluons. This reggeization picture [7] in QCD has now been tested at leading (LL) [1–4, 8, 9] and next-to-leading (NLL) [10, 11] accuracy, and it has been cross-checked by many different methods, including sophisticated techniques in string theory [12]. It is important to mention that reggeization and the existence of a Pomeron state also holds for electroweak [13], and gravitational interactions at high energies [14]. In particular, they have become of central interest in AdS/CFT duality and in string theory (integrability).

All this provides a very strong motivation to search for experimental evidence of the QCD Pomeron in high energy scattering processes. The LHC, because of the large center-of-mass energy, offers the unique possibility of testing this part of strong interaction dynamics.

8.2.2 Signals based upon inclusive all-order summation

From a phenomenological point of view, it is a pressing matter to find windows of applicability of the BFKL formalism. In the traditional approach, one searches for BFKL effects in a scattering process initiated by two hard partons with equal momentum scales: in pp scattering, this idea is realized in the Mueller-Navelet jets, and the momentum scales are related to the transverse momenta of the forward and backward jets (in ep scattering the analogous final state are the forward jet configuration). Whether the cross section for this process is described by BFKL or by the standard DGLAP [15–18] evolution depends upon the size of the rapidity separation of the two jets and upon the ratio of the momentum scales of the two jets: BFKL applies to configurations with large rapidity separations and (almost) equal momentum scales: for configurations with very different momenta it is DGLAP which provides the correct description. In a realistic scenario the situation may be not so clear: a characteristic example is the description of the growth of the proton structure functions at low values of Bjorken x where the two momentum scales are given by the photon virtuality and by the (lower) momentum scale of the proton. Indeed it is possible to get a good fit of the most recent combined HERA data for F_2 and F_L with a NLL BFKL calculation, see Fig. 8.1, taken from [19, 20]. However, it is equally possible

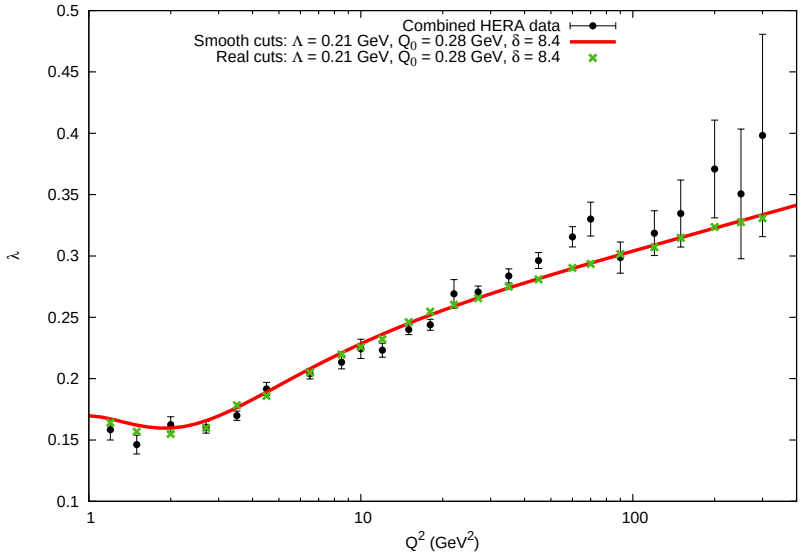

Fig. 8.1: BFKL calculation for $\lambda(Q^2)$ in the parametrization of the structure $F_2(x,Q^2) = c(Q^2)x^{-\lambda(Q^2)}$ at NLL with collinear improvements and a model for the proton impact factor of the form $\simeq (p^2/Q_0^2)^{\delta} e^{-p^2/Q_0^2}$, for values of $x < 0.01$. Λ enters in a regularization of the infrared behavior of the running coupling with the form $\alpha_s(\mu^2) = (4\pi/\beta_0)\left[1/\ln(\mu^2/\Lambda^2) + 125(1+4\mu^2/\Lambda^2)/((1-\mu^2/\Lambda^2)(4+\mu^2/\Lambda^2)^4)\right]$.

to fit these data with other approaches. Moreover, there is quite some model dependence in the BFKL calculation, which includes three free parameters for the structure of the coupling of the gluon ladder to the hadron, a model with a frozen behavior of the coupling in the infrared and the use of a collinear resummation together with a particular renormalization scheme which allows us to reach very low values of Q^2 in the fit.

All this indicates that particular attention has to be given to the ratio of the scales. As it has already been said, a clean BFKL test requires similar transverse momenta of both jets. However,

such a configuration becomes unstable [21, 22], in particular when a comparison at fixed order is performed. Thus, it would be very important phenomenologically to have also experimental data in a slightly asymmetric configuration with different transverse momenta of the tagged jets. This may allow to observe the transition from BFKL-like dynamics to collinear descriptions. This is not an easy task since the cross-section is strongly peaked near $|k_{\perp 1}| \sim |k_{\perp 2}|$. However, this could be offset by the larger cross-section at $\sqrt{s} = 13$ TeV compared to $\sqrt{s} = 7$ TeV. In addition, lowering the minimal value of the transverse momenta of the tagged jets would be a very motivating experimental challenge since it would further increase the cross-section and reduce the statistical uncertainties. A low transverse momentum of the jets also increases the contribution of multiparton corrections (see below). In general it may be safer to define 'windows' of transverse momenta rather than 'lower limits'. In the latter case, asymmetric configurations are included which may spoil BFKL signals.

8.2.2.1 Energy dependence: the BFKL intercept

Let us now look in more detail into possible measurements at the LHC. A natural test of BFKL dynamics is the growth of the cross section with increasing rapidity separation of the two jets. There is, however, a problem which is related to the fact that the BFKL-like growth due to the emission of gluons between the jets is contaminated by the x dependence of the parton densities of the two protons. The further the two jets are separated in rapidity, the deeper we are driven into the $x \to 1$ limit of the collinear parton distribution functions. This region is characterized by a drop of the cross section due to energy momentum conservation. This hides the BFKL effect inside the growth of the cross section, as it can be seen in Fig. 8.2 (obtained in Ref. [23]). Here the rapidity dependence of the cross section for Mueller-Navelet jets is investigated with the same values of the transverse momenta of the tagged jets. The calculations are performed for an LHC run at $\sqrt{s} = 14$ TeV, and we can see how the cross section decreases as Y increases. As

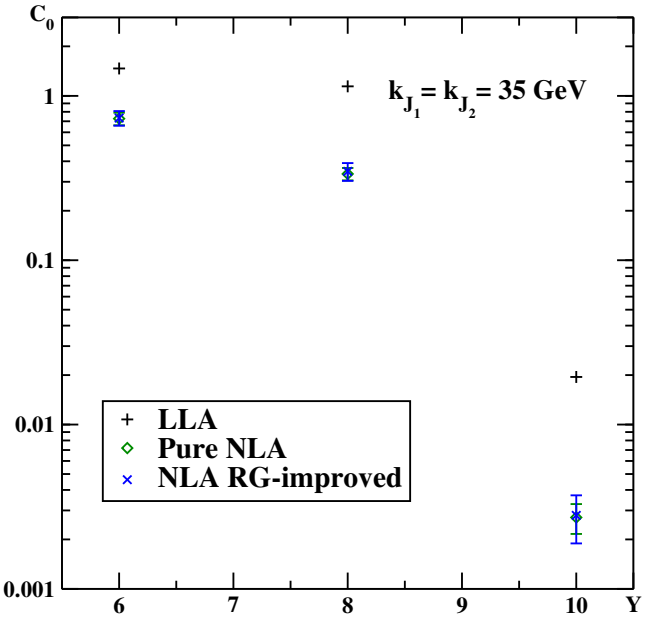

Fig. 8.2: Y dependence of Mueller-Navelet cross section C_0 for $|\vec{k}_{J_1}| = |\vec{k}_{J_2}| = 35$ GeV at $\sqrt{s} = 14$ TeV.

a possible way out of this difficulty, one should make use of different machine energies offered by the LHC and measure the cross-section at different center-of-mass energies s. By keeping the longitudinal momentum fractions of the jets, which are given by $x_{J,i} = \frac{k_{\perp i}}{\sqrt{s}} e^{y_{J,i}}$, fixed, the change

in the overall energy s directly translates into a change of the difference of the rapidities $y_{J,1}$ and $y_{J,2}$ of the tagged jets. In this way, at least in the LO description where the jet vertex imposes $x_i = x_{J,i}$, one should get access to the rapidity dependence of the partonic subprocess itself. In NLO the jet vertex contains an integral over x_i, and thus makes the theoretical prediction less straightforward.

8.2.2.2 Angular decorrelation

A very important signal for BFKL dynamics is contained in the angular dependence of the forward and backward jets, in particular in their decorrelation at large separation in rapidity [24, 25]. In practice, one can study the coefficients

$$\langle \cos(n\varphi) \rangle \equiv \langle \cos\left(n(\phi_{J,1} - \phi_{J,2} - \pi)\right) \rangle \,. \tag{8.1}$$

These coefficients are related to the azimuthal distribution of the jets $\frac{1}{\sigma}\frac{d\sigma}{d\varphi}$ through

$$\frac{1}{\sigma}\frac{d\sigma}{d\varphi} \;=\; \frac{1}{2\pi}\left\{1 + 2\sum_{n=1}^{\infty} \cos(n\varphi)\,\langle \cos(n\varphi)\rangle\right\}. \tag{8.2}$$

In a pure leading order (LO) collinear treatment, the two jets should be emitted back to back: $\varphi = 0$ and $k_{\perp 1}$=$k_{\perp 2}$, since there is no phase space for (untagged) emission between them. This simple picture should of course be corrected by radiative corrections. For large rapidities between the jets, the multiple emission of semi-hard gluons between these two jets is expected to modify dramatically this picture. This should lead to enhanced cross-sections as well as to strong decorrelation effects, i.e. a decrease of $<\cos(n\phi)>$.

Several comments are in place. First, it is known that passing from a leading logarithmic (LL) to a next-to-leading-logarithmic (NLL) treatment in the BFKL framework can modify significantly this picture. A complete NLL BFKL analysis of Mueller-Navelet jets (for more details, see refs. [26, 27]), including the NLL corrections both to the Green's function [10, 11] and to the jet vertex [28–34], showed that the NLL corrections to the jet vertex have a very large effect, of the same order of magnitude as the NLL corrections to the Green's function [35, 39], leading to a lower cross-section and a much larger azimuthal correlation [40]. However, these results are very dependent on the choice of the scales, especially the renormalization scale μ_R and the factorization scale μ_F, in particular in the case of realistic kinematical cuts for LHC experiments [26]. This dependency can be reduced by including a set of higher order contributions, according to the Brodsky-Lepage-Mackenzie (BLM) prescription [41] adapted to the resummed perturbation theory à la BFKL [42, 43]. Such a full NLL BFKL analysis supplemented by the BLM scale fixing procedure has been performed [27], leading to a very satisfactory description of the most recent LHC data extracted by the CMS collaboration for the azimuthal correlations of Mueller-Navelet jets at a center-of-mass energy $\sqrt{s} = 7$ TeV [44].

Second, in [35, 45] it has been noted that these differential distributions still suffer from a large influence of the collinear region. This is due to the fact that $<\cos(n\phi)> \simeq \exp(\alpha_s Y(\chi_n(1/2) - \chi_0(1/2)))$, where $\chi_n(\gamma)$ is, in Mellin space, the n-th Fourier component in azimuthal angle of the BFKL kernel where the region $\gamma \simeq 1/2$ gives the largest contribution to the cross section at high energies. It turns out that the $n = 0$ component is very sensitive to collinear dynamics well beyond the original multi-Regge kinematics. It is possible to take care of these collinear contributions in an approximated way by including their leading all-orders expression in a resummation "on top" of the BFKL original calculation. Nevertheless, at present it may be more important to fix the real region of applicability of the original BFKL

formalism at NLL by using observables which are far less sensitive to this collinear “contamination". It is only following this philosophy that one will be able to find “distinct" BFKL observables. An important step in this direction was taken in Ref. [35, 45] where instead of $<\cos(n\phi)>$ it was proposed to remove the $n=0$ dependence by studying “conformal ratios"[1] $\mathscr{C}_{m,n} = <\cos(m\phi)> / <\cos(n\phi)>$ which behave like $\simeq \exp(\alpha_s Y(\chi_m(1/2)-\chi_n(1/2)))$. It is important to note that the BFKL kernel for $n \neq 0$ is insensitive to collinear regions, as it was proven in Ref. [35, 45]. In that work it was shown that these new ratios are very stable under radiative corrections with the LO result (including running of the coupling) giving very similar results to the full NLL calculations. After the arrival of LHC data in recent years it has been seen that the NLL predictions, including NLO forward jet vertices, are in agreement with the experimental results. Furthermore, these observables are so fine tuned to the multi-Regge limit that it is difficult for other approaches to fit them with accuracy. This can be clearly seen in recent studies as those presented in Ref. [47] (Fig. 8.3), where a BFKL analysis at NLL is able to fit the large Y tail of the Mueller-Navelet “conformal ratios" proposed in Ref. [35, 45] whereas DGLAP Monte Carlos clearly deviate.

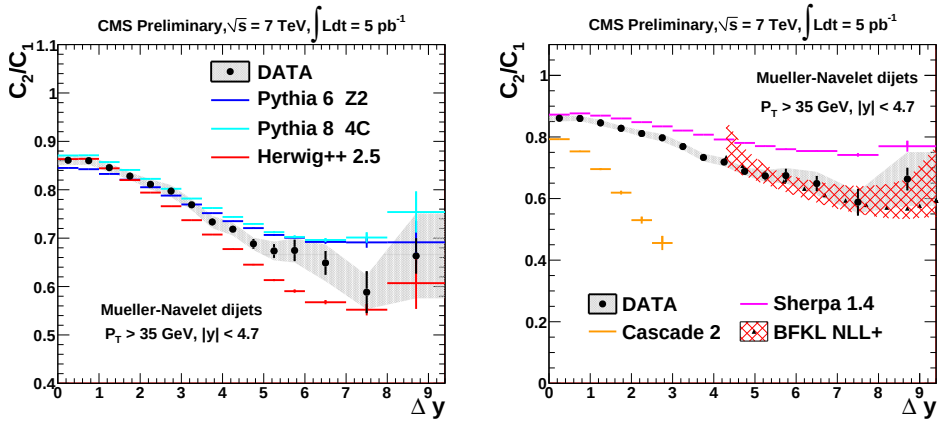

Fig. 8.3: Ratio C_2/C_1 as a function of Δy compared to various theory predictions.

Last, a general weakness of the BFKL approach is the fact that it does not respect strict energy momentum conservation. While such kinematic constraints are in principle subleading in the BFKL approach, numerically their effect could be sizable, in particular in the context of Mueller-Navelet jets at LHC. There have been many attempts to estimate these effects of energymomentum non-conservation [36–38]. An effective rapidity interval Y_{eff} to study energy momentum conservation effects in this process was introduced and studied in the BFKL LL approximation [36]. Later, an estimation with LO vertices and NLL Greens function was performed in [39]. Recently, a detailed study of the $2\gamma \to 2\gamma$ process at order $O(\alpha_s)$, treated either exactly or based on a NLL BFKL approximation has shown that one obtains a very significant improvement of energymomentum conservation when including NLO vertex corrections. This is true in the region where the two outgoing jets are in a slightly asymmetric configuration, the most important domain phenomenologically in view of a comparison with fixed-order approaches, as discussed at the beginning of section 8.2.2. We thus believe that energy-momentum non-conservation in NLL BFKL should not be a major issue in future phenomenological stud-

[1] We call them conformal because they capture the $SL(2,C)$ nature of the effective theory of QCD at high energies. When the same ratios are calculated in the $N=4$ supersymmetric Yang-Mills model, which enjoys four-dimensional conformal invariance, they are in agreement with those obtained in QCD using the Brodsky-Lepage-Mackenzie (BLM) scale-fixing procedure in momentum-subtraction (MOM) renormalization scheme (see Ref. [46]).

ies.

8.2.3 Multiple parton interactions (MPI) vs BFKL contribution

So far our discussion of BFKL signals has been restricted to the simplest set of diagrams with gluon emissions, the single chain process illustrated in Fig. 8.1a. There exists, however, another contribution to the Mueller-Navelet cross section which may become sizable for not too large transverse momenta of the jets, the two-ladder diagram illustrated in Fig-8.4. This correction

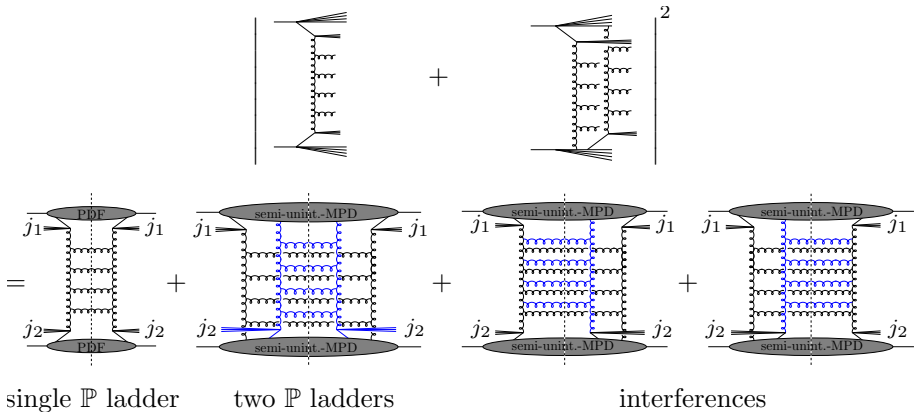

Fig. 8.4: The Mueller-Navelet squared amplitude, which involves a single chain à la BFKL (first line, left) added to a multipartonic contribution with two BFKL chains (first line, right). This squared amplitude can be expanded as the sum of a single BFKL ladder (second line, first term, scaling as $s^{\alpha_{\mathbb{P}}}$), of two BFKL ladders (second line, second term, scaling as $s^{2\alpha_{\mathbb{P}}}$) and of interference contributions (last terms of the second line, with an unknown scaling).

contains the product of two gluon densities. Since at small x each gluon density becomes large, this double parton contribution could be sizable, in particular when dealing with small transverse momenta of the tagged jets (which hopefully will become accessible at CMS and ATLAS). Note that as long as we do not integrate over the transverse momenta of the jets, the usual twist suppression is not applicable [48]. Thus it may happen that this MPI correction interferes with the BFKL signal. On the other hand, as an MPI contribution, it is of interest also in its own rights.

Let us report on a specific calculation [49]. We start with a sketch of the formalism. We considers the production of two pairs of jets, one in the forward, the other in the backward direction. We illustrate this process in Fig. 8.5. For a single pair of jets we write:

$$\frac{d\sigma(ij\to kl)}{dy_1 dy_2 d^2p_t} = \frac{1}{16\pi^2\hat{s}^2}\sum_{i,j} x_1 f_i(x_1,\mu^2)\, x_2 f_j(x_2,\mu^2)\, \overline{|\mathscr{M}_{ij\to kl}|^2}\,. \tag{8.3}$$

The calculations include only leading-order $ij\to kl$ partonic subprocesses. The K-factor for dijet production is rather small, of the order of $1.1-1.3$ (see e.g. [50, 51], but it can be easily incorporated. Below we shall show that already the leading-order approach gives results in sufficiently reasonable agreement with recent ATLAS [52] and CMS [53] data. With this the cross section for dijet production can be written as:

$$\frac{d\sigma^{DPS}(pp\to 4\text{jets}\,X)}{dy_1 dy_2 d^2p_{1t} dy_3 dy_4 d^2p_{2t}} = \sum_{i_1,j_1,k_1,l_1;i_2,j_2,k_2,l_2} \frac{\mathscr{C}}{\sigma_{eff}}\, \frac{d\sigma(i_1 j_1\to k_1 l_1)}{dy_1 dy_2 d^2p_{1t}}\, \frac{d\sigma(i_2 j_2\to k_2 l_2)}{dy_3 dy_4 d^2p_{2t}}\,, \tag{8.4}$$

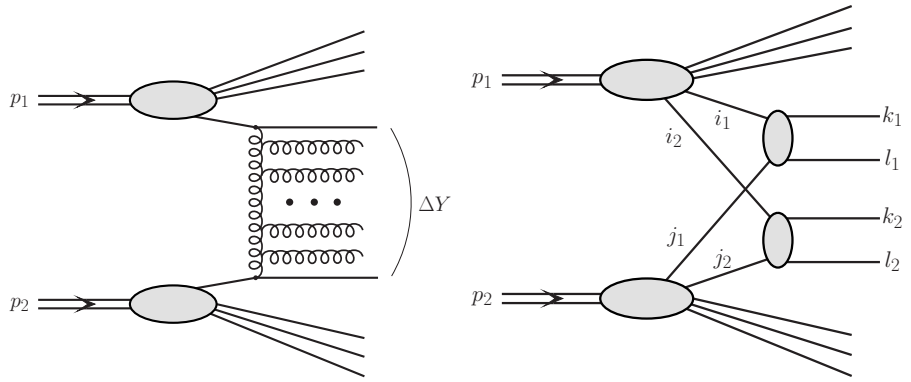

Fig. 8.5: The production of jets widely separated in rapidity via Mueller-Navelet mechanism (left) and within double-parton scattering mechanism (right).

where $\mathscr{C} = \left\{ \begin{array}{ll} \frac{1}{2} & \text{if } i_1 j_1 = i_2 j_2 \wedge k_1 l_1 = k_2 l_2 \\ 1 & \text{if } i_1 j_1 \neq i_2 j_2 \vee k_1 l_1 \neq k_2 l_2 \end{array} \right\}$, and the summation extends over the partons species $j,k,l,m = g,u,d,s,\bar{u},\bar{d},\bar{s}$. The combinatorial factors take care of the identity of the two subprocesses. Each step of DPS is calculated in the leading-order approach (see Eq.(8.3)). Experimental data from Tevatron [54] and LHC [55] provide an estimate of σ_{eff} in the denominator of formula (8.4). In the calculations, whose main results are presented here, we have taken σ_{eff} = 15 mb. As to the comparison with BFKL calculations, we consider the cross section integrated over ϕ (relative azimuthal angle between jets). Then the cross section can be simplified by including only one term n=0 in the sum over conformal spins. For comparison we also calculate correlations between jets obtained in the k_t-factorization approach. The calculations use Kimber-Martin-Ryskin unintegrated parton distributions [56]. The formulae for the off-shell matrix elements were obtained e.g. in [57], and corresponding formulae can be used in our calculations.

Let us present a few numerical results. In Fig. 8.6 we show distributions in the rapidity distance between two jets in leading-order collinear calculation and between the most distant jets in rapidity in the case of four double parton scattering (DPS) jets. In this calculation we have included cuts characteristic for the CMS experiments [58]. For comparison we show also results for BFKL calculation from Ref. [26]. For this kinematics the DPS jets give sizeable contribution only at large rapidity distance. However, the four-jet (DPS) and dijet (LO SPS) final state can be easily distinguished and in principle one can concentrate on the DPS contribution which is interesting by itself. The NLL BFKL cross section (long-dashed line) is sizeably lower than that for the LO collinear approach (short-dashed line). For higher LHC energies the suppression of the DPS-cross section becomes weaker. Fig. 8.7 shows results for smaller transverse momenta. Now the double parton scattering (DPS) contribution may even exceed the standard single parton scattering (SPS) dijet contribution. A measurement of such minijets may be, however, difficult. One could measure, for instance, correlations of semihard ($p_t \sim 10$ GeV) neutral pions with the help of so-called zero-degree calorimeters (ZDC). This will be discussed elsewhere.

Let us compare results of the different mechanisms still in another form. In Fig. 8.8 we show two-dimensional distributions in transverse momenta of dijets widely separated in rapidity ($8 < y < 9.4$)) at $\sqrt{s}$ = 14 TeV (Run II). Again we show results for k_t-factorization approach with KMR UPDF (left panel), the LL BFKL approach (middle panel) and the DPS mechanism calculated here in LO collinear approach (right panel). All mechanisms lead to cross sections

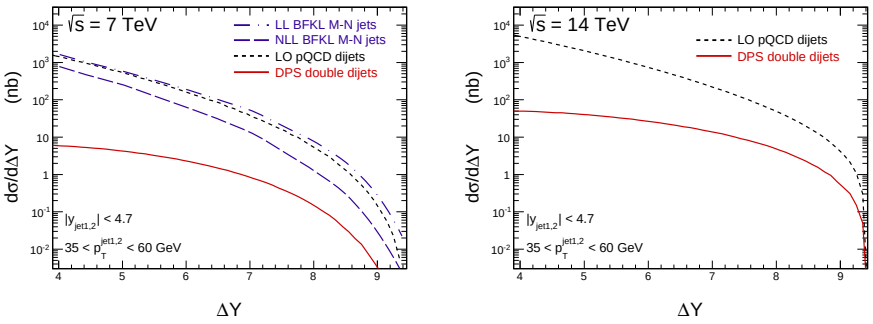

Fig. 8.6: Distribution in rapidity distance between the jet (35 GeV $< p_t <$ 60 GeV) with maximal (the most positive) and minimal (the most negative) rapidities. The collinear pQCD result is shown by the short-dashed line and the DPS result by the solid line for $\sqrt{s}$ = 7 TeV (left panel) and $\sqrt{s}$ = 14 TeV (right panel). For comparison we also show results for the BFKL Mueller-Navelet jets in leading-logarithm and next-to-leading-order logarithm approaches from Ref. [26].

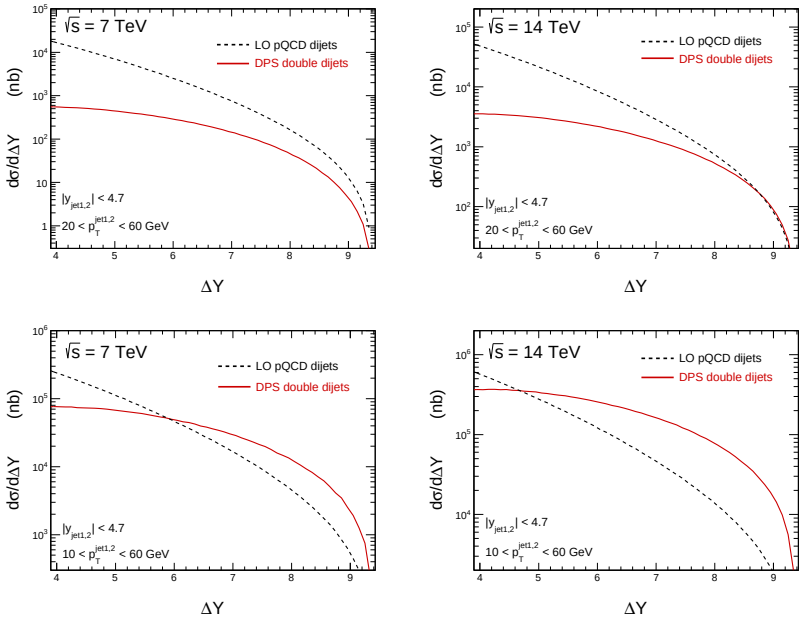

Fig. 8.7: The same as in the previous figure but now for somewhat smaller lower cut on minijet transverse momentum.

of the same order of magnitude. We obtain integrated cross section for $p_{1t}, p_{2t} > 35$ GeV σ = 18.7 nb (k_t-factorization, KMR PDF), 40.1 nb (LL BFKL), 2.8 nb (DPS, collinear LO), respectively. Such cross section could be measured in Run II both by the CMS collaboration and by ATLAS. The distribution in the BFKL approach and that corresponding to the DPS are rather similar as far as the shape is considered. The LL BFKL cross section is probably overestimated. NLL cross sections are much smaller than LL ones [40]. Corrections for energy-momentum conservation (violated in analytic BFKL) are expected to lower the cross section in addition. The distribution in the k_t-factorization approach is also interesting and shows a ridge along the diagonal $p_{1t} = p_{2t}$, which corresponds to back-to-back jets in the collinear LO approach. Therefore to understand which mechanism dominates one should study such distributions. This

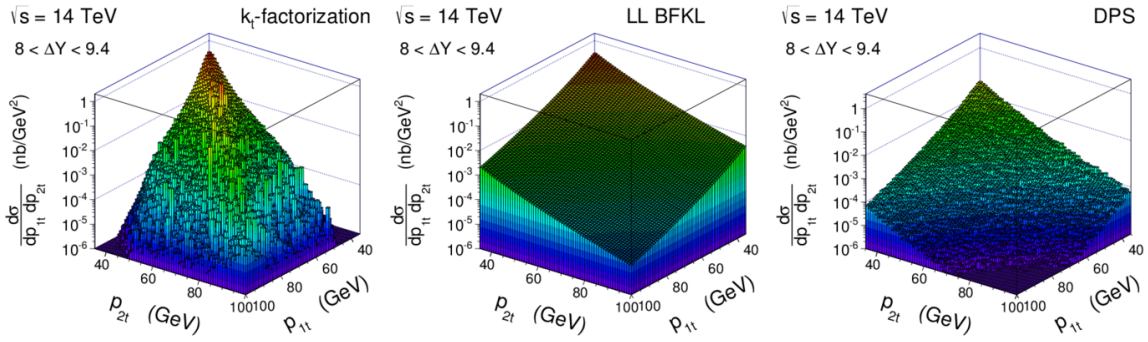

Fig. 8.8: Two-dimensional distributions in jets transverse momenta for large rapidity distance $8 < y < 9.4$ (CMS apparatus for jets) for k_t-factorization approach (left), LL BFKL (middle) and DPS (right).

would require rather good statistics. The presence of the ridge along the diagonal would clearly signal that the BFKL approach is insufficient in this context. Distribution in the azimuthal angle (to be discussed in [60]) would be another useful possibility to pin down the underlying mechanism. Many more interesting distributions will be discussed in Ref. [60].

As our main result, we have shown that
- the contribution of the DPS mechanism increases with increasing distance in rapidity between jets,
- the relative effect of DPS increases if one lowers the transverse momenta of jets (although such measurements may be difficult) .
The DPS effects therefore cannot be neglected completely when searching for BFKL signals. Also, double parton scattering contributions are interesting not only in the context how they contribute to distribution in rapidity distance between the jets but also per se. One could also make use of other observables like correlations in jet transverse momenta or jet transverse-momentum imbalance (see [59]) to enhance the relative contribution of DPS.

8.2.4 Exclusive radiation patterns: towards a new class of BFKL observables

In our opinion, it is mandatory to continue, in the coming years of analysis of LHC data, this line of searches for BFKL signals which are obtained from the all-order summation of gluon emissions. However, it is also needed to propose new quantities sensitive to multi-Regge kinematics and avoiding the influence of the, otherwise widely dominant, collinear regions of phase space. These analysis are more complicated from the theoretical point of view, since we need two key ingredients: new NLO impact factors and Monte Carlo techniques to control the gluon Green function and to fully extract its physical content in the most differential form. The former are mandatory to fairly test the theory and correctly control the dependence on the scales appearing in the calculations (running of the coupling and energy scale separating the universal gluon radiation in central regions of rapidity and that stemming from the fragmentation regions). The latter are needed in order to effectively generate differential distributions which are otherwise complicated to be calculated analytically.

In order to illustrate how details of the radiation pattern may influence some of the quantities we have discussed before, we return to the azimuthal angle projections and show that it is a good idea to distinguish among different approaches. Let us compare the above mentioned n-moments of the BFKL cross section with those obtained from the Catani-Ciafaloni-Fiorani-

Marchesini (CCFM) [61–64], which, in principle, interpolates the large x and small x limits of unintegrated gluon densities (we will see that this is only true for the $n = 0$ projection). This has been studied in Ref. [66] and we illustrate it here in Fig. 8.9. In the left plot we see the BFKL result, and in the right panel we show the CCFM analysis. We can see that the $n = 0$ component has a similar behavior in both cases since it grows with Y. But this is not the case for the other $n > 0$ components which in the BFKL case decrease with Y and for CCFM increase with Y. This is a fundamental difference between the Regge limit and approaches based on QCD coherence which should be exploited further in order to disentangle BFKL from other dynamics.

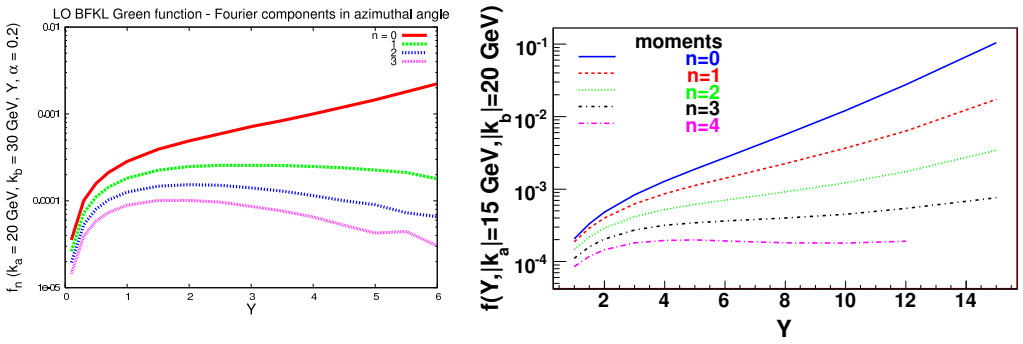

Fig. 8.9: Variation with rapidity of the different components of the Fourier expansion on the azimuthal angle of the BFKL (left) and CCFM (right) gluon Green function.

These two points were confirmed in another evaluation of the DPS contribution for this process [65], performed in a slightly different framework. Similarly to the results shown above, these predictions are based on the assumption that the DPS cross section can be factorized into the product of two SPS subprocesses. However, here each subprocess consists in the emission of a single jet in the forward (or backward) direction from one on-shell parton and one off-shell gluon. The former is described by a usual collinear PDF while the latter is described by an unintegrated gluon distribution (UGD), which is the source of the jet's transverse momentum. This is in the spirit of the second contribution shown in the first line of Fig. 8.4. The uncertainty on the DPS cross section, coming from the choice of the UGD parametrization and the variation of σ_{eff} in a range compatible with experimental determinations of this quantity, is rather large. Nevertheless, in this approach the DPS cross section is always smaller than the SPS one computed at NLL accuracy in the BFKL framework if one considers kinematics similar to those studied in Ref. [59]. When looking at the angular correlation between the jets, the effect of including the DPS contribution is always small, except for transverse momenta of the order of 10 GeV at $\sqrt{s} = 14$ TeV. For such small transverse momenta, double parton scattering could lead to a significantly smaller correlation than predicted by a SPS calculation, but the large uncertainty on the DPS cross section makes it impossible to draw firm conclusions in these kinematics at the moment.

There are other distributions which relate the average p_T of the mini jet radiation to its position in rapidity space, the so-called "diffusion plots" which can be connected to, *e.g.*, energy-energy correlations or with the distribution of mini jet multiplicity in different regions of rapidity in the detectors. With these tools at hand it is needed to be imaginative and try to tag different particles or jets in the final state which can serve as "projecting operators" on multi-Regge kinematics. It is clear that tagging different jets in the final state and allowing for associated mini jet radiation, together with stringent cuts on the p_T and rapidity separation of

the tagged jets, will allow for a much more precise identification of the multi-Regge region.

When using Monte Carlo methods it is possible to access very exclusive information not only related to multiple particle production, but also of the internal structure of the “pomeron ladder", which is relevant in diffractive events. As an example we show Fig. 8.10, from Ref. [67], where we can see the distribution in the number of minijets in the case of a total cross section (left) and the distribution in the number of rungs present in the pomeron exchange in a high energy elastic scattering with nonzero momentum transfer (right). The former includes final state radiation with any p_T, but a similar analysis can be performed for different bins in p_T at LL and NLL. These Poissonian shapes are characteristic of BFKL radiation. From these

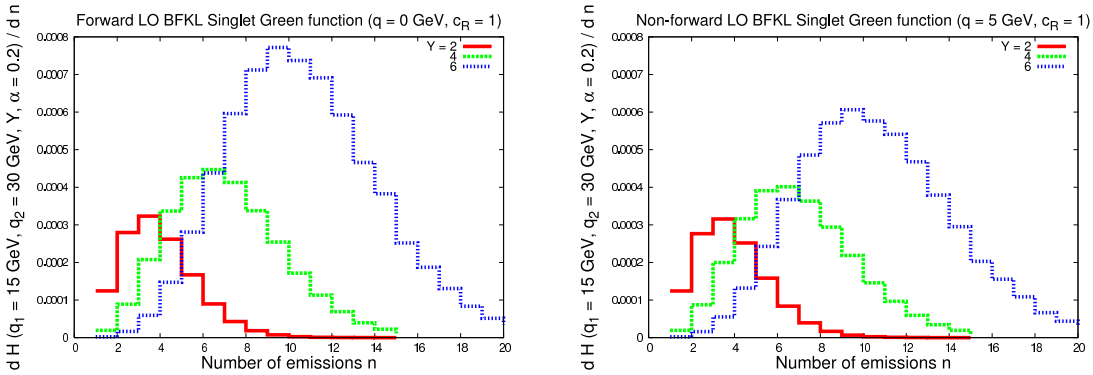
Forward LO BFKL Singlet Green function (q = 0 GeV, c_R = 1)
Non-forward LO BFKL Singlet Green function (q = 5 GeV, c_R = 1)
d H (q_1 = 15 GeV, q_2 = 30 GeV, Y, α = 0.2) / d n
Number of emissions n
Y = 2
4
6

Fig. 8.10: Distribution in the contributions to the BFKL gluon Green function (left is the forward and right the non-forward case) with a fixed number of iterations of the kernel, plotted for different values of Y and $\bar{\alpha}_s = 0.2$.

few examples it should be clear that the use of a BFKL-based Monte Carlo, in particular BFK-Lex described in [68] allows to address many more comparisons of exclusive final states with theoretical predictions.

Let us also mention a specific final state which allows to address BFKL physics: the jet-gap-jet configuration in which the jet plus proton remnants are attached to a color singlet exchange [69–71] without any activity inside the gap. As to the calculation of impact factors, the authors of [72–74] have developed a procedure based on Lipatov’s high energy effective action which is very powerful and useful in this regard. In [33, 34, 75, 76] the NLO forward jet vertex coupled to an octet has been reproduced which is related to forward jet production with associated mini jet radiation, and more recently [69–71] the impact factor through which the jet plus proton remnants are attached to a color singlet exchange. Further processes at full NLO, like forward production of electroweak bosons, will also require the calculation of NLO impact factors, a problem which can be suitably addressed with the high energy effective action approach. Turning to the color singlet exchange, because of the hard scales of the jets the color singlet exchange should be described by the exchange of a BFKL Pomeron: this makes this process an interesting candidate for BFKL searches. However, for these diffractive events we have the "traditional" problem of the gap survival probability which cannot be calculated yet in a reliable manner. As a step forward towards circumventing this problem, one should investigate exclusive distributions related to ratios of cross sections which somehow remove this gap factor and the influence of parton distribution functions.

Finally, it may also be useful to think about ’BFKL signals’ in a quite different way.

Most of the searches discussed so far look for signals which result from the inclusive radiation of a large (in most cases even 'infinite') number of gluons. Modern calculation techniques now allow for the computation of fixed order matrix elements of hard subprocesses with many partons (gluons) in the final state. At large rapidities, these matrix elements generate some of those logarithms which the BFKL approach sums to all orders (in LO or NLO accuracy). From this point of view BFKL can be seen as the most efficient tool for performing an all-order summation. A search for BFKL dynamics, therefore, could start from a close inspection of fixed-order calculations and a comparison with the corresponding BFKL predictions.

8.2.5 Previous measurements and experimental aspects

After this theoretical part let us now turn to experimental aspects. Some of the measurements discussed before have already been started at the Tevatron and in the previous LHC run. It may therefore be useful to briefly review these measurements and then say a few words about RUNII expectations and future experimental techniques.

8.2.5.1 Measurements from D0

Early measurements of forward-backward jet production in proton-(anti)proton collisions were performed by the D0 experiment. In [77], published in year 1996, azimuthal decorrelations between jets with large rapidity separation are presented. Jets above 20 GeV with $|\eta| < 3.0$ with largest rapidity separation in the event were selected from the data sample of 83 nb^{-1} collected at collision energy of 1800 GeV. If one of these jets was above 50 GeV the pair was selected for the analysis. An average cosine of $\Delta\phi$ between jets was measured as a function of rapidity separation, Δy, in the range $\Delta y < 5$. The measurements were compared with the HERWIG Monte Carlo (MC) generator [78] based on leading order matrix elements supplemented with parton shower, a NLO calculation based on JETRAD [79, 80] as well as LL BFKL calculations performed in [24, 81]. HERWIG has demonstrated the best agreement with the data. The LL BFKL calculation was above the measurements while the NLO calculations were below.

In [82] the ratio of dijet production at different energies was measured. Data samples of 0.7 nb^{-1} and 31.8 nb^{-1} obtained at collision energies of 630 GeV and 1800 GeV were used. The ratio was originally thought to demonstrate the strong growth of partonic cross-section with collision energy as predicted by BFKL. The measurements were compared to predictions of the HERWIG MC generator, fixed order calculation in LO pQCD and LL BFKL calculation [83]. The measurement showed considerably larger growth of cross-section with energy than all theory predictions. For a detailed discussion on the interpretation of this measurement see [21].

8.2.5.2 Forward backward jet production - measurements from CMS

CMS has performed two measurements of jets with large rapidity separation based on LHC data taken in 2010.

8.2.5.3 Inclusive to exclusive dijet production ratio

In this subsection the measurement [84] performed in collisions at $\sqrt{s} = 7$ TeV taken in 2010 is discussed. The measurement was performed with the effective luminosity of 5 pb^{-1}. The ratio of inclusive to exclusive dijet production was proposed in [85] as an observable sensitive to higher order QCD radiation and a potential manifestation of BFKL effects. Jets with transverse momenta above $p_{\mathrm{T,min}} = 35$ GeV are considered. Events with at least one pair of jets are denoted as "inclusive". Events with exactly one pair of jets within the acceptance are called "exclusive". In the inclusive case, the rapidity separation is evaluated for each pairwise combination of jets

above threshold. The ratio of inclusive to exclusive dijet production is measured in bins of rapidity separation Δy, covering a range up to $\Delta y = 9.2$.

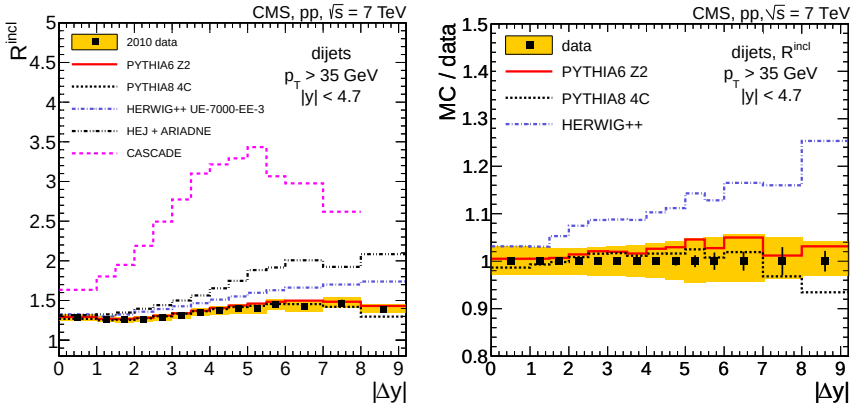

Fig. 8.11: Inclusive to exclusive dijet production ratio compared to predictions of DGLAP-based MC PYTHIA6, PYTHIA8, HERWIG++ and MC with elements of LL BFKL - HEJ and CASCADE (left). Comparison to DGLAP-inspired MCs is presented as data/MC ratio on the right.

The measurement of a ratio of cross sections allows to reduce many theoretical and experimental uncertainties with the jet energy scale calibration and model dependence of unfolding procedure being the most important systematic uncertainties. Total experimental uncertainty goes up to 5%.

The results of the measurement are presented at Fig. 8.11. The measurement is compared to predictions of DGLAP-based Monte Carlo generators PYTHIA6 [86], PYTHIA8 [87] and HERWIG++ [88] and to generators which include BFKL effects: HEJ [89] and CASCADE [90]. The HEJ MC generator accounts for wide-angle gluon emission to all orders of perturbation theory using LL BFKL formalism. CASCADE uses the CCFM evolution equation for initial state parton cascade. PYTHIA8 and PYTHIA6 predictions agree with the data within the experimental uncertainties. HERWIG++ shows stronger rise of the ratio with the rapidity separation increase. HEJ and CASCADE predict a too strong rise. However, CASCADE uses only gluon induced processes and thus the exclusive cross section at large rapidity separations becomes very small, leading to and increased ratio. This effect has been confirmed [91] by a simulation using gluon induced processes in PYTHIA6.

8.2.5.4 Azimuthal de-correlation of forward backward jets

The measurement [92] of azimuthal de-correlation for jets separated by a large rapidity interval was performed using 5 pb^{-1} of pp collisions at $\sqrt{s} = 7$ TeV in 2010.

Perturbative QCD at leading order predicts exactly two outgoing jets in a parton-parton interaction, which are back-to-back in azimuthal angle ϕ. In higher order calculations the jets can become de-correlated. In calculations based on BFKL, a significant de-correlation in azimuthal angle is predicted, however also higher order matrix element calculations and calculations supplemented with parton showers and multi-parton interactions predict significant de-correlation effects. Thus the study of azimuthal de-correlation of jets as a function of rapidity separation may give further insights into the production mechanism.

The dijet production cross section as a function of azimuthal angle difference can be

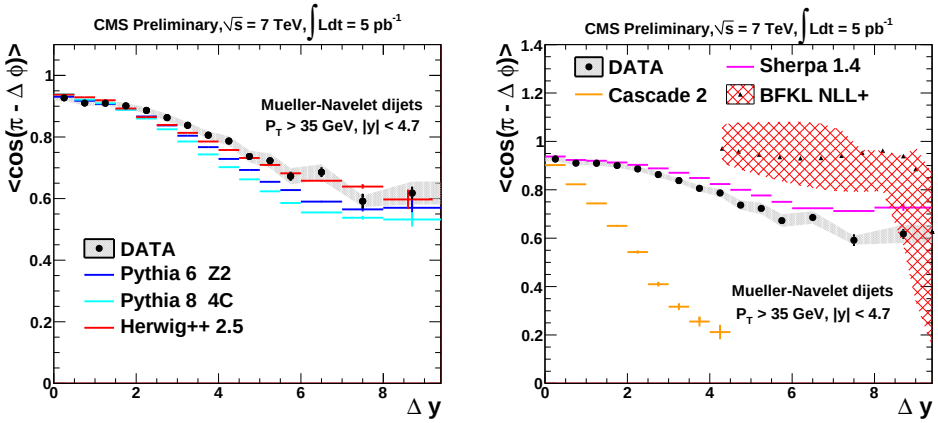

Fig. 8.12: C_1 as a function of Δy compared to various theory predictions.

written as a Fourier series:

$$\frac{1}{\sigma}\frac{d\sigma}{d(\Delta\phi)}(\Delta y, p_{\mathrm{Tmin}}) = \frac{1}{2\pi}\left[1+2\sum_{n=1}^{\infty} C_n(\Delta y, p_{\mathrm{Tmin}})\cdot cos(n(\pi-\Delta\phi))\right]. \tag{8.5}$$

The Fourier coefficients $C_n(\Delta y, p_{\mathrm{Tmin}})$ are equal to the average cosines of the de-correlation angle: $C_n(\Delta y, p_{\mathrm{Tmin}}) = \langle cos(n(\pi-\Delta\phi))\rangle$, where $\Delta\phi = \phi_1 - \phi_2$ is the difference between the azimuthal angles ϕ_1 and ϕ_2 of the jets most forward and backward in rapidity.

In [35] the ratio C_2/C_1 and C_3/C_2 was proposed as observables, which are particularly sensitive to higher order corrections and to BFKL effects. CMS has measured both C_n and the cosine ratios. The average cosines of the azimuthal angle and their ratios were measured in bins of the rapidity separation between the jets, Δy. Jets with p_{T} >35 GeV and $|y| < 4.7$ covering a rapidity separation of $\Delta y < 9.4$ were investigated. The measurements are compared to theoretical predictions in Fig. 8.12. The measurement of the ratio C_2/C_1 is shown in Fig. 8.3. The measurements are corrected for detector effects. The leading source of the experimental uncertainty is the jet energy scale of up to 24% depending on the observable and the rapidity separation range. The total experimental uncertainty, however, does not exceed 25%.

The next-to-leading logarithmic approximation (NLL) BFKL calculations [26] provides a good description of C_2/C_1. It should be noted that improved NLL BFKL calculations [27,93] were released later than the present measurement was published, in mentioned work comparison with the CMS data can also be found. However, also calculations supplemented with parton showers and multiparton interactions, PYTHIA6, HERWIG++, provide a reasonable good description of the measurement over the full range in Δy. CASCADE predicts too a large de-correlation.

8.2.5.5 Measurements from ATLAS

ATLAS detector [94] calorimeter system covers pseudorapidity range $|\eta| < 4.9$ allowing jet reconstruction up to $|y| < 4.4$. Tracking system extends to $|\eta| < 2.5$. Fine-segmented calibrated calorimeter energy deposits are combined in dedicated manner and clustered with anti-kT algorithm with distance parameter $R = 0.6$ (for measurements presented here). Jets are calibrated using various in-situ techniques [95, 96].

In [97] the measurement of dijet as a function of rapidity separation for different requirements on additional jets is described, either considering the two leading p_{T} jets or the most-

forward and most-backward jets using sets above $Q_0 = 20$ GeV. Two different cuts (veto) were applied on the additional jets between the jets defining the dijet system. In the first scenario, no additional jets above Q_0 are allowed, while in the second scenario no additional jets above $\overline{p_T}$ were allowed. Measurements were compared to the predictions from NLO MC POWHEG [98] interfaced to parton shower with PYTHIA6 or HERWIG++ and MC generator HEJ. Predictions for HEJ were obtained at parton level. The rapidity separation range covered by the measurement extends to $\Delta y = 6$. It was observed that for the veto $Q_0 = 20$ all predictions give smaller cross section than observed (Fig. 7 in [97]), while for veto scenario $Q_0 = \overline{p_T}$ POWHEG-based predictions show a good agreement with the data while HEJ overestimated the measurement (Fig. 8 in [97]). This is in qualitative agreement with the CMS dijet production ratio measurement (see Fig 8.11).

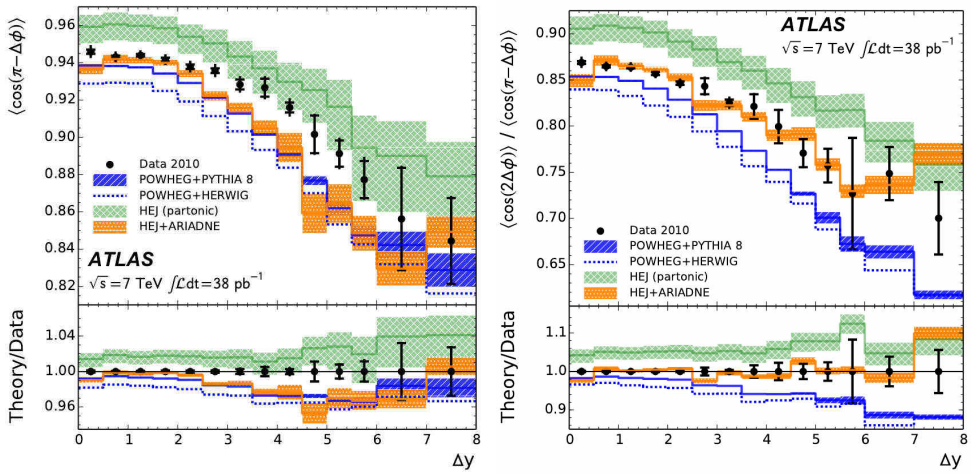

Fig. 8.13: ATLAS results on azimuthal decorrelation measurement, plots are taken from Fig. 5 in [99]. On the left average cosine as a function of rapidity separation is shown, on the right ratio C_2/C_1 is presented.

The azimuthal de-correlation between jets as a function of rapidity separation has been measured [99] for jets above $Q_0 = 20(30)$ GeV for data taken in 2010 (2011). The two leading jets were selected, and events were rejected if p_T of leading jet is below 60 or p_T of subleading jet is below 50 GeV. Events were also rejected if jets with transverse momenta of 20 (30) GeV were found between the leading jets. Jets were considered in the acceptance region of $|\eta| < 4.4$ for 2010 data. For data taken in 2011 the jets were restricted to the tracker acceptance $|\eta| < 2.4$ as this allows to identify jets belonging to the same interaction vertex in high-pileup environment.

The angular moments C_1 and C_2 as well as the ratio C_2/C_1 were measured. Below we will focus on measurement of C_1 and C_2/C_1 as functions of rapidity separation. The data are compared to predictions of NLO MC POWHEG supplemented with parton showers generated by PYTHIA or HERWIG++ and to HEJ. The measurements of the azimuthal decorrelations are shown at Fig. 8.13. The measurements extend to $\Delta y = 8$. The value of the average cosine obtained by ATLAS is bigger than the CMS result (0.8 for ATLAS and 0.6 for CMS in $7 < \Delta y < 8$ bin) which can be attributed to p_T ordering of jets and higher p_T of jets in case of ATLAS. POWHEG interfaced to PYTHIA as well as HERWIG overestimate the de-correlation. HEJ+ARIADNE package also overestimates the de-correlations. The ratio C_2/C_1 is well-described by HEJ+ARIADNE package while POWHEG + parton shower underestimates

the ratio.

To summarize, measurements of forward-backward dijet production performed by different experiments do not allow to make clear conclusions concerning observation of BFKL signal. Although a good description of the azimuthal de-correlation by the NLL BFKL calculations is obtained, the DGLAP MC parton shower calculations give a surprisingly good description of the measurement over the full acceptance region.

8.2.6 RunII expectations

BFKL resummation is performed for "pQCD high energy limit" asymptotic region or when the collision energy is much larger than the momentum transfer: $s \gg Q^2$. Obviously the validity of a given relation will increase for jets measured at the same p_{T}'s and increased collision energy (we imply here transition from 7 to 13 TeV). For further investigations, a dataset of $\sim$100 pb^{-1} is needed to perform careful measurements of dijet production at large rapidity intervals at pp collision energy of 13 TeV. An average pileup of 1 can be tolerated by analysis techniques used in LHC RunI.

The ability to measure jets with low p_{T} is important for approaching the high energy limit and revealing BFKL contributions into production of jets. There are two obstacles making this task rather challenging. The first one is the jet trigger efficiency. For example in CMS experiment for 2010 RunI data 99% efficiency was reached at around $p_{\mathrm{T}} = 35$ GeV. Another obstacle is the jet energy scale calibration. Due to nonlinear effects in the jet composition and calorimeter response, the jet energy resolution worsens for lower p_{T} which leads to larger uncertainties on the jet energy scale calibration. In measurements described here the energy scale was valid for jets above p_{T} of 20 GeV which can be considered as a realistic offline threshold for imposing vetoes or for Mueller-Navelet jet selection. Though it should be noted that the particle flow technique used for jet reconstruction allows to reconstruct jets starting from 10 GeV [100]. This technique uses all detector components to form particle candidates which are clustered into jets and that allows to improve jet energy resolution significantly.

For the measurement of Mueller-Navelet jets, a large rapidity acceptance of the detector is required. CMS calorimeter system covers the pseudorapidity range up to 5 allowing jet reconstruction within $|\eta| < 4.7$ range. In presence of additional interaction in the beam-crossing (pile-up) it is important to identify the pair with largest rapidity separation belonging to the same hard scattering. This may be possible in case the acceptance region is instrumented with a tracking detector. This is not the case for the forward region of CMS. The tracking system of CMS covers a pseudorapidity range of $|\eta| < 2.4$. Thus measurements of Mueller-Navelet jets across the full detector acceptance requires low-pileup collision events. The same is applicable to ATLAS detector where the calorimeter system allows to measure jets up to 4.4 in pseudorapidity while the tracking system extends to $\eta = 2.5$. Combinatorial background from pileup also saturates the bandwidth allocated to dijet triggers widely used for jet energy scale calibration in forward region or for selecting Mueller-Navelet jets. The pile-up scenario for data-taking should not have an average pileup of $\langle\mu\rangle > 1$. Note that both CMS and ATLAS analyses applied requirement of exactly one primary vertex per event to reduce or remove the combinatorial background in 2010 data. This requirement leaves $\sim$ 37% of events in case of mentioned scenario.

8.2.7 Summary

It is clear that we are entering a very exciting period where both rich data and new powerful calculations will be available allowing us to pin down in a precise fashion what is the underlying

dynamics governing the high energy limit of QCD. Some of the BFKL searches presented in this section have been discussed earlier and experimentally investigated before (HERA, Tevatron, low energy runs of the LHC). However, we have also listed new questions and proposed novel measurements which have not been addressed yet. In combination with the unprecedented high energy, this defines a really promising program for the coming years.

This program is important since there are uncertainties in the BFKL approach itself which need to be fixed. As an example, it is needed to find the dependence of each proposed observable on the renormalization schemes (the above mentioned conformal ratios were shown to be independent of these choices), but also the correct treatment of the running of the coupling must be addressed in an accurate way. Only a fair comparison to experimental data can solve many of these theoretical questions. Once we control a class of observables where only BFKL can fit them then we can introduce corrections to the original calculations in the form of hadronization, non-linearities, collinear radiation or even the possible connection with soft-collinear effective theories, in order to extend their applicability beyond the multi-Regge kinematics. Particularly interesting "deformations" of the original theory are those where non-perturbative effects (of confinement type, non related to high parton densities) are included [101–103]. But all of these can be studied only after we have a clear idea of the phenomenological window of applicability of the perturbative linear BFKL program.

Experimentally, with the large $\sqrt{s}$ reachable in run2, a study of the energy dependence of Mueller-Nevelet jets can be performed, by comparison with measurements from run1. Important are also dedicated measurements, where the transverse momenta of the forward and backward jets are in a p_T window as advocated in the introduction. Besides dedicated searches for BFKL effects, multi-jet measurements over the largest rapidity range are essential, as those measurements might not be well described by fixed higher order calculations (even supplemented with parton showers) and they could show the need for small x resummation to all orders. Experimentally challenging will be the high pileup scenario in run2 and dedicated methods for pileup identification and subtraction, in a region where there is no tracking, are desperately needed.

8.3 Inclusive forward di-jet production in pp

Let us now turn to our next topic, inclusive forward jets (Fig 8.1 b, left). Questions of highest interest include unintegrated gluon densities, saturation, and multiple interactions.

Unintegrated Gluon Densities (UGDs) are crucial ingredients of k_T-factorization-based approaches which once convoluted with off shell matrix elements allow to provide predictions for observables at low x. UGDs are in their nature more exclusive than collinear parton densities, since they depend not only on longitudinal degrees of freedom, but also on a transversal momentum of a gluon. However, the properties of UGD are still unexplored in wide kinematical regime [104]. A natural tool to access UGDs at low x are various configurations of forward jets. In particular, configurations with dijet or trijet system in a forward rapidity region and forward-central jet configurations are of great interest. They offer a possibility to perform a scan of UGDs in a large kinematical domain, in particular to access a kinematic region where the saturation phenomenon [105, 106] eventually emerges.

One of the frameworks which allows to access the observables sensitive to UGDs is so-called High Energy Factorization (HEF) [107] (see also [105], [108]). It relies on off-shell gauge invariant matrix elements and UGDs convolved together in longitudinal and transversal degrees of freedom. For the configurations of final states populating (at least partially) the

forward rapidity region, the following HEF formula may be used

$$d\sigma_{AB\to X} = \int \frac{d^2k_{TA}}{\pi} \int \frac{dx_A}{x_A} \int dx_B \sum_b \mathscr{F}_{g^*/A}(x_A, k_{TA})\, f_{b/B}(x_B)\, d\hat{\sigma}_{g^*b\to X}(x_A, x_B, k_{TA}), \quad (8.6)$$

where $\mathscr{F}_{g^*/A}$ is the UGD, $f_{b/B}$ are the collinear parton distribution functions and b runs over gluon and all the quarks that can contribute to the production of multiparticle state X (see also [109]). The off-shell gauge invariant matrix elements for multiple final states (residing in $d\hat{\sigma}_{g^*b\to X}$) can be calculated along the lines of Refs. [110, 111]. The restriction that the multiparticle state X populates the forward rapidity region follows from the fact, that Eq. (8.6) is valid when $x_B \gg x_A$, i.e. when the events are highly asymmetric.

Recently, some new forward jet observables were calculated within this framework for existing experimental setup [112–114] and some UGDs relevant for large p_t's [115] accounting for saturation phenomenon in both proton and lead. Below we briefly discuss the relevant observables and outline the main observations. We also give new predictions for a possible extension of CASTOR detector allowing for jet reconstruction.

8.3.1 Dijet production at forward and very-forward rapidities

Forward dijets offer practical advantages over forward-central dijets since the nearness in rapidity lowers the phase space for an emission of further jets. Moreover, the events are highly asymmetric as required in view of HEF formula (8.6). Depending on the cuts applied we probe x_A between 10^{-4} and 10^{-6} and x_B around unity.

An observable of particular interest in p+p and p+Pb collisions are angular decorrelations, i.e. the cross section as a function of the azimuthal angle between the two jets. Such a cross section reflects a pattern of gluon radiation as summed by the evolution equations. For instance when the jets are nearly back-to-back the transverse momentum of the incoming off-shell gluon is small and possibly affected by the saturation. In the other limit when the gluons are observed in a similar direction in the transversal plane the gluon density is probed at the large momentum and is subject to large sub-leading effects of higher orders. Those corrections come from non-singular pieces of DGLAP splitting function at low x and from energy conservation.

In Fig. 8.1 recent results [114] are presented for dijet system in forward rapidity region $3.2 < y < 4.9$. The potential singularities in matrix elements were cut by using the anti-k_T jet algorithm with $R = 0.5$ and the p_T cut of 20 GeV. We show both the absolute predictions and nuclear modification ratios R_{pA} defined as the ratio of the p+A cross section to p+p cross section normalized to the number of nuclei. The last observable is sensitive to the saturation effects. The calculations were made using two frameworks for UGDs: KS [112] and rcBK [116, 117]. Both of the approaches are extensions of the Balitsky-Kovchegov (BK) equation [118,119]. The KS is formulated in the momentum space and includes corrections of higher order coming from energy conservation, non-singular pieces of splitting functions at low x and running coupling [115]. It also assumes a homogeneous target. The rcBK is an extension of the BK equation to running coupling case and similarly to KS it assumes homogeneous target. Applying these densities to considered observables one clearly sees the sensitivity of the results to a particular evolution scenario (potentially this might be an effect of different initial conditions but the essential difference comes from different effects incorporated in the evolution kernel).

A particularly interesting observable is R_{pA} as a function of the p_T of the sub-leading jet. The striking feature is that the R_{pA} stays constant and is significantly lower than one in wide range of p_T. This suggests that the sub-leading jets are more affected by the saturation scale than the leading jet.

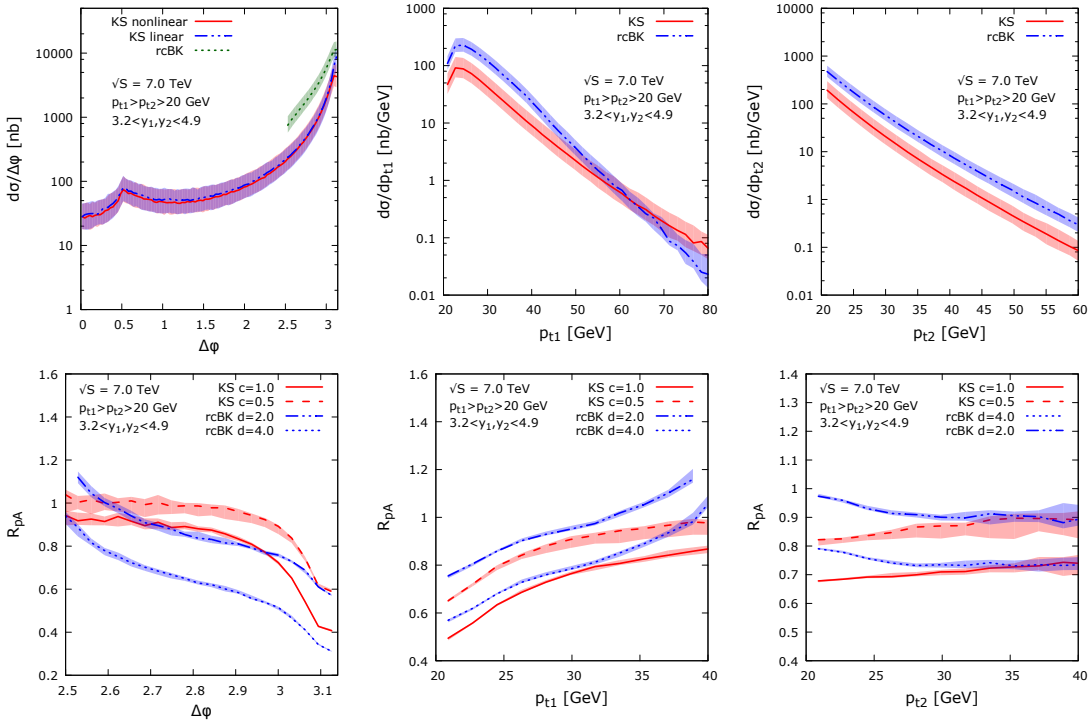

Fig. 8.1: The results for forward-forward dijet production within HEF framework with two models for UGDs described in the text. The uncertainty bands come from the scale choice uncertainty. We refer to [114] for further details.

In order to see an impact of possible upgrades of the LHC on our observables, and for the special purposes of this note, the calculation for a potential extension of the CASTOR detector, which would allow for jet reconstruction [120], is extended. We have assumed that the reconstruction of the jets is possible for $5\,\mathrm{GeV} < p_T < 30\,\mathrm{GeV}$ using anti-k_T algorithm with $R = 0.7$. We refer to this scenario as the very-forward case. The calculations were made using `LxJet` program [121] with the KS UGDs for p+p and p+A collisions. We present the results in Fig. 8.2. We see significant difference between the non-linear evolution of UGDs and the scenario where the non-linear term is removed from the equation. Saturation effects are very strong, as is also evident from the nuclear modification ratios. The values of x probed here lie between 10^{-5} and 10^{-6}.

There is another interesting scenario with an extension of the CASTOR detector. We may look also at the case where there is one (leading) jet with $p_{T1} > 20\,\mathrm{GeV}$ within rapidity interval $-4.9 < y_1 < -3.2$ and the second (soft) jet with $p_{T2} > 5\,\mathrm{GeV}$ is within $-6.6 < y_2 < -5.2$. This gives an opportunity to study UGDs at low x for large gluon off-shellness. The results prepared are shown in Fig. 8.3. An interesting feature is a relative flatness of the decorrelation distribution, meaning that one probes large transversal momenta of gluon density. A similar scan is also possible using three jet events, as explained below.

8.3.2 Trijet production at forward-central and purely forward rapidities

Three jets observables may give an additional insight into the UGDs due to possible additional cuts one may apply to scan certain regions of the phase space. For instance, one may consider the case where one of the jets is in the forward rapidity region while the two hardest jets are in the central rapidity region. In addition, we may restrict the two central jets to balance each

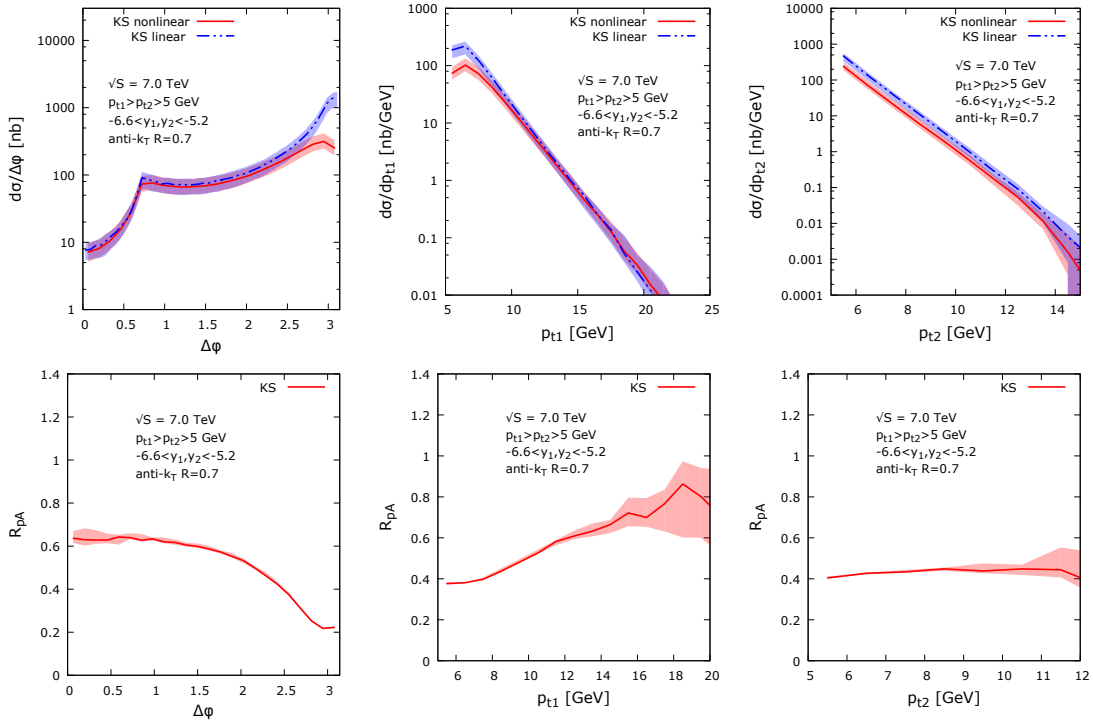

Fig. 8.2: The results for very-forward dijet production in a potential extension of the CASTOR detector [120]. The uncertainty bands come from the energy scale uncertainty (the scale enters the HEF factorization formula (8.6)).

other on the transverse plane within a cut on the sum of the two transverse momenta, D_{cut}. This allows to access the UGD at large transverse momentum almost directly by the third forward jet.

In Fig. 8.4 (left) the decorrelations are shown between the hardest and the softest jet [113] for the LHC setup available at present. The calculations were made for KS UGDs and for p+p and p+A collisions. The cuts applied are listed in the plots. An important feature of the result is a relative flatness of the distribution compared to calculations without the back-to-back cut on the central jets (right of Fig. 8.4). Such a distribution is very sensitive to the transversal degrees of freedom of UGDs.

Another interesting three jets observable is conveyed by configuration where all three jets are produced in the forward direction. This kinematical setup is similar to forward dijet case, i.e. the events are highly asymmetric, but the allowed phase space is larger. Particularly interesting is again the cross section for decorrelations measured as a dependence of the cross section on an angle between softest jet and hardest jet ϕ_{13}. We see on Fig. 8.5 (left) that this quantity is sensitive for large ϕ_{13} to gluon saturation, since we observe a depletion of the plateau as we move from KS linear to KS non-linear and KS for lead. This is also reflected in the nuclear modification ratio 8.5 (right).

8.3.3 Forward jet production - measurements at very large rapidities

The very forward calorimeter of CMS (CASTOR) in the acceptance region of $-6.6 < \eta < -5.2$ allows to access very small and very large x values in jet measurements (see Fig 8.1c). CASTOR has a 16-fold ϕ segmentation and a 14-fold longitudinal segmentation. While the longitudinal

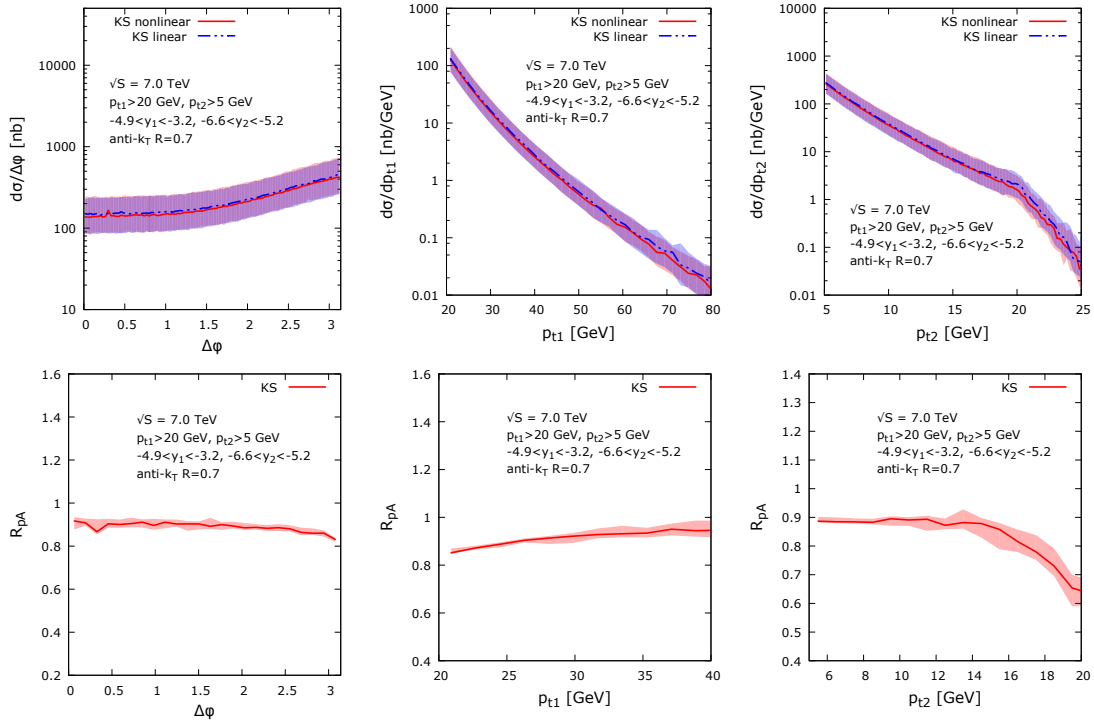

Fig. 8.3: The result for forward-very-forward scenario, i.e. the softest jet of the dijet system is in the CASTOR detector, while the harder is around HF detector. The uncertainty bands come from the scale choice uncertainty.

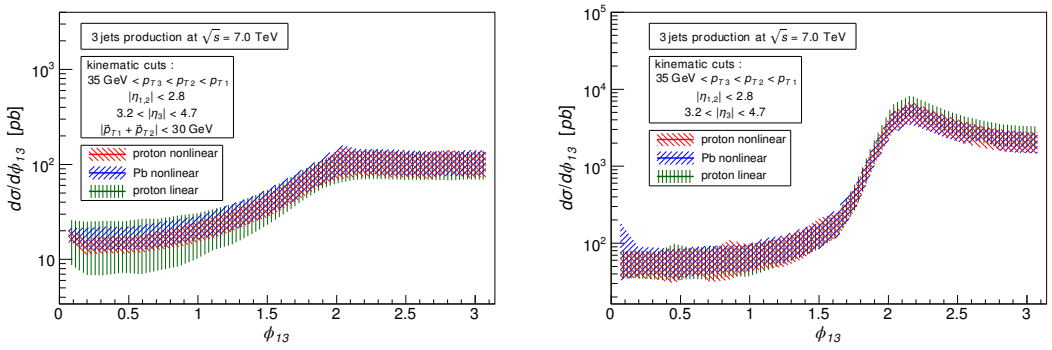

Fig. 8.4: Azimuthal decorrelations for forward-central three jet production. Two hardest jets are in the central detector, while the softest jet is in the forward region. For the left plot an additional cut is applied on the central jets, namely we require that they should almost balance each other. This flattens the distribution (left) comparing to the case without this cut (right) and makes it sensitive to UGDs for large transverse momenta. For more details refer to [113].

energy deposits are grouped together to yield a tower response, it was shown that an anti-kt algorithm with a radius parameter of 0.7 can reconstruct jets in CASTOR. Due to the missing η segmentation, all jets are reconstructed at a fixed pseudorapidity of 6.0. The p_T of these jets is within the lowest accessible at LHC and reaches up to only 6 GeV.

In Fig. 8.6 the cross section for di-jets with one jet with $p_T > 25$ GeV in the central region and another jet with $E > 500$ GeV in the CASTOR acceptance region is shown as predicted by different calculations. The predictions vary by more than factors of 10, so a measurement is

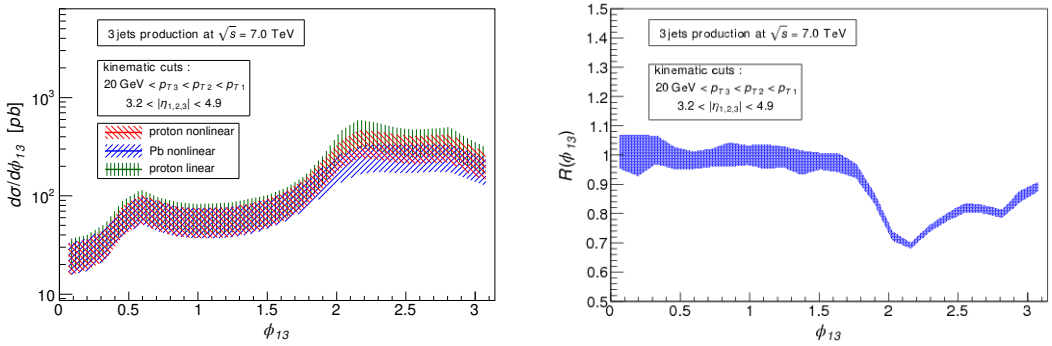

Fig. 8.5: Azimuthal decorrelations for forward-forward-forward three jet production. For large values of the azimuthal angle between the softest and the hardest jets we see significant differences between different evolution scenarios. For more details refer to [113].

needed to constrain the calculations.

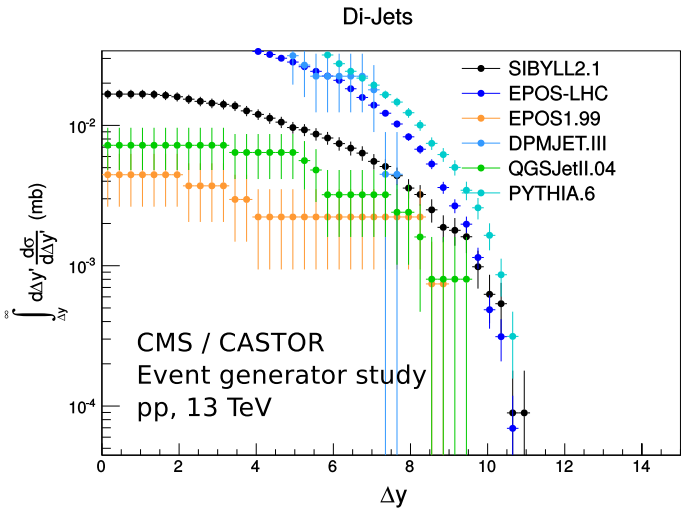

Fig. 8.6: Integrated cross sections for di-jets pairs with one jet reconstructed in CASTOR with E > 500 GeV and the other in the central part of CMS with $p_T > 25$ GeV. Very large model differences are visible as a function of di-jet opening angle Delta y.

Due to its 14-fold longitudinal segmentation, CASTOR is a very good detector to distinguish electromagnetic from hadronic energy deposits. Furthermore, when CASTOR is combined with the T2 tracking detector, charged electrons can be distinguished from neutral photons. First studies of isolated electrons with CASTOR and T2 have shown some of the potential behind this [122]. Given improved techniques to handle the underlying event subtraction in pp runs at 13 TeV, the detection of very forward electrons at $-6.6 < \eta < -5.2$ with fully resolved position (T2) and energy (CASTOR) has the potential to enhance the reach of Drell Yan and Z-production studies towards much smaller values of x compared to what is possible to study so far at LHC. For this purpose we implement a dedicated isolated electron trigger in CASTOR on L1 hardware trigger level, which can be used on HLT level to select the relevant event topologies. Given this trigger it will require 1 nb^{-1} in order to study very forward electrons up to 500 GeV and 100 nb^{-1} to extend this range towards 1 TeV. Since the current proposal assumes to analyse isolated electrons, small values of average pileup are needed. This is also mandatory if

a dedicated isolated electron trigger should be used. The pileup should not exceed one for this reason.

The first measurement of jets in the CASTOR calorimeter based on a sample of pp collisions at $\sqrt{s} = 7$ TeV is presented in [123]. Events are selected with at least one track-jet in the central CMS detector, with transverse momentum $p_T > 1$ GeV and $|\eta| < 2$. Track-jets are reconstructed with the anti-k_T jet clustering algorithm [124] with a distance parameter $R = 0.5$. The number of selected events in the minimum-bias sample is 4.6 million. The event selection is similar to that described in [125].

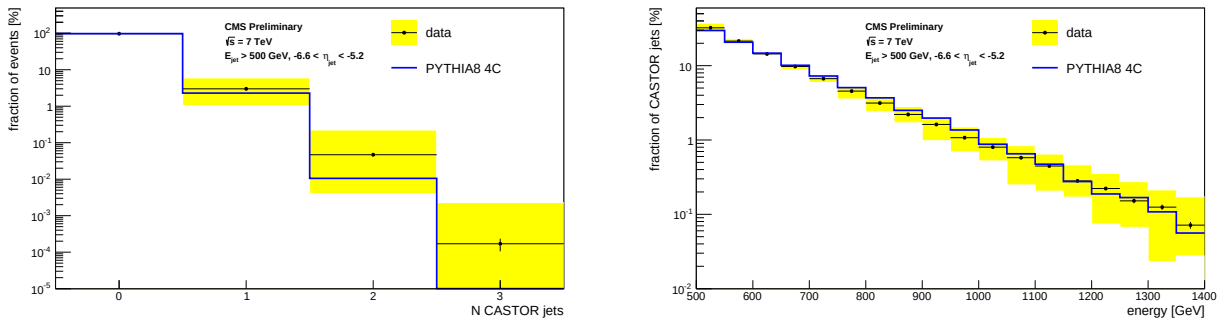

Fig. 8.7: Normalised distributions of the jet multiplicity and jet energy spectrum for jets reconstructed in CASTOR with an energy $E > 500$ GeV. The data are compared to the predictions of the MC event generator PYTHIA8-4C. The error band represents the 22% uncertainty on the CASTOR calorimeter absolute energy scale.

The normalised distributions of the jet multiplicity and jet energy spectrum are shown in figure 8.7 for jets reconstructed in $-6.6 < \eta < -5.2$ and $E > 500$ GeV. The data are compared to the predictions of the Monte Carlo (MC) event generator PYTHIA8 [126] with tune 4C [127]. The error band represents the 22% uncertainty on the absolute energy scale of the CASTOR calorimeter.

The energy weighted azimuthal ϕ profile [123] for jets reconstructed in CASTOR with an energy $E > 500$ GeV is presented in figure 8.8. The peak around the jet axis as well as the width of the distribution are found to reproduce the characteristics of the jet profile as determined in a generator level study.

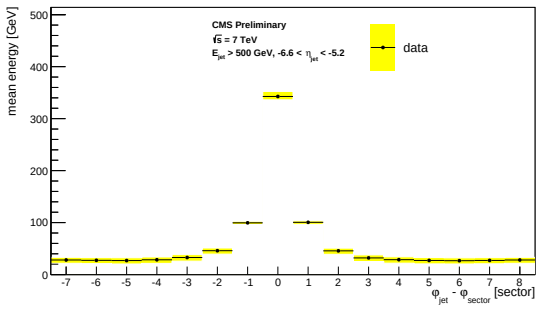

Fig. 8.8: Energy weighted azimuthal ϕ profile for jets reconstructed in CASTOR with an energy $E > 500$ GeV. The error band represents the 22% uncertainty on the CASTOR calorimeter absolute energy scale.

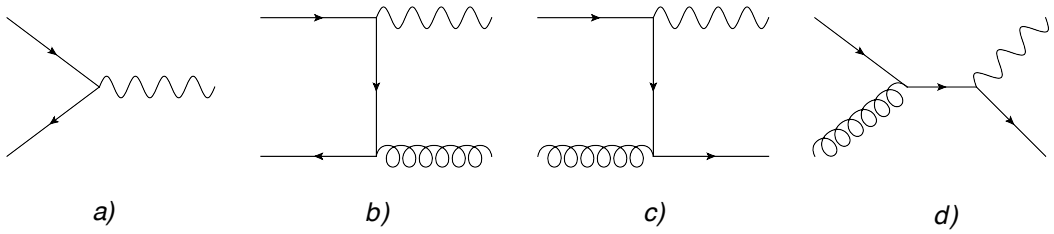

Fig. 8.1: The Drell-Yan production in the leading (a) and next-no-leading (b-d) order approximation. The diagrams c) and d) are enhanced in the small-x limit due to a strongly rising gluon distribution.

8.4 Saturation physics in p+p and p+A collisions

8.4.1 Introductory remarks

Saturation has attracted much interest, in connection with the behavior of the gluon density of the proton at small x and low Q^2, and for the understanding of the initial states in heavy ion collisions. First evidence for saturation has been found in electron-proton scattering at HERA (e.g. geometrical scaling), and in heavy ion collisions at RHIC and in the first run of LHC (e.g. two-particle correlations, nuclear modification factor). In pp collisions at the LHC, the best place to look for the small-x behavior of parton densities are Drell-Yan production processes in the forward direction; therefore, this also one of the most promising regions where saturation can be looked for.

8.4.2 Forward Drell-Yan production - collinear vs small-x approach

8.4.2.1 Drell-Yan cross section in the collinear approach

The Drell-Yan production is a unique process which offers high sensitivity to the parton distribution functions in hadrons. In the leading order (LO) approximation, the Drell-Yan lepton pair of invariant mass ($M > 1$ GeV) is produced by annihilation of two quarks from the colliding hadrons, see the diagram (a) in Fig. 8.1:

$$q_f \bar{q}_f \to \gamma^* \to l^+ l^- .$$

The cross section in this approximation is given by the quark/antiquark distributions in the colliding hadrons taken at the scale M^2:

$$\frac{d^2\sigma^{LO}}{dM^2 dx_F} = \frac{4\pi\alpha_{em}^2}{3N_c M^4}\frac{x_1 x_2}{x_1+x_2}\sum_f e_f^2 \left\{ q_f(x_1,M^2)\,\bar{q}_f(x_2,M^2) + \bar{q}_f(x_1,M^2)\,q_f(x_2,M^2) \right\}, \qquad (8.7)$$

where α_{em} is the fine structure coupling constant, N_c is the number of quark colors and $q_f, \bar{q}_f$ are quark/antiquark distributions. The quark momentum fractions, x_1 and x_2, are determined by the lepton pair kinematics:

$$x_1 = \frac{1}{2}\left(\sqrt{x_F^2 + 4\frac{M^2}{s}} + x_F\right), \qquad x_2 = \frac{1}{2}\left(\sqrt{x_F^2 + 4\frac{M^2}{s}} - x_F\right), \qquad (8.8)$$

where $x_F = x_1 - x_2$ is the Feynman variable of the lepton pair and s is the hadronic center-of-mass energy squared.

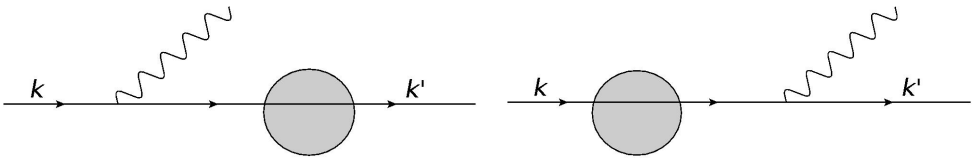

Fig. 8.2: The Drell-Yan process in the target rest frame point of view.

In the next-to-leading (NLO) approximation additional emissions of a parton into the final state has to be taken into account, see the diagrams (b-d) in Fig. 8.1. Because of the emission, one of the quarks entering the photon vertex carries a fraction $z < 1$ of the incoming parton momentum. Thus, the incoming parton momentum fractions take now the form:

$$x_1 = \frac{1}{2}\left(\sqrt{x_F^2 + 4\frac{M^2}{zs}} + x_F\right), \qquad x_2 = \frac{1}{2}\left(\sqrt{x_F^2 + 4\frac{M^2}{zs}} - x_F\right). \tag{8.9}$$

The NLO corrections to the Drell-Yan cross section are proportional to the strong coupling α_s and are given by [128–130]

$$\begin{aligned}\frac{d^2\sigma^{NLO}}{dM^2 dx_F} &= \frac{4\pi\alpha_{em}^2}{3N_c M^4}\frac{\alpha_s(M^2)}{2\pi}\int_{z_{min}}^1 dz \frac{x_1 x_2}{x_1 + x_2}\sum_f e_f^2 \Big\{ q_f(x_1, M^2)\,\bar{q}_f(x_2, M^2) D_q(z) + g(x_1, M^2) \\ &\times \left[q_f(x_1, M^2) + \bar{q}_f(x_2, M^2)\right] D_g(z) + (x_1 \leftrightarrow x_2)\Big\},\end{aligned} \tag{8.10}$$

where the coefficient functions $D_{q,g}$ are calculated perturbatively and g is a gluon distribution. Thus, up to the order α_s, the Drell-Yan cross section in the collinear approach is the sum of the leading and next-to-leading contributions:

$$\frac{d^2\sigma^{col}}{dM^2 dx_F} = \frac{d^2\sigma^{LO}}{dM^2 dx_F} + \frac{d^2\sigma^{NLO}}{dM^2 dx_F}. \tag{8.11}$$

8.4.2.2 Drell-Yan process in the small-x limit

In the small-x limit, the dilepton mass is much smaller than the center-of-mass energy of the colliding hadrons, $M_{\ell^+\ell^-} << \sqrt{s}$. In this case, a momentum fraction of one of the incoming partons is very small, e.g.:

$$x_1 \sim 1, \qquad x_2 = \frac{M_{\ell^+\ell^-}^2}{s x_1}. \tag{8.12}$$

If the small momentum fraction is carried by a gluon, the fast incoming quark probes high gluon density system in which saturation effects may occur.

The target rest frame point of view is particularly attractive for physical interpretation of these effects. In this frame, the fast incoming quark interacts with the target gluon field before or after scattering, emitting a virtual photon. This is shown by diagrams in Figs. 8.2. The photon then decays producing a lepton pair which moves into the region of forward rapidity.

The cross section for radiation of a photon with the momentum fraction z of the fast quark is given by [131]

$$\sigma(qp \to \gamma^* X) = \int d^2 r\, W(z, r, M^2)\, \sigma_{qq}(x_2, zr), \tag{8.13}$$

where r is the photon-quark transverse separation and W is the photon wave function squared, computed perturbatively in [132, 133]. The dipole cross section σ_{qq} [134] is known from DIS scattering at small Bjorken-x and describes the interaction of the incoming quark with strong gluon fields of the target hadron. The dipole form comes form the interference of the two shown amplitudes in the formula for the cross section. The final form of the Drell-Yan cross section in the dipole framework is given by the equation

$$\frac{d^2\sigma^{DY}}{dM^2\,dx_F} = \frac{\alpha_{em}}{6\pi M^2}\frac{1}{x_1+x_2}\int_{x_1}^{1}\frac{dz}{z}F_2\left(\frac{x_1}{z},M^2\right)\sigma(qp\to\gamma^* X), \tag{8.14}$$

where F_2 is the proton structure function. We will compare predictions given by this formula with those given by the collinear factorization approach (8.11). Before presenting our results, we will describe the dipole cross sections used in the analysis.

The following three models of the dipole cross sections σ_{qq} with gluon saturation effects have been used in the calculations:

– Golec-Biernat–Wüsthoff (GBW) [135, 136]

$$\sigma_{qq}(x,r)=\sigma_0\{1-\exp(-r^2Q_s^2(x)/4)\}, \tag{8.15}$$

– Bartels–Golec–Kowalski–Sapeta (BGKS) [137, 138]

$$\sigma_{qq}(x,r)=\sigma_0\Big\{1-\exp(-\pi^2r^2\alpha_s(\mu^2)xg(x,\mu^2)/3\sigma_0)\Big\}, \tag{8.16}$$

– Color Glass Condensate (CGC) [139, 140]

$$\sigma_{qq}(x,r)=\sigma_0\times\begin{cases} N_0\left(\frac{rQ_s}{2}\right)^{2(\gamma_s+\frac{1}{\kappa\lambda y}\ln\frac{2}{rQ_s})} & : \ rQ_s\le 2 \\ 1-e^{-A\ln^2(BrQ_s)} & : \ rQ_s>2 \end{cases} \tag{8.17}$$

In the formulas, Q_s is the saturation scale: $Q_s=Q_0x^{-\lambda}$. The parameters in the above formulas are determined from the analysis of the HERA data on deep inelastic scattering.

8.4.2.3 Results

In Fig. 8.3-left we present a comparison of the results from the collinear factorization (8.11) and the dipole approach (8.14) formulas with the existing data from the Fermilab E772 Collaboration [141]. We use the NLO CTEQ6.6M parton distributions [142] for the collinear factorization and the GBW parametrization [135, 136] for the dipole cross section. It is clearly seen that for the different values of the Feynman variable x_F, the E772 data are above the results from both approaches.

Fig. 8.3-right presents predictions for the Drell-Yan cross section as a function of the center-of-mass energy $\sqrt{s}$ at fixed $x_F=0.15$ for three values of the lepton pair mass $M=6,8,10$ GeV. At the LHC energy, saturation effects in the dipole model give results which are significantly below the collinear factorization predictions. The same results are shown using the linear scale in Fig. 8.4. The CTEQ6.6M and MSTW08 parton distributions, and the GBW and BGKS [137, 138] dipole models are used in these plots. The CGC model (8.17) gives results which are very close to the GBW lines.

Thus, the predictions from the dipole approach with gluon saturation give a significant suppression of the Drell-Yan production cross section in comparison to the collinear factorization results.

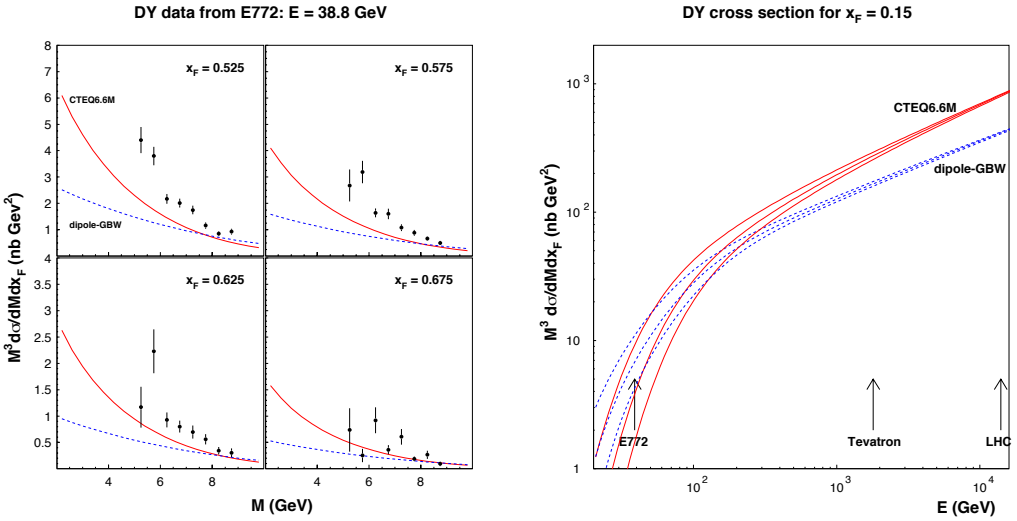

Fig. 8.3: Left: The Drell-Yan cross section in the collinear and dipole formulas against the E772 Collaboration data. Right: predictions for the LHC energies and three values of the lepton pair mass $M = 6, 8, 10$ GeV.

8.4.3 Forward Drell-Yan production - Further prospects in the collinear approach

Drell–Yan process is one of the standard observables used in parton distribution function determination. It has been measured in LHC at Atlas [143–145], CMS [146–149], and LHCb [150–152]. With this new very high energy data, new information about the parton distribution can be obtained. In particular, Drell–Yan is most sensitive to quark and antiquark parton distributions. In fact, most of the major parton distribution function parametrizations are already taking steps to include these data in their analyses.

In collinear factorization, one can schematically write the Drell–Yan cross section as (cf.(8.10)):

$$\frac{d\sigma}{d^3p} = \int dx_1 dx_2 \, \mathrm{PDF}(x_1, \mu_F) \, |\mathscr{M}(p; \mu_F, \mu_R)|^2 \, \mathrm{PDF}(x_2, \mu_F). \tag{8.18}$$

In the above equation we have the factorization scale μ_F, renormalization scale μ_R, and a sum over the different flavours of PDF is implied. The partons that take part in the process carry longitudinal momentum fraction given by:

$$x_{1,2} = \frac{m_{\mathrm{hard}}}{\sqrt{s}} \exp(\pm y) \tag{8.19}$$

where m_{hard} is the subprocess mass and y is its rapidity (at leading order $m_{\mathrm{hard}} = M$, i.e., the dilepton mass). The centre of mass energy is given by $\sqrt{s}$.

At forward rapidities, say, $y = 4$, for LHC compatible energy and dilepton mass of 5 GeV, one would probe the PDFs at $x_1 \approx 10^{-2}$ and $x_2 \approx 10^{-5}$, an uncharted region in x_2. Unfortunately, for such a small x the parton distributions are very sensitive to the factorization scale. Another point is that one cannot neglect the possibility that some saturation and multiple parton interactions take part in the process.

The factorization scale uncertainty is related with many gluon emissions during the evolution. The $g \to g$ DGLAP splitting function:

$$P_{g\to g}(z < 1) = 2C_A \left[\frac{1-z}{z} + \frac{z}{1-z} + z(1-z) \right] \tag{8.20}$$

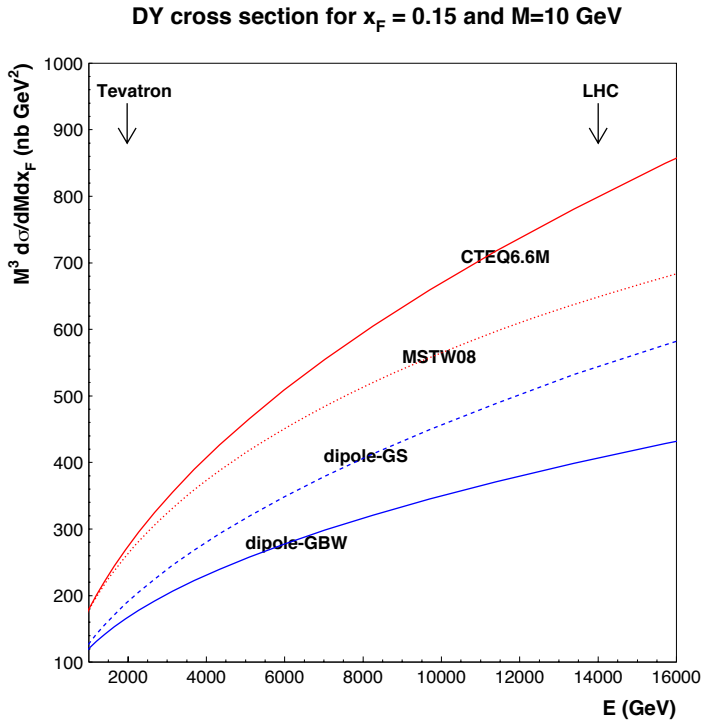

Fig. 8.4: The Drell-Yan cross section from the collinear and dipole approaches for fixed $x_F = 0.15$ and lepton pair mass $M = 10$ GeV.

has a divergence $1/z$. Therefore, for small x, when the factorization scale increases, many more gluons can be emitted in the DGLAP ladder, rapidly increasing the cross section. Ideally this would be compensated by the matrix element, however at next-to-leading order the matrix element can compensate only one gluon emission. In the view of this it is possible to understand the huge factorization scale uncertainty observed.

In Ref. [153] a method to reduce the factorization scale uncertainty was developed. The idea was to fix the factorization scale of the LO contribution based on the known NLO matrix element, determining the optimal scale at which all NLO contribution is already included in the DGLAP ladder at small x. The result of such calculation pointed that $\mu_F = 1.4M$ is the optimal scale. This choice was shown to greatly reduce the factorization scale dependence of the cross section, contributing for a better convergence of the perturbative series. Given that, observations of this process at the LHC can make a direct measurement of parton distribution functions (PDFs) in the low x region, $x < 10^{-4}$.

Unfortunately, LHC experiments do not have very good precision for such a small dilepton mass. Therefore one would like to probe a little larger dilepton mass ($M \approx 20$ GeV) at forward rapidities ($y > 3$). To do so while still probing PDFs in the important low-scale, low-x domain, a cutoff in the dilepton transverse momentum can be introduced [154]. The act of introducing a cutoff in the matrix element has to be matched by the inclusion of corresponding Sudakov form factors in the parton distribution evolution, as detailed in Ref. [154]. Taken into account that, the calculation of the optimal scale to reduce factorization scale uncertainty was redone, now with the cutoff. Therefore, a LHC measurement of such distribution is a direct measurement of an uncharted region of the PDFs.

While successful, collinear factorization for the Drell–Yan process only takes into ac-

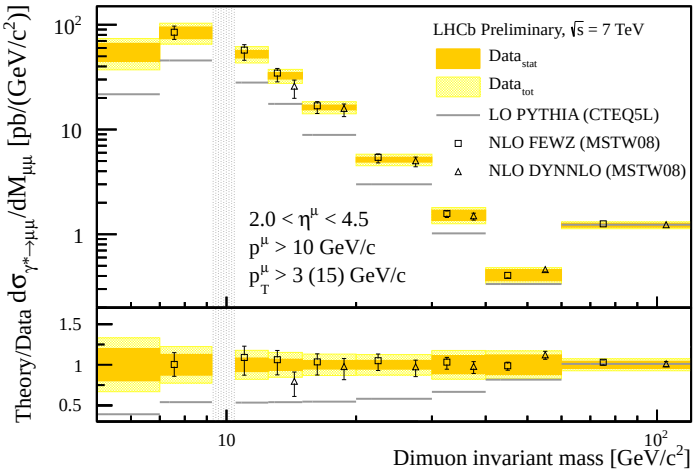

Fig. 8.5: Differential cross-section for $\gamma' \to \mu\mu$ as a function of $M_{\mu\mu}$. The dark shaded (orange) bands correspond to the statistical uncertainties, the light shaded (yellow) band to the statistical and systematic uncertainties added in quadrature. Superimposed are the PYTHIA predictions and the NLO predictions from FEWZ and DYNNLO; they are displaced horizontally for presentation. The shaded vertical band corresponds to the mass region of the Îě which is not included in the measurement. The uncertainties of the NLO predictions contain the PDF uncertainties evaluated at the 68% confidence level and the theoretical errors added in quadrature. The two bins with $M_{\mu\mu} > 40$ GeV/c have a cut of $p_{\mu T} > 15$ GeV/c for the data and the predictions. The lower plot shows the ratio of the predictions or the uncertainties to the data.

count the leading twist terms. Using the dipole formulation in Ref. [155], it was possible to include higher twist effects, as well as saturation effects. Saturation is expected to happen at sufficiently high energies, however the exact line where it becomes indispensable is not known. In Ref. [155] it was shown that, at forward rapidities, leading twist is a good approximation as long as the dilepton masses are larger than $M \approx 6$ GeV. For lower masses, the full twist resummation is necessary. Therefore, the observation of such low mass dileptons could test the boundaries of saturation and higher twist effects.

LHCb [156] has measured the Drell Yan cross-section at $\sqrt{s} = 7$ TeV differentially as functions of rapidity and mass down to 5 GeV with a small data sample corresponding to an integrated luminosity of just 37pb-1. Within the limited statistical precision consistency is seen with both FEWZ and Pythia predictions (Fig. 8.5). An analysis of the full Run 1 dataset of 3fb-1 will allow significant improvements to the measurement precision and could allow discrimination between theoretical models that include higher order twist or saturation effects.

From the theoretical point of view, everything that was done for pp collisions can be done as well for heavy ion collisions. In particular, for pA collisions there is a good possibility of analyzing nuclear parton distributions when one can disregard final state effects. One could study the same problems as before, except that saturation, multiple parton scattering and higher twist effects are much more important in the pA setup. In this case, backward and forward rapidities are different, but both are interesting. For backward rapidities, one is probing the nucleus at high x, but higher twist effects from the interaction between multiple nucleons should be present. For forward rapidities, one has small x in the nucleus and saturation effects should be important, on top of the fact that these nuclear distributions are now well known in this region. Higher twist effects should play a role as well, since for small x the effect of nuclear

shadowing is related to multiple nucleon interactions.

As discussed above, the LHC can contribute to the determination of the parton distribution functions in the low x and low scale region. Of course one could imagine an upgrade in the detectors to fully account for small mass dileptons in a run with low luminosity. However, it would be much easier to keep the experiments as they are and just have some analysis for more exclusive observables. Instead of only working with the integrated dilepton distribution, one could do the necessary cuts to guarantee that the partons are probed at small x. In this context, LHCb has a very promising potential with its geometry that covers forward rapidities.

8.4.4 Forward Drell-Yan production - Further prospects in the small-x approach

The current LHC detector configurations can explore small-x hard phenomena with nuclei and nucleons at photon-nucleon center-of-mass energies TeV scale, extending the x range of HERA by a factor of ten [157]. The LHC is in the kinematic range where nonlinear effects are several times larger than at HERA. In these regions, dileptons production in hadronic collisions (Drell-Yan process) can be used to investigate the limit of high partonic density, since this process probes the gluon distribution through QCD Compton process. In particular, the Drell-Yan transverse momentum (p_T) distribution can be extended to be sensitive to saturation effects. The Drell-Yan (DY) process in the kinematical region where the dilepton mass M is small compared to the center of mass energy $\sqrt{s}$ is of similar theoretical interest as deep-inelastic scattering (DIS) at low Bjorken-x. Both processes probe the target at high gluon density where one expects to find new physics. In contrast to DIS, where only the total cross section can be measured, there is a variety of observables which can be measured in the DY process, such as the transverse momentum distribution or the angular distribution of the lepton pair.

The Drell-Yan (DY) process cross sections have been proven to still fulfill the factorization property and are finite to first orders in perturbation theory at sufficiently large transverse momenta, p_T. The conventional factorization approaches to the DY process give divergent results at $p_T \to 0$, but the low p_T regions are treated in an extensive program of research. (see Ref. [158] and references therein). The differential cross section in the region $p_T \geq M_{\ell\ell}/2$ is driven by subprocesses initiated by incident gluons, and massive lepton-pair differential cross sections can be used to constrain the gluon density [159]. The DY cross section with large values of dileptons transverse momentum is related to deep-inelastic-lepton scattering (DIS), prompt photon production and jet production as an important probe of short-distance hadron dynamics. The production of dileptons in DY process in nuclear targets can help to constrain the parton distribution functions (PDFs) in the nucleons and are colorless probes of the dynamics of quarks and gluons [160]. Namely, they escape through the colored medium of the high-energy collision. The dileptons interact with the medium only electromagnetically, thus they can be a powerful probe of the initial state of matter created in heavy ion collisions. Refs. [161, 162] show that those electromagnetic probes are crucial to determine the dominant physics in the forward region at RHIC and at the LHC.

Direct (prompt) photon production and Drell-Yan dilepton pair production processes can be described within the same color dipole approach without any free parameters [163]. Such a formalism, developed in [164] for the case of the total and diffractive cross sections, can be also applied to radiation [165, 166]. In the target rest frame, the DY process looks like a bremsstrahlung [131] of a massive photon from an incoming quark. The photons can be emitted before or after a quark to be scattered on a proton. The cross section can be expressed through the more elementary cross section σ_{dip} of the interaction of a $Q\bar{Q}$ dipole [131], although no real quark dipole participates in the process of electromagnetic bremsstrahlung by a quark. The relation between this formalism and the usual collinear pQCD factorization has

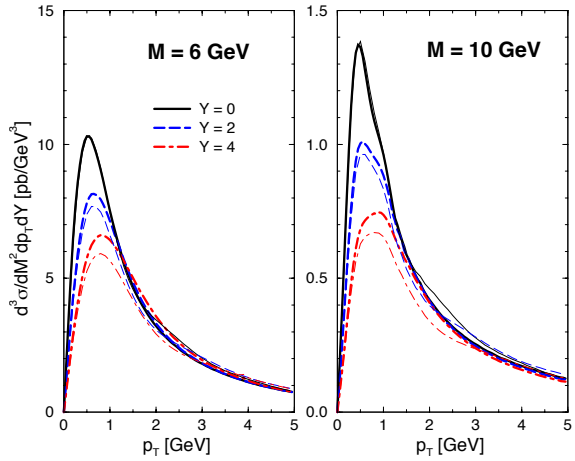

Fig. 8.6: Low mass DY differential cross sections, $d^3\sigma/dM^2dydp_T$, as a function of dilepton transverse momentum, p_T, at energy of $\sqrt{s} = 7$ TeV. The plots are shown for fixed dilepton mass ($M = 6$ and 10 GeV) and distinct lepton pair rapidities ($y = 0, 2, 4$). The results are presented using the GBW dipole cross section (bold curves) and the CGC dipole cross section (thin curves).

been studied in details in Ref. [167]. The dipole formalism offers an easy way to calculate the transverse momentum distribution in DY processes even in the low-p_T region. This contribution investigates the low mass DY cross section at the LHC energies using color dipole approach, discussing several phenomenological aspects. The main focus is at forward rapidities at the energy available at the LHC.

The Fig. 8.6, presents the results for the differential cross section, $d^3\sigma/dM^2dydp_T$ (in units of pb), as a function of the dilepton transverse momentum p_T. The bold curves present the predictions using the GBW dipole cross section and the thin curves present the predictions using the CGC dipole cross section. The hard scale considered is $\mu^2 = (1-x_1)M^2 + p_T^2$. The p_T-spectrum is quite sensitive to the particular model of dipole cross section (specially at large transverse momentum) as it depends on the behavior of effective anomalous dimension as discussed in the previous section. The left panel shows the case for fixed invariant mass $M = 6$ GeV and for sample values of dilepton rapidity including central and forward rapidities, i.e. $y = 0, 2$ and 4, respectively. The same notations hold for the right panel, where now the invariant mass is $M = 10$ GeV. As expected, the large rapidity cases give smaller cross sections and the peak on the distributions is shifted to larger values on transverse momentum. In the kinematical situation investigated here the peak is located at momentum around $p_T \approx 1$ GeV.

The Fig. 8.7 presents the invariant mass distribution at midrapidities considering the GBW model (dot-dashed line) and the phenomenological saturation model, labeled here CGC (solid line), which involves a running anomalous dimension. In the large p_T region occurs the main deviation between these two models, which gives distinct overall normalizations for the dilepton invariant mass distribution. The considered cuts are presented by the ATLAS analysis [168] for low mass Drell-Yan di-muon process. The selection cuts on that analysis at energy of $\sqrt{s} = 7$ TeV and integrated luminosity of 36 pb^{-1} were low muon transverse momentum, $p_T^\mu > 6$ GeV and low di-muon mass region $12 < M_{\ell\ell} < 66$ GeV. Here, we consider the integration over the boson rapidity in the range $|y_{\ell\ell}| < 2.5$ and dilepton transverse momentum $p_T \geq 1$ GeV. Distinct p_T cuts will lead to a different overall normalization for the invariant mass distribution. At this stage we did not impose the selected cuts on individual muons as done by ATLAS analysis. The results presented here are somewhat consistent with the extrapolated Born level differential

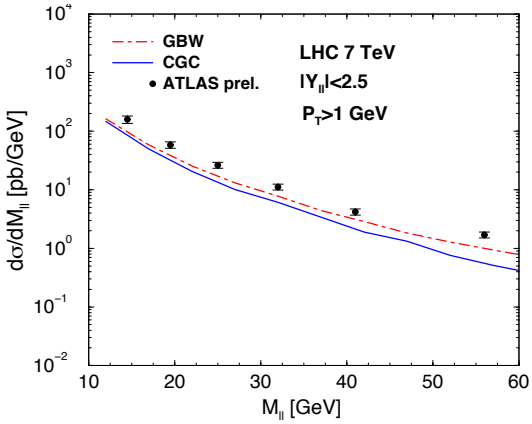

Fig. 8.7: Invariant mass distribution in the range $12 < M_{\ell\ell} < 60$ GeV. The imposed cuts at energy of $\sqrt{s} = 7$ TeV are lepton pair rapidities $|y_{\ell\ell}| < 2.5$ and dilepton transverse momentum $p_T \geq 1$ GeV. Preliminary ATLAS data [168] are shown for sake of comparison.

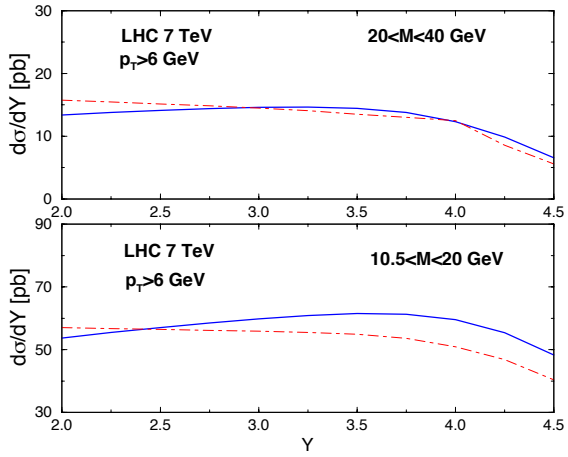

Fig. 8.8: The dilepton rapidity distribution at $\sqrt{s} = 7$ TeV imposing the cut on dimuon transverse momentum $p_T > 6$ GeV and two invariant mass regions: (upper plot) $20 \leq M_{\ell\ell} \leq 40$ GeV and (lower plot) $10.5 \leq M_{\ell\ell} \leq 20$ GeV.

cross section using the symmetric analysis. For sake of comparison, we include the preliminary data [168] in Fig. 8.7 (filled circles).

The rapidity distribution, $d\sigma/dy$, is computed for the interval $2 < y < 4.5$ in Fig. 8.8. The phenomenological models considered here are the same as the previous plot and the same notation was used. The hard scale, in this case, is $\mu^2 = \frac{1}{2}[(1-x_1)M^2 + p_T^2]$. The distinct anomalous dimension in the models causes the deviations between the predictions using distinct models. The cut imposed for the dilepton transverse momentum is $p_T > 6$ GeV and two distinct intervals of invariant mass are considered. In the upper plot one has $20 \leq M_{\ell\ell} \leq 40$ GeV whereas in the lower plot one has $10.5 \leq M_{\ell\ell} \leq 20$ GeV. The cut motivation is the recent LHCb collaboration [156] measurement of low mass DY cross section. The measurement collected with an integrated luminosity of 37 pb^{-1} are for the di-muon final state having muons within pseudorapidities of 2 to 4.5, muon transverse momentum $p_T^\mu > 3$ GeV ($p_T^\mu > 15$ GeV for higher masses) in two distinct mass regions. In the forward rapidities considered here, the saturation scale is

in the interval $0.6 \leq \langle Q^2_{\rm sat} \rangle \leq 1.2$ GeV^2 for $\langle M_{\ell\ell} \rangle \simeq 15.25$ GeV. Slightly lower values are found also for higher mass $\langle M_{\ell\ell} \rangle \simeq 30$ GeV. Fig.8.9 (upper panel) shows the invariant cross section as a function of p_T at energy $\sqrt{s} = 39$ GeV. The experimental results from the E866 Collaboration [169] are also presented ($\langle x_F \rangle \simeq 0.63$ and $4.2 \leq M_{\mu^+\mu^-} \leq 5.2$ GeV). The bottom panel shows the differential cross section $d^2\sigma/dMdy$ (for $|y| < 1$) for the energy $\sqrt{s} = 1800$ GeV as a function of dilepton invariant mass. The data from CDF Collaboration [170] are included in the plot, considering also the large invariant masses data points. The solid curves refer to CGC and dot-dashed curves to GBW dipole cross section, respectively. The color dipole picture reasonably describes the cross section from low to high energies in the kinematical regions where it is expected to be valid. The approach is also somewhat consistent with calculations carried out in next-to-leading order QCD at both fixed target and collider energies [159].

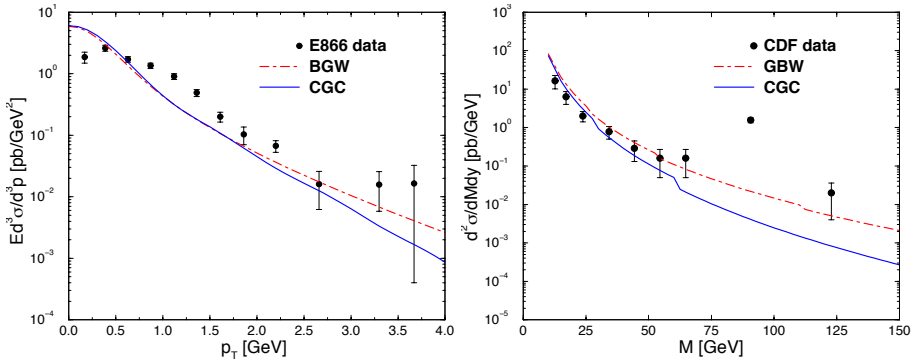

Fig. 8.9: The DY invariant cross section (left panel) at $\sqrt{s} = 39$ GeV as a function of p_T compared to the E866 Collaboration data [169]. In the left panel, the differential cross section $d^2\sigma/dMdy$ at $\sqrt{s} = 1800$ GeV as a function of invariant mass is presented and compared to the CDF Collaboration data [170].

As a summary, the main physics motivation for DY studies at the LHC are: extraction of PDFs in extended kinematics regions (high sensitivity to PDFs) and the saturation region study. This is due to the rather large cross sections (statistics) expected, the clear experimental signature and no uncertainties from fragmentation function. The low mass DY production can be addressed in the color dipole picture without any free parameters by using the dipole cross sections determined from current phenomenology in DIS. It has been shown before [171] that saturation physics is not directly relevant for RHIC at midrapidity, by considering in the kinematic range of data the saturation scale from the GBW model $Q^2_{sat} = (x_0/x_2)^\lambda = (x_0\sqrt{s}e^y p_T)^\lambda$, getting $0.1 \leq Q^2_{sat} \leq 0.5\ GeV^2$, which is very small compared to the transverse momenta $4 \leq p^2_T \leq 100\ GeV^2$. Therefore, saturation effects do not play an important role at RHIC midrapidity. The same statements about the role played by saturation effects remain valid for Tevatron at midrapidity, where the saturation scale is in the range $0.2 \leq Q^2_{sat} \leq 0.8\ GeV^2$. In the forward rapidities considered here, the saturation scale is in the interval $0.6 \leq Q^2_{sat} \leq 1.2\ GeV^2$ for $\langle M_{ll} \rangle \simeq 15.25\ GeV$. Thus, in the LHC this situation can be changed even at midrapidities as the saturation scale is enhanced by a sizable factor. So, the suppression of the DY cross section due to saturation effects can be large. The LHC opens a new kinematic regime at high energies, where QCD evolution leads to the fast growth of the gluon density. At these high densities it is possible that the novel phenomena related to the nonlinear dynamics of the gluon fields will occur, and DY production offers high sensitivity to the parton distribution in the hadron. Therefore, the LHC experiments will be important to study the production of low-mass Drell Yan with the goal to achieve higher PDF's precision.

8.4.5 Forward photon production and gluon saturation - theoretical overview and measurement proposal

8.4.5.1 Gluon saturation and photon production

Gluon saturation should affect the total multiplicity of produced particles in high-energy collisions. Furthermore, the predicted scaling properties of the momentum scales should lead to a behaviour called geometric scaling. Both the multiplicities and the scaling properties of particle distributions have been measured and compared to saturation models. The results appear to be consistent with expectations from the models, but unfortunately these observables are not specific enough to provide a proof for gluon saturation.

More discriminative power may come from more detailed studies of transverse momentum distributions and from two-particle angular correlations. The main interest lies here in the comparison of particle production in pp and p–A collisions, as saturation effects should be stronger for the higher gluon density in nuclei. Specifically, one expects that

- the nuclear modification factor

$$R_{pA} \equiv \frac{dN/dp_T\ (p+A)}{\langle N_{\mathrm{coll}} \rangle\, dN/dp_T\ (pp)} \tag{8.21}$$

  should show a suppression of particle production $R_{pA} < 1$ in a characteristic p_T range, and
- the jet-like peak at $\Delta\phi = 0$ usually observed in two-particle correlations in pp collisions should be modified (weakened and/or broadened) in nuclear collisions.

The interesting kinematic range is defined by the values of Bjorken x and the corresponding saturation scale Q_s. The relevant production processes will be affected by saturation when $Q < Q_s$, which calls for small to intermediate momentum probes. However, as one would like to use a calculable probe as a reference, this excludes too low momentum transfers – ideally one would want to study momentum ranges, where perturbative QCD should be applicable. To access small x, which for leading-order processes on the parton level can be approximated as $x \approx 2p_T \exp(-y)/\sqrt{s}$, particle production at large (i.e. *forward*) rapidities should be studied.

Transverse momentum spectra and angular correlations for neutral pions at forward rapidity have been studied in pp and d–A collisions at RHIC, and a suppression has been observed in the nuclear modification factor [172, 173] and a suppression and broadening in the angular correlation [174, 175]. However, the transverse momenta studied are still very small (on the order of 1 GeV or only slightly higher), a momentum range where particle production is anyhow not well understood. In addition, the relation between the kinematic variables in the final state are only weakly correlated to the parton kinematic parameters due to fragmentation and possibly other final state modifications of particle production.

Similar studies at LHC should allow to study both higher Q^2 and smaller x contributions, thus should be able to use well-defined particle production processes, while still being sensitive to saturation as the saturation scale should be much larger at the lower x values. First measurements of hadron production at forward rapidities have been performed at the LHC, but results are not conclusive. The production of ϕ mesons shows a strong suppression in p+A collisions compared to pp [176]. There is also a suppression of J/ψ production [177, 178], which is consistent with calculations using shadowing and final state energy loss. A CGC calculation predicts a stronger suppression than seen in the data, however this calculation has a number of uncertainties related to the coupling of the J/ψ to the gluon field, and it does not use a state-of-the-art CGC implementation. In general, also at LHC, hadron production will most likely not

provide an ideal probe because of final state modifications and their uncertainties, which will obscure the kinematics.

Probes, which directly access the parton kinematics, would be strongly preferable, which points to direct photons as an ideal probe. Direct photons have a number of advantages compared to other, in particular hadronic probes:

1. The production processes of direct photons are well understood theoretically.
2. The leading order process (q-g Compton scattering) is directly sensitive to the gluon density.
3. Fragmentation contributions, though significant at LHC, are less important than for hadrons, and can be suppressed by isolation cuts.
4. No other strong final state nuclear modification (like e.g. energy loss) is expected.

The advantage of photons with respect to the sensitivity to parton kinematics can be illustrated with the distribution of momentum fractions x_2 probed in the nucleus in p+A reactions at the LHC as displayed in Figure 8.10. The x_2 distribution for photon production with $4 < y < 5$ and $5 < p_T < 20\,\mathrm{GeV}/c$ is peaked between 10^{-5} and 10^{-4}, while the maximum contribution for pion production is generated from partons with x_2 about an order of magnitude larger. Thus, already the inclusive direct photon distribution has a clear sensitivity advantage, which can be further enhanced by applying isolation cuts on the photons, although the studies in Ref. [179] show that isolation may not be as effective as previously thought. Another advantage of photon

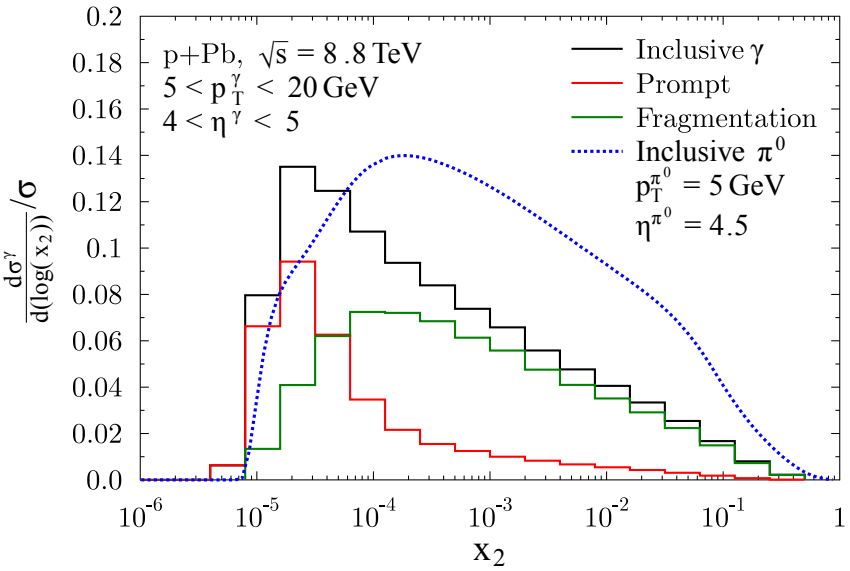

Fig. 8.10: Distribution of x_2 (momentum fraction of parton from the nucleus) probed in direct photon production at forward rapidity in p+Pb collisions at 8.8 TeV as calculated in JEPHOX using EPS09 structure functions in Ref. [179]. The different components of photon production are also shown separately. For comparison, the x_2 distribution for pion production of similar kinematics are included.

production is that the theoretical description also in the context of models of gluon saturation is very well understood. State-of-the-art calculations have shown a clear sensitivity to gluon saturation effects, as demonstrated in Figure 8.11, which shows the nuclear modifications factor R_{pA} of direct photons from the CGC calculation in Ref. [180] and from a pQCD calculation at NLO with EPS09 PDFs using JETPHOX. While the pQCD prediction shows only a slight

reduction of reaching $R_{pA} \approx 0.8$ at low p_T related to nuclear shadowing, the CGC calculation shows a strong suppression to $R_{pA} < 0.4$ for $p_T < 5\,\mathrm{GeV}/c$.

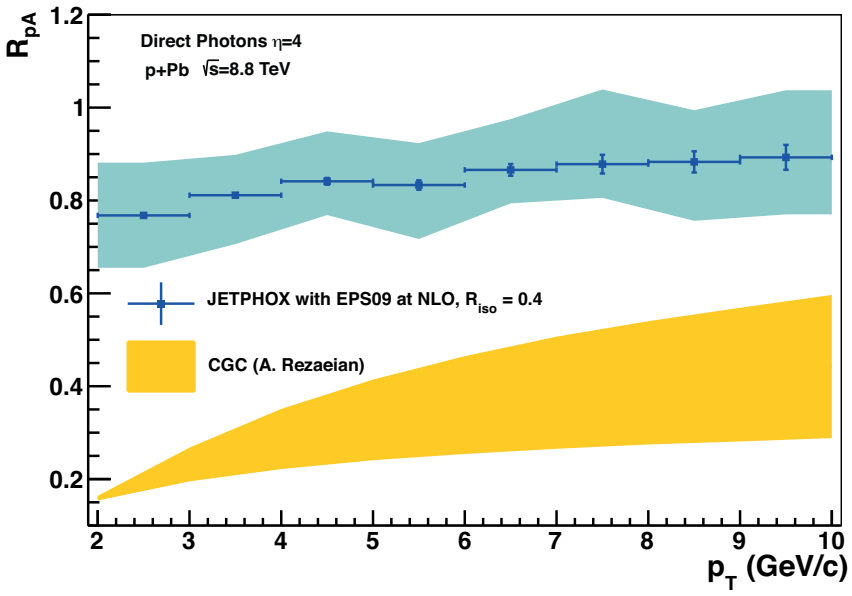

Fig. 8.11: Nuclear modification factor R_{pA} as a function of p_T for forward direct photon production. Shown are results of CGC calculations from Ref. [180] (orange) and from NLO pQCD calculations with JETPHOX (blue). The shaded bands show the systematic error estimates.

In principle the measurement of Drell-Yan production – i.e. virtual direct photons – would provide an alternative means of assessing low-x parton distributions with similar advantages, i.e. no final state modifications. The measurement is not as directly accessing the gluon distribution, however, as gluons play a role only via second order diagrams, or in the quark/antiquark PDFs via DGLAP evolution. It may be an additional complication for the interpretation to rely heavily on DGLAP evolution in theoretical predictions – finally a search for gluon saturation effects should *challenge* DGLAP evolution. Still this is likely not a major argument against using Drell-Yan.

The major disadvantage of Drell-Yan measurements is the very low cross section compared to real photon production. Ref. [181] shows a measurement of forward Drell-Yan muon pairs in pp collisions at 7 TeV from LHCb. For the low mass range relevant for this discussion ($5 < M < 7\,\mathrm{GeV}$) they quote a statistical error of $\approx 20\%$ for the rapidity-integrated measurement in a sample of 37 pb^{-1}. A low-mass rapidity-differential measurement would not be possible from this sample. The situation is considerably worse for p+Pb collisions, where an integrated luminosity of 50 nb^{-1} (corresponding to a nucleon-nucleon-equivalent luminosity of $\approx$10 pb^{-1}) is considered reasonable. Measurements of Drell-Yan production will therefore not be competitive to those of real photon production.

8.4.5.2 A new detector for measurements of forward direct photons in ALICE

A detector upgrade with a calorimeter at forward rapidities (FoCal) to measure forward direct photon production is currently being discussed in the ALICE collaboration [182]. This detector would be intended to measure direct photons, electrons/positrons and jets for rapidities $\eta > 3$. Such a detector would offer a wealth of physics possibilities, but its main focus is on measurements related to the structure of nucleons and nuclei at very low Bjorken-x and possible effects

of gluon saturation.

FoCal would consist of an electromagnetic calorimeter most likely positioned at a distance from the IP of $z \approx 7\,\mathrm{m}$ covering $3.2 < \eta < 5.3$ backed by a standard hadronic calorimeter. A distance of $z = 3.6\,\mathrm{m}$, which corresponds to a maximum reachable pseudorapidity of $\eta = 4.5$, has also been studied in simulations. Both positions are equivalent in terms of measurement conditions such as the particle density, such that it is sufficient at this stage to not explicitly perform all studies for both positions. The main challenge of an electromagnetic calorimeter in this region of phase space is the requirement to discriminate decay photons from direct photons at very high energy, which will require extremely high granularity.

The design option currently under study is a SiW sandwich construction. It consists of 20 layers of a 3.5 mm W plate ($\approx 1X_0$) interleaved with active layers with Si sensors. The active layers use two different sensor technologies: low granularity layers (LGL), which consist of sensors with 1 cm^2 pads summed longitudinally in segments and equipped with analog readout, and high granularity layers (HGL) based on CMOS monolithic active pixel sensors (MAPS). The MAPS will have a pixel size of a few $10 \times 10\,\mu\mathrm{m}^2$ with internal binary readout.[2] On-chip processing will convert the pixel count in a *macro-pixel* of $1\,\mathrm{mm}^2$ to a pseudo-analog value.

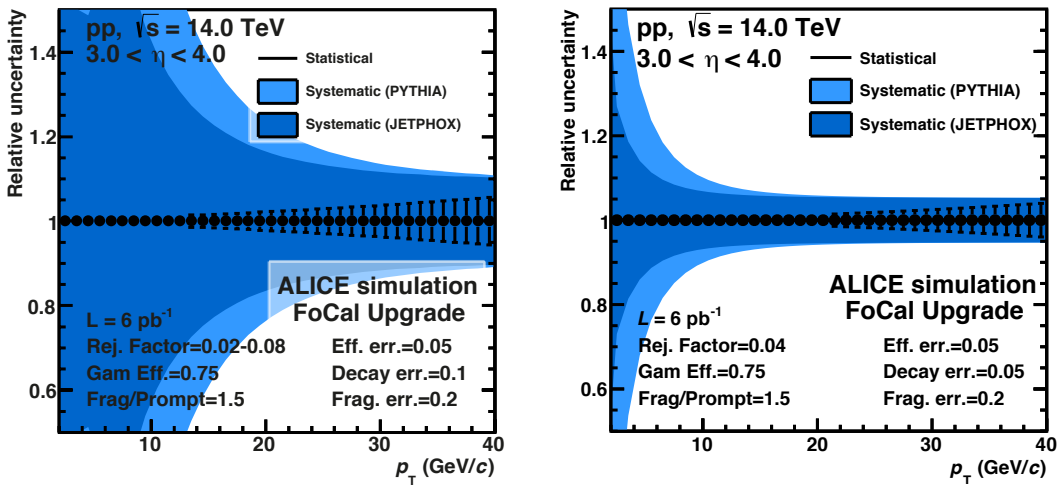

Fig. 8.12: Estimated relative uncertainties on the cross section measurement for direct photon production in p+p collisions at $\sqrt{s} = 14$ TeV, based on direct photon spectra from JETPHOX (dark band) and PYTHIA (light band), and background spectra from PYTHIA events. Statistical uncertainties are shown as error bars and the systematic uncertainty is shown as a band.

The HGL are crucial for γ/π^0 discrimination. The LGL have an effective tower width of the order of the Molière radius. Their two-shower separation power is similar to existing standard electromagnetic calorimeters.[3] However, the shape of electromagnetic showers allows us to make use of much finer granularity for shower separation and additional shower shape analysis for very high energy π^0, when the two photons can no longer be resolved. The impact of the granularity is shown in Fig. 8.12, which shows uncertainty estimates for a direct photon measurement in pp collisions at 14 TeV. The panel on the left hand side shows the expected performance using only the LGL, while the right panel shows the performance of the full detector.

[2] The current model for MC simulations uses a pixel size of $100 \times 100\,\mu\mathrm{m}^2$.

[3] Those conditions are in fact very similar to the ones of the electromagnetic calorimeter of the LHCb experiment.

A low-granularity detector would only determine the photon yield with a much larger systematic error, mainly due to the merging of π^0-decay photons. Only the high-granularity option has a good sensitivity for such a photon measurement. While FoCal would offer coverage towards higher rapidities than other LHC experiments, it is in particular the superior granularity at these large rapidities that would give FoCal a unique advantage.

8.4.5.3 Required beam times and luminosities

The detector upgrade would be installed in the LHC long shutdown 3 (2024), and measurements would be performed together with the full ALICE setup. Beam intensity conditions should thus be similar to the standard requirements of the upgraded ALICE experiment [183]. The main signal requires measurements of pp and p+Pb collisions – minimising systematic uncertainties requires running at the same $\sqrt{s}$ for both systems. The FoCal detector would also participate in additional Pb+Pb running of ALICE. The estimated requirements are summarised in table 8.1. Figure 8.13 shows an estimate of the measurement uncertainty for the nuclear modification factor for these conditions.

Table 8.1: Collision systems, beam conditions and integrated luminosities required for gluon saturation studies with FoCal in ALICE.

system	**luminosity**	**max. event rate**	**int. luminosity**
pp	$3 \times 10^{30}\,\mathrm{cm^{-2}s^{-1}}$	200 kHz	$\approx 6\,\mathrm{pb^{-1}}$
p–Pb	$10^{29}\,\mathrm{cm^{-2}s^{-1}}$	200 kHz	$50\,\mathrm{nb^{-1}}$
Pb–Pb[a]	$7 \times 10^{27}\,\mathrm{cm^{-2}s^{-1}}$	50 kHz	

[a] Not required for this measurement.

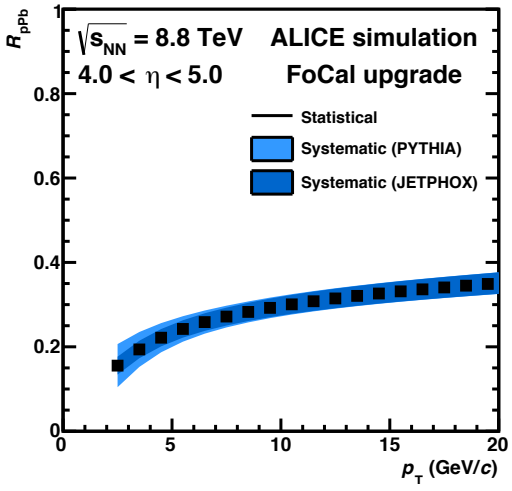

Fig. 8.13: Estimated relative uncertainties on measurement of the nuclear modification factor R_{pA} for direct photon production at $\sqrt{s} = 8.8$ TeV, based on direct photon spectra from JETPHOX (dark band) and PYTHIA (light band), and background spectra from PYTHIA events. Statistical uncertainties are shown as error bars and the systematic uncertainty is shown as a band. This simulation assumes a location of the detector at $z = 3.6\,\mathrm{m}$. Results are shown using only low granularity layers (*left*) and for the full detector including high granularity layers (*right*).

8.4.6 Summary

Forward Drell Yan production is a promising place for studying gluon densities at small-x and for finding saturation. For low lepton pair masses, dipole model predictions are significantly below the collinear predictions. Preliminary LHCb data indicate that, in fact, it will be possible to discriminate between different models. Distributions in transverse momentum of the Drell-Yan pair at low p_T should provide further hints for deviation from collinear factorization. Forward direct photon production is another final state sensitive to saturation. A detector upgrade at ALICE (FoCal) would offer a wide spectrum of physics possibilities.

8.5 Large-x physics in p+p and p+A collisions

One of the most important reasons to extend the capabilities of LHC experiments to high rapidities (high x_F) is to access the physics of heavy quarks and heavy hadrons [184].

The original discovery of the $\Lambda_c(cud)$ and $\Lambda_b(bud)$ [185] at the ISR was possible because of the "split-field" magnet which allowed the measurement of "leading hadrons" at high x_F. The hadroproduction of the J/ψ and even double J/ψ was originally observed by NA3 [186] in fixed-target experiments at high x_F. The production of the double-charm baryons ccd and ccu at forward rapidities has been reported by SELEX [187].

High x_F processes in proton collisions follow from the fact the heavy quarks in the five-quark $|uudQ\bar{Q}>$ light-front Fock state wave-functions of the proton appear at high light-front fraction x due to multi-connected diagrams – the "intrinsic heavy quark" distributions [188]. The high- x component is in addition to the usual low-x contribution from gluon splitting or DGLAP evolution. The intrinsic amplitude is maximal at minimal off-shellness; i.e., equal rapidity of the constituents and thus $x_i \propto m_{\perp i} = \sqrt{m_i^2 + k_{\perp i}^2}$ and the heavy quarks have the highest momentum fraction. The probability for intrinsic heavy quarks falls as $1/m_Q^2$ in non-Abelian QCD. These features are rigorous properties of QCD and the operator product expansion [189, 190].

The intrinsic charm distribution was measured at high x by the EMC collaboration [191]. The intrinsic contribution dominates at high x despite the $1/m_Q^2$ suppression since the DGLAP contribution falls rapidly as $(1-x)^5$.

The leading hadrons are formed in a collision when the quarks in the proton light-front wave-function coalesce at nearly equal rapidity. For example, in $pp \to \Lambda_c X$ the cud coalesce at equal rapidity. The momentum of the Λ_c is the sum of the three momenta of the cud and thus is dominated by the intrinsic high-x charm quark.

There are enormous implications for the LHC [192]: One can create a vast array of heavy-quark hadrons at high x_F. For example, the $B_c(b\bar{c})$ meson will be formed at high x_F in $pp \to B_c X$ collisions from the coalescence of the heavy quarks from the 7-quark $|uudccb\bar{b}>$ Fock state proton. One can make many other exotic heavy quark meson and and baryons, e. g., $|bcu>, |ccc>$, etc. One can also create tetraquark states at high x_F, such as the $Z_c(cc\bar{u}\bar{d})$ and $Z_b(bb\bar{u}\bar{d})$..

The existence of intrinsic heavy quarks in the proton leads to a novel mechanism for the production of the Higgs at high x_F. [193, 194] For example, the Higgs can couple to the b and $\bar{b}$ in the protonÕs five-quark Fock state $|uudb\bar{b}>$. Thus the Higgs will be produced in $pp \to HX$ at high $x_F = x_b + x_{\bar{b}}$ – at x_F as large as $x_F \simeq 0.9$. Similar contributions can arise from each of the $|uudQ\bar{Q}>$ Fock states, since the Higgs coupling compensates for the $1/m_Q^2$ fall-off of the intrinsic heavy-quark Fock state probability. The high x_F Higgs tends to travel down the LHC beam pipe. Thus the decay channels $\gamma\gamma$, and $\mu^+\mu^-\mu^+\mu^-$ could be particularly advantageous

channels for the detection of high-x_F very forward Higgs events.

References

[1] V. S. Fadin, E. A. Kuraev and L. N. Lipatov, Phys. Lett. B **60** (1975) 50.

[2] E. A. Kuraev, L. N. Lipatov and V. S. Fadin, "Multi - Reggeon Processes in the Yang-Mills Theory", Sov. Phys. JETP **44** (1976) 443 [Zh. Eksp. Teor. Fiz. **71** (1976) 840] [Erratum-ibid. **45** (1977) 199].

[3] E. A. Kuraev, L. N. Lipatov and V. S. Fadin, "The Pomeranchuk Singularity in Nonabelian Gauge Theories", Sov. Phys. JETP **45** (1977) 199 [Zh. Eksp. Teor. Fiz. **72** (1977) 377].

[4] I. I. Balitsky and L. N. Lipatov, "The Pomeranchuk Singularity in Quantum Chromodynamics", Sov. J. Nucl. Phys. **28** (1978) 822 [Yad. Fiz. **28** (1978) 1597].

[5] A. H. Mueller and H. Navelet, "An Inclusive Minijet Cross-Section and the Bare Pomeron in QCD", Nucl. Phys. B **282** (1987) 727.

[6] S. Dooling, P. Gunnellini, F. Hautmann and H. Jung, Phys. Rev. D **87**, no. 9, 094009 (2013) [arXiv:1212.6164 [hep-ph]].

[7] V. S. Fadin and R. Fiore, Phys. Lett. B **440** (1998) 359 [hep-ph/9807472].

[8] L. N. Lipatov, Sov. J. Nucl. Phys. **23** (1976) 338 [Yad. Fiz. **23** (1976) 642].

[9] L. N. Lipatov, Sov. Phys. JETP **63** (1986) 904 [Zh. Eksp. Teor. Fiz. **90** (1986) 1536].

[10] V. S. Fadin and L. N. Lipatov, Phys. Lett. B **429** (1998) 127 [hep-ph/9802290].

[11] M. Ciafaloni and G. Camici, Phys. Lett. B **430** (1998) 349 [hep-ph/9803389].

[12] Z. Bajnok, R. A. Janik and T. Lukowski, Nucl. Phys. B **816** (2009) 376 [arXiv:0811.4448 [hep-th]].

[13] J. Bartels, L. N. Lipatov and K. Peters, Nucl. Phys. B **772** (2007) 103 [hep-ph/0610303].

[14] J. Bartels, L. N. Lipatov and A. S. Vera, JHEP **1407** (2014) 056 [arXiv:1208.3423 [hep-th]].

[15] V. N. Gribov and L. N. Lipatov, "Deep inelastic e p scattering in perturbation theory", Sov. J. Nucl. Phys. **15** (1972) 438 [Yad. Fiz. **15** (1972) 781].

[16] L. N. Lipatov, "The parton model and perturbation theory", Sov. J. Nucl. Phys. **20** (1975) 94 [Yad. Fiz. **20** (1974) 181].

[17] G. Altarelli and G. Parisi, "Asymptotic Freedom in Parton Language", Nucl. Phys. B **126** (1977) 298.

[18] Y. L. Dokshitzer, "Calculation of the Structure Functions for Deep Inelastic Scattering and e+ e- Annihilation by Perturbation Theory in Quantum Chromodynamics", Sov. Phys. JETP **46** (1977) 641 [Zh. Eksp. Teor. Fiz. **73** (1977) 1216].

[19] M. Hentschinski, A. Sabio Vera and C. Salas, Phys. Rev. Lett. **110** (2013) 041601 [arXiv:1209.1353 [hep-ph]].

[20] M. Hentschinski, A. Sabio Vera and C. Salas, Phys. Rev. D **87** (2013) 076005 [arXiv:1301.5283 [hep-ph]].

[21] J. R. Andersen, V. Del Duca, S. Frixione, C. R. Schmidt and W. J. Stirling, JHEP **0102**, 007 (2001) [hep-ph/0101180].

[22] M. Fontannaz, J. P. Guillet, and G. Heinrich, *Is a large intrinsic k(T) needed to describe photon + jet photoproduction at HERA?*, *Eur. Phys. J.* **C22** (2001) 303–315.

[23] F. Caporale, B. Murdaca, A. Sabio Vera and C. Salas, Nucl. Phys. B **875** (2013) 134 [arXiv:1305.4620 [hep-ph]].

[24] V. Del Duca and C. R. Schmidt, "Dijet production at large rapidity intervals," Phys. Rev. D **49**, 4510 (1994) [hep-ph/9311290].

[25] W. J. Stirling, *Production of jet pairs at large relative rapidity in hadron hadron collisions as a probe of the perturbative Pomeron*, *Nucl. Phys.* **B423** (1994) 56–79.

[26] B. Ducloué, L. Szymanowski and S. Wallon, *Confronting Mueller-Navelet jets in NLL BFKL with LHC experiments at 7 TeV*, JHEP **1305**, 2013

[27] B. Ducloué, L. Szymanowski, and S. Wallon, *Evidence for high-energy resummation effects in Mueller-Navelet jets at the LHC*, *Phys.Rev.Lett.* **112** (2014) 082003.

[28] M. Ciafaloni, *Energy scale and coherence effects in small x equations*, *Phys.Lett.* **B429** (1998) 363–368.

[29] M. Ciafaloni and D. Colferai, *K factorization and impact factors at next-to-leading level*, *Nucl.Phys.* **B538** (1999) 187–214.

[30] J. Bartels, D. Colferai, and G. P. Vacca, *The NLO jet vertex for Mueller-Navelet and forward jets: The quark part*, *Eur. Phys. J.* **C24** (2002) 83–99.

[31] J. Bartels, D. Colferai, and G. P. Vacca, *The NLO jet vertex for Mueller-Navelet and forward jets: The gluon part*, *Eur. Phys. J.* **C29** (2003) 235–249.

[32] F. Caporale, D. Y. Ivanov, B. Murdaca, A. Papa, and A. Perri, *The next-to-leading order jet vertex for Mueller-Navelet and forward jets revisited*, *JHEP* **1202** (2012) 101.

[33] M. Hentschinski and A. Sabio Vera, Phys. Rev. D **85** (2012) 056006 [arXiv:1110.6741 [hep-ph]].

[34] G. Chachamis, M. Hentschinski, J. D. Madrigal Martinez and A. Sabio Vera, Phys. Rev. D **87** (2013) 7, 076009 [arXiv:1212.4992].

[35] A. Sabio Vera and F. Schwennsen, Nucl. Phys. B **776** (2007) 170 [hep-ph/0702158 [HEP-PH]].

[36] V. Del Duca and C. R. Schmidt, "Dijet production at large rapidity intervals", *Phys. Rev.* **D49** (1994) 4510, hep-ph/9311290.

[37] L.H. Orr, W.J. Stirling, "Dijet production at hadron hadron colliders in the BFKL approach", *Phys. Rev.* **D56** (1997) 5875, arXiv:hep-ph/9706529.

[38] J. Kwiecinski, L. Motyka, "Probing the QCD pomeron in doubly tagged e + e collisions", *Phys. Rev.* **B462** (1999) 203, arXiv:hep-ph/9905567

[39] C. Marquet and C. Royon, *Azimuthal decorrelation of Mueller-Navelet jets at the Tevatron and the LHC*, *Phys. Rev.* **D79** (2009) 034028.

[40] D. Colferai, F. Schwennsen, L. Szymanowski, and S. Wallon, *Mueller Navelet jets at LHC - complete NLL BFKL calculation*, *JHEP* **12** (2010) 026.

[41] S. J. Brodsky, G. P. Lepage, and P. B. Mackenzie, *On the Elimination of Scale Ambiguities in Perturbative Quantum Chromodynamics*, *Phys. Rev.* **D28** (1983) 228.

[42] S. J. Brodsky, V. S. Fadin, V. T. Kim, L. N. Lipatov, and G. B. Pivovarov, *The QCD pomeron with optimal renormalization*, *JETP Lett.* **70** (1999) 155–160.

[43] S. J. Brodsky, V. S. Fadin, V. T. Kim, L. N. Lipatov, and G. B. Pivovarov, *High-energy QCD asymptotics of photon photon collisions*, *JETP Lett.* **76** (2002) 249–252.

[44] CMS Collaboration, *Azimuthal angle decorrelations of jets widely separated in rapidity in pp collisions at* $\sqrt{s} = 7$ *TeV*, CMS Physics Analysis Summary CMS-PAS-FSQ-12-002, 2013.

[45] A. Sabio Vera, Nucl. Phys. B **746** (2006) 1 [hep-ph/0602250].

[46] M. Angioni, G. Chachamis, J. D. Madrigal and A. Sabio Vera, Phys. Rev. Lett. **107** (2011)

191601 [arXiv:1106.6172 [hep-th]].
[47] R. Ciesielski, arXiv:1409.5473 [hep-ex].
[48] M. Diehl, D. Ostermeier, and A. Schafer, *Elements of a theory for multiparton interactions in QCD*, *JHEP* **1203** (2012) 089.
[49] A. Szczurek, A. Cisek and R. MaciuÅĆa, AIP Conf. Proc. **1654** (2015) 070009 [arXiv:1411.4515 [hep-ph]].
[50] J. M. Campbell, J. W. Huston and W. J. Stirling, Rept. Prog. Phys. **70**, 89 (2007); arXiv:0611148 [hep-ph].
[51] A. Gehrmann-De Ridder, T. Gehrmann, E. W. N. Glover and J. Pires, Phys. Rev. Lett. **110**, 162003 (2013); arXiv:1301.7310 [hep-ph].
[52] G. Aad et al. (the ATLAS collaboration), Eur. Phys. J. **C 71**, 1512 (2011).; arXiv:1009.5908 [hep-ex]
[53] S. Chatrchyan et al. (the CMS collaboration), Phys. Rev. Lett. **107**, 132001 (2011); arXiv:1106.0208 [hep-ex].
[54] F. Abe et al. (CDF Collaboration), Phys. Rev. **D56**, 3811 (1997);
Phys. Rev. Lett. **79**, 584 (1997);
V. M. Abazov, Phys. Rev. **D81**, 052012 (2010).
[55] G. Aad *et al.* (ATLAS Collaboration), J. High Energy Phys. **06**, 141 (2012).
[56] M. Kimber, A.D. Martin and M. Ryskin, Eur. Phys. J. **C12** 655 (2000), arXiv:hep-ph/9911379;
M. Kimber, A.D. Martin and M. Ryskin, Phys. rev. **D63** 114027 (2001), arXiv:hep-ph/0101348.
[57] M. Nefedov, V. Saleev and A.V. Shipilova, Phys. Rev. **D87** 094030 (2013); arXiv:1304.3549 [hep-ph].
[58] I. Pozdnyakov, private communication
[59] R. Maciula and A. Szczurek, Phys. Rev. **D90** (2014) 014022.
[60] A. Cisek, R. Maciula and A. Szczurek, a paper in preparation.
[61] S. Catani, F. Fiorani and G. Marchesini, Phys. Lett. B **234** (1990) 339.
[62] G. Marchesini, Nucl. Phys. B **445** (1995) 49 [hep-ph/9412327].
[63] M. Ciafaloni, Nucl. Phys. B **296** (1988) 49.
[64] S. Catani, F. Fiorani, G. Marchesini and G. Oriani, Nucl. Phys. B **361** (1991) 645.
[65] B. Ducloué, L. Szymanowski and S. Wallon, arXiv:1507.04735 [hep-ph].
[66] G. Chachamis, M. Deak, A. Sabio Vera and P. Stephens, Nucl. Phys. B **849** (2011) 28 [arXiv:1102.1890 [hep-ph]].
[67] G. Chachamis and A. Sabio Vera, Phys. Lett. B **709** (2012) 301 [arXiv:1112.4162 [hep-th]].
[68] G. Chachamis and A. S. Vera, PoS DIS **2013** (2013) 167 [arXiv:1307.7750]; F. Caporale, G. Chachamis, B. Murdaca, A. Sabio Vera, preprint ArXiv:1508.07711.
[69] M. Hentschinski, J. D. Madrigal Martinez, B. Murdaca and A. Sabio Vera, Phys. Lett. B **735** (2014) 168 [arXiv:1404.2937 [hep-ph]].
[70] M. Hentschinski, J. D. Madrigal Martinez, B. Murdaca and A. Sabio Vera, Nucl. Phys. B **887** (2014) 309 [arXiv:1406.5625 [hep-ph]].
[71] M. Hentschinski, J. D. Madrigal Martinez, B. Murdaca and A. Sabio Vera, arXiv:1409.6704 [hep-ph].
[72] G. Chachamis, M. Hentschinski, J. D. Madrigal Martinez and A. Sabio Vera, Nucl. Phys.

B **876** (2013) 453 [arXiv:1307.2591].

[73] G. Chachamis, M. Hentschinski, J. D. Madrigal Martinez and A. Sabio Vera, PoS DIS **2013** (2013) 062 [arXiv:1307.7741].

[74] G. Chachamis, M. Hentschinski, J. D. Madrigal Martinez and A. Sabio Vera, Int. J. Mod. Phys. Conf. Ser. **25** (2014) 1460027 [arXiv:1308.0293 [hep-ph]].

[75] G. Chachamis, M. Hentschinski, J. D. Madrigal Martinez and A. Sabio Vera, Nucl. Phys. B **861** (2012) 133 [arXiv:1202.0649 [hep-ph]].

[76] G. Chachamis, M. Hentschinski, J. D. Madrigal Martinez and A. Sabio Vera, Phys. Part. Nucl. **45** (2014) 4, 788 [arXiv:1211.2050 [hep-ph]].

[77] S. Abachi *et al.* [D0 Collaboration], *The Azimuthal decorrelation of jets widely separated in rapidity*, Phys. Rev. Lett. **77**, 1996

[78] G. Marchesini et al., *HERWIG 6 : an event generator for hadron emission reactions with interfering gluons (including supersymmetric processes)*, **JHEP**, **1**, 2001

[79] W. T. Giele, E. W. N. Glover and D. A. Kosower, "Higher order corrections to jet cross-sections in hadron colliders," Nucl. Phys. B **403**, 633 (1993) [hep-ph/9302225].

[80] W. T. Giele, E. W. N. Glover and D. A. Kosower, "The Two-Jet Differential Cross Section at $\mathcal{O}(\alpha_s^3)$ in Hadron Collisions," Phys. Rev. Lett. **73**, 2019 (1994) [hep-ph/9403347].

[81] V. Del Duca and C. R. Schmidt, "BFKL versus O (alpha-s**3) corrections to large rapidity dijet production," Phys. Rev. D **51**, 2150 (1995) [hep-ph/9407359].

[82] B. Abbott *et al.* [D0 Collaboration], "Probing BFKL dynamics in the dijet cross section at large rapidity intervals in $p\bar{p}$ collisions at $\sqrt{s} = 1800$ GeV and 630-GeV," Phys. Rev. Lett. **84**, 5722 (2000) [hep-ex/9912032].

[83] L. H. Orr and W. J. Stirling, "The Collision energy dependence of dijet cross-sections as a probe of BFKL physics," Phys. Lett. B **429**, 135 (1998) [hep-ph/9801304].

[84] CMS Collaboration, *Ratios of dijet production cross sections as a function of the absolute difference in rapidity between jets in proton-proton collisions at* $\sqrt{s} = 7$ *TeV*, Eur. Phys. J. C **72**, 2012 [arXiv:1204.0696 [hep-ex]].

[85] V. T. Kim and G. B. Pivovarov, *BFKL QCD pomeron in high-energy hadron collisions: Inclusive dijet production*, Phys. Rev. D **53**, 1996

[86] T. Sjöstrand, S. Mrenna, P. Skands, *Pythia 6.4 Physics and Manual*, **JHEP**, 05, 2006

[87] Sjöstrand, T. and Mrenna, S. and Skands, P., *A Brief Introduction to PYTHIA 8.1*, Comput. Phys. Commun., **178**, 2008

[88] M. Bahr *et al.*, *HERWIG++ Physics and Manual*, Eur.Phys.J. C, **58**, 2008

[89] Andersen, J. R. and Smillie, J. M., *Multiple Jets at the LHC with High Energy Jets*, **JHEP**, 06, 2011

[90] Jung, H. and Baranov, S. and Deak, M. and Grebenyuk, A. and Hautmann, F. and others, *The CCFM Monte Carlo generator CASCADE version 2.2.03*, Eur. Phys. J. C, **70**, 2010, [arXiv:1008.0152]

[91] D. D. Damiani. Investigation of inclusive and exclusive jets production at the LHC. Comparison between cascade and pythia. Summerstudent Program DESY 2014.

[92] CMS Collaboration, *Azimuthal angle decorrelations of jets widely separated in rapidity at* $\sqrt{s} = 7$ *TeV*, CMS Physics Analysis Summary **FSQ-12-002**, 2013

[93] F. Caporale, D. Y. Ivanov, B. Murdaca and A. Papa, Eur. Phys. J. C **74** (2014) 3084 [arXiv:1407.8431 [hep-ph]].

[94] G. Aad *et al.* [ATLAS Collaboration], "The ATLAS Experiment at the CERN Large

Hadron Collider," JINST **3**, S08003 (2008).

[95] G. Aad *et al.* [ATLAS Collaboration], "Jet energy measurement and its systematic uncertainty in proton-proton collisions at $\sqrt{s} = 7$ TeV with the ATLAS detector," arXiv:1406.0076 [hep-ex].

[96] G. Aad *et al.* [ATLAS Collaboration], "Jet energy resolution in proton-proton collisions at $\sqrt{s} = 7$ TeV recorded in 2010 with the ATLAS detector," Eur. Phys. J. C **73**, 2306 (2013) [arXiv:1210.6210 [hep-ex]].

[97] G. Aad *et al.* [ATLAS Collaboration], "Measurement of dijet production with a veto on additional central jet activity in pp collisions at $\sqrt{s} = 7$ TeV using the ATLAS detector," JHEP **1109**, 053 (2011) [arXiv:1107.1641 [hep-ex]].

[98] P. Nason, "A New method for combining NLO QCD with shower Monte Carlo algorithms," JHEP **0411**, 040 (2004) [hep-ph/0409146].

[99] G. Aad *et al.* [ATLAS Collaboration], "Measurements of jet vetoes and azimuthal decorrelations in dijet events produced in pp collisions at $\sqrt{s} = 7$ TeV using the ATLAS detector," arXiv:1407.5756 [hep-ex].

[100] CMS Collaboration, "Determination of Jet Energy Calibration and Transverse Momentum Resolution in CMS," JINST **6**, 2011 [arXiv:1107.4277].

[101] H. Kowalski, L. N. Lipatov, D. A. Ross and G. Watt, Eur. Phys. J. C **70** (2010) 983 [arXiv:1005.0355 [hep-ph]].

[102] H. Kowalski, L. N. Lipatov and D. A. Ross, Phys. Part. Nucl. **44** (2013) 547 [arXiv:1205.6713 [hep-ph]].

[103] H. Kowalski, L. Lipatov and D. Ross, Eur. Phys. J. C **74** (2014) 2919 [arXiv:1401.6298 [hep-ph]].

[104] F. Hautmann and H. Jung. Transverse momentum dependent gluon density from DIS precision data. 2013.

[105] L.V. Gribov, E.M. Levin, and M.G. Ryskin. Semihard Processes in QCD. *Phys.Rept.*, 100:1–150, 1983.

[106] Javier L. Albacete and Cyrille Marquet. Azimuthal correlations of forward di-hadrons in d+Au collisions at RHIC in the Color Glass Condensate. *Phys.Rev.Lett.*, 105:162301, 2010.

[107] S. Catani, M. Ciafaloni, and F. Hautmann. High-energy factorization and small x heavy flavor production. *Nucl.Phys.*, B366:135–188, 1991.

[108] John C. Collins and R. Keith Ellis. Heavy quark production in very high-energy hadron collisions. *Nucl. Phys.*, B360:3–30, 1991.

[109] M. Deak, F. Hautmann, H. Jung, and K. Kutak. Forward Jet Production at the Large Hadron Collider. *JHEP*, 0909:121, 2009.

[110] Andreas van Hameren, Piotr Kotko, and Krzysztof Kutak. Multi-gluon helicity amplitudes with one off-shell leg within high energy factorization. *JHEP*, 1212:029, 2012.

[111] A. van Hameren, P. Kotko, and K. Kutak. Helicity amplitudes for high-energy scattering. *JHEP*, 1301:078, 2013.

[112] Krzysztof Kutak and Sebastian Sapeta. Gluon saturation in dijet production in p-Pb collisions at Large Hadron Collider. *Phys.Rev.*, D86:094043, 2012.

[113] Andreas van Hameren, Piotr Kotko, and Krzysztof Kutak. Three jet production and gluon saturation effects in p-p and p-Pb collisions within high-energy factorization. 2013.

[114] A. van Hameren, P. Kotko, K. Kutak, C. Marquet, and S. Sapeta. Saturation effects in forward-forward dijet production in p+Pb collisions. 2014.

[115] K. Kutak and A.M. Stasto. Unintegrated gluon distribution from modified BK equation. *Eur.Phys.J.*, C41:343–351, 2005.

[116] Ian Balitsky and Giovanni A. Chirilli. Next-to-leading order evolution of color dipoles. *Phys.Rev.*, D77:014019, 2008.

[117] Javier L. Albacete, Nestor Armesto, Jose Guilherme Milhano, and Carlos A. Salgado. Non-linear QCD meets data: A Global analysis of lepton-proton scattering with running coupling BK evolution. *Phys.Rev.*, D80:034031, 2009.

[118] I. Balitsky. Operator expansion for high-energy scattering. *Nucl.Phys.*, B463:99–160, 1996.

[119] Yuri V. Kovchegov. Small x F(2) structure function of a nucleus including multiple pomeron exchanges. *Phys.Rev.*, D60:034008, 1999.

[120] P. van Mechelen. Very forward jets with CMS-CASTOR. talk at the Small-x miniworkshop, DESY, February 19, 2014.

[121] Piotr Kotko. LxJet, 2013. C++ Monte Carlo program.

[122] H. Woehrmann for the CMS Collaboration, CMS DP 2014-014.

[123] CMS Collaboration [CMS Collaboration], "Jet measurement with the CASTOR calorimeter", CMS DP-2014/022.

[124] M. Cacciari, G. P. Salam and G. Soyez, "The Anti-k(t) jet clustering algorithm", JHEP **0804** (2008) 063 [arXiv:0802.1189 [hep-ph]].

[125] S. Chatrchyan *et al.* [CMS Collaboration], "Study of the underlying event at forward rapidity in pp collisions at $\sqrt{s}$ = 0.9, 2.76, and 7 TeV", JHEP **1304** (2013) 072 [arXiv:1302.2394 [hep-ex]].

[126] T. Sjostrand, S. Mrenna and P. Z. Skands, "A Brief Introduction to PYTHIA 8.1", Comput. Phys. Commun. **178** (2008) 852 [arXiv:0710.3820 [hep-ph]].

[127] R. Corke and T. Sjostrand, "Interleaved Parton Showers and Tuning Prospects", JHEP **1103** (2011) 032 [arXiv:1011.1759 [hep-ph]].

[128] G. Altarelli, R. K. Ellis and G. Martinelli, Nucl. Phys. **B143**, 521 (1978).

[129] G. Altarelli, R. K. Ellis and G. Martinelli, Nucl. Phys. **B157**, 461 (1979).

[130] J. Kubar-Andre and F. E. Paige, Phys. Rev. D **19**, 221 (1979).

[131] B. Z. Kopeliovich, J. Raufeisen and A. V. Tarasov, Phys. Lett. **B503**, 91 (2001).

[132] S. J. Brodsky, A. Hebecker and E. Quack, Phys. Rev. **D55**, 2584 (1997).

[133] M. A. Betemps, M. B. Gay Ducati and M. V. T. Machado, Phys. Rev. **D66**, 014018 (2002).

[134] N. N. Nikolaev and B. G. Zakharov, Z. Phys. **C49**, 607 (1991).

[135] K. Golec-Biernat and M. Wusthoff, Phys. Rev. **D59**, 014017 (1999).

[136] K. Golec-Biernat and M. Wusthoff, Phys. Rev. **D60**, 114023 (1999).

[137] J. Bartels, K. Golec-Biernat and H. Kowalski, Phys. Rev. **D66**, 014001 (2002).

[138] K. J. Golec-Biernat and S. Sapeta, Phys. Rev. **D74**.

[139] E. Iancu, K. Itakura and S. Munier, Phys. Lett. **B590**, 199 (2004).

[140] G. Soyez, Phys. Lett. **B655**, 32 (2007).

[141] E772, P. L. McGaughey *et al.*, Phys. Rev. **D50**, 3038 (1994).

[142] P. M. Nadolsky *et al.*, Phys. Rev. D **78**, 013004 (2008).

[143] G. Aad *et al.* [ATLAS Collaboration], Phys. Rev. D **85**, 072004 (2012) [arXiv:1109.5141 [hep-ex]].

[144] G. Aad *et al.* [ATLAS Collaboration], Phys. Lett. B **725**, 223 (2013) [arXiv:1305.4192 [hep-ex]].

[145] G. Aad *et al.* [ATLAS Collaboration], JHEP **1406**, 112 (2014) [arXiv:1404.1212 [hep-ex]].

[146] S. Chatrchyan *et al.* [CMS Collaboration], JHEP **1110**, 132 (2011) [arXiv:1107.4789 [hep-ex]].

[147] S. Chatrchyan *et al.* [CMS Collaboration], JHEP **1110**, 007 (2011) [arXiv:1108.0566 [hep-ex]].

[148] S. Chatrchyan *et al.* [CMS Collaboration], JHEP **1312**, 030 (2013) [arXiv:1310.7291 [hep-ex]].

[149] CMS Collaboration [CMS Collaboration], CMS-PAS-SMP-14-003.

[150] [LHCb Collaboration], LHCb-CONF-2012-013.

[151] RAaij *et al.* [LHCb Collaboration], JHEP **1206**, 058 (2012) [arXiv:1204.1620 [hep-ex]].

[152] RAaij *et al.* [LHCb Collaboration], JHEP **1302**, 106 (2013) [arXiv:1212.4620 [hep-ex]].

[153] E. G. de Oliveira, A. D. Martin and M. G. Ryskin, Eur. Phys. J. C **72**, 2069 (2012) [arXiv:1205.6108 [hep-ph]].

[154] E. G. de Oliveira, A. D. Martin and M. G. Ryskin, Eur. Phys. J. C **73**, 2361 (2013) [arXiv:1212.3135].

[155] K. Golec-Biernat, E. Lewandowska and A. M. Stasto, Phys. Rev. D **82**, 094010 (2010) [arXiv:1008.2652 [hep-ph]].

[156] LHCb Collaboration, *Inclusive low mass Drell-Yan production in the forward region at* $\sqrt{s} = 7$ *TeV*, LHCb-CONF-2012-013 (2012).

[157] A. J. Baltz, et al, Phys. Rept. **458** 1-171, (2008).

[158] Z.-B. Kang, J.-W. Qiu and W. Vogelsang, Phys. Rev. D **79**, 054007 (2009).

[159] E.L. Berger, L.E. Gordon and M. Klasen, Phys. Rev. D **58**, 074012 (1998).

[160] A.L. Ayala, M.B. Gay Ducati, L.N. Epele and C.A. Garcia Canal, Phys. Rev. C **49**, 489 (1994).

[161] M. A. Betemps and M. B. Gay Ducati, Phys. Rev. D **70**, 116005 (2004); Phys. Lett. B **636**, 46 (2006).

[162] F. Gelis and J. Jalilian-Marian, Phys. Rev. D **76**, 074015 (2007).

[163] B. Z. Kopeliovich, A. H. Rezaeian, H. J. Pirner and I. Schmidt, Phys. Lett. B **653**, 210 (2007).

[164] A. B. Zamolodchikov, B. Z. Kopeliovich and L. I. Lapidus, JETP Lett. **33**, 595 (1981).

[165] B.Z. Kopeliovich, proc. of the workshop Hirschegg '95: Dynamical Properties of Hadrons in Nuclear Matter, Hirschegg January 16-21, 1995, ed. by H. Feldmeyer and W. Nörenberg, Darmstadt, 1995, p. 102 (hep-ph/9609385).

[166] S.J. Brodsky, A. Hebecker and E. Quack, Phys. Rev. D **55**, 2584 (1997).

[167] J. Raufeisen, J. -C. Peng and G. C. Nayak, Phys. Rev. D **66**, 034024 (2002).

[168] ATLAS Collaboration, *Measurement of the low mass Drell-Yan differential cross section in the muon channel*, ATL-COM-PHYS-2012-469 (2012).

[169] J.C. Webb *et al.* [NuSea Collaboration], hep-ex/0302019.

[170] F. Abe *et al.* [CDF Collaboration], Phys. Rev. D **49**, 1 (1994).

[171] M.V.T. Machado and C. Brenner Mariotto, Eur. Phys. J **C61**, 871 (2009).

[172] J. Adams et al. (STAR Collaboration), Phys. Rev. Lett. 97 (2006) 152302.

[173] I. Arsene et al. (BRAHMS Collaboration) Phys. Rev. Lett. 93 (2004) 242303.
[174] E. Braidot et al. (STAR collaboration), Proceedings of the 45th Rencontres de Moriond (2010) preprint arXiv:1005.2378.
[175] A. Adare et al. (PHENIX Collaboration), Phys. Rev. Lett. 107, 172301 (2011).
[176] A. Uras, ALICE Collaboration, talk at Hard Probes 2013, http://indico.tlabs.ac.za/contributionDisplay.py?contribId=112&confId=30
[177] LHCb Collaboration, JHEP 02 (2014) 072.
[178] B. Abelev et al. (ALICE Collaboration), JHEP02 (2014) 073.
[179] I. Helenius, K.J. Eskola, H. Paukkunen, preprint arXiv:1406.1689.
[180] J. Jalilian-Marian, A. Rezaeian, Phys. Rev. D 86 (2012) 034016; A. Rezaeian, private communication.
[181] LHCb collaboration, LHCb-CONF-2012-013.
[182] T. Peitzmann, Proceedings of CHEF 2013, preprint arXiv:1308.2585.
[183] B. Abelev et al. (ALICE Collaboration), J. Phys. G: Nucl. Part. Phys. 41 (2014) 087001.
[184] S. J. Brodsky, A. Kusina, F. Lyonnet, I. Schienbein, H. Spiesberger and R. Vogt, arXiv:1504.06287 [hep-ph].
[185] G. Bari *et al.*, Nuovo Cim. A **104**, 1787 (1991).
[186] J. Badier *et al.* [NA3 Collaboration], Phys. Lett. B **114**, 457 (1982).
[187] J. Engelfried [SELEX Collaboration], eConf C **0610161**, 003 (2006) [hep-ex/0702001 [HEP-EX]].
[188] S. J. Brodsky, P. Hoyer, C. Peterson and N. Sakai, Phys. Lett. B **93**, 451 (1980).
[189] S. J. Brodsky, J. C. Collins, S. D. Ellis, J. F. Gunion and A. H. Mueller, DOE/ER/40048-21 P4, SLAC-PUB-15471.
[190] M. Franz, M. V. Polyakov and K. Goeke, Phys. Rev. D **62**, 074024 (2000) [hep-ph/0002240].
[191] J. J. Aubert *et al.* [European Muon Collaboration], Nucl. Phys. B **213**, 31 (1983).
[192] S. J. Brodsky, Nucl. Part. Phys. Proc. **258-259**, 23 (2015) [arXiv:1410.0404 [hep-ph]].
[193] S. J. Brodsky, B. Kopeliovich, I. Schmidt and J. Soffer, Phys. Rev. D **73**, 113005 (2006) [hep-ph/0603238].
[194] S. J. Brodsky, A. S. Goldhaber, B. Z. Kopeliovich and I. Schmidt, Nucl. Phys. B **807**, 334 (2009) [arXiv:0707.4658 [hep-ph]].

Chapter 9

Detectors

Conveners and Editors: V. Avati, J. Baechler
Internal Reviewers: M. Bruschi

LHC Forward Physics Working Conveners and Editors: N. Cartiglia, C. Royon

The following paragraphs describe the detector systems of the different LHC experiments optimized for the forward physics program as outlined in previous chapters of this report. Already existing detectors are described shortly, or a reference to the detailed articles [1] is given. The newly developed components that have been integrated during the long shutdown 1 (LS 1) and the ongoing R&D activities are described in more detail with possible reference to the corresponding technical design reports (TDRs) or upgrade proposals. The forward detector systems can in general be separated in two different types, the movable beam inserts with detectors and the standard detectors that are integrated in the central detector or installed in the LHC tunnel. The following table provides information on the coverage of LHC detectors with $|\eta| > 5$.

Experiment	Detector	Hardware Tecnology	Acceptance	Comment
ATLAS	LUCID	Gas Cherenkov tubes	$5.9 < \|\eta\| < 6.0$	
	ALFA	Scintillating fibres		Forward proton tracking $0 < \xi < 0.2$ high-β^*
	ZDC	Quartz rods, tungsten	$\|\eta\| > 8.3$	Neutrals only
	AFP	Tracking: Silicon		Forward proton tracking
		Timing:Quartz Cherenkov		$\approx 0.03 < \xi < 0.2$ low-β^*
ALICE	ADA	Scintillator	$-7.0 < \eta < -4.8$	
	ADC	Scintillator	$4.7 < \eta < 6.3$	
CMS	CASTOR	Quartz plates, tungsten	$-6.8 < \eta < -5.2$	
	FSC	Scintillator	$6 < \|\eta\| < 8$	
	ZDC	Quartz fibres, tungsten	$\|\eta\| > 8$	Neutrals only
TOTEM	T1	Cathode Strip Chambers	$3.1 < \|\eta\| < 4.7$	
	T2	GEM Chambers	$5.3 < \|\eta\| < 6.5$	
	RP	Silicon		Forward proton tracking $0 < \xi < 0.2$ high-β^*
CMS+TOTEM	CT-PPS	Tracking: Silicon		Forward proton tracking
		Timing: Quartz Cherenkov		$\approx 0.03 < \xi < 0.2$ low-β^*
LHCb	HERSCHEL	Scintillator	$5 < \|\eta\| < 8$	

Table 1 : Summary of very forward detector coverage of LHC experiments in Run II. Several numbers are approximate.

Movable beam inserts with detector sensors

The detector carriers which are integrated in the LHC beam tube and enter into the LHC beam vacuum are generically called "movable beam inserts". These beam inserts carry the detector sensors for tracking or timing and allow the approach of the sensor to a distance down to a millimetre from the beam center. The movable beam inserts have to comply with LHC requirements in view of impedance, ultra high vacuum and safety. The material budget plays an important role, as a fraction of the secondary particles which are generated by interaction of high energy particles with the material of the movable beam inserts are scattered in the material of the supra conducting LHC magnets close by. The beam insert design is universal and can be used in the different corresponding locations of the LHC machine.

The specific LHC optics generates a specific particle occupancy pattern in the sensors integrated in the movable beam inserts, depending on both, the distance of the sensor relative to the corresponding interaction point and the location in the tunnel (experiment). For each experiment and location, the size and pixelization of the sensor is specific and optimized accordingly and differs strongly for the high and low β^* optics. The insertion of the beam inserts is a complex procedure requiring the close collaboration with the LHC collimator experts and the operators in the LHCC control room. In this sense the movable beam inserts become an integral element of the LHC machine.

The movable beam inserts are also present in the parking position during the standard runs and interfere with the LHC machine mostly due to their impedance. The beam-induced heating of the movable beam device can lead to local vacuum degradation and thus create perturbations of the machine operation during the energy ramp-up phase and the later stable operation of the LHC machine.

Standard detectors

The standard detector for LHC forward physics can be either integrated in the central detector of an LHC experiment, or in the tunnel of LHC, outside of the vacuum beam pipe. The operation of these detectors is in the autonomy of the experiment.

Considerations for the Design and Operation of Forward Detectors at LHC with High and Low β^* Optics

Certain physics observables require that the forward detector information is combined with that of the corresponding central detector. In this case the synchronisation of the specific forward detector systems with the central detector needs to be considered in the design of the trigger and data acquisition. The distance of up to 250 m from the forward detectors to the central detectors requires fast signal transmission and precision clock distribution systems. An important impact on the detector design and general layout is given by the machine settings. The physics programme outlined previous chapters of this report specifies the different LHC beam optics, beam parameters and instantaneous luminosity for the measurement of a given physics variable. The requirements for the operation of detectors and movable beam inserts at low and high β^* are quite different.

The LHC beam intensity setting and instantaneous luminosity for the special runs (high β^*) will be defined by the forward physics community in agreement with the LHC operation group, while the integral time for these special runs is subject to negotiation with the LHC scientific management of CERN.

For high β^* runs, the integral luminosity per run and the integral beam time per year is much lower with respect to the standard runs, leading to significantly lower instantaneous and integral radiation exposure to ionizing and non-ionizing radiation of the dedicated detec-

tors and carriers. However, forward tracking detectors optimized in view of radiation hardness and multi-track resolution combined with timing detectors synchronized with precision clock distribution systems allow background elimination and vertex separation in the central detectors. Such optimized forward detector systems allow higher instantaneous luminosities with the advantage of reaching the physics goals with significantly shorter beam time.

The forward physics programme at low β^* in contrary needs to cope with the beam parameters determined by the mainstream LHC physics community, and all detector components to be used under these beam conditions are forced to be adopted accordingly. The detector components installed for this purpose can be exposed to very high radiation levels depending on the final location of the detector the tunnel or in the central detector. In particular, the movable beam inserts need to cope with these machine boundary conditions during insertion under standard run conditions. The design of the beam inserts in view of impedance and material budget is one key issue to avoid any impact on the machine stability. To assure the compliance of the beam inserts with the machine requirements, the design and production of the beam inserts undergoes strict quality control in close collaboration with the LHC machine safety experts. The requirements for movable beam inserts and their corresponding detectors differ for the usage in high and low β^* beams: the following sections describe the detector systems of the different experiments for the different optics settings.

9.1 ATLAS-ALFA Experiment

ATLAS is a multi-purpose detector designed to study elementary processes in proton–proton interactions at the TeV energy scale. It consists of an inner tracking system, calorimeters and a muon spectrometer surrounding the interaction point of the colliding beams. The tracking system covers the pseudorapidity range $|\eta| < 2.5$ and the calorimetric measurements range to $|\eta| = 4.9$.[1] To improve the coverage in the forward direction three smaller detectors with specialized tasks are installed at large distance from the interaction point. The most forward detector, ALFA, is sensitive to particles in the range $|\eta| > 8.5$, while the two others have acceptance windows at $|\eta| \approx 5.8$ (LUCID) and $|\eta| \approx 8.2$ (ZDC). A detailed description of the ATLAS detector can be found in Ref. [2].

The ALFA detector (Absolute Luminosity For ATLAS) is designed to measure small-angle proton scattering. Two tracking stations are placed on each side of the central ATLAS detector at distances of 237 m and 245 m from the interaction point. The tracking detectors are housed in Roman Pots which can be moved close to the circulating proton beams. Combined with special beam optics, this allows the detection of protons at scattering angles down to μrad.

Each station carries an upper and lower RP connected by flexible bellows to the primary LHC vacuum. The RPs are made of stainless steel with thin windows of 0.2 mm and 0.5 mm thickness at the bottom and front sides to reduce the interactions of traversing protons. Elastically scattered protons are detected in the main detectors (MDs) while dedicated overlap detectors (ODs) measure the distance between upper and lower MDs. The arrangement of the upper and lower MDs and ODs with respect to the beam is illustrated in Fig. 9.1.

Each MD consists of 2 times 10 layers of 64 square scintillating fibres with 0.5 mm side length glued on titanium plates. The fibres on the front and back sides of each titanium plate are orthogonally arranged at angles of $\pm 45^\circ$ with respect to the y-axis. The projections perpendicular to the fibre axes define the u and v coordinates which are used in the track reconstruction. To

[1] ATLAS uses a right-handed coordinate system with its origin at the nominal interaction point in the centre of the detector and the z-axis along the beam pipe. The x-axis points from the interaction point to the centre of the LHC ring and the y-axis points upwards. The pseudorapidity η is defined in terms of the polar angle θ as $\eta = -\ln \tan(\theta/2)$.

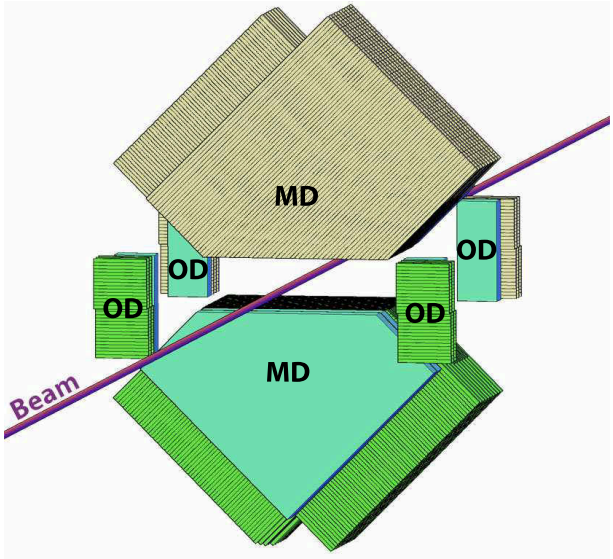

Fig. 9.1: A schematic view of a pair of ALFA tracking detectors in the upper and lower RPs. Although not shown, the ODs on either side of each MD are mechanically attached to them. The orientation of the scintillating fibres is indicated by dashed lines. The plain objects visible in front of the lower MD and ODs are the trigger counters. For upper MD and the lower ODs they are hidden at the opposite side of the fibre structures.

minimize optical cross-talk, each fibre is coated with a thin aluminium film. The individual fibre layers are staggered by multiples of 1/10 of the fibre size to improve the position resolution. The theoretical resolution of 14.4 μm per u or v coordinate is degraded due to imperfect staggering, cross-talk, noise and inefficient fibre channels. To reduce the impact of imperfect staggering on the detector resolution, all fibre positions were measured by microscope. In a test beam [3, 4] with 120 GeV hadrons, the position resolution was measured to be between 30 μm and 35 μm. The efficiency to detect a traversing proton in a single fibre layer is typically 93%, with layer-to-layer variations of about 1%. The overlap detectors (OD) consist of three layers of 30 scintillating fibres per layer measuring the vertical coordinate of traversing beam-halo particles or shower fragments.[2] Two independent ODs are attached at each side of both MDs, as sketched in Fig. 9.1. The alignment of the ODs with respect to the coordinate system of the MDs was performed by test-beam measurements using a silicon pixel telescope. A staggering by 1/3 of the fibre size results in a single-track resolution of about 50 μm. The signals from both types of tracking detectors are amplified by 64-channel multi-anode photomultipliers (MAPMTs). The scintillating fibres are directly coupled to the MAPMT photocathode. Altogether, 23 MAPMTs are used to read out each MD and its two adjacent ODs.

Both tracking detectors are completed by trigger counters which consist of 3 mm thick scintillator plates covering the active areas of MDs and ODs. Each MD is equipped with two trigger counters and their signals are used in coincidence to reduce noise contributions. The ODs are covered by single trigger counters and each signal is recorded. Clear-fibre bundles are used to guide all scintillation signals from the trigger counters to single-channel photomultipliers.

Before data taking, precision motors move the RPs vertically in 5 μm steps towards the beam. The position measurement is realized by inductive displacement sensors (LVDT) calibrated by a laser survey in the LHC tunnel. The internal precision of these sensors is 10 μm. In addition, the motor steps are used to cross-check the LVDT values.

[2] Halo particles originate from beam particles which left the bunch structure of the beam but still circulate in the beam pipe.

The compact front-end electronics is assembled in a three-layer structure attached to the back side of each MAPMT. The three layers comprise a high-voltage divider board, a passive board for signal routing and an active board for signal amplification, discrimination and buffering using the MAROC2 chip [5,6]. The buffers of all 23 MAPMT readout chips of a complete detector are serially transmitted by five kapton cables to the mother-board. All digital signals are transmitted via a fibre optical link to the central ATLAS data acquisition system. The analogue trigger signals are sent by fast air-core cables to the ATLAS central trigger processor.

The station and detector naming scheme is depicted in Fig. 9.2. The stations A7R1 and B7R1 are positioned at $z = -237$ m and $z = -245$ m respectively in the outgoing beam 1 (C side), while the stations A7L1 and B7L1 are situated symmetrically in the outgoing beam 2 (A side). The detectors A1–A8 are inserted in increasing order in stations B7L1, A7L1, A7R1 and B7R1 with even-numbered detectors in the lower RPs. Two spectrometer arms for elastic-scattering event topologies are defined by the following detector series: arm 1 comprising detectors A1, A3, A6, A8, and arm 2 comprising detectors A2, A4, A5, A7. The sequence of dipoles and quadrupoles between the interaction point and ALFA is also shown in Fig. 9.2. Among them, the inner triplet Q1–Q3 is most important for the high-β^* beam optics.

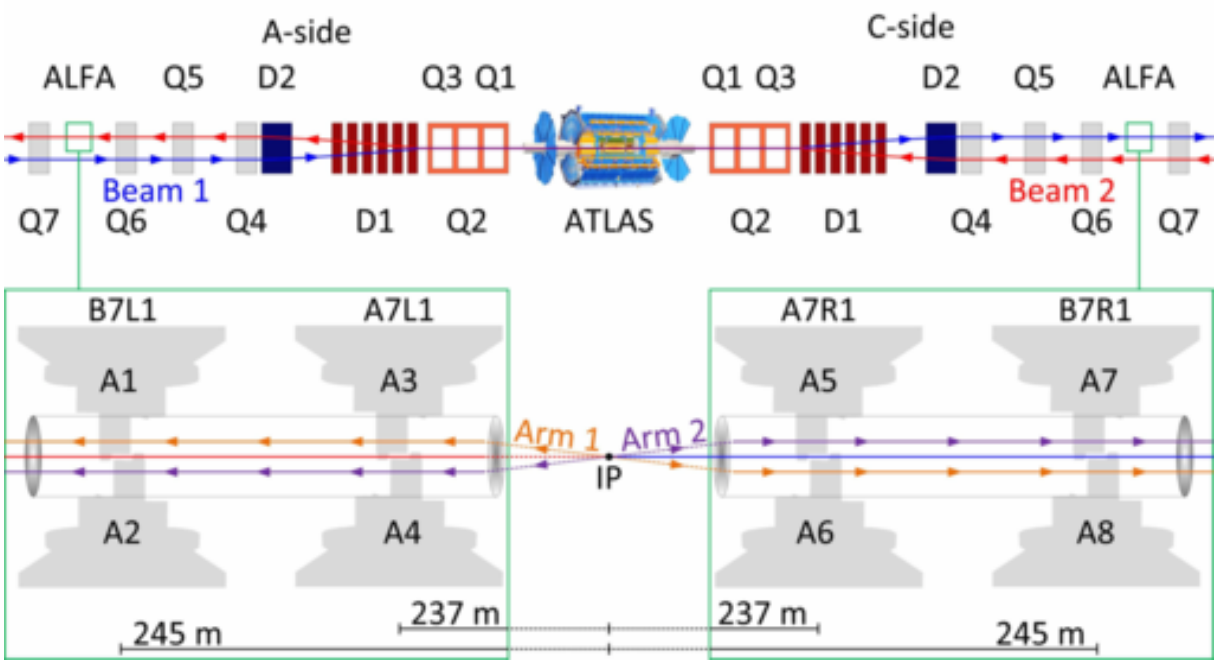

Fig. 9.2: A sketch of the experimental set-up, not to scale, showing the positions of the ALFA Roman Pot stations in the outgoing LHC beams, and the quadrupole (Q1–Q6) and dipole (D1–D2) magnets situated between the interaction point and ALFA. The ALFA detectors are numbered A1–A8, and are combined into inner stations A7R1 and A7L1, which are closer to the interaction point, and outer stations B7R1 and B7L1.The positions of the outer stations correspond to the new positions as defined for Run-II. The arrows indicate in the top panel the beam directions and in the bottom panel the scattered proton directions.

The ALFA detectors were operated in 2011 and 2012 under various beam conditions, with the nominal LHC collision optics but mostly at a dedicated high-β^* beam optics of 90 m. The latter setting was optimized to measure the total pp cross-section at the LHC at $\sqrt{s} = 7$ TeV (see Ref. [7]) and $\sqrt{s} = 8$ TeV. Data were also taken at a β^* value of 1 km to give access to even lower t, the momentum transfer, values. In addition to these low intensity pp runs, diffractive

data were taken with about 110 bunches with the detectors being as close as 7 mm to the beam as well as data in proton-lead collisions.

During operation of the ATLAS/ALFA system in Run-I a systematic increase of the temperature at the level of the detectors was noticed, starting at injection of the beam and reaching the maximum typically 3 hours after the energy ramp; the higher the densities of the bunches the higher the temperature increase. An increase of up to 20 degrees Celsius was observed for a total beam intensity of 2×10^{14}protons. Therefore absolute temperatures close to 40-45 degrees Celsius were reached, putting the gluing of fibers under stress and risking to put in danger the safe operation of the detector. The increase in temperature was traced back to be the consequence of RF losses in the cavity near the detector. Simulation work confirmed the hypothesis with an estimated power deposit of typically 10 W, which translate into the 20 degrees Celsius. Extrapolations to Run-II conditions gave values of up to 80 W in power dissipated; this would have damaged definitely the ALFA detectors.

During LS1 it was therefore decided to revise the design of the ALFA RP and stations to minimise the RF losses. Four main actions were taken. The first was to reduce the cavity to its minimum by extending the RP by a RP filler; the second was to move the ferrites to a more appropriate position to absorb more efficiently the wake field; the third was to add a heat distibution system in copper to extract more easily the heat if it gets to the detector and finally the fourth was to implemented an air cooling circuit. The three first options are illustrated on Fig. 9.3. After implementation of the changes and extensive testing, the four ATLAS/ALFA stations are back in operation. With all the measures taken a reduction of close to a factor 50 is expected in the power deposited on the detectors.

Two other important upgrades were undertaken during LS1; moving stations apart by 4 m (see Figure 9.2) and changing the Trigger system. Moving the B7L1 and B7R1 stations 4 m downstream from their original positions will improve the local angle resolution by factor of 2. The new trigger Back End boards will reduce the latency budget, making it possible for ATLAS to use the ALFA triggers with readout of the full detector system. The trigger Front End electronics of the ALFA detectors where upgraded to reduce dead time from about 550 ns to 87.5 ns. This makes efficient triggering possible with bunches separation down to 100 ns, corresponding to up to about 700 colliding bunches in LHC.

Before the forthcoming data taking period, Run-II, quite some activity will go into recommissioning of the system, in particular on the new Trigger system. The ALFA approved physics programme, total cross-section measurement and independant luminosity measurement, will be the main focus during Run-II. Data at a β^* of 90 m at $\sqrt{s} = 13\,\text{TeV}$ is the plan for 2015; during the shutdown 2015-2016 a new set of cables will be installed to power separately Q4 and Q7 allowing higher values in β^* and therefore giving access to lower $|t|$ values. If supported by ATLAS, ALFA will also participate in runs aiming at diffractive physics; in particular ALFA would have the capability to participate in high intensity runs with up to 700 bunches.

9.2 TOTEM Experiment

TOTEM [8, 9] is a LHC experiment with two detectors embedded in the CMS experiment (T1 and T2 telescopes) and Roman Pot units integrated in the LHC beam lines on both sides of the interaction point IP5/CMS. Since the start of LHC in 2010 the T1, T2 detectors and the 24 Roman Pot installed at $\pm147\,\text{m}$ and at $\pm220\,\text{m}$ from IP5 were operated successfully to perform the physics program of TOTEM during Run-I. The detectors of TOTEM, designed and optimized for special runs of low luminosity, were used for measurements at low- and high-β^* optics and fundamental results like the total p-p cross section at the LHC energy of $\sqrt{s}$ =

Fig. 9.3: Three of the main modifications implemented to minimise the effect of RF. From left to right: the RP filler with the copper contacts for proper grounding, the ferrites distributed as a ring on the flange of the station and the HDS (heat distribution system) in copper with the temperature probes attached to it.

7 TeV were measured and published in 2011. In 2012, TOTEM developed and proposed an upgrade strategy [10–13] with the goal to operate the Roman Pots at high luminosities in special and standard runs of LHC after LS1, allowing the reach of new physics observables. The "TOTEM upgrade proposal" which was approved by the LHCC in September 2013, comprises the relocation of the Roman Pot from ± 147 m in the ± 210 m region at IP5, the upgrade of four existing horizontal Roman Pots with a Radio Frequency shield, the installation of two newly developed low impedance Roman Pots in the ± 220 m region and the installation of additional collimators (TCL4 and TCL6) in the LHC beam line in the region of IP5. This newly proposed forward physics spectrometer at IP5 combining the existing Roman Pots with the upgraded and newly developed Roman Pots was going beyond the original goals and scope of the TOTEM collaboration and overlapped with the future CMS forward physics program. Therefore a new collaboration between CMS and TOTEM was created in the year 2014, to develop the CMS-TOTEM Precision Proton Spectrometer (CT-PPS) related to the physics goals reachable with low-β^* optics (standard LHC luminosity settings), using as baseline carriers the four standard horizontal Roman Pots (box shape) with RF shield to house pixel tracking detectors and the new horizontal circular Roman Pot to house timing detectors. The TOTEM collaboration will independently continue with its enlarged physics program related to special runs and started the development of timing detectors optimized for the vertical Roman Pots allowing the vertex separation at high luminosity, high-β^* runs.

In a common effort of CMS and TOTEM the spectrometer was installed during the LS1 period, while the development of the detectors (timing and tracking) is ongoing. The layout of the TOTEM experiment before LS1 can be found in all detail in [9] for both the telescopes (T1,T2) and the RPs. The following section puts the main focus on the new RP layout as it was realized during LSl. Figures 9.1, 9.2 shows the TOTEM experiment with the detectors T1 and T2 embedded in the CMS central detector and the RPs on both sides of CMS after LS1.

The following sections are based on different documents [10, 13, 21].

9.2.1 Standard TOTEM Detectors Operated during Run-I at High β^*

The Telescopes T1 and T2

Figure 9.3 shows the telescopes T1 and T2 and their integration in CMS. The T1 telescope consists of two arms, on either side of the IP5, fully integrated in the high-η cone of the CMS

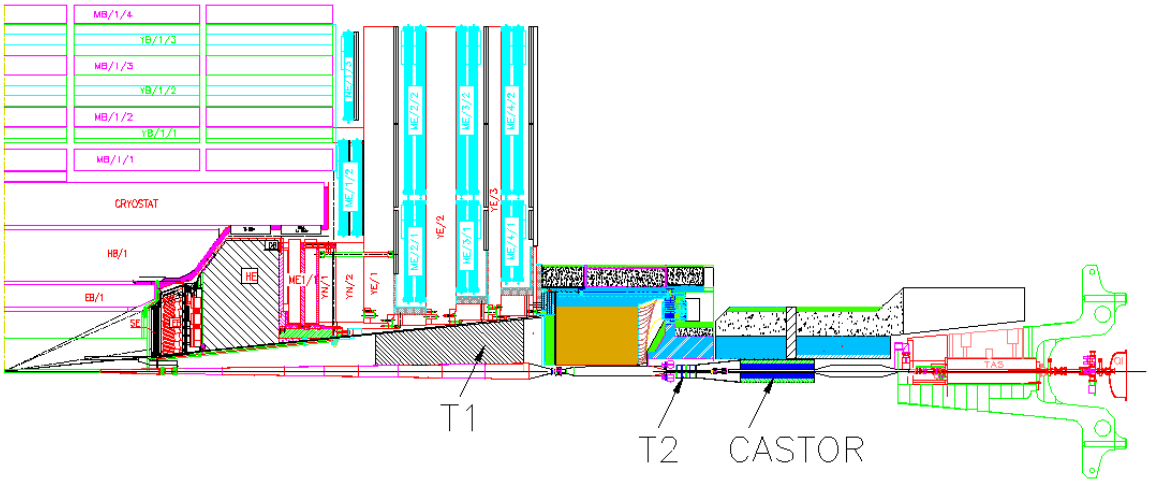

Fig. 9.1: The TOTEM forward trackers T1 and T2 embedded in the CMS detector

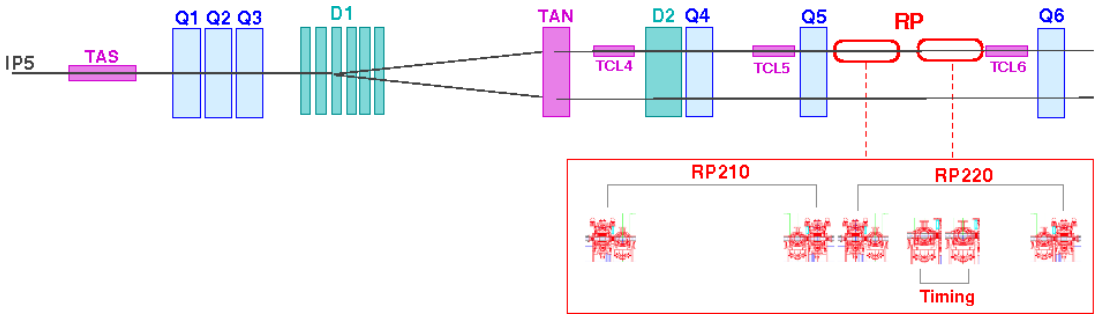

Fig. 9.2: The LHC beam line on one side of interaction point IP5 after LS1: the TOTEM Roman Pots are installed at distances of 210-220 m.

end-cap at a distance between 7.5 and 10.5 m from the IP. T1 detects charged particles in the pseudorapidity range $3.1 < |\eta| < 4.7$. Each arm is composed of 5 planes of Cathode Strip Chambers, with six chambers per plane [9]. The T2 telescope, based on "Gas Electron Multiplier" (GEM) technology [22], allows charged track reconstruction in the pseudorapidity range $5.3 < |\eta| < 6.5$. Each T2 telescope arm located at ~ 13.5 m on either side of IP5 is composed of 20 semi-circular GEM planes - with overlapping regions - interleaved on both sides of the beam vacuum chamber to form ten detector planes of full azimuthal coverage [9]. This novel triple GEM detector technology with the combined pad and strip readout was optimized to cope with the specific event topology and high radiation load close to the beam tube. In the triple GEM structure, a 3 mm drift space is followed by two 2 mm deep charge transfer regions (Transfer 1 and Transfer 2) and a 2 mm charge induction space. Each GEM readout board contains 256 concentric circular strips for the radial coordinate (80 μm wide, pitch of 400 μm) allowing a track resolution of about 100 μm, and a matrix of 1560 pads (with varying size from $2 \times 2\,\mathrm{mm}^2$ to $7 \times 7\,\mathrm{mm}^2$) for azimuthal coordinate reconstruction and for the T2 local trigger. The T2 GEM detector is operated with the gas mixture Ar/CO_2 (70%/30%).

Roman Pot System

The movable beam-pipe insertions called Roman Pots [9] are optimized to detect the leading protons scattered at very small angles. Each RP station is composed of two units (near and

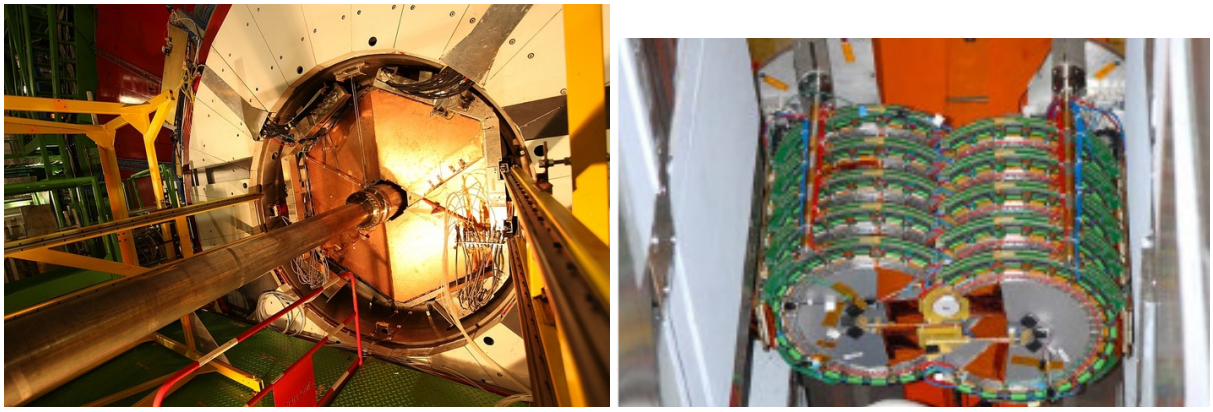

Fig. 9.3: The T1 (left) and T2 (right) telescopes integrated in CMS central detector.

far) separated by a distance of ~ 5 m, each consisting of two vertical pots and one horizontal pot. On each side of the interaction point IP5, 2 RP stations are installed, resulting in a total of 24 single RP detectors, not counting the two new horizontal RPs for timing, added during LS1. Each RP detector is equipped with a stack of 10 edgeless Si strip planes fixed in a frame with a high mechanical precision of better than 50 μm (Figure 9.4, left). The 512 strips with a pitch of 66 μm of a single Si-plane are oriented at an angle of $+45^\circ$ (u-planes) or -45° (v-planes) relative to the detector edge facing the beam. Each stack is composed of 5 pairs of u- and v-planes mounted back-to-back and centered inside the RP (Figure 9.4, right), that separates the sensors and the associated frontend electronics from the LHC vacuum via a thin window of 150 μm thickness. The Si detectors with the frontend electronics are operated at -30°C by means of evaporative cooling. The pressure in the pot is kept between 10 mbar and 40 mbar absolute to avoid condensation. In case of vacuum problems or increase of the absolute pressure above 50 mbar absolute, the cooling system is automatically switching to the 'warm mode', stabilizing the temperature at $+12^\circ$C. To optimize the acceptance for protons scattered at the smallest angles, the TOTEM experiment has developed planar edgeless silicon detectors [23] with a Current Terminating Structure (CTS) to reduce the insensitive area at the edge facing the beam down to 50 μm (Figure 9.5, left). The edgeless Si sensors are processed on very high resistivity n-type silicon wafers ($> 10\,\mathrm{k\Omega cm}$), with a thickness of 300 μm. The silicon detector hybrid carries the sensor with the 512 strips wire-bonded to the input channels of 4 VFAT readout chips. Beam tests have shown that the full detection efficiency is achieved at a distance of only 50 μm from the cut edge (Figure 9.5, right).

9.2.2 Detector Upgrade for Vertical Roman Pots

To reach the physics goals at high β^*, TOTEM stand-alone and combined runs of the CMS detector with the TOTEM RPs are envisaged. The operations of the RPs during Run-I have shown that the RP carriers and the Si strip detectors worked fully satisfactorily both in stand-alone mode and in combination with the CMS detector.

– Within the consolidation project performed during LS1, the RPs at 147 m have been relocated to the 210 m region upstream of the existing RPs at 220 m to improve the resolution of this proton spectrometer. The Roman Pot unit at 210 m far was rotated by 8 degrees around the LHC beam axis (Figure 9.6) relative to the 220 m station, to increase the multiple-track resolution of the silicon strip detector system [10]. Furthermore, all RPs of TOTEM were equipped with new ferrites [24] of higher Curie temperature as it was requested by the LHC machine committee with the aim to improve the beam vacuum.

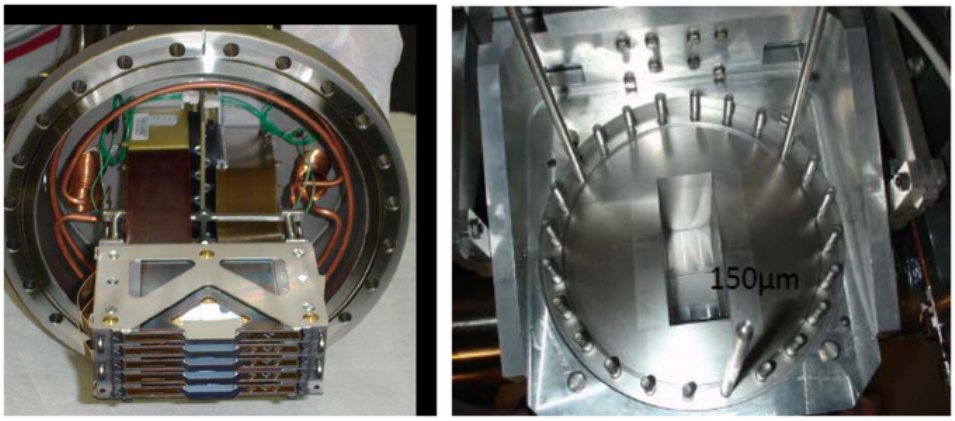

Fig. 9.4: Si detector package composed of 10 Si planes (left). Roman Pot, to separate the Si detector from the LHC vacuum via a thin window of 150μm thickness (right).

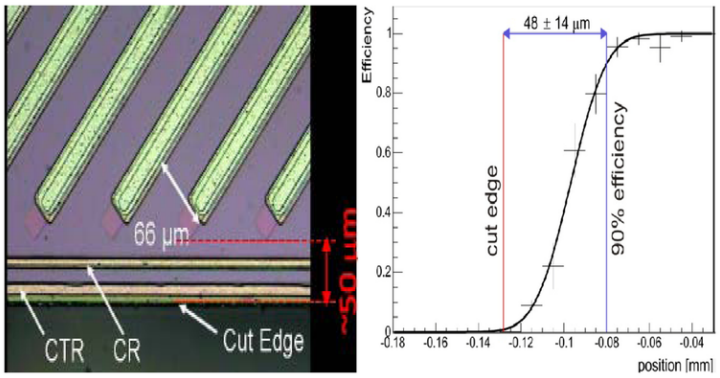

Fig. 9.5: (left) Edgeless Si strip sensor with Current Terminating Structure. The detector reaches full efficiency at 50μm distance from the cutting edge (right)

– As outlined in the physics chapter, high luminosity runs are needed to reach the integrated luminosity within reasonable beam time for special runs of the machine. Analysis of special Run-I data in combination with simulations have shown that the integration of timing detectors with a timing resolution of 50 ps can improve the vertex reconstruction significantly up to a pileup of $\mu \sim 1$.
Timing detectors with a resolution of 50 ps in combination with analogue and digital front-end electronics components are the main elements of the TOTEM upgrade programme as described in detail in [13]. The pixel size and occupancy of the timing detector sensor and the necessary rate capability of the sensor in combination with the full electronics chain were determined by detailed simulation studies. As part of the timing detector infrastructure, a precision clock distribution to synchronize the readout electronics of the timing detectors in the two arms of the $\pm$ 210 m stations will be integrated in the LHC tunnel. While the timing detector infrastructure will be already installed during LS1, the detector components – still under development – can be integrated, thanks to the design of the RPs, in short term technical stops.
– The space available to house the timing detectors in the Vertical RPs is limited by the dimensions of the carrier box allowing to stack detectors up to 5 cm. The Cerenkov detectors as proposed [25] for movable beam inserts cannot be integrated in the vertical RPs as the radiator bar requires at least 12 cm. However, the new horizontal RPs of the CT-

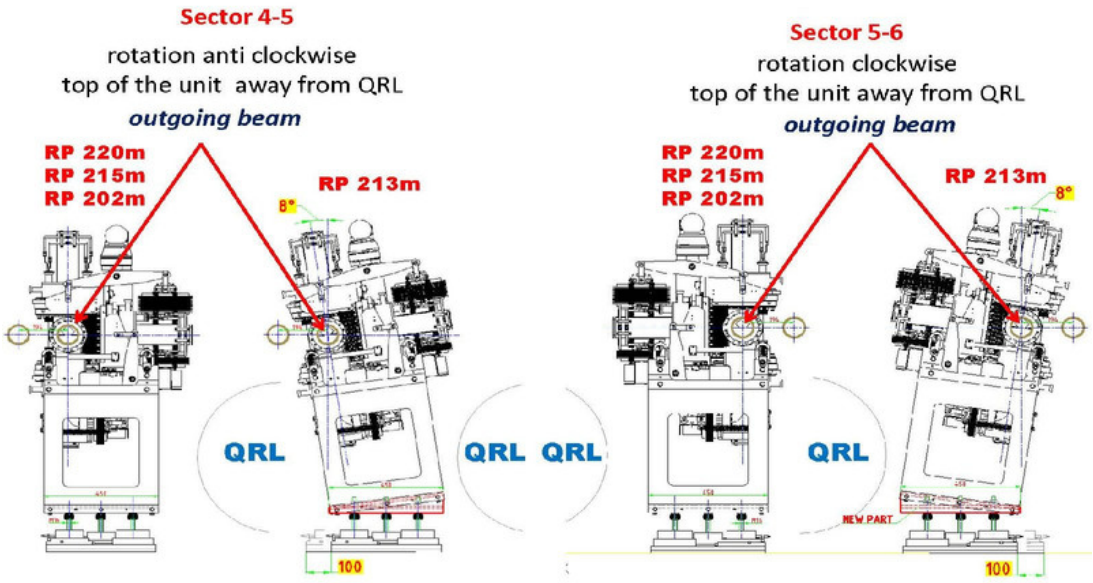

Fig. 9.6: Drawings of the rotated RP units. The view is directed along the outgoing beam.

PPS project, installed during LS1 with a cylindrical shape and a diameter of 12.5 cm, can house them. This technology will be explained in Section 9.4.1
To maintain a low occupancy for each detector channel, its segmentation must be properly tuned. A simple increase of the granularity reducing the pixel size would lead to an impractical growth of the number of channels, which in turn would reflect on the readout, requiring for example the development of custom ASICs.
These considerations led to study a design with pixels of different sizes since the track density due to diffractive events and overlapping background is not uniform as can be seen in the RP data recorded during Run-I . The pixel size is defined in view of having the same track occupancy in all pixels. The simulations to study the occupancy of a single pixel and the minimization of the number of channels required in each detector plane suggested that the minimal number of pixels of different sizes needed for a good efficiency at higher luminosity is 10 per plane with areas ranging from a few mm^2, for the pixels where the track density is larger, to several hundreds of mm^2 in the peripheral parts of the detection plane. The simulation is explained in detail in [13] (Section 4.2).

Diamond Detector as Baseline Technology for Timing Sensor

The selection of the detector technology has to take into account the required timing resolution and the variable size of the pixels. In the proposed diamond sensor, the pixel size minimally affects the time response of the signal due to the extremely high impedance of the material, guaranteeing the same resolution all over the detector plane. However the charge released from a diamond sensor is small in absolute terms ($\approx$ 15 000 e for a thickness of 500 μm, or $\approx$ 3 fC/MIP), and a low noise amplifier is needed to keep the S/N ratio large enough. Since the diamond resistivity is very high the main noise source is the first stage of the amplifier. It is also easy to implement a pattern with pixels of different sizes by means of a simple metallisation on the diamond crystal. The front end electronics design will be then a compromise between speed and low noise.

The present R&D considers ten channels per plane (as shown by simulation in [13]) and

the preamplifier stage located near the detector itself. A single plane is a $10 \times 20\,\mathrm{mm}^2$ diamond sensor. A board built with controlled impedance material (Roger) will be the mechanical support for the detectors, glued with the smallest pixel sizes located near the edge closer to the beam, and for the preamplifier electronics in order to reduce to the minimum the input capacitance (see Figure 9.7). A package of 4 detector planes, with thickness up to 500 μm, will fit in a vertical RP. Among the commercially available diamond substrates it is possible to choose detectors with resolution of the order of 100-150 ps, as the multiple measurements allow to reduce the overall time resolution down to the required $\sim 50\,\mathrm{ps}$. The readout board will be located as close as possible to the detector .

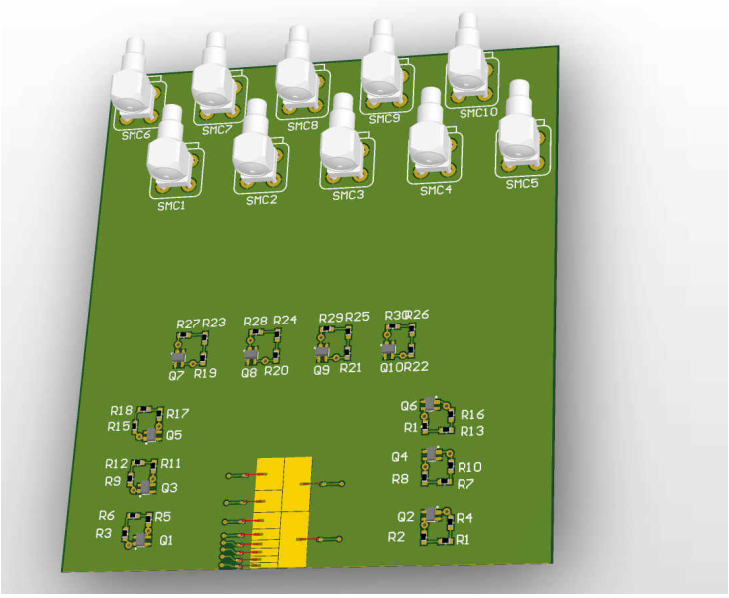

Fig. 9.7: The layout of the board showing the pixel position for one diamond detector plane.

Electronics for Timing Detectors

Given the small number of electronics channels required for the readout, TOTEM is developing a discrete component amplifiers. This single channel preamplifier is made up of two stages, i) the first is a simple CE transimpedance amplifier, with low amplification power and high bandwidth that allows fine tuning of the input impedance (Silicon-Germanium transistors from Infineon are under test). The controlled output signal has $50\,\Omega$ impedance. ii) The next stage amplifies the signal to an output voltage range of 0-1 V to match the readout requirements. The detector hybrid will contain only the first stage of the amplification chain and the signals are sent through coaxial cables to the second stage amplification board. The Hybrid is in the secondary vacuum and the cooling is performed passively through the metallic layers of the board itself.

Two possible ways of adding a time stamp to the recorded protons are: a TDC connected with single or multiple threshold discriminator or a high bandwidth signal sampler. The two possibilities considered have slightly different performances: the first gives a better trigger capability, while the second has a better time resolution.

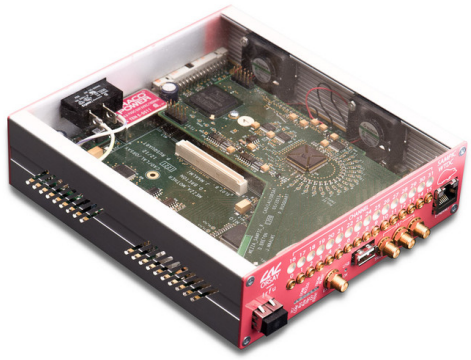

Fig. 9.8: The board with the SAMPIC chip used for the first tests.

Discriminator and time-over-threshold measurement with a TDC: each pixel is equipped with a wide bandwidth transconductance preamplifier and the output voltage is proportional to the input current generated from the collected charge that discharges on the input resistance. A single threshold discriminator detects the edge of the signal. The time walk of a single threshold discriminators, consequence of charge fluctuations, can be corrected measuring the time over threshold for each signal. In this case the signal rise time is limited by the bandwidth and with the present electronics is possible to obtain rise time down to ~ 180 ps. The criticality of this approach is that for a MIP the signal to noise ratio is lower than 2. A way to improve the S/N is either to add coherently with one preamplifier the signal produced in two (or more) diamond planes connected in parallel or to increase the input resistance of the amplifier as discussed in [26]. However the understanding of both solutions requires a certain amount of simulations and tests.

The NINO chip [27] provides this possibility, the output signal length being proportional to the time over threshold of the input analog signal. The maximum acquisition rate of this device is around 30 MHz which in turn implies an average rate for each pixel of less than 10 MHz, well below the maximum rate expected in the experiment. The front-end board for one plane will have 10 LVDS output signals each one providing both the pixel information of time of arrival with the leading edge and the charge released with the signal length.

Digital sampling: the signal from each pixel is integrated and then sampled with a high bandwidth signal sampler. To extract the timing information from the output of a preamplifier with a known transfer function, an appropriate algorithm reconstructs the original signal.

The sampling can be performed with the SAMPIC chip developed in Saclay and Orsay [28]. The chip has 16 input channels with a sampling rate up to 10 Gs/s which provides a good signal reconstruction, due to the fact that the preamplifier has a rise time of 2 ns (see Figure 9.8).

For each channel a circular buffer of capacitors continuously samples the input signal. Digitization of the buffer using a 11 bit Wilkinson ADC starts either when an external trigger is provided or when the input signals goes above a programmable threshold (see Figure 9.9 for a diagram of the chip).

A future version of the chip will allow a minimum 50 ns dead time on each independent channel by using a faster interleaved readout between two or four channels and a function to control the internal trigger, for instance start conversion only when the internal trigger fires

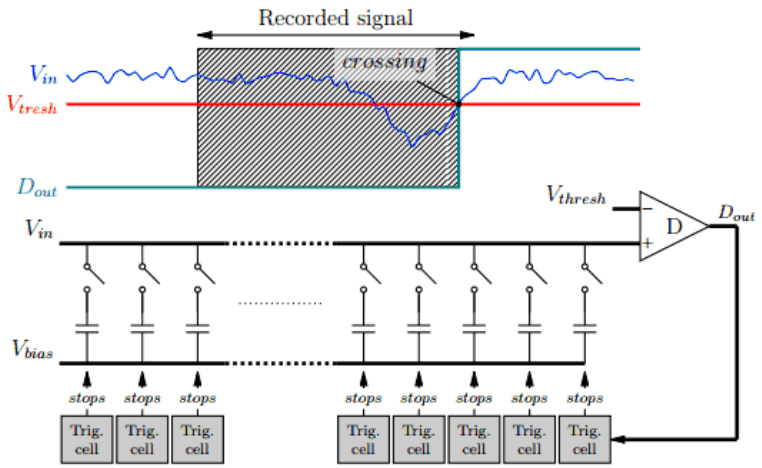

Fig. 9.9: Inside the SAMPIC, the input signal is continuously sampled in a ring analog buffer. In internal trigger mode, the signal is compared to a programmable threshold to stop the sampling and start the ADC conversion.

in coincidence with the bunch crossing, and the possibility of a fast read-out of the internal trigger time-stamp to be complemented with a more precise timing information after the digital analysis of the sampled signal will be completed.

The SAMPIC with a CSA preamplifier has been tested with a pair of "Ultra-Fast" Silicon detectors [29]. Figure 9.10 shows the time difference measured between the two detectors pulsed with the same laser via an optical splitter and using an off-line algorithm. The resolution achieved on the timing difference is of $\sim 40\,$ps, which indicates a resolution of $\sim 30\,$ps for a single measurement. More studies will follow with diamond detectors in a real test beam or cosmic rays.

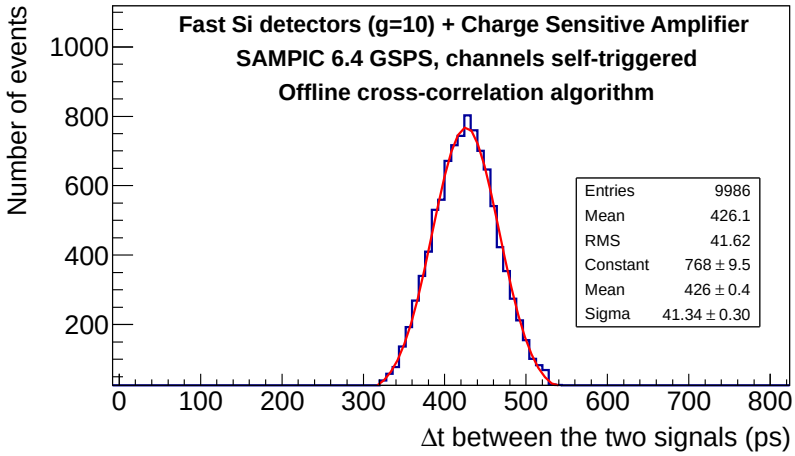

Fig. 9.10: Distribution of the time difference between two Ultra-Fast Silicon detectors pulsed with the same laser and read with fast CSA and SAMPIC, using an advanced off-line algorithm.

Preliminary Tests: Two diamond detectors, $0.5 \times 0.5\,\mathrm{mm}^2$ in size and 500 μm in thickness, have been purchased from Cividec Instrumentation [31] together with state of the art CSA and wide-band amplifiers with specs optimized to our request, and assembled in a telescope (Figure 9.11) for measurements with particles on a test beam (Figure 9.12). Moreover new transimpedance preamplifiers have been developed in house in order to study and optimise the input impedance of the circuits. Three beam test have been performed in PSI and Cern PS, with different configurations. The detectors where connected to the preamplifiers with SMA connectors. The input capacitance, of about 0.5 pF from the detector, was dominated by the connectors (5-10 pF). The rise time of the signals is strongly affected by this parameter and therefore a reduction in performance is expected. The resolution obtained is around 190 ps, well in line with the expected value, and an improvement is expected with a design of the hybrid that removes the connector. The final step is therefore to design and bring to a test-beam a hybrid with first-stage preamplifiers bonded as close as possible to the detector, in order to keep the capacitance below ~ 1 pF. A similar design has already been used successfully elsewhere [30]. Construction of the new hybrid has already started.

Other Technical Considerations: A cooling system will be provided for the electronics only, since the diamond detectors do not dissipate any power from the polarization power supply.

All the electronics that need to be as close as possible to the actual detector and that makes use of FPGAs (as the control/transmission board for the SAMPIC or, in alternative, the TDC board) can operate only in regions with reasonable radiation levels. Studies performed on Altera Cyclone FPGA with ion and neutron beams show that even in the surrounding area of the beam pipe we could expect for high luminosity runs a SEU (single event upset) rate of 1 every 3 hours, which is already orders of magnitude higher than what was experienced in the special high beta optics runs. For this reason space close to the Roman Pot station located in the floor of the tunnel will be available to keep the electronics as far possible from the beam pipes. In case of SEU a Resync request will be needed only for the TDC board.

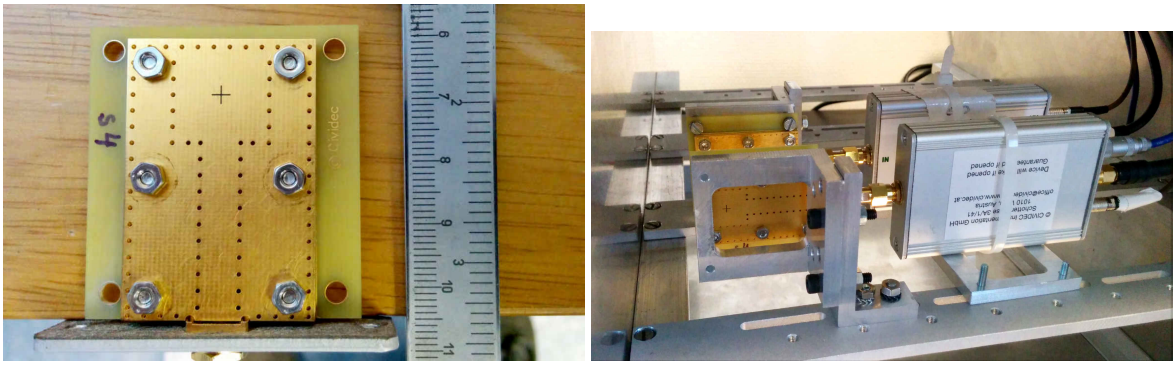

Fig. 9.11: Prototype of the diamond detector from Cividec Instrumentation (left) and the assembly of the test telescope (right).

TDCs with a time resolution of ~ 10 ps inside an FPGA are in an advanced stage of development by TOTEM and under evaluation. The time reconstruction algorithm measures the crossing time for a single threshold and the time over threshold and a correction matrix. In case we will use the SAMPIC chip, the data have to be fitted in a simple FPGA board. The advantage of using on board FPGAs is that the Trigger and DAQ information will be formatted on the same board. The event is formatted for DAQ with a header, a start of frame patterns

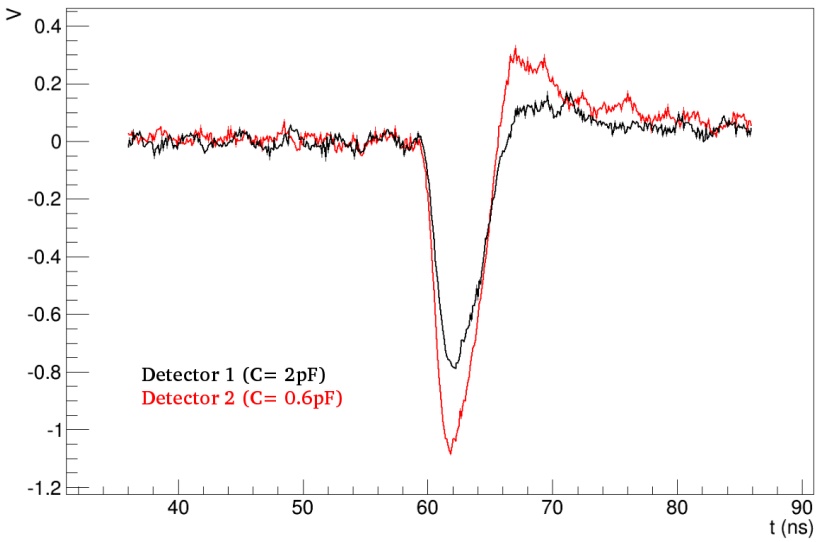

Fig. 9.12: Signals of two diamond detectors of different capacity recorded by the newly developed TOTEM Fast Amplifier in a test with 4 GeV electrons.

and counters, the list of TOA (Time Of Arrival) and TOT (Time Over Threshold) for each fired pixel, and a footer. The information is transmitted without on-line corrections.

The Trigger algorithm instead will perform an on-line rejection based on the number of tracks (see Section 4.2.2 in [13]). In order to filter out noisy channels that could contaminate the time measurement a trigger signal (a track road) is generated only if the signals from aligned pixels from adjacent planes satisfy a majority-AND condition. Track counting is done locally and, if the event is accepted, the time of arrival is formatted into 4 words and sent to the central trigger unit (TOTEM LONEG board).

Clock Distribution for Timing Detectors at ± 220 m from IP5

The challenge of combining measurements with picosecond range precision for Timing signals generated in locations separated by large distances (order of 220 m) requires a clock distribution system capable of the highest precision and of the utmost time stability.

The following pages aim at describing the Clock Distribution system for the TOTEM Timing Upgrade. The system is adapted from the *Universal Picosecond Timing System* [32], developed for FAIR (Facility for Antiproton and Ion Research), the new, unique international accelerator facility for research with antiprotons and ions presently under construction at GSI (D), where a Bunch phase Timing System (BuTiS) based on this concept has been implemented [33].

The optical clock distribution network will use a Dense Wavelength Division Multiplex (DWDM) technique that makes it possible to transmit multiple signals of different wave-lengths over a common single mode fibers. This will allow to use standard telecommunication modules compliant to ITU (International Telecommunications Union) international standards.

The experiment requires two very stable clocks for the precise timing reference of the measurement and the bunch identification. These reference clock signals are sent from the counting room to a set of receivers positioned near the timing detectors in various location of the LHC tunnel on both sides of IP5. A third signal added on the same optical fiber will be simply reflected back to be used to continuously measure the time delay of each optical transmission

line: these delay measurements are necessary to correct the time information generated at the detector location for fiber delay variations (thermal and mechanical instabilities).

The system can be logically subdivided in four major blocks: the Transmission Unit, the Distribution Unit, the Measurement Unit and the Receiving Unit. One Receiving Unit must be installed very near each Roman Pot location, the Transmission, Distribution and Measurement Units will be located in the TOTEM racks in the IP5 counting room. A block diagram of the entire system is reproduced in Figure 9.13.

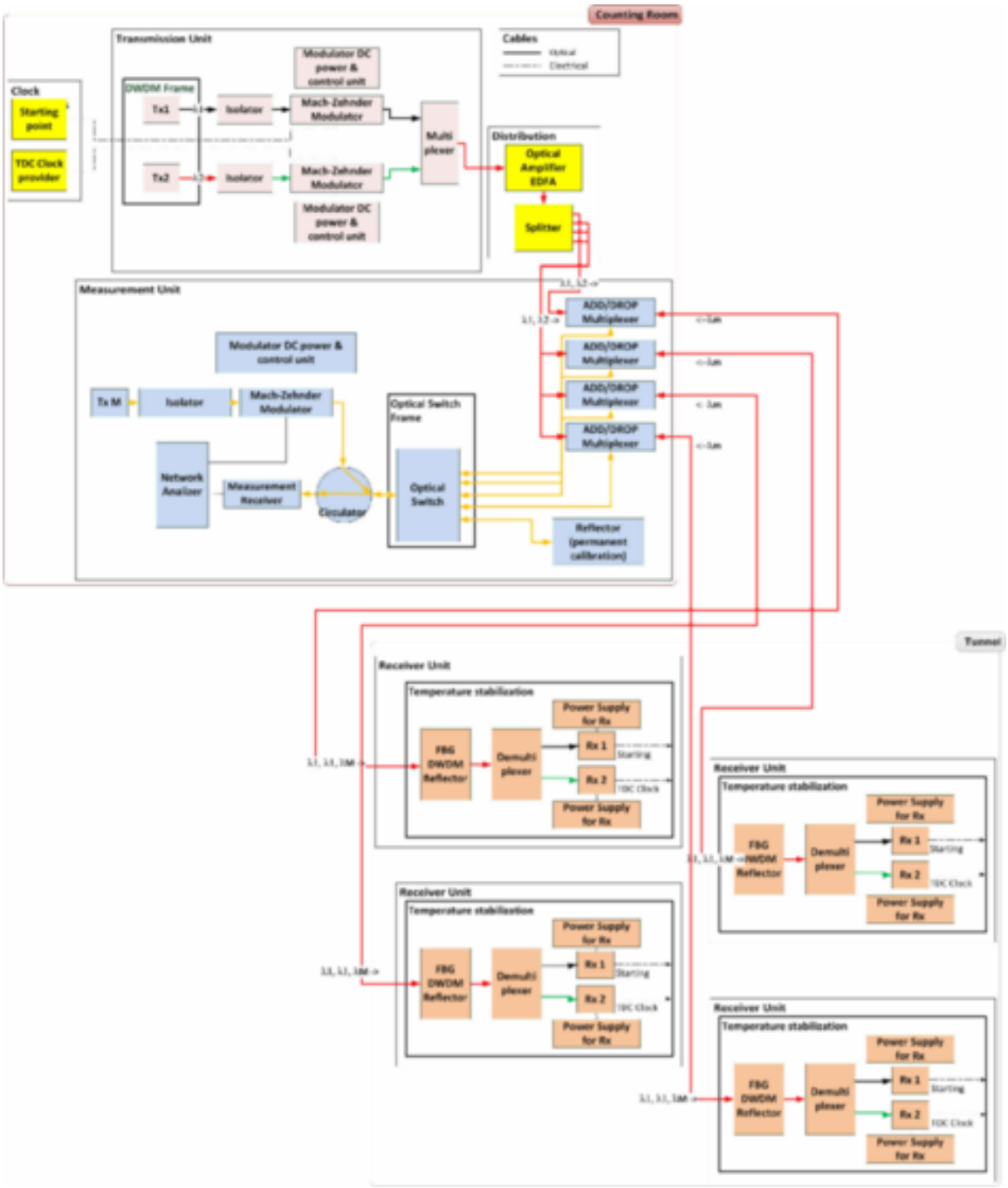

Fig. 9.13: The clock distribution system (see text).

Measurements performed with the prototype of the “BuTiS” system show that the in-

fluence of the transmission system on the signal jitter, is of the order of 0.4 ps [33], mainly dependent on the quality of the clock source signal, the noise added by the optical components and the bandwidth of the transmission system itself. Using a transmission system based on this concept, the total jitter of the TOTEM clock transmission system will also be due mainly to the inherent jitter of clock sources and the end user electronics.

- Transmission unit
  The Transmission Unit optically modulates the two reference clocks in signals with different wavelength λ_1 and λ_2. Via DWDM these optical signal are multiplexed into a single fiber and re-transmitted at a specific wavelength using a 1 550 nm band laser to the Distribution Unit. The signal is amplified with an erbium-doped fiber amplifier (EDFA) to compensate the attenuation due to further splitting and the multiplexers.
  A Thorlabs PRO8000 [34] platform has been chosen to generate the two DWDM wavelengths on channels ITU 32 and ITU 34. This complete platform is designed to operate and control electrical and optical modules for telecommunication testing and application developments from a broad family of interchangeable modular devices and can be controlled by an external computer using industrial control protocols. The modulation of the optical signals is performed by two military grade Mach-Zehnder modulators with a 20 GHz bandwidth. This unit can be rack mounted and is suitable for use in the experiment control room harsh environment.
- Distribution Unit
  The DWDM optical signal, as generated by the Transmission Unit, needs to be split in order to be transmitted to the four Receiving Units. Moreover a third DWDM modulated optical signal of wavelength λ_M is needed to measure the transmission delays over each fiber and is added to the other two clock signals.
  The JDSU [35] Multiple Application Platform (MAP-200) has been chosen for the Distribution Unit optical amplification, optical signal splitting and switching. This platform is a highly configurable, scalable and industrially controlled system that can host several optical modules with a wide range of functions. The EDFA amplifier developed for this platform will be used for the signal optical amplification.
- Measurement Unit
  The signals' delays are measured in this unit. A reference signal is generated, optically modulated using the wavelength λ_M and sent via an optical switch to every Receiving Unit and to a reflector, which will be used for calibration.
  Add/drop multiplexers combine this reference signal to each of the 4 DWDM optical signals generated in the Transmission Unit and split in the Distribution Unit. The multiplexed signal, that now contains the three modulated optical wavelengths: λ_1, λ_2 and λ_M, is transmitted to the Receiving Units located in the tunnel at $\pm$220m and $\pm$210m.
  The λ_M optical reference signal once at the Receiving Unit is reflected back to the Measurement Unit, where the optical add/drop multiplexer separates the λ_M optical signal coming back from the RUs and pass it back to the optical switch. A "circulator", placed between the DWDM modulator and the switch, distributes the reflected signals to a measurement instrument without interrupting the transmission from the generation module to the switch. A phase comparison of the reflected signal with the reference one is performed, using a vector network analyzer. The phase differences obtained by this measurement determine the delay of each clock signal distribution channel.
  As for the Transmission Unit, a Thorlab PRO8000 module, and the same Mach-Zender modulator, will be used. The DWDM wavelengths proper of channel ITU 36, will be used to modulate the reference signal.

– Receiving Unit
The Receiving Unit separates the multi-wavelength optical signal at the RP stations into individual signals.
The signal from the single mode fiber (SMF) encounters first a Bragg grating (FBG) DWDM reflector and reflects back the signal component of λ_M wavelength. The other components of the signal are routed to a DWDM demultiplexer that separates the two wavelengths, λ_1 and λ_2, and outputs them on separate fibers for conversion to electrical signals and delivered to the front end electronics and DAQ cards eventually.
This unit should be located as close as possible to every Roman Pot location. A temperature stabilization of this unit, depending on the temperature characterization of the installation point in the tunnel, may be needed to reduce the long term shift of the measured delay.

9.3 Forward Shower Counters in CMS

The true rapidities of the proton beams are $|y_{beam}| < 8.92$ (9.94) at $\sqrt{s} = 7$ TeV (13 TeV) respectively. Neutrons can be measured up to the beam rapidity with the Zero Degree Calorimeter, ZDC, which also measures photons, mostly from π^0's, at $\theta = 0$ ($\eta = \infty$). All charged particles have been swept by upstream magnets out of the ZDC acceptance. Up to the TAN at $z = 140$ m both incoming and outgoing beams are in a common vacuum pipe.

Apart from quasi-elastically scattered protons with $y \sim y_{beam}$ detected in Roman pots in TOTEM in high-β^* runs, and in future with CMS-TOTEM Precision Proton Spectrometers (CT-PPS) there are rapidity regions $+5 < \eta < +9$ and $-9 < \eta < -6.6$ not instrumented for *direct* particle detection. The asymmetry is because CASTOR has $-6.6 > \eta > -5.2$ but only on the negative-η side. Sets of scintillation counters, called Forward Shower Counters, FSC [14, 15], have been installed surrounding the outgoing beam pipes at $z = \pm 59$ m, ± 85 m and ± 114 m, see Figure 9.1.

These scintillation counters are fully efficient for minimum ionising particles, but their efficiency for primary particles is determined by the material of the beam pipes and surroundings and is a function not just of η but also of p_T, ϕ and charge Q, as well as the machine optics β^*. Particles in the region $6 \lesssim |\eta| \lesssim 8$ hit the beam pipes and surrounding material and may interact and cause showers of charged and neutral particles that will be detected in the FSC. Then η-coverage is not well defined.

An FSC gap by itself is not enough to select diffractive events efficiently it can be combined with either a proton in the TOTEM Roman pot in the same direction in the high-β^* runs, or gaps in other forward detectors: ZDC, CASTOR, T2 and also sometimes HF ($3 < \eta < 5$). GEANT was used [14] to simulate forward particle production, transport through the beam lines and showering in the materials. Fig. 9.2 shows estimated detection efficiencies for low mass diffraction, as a function of diffractive mass, for different combinations of forward detectors. At least five hits in any FSC counter were required, or a track or signal in the $|\eta|$ region covered by T1, T2, HF, CASTOR or the ZDC. Approximately 25% of the single diffractive cross section is for masses below 10 GeV/c^2.

CMS-TOTEM measurements at $\sqrt{s} = 8$ TeV [16] show $dN_{ch}/d\eta \sim 3$ at $\eta = 6$. Thus over two units of $\eta \sim 6 - 8$ most non-diffractive interactions have several charged particles plus neutrals (photons from π^0, K^0_L and neutrons) which may interact in the beam pipe or other material and make showers. Therefore the FSC counters are only useful for low pileup running, in particular for bunch crossings with only one inelastic collision. Using FSC as rapidity gap

detectors one can also require the adjacent T2 to be empty, and when using them to detect proton-dissociation products they can be used to extend the mass range.

During the mean pileup $\mu \sim 0.05$ TOTEM run with $\beta^* = 90$ m in July 2012 the FSC counters on the positive-η side were operational and correlations between their activity (hits or no-hits) and the direction of a proton, as well as with the mean-η of associated central jets, were observed. Their noise levels are low enough for them to be used as rapidity gap detectors.

In addition to their use as “gap detectors", they extend the rapidity coverage close to $\Delta\Omega = 4\pi$, which minimises the uncertainty in extrapolating the total inelastic cross section σ_{inel} to low diffractive masses. Events (in low pileup running) in which all the CMS detectors covering $-5 < \eta + 5$ are empty (in noise levels) but which have signals in the FSC counters (on one or both sides) from low-mass diffraction events can be measured and included. Furthermore the patterns of hits in the three stations (which cover different η-ranges) can be tested against models of low-mass diffraction, e.g. mass-dependent $p \to p\pi^+\pi^-$ or $n\pi^+$.

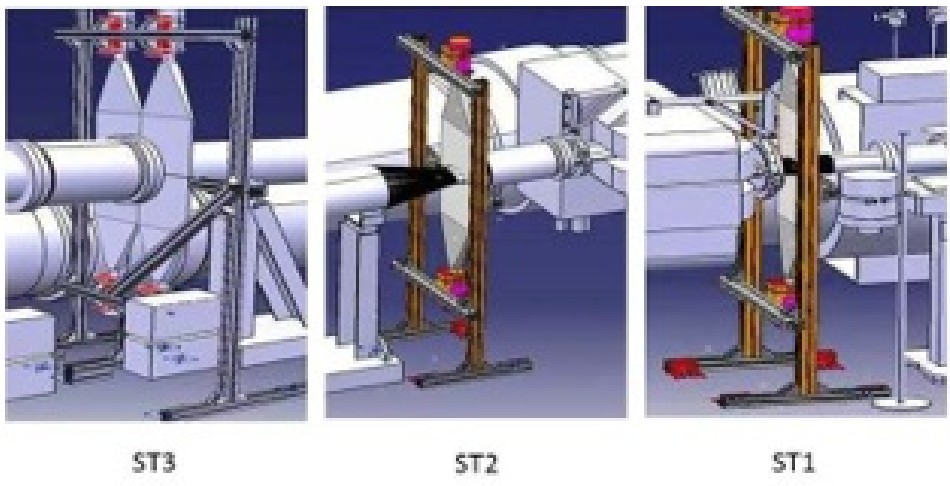

Fig. 9.1: The layout of three FSC stations in CMS. The fourth station is identical to ST3.

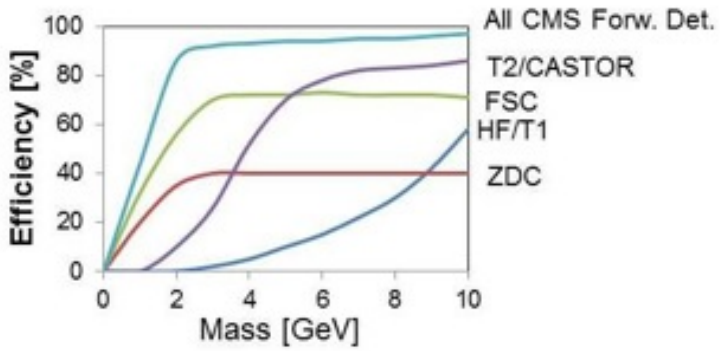

Fig. 9.2: Detection efficiency for single diffractive events as a function of diffractive mass, for different CMS detectors.

9.4 CMS-TOTEM Proton Spectrometer (CT-PPS)

A new collaboration between CMS and TOTEM was created to develop the CMS-TOTEM Precision Proton Spectrometer [21] related to the physics goals reachable with low β^* optics

(standard LHC settings). The baseline carriers of this spectrometer are the newly developed low-impedance RPs integrated in the beam line at $\pm(203 \div 214)$ m from IP5, designed to host future pixel and picosecond-timing detectors (Figure 9.1). To optimize the beam quality and to protect the LHC magnets near the RPs against collision debris, new collimators were installed upstream (TCL4) and downstream (TCL6) of the RPs during LS1. The TCL4 collimators were installed in the former locations of the RP147 stations, and TCL6 was installed between the most downstream unit of RP220 and the supra-conducting magnet Q6. Comprehensive simulation studies were performed and it could be shown that optimized collimator settings can result in a satisfactory machine protection without limitation of the physics goals. Additional beam loss monitors (BLMs) were installed in that region to monitor beam losses caused by RP and TCL6 insertions in that critical region. The installed spectrometer will consist of a total of 24 RPs (for tracking) and 2 RPs (for timing) that can be inserted selectively.

Within the CT-PPS collaboration new movable beam inserts, tracking and timing detectors for the low β^* forward physics were developed for the LHC straight line beam region of ± 210 m from the interaction point IP5. The requirements on beam inserts and detectors operated at low β^* are quite different from those at high β^*, as already outlined in Chapter 1. The underlying strategy foresees to integrate where possible the newly developed detectors in existing carrier systems of TOTEM and the use of existing infrastructure in the LHC tunnel. This concept lead to an inter weaved project of the TOTEM consolidation and upgrade program with the CT-PPS project. Timing detectors with a resolution better than 10 ps are required to achieve the necessary vertex separation in the CMS central detector with a O(mm) precision, for pileup of 25-50. The double hit probability per bunch crossing and the acceptable single proton rate of a single timing cell determine the pixel size. The detector systems with this time resolution and pixels size, combined with the high rate requirements, represent the forefront of present detector developments. With Cerenkov detectors, that can be integrated in the newly developed Roman Pots, the time resolutions in the range of 10 ps could already be achieved in test beams, however the high material budget and limited pixel size of this technology might turn out to be a limiting factor in the final operation under LHC conditions. Therefore R&D of different solid state detector have started to obtain the required time resolution with a lower material budget and smaller pixel cell size. The edgeless Si strip tracking detectors of TOTEM can not be used for the low β^* operation due to the intrinsic limited multi hit resolution. New slim edge radiation hard pixel detectors that cope with the required space resolution and optimized for the use in movable beam inserts are under development.

The upgrade of the present Roman Pots and the development of new cylindrical Roman Pots was mandatory for the ambitious goal to insert the detectors under standard LHC conditions close to the beam. At this point it is emphasized that alternative beam inserts like the movable beam pipe with low impedance (Hamburg Beam Pipe) have been studied for many years and are still under development [36]. The movable beam pipe concept, primarily developed for locations at LHC where the operation of horizontal Roman Pots is almost impossible due to space constraints of the LHC beam line, was as well proposed as alternative in that location, where the Roman Pots are at present integrated in the beam line of ± 220 m from IP5. However, till today was neither reached a final design nor the construction of a full size prototype, that complies with all requirements imposed on a beam insert for LHC. The possible usage of these type of beam inserts requires further R&D and the successful construction and test of a full size prototype.

In the absence of feasible alternatives to the concept of the Roman Pot at the time of LS1, the TOTEM collaboration decided for time and cost reasons to study and develop in close collaboration with the LHC Beams Impedance and engineering groups, the low impedance

Roman Pot concepts, based on the experience made during three years of operation during Run-I of LHC. These developments lead over a prototype phase, including mechanical & vacuum tests and RF measurements simulating the EM radiation field of the LHC beam close to the Roman Pot to a final design, that was approved for serial production. Even though the simulation and lab test have shown significant improvement of all critical parameters that determine the successful and safe operation of these beam inserts, a final prove of the expected performance can only be made under realistic conditions of LHC. In this sense the newly installed Roman Pots within the CT-PPS project can be considered as R&D for new beam inserts designs.

Test insertions of horizontal Roman Pots by TOTEM during Run-I have shown, that the generated secondary particle production rate impinging on the magnets downstream of the 220 m far Roman Pot stations can exceed the acceptable level. For that reason a new collimator system (TCL4 and TCL6) was proposed for IP1 and IP5, and installed during LS1 [37]. Figures 9.1 and 9.2 show the beamline in Sector 4-5 with the RPs installed.

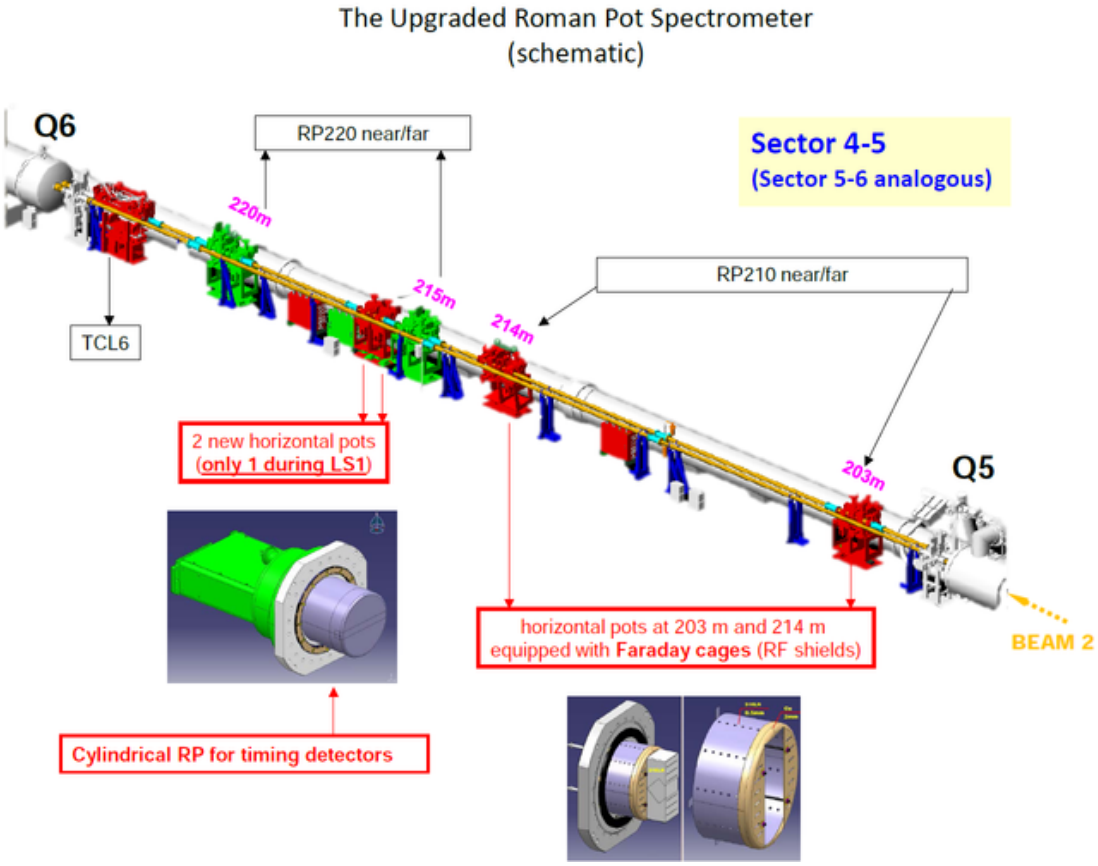

Fig. 9.1: The layout of the beam line in the 200 m region after LS1

9.4.1 Development of Low-Impedance Roman Pots

The new RPs installed between the existing units 220-N and 220-F are intended to host timing detectors. Hence their design was subject to the following main requirements:

1. Among several potential detector technologies for the timing measurements (see Section 9.4.2), Čerenkov counters [25, 38] are already at well advanced development stage. For the full timing resolution of $\sim$ 15 ps a total length of 24 cm of quartz is needed. Dis-

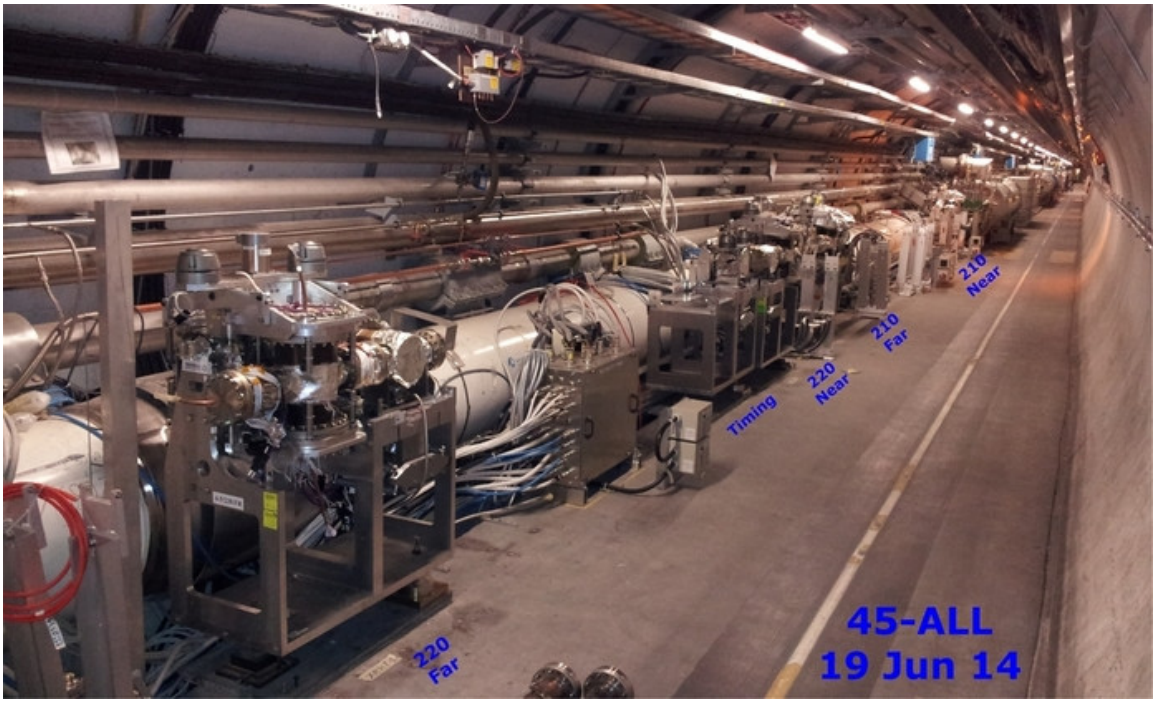

Fig. 9.2: The beamline in Sector 4-5 with the RPs installed

tributing this length over the two new pots requires each pot to accomodate two slabs of 6 cm length, too big for the space provided by the traditional TOTEM pots. If at a later stage thinner timing detectors (e.g. diamond detectors) become available, tracking and timing functionality may be combined in the same pots, reducing the number of pots to be inserted.

2. The RPs housing the timing detectors will have to operate in high luminosity running scenarios. They will have to approach very intense beams to the same distance as the tracking RPs, i.e. down to about a mm from the centre. At that distance beam-coupling impedance effects, machine vacuum compatibility in terms of outgassing, and particle shower development have to be taken into account in the geometrical design and in the choice of materials (Section 9.4.1.3).

After considering various options and after an iterative optimisation, the following design has been adopted for the new RPs (Figures 9.3 and 9.4) [39]. The volume housing the detectors will have a cylindrical rather than rectangular box shape. This choice provides the necessary space for all potential technologies of timing detectors and at the same time reduces the beam coupling impedance by minimising resonant cavities. The ferrite in this design will be integrated in the (stationary) flange rather than mounted on the moving detector housing. It will have a ring geometry (inner diameter = 150 mm, radial width = 15 mm, thickness = 5 mm). Furthermore, all vacuum-side surfaces of the RP stations are foreseen to receive a 2 μm thick Non-Evaporative Getter (NEG) coating.

9.4.1.1 The Mechanical Tests of New Roman Pot Cylinders

The new cylindrical Roman Pots with the thin window of 300 μm thickness have been produced (see Figure 9.3) in a collaboration of CERN with industries. After the production of the first prototype in fall 2013 a series of tests have been performed at CERN in collaboration

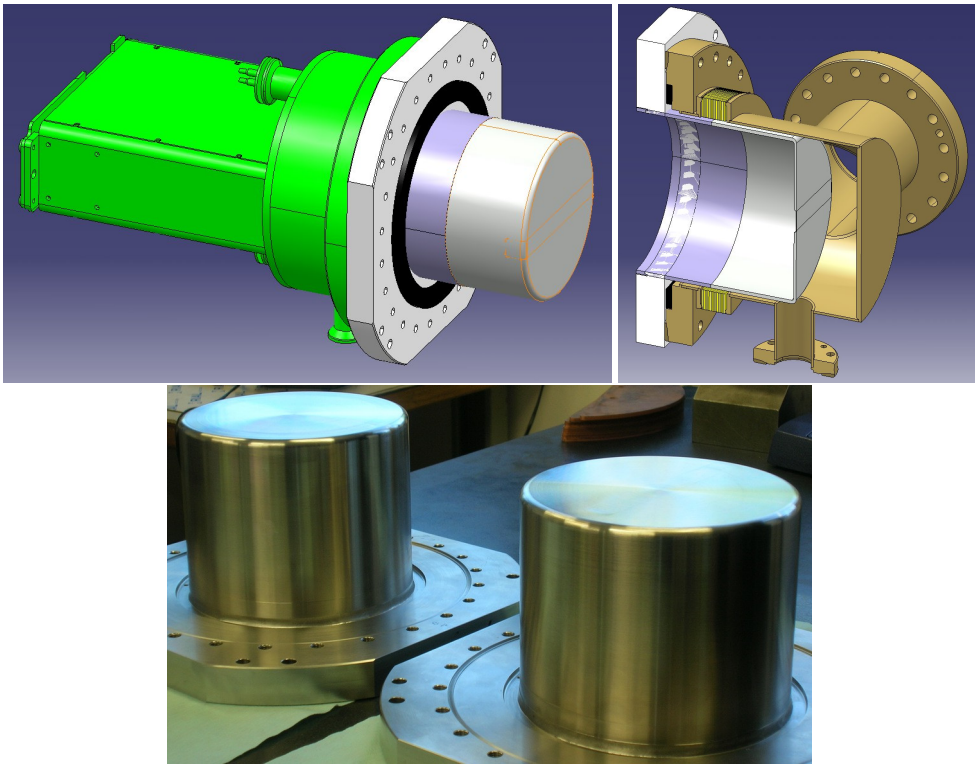

Fig. 9.3: Top: drawings of the cylindrical detector housing for the new RPs designed to accomodate timing detectors. Bottom: the manufactured pots.

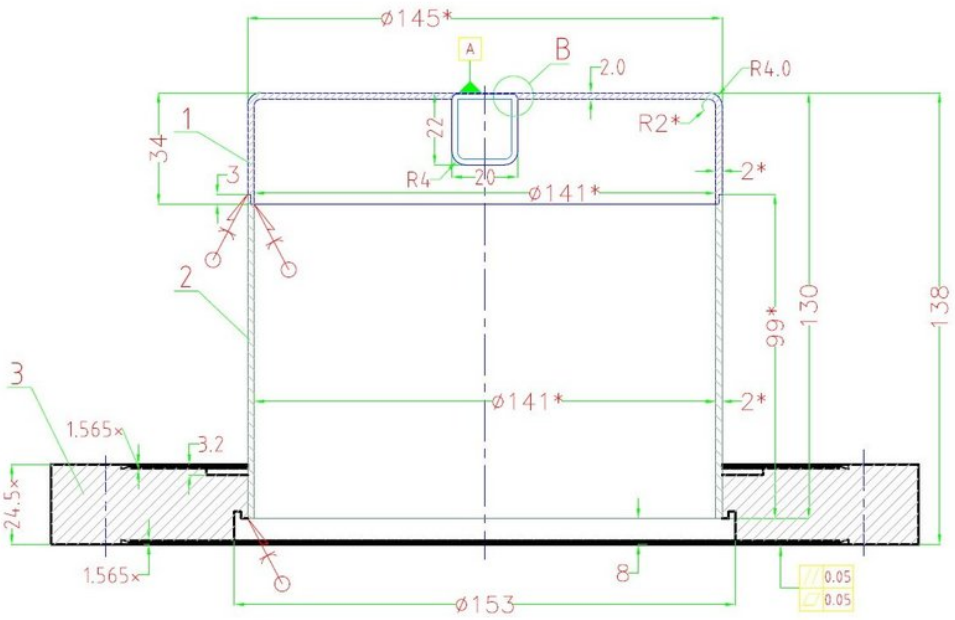

Fig. 9.4: Dimensions of the cylindrical RP.

with different support groups, to approve the compatibility of this new RP design with the LHC requirements. The deflection of the thin window was measured as function of the applied air overpressure simulating the possible pressure difference seen by the RP when the LHC beam

tube is under vacuum and the inner side of the RP is under atmospheric pressure. Such pressure difference will occur during the installation of the detector components or a failure of the vacuum system and a leak of the feedthrough integrated in the flange separating the atmosphere from the inner side of the RP [40]. Furthermore the He transmission was measured in a special setup and the compatibility of this design with the LHC leak rate requirements was shown [41].

9.4.1.2 The RF Shield for the Box-Shaped Horizontal Roman Pots

Given that the existing horizontal pots housing tracking detectors will have to cope with the same high luminosity conditions as the new timing RPs, some adaptations will be made:

- To reach the same impedance reduction as for the new cylindrical pots (see Section 9.4.1.4), the rectangular detector boxes will be successively equipped with 1 mm thick cylindrical copper RF shields (Figure 9.5). Holes in the shield allow for the gas flow necessary to establish a vacuum equilibrium inside and outside the shield. The number and dimensions of these holes have been defined in cooperation with the LHC vacuum group: In the lateral, cylindrical wall there are 3 rows of 15 circular holes each with a diameter of 1 cm; the wall facing the beam has 8 slits of $3 \times 12\text{mm}^2$ with rounded corners (2 mm radius). The shield is retracted by 30 mm from the box window facing the beam, in order not to intercept any signal protons with the shield material. In the first step, during LS1, the horizontal pots of the RP210 station will receive the RF shields, in order to gain experience without touching the RP220 station.
- The horizontal RP210 stations will be equipped with new vacuum bellows and modified flanges that allow to integrate the same ferrite geometry as used in the new RPs. The ferrites of the vertical RPs of the RP210 stations will be exchanged with the new TT2 material as in the RP220 stations.

9.4.1.3 Interaction of the Roman Pot with the Beam Environment

In October and November 2012 several test insertions of the RPs in normal high-luminosity fills at $\sqrt{s} = 8\,\text{TeV}$ with $\beta^* = 0.6\,\text{m}$ were performed. While the vertical pots had no problems to reach the target distance of 12 σ from the beam centre, the horizontal pots encountered a very intense collision debris halo, and repeatedly the beam was dumped by showers hitting the Beam Loss Monitors at a pot position of about $30\,\sigma$. Separating the beams in IP5 finally reduced the luminosity – hence the debris halo – by a factor 22.7, enabling the approach to the horizontal target distance of $14\,\sigma = 1.6\,\text{mm}$ from the beam containing 1368 bunches of – at RP insertion time – 1.1×10^{11} protons or a total charge of 1.45×10^{14} protons. The beam profiles (Figure 9.6) measured during these insertions can be used to benchmark shower simulations (Section 9.4.1.7). The first lesson for the upgrade from this exercise is that a horizontal RP approach to physics-relevant positions of $10 \div 15\,\sigma$ will require to absorb the showers produced by the RPs in order to protect the quadrupole Q6. The solution is the addition of the new collimators TCL6 between the RR220 station and Q6 (see Section 9.4.1.8).

While the horizontal pots were stationary at $14\,\sigma$ from the beam centre, i.e. for about 30 minutes, the temperature sensors on the detector hybrid boards in those RPs registered a temperature increase by about 4°C, despite the active cooling of the detector packages. This effect is explained by impedance heating of the ferrite collar mounted around the box-shaped housing on the beam vacuum side. A direct temperature measurement near the ferrite was not available, but given the long thermal conduction path from the heat source to the detector package, and the absence of convection inside the pot due to the secondary vacuum, the temperature of the

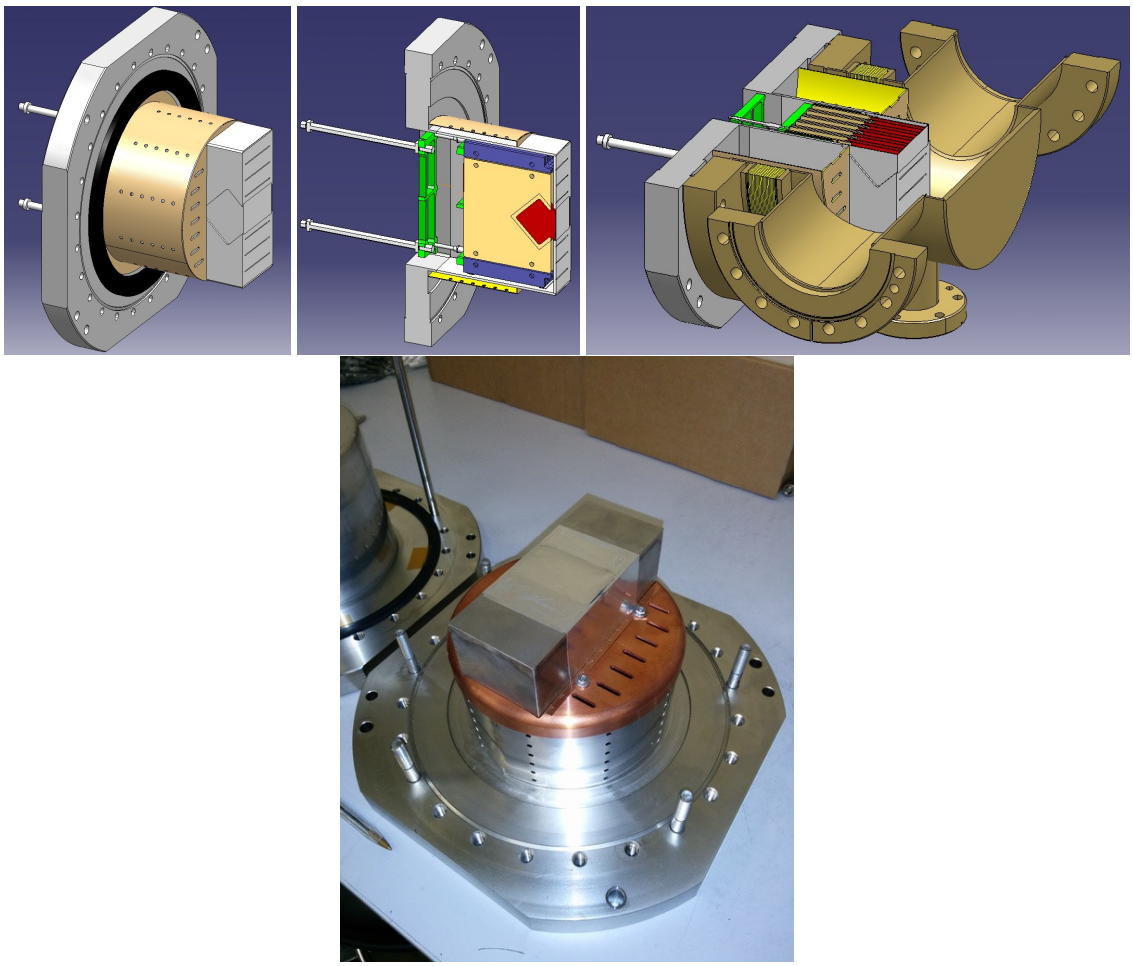

Fig. 9.5: Top: Drawings of the cylindrical RF shield for the box-shaped horizontal RPs. Bottom: the manufactured shield.

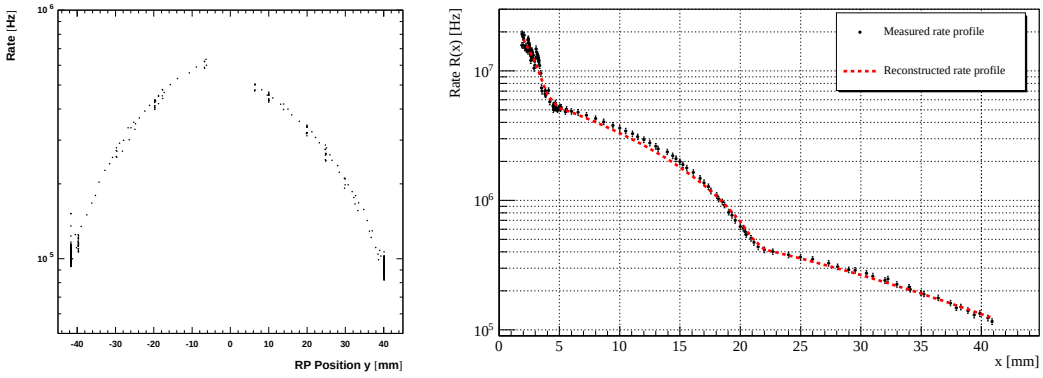

Fig. 9.6: Left: vertical beam profile measured via the trigger rates in the detectors of the top and bottom pots of Sector 56, 220-N. Right: horizontal beam profile measured in Sector 45, 220-N; the luminosity reduction by beam separation has been corrected for. The reconstructed curve is the result of a convolution fit discussed in [42].

ferrites may have reached values well above 100°C, the Curie temperature of the ferrites (material 4S60 from Ferroxcube) above which they are ineffective. Another piece of evidence for substantial heating of the ferrites was given by the vacuum deterioration observed after the very close insertion of the horizontal RPs. First laboratory tests have shown that the ferrite material installed around the pots shows substantial outgassing at high temperatures.

Triggered by the problems and observations described above, a programme of simulations, extended laboratory tests, and design optimisations was defined; it is discussed in the following section.

9.4.1.4 Impedance

As mentioned in the previous section, during a RP insertion to 1.6 mm from a high-intensity beam (1368 bunches of 1.1×10^{11} protons) a temperature increase was observed on the detector hybrid boards. This effect can probably be attributed to impedance heating. It is hypothesised that the 4S60 ferrite mounted around the RP box reached a temperature above 100°C, the Curie temperature, which resulted in the loss of ferrite effectiveness and hence even stronger heating by the now non-damped cavity resonance near 550 MHz [43]. Note, however, that no other impedance effects were observed, in particular, no beam instabilities.

The aim of the work presented here [44] is the optimisation of the RP design to minimise the beam-coupling impedance, in particular at very close distances to the beam, in view of more regular and extended RP insertions in the future.

The impedance seen by a beam of particles has contributions from the shape of the vacuum chamber (geometrical impedance) and from the finite conductivity of the material used for its construction. The remainder of this section focusses on the dominant geometrical contribution of three RP designs: the standard box-shaped RP, the new cylindrical RP, and the improved box-shaped RP with shield (introduced in Section 9.4.1.2).

The study was performed by simulating the passage of a charge distribution (source charge) through a cavity, in this case through a RP, and computing the wake field felt by a longitudinally or transversely displaced second charge (test charge). The potential felt by the test charge is then used to compute the longitudinal or transverse impedance using Fourier Transforms.

Three impedance effects have to be addressed:

- **Beam-induced heating**, i.e. the transfer of power from the beam to the lossy wall of a cavity, is determined by the frequency-dependent real part of the longitudinal impedance in conjunction with the power spectrum of the beam
  The main contribution to the heating comes from resonances below 1.5 GHz; at higher frequencies the beam power spectrum is attenuated by more than ~ 30 dB relative to its value at $f = 0$ [45]. For all power calculations a current of 0.6 A (corresponding to M=2808 and N_B= $1.2 \cdot 10^{11}$ protons) was used.
- **Longitudinal instabilities** are related to the effective longitudinal impedance. The effective impedance is the impedance actually felt by the beam: it is given by the impedance convoluted with a weighting function $\sigma(f)$ which is determined by the bunch profile.
  A conservative estimation of the effective longitudinal impedance is the slope of the imaginary part of the longitudinal impedance at low frequencies Z^0_{long}/n where $n = f/f_{\text{rev}}$ is the harmonic number. It is possible to show [44] that $\Im Z^0_{\text{long}}/n < (\Im Z_{\text{long}}/n)^{\text{eff}}$.
  The simulated value for $\Im Z^0_{\text{long}}/n$ will be compared with the measured value for $(\Im Z_{\text{long}}/n)^{\text{eff}}_{\text{LHC}} = 90\,\text{m}\Omega$ [46].

– **Transverse instabilities** have, analogously, their origin in the low-frequency behaviour of the transverse impedance. Following the same approach for the effective transverse impedance, it is possible to compute the *driving* (or *dipolar*) impedance and relate it to the transverse impedance [47], $\Im Z_{\mathrm{t}}^{\mathrm{driving}}$.
A normalisation with the ratio of the beta function value at the equipment under study, β_t, and the average over the ring, $\langle\beta_t\rangle = 70\,\mathrm{m}$, facilitates the comparison with other equipments at different positions in the machine:

$$\overline{\Im Z_{\mathrm{t}}^{\mathrm{driving}}} = \Im Z_{\mathrm{t}}^{\mathrm{driving}} \frac{\beta_t}{\langle\beta_t\rangle} \tag{9.1}$$

The new RP will be horizontal ($t = x$); moreover, among all the RPs the highest value (worst case) of $\beta_x = 98\,\mathrm{m}$ is reached at the unit 210-N. This value can be compared with $25\ \mathrm{M\Omega/m}$, a conservative value of the value expected for the full machine [48].

For the new cylindrical pots, simulation results indicate that no low frequency resonances ($<$ 1.4 GHz) are present if the gap between the detector housing and the flange is completely closed, which of course prevents any RP movement. Mechanical constraints require at least 2.5 mm gap between the housing and the flange. With this gap a resonance at 470 MHz appears, however its impedance is smaller than for the standard box-shaped RP. The position and the dimensions of the ferrite has been optimised through various iterations considering also vacuum and mechanical construction. The final design consists of a ferrite ring (inner diameter = 150 mm, radial width = 15 mm, thickness = 5 mm) integrated into the flange, as far as possible from the beam

In all cases, the 470 MHz resonance is damped and smeared beyond recognition. At low frequencies, the cylindrical and shielded RPs have a smaller $\Re[Z_{\mathrm{long}}]$ than the standard RP. This is also reflected by the reduced heating for the new designs (Figure 9.7). Figure 9.8 shows the

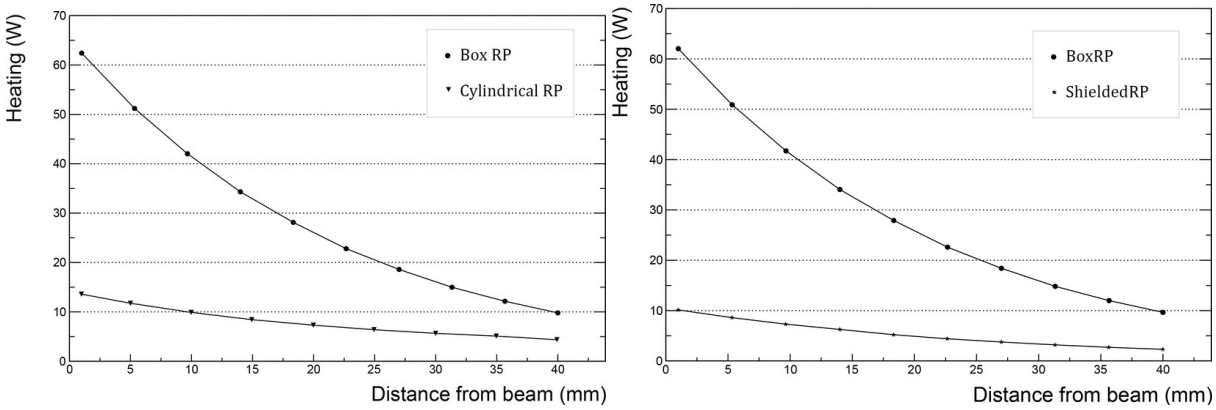

Fig. 9.7: Power lost by the beam passing through the RP, for the three RP designs ($I = 0.6\,\mathrm{A}$).

effective longitudinal impedance as a function of the RP distance from the beam. Also here, the new designs have led to a significant reduction.

These results are numerically summarised in Table 9.1.

9.4.1.5 The RF Test in the Lab

The new cylindrical RP and the RF shield in combination with ferrites were developed to reduce the RF interaction with the LHC beam. Prior the serial production of components a new RP

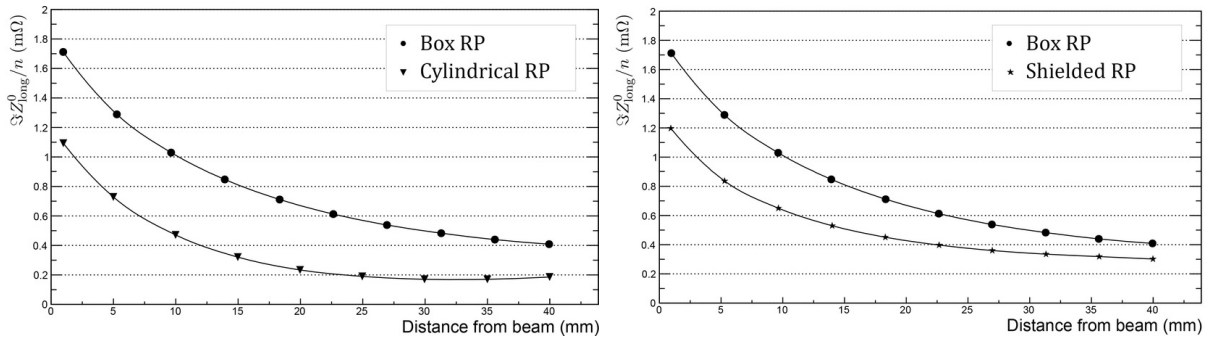

Fig. 9.8: Effective longitudinal impedance as a function of the RP distance from the beam, for the three RP designs.

	Distance from the beam [mm]	$\frac{\Im Z^0_{\text{long}}}{n}$ [mΩ]	fraction of $(\frac{\Im Z_{\text{long}}}{n})^{\text{eff}}_{\text{LHC}}$ (90 mΩ)	$\overline{\Im Z^{\text{driving}}_{\text{trans}}}$ [MΩ/m]	fraction of $\Im(Z_x)^{\text{eff}}_{\text{LHC}}$ (25 MΩ/m)	Heating [W] I=0.6 A
Box RP	1	1.7	$< 1.9\,\%$	0.15	$< 0.6\,\%$	62
	5	1.3	$< 1.4\,\%$			52
	40 (garage)	0.41	$< 0.45\,\%$			10
Cylindrical RP	1	1.1	$< 1.2\,\%$	0.11	$< 0.5\,\%$	13
	5	0.73	$< 0.81\,\%$			11
	40 (garage)	0.18	$< 0.20\,\%$			4
Shielded RP	1	1.2	$< 1.3\,\%$	0.2	$< 0.8\,\%$	10
	40 (garage)	0.30	$< 0.33\,\%$			2

Table 9.1: Main results of the simulation of the present box RP (Box RP), the cylindrical RP (Cylindrical RP), and the Box RP with Shield. Longitudinal and transverse impedances are compared with the total values estimated for the present LHC effective impedances.

cross with flanges and bellow was manufactured. The prototype of the cylindrical RP and the RF shield in combination with the box-shaped RP have been integrated in this new RP cross for RF measurements. In February 2014 measurements were performed by TOTEM and the LHC impedance group in the TIF lab of CERN. In detailed measurements with and without the new ferrites and at different insertion positions of the RP, the RF characteristics of this new geometry could be determined and good agreement with the predictions, based on simulations could be found [49].

9.4.1.6 Impact of Ferrite outgassing on LHC Vacuum

The vacuum degradations observed in 2012 after very close horizontal RP insertions to high-intensity beams triggered the following consolidation activities for improving the vacuum compatibility of the RP system:

– Ferrite material improvements:
The 4S60 ferrites used in the RP system before LS1 are now (but not in 2006) known to show high outgassing rates unless they are baked out at 1000°C [50]. In the TOTEM RPs these ferrites were installed as received from the manufacturer and then baked out *in situ* at about 200°C like all other beam-pipe components, which turned out not to be sufficient.

Since the 4S60 ferrites have in addition a low Curie temperature of only 100°C, alternative ferrite materials are being investigated instead of only baking out the 4S60 material at 1000°C. The material used for the TOTEM RPs is TT2-111R from TransTech with a Curie temperature of 375°C and an acceptable outgassing after bake-out at 1000°C [51]. An alternative material for possible future use is 4E2 (Ferroxcube) with a Curie temperature of about 400°C; its outgassing behaviour remains to be tested.

– The new geometrical ferrite configuration reduces the ferrite surfaces exposed to the vacuum by an order of magnitude from 220 cm^2 per standard RP to 23 cm^2 per cylindrical RP.
– All components exposed to the primary beam vacuum have been proposed by the vacuum group to be coated with NEG, as far as technically possible.

9.4.1.7 Generation of Particle Showers

To assess the generation of particle showers by RPs interacting with the intense debris halo (see 2012 experience discussed in Section 9.4.1.3), Geant4 simulations implementing detailed models of the rectangular and the new cylindrical RPs have been carried out [42].

The first goal of the study was to identify the contributions from the different structural elements of a RP to the shower creation.

As expected, the number of secondary particles is mostly determined by the amount of material traversed. The key observations are:

– In both RP designs, the bottom foil produces by far the highest number of secondary particles, followed by the thick body walls with 2 to 3.5 orders of magnitude lower rates. The orthogonally traversed thin front and back windows produce the lowest numbers of secondaries.
– The bottom foil of the cylindrical pots produces more than 10 times more secondaries than the much shorter foil of the standard pots. In the other elements the shower production is similar in the two designs.
– The showers from the bottom foil of the cylindrical pot are 3 times wider than the ones from the standard pots: 99% contained in 0.6 rad = 34° rather than in 0.2 rad = 11°.
– The two projections, horizontal and vertical, are almost identical.

The simulated secondary particle distribution in a scoring plane 6 m downstream of a standard horizontal RP inserted to 2 mm from the beam centre shows that at the entrance point of TCL6, 25 % of the secondary particles, carrying 90 % of the energy, are contained within the beam-pipe radius and thus intercepted by TCL6. How much of this flow leaks through the TCL6 aperture and thus hits Q6 will be the subject of the FLUKA study discussed in Section 9.4.1.8.

9.4.1.8 Interplay between Roman Pots and Collimators

The modified RP system with relocated and additional units will be embedded in an upgraded collimation system. This section discusses the performance of the new combined layout in terms of physics acceptance and machine protection.

The New Collimators TCL4 and TCL6

LHC operation at highest luminosities may require additional protection of the quadrupoles Q5 and Q6 against collision debris from IP5 [52].

To protect Q5, new collimators, TCL4, have been installed on the outgoing beams in the old location of the RP147 station, and the already existing collimators TCL5 may be partially closed. Since both TCL4 and TCL5 are located upstream of the RP stations and can intercept diffractive protons if too tightly closed, the aperture settings of these collimators will be the result of an optimisation study maximising the physics acceptance as far as compatible with the necessary magnet protection.

Downstream of the last RP unit, 220-F, another collimator, TCL6, has been installed [37] on the outgoing beam to protect the quadrupole Q6 against debris from IP5, thus taking over a part of the original role of TCL5 which cannot be too tightly closed without intercepting all the signal protons to be measured by the RP system. Another beneficial effect of this new collimator is its capability to absorb showers created by the insertions of the horizontal RPs close to the beam. RP operations at low β^* and high luminosities in 2012 have demonstrated that without any absorber behind the RP stations, insertions were limited to distances greater than $30\,\sigma$, because the showers caused by the pots' interaction with the debris halo brought the dose rates measured by the Beam Loss Monitors above the beam dump thresholds. The improvement by the addition of TCL6 will be the subject of a FLUKA study.

Optimisation of Roman Pot and Collimator Settings

This section discusses the strategy for defining an optimal combined set of jaw positions for the RPs and the collimators TCL4, TCL5 and TCL6. Given that the TCLs are only required at highest luminosities, only the low-β^* running scenarios are relevant for these considerations. The TCL collimators are designed to protect the quadrupoles Q5 and Q6 against debris from collisions at IP5. Their jaws approach the beam horizontally and potentially intercept diffractively scattered protons, thus interfering with the physics measurements in the RPs. Therefore, the aim of the optimisation is to find:

1. jaw positions for TCL4 and TCL5 that leave the aperture as widely open as allowed by the protection needs of Q5, i.e. the dose rate received by Q5 has to stay well below the magnet quench threshold;
2. RP positions as close to the beam as allowed by the protection capacity of TCL6 to prevent Q6 from quenching.

The upper limit $\xi_{\max}$ for accepted momentum losses of diffractive protons is given by minimum value of the ratio d_x/D_x between horizontal aperture and dispersion along the path from the interaction point to the RP. Table 9.2 gives the values of $10\,\sigma_x$ beam width and the dispersion D_x in all TCL collimators and in some RP locations for the $\beta^* = 0.55\,\text{m}$ optics at $\sqrt{s} = 14\,\text{TeV}$.

Beam Element	Position s [m] from IP5	$10\,\sigma_x(s)$ [mm]	$D_x(s)$ [mm]	$\lvert\xi(10\,\sigma)\rvert$
TCL4	149	5.2	-66	0.079
TCL5	185	2.8	-83	0.034
RP 210-N	202	2.2	-90	0.024
RP 220-F	220	0.90	-80	0.011
TCL6	221	0.89	-80	0.011

Table 9.2: Horizontal beam envelope ($10\,\sigma$) and dispersion at the TCL collimators and at the first and last RP unit. The last column gives the ξ-value at $10\,\sigma$ from the beam centre (for $t = 0$).

The most stringent impact on diffractive proton acceptance is made by TCL5 which at its nominal jaw position of $10\,\sigma$ from the beam centre would intercept all protons with $\xi > 0.034$

while for the physics programme a cut-off greater than 0.1 would be desirable. Therefore the collimation group developed an alternative scheme for fills with RP operation where TCL5 would be fully open and both TCL4 and TCL6 closed to $10\,\sigma$. However, in that scheme TCL4 would be the bottleneck producing a cut at 0.079. A new study presently carried out by the FLUKA team investigates the possibility to open TCL4 to $15\,\sigma$ and complement its protection by closing TCL5 to $35\,\sigma$. In this way, both collimators would lead to the same upper ξ cut-off at 0.11.

Once the optimal settings for TCL4 and TCL5 will be fixed, another FLUKA study will focus on the impact of RP insertions on Q6 and its mitigation by closing TCL6 to $10\,\sigma$. It is expected that a horizontal RP approach to a minimum distance between 11 and $14\,\sigma$ should be possible, corresponding to minimum accepted ξ-values between 0.012 and 0.016.

9.4.2 Requirements on the Timing Detectors and Strategy

The need for precise timing detectors measuring the time difference of the protons in the two arms of the spectrometer is justified as an effective way to reduce the pileup background. A baseline time resolution of $\sigma(t) = 10\,\text{ps}$, corresponding to a vertex resolution $\sigma(z_{pp}) = 2.1\,\text{mm}$, is set as an ambitious target of the CT-PPS project.

The required detector area is small ($\leq 4\text{cm}^2$). In addition to a good time resolution, the use of a detector with a small dead region is a key requirement. On the side adjacent to the beam, the dead region should be at the level of $\sim 200\,\mu\text{m}$ or below, matching that of the tracking detectors. The distance between the active area and the vacuum includes in addition the bottom of the RP ($0.3^{+0.02}_{-0.10}\,\text{mm}$). The scattered protons are deflected out of the beam by the LHC magnets, but at the z position of the detectors they are displaced by only a few mm, so any inactive area (on the inner edge) causes a loss in acceptance at low masses.

The detectors should be radiation hard. Close to the beam where the detectors are located, we expect a proton flux of about $5 \times 10^{15}\,\text{cm}^{-2}$ per $100\,\text{fb}^{-1}$. The expected thermal neutron flux extrapolated from TOTEM measurements is about $10^{12}\,\text{cm}^{-2}$ per $100\,\text{fb}^{-1}$. In the case of Cherenkov detectors the photodetectors will be farther from the beam, where radiation field is reduced to the neutron component. Replacing the photodetectors or solid-state timing detectors approximately once a year is feasible, as they are accessible and relatively inexpensive.

As there is often more than one proton in the acceptance from the same bunch crossing, a fine segmentation is also required. The detectors should have the capability of measuring the times of two or more particles from the same bunch crossing, and of being read out every 25 ns, with no significant remnant signals from earlier crossings. This implies segmentation.

A detector based on Cherenkov technology is developed for precise timing as the baseline proposal.

Presently, the state-of-the-art of time resolution with minimum ionizing particles in a single detector layer is the following: 1) gas Cherenkov $\sim 15\,\text{ps}$ [54]; quartz Cherenkov $\sim 30\,\text{ps}$ [55]; diamond sensors $\sim 100\,\text{ps}$ [56, 57]; silicon sensors $\sim 100\,\text{ps}$ [58]. Complete systems with several detector layers allow for improved performance.

While Cherenkov based detectors have intrinsically better time resolution and are more mature timing technologies, they have some important drawbacks. In the existing prototype implementations, the quartz detector is segmented in elements of $3 \times 3\,\text{mm}^2$, which implies a large rate of double hits in the same bar per bunch crossing, approaching 50% in the sensors close to the beam. We assume that two hits in the same channel cannot be resolved. Finer granularity near the beam, where it is most needed, may be possible but needs further development.

The amount of material introduced by the quartz detector itself is not negligible. In the foreseen configuration, the probability that a proton has a nuclear interaction in one detector is between 7.2% and 14.6% (depending on the proton position in the detector). As the timing detector is located downstream of the pixel detectors these interactions do not affect the track measurement, however they may smear or fully corrupt the time measurement introducing another source of inefficiency.

Solid state timing detectors have the important advantage of being very thin and allowing for fine granularity. Typically solid state detectors are a few hundred microns thick making it possible to stack ten or more detectors, which to a first approximation improves the time resolution by the square root of the number of layers. A resolution of 30 ps per detector, possibly achieved as a result of the current R&D effort, would allow for a timing system with the baseline 10 ps resolution. On the other hand the possibility of defining small size pixels permits reducing the rate per channel, which improves the time measurement and reduces significantly the inefficiency due to double hits. Of course the detectors should be able to sustain the high radiation doses involved in this application, which requires still considerable development.

Taking into account the previous considerations, we have chosen as the baseline timing detector the L-bar Quartic (Quartz Timing Cherenkov) design with $5 \times 4 = 20$ independent channels of $3 \times 3\,\mathrm{mm}^2$ area. The SiPM photodetectors are relatively far from the beam, in a region where the neutron flux is $\sim 10^{12}$ neq/cm^2 per $100\,\mathrm{fb}^{-1}$. SiPM devices that tolerate this radiation level are available, as found in the framework of the HCAL Upgrade project, however a increase of the leakage current is observed [59]. The SiPMs will probably require replacement after $100\,\mathrm{fb}^{-1}$, which is feasible given the small number of devices involved. We will also consider the possibility of using GaInP photosensors, under development for the upgrade of the CMS endcap calorimeter, given its potentially better tolerance to radiation. Two Quartic detectors fit inside a cylindrical Roman Pot, providing a combined resolution of the order of 20 ps. The Quartic baseline is presented in Section 9.4.2.1.

The relatively high fraction of nuclear interactions in the quartz bars prevents the use of more than two Quartic detectors per spectrometer arm. In order to reduce the amount of the dense material, we explore the possibility of complementing the Quartic measurement by using a short (~ 10 cm) Gas Cherenkov Time-of-Flight detector (GasToF) inside a second, upstream, cylindrical RP. The GasToF detector with a multi-anode MCP-PMT may be able to time individual photoelectrons to achieve multi-proton capability. Combined with the Quartic measurements, this additional detector could allow to approach the 10 ps time resolution. While GasToF prototypes have been built and validated, there are not yet test beam results confirming the multi-hit performance predicted from simulation. The possible use of GasToF in the experiment is therefore dependent on successful test beam results with final prototypes. The GasToF option is described in [21] (Section 5.3).

Both the Quartic and GasToF detectors have a relatively small number of channels and produce electrical pulses with similar characteristics. Therefore the proposed readout system, based on two well known integrated circuits (the amplifier-discriminator NINO and the High Performance time-to-digital converter HPTDC), can be used by both detectors. This solution offers a potential for possible future upgrades as new improved versions of the HPTDC and of the NINO chips are already in the pipeline. A reference clock system, complementary to the CMS timing system, provides time synchronization with less than 1 ps jitter between the detectors in opposite arms.

In parallel we intend to pursue the R&D on solid state options for timing, in particular diamond sensors and silicon sensors with avalanche gain. There are still many challenges to

overcome before any of these options become a viable timing detector for CT-PPS. This includes the improvement of the intrinsic detector resolution, the demonstration of resistance to radiation, and the development of suitable low noise and fast electronics. Prototypes will be built and evaluated in test beams. The small area, and therefore cost, of the timing detectors allows to foresee the replacement of the CT-PPS timing baseline when a better solution is available. The solid state options and respective R&D plans are described in Sections 5.5 and 5.6 in [21].

9.4.2.1 The Cherenkov Quartic Detector as Baseline for Timing

Cherenkov light is prompt and therefore ideal for fast timing, although the amount of light is small compared to that in scintillator. Radiators need to be transparent, i.e. with a long absorption length $L_{abs}(\lambda)$, where λ is the optical wavelength, preferably into the ultraviolet, $\lambda \approx 200\,\text{nm}$, where most photons are generated. The number of Cherenkov photons radiated is proportional to $1 - 1/n^2(\lambda)$; more completely (for charge $Q = 1$, and $\beta = 1$):

$$\frac{d^2N}{dxd\lambda} = \frac{2\pi\alpha}{\lambda^2}\left(1 - \frac{1}{n^2(\lambda)}\right), \tag{9.2}$$

where α is the fine structure constant.

The approximate rule for the number of photoelectrons in a typical detector is:

$$N_{pe} \sim 90\,\text{cm}^{-1} \cdot \text{L(cm)} \sin^2\theta_{ch} \sim 50\,\text{cm}^{-1},$$

which gives about 200 photoelectrons for a quartz detector of length 40 mm, to be scaled by a factor for the acceptance of the photons.

The light is emitted along the particle's path in a cone with half angle (Cherenkov radiation angle) θ_{ch} given by $\cos(\theta_{ch}) = 1/n(\lambda)$. We have developed fast detectors with both gas and solid radiators.

Among solid radiators, fused silica, SiO_2, or quartz (ultraviolet grade, UVT) is commonly used, and it is chosen as our baseline material. As $n(\lambda) \sim 1.48$, there is much more light per cm than in a gas, but since $\theta_{ch} \sim 48^\circ$, the light does not arrive as promptly, and fine segmentation, in our case with quartz bars, is limited.

9.4.2.2 Quartic Design for Roman Pots, with L-Bar Geometry

We have developed detectors [25] with quartz bars of $3 \times 3\,\text{mm}^2$ cross section in the form of an 'L', called L-bar Quartic (QUARtz TIming Cherenkov), the light being detected with SiPMs.

This configuration allows segmentation in both x and y. The photodetectors are located at $\sim 8\,\text{cm}$ from the beam in the horizontal plane and can be partially shielded to reduce their radiation dose.

In the Quartic design there is an array of $3 \times 3\,\text{mm}^2$ "radiator bars", R, parallel to the beam. The Cherenkov angle is the complement of the critical angle for Total Internal Reflection (TIR) on the bar sides, and as the proton paths are almost exactly parallel to the bars all the Cherenkov light is internally reflected to the back end of the radiator, as shown schematically in Figure 9.9. Most (about 2/3) of the light is transmitted to the SiPM along the light-guide (LG) bar, also with total internal reflection. The remaining $\sim 1/3$ is reflected back to the entrance of the radiator bar, where there will be a black absorbing surface. The LG bars end in a (vertical in the horizontal RP) plane, 73 mm from the beam pipe wall. This distance is a compromise between being away from the beam for radiation issues, and keeping the LG bars short to minimise the absorption, number of reflections, and optical dispersion. The spread of the travel

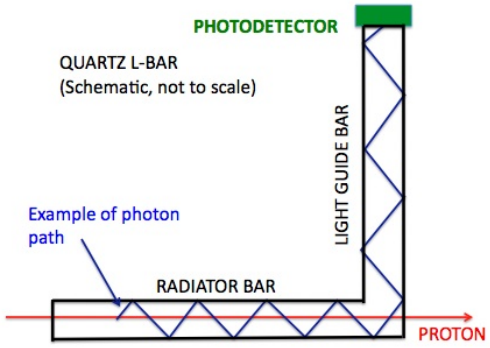

Fig. 9.9: Cherenkov light rays in the radiator and light guide bar, for n = 1.48, in the plane of the 'L' ($\phi_{ch} = 90°$).

time of the photoelectrons is mainly caused by the length of the radiator bar. The component of the speed of the light along the radiator bar is $dz/dt = c/n^2 \sim 0.140$ mm/ps.

Detailed studies of the Quartic and other timing detectors can be found in Refs. [25, 55, 60–62].

The CT-PPS Quartic "module" is a light tight box with a very thin ($\sim 100\,\mu$m) side wall on the beam side, and blackened interior. This side wall may be removed on insertion in the pot as the interior will be dark; it is to protect the inside prior to insertion and to optically close the box for beam tests. One module consists of ($4 \times 5 = 20$) independent $3 \times 3\,\text{mm}^2$ bar elements. This allows a time measurement of two or more protons from the same bunch crossing (which has a time spread $\sigma_t \sim 150$ ps) if they are in different elements. The active area is 12.6 mm (vertically, y) $\times$ 15.8 mm (horizontally, x). This includes 200 μm spacers (a wire grid) to separate the bars, allowing total internal reflection, and avoiding light leakage. The dimensions of the bars are given in Figure 9.10. The ends of the light guide bars arrive at an array of SiPMs, coupled with a thin silicon "cookie" for good optical coupling. We use SiPMs Hamamatsu MPPC Type S12572-050 mounted in a flat plate holder. The SiPMs fit in rectangular holes in the plate and as they are not fixed to the read-out board they can be very simply replaced. The SiPMs are connected to the read-out board through an anisotropic conducting sheet (embedded very short wires give an electrical connection through the sheet but not in the plane).

The bars pass through circular holes for locating the bars against the SiPMs, with better than 25 μm accuracy. These holes are countersunk, as the 20 bars all have to be inserted together. The complete bar assembly is then inserted in the box on precision grooves; the front window is placed in position later, after position and optical checks are done. Figure 9.11 shows the assembly of two modules in one RP. We have the option of displacing one module in (x, y) with respect to the other by 250 μm (e.g.) to avoid any dead regions between the bars. Alignment of the radiator bars parallel to the protons (at the level of $\lesssim 10$ mrad) will be needed to maximise light collection and avoid light leakage into neighbouring bars.

9.4.2.3 Integration with Roman Pots

The longitudinal space in the RPs is approximately 140 mm. The L-bar geometry allows installation of Quartic two modules in one RP (Figure 9.11) The two modules in a pot will be fitted together precisely using dowel pins.

Figure 9.11 shows the design of the module for insertion into the horizontal RP. A slightly modified version (Figure 9.12) reduces the material close to the beam. The protons enter

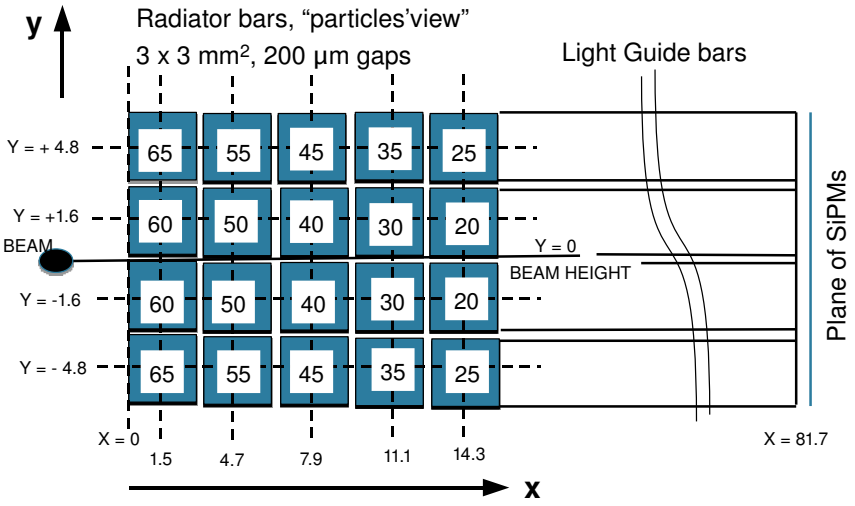

Fig. 9.10: Schematic layout of quartz bars looking in the direction of the protons. Numbers on the $3 \times 3\,\mathrm{mm}^2$ radiator bars are their lengths in mm, and coordinates (mm) are the centers of the bars. The light guide bar lengths are chosen to all end in a common plane 81.7 mm from the edge closest to the beam.

through a thin window (nominally $100\,\mu$m aluminium, but it has no mechanical purpose, it is for absorption of reflected light and light exclusion). The array of radiator bars is clamped on the three sides away from the beam with a plastic U-clamp, touching each bar only along a fine line. For assembly of the bar array a 4-sided clamp is placed temporarily around the front of the array. The SiPM plate and read-out board are precisely positioned by dowels with respect to the L-bar positioning plate.

9.4.2.4 Photodetectors: Silicon Photomultipliers

Silicon photomultipliers, SiPMs, are solid state photon counters comprised of a large number of avalanche photodiodes (APDs) or "pixels" of order $20\,\mu$m dimensions, with a high gain (up to 10^6) in Geiger mode, with an applied voltage just above the breakdown voltage (about 30 V to 70 V depending on the type). Each discharged pixel has a recovery time of ~ 50 ns, but with e.g. 100 photoelectrons per event and thousands of pixels per mm^2 this is acceptable with 25 ns bunch-crossing time. For the SiPMs, the single photon detector efficiency is the product of the quantum efficiency and the fractional area coverage of the APDs. SiPMs are rugged, simple to use and relatively cheap per unit, but at present are only available commercially with effective active areas from $1 \times 1\,\mathrm{mm}^2$ to $3.5 \times 3.5\,\mathrm{mm}^2$. Smaller SiPMs have less capacitance and are intrinsically faster.

The SiPMs, Hamamtsu MPPC type S12572-050, operate at ~ 72 V, just above the breakdown voltage (they operate in Geiger mode, discharging one or two pixels per detected photon). These have 3600 pixels of $50\,\mu$m diameter. The single photon detection efficiency and the wavelength-dependence of the response is shown in Figure 9.13. Improved efficiency in the UV is being investigated. Individual HV values can be applied to each SiPM, and their leakage

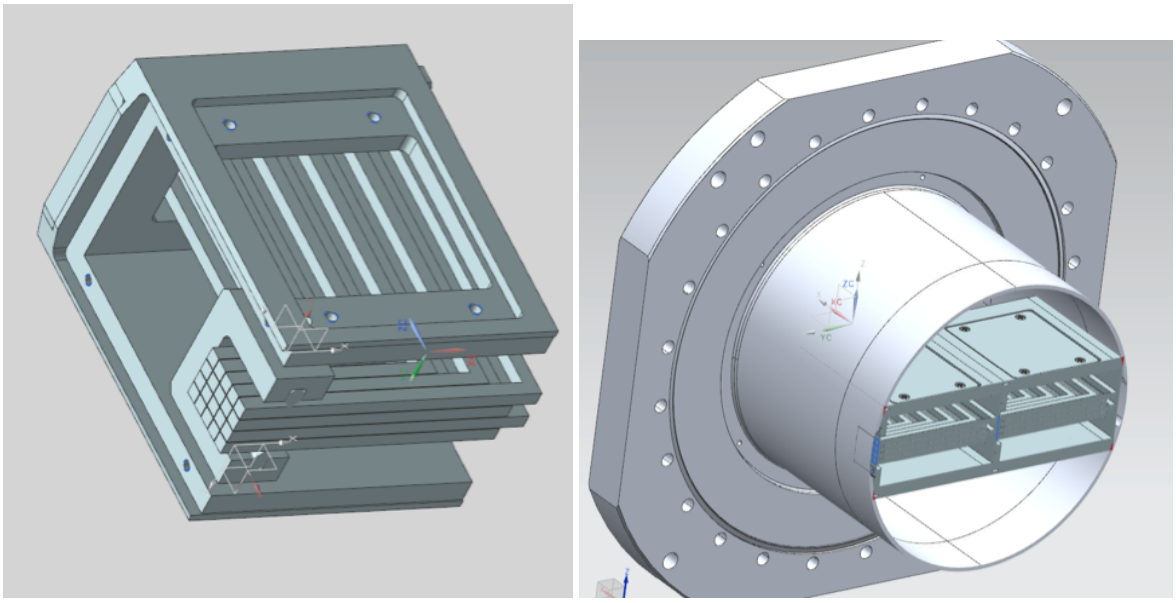

Fig. 9.11: Left: Design of module for insertion in Roman Pot (two in one pot). Right: Assembly of two Quartic modules in Roman Pot. The beam comes from the left.

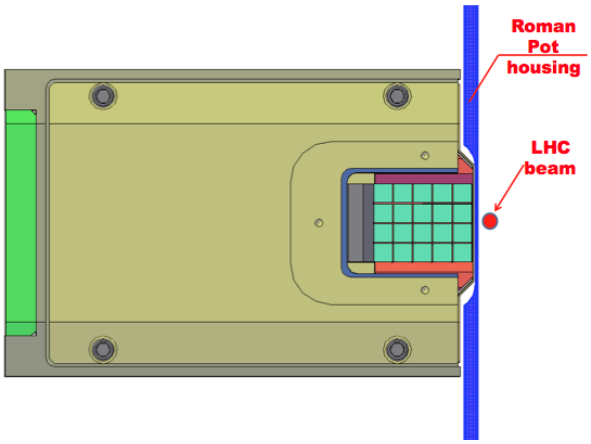

Fig. 9.12: "Particle eye view" of bar array in pot. This is a modified design reducing the material close to the beam.

currents monitored through a high-resistance (6.4 MΩ) bleed resistor to ground. While the gains of SiPMs are very sensitive to temperature, the time resolution is not. Air cooling is expected to be sufficient; an alternative is to use the same cooling system as for the tracking detectors. The temperature of the SiPM boards will be monitored with thermistors. The SiPM board receives an individually controllable bias voltage ~ 72 V from a local programmable supply. The signals are read out with miniature coaxial cable with SMA connectors.

9.4.2.5 Monitoring, Alignment, and in situ Calibration

The rates in each bar are monitored both online and offline. The rates are expected to be up-down symmetric about the beam height (as can also be determined from the tracker), column-by-column. This gives a measure of the centre of the beam in y, assuming the backgrounds are relatively small. For a given row in y the rates will fall with x with two components: protons from collisions and beam halo background. The former will be compared with predicted t-

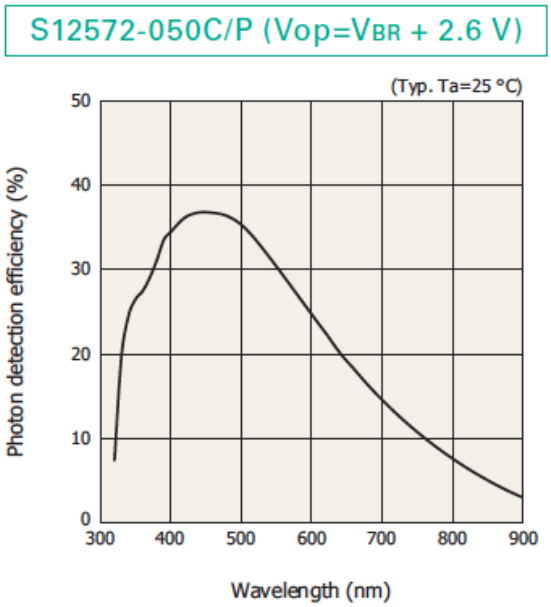

Fig. 9.13: Photon detection efficiency of Hamamatsu S12572 SiPM. This is the product of the quantum efficiency and the fill factor (50 μm pixels).

distributions, and it is valuable to measure the latter. When the RPs are inserted at the beginning of stores the rates will be carefully monitored, e.g. partially withdrawing in the event of an abnormal increase.

Initial relative alignment of the Quartic bars and tracker will be achieved by matching the individual bar edges in x and y with the track distributions.

A pair of light-emitting diodes will be mounted inside the module in such a way that some light is captured in each bar. This will be pulsed when there is no beam as a control of all the SiPMs and their readout.

Occupancy of the bars will be monitored in real time, as functions of the instantaneous luminosity and background conditions. Geometrical matching between the bar array and the trackers will also be measured; the 200 μm gaps between the bars can also provide a check.

A calibration of the absolute time difference between the protons, Δt_{pp}, can be derived by matching $z_{pp} = z_X$ using real events of the type $p + p \to p + X + p$, where X is a set of particles measured in the central detector. After kinematic matching of X to the protons (four-momentum conservation) the 2D plot of z_{pp} vs z_X will show a ridge which calibrates both $z_{pp} = 0$ as well as checking the time scale.

While the time difference between the "left" and "right" protons, $t_L - t_R$, gives z_{pp}, the time sum, or $(t_L + t_R)/2$ (minus a constant), would provide another, orthogonal, variable for pileup rejection if the actual event time were known much better than the spread in collision times, $\sim$150 ps.

9.4.2.6 Beam Tests

A prototype Quartic with L-bars was tested in the Fermilab test beam, with 120 GeV protons, using a mechanical design that does not include some features needed for the CT-PPS version. Figure 9.14 shows one example, with $\sigma(\Delta t) = 34.9$ ps, showing no background or inefficiency. The single-photon time resolution of the SiPM we used is quoted by Hamamatsu to be $\sim$ 300 ps;

giving an expected time resolution for 100 p.e. of $300\,\text{ps}/\sqrt{100} = 30\,\text{ps}$, in reasonable agrement with the observations. See [25] for more details of the test procedures and results.

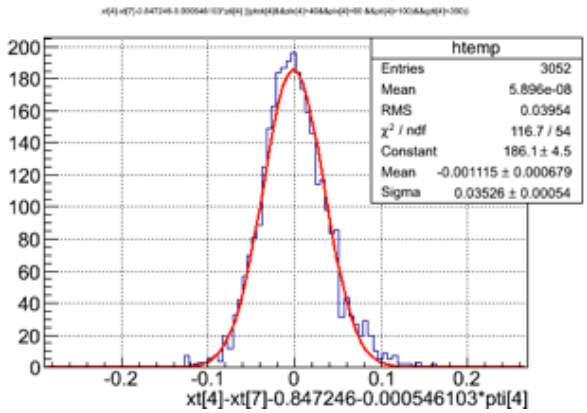

Fig. 9.14: The time difference between one L-bar (30 mm radiator, 40 mm light guide, Hamamatsu MPPC type S10362-330050C) and the reference time signal (PMT240 in beam). It shows $\sigma = 35.3$ ps.

9.4.2.7 Future Developments

We have described the baseline Quartic detectors, which will be ready for installation in 2015 when the RPs have been installed and commissioned. Several potential improvements will be investigated. These include finer segmentation, especially near the beam, a more compact SiPM array ("buttless" type), and the use of a multi-anode MCP-PMT in place of SiPMs. The latter have had photocathode lifetime problems limiting their use in such a high-rate environment, but developments to mitigate that have been made.

Also, faster SiPMs with higher photon detection efficiency and possibly more sensitivity in the UV may become available, potentially allowing easy replacement.

SiPMs from STMicroelectronics (STM) with new p-on-n structure (rather than N-on-P SiPMs, also from STM) show significantly better timing properties [60] [3]. Tests with a PiLas (Picosecond Injection Laser) showed the photon detection efficiency at $\lambda = 405$ nm, 5 V above breakdown voltage (28 V), to be 43% higher (31.1% cf. 21.7%). Also the SPTR, is 174 ps cf. 231 ps, i.e. smaller by 25% than for STM n-on-p detectors. Together these improvements lead one to expect that the single bar resolution can be improved from the measured 32 ps to ~ 20 ps.

Unlike the large central CMS detectors, due to the small number of channels, upgrades to the timing detectors can be considered on a yearly timescale, and we expect to continue the necessary R&D. Also, if timing detectors based on other principles, e.g. solid state detectors, demonstrate good performance and acceptable properties (e.g. radiation hardness) they can supplement, or possibly replace, the Quartic detectors.

Readout System of the Cherenkov Detectors

The task of the readout system is to provide time and amplitude measurements of the pulses generated by the photosensors associated to the Cherenkov detectors, and to transmit the digitized data to the data acquisition system.

The Cherenkov timing detectors are composed of a number of modules installed in one or more RP. The readout system follows the same modularity, and is composed of independent

[3] We thank STMicroelectronics for providing samples.

units (readout module) interfacing to the CT-PPS DAQ/Trigger system. Each readout module has 64 channels suitable for use with the baseline Quartic module (20 channels), but also with possible Quartic modules with finer granularity.

The readout system is also required to provide the measurement of the input pulse amplitude. While this measurement is not directly used in the reconstruction of the collision vertex, the knowledge of the amplitude is mandatory for detector calibration, time corrections (e.g. "time-walk") and pulse pile-up rejection.

The readout system is required to have double hit resolution better than 25 ns, suitable for operation with 25 ns bunch separation without loss of efficiency, and to sustain a maximum rate of 6 MHz per channel, corresponding to a maximum channel occupancy of 20% at 25 ns LHC beam operation, averaged over all channels. While the average occupancy of the Quartic channels ($3 \times 3\,\mathrm{mm}^2$ quartz bars) is 20% for average pile-up of 50 events, the highly non-uniform occupancy of the detector (the occupancy of the innermost channels reach 70%) induces a significant readout inefficiency for a number of pile-up events larger than 25.

The readout system is required to provide on-detector L1 trigger matching, allowing extraction of the detector data in a time window around the L1 time, local event building and data transmission to the DAQ system. The data rate of a readout module, assuming readout of 10 channels after zero suppression, 3 bunch crossings time window, 32 bit event data per channel, and 100 kHz L1 rate, is estimated to be 100 Mb/s.

The timing detector readout system is expected to provide hit information and time measurement at the bunch crossing rate to be used by the trigger system. By combining the information from the two PPS arms, the L1 can estimate the z-vertex coordinate, allowing to select events in the tails of the z-vertex distribution where the pileup density is smaller. This capability would provide a reduction of the L1 rate of high cross-section processes so that it fits within the L1 rate constraints, selecting at the same time the events less affected by pileup. The trigger requirement implies the use of a low latency TDC delivering conversion data at the bunch crossing rate.

In order to achieve the desired time resolution, the front-end timing electronics must be located in the RPs or a nearby region (1-2 m distance). This raises issues of radiation tolerance since the radiation levels in the RPs, in the region 200 m from IP, are expected to be 100 Gy and 10^{12} neq/cm^2 for 100 fb^{-1} of integrated luminosity.

System Design

The main guideline in the design of the timing detector readout system was to reuse well known components with adequate performance, allowing to streamline the design and implementation of the system so that it may be possible to evaluate the timing detectors in the LHC beam in 2015.

We have therefore decided to base our system on the amplifier-discriminator NINO and the time-to-digital converter HPTDC. Both chips have been developed by CERN's microelectronics group for the LHC experiments. The HPTDC chip is used in the CMS muon system, while the NINO and HPTDC chips are associated in the time-of-flight detector of the ALICE experiment. These chips are now widely used in many applications, including PET Time-of-Flight.

The EndoTOFPET-US collaboration[4] has studied the time resolution of the NINO-HPTDC

[4]This project have been funded by the European Union 7th Framework Program (FP7 / 2007-2013) under Grant Agreement No. 256984 (EndoTOFPET-US)

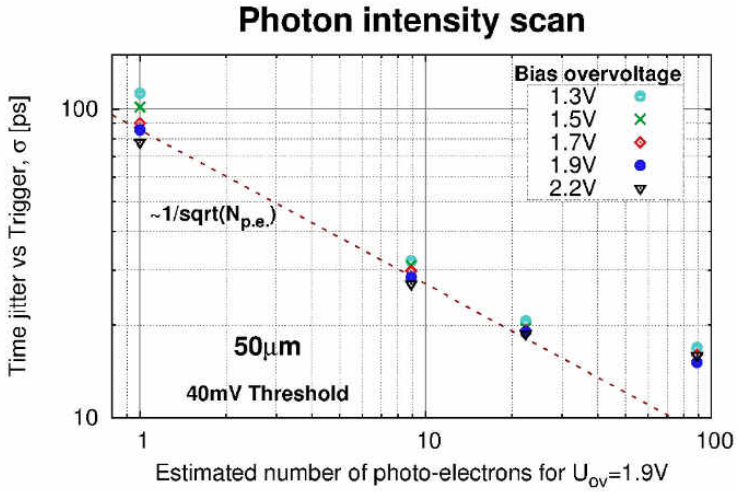

Fig. 9.15: Time resolution of laser pulses as a function of the number of photo-electrons measured with MPPC and the NINO-HPTDC electronics chain.

readout chain, using laser pulses detected by $3 \times 3\,\mathrm{mm}^2$ SiPMs (Hamamatsu MPPC) with SPAD size of $50\,\mu\mathrm{m}$ [64]. The measured time resolution as a function of the number of photo-electrons is shown in Figure 9.15. For 100 photoelectrons a resolution better than 20 ps is achieved.

The NINO amplifier-discriminator is implemented in a 8 channel ASIC. The time binning and number of channels of the HPTDC ASIC is configurable. In our case we use the HPTDC high-resolution mode, which provides 8 channels with 25 ps time binning. The timing readout system is designed to be integrated in the common CT-PPS DAQ and Control system, based on the CMS Pixel FED and FEC boards. The FED board provides input to 400 Mb/s optical links transmitting detector data, builds event packages and transmits them to the central DAQ. The FEC board transmits fast controls (LHC clock, L1 and fast signals) to the detector, as well as front-end configuration data. We plan to use the same components used in the Pixel detector to implement the on-detector interface to the FED and FEC board, namely the transmission and reception optical hybrids and the CCU control chips.

Physically, the timing readout system is implemented in two electronics boards: 1) the frontend board, housing 8 NINO chips and installed in the RP, which receives the SiPM signals transmits the LVDS output on the feed-through connector; 2) the digital board, which receives the LVDS output of the discriminators and houses 8 HPTDC chips. The digital board integrates a radiation resistant FPGA to serve as readout controller of the HPTDC chips, and provides on-board connectors to the opto-hybrid mezzanines (PoH and DoH). If required, the digital board could be installed a few meters away of the RPs in a radiation protected place.

9.4.3 Pixel Tracking System

The key requirements for the CT-PPS tracking system are:

- Efficient pixel based tracking as close as possible to the sensors physical edge, providing hit resolution better than 30 μm.
- Radiation hardness: a design figure of $5 \cdot 10^{15}$ protons/cm^2 for 100 fb^{-1} of integrated luminosity is required (Figure 9.16).
- Reliable operation at the highest LHC luminosity.

Since the construction of the original pixel tracking systems for the LHC experiments, there has been considerable progress in silicon sensor technology. Both CMS and ATLAS have

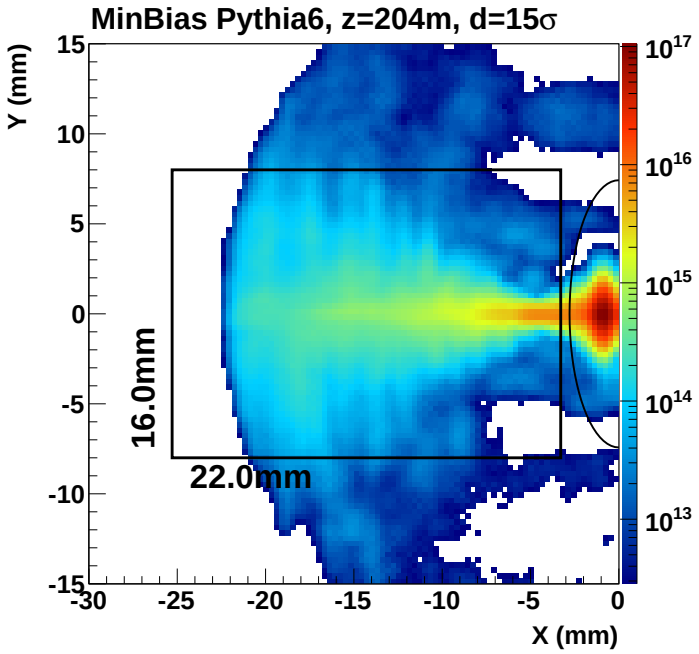

Fig. 9.16: Simulated proton fluence in the tracking station at 204 m from the IP for the integrated luminosity of $100\,\text{fb}^{-1}$. The rectangle indicates the detector surface transverse to the beam assuming a detector tilt angle of 20°. The ellipse shows the 15 sigma beam contour. In the detector edge a value of the order of $5 \times 10^{15}\,\text{p/cm}^2$ is obtained. This value is compatible with the extrapolation from TOTEM data.

pursued improved pixel designs for the high-luminosity upgrades of the LHC. These ongoing R&D efforts have already achieved two proven sensor designs that meet the needs of CT-PPS and can be produced by industry: 3D and planar slim-edge silicon pixel sensors. Both types of sensors are being installed in the new Insertable Barrel Layer (IBL) of the ATLAS vertex detector [65].

3D sensors [66] consist of an array of columnar electrodes (radius $\sim 5\,\mu$m) of both doping types that penetrate through the silicon bulk perpendicularly to the surface, as shown in Figure 9.17. The bulk is usually of type p. Junction n-type electrodes are read out on the front side of the sensor while ohmic p-type electrodes are connected on the back side for applying the bias voltage. This structure decouples the inter-electrode distance from the sensor substrate thickness, allowing to reduce the drift path of the charge carriers without decreasing the total generated charge.
The close electrode spacing provides several advantages compared to the planar sensor design:

- low full depletion voltage ($\sim 10\,\text{V}$),
- fast charge collection time,
- reduced charge-trapping probability and therefore high radiation hardness.

The baseline CT-PPS tracking system is based on 3D pixel sensors, produced either by FBK (Trento, Italy) [72] or CNM (Barcelona, Spain) [73], which we think provide the best performance in terms of active region and radiation hardness. These companies have already produced 200 μm slim-edge 3D sensors for the IBL project with satisfactory yield. However,

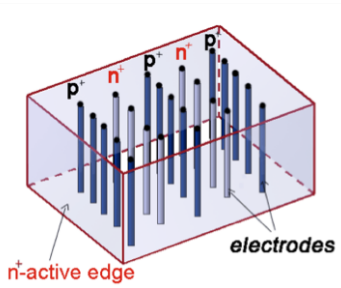

Fig. 9.17: Sketch of a 3D sensor.

for CT-PPS we would like to pursue the option with a 100 μm, or better, slim-edge design, where the active region of the sensor is as close as 100 μm to the edge. Since such slim edges have not yet been produced, we mitigated our schedule risk by designing the CT-PPS tracking system to allow rapid installation, or replacement, of the unit during a LHC technical stop.

The chosen configuration for the tracking system consists of two detector units in each arm, for a total of four detector units. These are the horizontal RPs located at $\sim$210 m. Each station will contain one stack of silicon tracking detectors. Each stack will consist of six planes, where each plane contains a $1.6\times2.4\,\text{cm}^2$ pixel sensor read out by six PSI46dig readout chips ROCs [68]. Each ROC reads 52×80 pixels with dimensions $150\times100\,\mu\text{m}^2$. Given the small area of the detector, covered by a small number of individual sensors, we have chosen a number of planes that provide confortable redundancy making the system resilient to possible failures. The design of the front-end electronics and of the DAQ is based on that developed for the Phase 1 upgrade of the CMS silicon pixel detectors [69].

The resolution of the x-coordinate is determined by the sharing of charge in the pixel clusters, which depends on the detector tilt angle in the x-z plane. While this parameter is not yet defined, test beam results with similar sensors indicate that for an angle of $<$20 degrees the two-pixel clusters have resolution of the order of 10 μm. Since there is no tilt in the y-z plane, the resolution of the y-coordinate is of the order of 30 μm.

The Readout System

The readout of the pixel detector is largely based on components developed in the framework of the CMS Pixel Upgrade Phase 1 readout project. Most components are currently at an advanced test stage and/or in final production. Extensive documentation of each component can be obtained elsewhere [69].

By convention a detector package is a set of six modules, one for each sensor present in a RP. There are in total four detector packages. The specific CT-PPS elements in the readout system are the six RPix Modules (Roman Pot PIXel Modules) and the RPix Portcard. The low voltage system and high voltage system are part of the low voltage and high voltage system of TOTEM, already in place. The backend DAQ electronics, to be installed in the service cavern, is being actively developed by CMS as part of the Pixel Upgrade Phase 1 project.

Each RPix Module consists of a flexible hybrid circuit hosting: a silicon sensor, six ROCs "bump-bonded" to the silicon sensor, and one Token Bit Manager (TBM) chip. The ROC is responsible for charge collection, charge discrimination and data sparsification.

The TBM is responsible for reading out the six ROCs in the module (it can manage up to 16) using a token ring protocol and serialising the data over a single output line. The TBM

manages two token bit ring protocols at the same time, multiplexing the two data streams on the same output line before encoding the data stream. The net result is an uplink data stream running at 400 Mb/s. Dispatching these high speed signals on the flexible hybrid without degrading them is one of the major design requirements of the RPix Module, together with the need to deliver the high voltage to the sensor safely.

The RPix Portcard accomplishes a variety of tasks. The board receives the output data from six RPix modules and retransmits them on six optical fibres towards DAQ modules, using a POH7 opto-electrical converter mezzanine card [70]. This board also receives fast configuration commands from the Pixel FEC via optical fibres, translates these signals using detector optical receivers (DOH) and dispatches them to the modules. These functionality are similar to those of the Forward Pixel project portcard developed by Fermilab. Moreover the RPix Portcard integrates other components such as the radiation sensors, part of the TOTEM DCS radiation monitoring system, and the CMS Tracker Optical Control Link components which are capable of receiving and decoding the commands sent from the Tracker FEC. Finally, the newly developed DC/DC converters [71], developed by CMS, are installed on the board, in order to generate the different voltages needed by the portcard itself and by the attached modules.

For the backend DAQ system, the plan is to use the new uTCA crates and boards developed for the Pixel Upgrade Phase 1 project. A fallback solution, using VME electronics, is available in case the baseline solution could suffer long delays.

It should be noted that the tracking front-end based on the CMS pixel readout chip PSI46dig chip does not have trigger outputs and therefore can not be integrated in the L1 Trigger.

9.5 The AFP Detector

The ATLAS Forward Proton (AFP) program aims to intercept and measure protons emitted in the very forward directions from the ATLAS interaction point (IP). Forward protons are characterized by their energy fractional loss $\xi = (E - E_{beam})/E_{beam}$ and by the four-momentum transfer squared $t = (p - p_{beam})^2 \simeq (p\theta)^2$, where E and p characterize the forward proton, and θ is its scattering angle. The program and its detectors is described in detail in the AFP Technical Design report. [76]

A varied physics program using forward protons becomes available with AFP: single and double diffraction measurements, Pomeron structure functions, rapidity gap survival probability, and double Pomeron exchange (DPE) and double photon exchange (DPhE) processes. The latter give access to anomalous quartic coupling measurements of interest to beyond-Standard-Model Physics signals.

The AFP detectors consist of two forward arms, with two detector station per arm located at 206 m and 214 m from the ATLAS IP. The detectors are housed inside so-called Roman Pots, stainless steel pots that are able to move inside the beam pipe aperture after stable collisions are established. The pots have thin 300 μm windows facing the beam, to minimize interactions and to enable the detectors to approach the beam as close as possible to intercept protons with energy losses as low as $\xi \simeq 1.5\%$. The upper limit to the ξ-acceptance is about 15% and determined by the LHC optics and the upstream beam apertures.

Although the non-exhaustive list of AFP physics processes covers a wide range of cross sections, some of the more interesting processes are rare and require running at the highest luminosity available. Characterizing the instantaneous luminosity by the average number of interactions, μ, occurring at a bunch crossing, μ is expected to be in excess of 25 for the upcoming LHC run period and may well reach 50 or more interactions per bunch crossing.

9.5.1 Beam Interface

The AFP Beam interface of choice is the Roman Pot (RP) because of its proven service record in the ALFA and TOTEM experiments, and the acceptable additional impedance that the RP presents to the circulationg LHC beams: less than 1% of the total LHC transverse impedance. This was extensively simulated by the LHC Impedance team.

The TOTEM collaboration has developed a full design of a cylindrical horizontal RP station based on the existing horizontal and vertical RP stations of TOTEM and ALFA, see the relevant chapters in this report. The AFP RP station is a single-sided horizontal cylindrical RP station virtually identical to the TOTEM design presented in this report. Differences concern the support table, which is specific to the AFP locations near the ATLAS Interaction Point 1 (IP1). Also, the RP itself has a slightly different design: whereas the TOTEM RP design has a beam window of 300 µm thick formed by a 'groove' of 1.7 mm deep and 18 mm wide on the inside of the RP bottom, the AFP RP is instead flat on the inside of the RP, with a similar 'groove' facing the circulating beam. Fig. 9.1 shows the AFP RP design. In normal operation the AFP RP will have a secondary vacuum inside the pot, and only during the installation and removal of the detectors will the inside RP pressure go to 1 bar. The AFP RP design was simulated for mechanical stability in two extreme cases: inside pressure of 1 bar, and outside vacuum, and the reverse. The maximum stress of 0.14 GPa, see Fig. reffig:AFP-RP-Stresses, is 70% of the assumed 0.20 GPa yield strength of the 316LN Stainless Steel and occurs near the outside corners of the thin window facing the beam. The maximum displacement occurs at the center of the thin window and is approximately 0.8 mm.

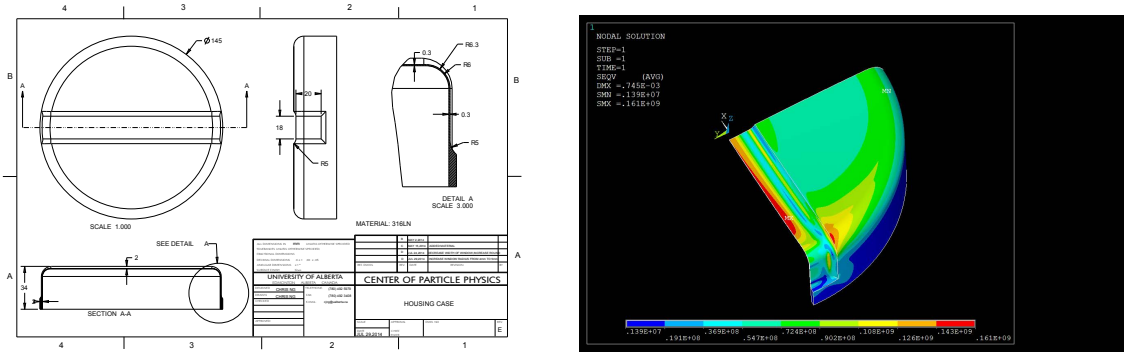

Fig. 9.1: Left: the design of the AFP Roman Pot with 300 µm windows. Note the exterior 'groove' forming the window facing the beam. Right: the calculated stresses in the material

The upstream pot, closest to the ATLAS IP, will contain a Silicon Tracker (SiT) using 3D pixel sensors of the ATLAS IBL design. The upstream pot, at 214 m, will contain both a SiT and a Time-of-Flight detector (ToF) using L-shaped Quartz radiator bars (LQbar). A draft design is shown in Fig. 9.2. The detectors are described in the following sections.

9.5.2 Silicon Tracker

The AFP design foresees a high resolution pixelated silicon tracking system placed at 210 m from the ATLAS interaction point (IP). Combined with the magnet systems of the LHC accelerator, the AFP tracker will provide the momentum measurement of the scattered protons. The full AFP tracker will consist of four units, each composed of four to five pixel sensor layers, which will be placed in Roman Pots, two on each side of the ATLAS IP.

To ensure good momentum resolution, the AFP tracker is required to provide high spatial resolution (about 10 µm) in the short pixel direction. Furthermore, it is vital for the physics

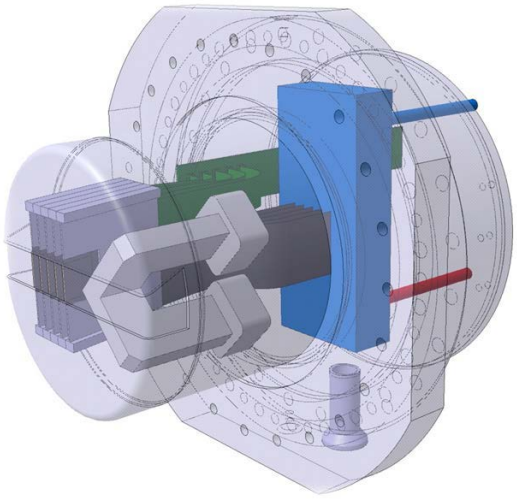

Fig. 9.2: The design of the AFP Roman Pot with a 5-plane Silicon 3D Pixel tracker and a double LQbar Time-of-Flight detector. Note the cold-air heat exchanger near the top flange (dark blue) which is using cold air from a vortex 'aircooler' apparatus.

program to measure very small scattering angles. To this end the detectors will be placed almost perpendicular to the beam (under a small tilt of 15°) with one side only 2-3 mm away from it. This leads another two critical requirements for the pixel detectors:

1. The inactive region of the detector side facing the beam has to be minimized to about 100-200 µm.
2. Due to the proximity to the beam, the detectors have to withstand a highly non-uniform irradiation profile with a high maximum fluence in the area closest to the beam and several orders of magnitude lower away from it. The magnitude of the maximum fluence depends on the run scenario: about 5×10^{12} p/cm^2 are expected for initial low-luminosity runs and about 5×10^{15} p/cm^2 for a possible later high-luminosity scenario.

9.5.2.1 Modules

The most critical component of the AFP tracking system is the pixel module. It consists of a 3D pixel sensor bump-bonded (connected) to a front-end chip which in turn is glued and wire-bonded to a flexible printed circuit (flex). The flex provides clock and command signals and routes the data output. The AFP module will consist of a single FE-I4B front end chip, which will provide an active area of 1.68×2.00 cm^2. The AFP single-chip 3D pixel modules are similar to the ones used in the ATLAS Insertable B-Layer (IBL) detector. However, some important modifications have to be implemented to meet the specific requirements for AFP.

3D Sensors

In 3D pixel sensors, n- and p-type column-like electrodes penetrate the substrate defining the pixel configuration. Though the fabrication process is complex, the technology is less demanding in terms of bias voltage and cooling than the standard planar approach, and the reduced drift path makes 3D devices more radiation hard. In recent years significant progress has been made in the development of 3D sensors, which culminated in the sensor production for the ATLAS IBL [77]. The AFP pixel detectors will be based on the 3D double sided sensors developed by CNM (Barcelona) and FBK (Trento) for the IBL.

The AFP 3D sensors were already fabricated at CNM on Float Zone, p-type, 100 mm diameter, wafers, with $< 100 >$ crystal orientation, 230 µm thickness, and a very high resistivity (10 to 30 kΩ cm). Columnar electrodes, 12 µm wide, were obtained by Deep Reactive Ion Etching (DRIE) and dopant diffusion from both wafer sides (n+ columns from the front side, p+ columns from the back side), without the presence of a support wafer. By doing so, the substrate bias can be applied directly on the back side. The sensor design features an array of 336×80 pixels with a pixel size of 50×250 µm^2. Each pixel consists of 2 n+-junction columns and 6 surrounding p+-ohmic columns. Figure 9.3 shows details of the 3D sensor layout.

The CNM production for AFP concluded in July 2014. Unfortunately, due to a machine problem, a large portion of the 13 wafers of the run were damaged and only 6 are expected to work. Each wafer provides 8 3D sensors, so this is not a problem for the first phase of the AFP program.

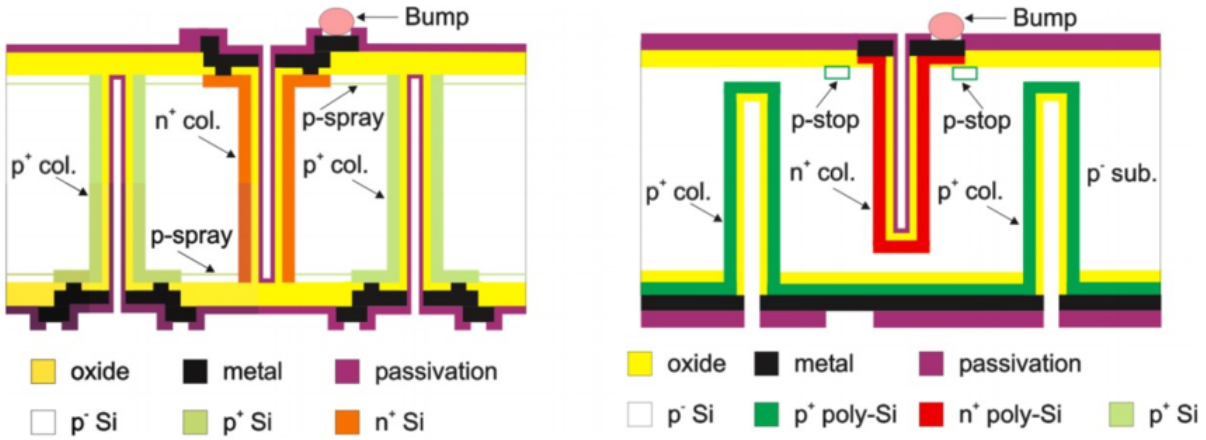

Fig. 9.3: **Design of the columns of the FBK (left) and CNM (right) 3D sensors.**

Front-end Electronics

The pixel readout electronics will be the FE-I4B [78]. The sensors are DC coupled to the chip with negative charge collection. Each readout channel contains an independent amplification stage with adjustable shaping, followed by a discriminator with independently adjustable threshold. The chip operates with a 40 MHz externally supplied clock. The time over threshold (ToT) with 4- bit resolution together with the firing time are stored for a latency interval until a trigger decision is taken. The FE-I4 chip can also send a trigger signal via the HitOr line. This HitOr will be used for the first-phase AFP trigger, when there is no installed Time-of-Flight detector.

The FEI4 chip has been extensively tested for the ATLAS IBL detector. The radiation hardness has been well established to fluencies of 250 Mrad and beyond, surpassing the AFP requirements. The trigger capabilities have also been proven, as the chip is used to trigger the ATLAS Diamond Beam Monitor detector.

9.5.3 Time-of-Flight Detector

Because single diffraction, which produces a single forward proton, are relatively common (about 10% of the total cross section), an interaction of high interest, like Double Pomeron or Photon Exchange, which yields two forward protons, may easily be faked by the occurrence of two single-diffraction interactions in the same bunch crossing. The only possible rejection

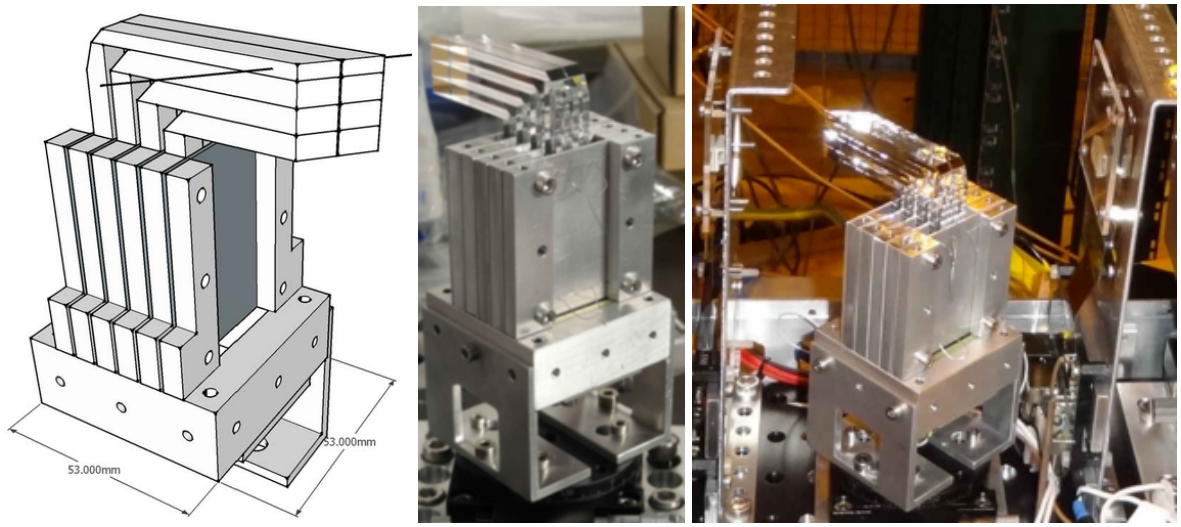

Fig. 9.4: Left: the design of the AFP Time-of-Flight Detector (LQbar). The straight line is an example of a diffractive proton entering one of the quartz radiator bars from the right. Middle: The LQbar detector before test beam installation in November 2014. Note the quartz radiator bars with the 45° Aluminized mirrors. Right: the LQbar ToF installed in the beam test. Two 3D Silicon tracker planes are also visible.

of this background is to measure the arrival time difference of the forward protons in the two arms with pico-second accuracy. For a genuine two-proton event, the arrival time difference of the forward protons $\Delta t = t_{Leftarm} - t_{Rightarm}$ is directly related to the interaction vertex location z_{vertex} (z measured along the beam from zero at the ATLAS IP and positive toward the 'Right' arm) as: $z_{vertex} = c\Delta t/2$. Thus, a $\sigma_t = 10$ ps time-of-flight resolution translates into a $\sigma_z = 2.1$ mm vertex resolution. The vertex location derived from fast timing is compared to the location measured from the ATLAS inner detector tracking; if the two locations differ, the protons stem from unrelated background events. Extensive simulations have shown that a 10 ps Time-of-Flight measurement provides a background rejection factor around 20.

The proposed AFP Time-of-Flight detectors consist of Quartz bars positioned at the Cerenkov angle with respect to the proton directions. Because of the constraints imposed by the Roman Pot housing, the quartz bars must be bent out of the z(beam) - y(vertical) plane into the x(horizontal) direction; a structure that was named 'LQbar'. A picture of an 8-channel LQbar detector, and its protype implemented for the November 2014 AFP Beam Test is shown in Fig. 9.4. The Cerenkov light travels up the bars and is converted to a signal by a specialized 4×4-pixel Multi-Channel-Plate Photomultiplier tube by Photonis. [79]

A possible upgrade of this detector allowing a better pixelisation is under study, it could benefit from other technologies such as fast Si or damonds as for CMS-TOTEM.

The PMT output signal is approximately Gaussian with a 700 ps full width at half maximum (rms$\simeq$ 300 ps). Photon statistics (the mean number of photo-electrons is about 10) affect the signal amplitude but preserve the shape precisely. The goal of the electronics is to preserve the signal shape information and derive the best possible timing of the signal, independent of the signal amplitude.

The approach chosen by the AFP timing group is low-noise amplification followed by constant-fraction discrimination (CFD) and high-precision time digitization (HPTDC) and read-out, see Fig. 9.5 where the various components and their locations are depicted. [80] (with a possible upgrade using SAMPIC).

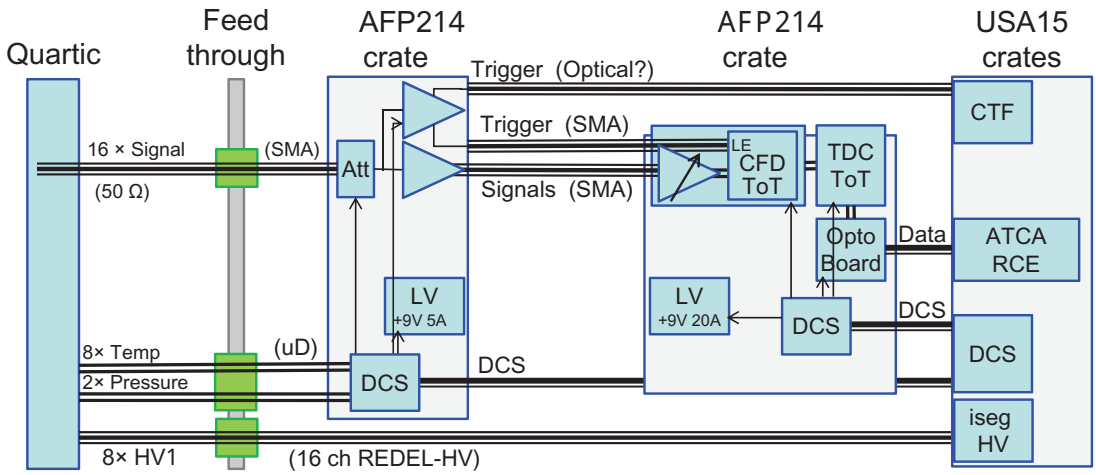

Fig. 9.5: A schematic diagram of the components of the fast timing electronics chain described in the text, together with their physical locations in the LHC tunnel.

Other approaches are possible, as discussed for example by E. Delagnes, E. Breton, and S. Ritt in Ref. [81]. The sampling methods described by these authors are best performing, and the cost reduced compared to CFD, and the SAMPIC chip is considered as an upgrade for the readout electronics [82].

Beam tests (Fermilab 2012, CERN 2013) have shown that the single-channel resolution of PMT, Preamplifiers and CFD is 20 ps, limited by the PMT signal shape, statistics, and noise. Two or more sequential measurements (two or more successive quartz bars) will reduce the proton ToF resolution accordingly; four sequential measurements will provide 10 ps resolution (although this configuration has to be tested due to the material budget).

The beauty of the system is its modularity: the resolution can be tuned by the changing the number of quartz bars in succession, while the resolution requirement per-channel is somewhat relaxed. Somewhat arbitrarily, in order to preserve the per-channel timing resolution, we require the time jitter of the electronics to be 5 ps or less.

Adjacent sequences of quartz bars cover intervals in proton energy loss ξ. It is assumed that the ξ acceptance is subdivided into 4 intervals, each individual ξ interval covered by a sequence of 2-4 quartz bars. Because the central missing mass MM measured from the two protons is directly related to their ξ, $MM^2 = \xi_1\xi_2(2E_{beam})^2$, a selection for events in which a large missing mass is produced can be formed already at the trigger level.

9.5.3.1 Preamplifiers

The PMT is used at a low gain of about 5×10^4 to maximize the lifetime of the tube in the high-rate LHC environment close to the circulating beam. The typical PMT output signal at this gain is about 8 mV for 10 photoelectrons. The AFP CFD used has a dynamic range from 250 - 1200 mV (a new design is in the works with a further improvement anticipated in dynamic range).

In order to match the CFD dynamic range, and to provide for gain variations as function of PMT pixel and ageing, the preamplification is done in two 20 dB stages. The first stage PA-a is located directly on the base of the PMT. The 8-channel preamplifier PCB is based on the PSA4-5043+ low-noise (NF=0.7 dB) InGaP E-PHEMT MMIC gain block (gain 18.6 dB

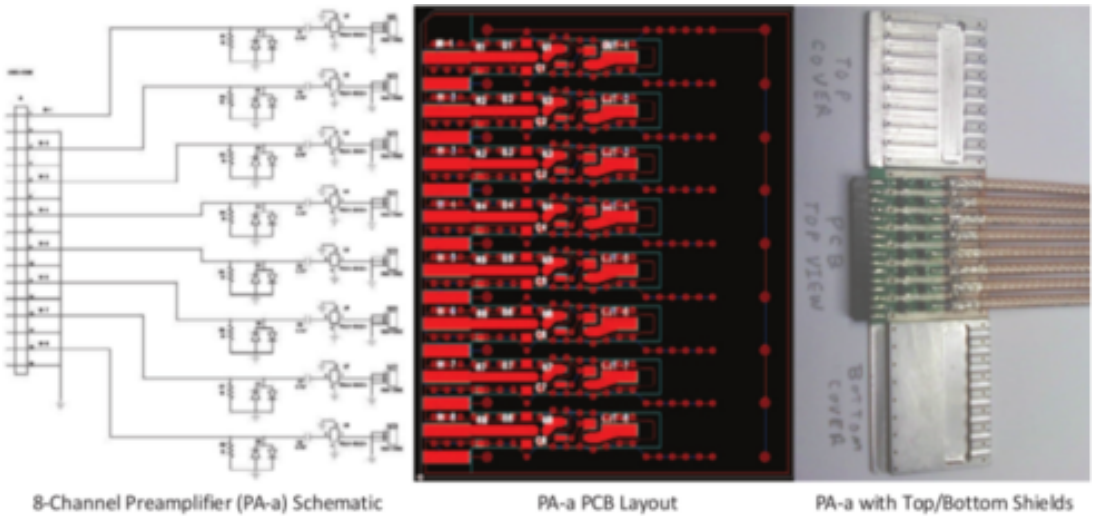

Fig. 9.6: The schematic diagram, layout, and photo of the low noise pre-amplifier, to be located on the photodetector base in the secondary vacuum.

at 1 GHz) from MiniCircuits.com, see Fig. 9.6. The PA-a has been tested under power and demonstrated to be radiation tolerant to at least 9 kGy (LANSCE, February 2014 run with 800 MeV protons, 2.2×10^{13} p/cm^2); this dose corresponds to the dose expected at the preamplifier location for 300 fb^{-1} or three years at a luminosity of 10^{34} cm^{-2}s^{-1}.

The first preamplifier stage is connected by coaxial cable to the second preamplification stage (PA-b) located at floor level below the detector, where the high-energy proton flux is expected to be a factor 20 lower (the low energy neutron flux is a factor 10 lower there).

The PA-b provides DC power (5 V) to the PA-a via the coaxial connection. The PA-b further includes (in order): a programmable 3-bit attenuator (Hittite HMC288MS8 2 dB LSB GaAs MMIC, range 1 dB - 15 dB), a 2 Way-0^o splitter (MiniCircuits TCP-2-33W+, -4 dB insertion loss) providing a trigger pick-off, and a ADL5611 gain block (Analog Devices, gain 22(20) dB at 1(4) GHz), see Fig. 9.7. The PA-b has successfully survived the same irradiation runs and doses as PA-a.

9.5.3.2 Trigger

A trigger board has been designed and will be produced in the near future. The design is based on the 8-channel GaAs Discriminator MMIC 'NINO' (developed and produced by CERN. [83]), followed by programmable majority circuitry to form a 'N out of M' type trigger combination on two LVPECL outputs. The option to include a (properly timed) bunch crossing gate (LVPECL) is implemented. The PCB has been laid out but not yet been produced. Let us notice that the upgrade SAMPIC solution will provide a trigger directly.

The trigger signals from several adjacent quartz bar sequences are combined into a bit stream and sent over fast air-core coax cables to the ATLAS Central Trigger Processor. The trigger information from the two AFP arms can be used to form a large proton-proton 'missing mass' trigger and can be combined with various central ATLAS trigger terms.

9.5.3.3 Constant Fraction Discriminator

The Constant Fraction Discriminator principle has long be used to correct for time walk in cases where the signal fluctuates in amplitude but is constant in shape. The AFP design was

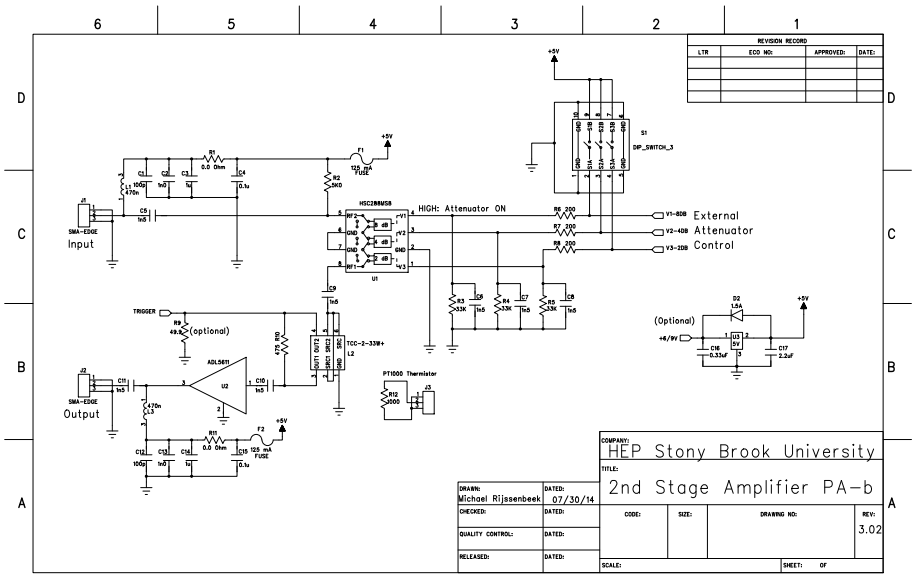

Fig. 9.7: The schematic diagram of the new second-stage variable-gain amplifier PA-b, to be located below the detector at floor level.

initially developed for FP420 by Luc Bonnet of the Université Catholique de Louvain, and was further developed for AFP by the HEP group (J. Pinfold, S-L. Liu) at the University of Alberta at Edmonton (Alberta). The measured time-walk is 5 ps or less over the range 250 - 1200 mV. The design is currently revisited to obtain a larger dynamic range and to implement a time-over-threshold functionality, which will allow off-line timing corrections if so required. Moreover, the new CFD design includes an optional bunch crossing gate to reduce output rates.

A single CFD channel is implemented on a small 28×70 mm^2 daughter board, with RF I/O connectors for signal in and signal NIM out, and differential LVPECL outputs.

9.5.3.4 High Precision Time Digitizer

The High Precision Time Digitizer board, HPTDC, was developed by Alberta. The 12-channel board uses 4 HPTDC ASICs developed and produced by CERN in 0.25 μm CMOS technology (HPTDC, J. Christiansen et al., http://tdc.web.cern.ch/tdc/hptdc/hptdc.htm). The four ASICs are controlled by an on-board FPGA which also handles the flow of data and controls. This and previous versions of the HPTDC board have been used successfully at various beam tests. The HPTDC and new developments were presented in Ref. [84].

The intrinsic resolution of the current HPTDC is 16 ps, which is a significant contributor to the per-channel resolution. However, new HPTDC ASIC development with smaller feature size are ongoing at CERN and may lead to significant improvements in the near future. Note that the 16 ps resolution of the HPTDC is per channel and that the contribution for a system of four quartz bars in sequence would only be 8 ps.

The radiation tolerance of the HPTDC is not guaranteed. The HPTDC ASIC is expected to be radiation tolerant to a degree sufficient for it to be located on the tunnel floor, near the the detectors. The FPGA firmware must be re-designed to provide the appropriate checking of HPTDC registers for upsets. Moreover, the FPGA itself has to be radiation tolerant, which can be done by choosing a radiation-hard part (expensive!) or going to a fuse-programmable part. Alternatively, the FPGA can be programmed to do self-checking and organized with majority decisions in critical paths. It is the latter choice that will be pursued.

9.5.3.5 Reference Clock

A major component of any time-of-flight system using two widely separated detector arms (424 m apart measured along the beam line), is a synchronizing Reference Clock. As for other components, the requirement is that the two local detector clocks are synchronized to well within 5 ps.

The University of Texas group (A. Brandt, V. Shah, et al.) has developed a prototype Reference Clock based on a design originally by SLAC. Every Daughter Clock sends its signal to a central Reference Clock which produces a DC phase error signal that is read (on the same cable) by the Daughter Clock. The Daughter Clock adjusts its phase until the phase error signal is zero.

The design is not fully complete at this time but initial tests indicate the desired performance can be reached.

In addition to the synchronized local clock, clock fanouts at the local detectors are required. We intend to implement these with high performant LVPECL Clock FanOut buffers from Micrel.

9.5.4 Data Acquisition

The Data Acquisition system currently foreseen is based on the Reconfigurable Cluster Element (RCE) computer daughterboards in the ATCA telecom standard. [85] This system has successfully been employed for the testing of the ATLAS Intermediate B-Layer Silicon pixel detectors. Because the same Silicon sensors are used for the AFP tracker, the RCE-based DAQ system can be used essentially without any new development. However, the HPTDC board has to be interfaced to the RCE readout. This requires new FPGA firmware (also required for radiation tolerance!) as well as additions and modifications to the RCE software.

Recently, the Time-of-Flight time digitizer HPTDC board was successfully interfaced to the RCE DAQ with an interfacing very similar to the interfacing with the FE-I4 silicon tracker front-end chip. Both tracker and Time-of-Flight detectors can therefore be read with the same RCE-based DAQ. The IBL Optoboard, the optical data and command interface board for the ATLAS Intermediate B-Layer detector, will be used to interface between the optical data cable and the copper lines to the front-ends in the same way as for the ATLAS IBL.

Because the RCE hardware is located in a low radiation and accessible area near the ATLAS detector, radiation tolerance is not an issue for the DAQ.

.

9.6 LHCb Experiment

As described in Chapter 5 LHCb is well suited for central exclusive production (CEP) physics [86]. It has excellent acceptance, tracking and particle identification in the forward region, good sensitivity to low p_T particles, and is able to reject activity in the backward region using tracks reconstructed in the VELO. The experiment runs at lower luminosity using β^* settings and offset levelling techniques, and so benefits from low pile-up conditions and is able to select CEP events with no additional interactions. Of the 3.2 fb^{-1} accumulated in Run I about 21% is useful for studying exclusive events with no additional pile-up activity. Run II will extend this potential; after the move to a 25 ns filling scheme, LHCb plans to accumulate more than $5\,fb^{-1}$, of which the useful fraction for CEP studies with no pile-up will rise to 37%. A further advantage of LHCb is the availability of the low level trigger operating at 40 MHz, which has access to information about backwards activity and has been used since 2012 to enhance the event yield for CEP hadronic final states.

Previously published LHCb results have shown that with the current coverage there is still a significant irreducible background to the central exclusive signal consisting of events where the proton has dissociated in the forward direction outside the experimental acceptance. For this reason LHCb is currently installing a new system of scintillator detectors in the LHC tunnel to detect showers from high rapidity particles interacting with beam-pipe elements. The concept is modelled on previous successfully operating systems, in particular at CDF at the Tevatron [87] and CMS for low pile up LHC running. The absence of activity in the scintillators can be used to confirm the existence of a rapidity gap extending beyond the spectrometer acceptance, and to reduce backgrounds to CEP candidates and allow the study of many interesting central states with lower masses which are currently systematics limited. The HERSCHEL (High Rapidity Shower Counters for LHCb) system will also act as a general rapidity gap detector, identifying very forward showers in low mass diffractive excitation. The LHCb readout offers the potential to incorporate scintillator signals into the low level trigger. In this way a highly efficient trigger can be developed which will allow LHCb to exploit dedicated low luminosity running for forward physics purposes. In addition to their value for studying rapidity gaps without pile-up, the FSC counters can provide real-time monitoring of beam conditions and may extend the usefulness of the Beam Gas Imaging luminosity measurement by complementing existing coverage in the backwards direction.

9.6.1 HERSCHEL configuration

As illustrated in Fig. 9.1, the Herschel system comprises three stations in the RB84 section of the LHC on the left side of the LHCb interaction region IP8, and two stations in the RB86 section on the right side of IP8. The left-side stations, which are upstream of the VELO, are labelled B (backwards) and the right side stations downstream of the muon chambers are labelled F (forwards). The z-positions of the stations with respect to IP8 are largely defined by the available space, and are placed as symmetrically as possible. The outermost stations (B1,B2,F1 and F2) are at $\pm$ 20 m and 114 m, and on the backward side an additional station (B0) is placed at -7.5 m. Due to differences in the vacuum chamber layout at the proposed locations, the innermost cut-out of the scintillator panels are adapted appropriately. The smallest achievable radii are at B0 and B1, where the vacuum chamber has a circular cross-section with an outer diameter of 84 mm. At station F1 the scintillator plates must fit around the vacuum bellow, and the far stations are situated in the region where each beam has an individual chamber, and are enlarged accordingly. Each station is equipped with four scintillator plates, with outer quadrant dimensions of 300×300 mm^2. The layout is indicated schematically in Fig 9.2 9.3 9.4. The stations start to be efficient for primary particles with a pseudorapidity of about 7.5 or less,

due to the presence of beam elements where showering can be initiated giving signals in the scintillators.

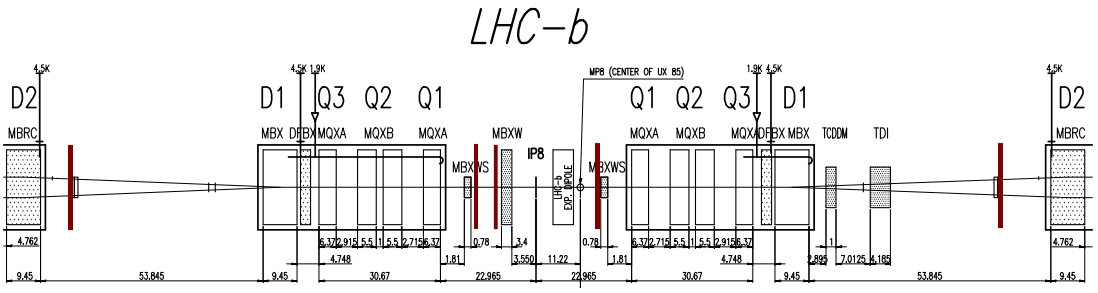

Fig. 9.1: Layout of IR8. The positions of the shower counter stations are indicated by the red arrows.

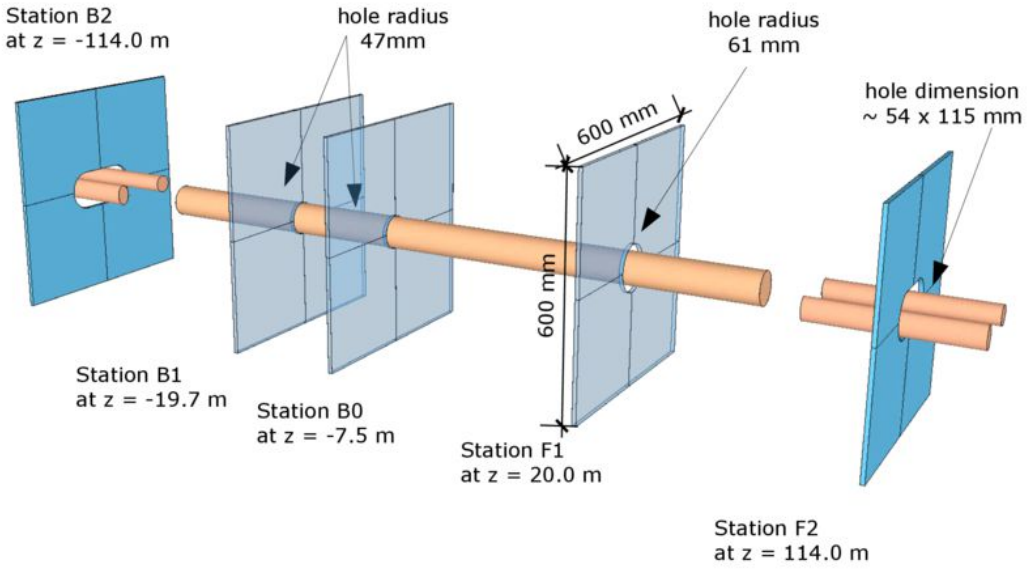

Fig. 9.2: Schematic overview of the scintillator configuration. The z scale has been compressed and the long section of the beam pipe between the B/F1 and B/F2 stations omitted.

The shower counter environment has been fully simulated with a description of the beam material and magnetic fields, and the scintillator occupancy has been studied with single particles and full LHCb events. A typical inelastic collision will give rise to showers that will produce a high level of activity in most or all of the scintillator stations. In these events the number of charged particles that will give light is expected to be ~ 100 per quadrant in stations B0, B1 and F1, and up to ten times this value in B2. The photomultipliers must be able to with-

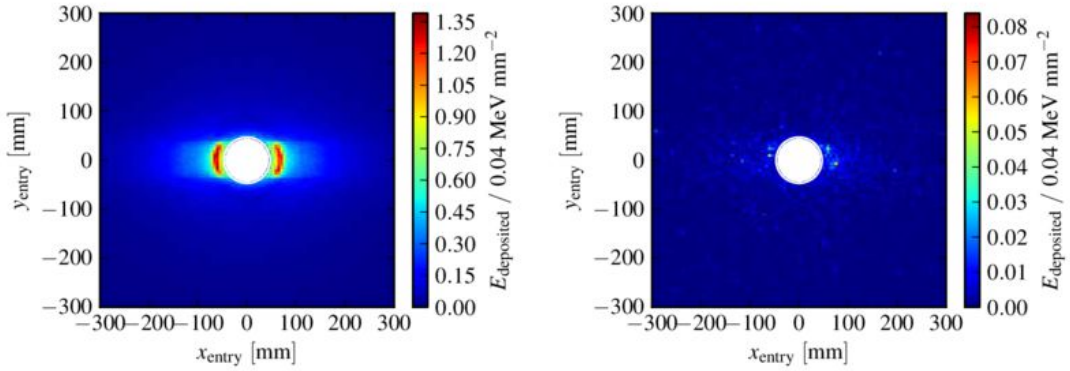

Fig. 9.3: Simulated energy deposited in the innermost backward Herschel counter (B0) for inelastic collisions (left) and for events mimicking a CEP-like physics event with a disassociated proton (right)

stand the light flux produced from such activity occurring in the majority of beam-crossings. At the same time the system must be sensitive to the activity from classes of interaction that constitute background to the CEP analyses, for example a single diffractive interaction that gives rise to a low level of activity in the spectrometer acceptance. Simulation studies indicate that the hit multiplicity in such interactions is about five times lower than in other classes of inelastic events.

The radiation environment is most severe for B2 and F2. Here simulation indicates that the dose in the innermost region of the scintillator plane will approach 1 MRad/fb^{-1}, and to be an order of magnitude lower for those regions more than 5 cm from the closest acceptance. The other stations will experience a lower dose, following the reduced multiplicity in these planes. Irradiation measurements for calorimeter modules exposed in the tunnel during Run 1 close to the location of B0 give results that are compatible with these estimates. In order to protect the scintillators from accumulating irradiation while not in use, each station is equipped with a remoted controlled pneumatic moving system allowing the planes to be retracted and rotated away from the beamline. The stations are not located in a high magnetic field, the largest being ~ 30 G at F1.

9.6.2 Detector Design and Installation

The scintillators are manufactured from EJ-200[5] plastic scintillator material, which features a rise time of 0.9 ns, a decay time of 2.1 ns and a light yield of 10000 photons/1 MeV e$^-$. Light guides in the shape of a fish tail are glued to the top or bottom of the scintillator plates. For calibration purposes, two "Mega Bright Blue" LEDs [6] are included with each scintillator, close to and far away from the light guide. The scintillators and light guides are covered by thin aluminium sheets appropriate for the LHC tunnel environment.

The main challenge for the photomultiplier tube is the high photon flux, which even when the tube is operated with reduced gain will lead to a high anode current. The Hamamatsu[7] R1828-01 2$''$ diameter PMT is used, which allows a maximum average anode current of 200 μA. It has a relatively fast signal response of 1.3 ns rise time. This 12-stage PMT also has a large range of gain adjustment which is suitable for both a low gain operation ($\sim 10^3 - 10^4$) in the

[5] Eljen Technology, Sweetwater, Texas 79556, United States (`http://www.eljentechnology.com`

[6] Manufactured by Multicomp

[7] Hamamatsu Photonics K. K., Hamamatsu City, Japan (`www.hamamatsu.com`)

Fig. 9.4: Photographs of the installed Herschel scintillators in the LHC tunnel. a) shows station B0, 7.5 m upstream of LHCb, b) shows station B1 at 19.7m upstream and c) shows station B2 at 114 m upstream. On the downstream side, d) shows station F1, here in the open position such that the scintillator shape can be clearly seen, and e) shows station F2.

experimental environment of the LHC, and a high gain operation ($\sim 10^6 - 10^7$) required for the calibration of the counters with cosmic muons. In order to cope with the rates a special resistive divider design is used which features Zener diodes to stabilise the dynodes and a bias extra-current to allow sufficient current in the vicinity of the anode. Such a design has already been operated successfully in the LHCb Beam Loss Scintillator (BLS) system in similar radiation conditions. Each photodetector is mounted in a standard steel housing, including a shielding tube that together provides protection against magnetic fields up to ~ 1 kG.

All scintillators were calibrated before installation using cosmic and LED signals. The light yield is estimated to be 200 electrons per mip and the cosmic signals show a clear separation from the pedestal. A clipping scheme is used to contain the signals within a 25 ns window. The scintillators and cables were installed during available access times in the LHC tunnel over a six month period towards the end of 2014 and the start of 2015. Photographs of the complete set of stations can be seen in figure 9.4.

The Herschel system is required to identify events with low signals, which typically occur after a minimum bias event with large energy deposition in the scintillators, with the event occupancy being very close to 100%. For this reason careful attention was paid to the signal speed and choice of electronics. The readout system uses components from the readout system of the LHCb preshowerdetector. Each channel is treated by alternately by two integrators, which are each reset after 50 ns. The electronics for the backwards and forwards stations are installed

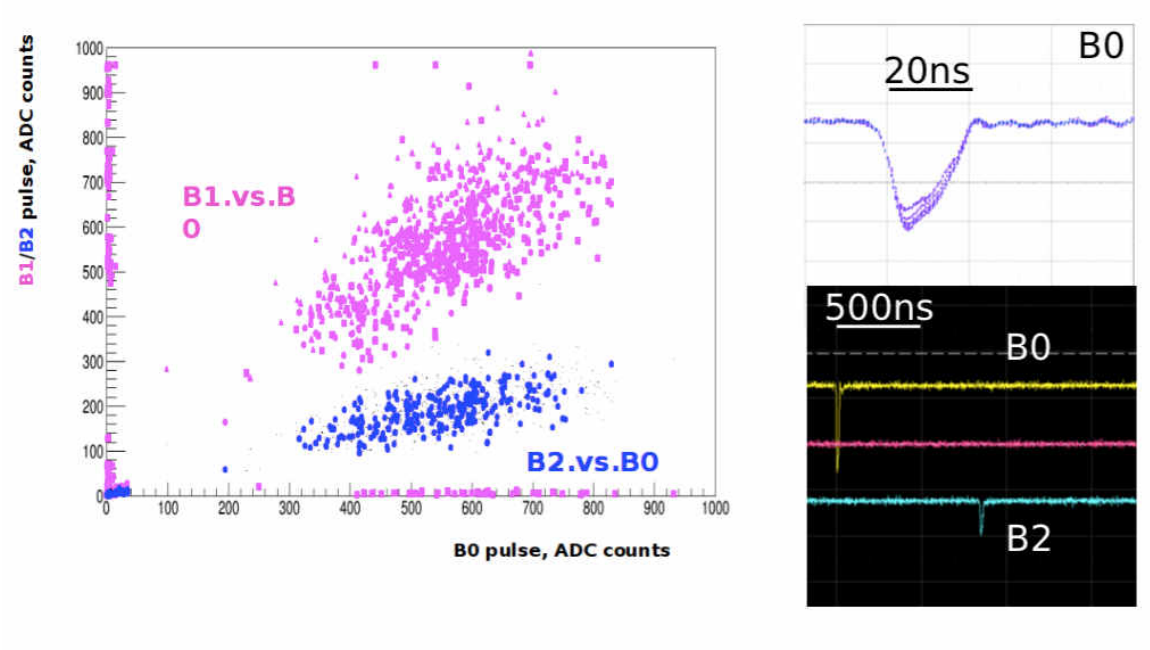

Fig. 9.5: Preliminary plots giving a qualitative indication of the Herschel data quality from the November 2014 "TED" run. The scatter plot shows the correlation between the three downstream stations. As expected, B2 is less populated than B0 or B1. The right figures show the characteristics of the signals in the channels connected to the oscilloscope. The signal is contained within 25 ns.

in independent crates on either side of the LHCb cavern, before routing to the barracks and combination with the other LHCb sub detectors. The commissioning of the system started in November 2014 and March 2015, when data was provided in LHCb during the so called "TED" shots during LHC sector tests, where particles emerge from the beam stopper downstream of LHCb. This provided an opportunity to check the synchronisation of Herschel relative to the rest of LHCb, tune the time alignment, and evaluate the readout chain. For the purposes of this test some Herschel channels were connected directly to an oscilloscope. The first performance indications showed that the scintillators were working well, that the signal is contained within 25 ns, and that correlations in signals are seen between the stations. Data from the November 2014 TED run is shown in figure 9.5 and a more detailed analysis is ongoing.

It is also of great interest to include Herschel information in the LHCb L0 trigger, which is the lowest level trigger of the experiment running at 40 MHz. By vetoeing events with activity in the scintillator, it should prove possible to extend the kinematic range of exclusive hadronic channels by relaxing the multiplicity and transverse momentum cuts which are currently imposed to suppress the rate. In addition it should be possible to exploit Herschel to enhance the L0 trigger for single diffractive physics events. The LHCb luminosity monitoring also needs to suppress background pp interactions where there are particles in both directions but may mimic beam-gas interactions due to the lack of angular coverage of LHCb and the Herschel trigger is expected to play a role. The commissioning of Herschel at L0 requires additional hardware

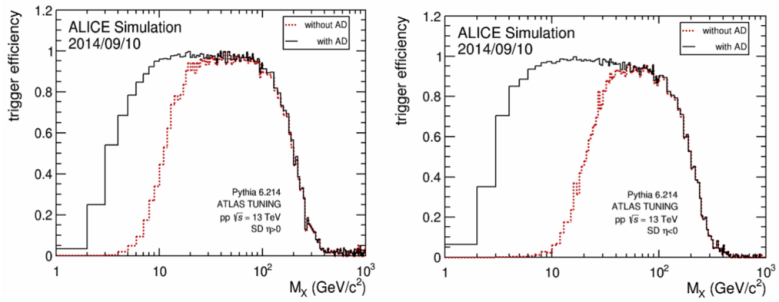

Fig. 9.1: Trigger efficiency for single diffractive events (SD) for $\eta > 0$ (right) and $\eta < 0$ (left). In both cases the efficiency of the trigger given by AD increases considerably at low diffractive masses

interventions and is scheduled for the first technical stop after a few months running at Run II.

9.6.3 Conclusions

The addition of the Herschel scintillation counters around the beam pipes on both sides of LHCb increases their rapidity coverage and enables studies of diffractive processes, both as gap detectors and as detectors of propton diffractive dissociation. The system is currently being installed and commissioned and is expected to operate fully during Run II.

9.7 AD: The Alice Diffractive Detector

There are only a few sub-detectors in ALICE that are used to measure charged particle multiplicity at large pseudo-rapidities η, ($|\eta| > 2$). The VZERO detector, made of scintillator plastic, is used as a level zero trigger and it is suitable for multiplicity measurements, the Forward Multiplicity Detector (FMD) made of silicon detectors and the Photon Multiplicity Detector (PMD) at moderately large forward rapidity, the Zero Degree Calorimeter (ZDC), which can be used to tag neutrons and protons from the nuclear break-up, are some of the devices used for diffractive physics studies.

ALICE has excellent particle identification capabilities in the central rapidity region and can resolve low transverse momentum tracks, ($p_T > 150$ MeV), i.e. ALICE is in a position to study soft and hard diffractive events at the LHC. In order to extend the rapidity coverage of ALICE and enhance the efficiency for detecting events with rapidity gaps, during LS1 a small detector was installed made of scintillation counters with optical fibre readout (AD, the ALICE Diffractive detector).

The AD detector will increase the sensitivity to diffractive masses close to threshold ($m_p + m_\pi$) and also partially compensate for the loss of trigger efficiency for Minimum Bias events and diffractive events when reaching the design LHC energies (see figure 9.1). This detector will provide a level zero trigger signal which will be useful for diffractive cross section measurements. It will extend the pseudorapidity gap trigger, crucial in the study of central diffraction, where the physics reach is limited by statistics. In addition, the possibility of triggering on the charge deposited in the AD scintillator modules will provide an extended centrality trigger in both Pb–Pb and pPb collisions studies.

9.7.1 Design of AD

The AD detector consists of two stations of scintillator pads (see figure 9.2), one on each side of the interaction point (see figure 9.3), ADA on the cavern A-side, ADC on the tunnel C-side).

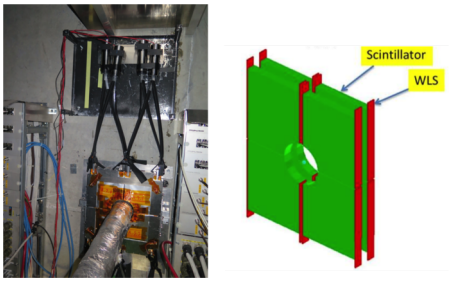

Fig. 9.2: Picture of one AD station installed inside the ALICE' cavern (left). Drawing of one AD station (right) showing eight scintillator cells (green) and two WLS bars per cell (red)

Each station has two layers, each with four BC404 scintillator pads of dimension $181 \times 216 \times 25$ mm^3, arranged around the beam pipe. In each station, a coincidence between corresponding pads is required to reduce background and electronic noise. On the C-side the two layers are placed inside the LHC tunnel next to the compensator dipole magnet, a position that avoids synchronization with beam-gas when LHC runs with 25 ns bunch spacing.

9.7.2 Commissioning of AD

The light produced by BC404 plastic scintillator material is collected by two Wave Length Shifting bars (WLS) attached, but not glued, on each side of the pads. Each WLS bar transfer the collected light to a bundle of 96 transparent optical fibres, which conducts the light to the PMTs (inside the ALICE cavern). The light is converted into an electric pulse by a fine mesh PMT from Hamamatsu R5946 (hybrid assembly H6153-70). The signal from the PMT is sent to a preamplifier card which delivers two signals: one, amplified by a factor of 10 and clamped at about 300 mV which is used for timing measurement, the second, direct unmodified signal, is used for charge integration. The preamplifiers are installed close to the Front End Readout electronics. The Front End Electronics provides signals for the level 0 trigger of ALICE. It is of the same kind as that presently used in the VZERO detector [91]. The trigger signals of the AD counters will expand the acceptance of the Minimum Bias trigger. Moreover it will be possible to trigger on charge deposition in the two AD detectors providing an extended centrality trigger in both Pb-Pb and proton-Pb collision studies.

The photomultipliers and scintillators were calibrated with cosmic ray data and LED signals in the laboratory. The measured time resolution is about 0.8 ns and a clear separation obtained between the signal and the pedestals as shown in figure 9.4 for cosmic muons.

Conclusion

Diffraction is an important part of non-perturbative QCD studies. It is also important in the tuning of Glauber models used to simulate Pb-Pb and pPb collisions. For this purpose, during LS1 the ALICE collaboration installed the AD detector, which will increase the trigger efficiency for diffractive events. The system is fully installed and currently is being commissioned so as to be completely operational during Run-II.

9.8 LHCf Detectors

The Large Hadron Collider forward (LHCf) experiment installed two independent detectors at either sides of IP1 (ATLAS) [92] . The detectors are installed in the instrumentation slots of the TAN absorbers 140 m away from the IP. The detector at the IP8 (LHCb) side is called Arm1

ADA/ADC layer positions

Station	Inner radius (cm)	η_{min}	η_{max}	Z (cm)
ADC layer 0	3.7	-6.96	-4.92	-1955.75
ADC layer 1	3.7	-6.96	-4.92	-1953.05
ADA layer 2	6.2	+4.77	+6.30	+1693.65
ADA layer 3	6.2	+4.77	+6.30	+1696.35

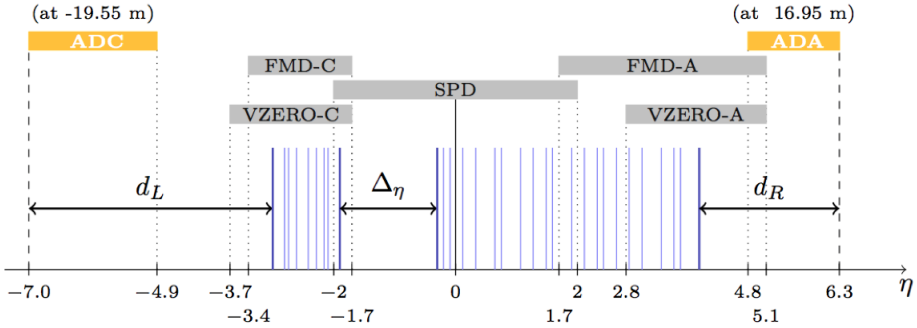

Fig. 9.3: Pseudorapidity coverage of the AD system. The diffractive trigger will be generated by AD, VZERO and SPD systems.

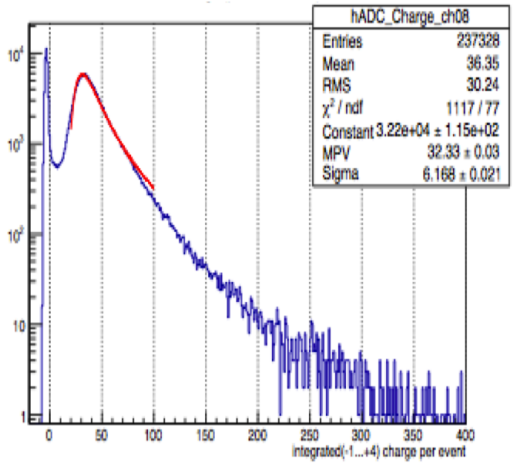

Fig. 9.4: Charge distribution of one channel of AD. The pedestal is well separated from the signal.

and the other at the IP2 (ALICE) side is called Arm2. This location allows the detection of neutral particles with $\eta > 8.4$. Photons, predominantly decay products of π^0, and neutrons are dominant particles arriving at the detectors. The detectors to be used in Run-II are essentially the same used in Run-I except some upgrades described below.

Each of the LHCf detectors consists of two small calorimeters with a double tower structure [93]. The dimensions of the towers transverse to the beam direction are 20 mm×20 mm and 40 mm×40 mm for Arm1 and 25 mm×25 mm and 32 mm×32 mm for Arm2. The longitudinal structure of the towers is a stack of 44 radiation lengths of Tungsten interleaved with 16 sampling scintillators. Plastic scintillators were used during Run-I but they have been replaced with Gd_2SiO_5 scintillators for Run-II [94] to make the calorimeters radiation harder. Four X-Y pairs of strip sensors, SciFi in Run-I [95] and GSO-bar bandles in Run-II [96] for Arm1 and Silicon strip sensors for Arm2 [97], are inserted to measure the lateral distribution of the show-

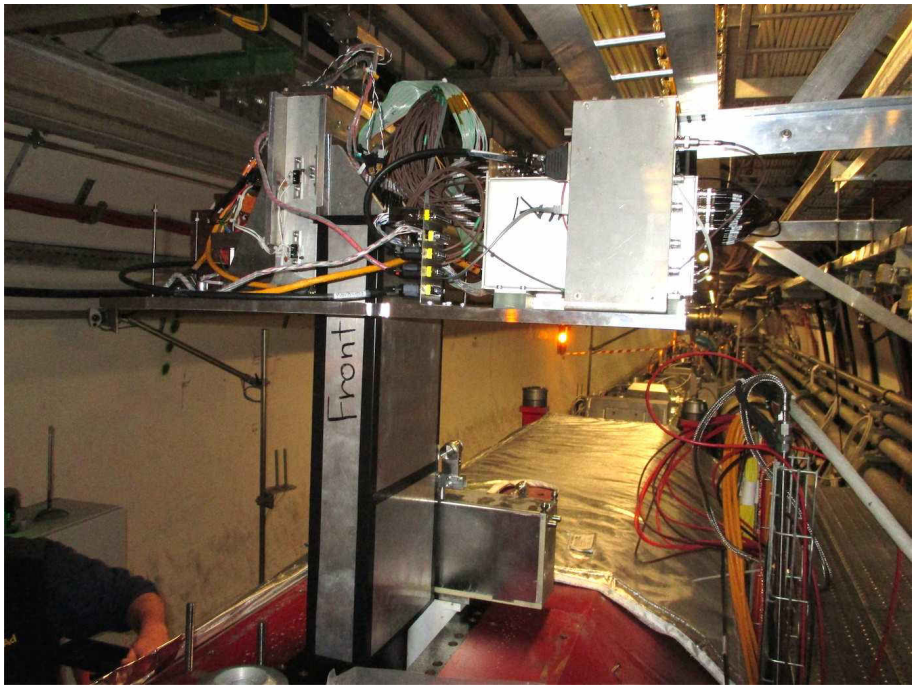

Fig. 9.1: LHCf Arm1 detector and its front-end electronics being installed into the TAN instrumentation slot.

ers. The longitudinal locations and the readout circuit of the Silicon strip sensors have also been updated in Run-II to optimize the energy determination ability using the Silicon sensors. Thanks to the double tower structure and position sensitivity, invariant mass of photon pairs hitting each calorimeter can be estimated. By selecting $\pi^0 \to \gamma\gamma$ events, momenta of π^0 are obtained [98] [99].

The performances of the LHCf detectors have been carefully studied by using data from SPS beam test and LHC Run-I, as well as through detailed MC simulations, and are summarized in [100] [101] [102].

References

[1] A. Breskin, R. Voss ed., "The CERN Large Hadron Collider: Accelerator and Experiments", JINST 3 (2008) S08001-S08007.

[2] ATLAS Collaboration, "The ATLAS Experiment at the CERN Large Hadron Collider", JINST 3 (2008) S08003.

[3] F. Anghinolfi et al., "Hadron beam test of a scintillating fibre tracker system for elastic scattering and luminosity measurement in ATLAS", JINST 2 (2007) P07004.

[4] S. Ask et al., "Luminosity measurement at ATLAS: Development, construction and test of scintillating fibre prototype detectors", Nucl. Instrum. Meth. **A 568** (2006) 588.

[5] P. Barrillon et al., "PMF: The front end electronic of the ALFA detector", Nucl. Instrum. Meth. **A 623** (2010) 463.

[6] S. Blin, P. Barrillon, Ch. de La Taille, "MAROC, a generic photomultiplier readout chip", IEEE Nucl. Sci. Symp .Conf. Rec. (2010) 1690-1693.

[7] ATLAS Collaboration, "Measurement of the total cross section from elastic scattering in pp collisions at $\sqrt{s} = 7$ TeV with the ATLAS detector", accepted by Nucl. Phys. B.,

arXiv:1408.5778, CERN-PH-EP-2014-177.

[8] TOTEM Collaboration, "Technical Design Report", CERN-LHCC-2004-002; addendum CERN-LHCC-2004-020.

[9] TOTEM Collaboration, "The TOTEM Experiment at the CERN Large Hadron Collider", JINST 3 (2008) S08007.

[10] TOTEM Collaboration, "TOTEM Upgrade Proposal", CERN-LHCC-2013-009 / LHCC-P-007.

[11] J. Baechler and D. Pfeiffer, "Engineering Change Request: TOTEM Consolidation Project", LHC-XRP-EC-0010, EDMS 1314925.

[12] M. Deile et al., "Engineering Change Request: TOTEM Upgrade Project", LHC-XRP-EC-0011, EDMS 1361537.

[13] TOTEM Collaboration, "Timing Measurements in the Vertical Roman Pots of the TOTEM Experiment, Technical Design Report", CERN-LHCC-2014-020; addendum CERN-LHCC-2014-024.

[14] M.G.Albrow *et al.*, Forward physics with rapidity gaps at the LHC, J. Inst. **4** P10001 (2009) and *LHCC-G-124*

[15] M.G.Albrow, P. Collins and A Penzo, Int. J. Mod. Phys. A **29** 1446018 (2014).

[16] The CMS Collaboration, CMS PAPER FSQ-12-026, arXiv:1405.0722 [hep-ex].

[17] C.J. Morningstar and M. Peardon, Phys. Rev. D **60** 034509 (1999).

[18] C-F. Qiao and L. Tang, Phys. Rev. Lett. **113** 221601(2014) and references therein.

[19] V.P.Goncalves and M.V.T.Machado, Eur.Phys.J **C56** 33 (2008).

[20] L.Motyka and G.Watt, Phys. Rev. **D78**:014023 (2008).

[21] CMS and TOTEM Collaborations, "Technical Design Report for CMS-TOTEM Precision Proton Spectrometer, CERN-LHCC-2014-021.

[22] F. Sauli, Nucl. Instrum. Methods A 386, 531 (1997).

[23] G. Ruggiero et al., "Planar edgeless silicon detectors for the TOTEM experiment", IEEE Trans. Nucl. Sci. 52 (2005) 1899
G. Ruggiero et al., Final size planar edgeless silicon detectors for the TOTEM experiment, Nucl. Instrum. Meth. A 563 (2006) 41
E Alagoz et al., "Performance of almost edgeless silicon detectors in CTS and 3D-planar technologies", 2013 JINST 8 P06009.

[24] F. Carra, "Choice of material for TCTP ferrite and support", LHC Collimation Working Group meeting 159, 22 April 2013,
`https://indico.cern.ch/conferenceDisplay.py?confId=246742`

[25] M.G. Albrow et al., "Quartz Cherenkov Counters for Fast Timing: QUARTIC", JINST 7 (2012) P10027.

[26] M. Osipenko *et al.*, "Comparison of Fast Amplifiers for Diamond Detectors", arXiv:1310.1000 (2013).

[27] F. Anghinolfi *et al.*, "NINO: an ultra-fast and low-power front-end amplifier/discriminator ASIC designed for the multigap resistive plate chamber", Nucl. Inst. and Meth.**A** 533 (2004) 183-187.

[28] H. Grabas, "Developing Picosecond Time of Flight detectors", PhD Thesis - Université Paris Sud - (2013).

[29] N. Cartiglia *et al.*, "Performance of Ultra-Fast Silicon Detectors", arXiv:1312.1080 (2013).

[30] J. Pietraszko,L. Fabbietti, W. Koenig, M. Weber, NIM **A 618** (2010) 121-123

[31] Cividec Instrumentation: http://www.cividec.at

[32] M. Bousonville and J. Rausch, "Universal picosecond timing system for the Facility for Antiproton and Ion Research", Phys. Rev. ST Accel. Beams **12** (2009) 042801.

[33] P. Moritz and B. Zipfel, "Recent Progress on the Technical Realization of the Bunch Phase Timing System BuTiS", IPAC-2011-MOPC145 Conf.Proc. C110904 (2011) 418-420.

[34] Thorlabs, Inc.: www.thorlabs.com . PRO8000 platform: http://www.thorlabs.com/newgrouppage9.cfm?objectgroup_id=895 .

[35] JDS Uniphase Corporation: www.jdsu.com . Multiple Application Platform (MAP-200) http://www.jdsu.com/en-us/test-and-measurement/products/a-z-product-list/Pages/map.aspx .

[36] K. Piotrzkowski and U. Schneekloth, ZEUS collab. meeting, march 1994, DESY, Hamburg.
B. Salvant, presentation at the 22nd LEB meeting, Sep. 10, 2012.
http://indico.cern.ch/conferenceDisplay.py?confId=204787
B. Salvant, presentation at 17th LTEX meeting, March 21, 2013.
https://indico.cern.ch/event/233129/material/slides/1?contribId=0

[37] "Installation of Physics Debris Absorbers (TCL) on both sides of IP1 and IP5 in front of Q6 Quadrupole", LHC-LJ-EC-0040, EDMS 1357736.

[38] ATLAS Collaboration, "Letter of Intent for the Phase-I Upgrade of the ATLAS Experiment", CERN-LHCC-2011-012 ; LHCC-I-020.

[39] J. Baechler, D. Druzhkin, "Design and production of a cylindrical Roman Pot for LHC", EDMS note in preparation.

[40] J. Baechler et al., "Measurement of thin window deflection under variable air pressure exposure",EDMS note in preparation.

[41] J. Baechler et al., "Leak test of the new cylindrical Roman Pot with thin window", EDMS note in preparation.

[42] F. Nemes: "Geant4 simulations for the TOTEM upgrade program", CERN-TOTEM-NOTE-2013-002.

[43] M. Deile et al., "Beam Coupling Impedance Measurement and Mitigation for a TOTEM Roman Pot", Proceedings of EPAC08, arXiv:0806.4974 .

[44] N. Minafra, "RF Characterization of the New TOTEM Roman Pot", CERN-TOTEM-NOTE-2013-003.

[45] P. Baudrenghien et al., "The LHC RF System – Experience with beam operation", CERN-ATS-2011-048.

[46] E. Chapochnikova, "First measurements of longitudinal impedance and single-bunch effects in the LHC",
https://www.cern.ch/emetral/ICEsection/2010/Meeting_01-09-10/Longitudinal%20impedance.pptx

[47] E. Metral, "Procedures for frequency and time domain EM simulations in asymmetric structures",
http://sps-impedance.web.cern.ch/sps-impedance/documents/ProceduresForFrequencyAndTimeDomainEMSimulationsInAsymmetricStructures_EM.pdf

[48] E. Metral, "Pushing the limits: beam", Chamonix 2011 Workshop on LHC Performance,

http://indico.cern.ch/getFile.py/access?contribId=14&sessionId=6&resId=0&materialId=paper&confId=103957

[49] N. Minafra, "RF Measurement of the New TOTEM Roman Pot", in preparation.

[50] F. Carra, "Choice of material for TCTP ferrite and support", LHC Collimation Working Group meeting 159, 22 April 2013, https://indico.cern.ch/conferenceDisplay.py?confId=246742

[51] G. Cattenoz, "Vacuum degassing test report of TT2-111R ferrite after bake-out", EDMS 1287626.

[52] S. Redaelli: Plans for collimation upgrade of IR1 and IR5 in LS1, 13th LTEX meeting, 11.10.2012, https://indico.cern.ch/conferenceDisplay.py?confId=211226

[53] M.G. Albrow et al., "The FP420 R&D Project: Higgs and New Physics with forward protons at LHC", JINST 4 (2009) T10001.

[54] L. Bonnet, J. Liao and K. Piotrzkowski, "Study on GasToF: A 10 ps resolution timing detector", NIM A762 (2014) 77..

[55] M.G.Albrow, "Fast timing detectors for leading protons at LHC: QUARTIC", Proc. Workshop on Picosecond Photon Sensors for Physics and Medical Applications, Clermont-Ferrand, March 2014 (to be published in Acta Physica Polonica).

[56] G. Chiodini, "Timing Diamond Detector for MIP", Workshop on Picosecond Photon Sensors for Physics and Medical Applications, Clermont-Ferrand, March 2014.

[57] M. Ciobanu et al., "In-beam diamond start detectors", IEEE Trans. Nucl. Sci. 58 (2011) 2073.

[58] N. Cartiglia et al., "Timing capabilities of Ultra-Fast Silicon Detector", Workshop on Picosecond Photon Sensors for Physics and Medical Applications, Clermont-Ferrand, March 2014

[59] CMS Technical Design Report for the Phase 1 Upgrade of the Hadron Calorimeter, Technical Report CERN-LHCC-2012-015. CMS-TDR-010, CERN, Geneva, (Sep, 2012).

[60] M. Mazzillo *et al.*, IEEE Nucl. Sci. Symposium NI-187 p.391.

[61] A. Ronzhin *et al.*, Nucl. Inst. Methods A **616** (2010) p.38.

[62] J. Va'vra *et al.*, Nucl. Inst. Methods A **606** (2009) p.404

[63] Specialty Glass Products, 2885 Terwood Rd., Willow Grove, PA 19090, USA.

[64] S. Gundacker et al., "Time of flight positron emission tomography towards 100 ps resolution with L(Y)SO: an experimental and theoretical analysis", JINST 8 (2013) P07014.

[65] ATLAS Insertable B-Layer Technical Design Report, ATLAS IBL Collaboration, CERN-LHCC-2010-013, ATLAS-TDR-19, 15 September 2010 (2010).

[66] S.I. Parker et al., "3D - A proposed new architecture for solid-state radiation detectors", Nucl. Instr. and Meth. A 395 (1997) 328.

[67] C.J. Kenney et al., "Results From 3-D Silicon Sensors With Wall Electrodes: Near-Cell-Edge Sensitivity Measurements as a Preview of Active-Edge Sensors", IEEE Trans. Nucl. Sci. 48 (2001) 2405.

[68] H.Chr. Kästli, "Frontend electronics development for the CMS pixel detector upgrade", Nucl. Instr. and Meth. A 731 (2013) 88.

[69] CMS Technical Design Report for the Pixel Detector Upgrade, CMS Collaboration, CERN-LHCC-2012-016; CMS-TDR-11, 7 September 2012 (2012).

[70] J. Troska *et al.*, "Prototype pixel optohybrid for the CMS phase 1 upgraded pixel detector",

JINST 7 (2012) C01113.

[71] L. Feld *et al.*, “Development of a DC-DC conversion powering scheme for the CMS Phase-1 pixel upgrade", JINST 9 (2014) C01048.

[72] A. Zoboli *et al.*, “Double-Sided, Double-Type-Column 3-D Detectors: Design, Fabrication, and Technology Evaluation", IEEE Trans. Nucl. Sci. 55 (2008) 2775.

[73] G. Pellegrini *et al.*, “First double-sided 3-D detectors fabricated at CNM-IMB", Nucl. Instr. and Meth. A 592 (2008) 38.

[74] C. Da Viá *et al.*, “3D silicon sensors: Design, large area production and quality assurance for the ATLAS IBL pixel detector upgrade", Nucl. Instr. and Meth. A 694 (2012) 321.

[75] M. Povoli *et al.*, “Slim edges in double-sided silicon 3D detectors", JINST 7 (2012) C01015.

[76] AFP Collaboration (ATLAS Collaboration), “The ATLAS Forward Proton Detector, Technical Design Report", to be published.

[77] IBL Community (ATLAS Collaboration), "ATLAS Insertable B-Layer, Technical Design Report", CERN-LHCC-2010-013, ATLAS TDR 19, `https://indico.cern.ch/event/234328/session/0/contribution/15/material/slides/1.pdf`

[78] M. Barbero *et al.* (ATLAS FE-I4 Collaboration), “FE-I4 ATLAS Pixel Chip design”, Proceedings of Science, PoS027, VERTEX 2009, Veluwe, The Netherlands, 13-18 September 2009.

[79] , Photonis Corporation, `www.photonis.com`

[80] M. Rijssenbeek (AFP Collaboration), "ATLAS Forward Proton Detectors: Time-of-Flight Electronics", Acta Phys. Pol. B, Proc. Suppl. 7-4 2014.

[81] “Workshop on Picosecond Photon Sensors for Physics and Medical Applications”, Clermont-Ferrand, 12-14 March 2014

[82] J.F. Genat, “Signal Processing for Fast Photo-detectors”, “Workshop on Picosecond Photon Sensors for Physics and Medical Applications”, Clermont-Ferrand, 12-14 March 2014

[83] F. Anghinolfi, P. Jarron, F. Krummenacher, E. Usenko, and M.C.S. Williams “NINO: An Ultrafast Low-Power Front-End Amplifier Discriminator for the Time-of-Flight Detector in the ALICE Experiment", IEEE Trans. Nucl. Sci. 51 (2004) 1974-8

[84] J. Pinfold, “Plans for a Picosecond HPTDC”, “Workshop on Picosecond Photon Sensors for Physics and Medical Applications”, Clermont-Ferrand, 12-14 March 2014,

[85] `http://www.picmg.org/openstandards/advancedtca/`

[86] Missing LHCb ref

[87] Missing LHCb ref

[88] M.Bombara et al ALICE-INT-2010-014 version 1.0

[89] ALICE Collab. , (B. Abelev et al.), arXiv: 1208.4968, CERN-PH-EP-2012-138

[90] C. Royon, arXiv:1008.3207 hep-ex, 18th International Workshop on Deep Inelastic Scattering and Related Subjects (DIS 2010), Florence Italy, 19-23 Apr. 2010. M.M. Obertino, (on behalf of CMS Collaboration), Nuovo Cimento C32 (2009) 119.

[91] Y. Zoccarato, et al, Nucl. Instrum. Meth. A626-627(2011)90-96.

[92] LHCf Technical Design Report, CERN-LHCC-2006-004.

[93] O. Adriani *et al.*, *JINST* **3**, S08006 (2008).

[94] K.Kawade *et al.*, *JINST* **6**, T09004 (2011).

[95] M. Mizuishi *et al.*, *J. Phys. Soc. Jpn* **78**, Suppl. A, 173 (2009).

[96] T.Suzuki *et al.*, *JINST* **8**, T01007 (2013).
[97] O. Adriani *et al.*, *JINST* **5**, P01012 (2010).
[98] H.Menjo *et al.*, *Astropart. Phys.* **34**, 513-520 (2011).
[99] O.Adriani *et al.*, *Phys. Rev. D* **86**, 092001 (2012).
[100] T. Mase *et al.*, *NIM* **A671**,129 (2012).
[101] K.Kawade *et al.*, *JINST* **9**, P03016 (2014).
[102] O. Adriani *et al.*, *IJMPA* **28**, 1330036 (2013).

Summary and Conclusion

This yellow report presents a summary of our current understanding in the field of high-energy forward particles physics and indicates a path for future studies.

Forward physics in the next few years has the potential to provide strong new contributions to the understanding of perturbative and non perturbative QCD, to be instrumental in the understanding of processes involving forward jets, and to open a new window on Beyond Standard Model searches.

The activities that have lead to this document have lasted about 18 months, with regular meetings at CERN and in several countries. These meetings have been characterized by a strong participation from many experiments at LHC and in cosmic rays and from the theory community, bringing together the experts working in different fields and theory divisions.

High cross studies, mostly centered around the physics of diffractive processes and particle multiplicities, will be carried out first while central exclusive production, with its unique capabilities of studying events completely contained in the detector, and saturation processes require more luminosity.

The forward physics program, as outlined in the report, relies strongly on new detectors added to current LHC experiments to gain access to part of the final state phase space currently not reachable. These new detectors, combined with both dedicated and standard LHC running conditions will enable in the next few years to explore the physics program here detailed.

Acknowledgements

We are very grateful to the LPCC for all their help in creating an excellent scientific environment while organizing the Forward Working Group meetings at CERN. V.A. Khoze thanks the Leverhulme Trust for an emeritus fellowship. This work was also supported in part by the Polish National Science Centre grant UMO-2012/05/B/ST2/02480.